*Physics of Atomic Nuclei, Vol. 65, No. 7, 2002, pp. 1153–1154. Translated from Yadernaya Fizika, Vol. 65, No. 7, 2002, pp. 1187–1188.
Original Russian Text Copyright © 2002 by the Editorial Board.*

90th ANNIVERSARY OF I.I. GUREVICH'S BIRTHDAY

Isai Isidorovich Gurevich (July 13, 1912–December 6, 1992)

Nearly ten years has passed since the death of I.I. Gurevich, a corresponding member of the Russian Academy of Sciences, an eminent physicist, who had a broad range of scientific interests and a profound understanding of the essence of physical phenomena that he studied. Gurevich mastered equally well the subtleties of physics experiments and of their theoretical interpretation. He was the author of more than 100 scientific studies, and some of them became classic even during his life.

Gurevich was born on July 13, 1912, in Riga. In 1934, he graduated from Leningrad State University. In the same year, he performed his first studies, which were devoted to neutron physics. Of greatest interest among the studies of this series were those that explored the structure of levels in heavy nuclei and which culminated in formulating the hypothesis of phase transitions in nuclear matter. This hypothesis was fully confirmed in the modern superconducting model of nuclear matter. During the same early period of his scientific activities, Gurevich was able to discover the effect of the cosmic-ray-induced spallation of nuclei. As a matter of fact, this was the first study aimed at exploring the strong interaction of ultrahigh-energy cosmic-ray particles.

From 1941 to 1948, Gurevich was involved in the work on the physics of nuclear reactors. His studies, performed together with Ya.B. Zeldovich, I.Ya. Pomeranchuk, and Yu.B. Khariton, resulted in the formulation of a qualitative theory of nuclear reactors. Of particularly great importance were his investigations into the theory of exponential experiments with thermal neutrons and the theory that he developed, together with Pomeranchuk, for the phenomenon of resonance absorption in uranium–moderator heterogeneous systems. It was precisely this study that validated the possibility of creating natural-uranium reactors. Gurevich took an active part in the calculations of critical dimensions of the first soviet nuclear reactor put into operation by I.V. Kurchatov in 1946.

The approximate method for solving integral equations that was developed by Gurevich formed the basis of his doctoral dissertation that he defended in 1944.

Beginning in 1952, Gurevich performed studies in nuclear, elementary-particle, and high-energy physics, as well as in the physics of weak interaction.

By analyzing experimental data on nuclear resonances in 1956 and 1957, Gurevich, together with M.I. Pevzner, showed for the first time that the distribution of nuclear levels around a mean value is not chaotic—that is, there is a repulsion between nuclear levels, which is manifested in a low probability of very closely spaced levels. This study initiated a whole series of subsequent experimental and theoretical investigations.

In connection with the discovery of parity conservation in weak interaction, Gurevich and his colleagues performed investigations spanning the period between 1958 and 1967 that were aimed at verifying the $V-A$ theory of weak interactions by the angular asymmetry of electrons originating from muon decays. These studies yielded the asymmetry-coefficient value of $a = 0.325 \pm 0.005$, which was the best one in the world scientific literature and which was in excellent agreement with theoretical predictions.

In 1964, Gurevich, together with V.M. Galitsky, investigated theoretically coherent effects in bremsstrahlung from ultrarelativistic electrons. They discovered the new effect of medium-induced brems-

1063-7788/02/6507-1153$22.00 © 2002 MAIK "Nauka/Interperiodica"

strahlung suppression due to photon absorption in matter.

From 1968, Gurevich gave much attention to the method developed in his laboratory for studying matter with the aid of positively charged muons. By applying this method, which is based on measuring the precession and relaxation of the spin of polarized muons, Gurevich and his colleagues were able to discover the two-frequency precession of a hydrogen-like muonium atom (discovery certificate) and the subbarrier (quantum) diffusion of muons and to measure intrinsic magnetic fields in magnets and superconductors. The muonic method for studying matter was recognized worldwide, along with other classic methods in solid-state physics, such as neutron diffraction, Mössbauer effect, and nuclear magnetic resonance. For work on evolving the new method for studying matter with the aid of muons, the USSR Academy of Sciences awarded Gurevich a Kurchatov Gold Medal of 1980.

The development of nuclear physics is impossible without creating complex experimental facilities and without introducing methodological novelties. Gurevich devoted much time to this facet of scientific activities. Among his methodological achievements, of special note is the creation of a facility for generating strong pulsed magnetic fields, whose strength in a volume of 1 l may reach 300 kOe within a few milliseconds. Such pulsed magnetic fields are of great value both for elementary-particle and for solid-state physics. In particular, a series of experiments aimed at searches for the Dirac monopole and an investigation of the properties of superconducting materials in high-strength magnetic fields were performed with the aid of pulsed magnetic fields.

In 1968, Gurevich was elected to corresponding membership in the USSR Academy of Sciences. He gave much of his time to teaching young scientists. His disciples included Academician L.M. Barkov; B.A. Nikolsky, corresponding member of the Russian Academy of Sciences; and doctors and candidates of sciences. Since 1946, Gurevich had been a professor at the Department of Nuclear Physics at the Moscow Engineering Physics Institute. His lecture courses, highly pedagogical in form, always covered the most topical problems of contemporary nuclear physics. The monograph of Gurevich and L.V. Tarasov *The Physics of Low-Energy Neutrons*, which appeared in 1965 (and which was shortly afterward translated into English), has been so far of great scientific and pedagogical value.

For active and seminal research activity, Gurevich was decorated with two Red Banner of Labor and two Badge of Honor orders. In 1949, he was awarded a USSR State Prize.

The blessed memory of Isai Isidorovich Gurevich, an outstanding physicist and a charming personality, will always be cherished by his numerous disciples and by all those who had the privilege of experiencing his beneficial influence. His scientific legacy will undoubtedly be studied by many generations of physicists.

Editorial Board

Physics of Atomic Nuclei, Vol. 65, No. 7, 2002, pp. 1155–1172. Translated from Yadernaya Fizika, Vol. 65, No. 7, 2002, pp. 1189–1205.
Original Russian Text Copyright © 2002 by Mukhin, Patarakin, Tikhonov.

90th ANNIVERSARY OF I.I. GUREVICH'S BIRTHDAY

Pion, Pion–Pion, and Pion–Nucleus Interactions

K. N. Mukhin, O. O. Patarakin, and V. N. Tikhonov

Russian Research Centre Kurchatov Institute, pl. Kurchatova 1, Moscow, 123182 Russia

Received October 16, 2001

Abstract—This survey is devoted to describing the early studies of I.I. Gurevich on pion physics that were performed by the photoemulsion method and the studies of the pion–pion interaction that were made by his colleagues on the basis of the hydrogen-bubble-chamber and the magnetic-spectrometer method (as well as on the basis of the photoemulsion method). Two approaches—an extrapolation of experimental data from the physical region to the pion pole and a theoretical calculation based on the Roy integral equations—are used to deduce information about the pion–pion interaction. The first results obtained for pion–pion and pion–nucleus interactions in the experiments that are being currently performed in Brookhaven and at CERN ($\pi\pi$ interaction) and at TRIUMF (Canada) and in Brookhaven (pion–nucleus interaction) are presented, along with the existing theoretical concepts in these realms of physics.

One of the authors of the present article (K.N. Mukhin) had had a privilege to associate with I.I. Gurevich (further I.I.) for about 45 years, not only at the laboratory and at the seminars that he headed but also during our mutual pedagogical activities at the Moscow Engineering Physics Institute (we delivered lectures in neighboring rooms and went home together, visiting bookshops on the way), at his home (editorship work), and even during vacations. Of course, physics was one of the permanent topics of our association. I.I. loved any kind of physics, including so-called general physics, nuclear physics, elementary-particle physics, and astrophysics. But he was especially fond of nuclear physics, nourishing tenderness, in particular, to the simplest version of the nuclear reactor—namely, the uranium–graphite reactor employing natural uranium. He used to say, "Only imagine what a wonderful combination made it a physical reality. If the cross section for ^{235}U fission induced by thermal neutrons and the number of secondary neutrons formed had been slightly smaller and if the cross section for resonance-neutron capture by ^{238}U had been slightly larger, the success could not have been achieved."

It is no wonder that the neutron was of course his first love in elementary-particle physics. But when the problem was by and large solved (owing, in particular, to a very serious contribution of I.I.), there appeared his second love—the pion (after that, the muon; then, the monopole; and, finally, the neutrino). In the present article, we would like to tell how this second love of I.I. began, how he could inspire this feeling in the souls of some of his collaborators, and how investigation with I.I. into the physics of pions and of pion–nucleus interaction made its first steps; we will also list the results at which these lines of investigation arrived today.

Apart from describing our studies, we will discuss, in the last sections of this article, the currently prevailing situation in the theoretical and experimental physics of the pion–pion interaction—in particular, the first results of unique experiments that are being presently performed in Brookhaven and at CERN. We will also give an account of intriguing data from the latest experiments that studied pion-production processes in pion–nucleus interactions.

1. STUDIES OF I.I. GUREVICH AND HIS COLLEAGUES ON PION PHYSICS

As is well known, pions, which were predicted by Yukawa as quanta mediating strong interaction, were discovered in the composition of cosmic rays in 1947 by the photoemulsion method. Both these circumstances (the very fact of this discovery and the method by which it was made) strongly affected the attitude of I.I. to the pion as one of his favorite particles. As soon as the synchrocyclotron of the Joint Institute for Nuclear Research was commissioned at Dubna, I.I. headed a group of his collaborators who began conducting experiments devoted to pion physics by using precisely the photoemulsion method.

I.I. had been acquainted with the photoemulsion method for studying the properties of elementary particles since 1935, when, together with A.P. Zhdanov, he tried to improve this method, which was first developed by L. Mysovskii and P. Chizhov in 1927 [1]. At the time that we are now describing (the late

1940s and the early 1950s), I.I. continued intensively developing this procedure, organizing, in his division, a photoemulsion group headed by D.M. Samoilovich, who evolved and fabricated special thick-layered nuclear photographic plates that were capable to detect the tracks of singly charged elementary particles. In the same years, another collaborator of I.I. (V.V. Alpers) developed the emulsion-chamber procedure (it employs stacks of emulsion layers without glass, where, owing to the common coordinate grid, it is possible to trace the tracks of particles that go over from one layer to another) [2], which is more elaborate than that based on photographic plates. It is precisely these plates and chambers that were used in the pion-physics studies that were performed by I.I. and his colleagues and which are described below. (For purely technical reasons, these studies were published much later than they had been performed or have not been published altogether.)

One of the first studies of I.I. and his colleagues was devoted to determining the pion mass by the photoemulsion method that involves counting the developed grains on the tracks of pions (π) and protons (p). Negative pions were produced in the interaction of 560-MeV alpha particles with lead nuclei in a special device installed in the synchrocyclotron chamber and, after being deflected by the magnetic field of the accelerator, were incident on photographic plates at sliding angles. The geometry of the experiment was chosen in such a way that slow negative pions of energy in the range 1–30 MeV hit the photographic plates.

Horizontal tracks situated rather far off the emulsion surface and the glass were selected for viewing and measurements. Grains were counted at a 2025 magnification by using a dedicated procedure for analyzing the ends of the tracks, where the density of the grains was so high that they formed so-called conglomerations. The counting yielded the dependences $N(R)$, where N is the number of the grains and R is the residual range (that is, the particle range measured from the point of its stopping). From the theory of the method, it follows that $N = R\varphi(R/m)$; that is, the pion mass can be estimated by comparing $N_\pi(R_\pi)$ and $N_p(R_p)$ at specific values of R_π and R_p (protons, whose mass is known, served as a reference).

For the negative-pion mass, the processing of these data yielded the value

$$m_{\pi^-} = (273.6 \pm 2.9)m_e, \tag{1}$$

which was the closest to the modern value ($\sim$273.1m_e) among all of the values obtained at that time in other laboratories worldwide. Unfortunately, we were unable to publish this study, and the traces of it remain only in the form of a report in the archives of our institute [3].

Within the same period (1950–1952), I.I. and his collaborators performed investigations in which they exposed nuclear photographic plates and emulsion chambers to cosmic rays. The irradiation of photographic materials was implemented in balloon-borne experiments (the balloons used were launched in Dolgoprudnyĭ) performed by physicists from the Research Institute of Physics (Moscow State University), who were directly involved in cosmic-ray studies. Our efforts were aimed at discovering, in cosmic rays, particles of mass that would have intermediate values between the pion and the proton (this was a popular topic of investigation at that time), but our attempts proved to be futile [4, 5].

In 1952 and 1553, I.I. relaunched their investigations at the synchocyclotron, where they explored the features of the production of slow charged pions on photoemulsion nuclei exposed to 460-MeV protons and to neutrons of 400-MeV effective energy [6]. Two photoemulsion chambers, each consisting of 20 photoemulsion layers and having a total thickness of 6 mm, were used in that study. One of the chambers was exposed to an extracted beam of protons, while the other was exposed to a neutron beam.

The use of the emulsion-chamber procedure enabled us to trace the entire path of charged pions from the point of their ionization stopping to the production vertex. This made it possible to observe a large number of stars[1] associated with the production of charged pions and to construct angular and energy distributions of product pions in the region of low energies.

Inspecting the resulting curves, one can clearly see that the energy spectra of negative and positive pions are shifted with respect to each other by $\Delta \approx 15$ MeV. This shift is naturally explained by the effect of the Coulomb barrier, whose mean height for photoemulsion nuclei with respect to singly charged particles is 7.5 MeV. In addition, the cross sections for the production of slow ($0 < E < 40$ MeV) charged pions were estimated at

$$\begin{gathered}\sigma_{\pi^+} = (2.9 \pm 0.9) \times 10^{-27}\ \mathrm{cm}^2, \qquad (2)\\ \sigma_{\pi^-} = (1.3 \pm 0.5) \times 10^{-27}\ \mathrm{cm}^2,\\ \sigma_{\pi^+ + \pi^-} = (4.2 \pm 1.4) \times 10^{-27}\ \mathrm{cm}^2,\end{gathered}$$

and the ratio of the numbers of product positive and negative pions was found to be

$$\pi^+/\pi^- = 2.5 \pm 0.5. \tag{3}$$

---

[1] By a star, we mean a microphotograph of a particle–nucleus interaction resulting in the formation of starlike rays of tracks generated by charged particles emitted from the nucleus involved.

Stars that are associated with the production of unlikely charged pions as contrasted against mesonless stars are also of interest in themselves from the point of view of the theory of an intranuclear cascade. In particular, a comparison of these two types of stars revealed a considerable anisotropy of slow particles in pion-production stars. This suggests the presence of a large number of slow cascade particles, especially in mesonic stars.[2)]

Also, the mean energy $\bar{E}$ deposited in a star was calculated for mesonic stars and was proved to be approximately equal to the incident-nucleon energy $\bar{E}_N = (460 + 400)/2 = 430$ MeV; that is,

$$\bar{E}_{\text{star}} = 2(\bar{E}_{ch} + Q\bar{N}_{ch}) + E_\pi \tag{4}$$
$$= 2(104 + 9 \cdot 4) + 160 = 440\ MeV \simeq \bar{E}_N,$$

where $\bar{E}_{ch}$ is the mean total energy of charged particles outgoing from a star, Q is the nucleon binding energy in the nucleus involved, N_{ch} is the mean number of charged particles in the nucleus, E_π is the total energy of the pion, and the factor of 2 takes into account the formation of neutrons in a star.

In 1954 and in 1955, investigation of the production of slow charged pions on photoemulsion nuclei was continued [7]. That time, use was made of a chamber formed by 45 layers of more sensitive NIKFI photoemulsion, its total thickness being 15 mm. The chamber was exposed to a proton beam of energy $E = 660 \pm 10$ MeV. A greater thickness of the emulsion chamber and a higher sensitivity of the emulsion used made it possible to analyze the pattern of slow-pion production on photoemulsion nuclei. This investigation resulted in obtaining the angular and energy distributions of product positive and negative pions. From the angular-distribution pattern, it followed that the pion-production cross section depends only slightly on the pion emission angle with respect to the axis of the incident-particle beam. What was observed for the energy distributions of product pions confirmed the distinction between the spectra of positively and negatively charged pions that had been observed at a lower proton energy in [6], although this distinction became less pronounced. The ratio of the numbers of the product positive and negative pions proved to be

$$\pi^+/\pi^- = 2.3 \pm 0.5, \tag{5}$$

which, within the experimental errors, agrees with the previous result obtained at a proton energy of 460 MeV. The cross sections for the production of slow ($0 < E < 40$ MeV) pions were found to be

$$\sigma_{\pi^+} = (4.4 \pm 15) \times 10^{-27}\ \text{cm}^2, \tag{6}$$
$$\sigma_{\pi^-} = (2.8 \pm 1) \times 10^{-27}\ \text{cm}^2,$$
$$\sigma_{\pi^+ + \pi^-} = (7.2 \pm 1.8) \times 10^{-27}\ \text{cm}^2.$$

The experiments reported in [7] explored not only the properties of product charged pions but also the stars themselves. In particular, the angular and energy distributions were obtained for particles outgoing from stars of three types: those that are associated with the production of positively charged pions, those that are associated with the production of negatively charged pions, and those that are mesonless. In analyzing mesonic stars, the tracks of outgoing particles were traced up to the point of their stopping in the emulsion chamber or up to their escape from it. In the first case, the particle energy was determined on the basis of the curve $E = f(R)$, where R is the ionization particle range, while, in the second case, this was done by using curves representing the dependence of the energy on the grain density, $E = f(dN/dR)$. Mesonless stars were found by tracing the tracks of primary protons from their entrance to the emulsion chamber up to stars caused by them.

As the result of this analysis, it was noticed that mesonless stars are characterized by a comparatively greater number of charged particles outgoing from them and by a greater amount of kinetic energy $\bar{E}_{ch}$ carried away by them, but this is quite natural for stars whose energy balance does not include expenditures for pion production. For mesonic stars associated with the production of negatively charged pions, a more copious generation of slow ($E < 100$ MeV) particles was found in relation to what was observed for positive-pion stars; this is naturally explained by the distinction between the changes in the charge of the nucleus in the two cases: in the case of proton-induced production, the nuclear charge does not change upon positive-pion generation, but it changes by $\Delta Z = 2$ upon negative-pion generation. The numbers of product fast ($E > 100$ MeV) particles are approximately identical in the two cases.

An investigation of the angular distribution of particles formed in stars revealed the presence of a forward anisotropy, which survives down to the lowest particle energies (although it became somewhat less pronounced in relation to the results that had been obtained in the previous study reported in [6]). For fast particles, the asymmetry remained at the same high level. Needless to say, it was verified that the anisotropy in question cannot be due to the motion of the nucleus as a discrete unit in that case as well.

Yet another result obtained in [7] refers to experimentally estimating the mean range of 660-MeV

[2)] A trivial verification shows that the anisotropy observed experimentally cannot be explained by the motion of the nucleus involved.

protons with respect to inelastic interactions. It was obtained by dividing the total length of the proton tracks studied there (4360 cm) by the number of inelastic interactions (123). This yielded the value

$$\lambda = 35.4 \pm 3.1 \text{ cm}, \quad (7)$$

which agrees well with the average of two calculated values (37.3 and 33.6 cm).

The experiments reported in [7] were the last pion-physics studies in which I.I. participated directly. After their completion, there was altogether a rather long-term pause in the work devoted to these realms, since there appeared a few new lines of investigation in the division headed by Gurevich. One of these (that in which the present authors were involved) was aimed primarily at developing bubble-chamber procedures employing pulsed magnetic fields [8–10] and semiautomated measuring devices for viewing and processing photographs taken at these (and other) chambers [11]. The created chambers were irradiated at the accelerators installed at the Laboratory of High Energies, Joint Institute for Nuclear Research (JINR, Dubna), and at the Institute of Theoretical and Experimental Physics (ITEP, Moscow). A propane chamber was exposed to a proton, a pion, and a kaon beam from the LHE accelerator, where investigations into the physics of protons [12], pions [13] (the first study on pion physics after a long-term pause), and kaons [14] (a continuation of searches for new particles) were performed. At the ITEP accelerator, a pion beam was created [15] and the efficiency of a xenon chamber supplemented with a pulsed magnetic field of a record-breaking strength of 70 kG and with a high-pressure (100 atm) gas hydrogen target [16] was proven.

Concurrently (from the early 1970s), a continually expanding group of I.I.'s associates who worked at chambers and measuring devices initiated a vast series of investigations into pion physics (including pion–pion interaction) [17–21] by using photographs kindly placed at their disposal by colleagues from ITEP [22].

As before, these new pion-physics studies (in the next section of the article, we will describe them in detail) were conducted in the division headed by I.I., but without his direct participation this time (he then cherished his third love, the muon!). Eventually, the appearance of new lines of investigation and of new interests led, in 1977, to the separation of I.I.'s division into three laboratories, including the Laboratory of Pion Interactions (LPI), which arose from our pion group and which embarked on continuing investigations into the pion–pion interaction, originally one of the main lines of LPI activities.[3] As a matter of fact, our work along these lines has been continued, with short pauses, up to the present moment [25–43]. By convention, it can be divided into two stages. At the first stage, we processed $\pi^{\pm}p \to \pi\pi N$ events recorded with the aid of the ITEP hydrogen bubble chamber, as well as with the aid of the photoemulsion method; at the second stage, we treated similar events recorded by the CHAOS facility at the TRIUMF accelerator in Canada. A comparison with other data is given in the review articles [30, 43] and in the monograph [33]. In the sections of this article that follow, we will describe those studies in detail and outline the current situation around the problem of the pion–pion interaction. To conclude this section, it would be worthwhile to indicate that the aforementioned separation of Gurevich's division into three laboratories was of a purely formal character—by this, we mean that, as a matter of fact, I.I. had continued to supervise the activities of all three of these until his death. At any rate, he always showed interest in and lent support to our pion-physics studies, which were conducted in close scientific contact with him.

2. INVESTIGATION OF THE PION–PION INTERACTION BY THE METHOD OF A HYDROGEN BUBBLE CHAMBER

2.1. Introductory Remarks

By the instant at which we embarked on our investigation into pion–pion interactions (1970), the following had been known. Since the pion is a quantum mediating strong interactions, the effect of scattering of one quantum on another was expected to be pronounced in hadron interactions—that is, the interaction of pions may significantly affect the mechanism of any reaction involving hadrons. It follows that information about pion–pion interactions is required for obtaining deeper insight into hadron physics. It was (and it has remained) impossible to obtain this information directly by studying the scattering of a pion on a pion. But one can consider the inverse problem: since the pion–pion interaction contributes significantly to the mechanisms of reactions featuring hadrons, an attempt can be made to extract, by means of a theoretical analysis, information about the pion–pion interaction from experimental data on such reactions. This was precisely the idea of all theoretical methods developed by that time for studying the pion–pion interaction [44–51].

---

[3] Later on, there appeared, at LPI, a second main line that consisted in the joint work with the Institute for Nuclear Research (INR, USSR Academy of Sciences, Moscow) and LHE on designing, manufacturing, and employing the AMPIR universal detector equipped with a superconducting radiation-transparent solenoid [23, 24].

In our investigations, we employed the method that was proposed by Goebel [44] and by Chew and Low [45] and which is based on the assumption that one-pion-exchange (OPE) processes play a dominant role in the mechanisms of the reactions being discussed. Under this assumption, the method makes it possible to obtain the cross sections for pion–pion scattering from $\pi N \to \pi\pi N$ cross sections, which are accessible to a direct measurement. The relationship between these two types of cross sections is given by the Chew–Low formula [45]

$$\sigma_{\pi\pi}(m_{\pi\pi}) = \lim_{t\to\mu^2}\left[\frac{\partial^2\sigma_{\pi\pi N}}{\partial t\partial m^2_{\pi\pi}}\frac{2\pi}{\alpha f^2}\frac{p^2(t-\mu^2)^2\mu^2}{tm_{\pi\pi}k}\right], \tag{8}$$

where α is a numerical factor that is equal to unity for the reactions $\pi^{\pm}p \to \pi^{\pm}\pi^0 p$ and to two for the reactions $\pi^{\pm}p \to \pi^{\pm}\pi^{+}n$, $f^2 = 0.08$ is the πN coupling constant, p_π is the incident-pion momentum, $k = (m^2_{\pi\pi}/4 - \mu^2)^{1/2}$ is the secondary-pion momentum in the dipion rest frame, $\mu = m_\pi$, and t is the 4-momentum transfer in μ^2 units. Within this approach, the features of the pion–pion interaction (cross sections, phase shifts, scattering length) can be obtained by fitting experimental results in the physical domain or by extrapolating them to the pion pole.

A remarkable feature peculiar to the Goebel–Chew–Low method is that it is possible in principle to obtain all phase shifts for pion–pion scattering at all values of the dipion mass $m_{\pi\pi}$, provided that use is made of various channels of the $\pi N \to \pi\pi N$ reactions with various signs of incoming and outgoing pions. Having such a possibility at our disposal, we were able to obtain, by using a single method within the same laboratory, self-consistent values of five phase shifts for pion–pion scattering in the elastic region, δ^0_0, δ^2_0, δ^1_1, δ^0_2, and δ^2_2, and of some other parameters of the pion–pion interaction for four charged channels ($\pi^-\pi^+$, $\pi^-\pi^0$, $\pi^+\pi^0$, and $\pi^+\pi^+$). We note that each of a few experimental studies that we know to have been performed prior to our investigation [52–55] reported information only about one of the properties of the pion–pion interaction (for example, δ^0_0 near the threshold [52] and the parameters of the ρ resonance [53, 54]). But later on (simultaneously with the commencement of our activities in these realms), there began to appear articles that reported on an investigation of the pion–pion interaction by a method similar to that which we adopted. In this connection, we would like to mention the studies of Colton *et al.* [56] and of Protopoppescu *et al.* [57], who showed that, for πN interactions, the cross sections and angular distributions found experimentally on the mass shell agree with those that were calculated by the Goebel–Chew–Low method, whence it follows that one-pion exchange makes a dominant contribution to the mechanism of such reactions. Between 1973 and 1979, the authors of [58–61] reported on investigations of the pion–pion interaction on the basis of high-statistics data samples; however, those authors explored predominantly the region of large dipion masses ($m_{\pi\pi} > 1$ GeV).

2.2. Description of the Procedure

As was indicated above, reactions of the $\pi^{\pm}p \to \pi\pi N$ type were studied by using data obtained by irradiating the 50-cm hydrogen bubble chamber installed at ITEP and placed in a magnetic field of strength 20 kG [22]. The chamber was photographed onto a 80-mm-wide photographic film by three photocameras. The films were viewed through projection devices of the Mikrofot type with the aim of selecting two-prong events characteristic of the reactions

$$\pi^-p \to \pi^-\pi^+n, \quad \pi^-p \to \pi^-\pi^0p, \tag{9}$$
$$\pi^+p \to \pi^+\pi^0p, \quad \text{and} \quad \pi^+p \to \pi^+\pi^+n,$$

and of the elastic-scattering processes

$$(\pi^-p \to \pi^-p)_{el} \quad \text{and} \quad (\pi^+p \to \pi^+p)_{el}, \tag{10}$$

which were used not only to investigate elastic scattering as such but also to perform a normalization.

In all, we viewed about 130 000 stereophotographs obtained in exposing the chamber to negative pions with a momentum of $p_{\pi^-} = 4.5$ GeV/c and about 84 000 stereophotographs obtained in exposing the chamber to positive pions with a momentum of $p_{\pi^+} = 3.05$ GeV/c and discovered on them, respectively, 19 000 and 18 000 two-prong events. These events were then measured by the method of mismatched points at a semiautomated facility of the stereocomparator type [11] and with a measuring microscope.

In order to reconstruct the precise spatial pattern of an event, it is sufficient to measure two different frames of the three that are taken; in order to achieve, however, the preassigned accuracy of reconstruction, this pair of frames was chosen from the three possible combinations (the first and the second, the first and the third, or the second and the third) according to a specific criterion.

The two-prong events selected in this way were processed on the basis of the ASP code [62], which reconstructs the geometry of an event; calculates the parameters of the track; and, with the aid of the χ^2 criterion, hypothetically associates events with one of the processes listed in (9) and (10). As an output, the code yielded the momenta and the direction cosines for all charged particles involved in the adopted hypothesis, as well as the degree of primary-track ionization (it is taken to be equal to unity) and the

Table 1

Process	Primary-pion momentum, GeV/c	Cross section, mb
$(\pi^- p \to \pi^- p)_{\rm el}$	4.5	6.21 ± 0.19
$(\pi^+ p \to \pi^+ p)_{\rm el}$	3.05	7.02 ± 0.23
$\pi^- p \to \pi^- \pi^+ n$	4.5	3.04 ± 0.20
$\pi^- p \to \pi^- \pi^0 p$	4.5	2.01 ± 0.16
$\pi^+ p \to \pi^+ \pi^0 p$	3.05	3.26 ± 0.24
$\pi^+ p \to \pi^+ \pi^+ n$	3.05	2.18 ± 0.16

predictions of the code for the degree of secondary-particle ionization (it is different for a proton and a pion of given momentum).

The correctness of identifying events was tested by measuring the degree of ionization, which was compared with that which was predicted by the above code. A mismatch implied that a given event can be associated with none of the types listed in (9) and (10), but that it additionally involves one or a few neutral pions [20, 28].

For each of the types listed in (9) and (10), a few thousand correctly identified events were obtained upon measuring and additionally viewing them for ionization. These events were then processed by using dedicated codes, whereby it was possible to deduce values of the invariant dipion mass $m_{\pi\pi}$, of the invariant variable t, of the cosines of the angles of divergence of the particles involved in the c.m. frame and in the dipion rest frame, and of other relevant variables. This information was sufficient for deriving all of the aforementioned features of the pion–pion interaction.

2.3. Results

The cross sections for the processes in (9) and (10) were the first results obtained by studying the above two-prong events. Of these cross sections, those for the processes in (10) were used for normalization purposes. In studying them, special attention was therefore given to introducing corrections for losses of events having short proton tracks (because of low momenta or because of the coincidence of their direction with that toward the photocameras used—for details, see [20]). Similar azimuthal corrections were also introduced for events of the reactions $\pi^\pm p \to \pi^\pm \pi^0 p$, which have proton tracks, but they were not required for reactions like $\pi^\pm p \to \pi^\pm \pi^+ n$, since the tracks of pions are much longer than the tracks of protons.

In calculating the cross sections, use was made of the optical theorem. The resulting cross-section values are quoted in Table 1.

The reactions $\pi^- p \to \pi^- \pi^+ n$ and $\pi^\pm p \to \pi^\pm \pi^0 p$ may proceed through resonance states formed by two pions or by a pion and a neutron—that is, through the production of ρ^0, ρ^+, ρ^-, f^0, g^-, g^0, and $\Delta^\pm$ resonances. The cross sections for the production of $\Delta^\pm$ resonances are rather modest at the energies considered here, but the reflections of these resonances affect the distribution of events with respect to the effective dipion mass $m_{\pi\pi}$. This point was taken into account by means of a dedicated calculation. By way of example, the effective-dipion-mass ($m_{\pi\pi}$) distribution of $\pi^- p \to \pi^- \pi^+ n$ events is shown in Fig. 1 with allowance for the contribution from the phase spaces of the ρ^0, f^0, and g^0 resonances and for the reflection of Δ resonances [32]. By investigating this distribution (and analogous distributions for other reactions), it was possible to deduce the parameters of identified dipion and Δ resonances and their cross sections (see Table 2).

In order to prepare the data in question for a partial-wave analysis, some cuts were imposed on them, including a cut on t—specifically, the cut $|t| \le 0.3$ (GeV/c)^2 for the reaction $\pi^- p \to \pi^- \pi^+ n$ and the cut $0.1 \le |t| \le 0.5$ (GeV/c)^2 for the reactions induced by incident positively charged pions. Upon imposing all the cuts, the remaining number of events was about 1100 to 3000 for the different reactions. This made it possible to perform a reliable partial-wave analysis in the dipion-mass range $320 \le m_{\pi\pi} \le 980$ MeV for the reaction $\pi^- p \to \pi^- \pi^+ n$ and in the pion-mass range $387 \le m_{\pi\pi} \le 1215$ MeV for the reactions $\pi^\pm p \to \pi^\pm \pi^0 p$ and $\pi^+ p \to \pi^+ \pi^+ n$.

The cross section $\sigma_{\pi\pi}$ for pion–pion scattering and the angular distributions of secondary pions formed the input data for the partial-wave analysis. According to Eq. (8), $\sigma_{\pi\pi}$ is obtained by extrapolating the differential cross section for the $\pi N \to \pi\pi N$ reactions to the pion pole. Usually, an extrapolation to the pion pole is constructed for the auxiliary function

$$F(t, m_{\pi\pi}) = \frac{\partial^2 \sigma}{\partial t \partial m_{\pi\pi}^2} \frac{2\pi p_\pi^2 (t - \mu^2)^2}{\alpha f^2 m_{\pi\pi} k}, \qquad (11)$$

where the notation is identical to that in Eq. (8). As a result, $\sigma_{\pi\pi}$ is obtained in the form

$$\sigma_{\pi\pi}(m_{\pi\pi}) = \lim_{t \to \mu^2} F(t, m_{\pi\pi}) \mu^2 / t. \qquad (12)$$

In the study that we now describe, use was made of the pseudoperipheral approximation proposed by Baton *et al.* [63]. This approximation employs the additional assumption that $F(0) = 0$ and involves constructing the auxiliary function $F'(t) = F(t)/t$,

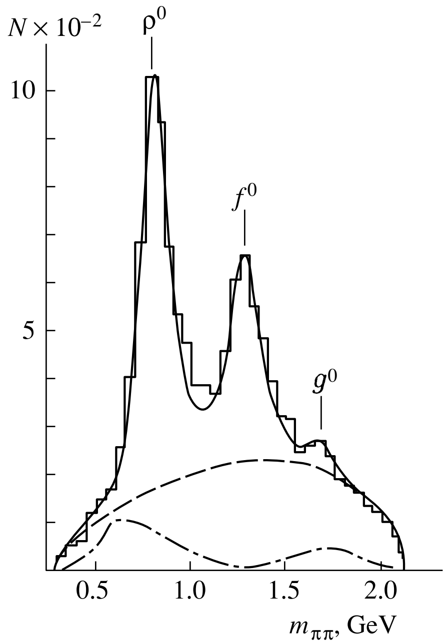

Fig. 1. Dipion-mass distribution of $\pi^- p \to \pi^- \pi^+ n$ events (histogram). The dash-dotted curve corresponds to the reflection of the $\Delta(1232)$ resonance (the relevant values are magnified by a factor of 5). The dashed curve represents the phase space. The solid curve is the sum of the Breit–Wigner curves for the ρ^0, f^0, and g^0 resonances; the phase space; and the reflection of $\Delta(1232)$.

which is precisely the function that is extrapolated to the pion pole. For all charged states, the resulting cross sections $\sigma_{\pi\pi}$ are displayed in Fig. 2. The angular distributions of secondary pions were described in terms of the averaged spherical harmonics $\langle Y_L^0 \rangle (m_{\pi\pi})$, which were also extrapolated to the pion pole.

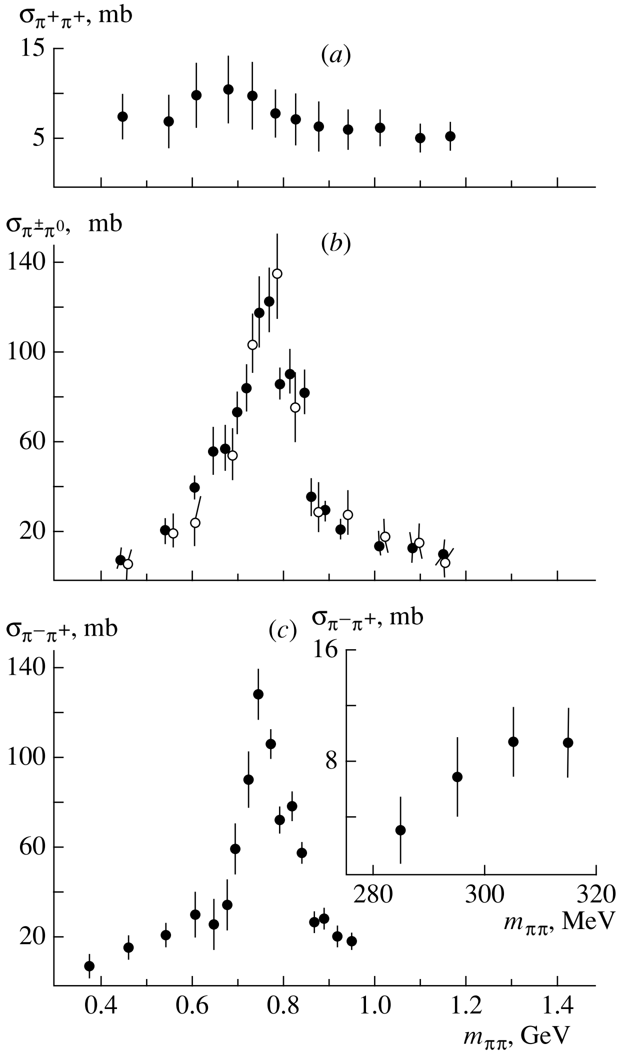

Fig. 2. Pion–pion cross sections $\sigma_{\pi\pi}$ for various charged channels: (*a*) $\pi^+\pi^+ \to \pi^+\pi^+$, (*b*) $\pi^-\pi^0 \to \pi^-\pi^0$ (closed circles) and $\pi^+\pi^0 \to \pi^+\pi^0$ (open circles), and (*c*) $\pi^-\pi^+ \to \pi^-\pi^+$. The inset shows $\sigma_{\pi\pi}$ values near the threshold that were obtained from the analysis of photoemulsion data.

The partial-wave analysis can be performed either by the energy-independent method, in which case solutions for the phase shifts and elasticity factors are found individually for each interval of $m_{\pi\pi}$ values, or by the energy-dependent method, in which case the behavior of the S-, P-, and D-wave phase shifts is parametrized by different functions of $m_{\pi\pi}$ and q. In our study, we employed both methods, which yielded consistent results. By way of example, the result obtained for the phase shift δ_0^0 from the energy-independent version of the calculation is presented in Fig. 3. Here, attention is caught by the ambiguous behavior of the phase shift δ_0^0 (so-called "up–down" problem, which has so far been the subject of lively discussions—see, for example, [43]). Given the phase shifts δ_l^I for pion–pion scattering, one can find the corresponding scattering lengths by extrapolating them to the threshold; that is,

$$a_l^I = \lim_{q \to 0} \frac{\delta_l^I(q)}{q^{2l+1}}, \tag{13}$$

where q is the secondary-pion momentum in the dipion rest frame.

It should be noted that the pion–pion scattering lengths are very important quantities. They are predicted by a number of theoretical models. Moreover, their values can in principle be deduced from data on several processes, whereas all phase shifts for pion–pion scattering over the entire region of the dipion masses can be determined only from data on the $\pi N \to \pi\pi N$ processes.

Table 2

Resonance	$m_{\pi\pi}$, MeV	Γ, MeV	σ, mb	p, GeV/c
ρ^-	790 ± 15	180 ± 15	0.50 ± 0.04	4.5
ρ^0	790 ± 10	170 ± 10	0.85 ± 0.05	4.5
ρ^+	780 ± 15	140 ± 15	1.07 ± 0.11	3.05
f^0	1270 ± 20	200 ± 30	0.52 ± 0.04	4.5
g^-	1680 ± 20	190 ± 25	0.03 ± 0.03	4.5
g^0	1680 ± 20	190 ± 25	0.05 ± 0.03	4.5
$\Delta^\pm$	1232 (fixed)	120 (fixed)	0.06 ± 0.02	4.5

Frequently, there arises the question of whether the aforementioned extrapolation is reliable in the physics of the pion–pion interaction. In our studies, we had had to deal with this question in extrapolating cross sections and spherical harmonics to the pole. Here, we ran into it once again in studying the scattering length. The point is that the real part of the S-wave amplitude has, as theorists assumed (see, for example, [64]) and as we confirmed experimentally in our joint study with physicists from Dubna [27], a subthreshold zero not far from the physical region. In view of this, it was illegitimate to employ, in the case of the S wave, the familiar effective-range approximation, which had been conventionally used in constructing extrapolations from the region $m_{\pi\pi} > 400$ MeV, but which led in this case to an overestimated value of the scattering length a_0^0. In [27], we sidestepped this difficulty by employing, for extrapolation purposes, data in the threshold region $280 \leq m_{\pi\pi} \leq 320$ MeV that were obtained in [52] by the photoemulsion method. The value of $a_0^0 = (0.24 \pm 0.07)\ \mu^{-1}$ found in this way is consistent with the value of $a_0^0 = (0.25 \pm 0.05)\ \mu^{-1}$, which was calculated by means of extrapolation from the farther region $280 \leq m_{\pi\pi} \leq 700$ MeV with the aid of the Serebryakov formula [64], which takes into account the existence of the subthreshold zero.

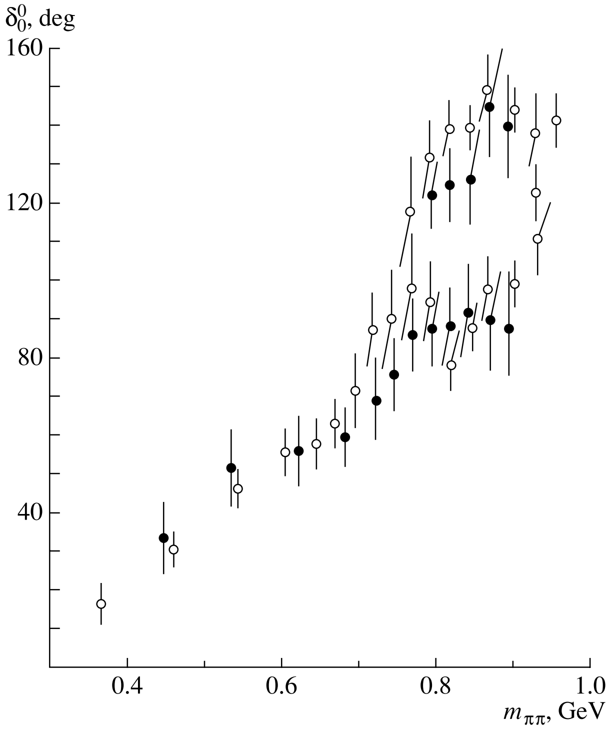

Fig. 3. Two versions of the calculations for the phase shift δ_0^0 obtained by the energy-independent method from data on the reaction $\pi^- p \to \pi^-\pi^+ n$ at $p_{\pi^-} = 4.5$ GeV/c.

Apart from the extrapolation method for determining scattering lengths, which was described above, we also employed, in our studies, the theoretical method for computations that is based on the Roy equations [65]. Roy derived exact equations by using double-subtraction dispersion relations at a fixed value of t and the analyticity and the crossing-symmetry properties of the scattering amplitude. These equations determine partial-wave amplitudes in the region $-4 \leq s \leq 60$ ($s = m_{\pi\pi}^2/\mu^2$), which includes the unphysical part $-4 \leq s \leq 4$, in terms of quantities in the physical region $4 \leq s \leq \infty$. Supplemented with the unitarity relation, the Roy equations form a set of nonlinear singular equations containing all partial-wave amplitudes. This set of equations makes it possible in principle to reconstruct part of unknown partial-wave amplitudes on the basis of their known components (e.g., to determine the amplitudes in the low-energy region from their known behavior at high energies); to evaluate the scattering length; to determine the positions of subthreshold zeros; and to resolve the up–down problem.

Here, we will not write here the complete set of Roy equations, including integral equations with complicated kernels (see, for example, [31, 32]), restricting ourselves to presenting the subtraction terms for the S and P waves. These terms are explicitly expressed in terms of the S-wave scattering lengths and are given by

$$\lambda_0^0(s) = a_0^0 + \frac{1}{12}(2a_0^0 - 5a_0^2)(s-4), \qquad (14)$$

$$\lambda_0^2(s) = a_0^2 - \frac{1}{24}(2a_0^0 - 5a_0^2)(s-4),$$

$$\lambda_1^1(s) = \frac{1}{72}(2a_0^0 - 5a_0^2)(s-4).$$

We will not describe here the rather cumbersome procedure of applying the Roy equations to studying pion–pion interactions either. We only note that, in using a general theoretical method for their analysis, there arises an entire set of solutions. In order to restrict their number, one has to impose specific constraints known from experimental data (for example, the conditions ensuring the existence of the rho resonance in the P wave or the absence of resonances in the $I = 2$ waves for $m_{\pi\pi} < 1$ GeV). But even in this case, one does not arrive at a unique solution for a_0^0 and a_0^2; instead, there appears, in the (a_0^0, a_0^2) plane, a so-called universal curve that represents the set of correlated values of a_0^0 and a_0^2. By using known experimental data—the methods for obtaining such data were described in the preceding section—as inputs for the Roy equations, we were able to reduce, in [32], the limits of the universal curve to the boundaries of a rather small region of a_0^0 and a_0^2, namely,

$$0.21\,\mu^{-1} \le a_0^0 \le 0.27\,\mu^{-1}, \qquad (15)$$

$$-0.04\,\mu^{-1} \le a_0^2 \le 0.00\,\mu^{-1}.$$

The same method was employed to determine the positions of the subthreshold zeros of the S-wave amplitudes near the physical region. The results are

$$s_0 = -0.2, \qquad s_2 = 2.4. \qquad (16)$$

To conclude our analysis of problems that are associated with the singularities in the behavior of the partial-wave amplitudes for pion–pion scattering in the low-energy region and which have been treated at this stage of our work, we present the values obtained for the scattering lengths a_0^0, a_0^2, a_1^1, a_2^0, and a_2^2 by averaging data from measurements of these quantities by different methods:

$$a_0^0 = (0.24 \pm 0.03)\,\mu^{-1}, \qquad (17)$$

$$a_0^2 = (-0.04 \pm 0.04)\,\mu^{-1},$$

$$a_1^1 = (0.034 \pm 0.003)\,\mu^{-3},$$

$$a_2^0 = (7.8 \pm 6.0) \times 10^{-4}\,\mu^{-5},$$

$$a_2^2 = (3.8 \pm 1.4) \times 10^{-4}\,\mu^{-5}.$$

Since 1996 [36], we have repeatedly employed the method of the Roy equations to process available experimental results on the phase shifts for pion–pion scattering.

3. INVESTIGATION OF THE REACTIONS $\pi^{\pm}p \to \pi\pi N$ WITH THE CHAOS SPECTROMETER AT THE TRIUMF ACCELERATOR IN CANADA

Various calculations revealed that the method for determining scattering lengths on the basis of dispersion relations (for example, the Roy equations) is very sensitive to variations in experimental data near the threshold. A particular interest in the threshold region of energies is also associated with the fact that the pion–pion scattering lengths vanish there in the chiral limit; therefore, their precise experimental values furnish information about the degree of chiral-symmetry breaking, eventually enabling one to choose between the existing theoretical scenarios of this symmetry breaking. At the same time, there had been virtually no statistically reliable data on the features of pion–pion scattering near the threshold.

This gap in studying the pion–pion interaction was filled by an international collaboration that performed experiments with the CHAOS spectrometer [66] at the TRIUMF meson factory in Canada [40] and which included some members of our group.

The layout of the CHAOS facility is shown in Fig. 4. It includes a dipole magnet creating a field of 0.5 T, four concentric cylindrical wire chambers (two proportional and two drift ones), and a set of plastic scintillators equipped with lead-glass Cherenkov counters. A liquid-hydrogen target (ø = 25.5 mm, $l = 50$ mm, $T = 18$ K) was inserted at the center of the magnet through a special hole. The solid angle covered by the spectrometer was 324° in the horizontal plane and ±7° in the vertical plane.

The experiment employed 223-, 243-, 264-, and 284-MeV pion beams at a resolution of $\Delta p/p = 0.01$–0.05. A comparatively low energy of incident pions made it possible to obtain the parameters of pion–pion scattering directly in the threshold region of energies. For each value of the charged-pion energy, the collected data sample included 10 000 $\pi^-\pi^+$ and 10 000 $\pi^+\pi^+$ events, which were distributed over a 10 × 10 × 10 three-dimensional grid in terms of the variables $m_{\pi\pi}^2$, t, and $\cos\theta$. A general normalization of the data on the reaction in question was performed by comparing the measured values of the cross section for elastic pion–proton scattering with known data from other experiments.

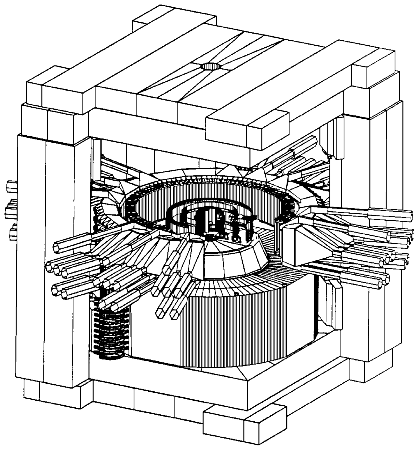

Fig. 4. Layout of the CHAOS facility.

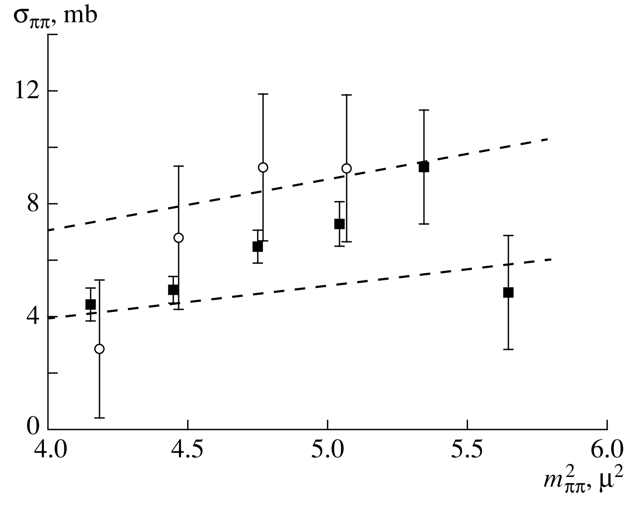

Fig. 5. Cross section for pion–pion scattering near the threshold: (closed boxes) results obtained by extrapolating data on the reaction $\pi^- p \to \pi^-\pi^+ n$ from the CHAOS facility, (open circles) data of the photoemulsion study reported in [52], and (region between the dashed lines) predictions of the calculations based on the Roy equations.

The results obtained in this way were processed by the Goebel–Chew–Low extrapolation method described above, which was supplemented with the Baton pseudoperipheral approximation [63]. The possibility of simultaneously using data obtained at different incident-pion energies was an important feature that was peculiar to the treatment of the experimental data being discussed and which enabled one to exercise an additional control over the correctness of the adopted extrapolation procedure by requiring that the cross section $\sigma_{\pi\pi}(m_{\pi\pi})$ be independent of the total energy of the process $\pi N \to \pi\pi N$.

The resulting values of the cross sections for $\pi^-\pi^+$ scattering near the threshold are shown in Fig. 5, along with the data from the aforementioned photoemulsion study in [52] and the results of the calculations based on the Roy equations. From this figure, it can be seen that the cross-section values directly obtained from experiments in the threshold region comply well with the results of the calculations that employ data from the reactions $\pi p \to \pi\pi N$ at a higher incident-pion momentum. This suggests that the Goebel–Chew–Low extrapolation procedure is self-consistent; that is, it is equally applicable in the case of low and in the case of high momenta of pions inducing relevant reactions.

The cross sections for pion–pion scattering near the threshold enabled us to determine the scattering length a_0^0 [40]. Its value was obtained directly from the cross section for $\pi^-\pi^+$ scattering at the threshold, where this cross section is associated primarily with the S_0 wave (for the $\pi^-\pi^+$ channel, the contribution of the S_2 wave is small). The resulting value of a_0^0 is

$$a_0^0 = [0.204 \pm 0.014(\text{stat.}) \pm 0.008(\text{syst.})]\mu^{-1}. \tag{18}$$

In order to check the correctness of this result, the scattering length a_0^0 was also estimated by a few other methods that yielded the following values (in μ^{-1} units):

$$a_0^0 = 0.229 \pm 0.008$$

from a comparison with a_1^1 according to the Basdevant method [67],

$$a_0^0 = 0.214 \pm 0.011 \tag{19}$$

from the preliminarily found value of the phase shift δ_0^0,

$$a_0^0 = 0.223\,^{+0.027}_{-0.023}$$

from the substitution of the phase shift δ_0^0 into the Roy equations, and

$$a_0^0 = 0.21 \pm 0.02$$

from a comparison of the experimental threshold value of the cross section for pion–pion scattering with the cross section calculated on the basis of the method proposed in [36].

Within the errors, all of them agree with the value of a_0^0 in (18); therefore, the value in (18) can be considered not only as a correct value, but also as the value that is characterized by the highest statistical significance. It should be noted, however, that this statement is valid under the assumption that the one-pion-exchange diagram is dominant. Unfortunately, the modern theory is unable to assess the error stemming from the possible contribution of background diagrams.

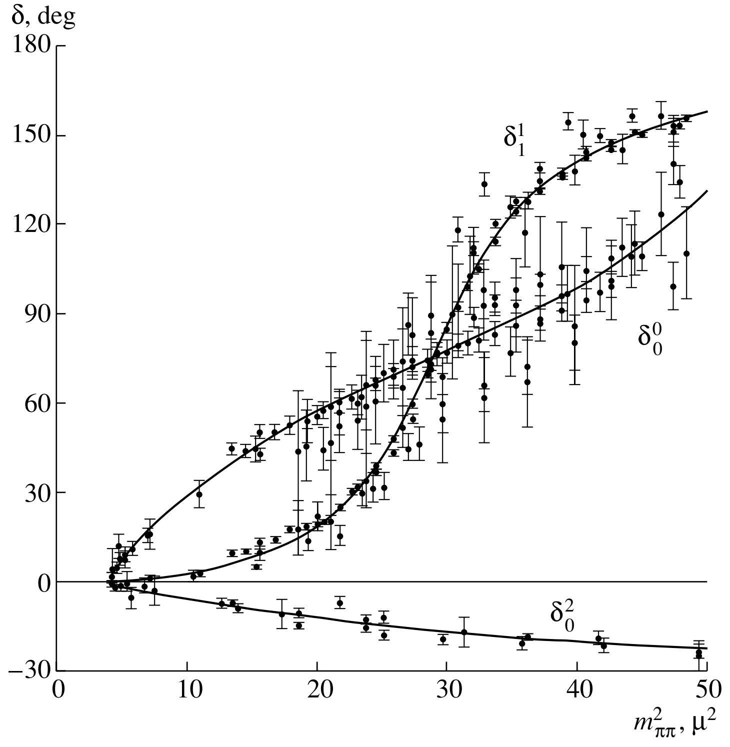

Fig. 6. Set of the experimental values of the S- and the P-wave phase shifts for pion–pion scattering and their approximation.

4. CURRENT SITUATION AROUND THE INVESTIGATION OF THE PION–PION INTERACTION: THEORY VERSUS EXPERIMENT

The current stage of the experimental investigation of the pion–pion interaction is characterized by the endeavor to obtain very precise (approximately an order of magnitude more precise than at present) values of the cross sections for pion–pion scattering and of the relevant phase shifts and especially scattering lengths. The need for such precise data is dictated by the achievements of chiral perturbation theory, which makes it possible to compute the characteristics of low-energy processes involving pions [68–71]. The structure of chiral perturbation theory is based on the principle of spontaneous chiral-symmetry breaking, whose scenario depends on important QCD parameters embedded in the theory, such as the quark condensate and the light-quark masses. The assumption of a significant value of the quark condensate (~1 GeV) leads to so-called standard chiral perturbation theory, while the assumption of its very small value leads to generalized chiral perturbation theory.

Standard chiral perturbation theory and generalized chiral perturbation theory predict different values of the pion–pion scattering length a^0_0 ($0.20\,\mu^{-1}$ and $0.27\,\mu^{-1}$, respectively). Therefore, an experimental corroboration of one of these would make it possible to choose a version of the theory, whereby one could draw definitive conclusions on the values of the aforementioned QCD parameters.

Although the values of a^0_0 that are predicted by these two versions of chiral perturbation theory are distinct, their difference is insufficient, at the current level of errors in available experimental data, for deciding on one of them, the more so as the accuracy in some of them is considerably overrated, as follows from modern investigations of the correctness of solving data-analysis problems [43]. Moreover, the most accurate value of a^0_0 [see (18)] that we obtained in [40], albeit being very close to that which is predicted by standard chiral perturbation theory, takes no account of the possible error associated with the contribution of background diagrams, which is impossible to evaluate at the present stage of development of the theory.

Several different methods are used at the present time in order to improve the accuracy of relevant experimental results.

First, a global treatment of numerous data from investigations of reactions like $\pi N \to \pi\pi N$ (including the reaction $\pi^- p \to \pi^0\pi^0 n$, which is difficult for observation, as well as some recent results obtained for other channels near the threshold and the results of polarization experiments) in terms of the Roy equations is being continued. For example, the database

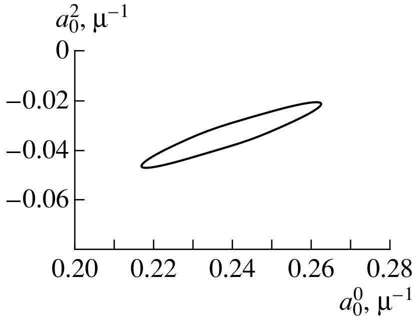

Fig. 7. Resulting scattering ellipse for a_0^0 and a_0^2.

comprising the phase shifts for pion–pion scattering that were obtained from analyses of five charged channels over the energy range from the threshold to 1 GeV of the dipion mass was used in [42]. For the first time, this analysis employed experimental data on both S-wave phase shifts near the threshold, which have a decisive effect on the accuracy in solving the Roy equations.

Figure 6 displays the entire body of experimental data on the S- and P-wave phase shifts for pion–pion scattering and their approximations by smooth curves. These curves were introduced as inputs in the Roy equations to determine solutions for the subtraction constants $\lambda(s)$—that is, in integrating the Roy equations for each set of phase-shift values. The values of the real parts of partial-wave amplitudes were chosen at each point where there were experimental data on phase shifts. It was shown that the resulting values of $\lambda(s)$ are indeed described well, as follows from the structure of the Roy equations [see Eqs. (14)], by linear functions of the dipion mass s; that is, the procedure employed is self-consistent. On the basis of the resulting dependences it was possible to determine values of the S-wave scattering lengths such that the principles of analyticity, unitarity, and crossing symmetry are satisfied for the corresponding partial-wave amplitudes and that they are consistent with the available experimental values of the phase shifts in terms of the χ^2 criterion:

$$a_0^0 = (0.240 \pm 0.023)\,\mu^{-1}, \tag{20}$$
$$a_0^2 = (-0.034 \pm 0.013)\,\mu^{-1},$$
$$a_1^1 = (0.0356 \pm 0.0017)\,\mu^{-3}.$$

The region of possible values of a_0^0 and a_0^2 is shown in Fig. 7.

Investigations of reactions like $\pi N \to \pi\pi N$ made it possible to construct more precisely the phase-shift curves from the threshold to the dipion-mass value of about 1.2 GeV and to shrink the interval of the possible scattering-length values [42]. Needless to say, they could not remove the main qualification concerning the analysis of $\pi N \to \pi\pi N$ data with the aim of extracting information about the pion–pion interaction—the results cannot be obtained in a completely model-independent way.

Second, an experiment studying K_{e4} decay is being presently performed in Brookhaven. This decay ($K^+ \to \pi^+\pi^-e^+\nu_e$) is one of the most reliable sources of information about low-energy pion–pion interaction. It enables one to deduce, under minimal model assumptions, information about the phase-shift difference $(\delta_0^0 - \delta_1^1)$ near the threshold. The kinematical dependence of the amplitude due to weak interaction is known rather well, and all deviations observed experimentally are associated with strong interaction, which causes the rescattering of final pions. Since the dipion possesses a low energy in the process being considered, it is legitimate to disregard the effect of higher partial waves; in view of this, the $\Delta I = 1/2$ rule restricts the isospin structure of the amplitude to $I = 0, 1$ states. Unfortunately, K_{e4} decay is a rare decay mode, its branching ratio being 3.4×10^{-5}, which severely complicates the accumulation of statistics. This is the reason why previous experiments were unable to yield results on the phase shifts at the required level of precision.

A new experiment (E865 [72]) has been performed since 1993. Its layout is shown in Fig. 8. This experiment employs a 6-GeV/c kaon beam, a 5-m decay chamber, a magnet ($D5$) for separating positively and negatively charged particles, and a triggering hodoscope (A counter). The momenta are determined with the aid of proportional wire chambers ($P1$–$P4$) and a second magnet ($D6$). The identification of particles is performed by means of an electromagnetic shower calorimeter, four gas Cherenkov counters ($C1$, $C2$), a stack of iron layers for measuring the muon range, wire chambers, muon hodoscopes (B and C counters), and a device measuring the beam trajectory in the upper section of the decay chamber.

In planning this experiment, the accumulation of enormous statistics of 3×10^5 events for this very rare channel of kaon decay was foreseen, which would make it possible to determine a_0^0 with a 5% precision—that is, to select reliably one of the two versions of the theory. At present, about 400 000 events have been selected and analyzed. According to a preliminary report on the first results of this experiment [73], this results in the a_0^0 value

$$a_0^0 = [0.228 \pm 0.012(\text{stat.}) \pm 0.003(\text{syst.})]\mu^{-1}, \tag{21}$$

which does indeed have a 5% precision and which is rather close to that which was found by processing

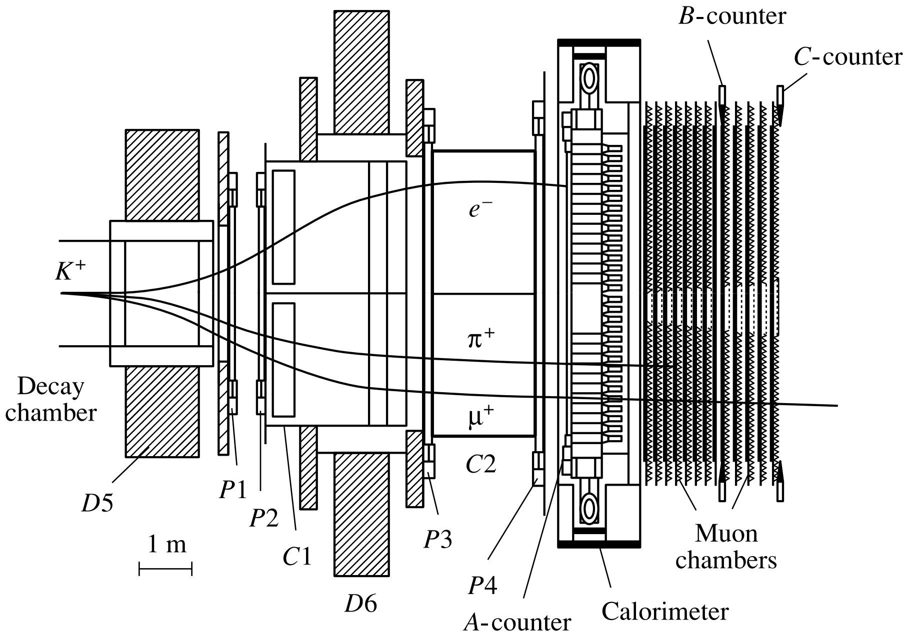

Fig. 8. Project of an experiment intended for studying K_{e4} decay: ($D5$) separating magnet, ($P1$–$P4$) proportional wire chambers, ($D6$) magnet for determining particle momenta, ($C1$, $C2$) Cherenkov detectors, (A counter) triggering hodoscope, and (B and C counters) muon hodoscopes.

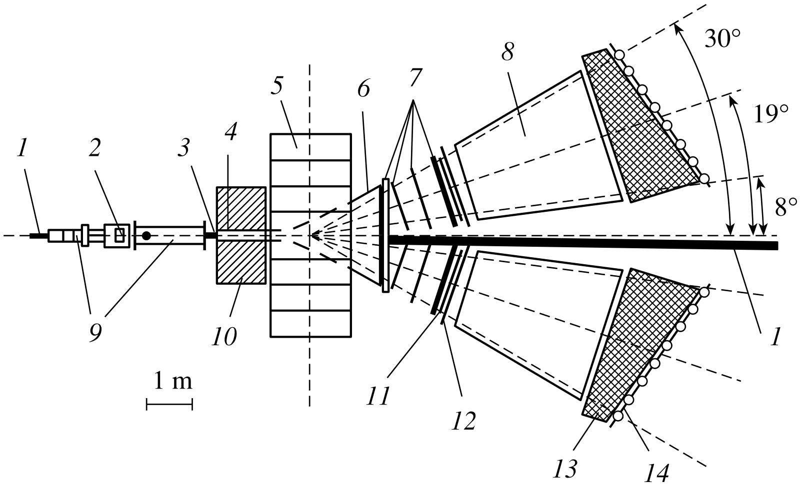

Fig. 9. Layout of the DIRAC experiment: (*1*) proton beam, (*2*) foiled targets, (*3*) scintillation fiber coordinate detectors, (*4*) collimator, (*5*) magnet of the spectrometer, (*6*) vacuum chamber, (*7*) drift chambers, (*8*) Cherenkov counters, (*9*) vacuum tube, (*10*) radiation protection, (*11*) vertical hodoscopes, (*12*) horizontal hodoscopes, (*13*) cast-iron absorbers, and (*14*) muon scintillation counters.

data on the reactions $\pi N \to \pi\pi N$ (see, for example, [42]).

Third, the DIRAC experiment [74], which is aimed at studying the properties of pionium, the exotic, unstable hydrogen-like $\pi^+\pi^-$ atom, is being performed at CERN. A theoretical analysis of this experiment makes it possible to relate the ratio of the branching fractions for pionium decay through the $2\pi^0$ and the 2γ channel to the scattering-length difference squared $(a_0^0 - a_0^2)^2$. In order to achieve a 5% precision in determining $(a_0^0 - a_0^2)$ and, hence, a_0^0, since $|a_0^0| \gg |a_0^2|$, it is sufficient in this case to measure the pionium lifetime with a 10% precision. Preliminary results supporting the correctness of the idea underlying the method were obtained in 1994 at the Serpukhov accelerator [75].

The layout of the DIRAC (Dimeson Relativistic Atom Complex) experiment is displayed in Fig. 9.

The experiment employs a 24-GeV/c proton beam from the PS accelerator and a few different targets; of these, a tantalum target is thought to be optimal. It is planned that the resolving power of the equipment for recording pions will be about 1 MeV/c, which will make it possible to see, at a high statistical level, an excess of atomic pion pairs near zero relative momenta in several ranges of its variation. The authors of this project (physicists from JINR and some other institutions) hope to obtain, within two to three years, about 20 000 atomic pairs from pionium disintegration with a relative momentum below 3 MeV/c and the opening angle smaller than 3 mrad.

More details on the two experiments in question, on the current state of affairs in the physics of the pion–pion interaction, and on the advances made in these realms can be found in the review article [43].

5. INVESTIGATION OF $(\pi,\ 2\pi)$ PION-PRODUCTION PROCESSES ON NUCLEI

In 1991, Chanfray *et al.* [76] predicted that, under the effect of a nuclear medium, the yield of $\pi^-\pi^+$ pairs having small invariant masses must be considerably enhanced—that is, the pion–pion interaction in the $I=0$ channel becomes stronger in this case. Although the authors later disavowed their prediction, the value of it was in that they initiated experimental investigations along these lines.

One relevant experiment [77] was performed at the accelerator of the TRIUMF meson factory (in Canada) with the CHAOS magnetic spectrometer [66], which was described above. The first series of measurements was performed in a 283-MeV pion beam, which was focused at the center of the spectrometer, where a solid nuclear or a liquid-hydrogen target was placed. The experimentalists recorded in coincidence two pions from each reaction in the following pairs:

$$\pi^+ + d \to X\pi^+\pi^+ \text{ and } \pi^+ + d \to X\pi^+\pi^-, \quad (22)$$
$$\pi^+ + {}^{12}\mathrm{C} \to X\pi^+\pi^+ \text{ and } \pi^+ + {}^{12}\mathrm{C} \to X\pi^+\pi^-,$$
$$\pi^+ + {}^{40}\mathrm{Ca} \to X\pi^+\pi^+ \text{ and } \pi^+ + {}^{40}\mathrm{Ca} \to X\pi^+\pi^-,$$
$$\pi^+ + {}^{208}\mathrm{Pb} \to X\pi^+\pi^+ \text{ and } \pi^+ + {}^{208}\mathrm{Pb} \to X\pi^+\pi^-.$$

The sought events were identified by using information both from the wire chambers (the sign of the charge and the momentum) and from the telescopes formed by scintillation and Cherenkov counters (separation of π from p and of π from e). The relevant sample of experimental data included fully reconstructed $\pi^+ \to \pi^+\pi^-$ and $\pi^+ \to \pi^+\pi^+$ events, whose numbers were 3690 to 7270 for the former and 310 to 1060 for the latter. In order to calculate the double-differential cross sections, these events were distributed over multidimensional shells and were multiplied by a weight that corresponded to each cell and which was obtained via a Monte Carlo simulation with allowance for the rate of formation of relevant events in the spectrometer. The measurement of the kinetic energies and of the laboratory angles for both final-state pions made it possible to calculate the fivefold-differential cross section

$$d^5\sigma/(dEd\theta)_{\pi 1}(dEd\theta)_{\pi 2}d\phi, \quad (23)$$

where ϕ is the zenith angle between the momenta of the two pions; it could be measured in the range $0^\circ \pm 7^\circ$ (or in the range $180^\circ \pm 7^\circ$). All the required distributions, including those with respect to the invariant dipion mass, the kinetic energies of pions, and their angles, were calculated on the basis of this differential cross section. Figure 10 displays the graphs of the function $d^3\sigma/dm_{\pi\pi}d\Omega d\phi$ versus the dipion mass for the reaction channels $\pi^+ \to \pi^+\pi^-$ and $\pi^+ \to \pi^+\pi^+$. From this figure, it can be seen that, in contrast to what is observed for the channel $\pi^+ \to \pi^+\pi^+$, the cross section for the interaction with nuclear targets in the channel $\pi^+ \to \pi^+\pi^-$ at near-threshold invariant masses (from $2m_\pi$ to 310 MeV) shows distinct peaks, which become more pronounced with increasing atomic number of the target. It can also be seen from the figure that there is no such effect for $\pi^+\pi^+$ pairs, which have $I = 2$.[4)]

Since the experiment resulted in an unambiguous observation of the "predicted" effect, new theoretical models were required for explaining it.

In 1999, Vicente-Vakas and Oset [79] presented the results that they obtained by simulating $(\pi,\pi\pi)$ processes on nuclei. They took into account the effect of Fermi motion and rescattering effects and attained good agreement with experimental data for processes resulting in the production of $\pi^+\pi^+$ pairs, but they were unable to reproduce data for $\pi^-\pi^+$ pairs without introducing an arbitrary and large final-state interaction for the isospin-zero channel. Also in 1999, Hatsuda *et al.* [80] studied a variation of the pion–pion interaction in the isospin-zero channel in response to variations of the nuclear density under the conditions

---

[4)] Recently, the Crystall Ball collaboration reported its experimental data obtained by studying the processes $\pi^- A \to \pi^0\pi^0 A'$ on H, ^{12}C, ^{27}Al, and ^{64}Cu nuclei at the pion momenta of 408 and 750 MeV/c [78]. From these data, it also follows that the yield of $\pi^0\pi^0$ pairs is enhanced near the threshold of $2m_\pi$ and that it increases with increasing target mass number. Since this process involves the $I = 0$, 2 channels, the fact that the effect is qualitatively the same as that which was observed at the CHAOS facility (where $I = 0$, 1 could occur and where $I = 2$ was rejected because of the absence of the effect in the $\pi^+\pi^+$ channel) leads to the conclusion that, in all probability, the enhancement in question is associated with the $I = 0$ channel.

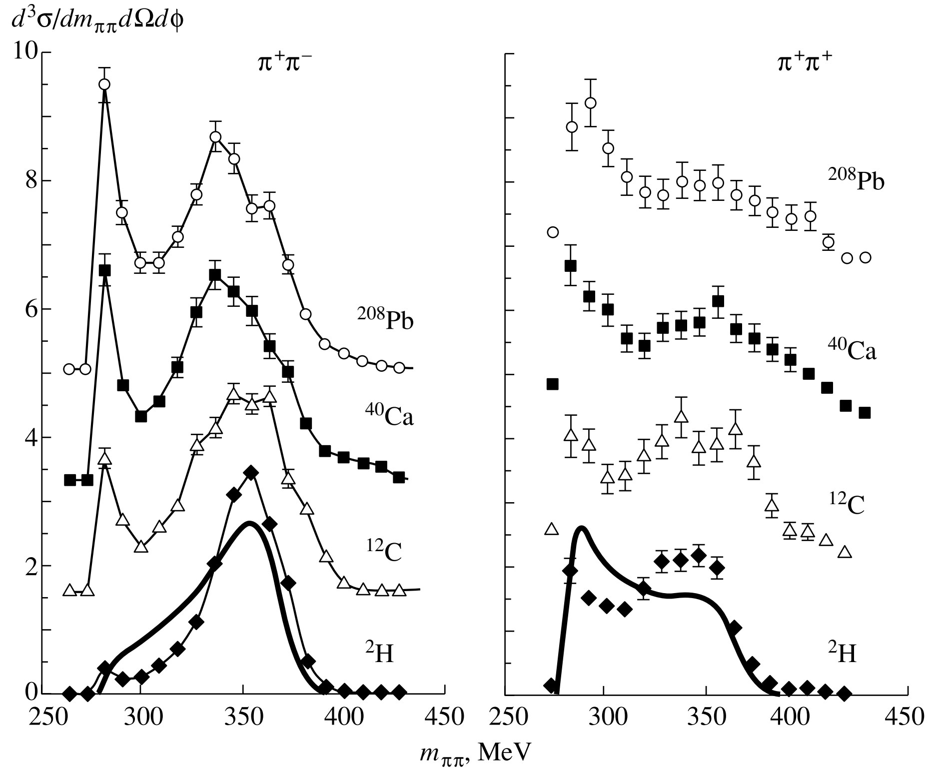

Fig. 10. Differential cross sections (in arbitrary units) for the yield of dipions versus the dipion mass for pion interactions with various nuclei.

of a partial restoration of chiral invariance. They predicted an enhancement of the pion–pion interaction near the threshold. This explanation could be treated as an example of manifestations of quark effects in nuclear physics. Different explanations of the effect had also been proposed. The situation around this question had been such that a continuation of experiments along these lines became mandatory.

For a further investigation of the observed effects, measurements were performed for the reactions

$$^{45}\mathrm{Sc}(\pi^+,\pi^+\pi^+)X \text{ and } ^{45}\mathrm{Sc}(\pi^+,\pi^+\pi^-)X \quad (24)$$

at the incident-pion energies of 240, 260, 280, 300, and 320 MeV [41]. The motivation of this experiment was that, if the enhancement of the yield of pion pairs near the threshold was due to final-state interaction, the effect should be independent of the primary energy. But if it is new pion-production mechanisms in a nuclear medium that are responsible for the enhancement in question, the effect should depend on the primary energy. Moreover, a scandium target represents nuclei having incompletely filled shells, in contrast to target nuclei used previously. Although the dependence of the effect on the specificity of nuclear properties seemed improbable, it was desirable to verify this possibility. Finally, the measurements of the features of the process within a single experiment covered the case of a deuterium target as well.

The measurements demonstrated that the earlier observation of a considerable enhancement of the yield of $\pi^+\pi^-$ pairs with near-threshold invariant masses in the interaction of pions with nuclei is reproduced at nearly the same level for all primary pion energies. This result favors the explanation of the observed effect as that which is due to the existence of a strong final-state interaction in the $I = 0$ $\pi^+\pi^-$ channel (channel whose quantum numbers are those of the sigma meson) in a nuclear medium.

6. CONCLUSION

At the beginning of the article, we talked about the first studies in the region of pion physics, which were performed in the late 1940s and in the early 1950s and in which Gurevich participated directly. Some important methodological and physical results concerning pion physics and the physics of pion–nucleus interactions were obtained in those early studies by the photoemulsion method. Among other things, Gurevich and his collaborators found the charged-pion mass. Among the values found by that time, their result proved to be the closest to the modern value.

The next step in studying the pion and the pion–pion interaction was made by I.I.'s disciples, whom he actively supported. These investigations continued for many years by using various experimental procedures based on hydrogen bubble chambers, photoemulsions, and magnetic spectrometers and various methods for data treatment and analysis. They resulted in deducing self-consistent results for four charged channels of pion–pion scattering, precise values of the pion–pion cross sections near the threshold, and scattering lengths. Also, a complete database of the phase shifts for pion–pion scattering was analyzed on the basis of dispersion relations (the technique of Roy equations), and the region of the S-wave scattering lengths was obtained where the solutions to the dispersion equations for the partial-wave pion–pion amplitudes are adequate to experimental data and meet the requirements of analyticity, unitarity, and crossing symmetry.

Considerable advances have been made in determining the S_0-wave scattering length a_0^0, which is of crucial importance for the theory. Two versions of modern chiral perturbation theory—standard chiral perturbation theory and generalized chiral perturbation theory—lead to different scenarios of chiral-symmetry breaking. The values of a_0^0 ($0.20\,\mu^{-1}$ and $0.27\,\mu^{-1}$, respectively) represent one of the few experimentally verifiable consequences of these theories. The value of $a_0^0 = [0.204 \pm 0.014(\text{stat.}) \pm 0.008(\text{syst.})]\mu^{-1}$, which was obtained in [40], favors the standard version of the theory and, hence, a strong quark condensate, but, of course, the conclusive choice would be premature at this stage.

In the last sections of the article, we tried to demonstrate what has become of pion physics today. Instead of counting grains in photoemulsions, present-day experimentalist are taking readings of a few tens of thousands of sensitive channels of giant experimental facilities, studying the properties of the unstable $\pi^+\pi^-$ atom (DIRAC experiment), and accumulating formidable statistics of millions of events of K_{e4} decay, whose branching ratio is as small as 10^{-5}! A systematic investigation of pion interactions in a nuclear medium has been begun, and an intriguing enhancement of the yield of pairs of oppositely charged pions near the threshold has already been discovered. The origin of the effect has not yet been clarified conclusively, but the very fact that the problem of a partial restoration of chiral symmetry in a nuclear medium (it is broken in a vacuum)—that is, the problem of the manifestation of QCD effects in nuclear physics—has been addressed demonstrates the achieved level of development along these lines of investigation. We are confident that, in the near future, the concerted efforts of experimentalists and theorists will lead to still more considerable advances in the understanding of pion physics, which Gurevich loved so much!

ACKNOWLEDGMENTS

We are grateful to V.P. Martemyanov and E.E. Saperstein, who proposed that we write this article and who permanently showed interest in our work on it. Special thanks are also due to A.A. Kartamyshev, A.F. Sustavov, and V.N. Maiorov, who took part in a considerable part of the investigations described in this article.

This work was supported by the Russian Foundation for Basic Research (project no. 00-02-17852).

REFERENCES

1. L. Mysovskii and P. Chizhov, Z. Phys. **44**, 408 (1927).
2. V. V. Alpers and A. A.Varfolomeev, Prib. Tekh. Éksp., No. 1, 1 (1956).
3. R. I. Gerasimova, I. I. Gurevich, and K. N. Mukhin, Report No. 440A (Institute of Atomic Energy, 1951).
4. I. I. Gurevich, K. N. Mukhin, and D. M. Samoĭlovich, Report No. 435A (Institute of Atomic Energy, 1950).
5. V. V. Alpers, I. I. Gurevich, and K. N. Mukhin, Report No. 518A (Institute of Atomic Energy, 1951).
6. V. V. Alpers, I. I. Gurevich, K. N. Mukhin, *et al.*, Zh. Éksp. Teor. Fiz. **30**, 1025 (1956) [Sov. Phys. JETP **3**, 914 (1956)].
7. V. V. Alpers, I. I. Gurevich, K. N. Mukhin, *et al.*, Zh. Éksp. Teor. Fiz. **30**, 1034 (1956) [Sov. Phys. JETP **3**, 735 (1956)].
8. L. M. Barkov, K. N. Mukhin, and R. S. Shlyapnikov, in *Proceeding of the International Conference on High Energy Accelerators and Instruments, CERN, Geneva, 1959,* p. 514.
9. V. K. Makar'in, V. P. Martem'yanov, K. N. Mukhin, *et al.*, in *Proceedings of the XII International Conference on High Energy Physics, Dubna, 1964* (Atomizdat, Moscow, 1964), Vol. II, p. 469.
10. V. K. Makar'in, Preprint No. IAÉ-2485 (Institute of Atomic Energy, Moscow, 1975).
11. L. M. Barkov, K. N. Mukhin, V. A. Suetin, *et al.*, Prib. Tekh. Éksp., No. 6, 48 (1963).
12. S. P. Kruchinin, K. N. Mukhin, and A. S. Romantseva, Preprint No. IAÉ-700 (Institute of Atomic Energy, Moscow, 1964).
13. S. P. Kruchinin and K. N. Mukhin, in *Elementary Particles: Collection of Articles of Moscow Engineering Physics Institute* (Atomizdat, Moscow, 1967).
14. L. M. Barkov, K. N. Mukhin, V. V. Ogurtsov, *et al.*, Zh. Éksp. Teor. Fiz. **43**, 335 (1962) [Sov. Phys. JETP **16**, 240 (1963)].
15. V. I. Baranov, V. K. Makar'in, O. O. Patarakin, *et al.*, Preprint IAÉ-3211 (Institute of Atomic Energy, Moscow, 1970).

16. V. I. Baranov, V. K. Makar'in, K. N. Mukhin, *et al.*, Preprint No. IAÉ-3772/2 (Institute of Atomic Energy, Moscow, 1983).
17. O. I. Kutlina, K. N. Mukhin, A. S. Romantseva, *et al.*, Preprint No. IAÉ-1975 (Institute of Atomic Energy, Moscow, 1970).
18. A. A. Kartamyshev, K. N. Mukhin, A. F. Sustavov, *et al.*, Yad. Fiz. **15**, 294 (1972) [Sov. J. Nucl. Phys. **15**, 166 (1972)]; **16**, 535 (1972) [**16**, 298 (1972)]; **17**, 81 (1973) [**17**, 42 (1973)].
19. A. A. Kartamyshev, K. N. Mukhin, A. F. Sustavov, *et al.*, Phys. Lett. B **44B**, 310 (1973).
20. A. A. Kartamyshev, K. N. Mukhin, O. O. Patarakin, *et al.*, Preprint No. IAÉ-2374 (Institute of Atomic Energy, Moscow, 1974).
21. A. A. Kartamyshev, K. N. Mukhin, O. O. Patarakin, *et al.*, Pis'ma Zh. Éksp. Teor. Fiz. **20**, 748 (1974) [JETP Lett. **20**, 346 (1974)]; **23**, 478 (1976) [**23**, 432 (1976)].
22. M. S. Aĭnutdinov, G. V. Beketov, *et al.*, Prib. Tekh. Éksp., No. **2**, 47 (1968).
23. A. B. Kurepin, K. N. Mukhin, O. O. Patarakin, *et al.*, Preprint No. P0484, IYaI AN SSSR (Institute for Nuclear Research, USSR Academy of Sciences, Moscow, 1986).
24. O. O. Patarakin, A. B. Kurepin, K. N. Mukhin, *et al.*, Preprint No. 76992, IYaI RAN (Institute for Nuclear Research, Russian Academy of Sciences, Moscow, 1992).
25. A. A. Kartamyshev, K. N. Mukhin, and O. O. Patarakin, Pis'ma Zh. Éksp. Teor. Fiz. **25**, 68 (1977) [JETP Lett. **25**, 61 (1977)]; **26**, 422 (1977) [**26**, 296 (1977)].
26. E. A. Alekseeva, K. N. Mukhin, and O. O. Patarakin, Pis'ma Zh. Éksp. Teor. Fiz. **29**, 109 (1979) [JETP Lett. **29**, 100 (1979)].
27. A. A. Bel'kov, S. A. Bunyatov, K. N. Mukhin, and O. O. Patarakin, Pis'ma Zh. Éksp. Teor. Fiz. **29**, 652 (1979) [JETP Lett. **29**, 597 (1979)].
28. E. A. Alekseeva, K. N. Mukhin, O. O. Patarakin, *et al.*, Preprint No. IAÉ-3241/1 (Institute of Atomic Energy, Moscow, 1980).
29. K. N. Mukhin, O. O. Patarakin, A. F. Sustavov, *et al.*, Pis'ma Zh. Éksp. Teor. Fiz. **32**, 616 (1980) [JETP Lett. **32**, 601 (1980)].
30. K. N. Mukhin and O. O. Patarakin, Usp. Fiz. Nauk **133**, 377 (1981) [Sov. Phys. Usp. **24**, 161 (1981)].
31. E. A. Alekseeva, K. N. Mukhin, and O. O. Patarakin, Yad. Fiz. **35**, 917 (1982) [Sov. J. Nucl. Phys. **35**, 533 (1982)].
32. E. A. Alekseeva, K. N. Mukhin, O. O. Patarakin, *et al.*, Zh. Éksp. Teor. Fiz. **82**, 1007 (1982) [Sov. Phys. JETP **55**, 591 (1982)].
33. A. A. Bel'kov, S. A. Bunyatov, K. N. Mukhin, and O. O. Patarakin, *Pion–pion Interaction* (Énergoatomizdat, Moscow, 1985).
34. O. O. Patarakin and V. N. Tikhonov, Preprint No. IAÉ-5629/2 (Institute of Atomic Energy, Moscow, 1993).
35. O. O. Patarakin and V. N. Tikhonov, in *Proceedings of the International Conference on Meson and Nuclei at Intermediate Energies, Dubna, Russia, 1994,* Ed. by V. Khanhasayev, p. 255.
36. O. O. Patarakin, V. N. Tikhonov, and K. N. Mukhin, Nucl. Phys. A **598**, 335 (1996).
37. CHAOS Collab. (O. Patarakin), in *Proceedings of the Workshop on Chiral Dynamics, Mainz, Germany, 1997,* Ed. by A. M. Bernstein, D. Drechsel, and T. Walcher (Springer-Verlag, Berlin, 1998), p. 376.
38. J. B. Lange *et al.*, πN-Newsletter **13**, 32 (1997).
39. M. Kermani, O. O. Patarakin, V. N. Tikhonov, *et al.*, πN-Newsletter **13**, 27 (1997).
40. M. Kermani, O. O. Patarakin, G. R. Smith, *et al.*, Phys. Rev. C **58**, 3431 (1998).
41. M. E. Sevior, P. A. Amadruz, F. Bonutti, *et al.*, πN-Newsletter **15**, 48 (1999).
42. V. N. Maĭorov, O. O. Patarakin, and V. N. Tikhonov, Yad. Fiz. **63**, 1699 (2000) [Phys. At. Nucl. **63**, 1612 (2000)].
43. V. V. Vereshchagin, K. N. Mukhin, and O. O. Patarakin, Usp. Fiz. Nauk **170**, 353 (2000).
44. C. Goebel, Phys. Rev. Lett. **1**, 337 (1958).
45. G. Chew and F. Low, Phys. Rev. **113**, 1640 (1959).
46. V. N. Gribov, Nucl. Phys. **5**, 653 (1958).
47. V. V. Anisovich, A. A. Ansel'm, and V. N. Gribov, Zh. Éksp. Teor. Fiz. **42**, 224 (1962) [Sov. Phys. JETP **15**, 159 (1962)].
48. A. V. Aref'ev *et al.*, Yad. Fiz. **5**, 1060 (1967) [Sov. J. Nucl. Phys. **5**, 757 (1967)]; **10**, 797 (1969) [**10**, 460 (1969)].
49. S. Weinberg, Phys. Rev. Lett. **17**, 616 (1966); **18**, 188 (1967).
50. M. G. Olson and L. Turner, Phys. Rev. Lett. **20**, 1127 (1968).
51. F. Pais and S. B. Treiman, Phys. Rev. **168**, 1858 (1968).
52. Yu. A. Batusov, S. A. Bunyatov, V. M. Sidorov, and V. A. Yarba, Yad. Fiz. **1**, 526 (1965) [Sov. J. Nucl. Phys. **1**, 374 (1965)].
53. P. I. Golubnichiĭ *et al.*, At. Énerg. **22**, 108 (1967).
54. V. Auslander *et al.*, Phys. Lett. B **25B**, 433 (1967).
55. V. L. Auslender *et al.*, Yad. Fiz. **9**, 114 (1969) [Sov. J. Nucl. Phys. **9**, 69 (1969)].
56. E. Colton *et al.*, Phys. Rev. D **7**, 3267 (1973).
57. S. Protopoppescu *et al.*, Phys. Rev. D **7**, 1279 (1973).
58. B. Hyams *et al.*, Nucl. Phys. B **64**, 134 (1973).
59. P. Estabrooks and A. D. Martin, Nucl. Phys. B **95**, 322 (1975).
60. W. Hoogland *et al.*, Nucl. Phys. B **126**, 109 (1977).
61. M. J. Corden *et al.*, Nucl. Phys. B **157**, 250 (1979).
62. F. M. Filler, Dokl. Akad. Nauk SSSR **177**, 1058 (1967) [Sov. Phys. Dokl. **12**, 1138 (1968)].
63. J. P. Baton, G. Laurens, and J. Reignier, Nucl. Phys. B **3**, 349 (1967).
64. V. V. Serebryakov and D. V. Shirkov, Phys. Lett. B **25B**, 138 (1967).

65. S. M. Roy, Phys. Lett. B **36B**, 353 (1971).
66. G. R. Smith *et al.*, Nucl. Instrum. Methods Phys. Res. A **362**, 349 (1995).
67. L. L. Basdewant, Nucl. Phys. B **72**, 413 (1974).
68. S. Weinberg, Physica A (Amsterdam) **96**, 327 (1979).
69. S. Weinberg, *The Quantum Theory of Fields* (Cambridge Univ. Press, Cambridge, 1995), Vols. 1, 2.
70. J. Gasser and H. Leutwyler, Phys. Lett. B **125B**, 325 (1983).
71. J. Gasser and H. Leutwyler, Nucl. Phys. B **250**, 465 (1985); **250**, 517 (1985); **250**, 539 (1985).
72. J. Lowe, Lect. Notes Phys. **513**, 375 (1998).
73. P. Truol, in *Proceedings of the 5th Workshop on Heavy Quarks at Fixed Target (HQ2K), Rio de Janeiro, Brazil, 2000,* Frascati Phys. Ser. **20**, 49 (2001); hep-ex/0012012.
74. B. Adeva *et al.*, CERN SPSLC Proposal (1994).
75. L. G. Afanasyev *et al.*, Phys. Lett. B **308**, 200 (1993).
76. G. Chanfray *et al.*, Phys. Lett. B **256**, 325 (1991).
77. F. Bonitty *et al.*, Phys. Rev. Lett. **77**, 603 (1996).
78. Crystall Ball Collab. (B. M. K. Nefkens and A. B. Starostin), πN-Newsletter **15**, 78 (1999).
79. M. J. Vicente-Vakas and E. Oset, Phys. Rev. C **60**, 64621 (1999).
80. T. Hatsuda, T. Kunihiro, and H. Shemizu, Phys. Rev. Lett. **82**, 2840 (1999).

Translated by A. Isaakyan

Physics of Atomic Nuclei, Vol. 65, No. 7, 2002, pp. 1173–1187. Translated from Yadernaya Fizika, Vol. 65, No. 7, 2002, pp. 1206–1219.

90th ANNIVERSARY OF I.I. GUREVICH'S BIRTHDAY

Investigation of Neutrino Properties in Experiments at Nuclear Reactors: Present Status and Prospects

L. A. Mikaelyan

Institute of General and Nuclear Physics, Russian Research Centre Kurchatov Institute,
pl. Kurchatova 1, Moscow, 123182 Russia

Received April 20, 2001; in final form, August 24, 2001

Abstract—The present status of experiments that are being performed at nuclear reactors in order to seek the neutrino masses, mixing, and magnetic moments, whose discovery would be a signal of the existence of physics beyond the Standard Model, is considered, along with their future prospects.

INTRODUCTION

Presently, searches for neutrino oscillations and a determination of the neutrino mass structure are among the foremost lines of investigation in experimental particle physics. After a long period of searches for neutrino oscillations in short-baseline experiments, explorations at nuclear reactors have entered a new phase. Investigations in these realms are now being conducted at ever greater distances, and, for the first time, the masses of the neutrinos and their mixing are being investigated precisely in those regions that are suggested by the observations of atmospheric and solar neutrinos.

Specifically, we consider the following experiments and projects:

(i) the CHOOZ experiment that had been performed by a collaboration of laboratories from Italy, France, Russia, and the United States of America and which had been devoted to searches for antineutrino oscillations at long distances from the reactor used (the experiment had been completed in 1999; the results were published in [1]);

(ii) the Palo Verde reactor-based experiment that had been performed by a collaboration of laboratories from the United States of America and which had been aimed at long-baseline searches for neutrino oscillations (the measurements had been completed by the middle of 2000; the results obtained in the exposures of 1998 and 1999 were published in [2]);

(iii) the project of the Kr2Det experiment that will seek oscillations at long distances from the reactor used the project, which will pursue oscillations characterized by rather small mixing angles, currently being developed for the Krasnoyarsk underground laboratory (600 mwe) [3] (it is foreseen that the development of the project will have been completed by 2003);

(iv) the KamLAND experiment that is being performed at Kamioke by researchers from Japan and the United States of America and which is devoted to searches of neutrino oscillations at very long distances [4] (it is expected that the first results will have been obtained in 2002).

The results of these laboratory experiments will make it possible to reveal the role of electron neutrinos in the anomalies of atmospheric neutrinos, to verify the hypothesis of solar-neutrino oscillations, and to establish the mass structure of the electron neutrino within the model involving the mixing of three neutrinos.

By searches of oscillations at long distances, one usually implies experiments in which detectors are positioned at distances of about 1 km from the reactor employed (long-baseline experiments). Experiments where the reactor-to-detector distance is 100 km or more are referred to as very long baseline ones. It should be emphasized that it is owing to impressive advances in developing procedures for reactor-antineutrino detection that long-baseline and very long baseline investigations became possible.

An extensive list of references on the problem of neutrino oscillations from the studies of Pontecorvo and his colleagues [5], an account of the theory and of the phenomenology of this phenomenon, and a description of the experiments that had been performed prior to 1997 can be found in the review articles [6, 7].

Another line of neutrino investigations at nuclear reactors focuses on attempts at observing the neutrino magnetic moment. A discovery of the neutrino magnetic moment at a level of $10^{-11}\mu_B$ (μ_B is the Bohr magneton) in a laboratory experiment would be of crucial importance for particle physics and neutrino astrophysics [8, 9]. In order to explain so "large" a value of the neutrino magnetic moment, it would be necessary to introduce, in the theory of weak interaction, the right-handed W boson in addition to the left-handed one; moreover, the interaction of the neutrino magnetic moment with the magnetic field in the convective zone of the Sun could enhance $\nu_e \to \nu_{\mu,\tau}$ transitions (spin—flavor precession) and lead to the emergence of a correlation between the recorded solar-neutrino flux and the magnetic activity of the Sun. It should be noted that such a correlation was indeed observed [10].

The experiments that were performed at the reactors in Rovno [11] and in Krasnoyarsk [12] (see also the review article of Derbin [13]) yielded the constraint $\mu_\nu \leq 2 \times 10^{-10}\mu_{\rm B}$, which is still far from the desired region of values. In Section 2, we consider the attempts that are being undertaken at present to improve the sensitivity of nuclear-reactor experiments to the neutrino magnetic moment. Projects that are based on the use of intense artificial sources of neutrinos and antineutrinos and which seem rather promising are beyond scope of this article.

1. SEARCHES OF ANTINEUTRINOS

1.1. Reactor Antineutrinos

A liquid organic scintillator serves as a target for reactor antineutrinos in all experiments that are devoted to searches for neutrino oscillations and which are considered here. Antineutrinos are recorded by the products of the inverse-beta-decay reaction

$$\bar{\nu}_e + p \to e^+ + n, \tag{1}$$

whose threshold is 1.804 MeV. The cross section for reaction (1) can be represented as

$$\sigma(E) = 9.556 \times 10^{-44}(886/\tau_n) \tag{2}$$
$$\times [(E-\Delta)^2 - m^2]^{1/2}(E-\Delta)(1+\delta)\ ({\rm cm}^2),$$

where $\Delta = 1.293$ MeV, the incident-antineutrino energy E and the electron mass m are expressed in MeV; the quantity $\delta \ll 1$ takes into account recoil and weak-magnetism effects and the radiative correction [14], and τ_n is the free-neutron lifetime expressed in seconds.

The positron kinetic energy T in reaction (1) is related to the absorbed-antineutrino energy by the equation

$$T \approx E - 1.8\,{\rm MeV}. \tag{3}$$

In the majority of the cases, photons arising in positron annihilation are absorbed in the sensitive volume, with the result that the recorded positron energy increases by about 1 MeV in relation to than in (3). In all experiments, use is made of the method of delayed coincidences between the signals from the positron and the neutron. In the CHOOZ and the Palo Verde experiment, neutrons are recorded by the photon cascade having the total energy of about 8 MeV and arising upon neutron capture by gadolinium nuclei that are introduced in the target scintillator. Neither the KamLAND nor Kr2Det project employs gadolinium—the neutron signal is generated there by 2.2-MeV photons accompanying neutron capture in hydrogen.

In order to analyze the results of relevant experiments, it is of crucial importance to know the properties of a reactor as a source of antineutrinos. Per gigawatt of thermal power, a nuclear reactor generates more than 2×10^{20} electron antineutrinos per second, the majority of which originate from the beta decay of nuclear fragments produced in the reactor core upon the fission of uranium and plutonium isotopes; about a quarter of these antineutrinos fall in the energy region above the threshold for reaction (1). Since the second half of the 1970s, it has been known that the fragments of different fissile isotopes emit electron antineutrinos having noticeably different spectra. For the fission of ^{235}U, ^{239}Pu, and ^{241}Pu, the most precise information about the spectra in the region above 1.8 MeV was obtained at the Institute Laue—Langevin (ILL, Grenoble) by the method of conversion of the beta spectra measured for the mixture of fragments [16]; for ^{238}U, use is made of the calculated value [17]. Data that concern the reactor power and the current isotope composition of the burning nuclear fuel and which are necessary for computing the flux and the spectrum of antineutrinos are presented by the reactor personnel.

With the aim of obtaining a reference for normalizing data from the CHOOZ experiment, which had already been planned at that time, the collaboration of College de France (Paris), Kurchatov Institute (Moscow), and LAPP (Annecy) measured in 1992—1994 the total cross section for reaction (1) at a distance of 15 m from the Bugey reactor, whose power is 2.8 GW. The result was [18]

$$\sigma_{\rm expt} = 5.750 \times 10^{-43}\ {\rm cm}^2/({\rm fission\ event}) \pm 1.4\%, \tag{4}$$

which is in good agreement with the cross section σ_{V-A} calculated by taking the convolution of the cross section from relation (2) and the spectrum of reactor electron antineutrinos:

$$\sigma_{\rm expt}/\sigma_{V-A} = 0.987 \pm 1.4\%\ ({\rm expt.}) \pm 2.7\%(\sigma_{V-A}). \tag{5}$$

Thus, the cross section measured experimentally is more accurate than the computed value and can serve as a metrological reference for cross sections in the absence of oscillations. It should be noted that the fine features recently revealed in the emission of reactor electron antineutrinos above the threshold for reaction (1) increase the error in the cross section (4) by about 0.5% [19]. This circumstance was taken into account in determining the parameters of oscillations in the CHOOZ experiment.

In the next section of the article, we will consider the spectrum of reactor electron antineutrinos below the threshold for reaction (1), because knowledge of this spectrum is necessary for performing and interpreting experiments that seek the neutrino magnetic moment.

1.2. Motivation

First of all, we recall basic relations that are valid in the case of mixing of two neutrino-mass eigenstates ν_1 and ν_2, with the corresponding masses being m_1 and m_2. We have

$$\nu_e = \cos\theta\nu_1 + \sin\theta\nu_2. \tag{6}$$

In this case, the survival probability $P(\nu_e \to \nu_e)$—that is, the probability that a neutrino that is produced in the source used will retain its original nature at a distance L (m) from the source—is given by

$$P(\nu_e \to \nu_e) = 1 - \sin^2 2\theta \sin^2(1.27\Delta m^2 L E^{-1}), \tag{7}$$

where $\sin^2 2\theta$ is the mixing parameter, $\Delta m^2 \equiv m_2^2 - m_1^2$ (eV^2) is the mass parameter, and E (MeV) is the neutrino energy.

In experiments, oscillations are sought by a characteristic distortion of the spectrum of electron antineutrinos (positrons) and by the reduction of the event-counting rate. For reactor electron antineutrinos, the relevant distortions of the spectrum and the accompanying reduction of the counting rate are maximal, provided that

$$\Delta m^2 L \approx 5 \text{ eV}^2 \text{ m}. \tag{8}$$

Relations (7) and (8) demonstrate that, for example, at a distance of 1 km from the reactor, the sensitivity of the experiment being discussed is the highest at $\Delta m^2 \approx 5 \times 10^{-3}$ eV^2 and that it becomes poorer fast as Δm^2 decreases.

In the early 1990s, there appeared motivations for seeking reactor-neutrino oscillations in the range $\Delta m^2 = 10^{-2}$–10^{-3} eV^2, which had not yet been explored by that time. The investigation of atmospheric neutrinos with the aid of the Kamiokande II and IMB Cherenkov detectors in [20] revealed that the ratio of the muon-neutrino flux to the electron-neutrino flux is two-thirds as great as its computed counterpart. This discrepancy, known as the atmospheric-neutrino anomaly, could be explained under the assumption that intense transitions occur through the $\nu_\mu \leftrightarrow \nu_e$ channel, through the $\nu_\mu \leftrightarrow \nu_\tau$ channel, or through both these channels simultaneously. As to the mass parameter Δm^2_{atm}, it could lie within a wide range of values between 10^{-1} and 10^{-3} eV^2. At present, observations of atmospheric neutrinos have yielded even more compelling grounds to believe that neutrino oscillations do indeed exist. If the SuperKamiokande data are analyzed under the assumption that only the $\nu_\mu \leftrightarrow \nu_\tau$ channel is operative, the best description is obtained at the following parameter values [21]:

$$\Delta m^2_{\text{atm}} \approx 3 \times 10^{-3} \text{ eV}^2 \tag{9}$$

(the most probable value),

$$\sin^2 2\theta_{\text{atm}} > 0.88.$$

It should be emphasized that the SuperKamiokande data do not at all rule out a noticeable contribution from the $\nu_e \leftrightarrow \nu_\mu$ channel [22].

For more than three decades, the deficit of solar neutrinos in relation to the computed data has been considered as a strong argument in favor of the existence of electron-neutrino oscillations. An analysis of solar-neutrino data accumulated by 1998 and the inclusion of the solar-matter effect, known as the Mikheev–Smirnov–Wolfenstein (MSW) effect, made it possible to find, in the ($\sin^2 2\theta$, Δm^2) plane, a few regions where parameter values ensure a solution to the solar-neutrino problem [23]. According to [24], the situation changed as soon as new data appeared after the commissioning of the SuperKamiokande facility in 1998. At present, one of the solutions—it is referred to as the Large Mixing Angle (LMA) MSW solution—provides the best fit to the observation data. The most probable values of the parameters that characterize this solution are

$$\Delta m^2_{\text{sol}} \approx 3 \times 10^{-5} \text{ eV}^2, \quad \sin^2 2\theta_{\text{sol}} \approx 0.8. \tag{10}$$

In the case where two mass eigenstates ν_1 and ν_2 are mixed, there is obviously one mass parameter $\Delta m^2 = m_2^2 - m_1^2$. The mixing of at least three mass eigenstates is necessary for two mass parameters Δm^2_{atm} and Δm^2_{sol} to exist. In the case where three mass eigenstates ν_1, ν_2, and ν_3 undergo mixing and where three active neutrino flavors ν_e, ν_μ, and ν_τ oscillate, there are generally three mass parameters: $\Delta m^2_{21} = m_2^2 - m_1^2$, $\Delta m^2_{31} = m_3^2 - m_1^2$, and $\Delta m^2_{32} = m_3^2 - m_2^2$. Of these, only two are independent, since $\Delta m^2_{21} \equiv \Delta m^2_{31} - \Delta m^2_{32}$. According to (9) and (10), one of these parameters is two orders of magnitude greater than the other; therefore, we have

$$\Delta m^2_{\text{sol}} = \Delta m^2_{21} \approx 3 \times 10^{-5} \text{ eV}^2, \tag{11}$$

$$\Delta m^2_{\text{atm}} \approx \Delta m^2_{31} \approx \Delta m^2_{32} \approx 3 \times 10^{-3} \text{ eV}^2.$$

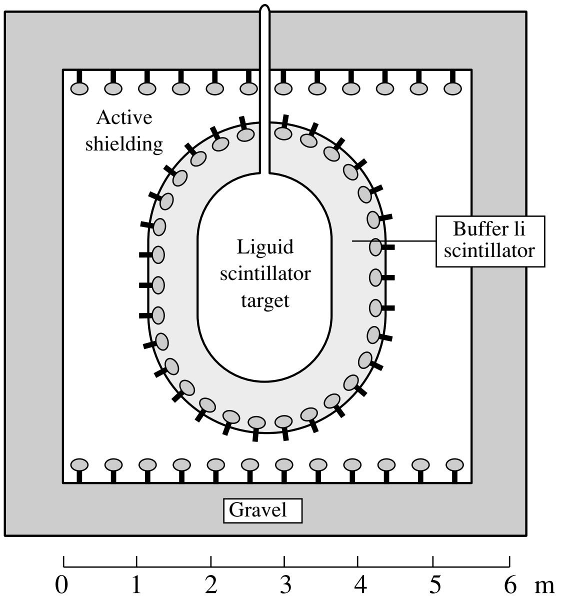

Fig. 1. Layout of the CHOOZ detector (its description is given in the main body of the text).

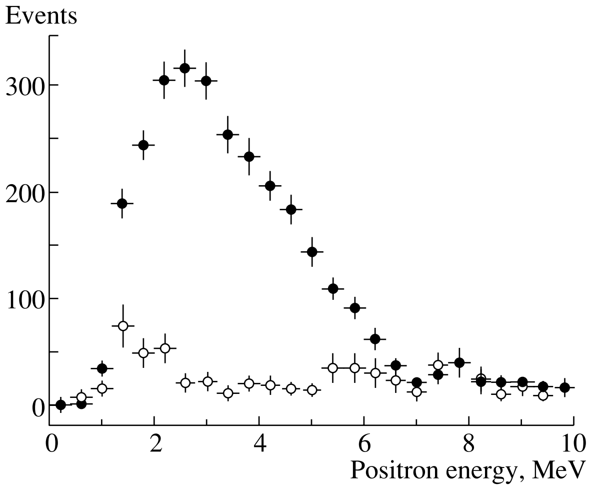

Fig. 2. Spectra of positrons in the CHOOZ experiment during the reactor (closed circles) operating and (open circles) shutdown periods.

In the case of reactor neutrinos that is considered here, there are two mixing parameters in the adopted scheme. They are expressed in terms of the mixing-matrix elements U_{ei} appearing in the superposition $\nu_e = U_{e1}\nu_1 + U_{e2}\nu_2 + U_{e3}\nu_3$ $(\sum U_{ei}^2 = 1)$; that is,

$$\begin{aligned} \sin^2 2\theta_{\rm LBL} &= 4U_{e3}^2(1 - U_{e3}^2), \\ \sin^2 2\theta_{\rm VLBL} &= 4U_{e1}^2 U_{e2}^2, \end{aligned} \tag{12}$$

where LBL and VLBL stand for, respectively, long-baseline and very long baseline reactor-to-detector distances.

Thus, long-baseline and very long baseline reactor experiments make it possible to (i) study the role of the electron neutrino in the region of atmospheric-neutrino oscillations; (ii) verify whether the hypothesis specified by (10) is valid for solar-neutrino oscillations; and (iii) obtain, within the model of three neutrino flavors, the full pattern of the mass structure of the electron neutrino.

The question of the number of neutrino flavors that is greater than three is beyond the scope of the present article. Yet, it is worth noting that, according to the data of the LSND experiment (Los Alamos), $\nu_\mu \to \nu_e$ transitions, which are characterized by a rather small mixing angle, are observed in the region of large mass-parameter values of $\Delta m^2_{\rm LSND} \sim 1$ eV^2 [25]. The existence of three mass parameters, $\Delta m^2_{\rm sol}$, $\Delta m^2_{\rm atm}$, and $\Delta m^2_{\rm LSND}$, requires introducing, at least, yet another mass eigenstate ν_4 and one sterile neutrino ν_s (either sterile neutrinos do not interact with other particle species at all, or the corresponding coupling constant is much less than the Fermi constant). The problem of sterile neutrinos has been discussed in the literature since the first studies of Pontecorvo [5]; in recent years, interest in this problem has become especially acute in connection with reports on the LSND experiments (see, for example, [26, 27] and references therein). The potential of nuclear reactors for sterile-neutrino searches was schematically considered in [28].

1.3. Experiments and Projects

CHOOZ

The antineutrino detector used was constructed in an underground (300 mwe) gallery at distances of 1000 and 1100 m from two PWR reactors. The total rated power of the reactors was 8.5 GW. The detector (see Fig. 1) was formed by three concentric spheres. The central zone, which contained 5 t of a liquid organic scintillator with an addition of gadolinium (about 1 g/l), served as a target for electron neutrinos. The target was surrounded by a liquid-scintillator layer (not containing gadolinium) of thickness 70 cm followed by third layer (90 t of a scintillator), which acted as a passive and an active shielding of the detector. Two inner zones of the detector were viewed by 192 eight-inch phototubes mounted on a nontransparent screen. The second zone (buffer volume), which absorbed annihilation photons and photons arising upon neutron capture in gadolinium that escaped from a comparatively small target, improved considerably the calorimetric properties of the detector.

The experiments was conducted from April 1997 to July 1998. This was the period within which the newly constructed reactors gradually approached the rated mode of operation. This circumstance made it possible to have sufficient time for performing measurements during the operation of each of the two reactors, with the other reactor being off; during the simultaneous operation of the two reactors; and during the period within which the reactors were both off (see Table 1).

Neutrino events were required to satisfy the following selection criteria: (a) The energy of the first (positron) event and the energy of the second (neutron) event must lie within the ranges 1.3–8 and 6–12 MeV, respectively. (b) The time interval between the positron and the neutron event must be in the range 2–100 μs. (c) The spatial conditions are such that the distance between the phototube surface and any event must not be less than 30 cm and that the first and the second event must not be separated by a distance longer than 100 cm. As soon as these selection criteria are imposed, the efficiency of neutrino-event detection becomes $\epsilon = (69.8 \pm 1.1)\%$.

In all, about 2500 antineutrinos were recorded over the time of measurements, with the measured counting rate being 2.58 $\bar{\nu}_e$/d per 1 GW of reactor power; the typical event-to-background ratio was 10 : 1. The positron spectra measured within the reactor operating and shutdown periods are displayed in Fig. 2. The ratio $R_{\text{meas/calc}}$ of the measured neutrino events to that which is expected in the absence of oscillations proved to be

$$\text{CHOOZ}: R_{\text{meas/calc}} \tag{13}$$
$$= 1.01 \pm 2.8\% \text{ (stat.)} \pm 2.7\% \text{ (syst.)}.$$

In this result, the main contribution to the systematic error comes from the uncertainties in the reaction cross section (1.9%—see Subsection 2.1 below), in the efficiency of the neutrino-event detection (1.4%), and in the number of target protons (0.8%).

Constraints on the oscillation parameters were obtained by comparing the entire body of information accumulated in the experiment with the values that are expected in the absence of oscillations. The result (the "CHOOZ" curve in Fig. 3) depends directly on knowledge of the absolute values of the characteristics of the neutrino flux and spectrum, on the cross section for the inverse-beta-decay reaction, and on the features of the detector. As can be seen from Fig. 3, electron neutrinos do not show, at the achieved level of accuracy, oscillations in the region Δm^2_{atm}:

$$\sin^2 2\theta_{\text{CHOOZ}} \leq 0.1, \tag{14}$$
$$U^2_{e3} \leq 2.5 \times 10^{-2} \text{ (at } \Delta m^2 = 3 \times 10^{-3}\ \text{eV}^2\text{)}.$$

The result presented in (14) establishes definitively that $\nu_\mu \leftrightarrow \nu_e$ oscillations cannot play a decisive role in the atmospheric-neutrino anomaly.

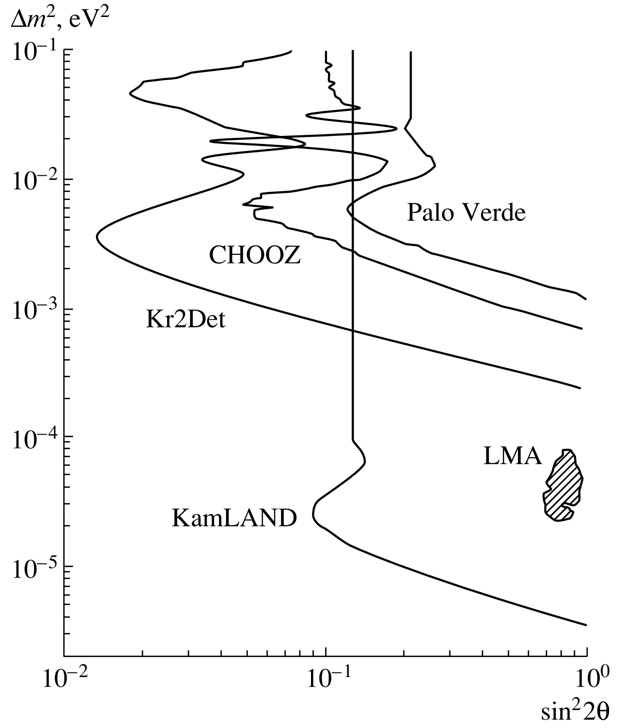

Fig. 3. Constraints obtained for the oscillation parameters in the CHOOZ and Palo Verde experiments at a 90% C.L. and constraints expected in the Kr2Det and KamLAND projects.

Searches for oscillations in long-baseline and very long baseline experiments in ever lower fluxes of electron antineutrinos require drastically improving the techniques for recording reactor neutrinos. The background level of about 0.25 event/d per 1 t of target mass achieved in the CHOOZ experiment is nearly 1000 times lower than in any of the previous experiments of this kind. In this connection, we would like to note two key points. First, this is the underground deployment of the experiment. Under a rock layer of thickness 300 mwe, the muon flux, which is the main source of a correlated background, decreases in relation to that at the Earth's surface by a factor of about 300 down to a level of 0.4/m^{2}s. The second point is associated with the design of the detector. The intro-

Table 1. Modes of data accumulation in the CHOOZ experiment

Reactor 1	Reactor 2	Time, d	W, GW
+	0	85.7	4.03
0	+	49.5	3.48
+	+	64.3	5.72
0	0	142.5	–

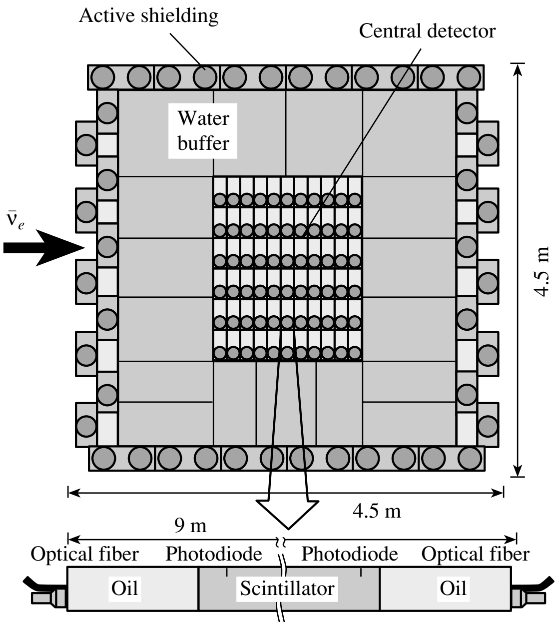

Fig. 4. Layout of the Palo Verde detector.

duction of the buffer zone (see Fig. 1) reduces the level of the random-coincidence background, shielding the fiducial volume from the high natural radioactivity of the phototube glass and structural materials.

Palo Verde

In the Palo Verde experiment, three PWR reactors belonging to the same type and having the total (thermal) power of 11.6 GW are at distances of 890, 890, and 750 m from a detector constructed in an underground laboratory (32 mwe). Once a year, each of the reactors is shut down for about 40 days, while the other reactors continues operating over this time interval.

The experiment being discussed employs a detector whose design is totally different from that of the CHOOZ detector and uses more involved methods for selecting neutrino events. These distinctions are dictated by a much more intense muon flux to the detector (about $20/\mathrm{m}^2$ s) and by a less favorable schedule of reactor operation. The electron-antineutrino detector has the form of a 6×11 matrix composed of long sections whose dimensions are $12.7 \times 25 \times 900$ cm. The 7.4-m-long central part of each section contains a liquid scintillator with an addition of gadolinium; the endface parts of a section are filled with mineral oil, each of such endface parts housing a phototube (see Fig. 4). The total mass of the target scintillator is 12 t. From all sides, the target is surrounded by a purified-water layer (passive shielding) followed by the scintillation sections of an active shielding, which generate, in response to the propagation of cosmic-ray muons through them, anticoincidence signals, whose frequency is 2 kHz.

A preliminary selection of candidates for events of reaction (1) is accomplished according to the following criteria: (a) The positron event must be fast (30 ns), and there must be a coincidence between three sections, with the thresholds being 500 keV (positron ionization) in one of them and 40 keV (Compton electrons from annihilation photons) in the other two. (b) The same conditions must hold for the neutron event. (c) The expectation time for the second event must be 450 μs, which is much longer than the neutron lifetime in the scintillator (about 30 μs); useful and background events are detected in the first part of the interval, while the background of random coincidences is recorded within its second part. Events satisfying the above criteria were accumulated and were subjected to additional amplitude and spatial criteria in the course of a subsequent treatment. Upon imposing all the selection criteria, the efficiency of electron-antineutrino detection became 11% at the effect-to-background ratio of 1 : 1.

The total time of data accumulation in 1998 and 1999 was about 202 days; for 59 days of these, two of the three reactors operated. Two different methods were applied to single out the neutrino signal. Of these, one was the usual on–off method, which was based on measuring the electron-antineutrino flux within the shutdown period of one of the reactors, in which case the electron-antineutrino flux from the operating reactors was considered as a background component. To the best of my knowledge, the other method was applied for the first time. This method made it possible to employ the entire body of accumulated data and to separate the useful effect from the background directly in these data. This method, dubbed by the authors a swap method, relies on the similarity of the amplitude spectra of the the first and the second signal in time that stem from a background event and on their pronounced distinction in the case of the positron and neutron originating from reaction (1).

As a result, it was found that the measured number of neutrino events and that which was expected in the absence of neutrino oscillations satisfy the relation

$$\begin{aligned} &\text{Palo Verde:} \quad R_{\mathrm{meas/calc}} \\ &= 1.04 \pm 3\% \text{ (stat.)} \pm 8\% \text{ (syst.)}. \end{aligned} \tag{15}$$

In this result, the systematic uncertainty is presently three times as great as the analogous uncertainty in the CHOOZ experiment [see relation (13)]. It is foreseen that a further data treatment will lead to a reduction of the uncertainties (F. Boehm, private communication). Figure 3 shows the constraints that were obtained for the neutrino-oscillation parameters by using the entire body of information accumulated by the end of 1999 (Palo Verde curve).

Kr2Det project

The Kr2Det project is that of an experiment that will seek oscillations in the region around $\Delta m^2_{\text{atm}} \sim 3 \times 10^{-3}$ eV^2, but which is expected to have a much higher sensitivity to the mixing parameter than the CHOOZ and the Palo Verde experiment. The implementation of this project would make it possible to measure the mixing-matrix element U_{e3} or to set a more stringent limit on it. It is interesting to note that, if the LMA MSW version does indeed solve the solar-neutrino problem, the analysis [29] shows that the value of U^2_{e3} may be close to the limit that is set by the current constraint $U^2_{e3} \leq 2.5 \times 10^{-2}$.

The basic features of the experiment being discussed are the following:

(i) In order to achieve a higher rate of data accumulation, the target mass is enhanced in relation to that of the CHOOZ detector by nearly one order of magnitude. For a target, use is made of an organic scintillator of mass 45 t without gadolinium additions.

(ii) In order to eliminate the majority of methodological errors, measurements will be performed by simultaneously using two identical spectrometers of electron antineutrinos—a far and a near one that are positioned at distances of, respectively, 1100 and 150 m from the reactor.

(iii) The experiment will be performed at a depth of 600 mwe, whereby the cosmic-ray component of the background is suppressed down to a rather low level.

The detectors have a three-zone structure (see Fig. 5). The phototubes used are mounted on a metal sphere that separates zones *2* and *3* by light, which are filled with nonscintillating mineral oil. The expected magnitude of a scintillation signal is 100 photoelectrons per 1 MeV of energy absorbed in the scintillator. The energy resolution is $\sigma \approx 0.14\sqrt{E(\text{MeV})}$.

Candidates for a neutrino event are required to satisfy the following selection criteria: (a) The energy of the first (positron) event and the energy of the second (neutron) event must lie in the ranges 1.2–9.0 and 1.7–3.0 MeV, respectively. (b) The second event must be recorded within the time window 5–500 μs. (c) The spatial distances between the events must not exceed 100 cm. The duration of an anticoincidence signal is 1000 μs at a repetition frequency of about 10/s. Under these conditions, events of reaction (1) are recorded with an efficiency 80%, the counting rate in the far detector being $N_\nu = 52\bar{\nu}_e/\text{d}$; the expected background level is about 10% of the magnitude of the useful effect.

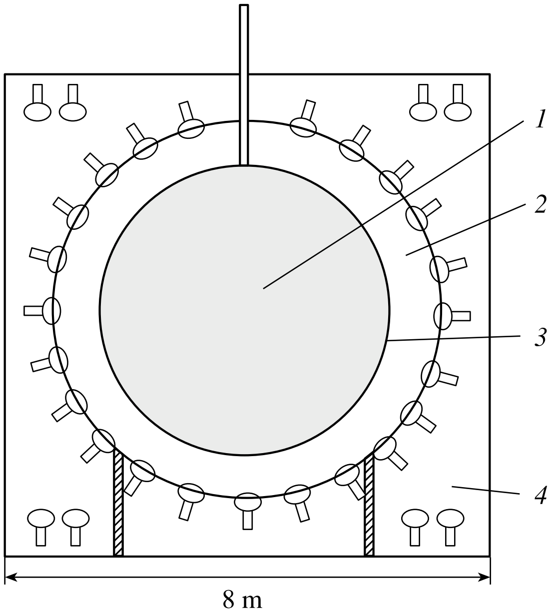

Fig. 5. Layout of the Kr2Det detector: (*1*) target (liquid scintillator), (*2*) buffer (paraffin oil), (*3*) transparent film, and (*4*) anticoincidence region (paraffin oil).

In the case where there are no oscillations, the ratio $X_{f,n}$ of the positron spectra measured in reaction (1) simultaneously by the far (f) and by the near (n) detector,

$$X_{f,n} = C(1 - \sin^2 2\theta \sin^2 \varphi_f)(1 - \sin^2 2\theta \sin^2 \varphi_n)^{-1} \tag{16}$$

($\varphi_{f,n} = 1.27\Delta m^2 L_{f,n} E^{-1}$, $L_{f,n} = 1100$, 150 m), is independent of the positron energy. Searches for nonzero values of the oscillation parameters $\sin^2 2\theta$ and Δm^2 are based on an analysis of small deviations of the ratio in (16) from a constant value. The results of this analysis do not depend on precise knowledge of the spectrum of reactor antineutrinos, on the reactor power, on the number of protons in the target, or on the detection efficiency. However, the possible distinction between the spectral features of the detectors used requires monitoring. A method is being developed that would make it possible to reveal this distinction and, if necessary, to introduce relevant corrections. It is assumed that the corresponding systematic uncertainty will not exceed a few tenths of a percent. The expected constraints are displayed in Fig. 3 (Kr2Det curve). It is foreseen that the experiment will record 40000 electron antineutrinos.

KamLAND

The electron-antineutrino flux is 1000 times less in this experiment than in the CHOOZ experiment. Fifty reactors of an atomic power plant in Japan,

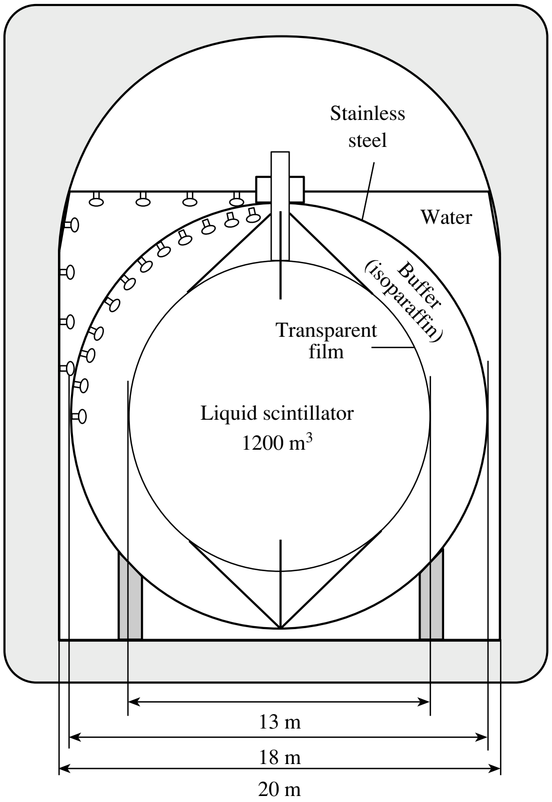

Fig. 6. Layout of the KamLAND detector

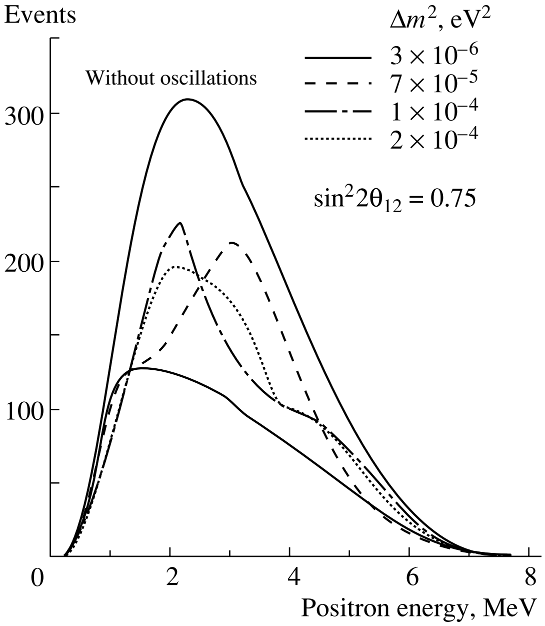

Fig. 7. Positron spectra in the KamLAND experiment for a few values of the mass parameter from the LMA MSW region (calculation).

which have a total thermal power of about 130 GW, serve as a source of antineutrinos. The detector is positioned at distances of about 100 to 800 km from the reactors. About 70% of the electron-antineutrino flux is generated by the reactors occurring at distances of 145 to 214 km from the detector. The flux never decreases down to zero, but it undergoes seasonal variations, changing by ±(10–15)% around its mean-annual value.

The detector is being constructed at a depth of 2700 mwe in the cavern that previously housed the Kamiokande facility. Phototubes that cover 30% of the surface view, through the oil layer of the buffer zone of thickness 2.5 m, a spherical target containing 1000 t of a liquid scintillator (see Fig. 6). In contrast to the detectors described above, the outer layer is filled with water here. In just the same way as in the other cases, this zone plays the role of a passive and an active shielding. The expected muon flux to the detector is about 0.3/s. In order to reduce the background associated with natural radioactivity, it is proposed to purify the target scintillator from uranium and thorium to a level of 10^{-16} g/g. Special measures are taken to prevent the penetration of radon into the scintillator. In addition to conventional criteria for selecting neutrino events in amplitude, in time, and in positron–neutron spacing, some additional criteria will be imposed to eliminate the background (for more details, see [4]). At a 100% detection efficiency, the neutrino-event counting rate computed in the absence of oscillations is about 800/yr, the event-to-background ratio being not poorer than 10 : 1. However, it is indicated in the project that, in the positron-energy region extending up to about 2.5 MeV, there must be an irremovable background of so-called terrestrial antineutrinos originating from the chains of uranium and thorium decays, its magnitude in this energy region being commensurate with the signal from the reactors used. In passing, we note that problems associated with studying the antineutrino activity of the Earth, which are of prime interest for geology, were posed more than forty years ago [30].

In Fig. 7, the positron spectra expected in the experiment are shown for a few values of Δm^2. It is believed that measurements spanning a period of three years will make it possible to establish with confidence whether the electron neutrino oscillates with parameters from the LMA MSW region (see the KamLAND curve in Fig. 3).

2. SEARCHES FOR THE NEUTRINO MAGNETIC MOMENT

2.1. Spectra and Cross Sections

Information presented in this section may be of use in considering and planning reactor experiments aimed at improving the sensitivity of searches for the neutrino magnetic moment.

Electron-antineutrino scattering on free electrons

An antineutrino that possesses a magnetic moment μ_ν can be scattered by an electron. The cross section for magnetic scattering on a free electron at rest, $d\sigma^m/dT$, is proportional to μ_ν^2 [31]; that is,

$$d\sigma^m/dT = \pi r_0^2(\mu_\nu/\mu_{\rm B})^2(1/T - 1/E), \qquad (17)$$

where $\pi r_0^2 = 2.495 \times 10^{-25}$ cm^2, E is the incident-neutrino energy, and $\mu_{\rm B}$ is the Bohr magneton.

The cross section for $\bar{\nu}_e e$ scattering associated with weak interaction (see, for example, [8]) is given by

$$d\sigma^w/dT = G_{\rm F}^2(m/2\pi)[4x^4 + (1+2x^2)^2 \qquad (18)$$
$$\times (1 - T/E)^2 - 2x^2(1+2x^2)mT/E^2],$$

where $x^2 = \sin^2\theta_{\rm W} = 0.232$ is the Weinberg angle and $G_{\rm F}^2(m/2\pi) = 4.31 \times 10^{-45}$ cm^2/MeV.

For a given value of the incident-neutrino energy, the kinetic energy of the recoil electron is constrained by the condition

$$T \le T_{\rm max} = 2E^2/(2E + m). \qquad (19)$$

An experiment consists in measuring the total spectrum of recoil electrons upon scattering associated with weak and magnetic interaction, $S^w(T) + S^m(T)$. The spectra $S^w(T)$ and $S^m(T)$ (cm^2 MeV^{-1} fission event^{-1}) are represented as the convolutions of the cross sections in (17) and (18) with the reactor-antineutrino spectrum $\bar{\nu}_e \rho(E)$ (MeV^{-1} fission event^{-1}). Here, scattering associated with weak interaction—a process of importance in its own right—plays the role of a background that is correlated with the operation of the reactor used. As the kinetic energy T of the recoil electron decreases, the spectrum $S^m(T)$ grows indefinitely, whereas the spectrum $S^w(T)$ tends to a constant limit (see Fig. 8). The two spectra become equal at $T = 300$ (2.5) keV for $\mu_\nu = 10^{-10}\mu_{\rm B}$ ($\mu_\nu = 10^{-11}\mu_{\rm B}$).

In order to discover the magnetic moment at the level of $\mu_\nu = 10^{-11}\mu_{\rm B}$, it is therefore necessary to measure the recoil-electron spectra in the energy region below a value of about 10 keV. At such low values of the recoil energy, the differential cross sections in (17) and (18) for the spectrum of reactor electron antineutrinos assume the asymptotic form

$$d\sigma^m/dT = 2.495 \times 10^{-47}\ {\rm cm}^2/T \qquad (20)$$
$$(\text{for } \mu_\nu = 10^{-11}\mu_{\rm B}),$$
$$d\sigma^w/dT = 10.16 \times 10^{-45}\ {\rm cm}^2/{\rm MeV}.$$

In this approximation, the recoil-electron spectra $S^{m,w}(T)$ are independent of the details of the shape of the spectrum $\rho(E)$—they are determined exclusively by the total number of antineutrinos per fission event, $N_\nu = \int \rho(E)dE$ (fission event^{-1}); that is,

$$S^m(T) = 2.495 \times 10^{-47} N_\nu/T\ {\rm cm}^2\ \text{fission event}^{-1} \qquad (21)$$
$$(\text{for} \quad \mu_\nu = 10^{-11}\mu_{\rm B}),$$
$$S^w(T) = 10.16 \times 10^{-45} N_\nu$$
$${\rm cm}^2\ {\rm MeV}^{-1}\ \text{fission event}^{-1}.$$

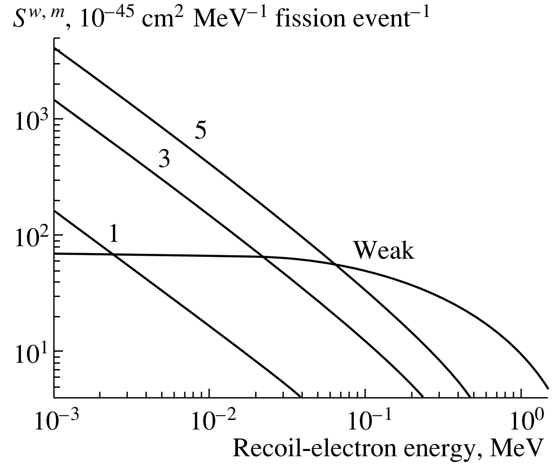

Fig. 8. Spectra for $\nu_e e$ scattering associated with weak and magnetic interaction (results of the calculations). The figures on the curves representing the spectra for magnetic scattering are the values of μ_ν in $10^{-11}\mu_{\rm B}$ units.

Spectrum of reactor antineutrinos

The reduction of the recoil-electron-detection threshold increases the contribution that electron antineutrinos from the region lying below the threshold for inverse beta decay make to scattering associated with magnetic and weak interaction; as was indicated above, nearly the entire spectrum of electron antineutrions comes into play as soon as the threshold becomes less than some 15 keV.

Here, we would like to highlight the qualitative features of the soft section of the reactor-antineutrino spectrum that were revealed in recent years [32, 33].

About three-fourths of all electron antineutrinos emitted by a reactor fall within the energy range 0—2 MeV. A significant contribution to the spectrum in this range comes from antineutrinos originating from the beta decay of nuclei that are formed in the reactor core upon radiative neutron capture. This contribution can be evaluated on the basis of the data given in Fig. 9, which depicts a typical total spectrum of electron antineutrinos and, separately, its component associated with the beta decay of fission fragments.

The spectrum and the intensity of the electron-antineutrino flux are not determined unambiguously

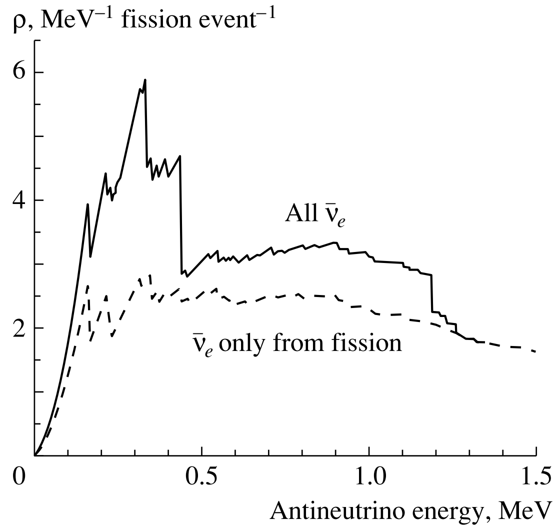

Fig. 9. Soft section of the spectrum of reactor electron antineutrinos.

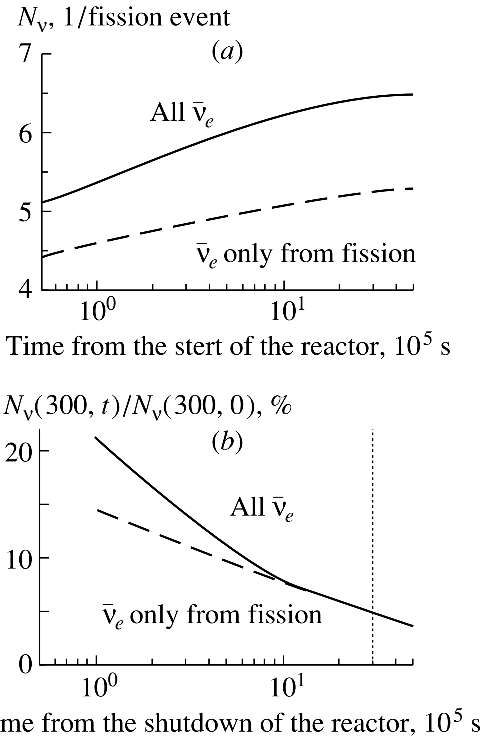

Fig. 10. Time evolution of the flux of reactor electron antineutrinos: (*a*) growth of $N_n = \int \rho(E)dE$ after the start of the reactor and (*b*) falloff after the shutdown of the reactor (in percent with respect to the flux at the end of the reactor operating period). The vertical dotted line in Fig. 10*b* indicates the instant at which the next operating period begins.

by the current reactor state, which is specified by the preset power level and by the isotopic composition of the burning nuclear fuel—they also depend on the prehistory of this state. From the start of the reactor, there begins a long-term process through which the flux approaches its equilibrium value; after the reactor shutdown, the flux begins to fall off slowly, and this falloff does not have time to be completed by the instant at which the next operating period starts (see Fig. 10). In experiments of the type being discussed, the detector background is measured within shutdown periods (that is, between two successive operating periods), but, in such periods, there is, in fact, a residual radiation of nuclear fuel occurring in the shutdown reactor. The growth of the flux and its falloff are accompanied by changes in the spectral content of electron antineutrinos and, hence, in the spectra of recoil electrons.

In order to describe accurately the total spectrum of reactor antineutrinos, it will be necessary to refine further available data on the contributions of its individual components and their time dependences and to make use of specific information about the previous operation of the reactor used throughout 2 to 3 years. As a rule, such information can be provided by the personnel of the corresponding atomic power plant. The need for such refinements is dictated by the demands of the experiments that are being performed and planned.

Inelastic scattering on atomic electrons

As the energy lost by a neutrino in a collision event decreases, effects associated with the binding of atomic electrons become operative. In the case of inelastic scattering on an electron occurring in the ith subshell, the energy transfer q from the electron antineutrino is equal to the sum of the kinetic energy of the knock-on electron and its binding energy ε_i in this subshell; that is,

$$q = \varepsilon_i + T. \tag{22}$$

The filling of the vacancy formed is accompanied by the emission soft x-ray photons and Auger electrons of total energy ε_i that is absorbed in a detector material. As a result, the event energy observed in the experiment being discussed coincides with the energy transfer q in a collision. The differential cross sections and spectra for inelastic scattering on an electron of the ith shell due to magnetic and weak interaction vanish for $q \leq \varepsilon_i$.

To a precision of 2 to 3%, the results obtained by numerically calculating the spectra for the magnetic-interaction-induced (S^m_{in}) and the weak-interaction-induced (S^w_{in}) inelastic scattering of reactor antineutrinos on the electrons of a iodine ($Z = 53$) and a ger-

Table 2. Binding energies (in keV) of the electrons in the iodine ($Z = 53$) and the germanium ($Z = 32$) atom

Z	$1s_{1/2}$ K	$2s_{1/2}$ L_{I}	$2p_{1/2}$ L_{II}	$2p_{3/2}$ L_{III}	$3s_{1/2}$ M_{I}	$3p_{1/2}$ M_{II}	$3p_{3/2}$ M_{III}	$3d_{3/2}$ M_{IV}	$3d_{5/2}$ M_{V}
53	32.9	5.09	4.78	4.48	1.03	0.90	0.84	0.61	0.60
32	10.9	1.37	1.22	1.19					

manium ($Z = 32$) atom can be approximated as [34]

$$S_{\mathrm{in}}^{m(w)}(q) \approx \left[\frac{1}{Z}\sum_i n_i\theta(q-\varepsilon_i)\right] S_{\mathrm{free}}^{m(w)}(q), \quad (23)$$

where summation is performed over the subshells of the atom involved; n_i is the number of electrons in the ith subshell; $\theta(q-\varepsilon_i)$ is the Heaviside step function, which is equal to unity for $q \geq \varepsilon_i$ and to zero for $q < \varepsilon_i$; and $S_{\mathrm{free}}^{m,(w)}(q)$ is the kinetic-energy spectrum for magnetic-interaction-induced (weak-interaction-induced) scattering on free electrons (see above), in which case $\varepsilon = 0$ and $q = T$. It is worthy of note that, in this approximation, the binding of atomic electrons exerts the same effect on magnetic-interaction-induced and weak-interaction-induced scattering.

The calculated binding energies of electrons are given in Table 2.

The actual calculations of inelastic scattering were performed in the energy-transfer (q) range from 1–1.5 to 200–300 keV for the K, L, and M shells of the iodine atom and the K and L shells of the germanium atom, the remaining electrons being considered to be free.

Relation (23) can be formulated in the form of the following rule:

In order to find the distribution of observed energies for the case of inelastic scattering on an atom due to magnetic (weak) interaction, it is necessary to compute the spectrum of kinetic energies for inelastic scattering on a free electron due to magnetic (weak) interaction and multiply the result by the response function R,

$$R = \frac{1}{Z}\sum_i n_i\theta(q-\varepsilon_i), \quad (24)$$

which depends only on the binding energy of the electrons in the atom.

As can be seen from relations (23) and (24) and from Fig. 11, the spectra for elastic scattering do not differ from the spectra for inelastic scattering if the energy transfer exceeds the binding energy of a K electron in the target atom. As the energy transfer decreases, an ever greater number of internal atomic electrons successively cease to take part in the scattering process, with the result that the spectra for inelastic scattering constitute an ever smaller fraction of the spectra for elastic scattering. At the energy-transfer value as low as 1 keV, the ratio of the spectrum for inelastic scattering to the spectrum for elastic scattering reduces to 41/53 for iodine and to 22/32 for germanium.

The authors of [34] discussed the accuracy and the applicability range for the recipe in (23) and presented some examples where this recipe is hardly workable or where it is not at all applicable.

2.2. Experiments

The experiments reported in [11, 12], as well as the earlier experiment described in [35], were intended for verifying theoretical predictions for the structure of weak $\nu_e e$ interaction. In practice, it turned out, however, that the main problem that arises in detecting single electrons from $\bar{\nu}_e e$ scattering is that of the detector background, which could not be reliably removed despite massive efforts mounted for many years to solve this problem. As a result, it proved to be impossible to test, in reactor experiments, the Standard Model in the sector of first-generation leptons, which is the clearest sector from the theoretical point of view. The cross section for scattering due to weak interaction was experimentally determined in [11, 12] to a relative precision of 50%. Searches for the neutrino magnetic moment involve still greater difficulties.

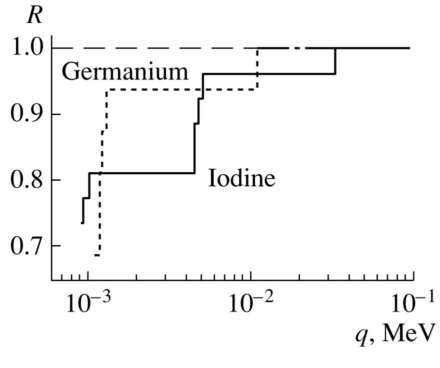

Fig. 11. Response functions for iodine and germanium [see Eq. (24)].

Table 3. Number of recoil electrons for a target exposure of 1000 kg d that are associated with electron-antineutrino scattering on free electrons due to weak (w) and magnetic (m) ($\mu_\nu = 3 \times 10^{-11}\mu_\mathrm{B}$) interaction

Range of recoil-electron energies, keV	Bugey		Krasnoyarsk	
	w	m	w	m
1–4	11	122	6	67
4–16	43	120	24	66
16–60	140	100	77	55
60–250	360	90	200	50
250–1000	750	50	410	27

In this section, we will consider attempts at reducing the limit on μ_ν that are being undertaken by the MUNU collaboration (Grenoble–Munster–Neuchatel–Padova–Zurich) at the reactor in Bugey [36] and by the Kurchatov Institute in a collaboration with the Petersburg Nuclear Physics Institute at the reactor in Krasnoyarsk [37]. Also, mention is briefly made of new-type detectors developed at the Institute for Theoretical and Experimental Physics (ITEP, Moscow) and at the Joint Institute for Nuclear Research (JINR, Dubna). The expected event-counting rates that are quoted in Table 3 give an idea of the orders of magnitude of the quantities with which one has to deal in experiments studying electron-antineutrino scattering on electrons.

MUNU

The MUNU collaboration has constructed a time-projection chamber (TPC) of volume about 1 m^3, the chamber being filled with a CF$_4$ gas. At a pressure of 5 atm, the target mass is 18 kg. The chamber is surrounded by a liquid scintillator (LS) playing the role of an active and a passive shielding (see Fig. 12). The gas circulates, passing through filters absorbing oxygen. Since 1998, the detector has been arranged at a distance of 18.6 m from the center of the Bugey reactor. The structural materials of the reactor edifice that are situated above the detector and which are of thickness approximately equal to 20 mwe ensure shielding from the hadronic component of cosmic rays.

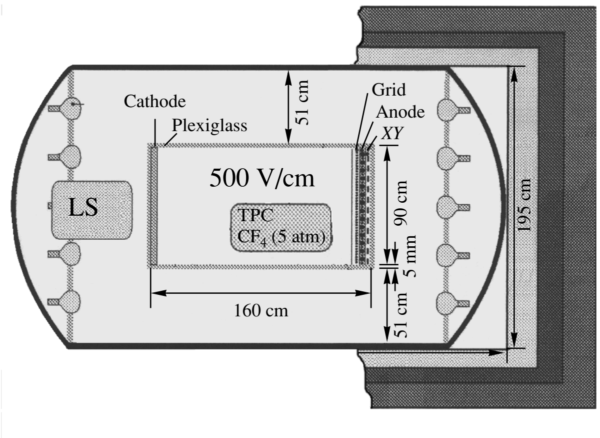

Fig. 12. MUNU detector of $\bar{\nu}_e e$ scattering in Bugey.

The experiment being discussed has measured the energy and the angular distribution of electrons with respect to the momentum of incident electron antineutrinos. Within the reactor shutdown periods, it was found that the distribution of background events is nearly isotropic. However, the absolute value of the background proved to be unacceptably large, and test measurements were performed at a detection threshold of 800 to 1000 keV. Investigations made it possible to establish the origin of the main background sources. It turned out that the oxygen filter is a source of radon and that the material of the chamber cathode contains an admixture that emits beta particles with an endpoint energy of about 1.2 MeV. The removal of the filter and a replacement of the cathode reduced considerably the background, whereupon the threshold was lowered to 300 keV.

Krasnoyarsk

The detector is being arranged at a depth of 600 mwe in the new laboratory room, where the flux of electron antineutrinos is about 40% less than in the MUNU experiment. The target for electron antineutrinos consists of 604 silicon crystal detectors forming a compact assembly of four hexahedral matrices, each containing 151 crystals. An individual detector is made in the form of a cylinder of diameter 29 mm and height 100 mm. The total mass of silicon is 80 kg. A HPGe detector of volume 116 cm^3 is positioned at the center of the assembly. The carrying part of the matrices is manufactured from radiation-pure fluoroplastic. The target is placed in a cooled chamber with walls of oxygen-free copper. Signals from individual crystals are transmitted through stepwise channels to vacuum joints and, further, to preamplifiers. The vacuum casing of the detector—it is 64 cm in diameter and 62 cm in height and is manufactured from titanium of thickness 4 mm—protects the detector from the penetration of radon (see Fig. 13). This casing is followed by a few layers of a passive and an active shielding, the layer closest to the chamber being made of lead.

It is planned that the detector will have been commissioned at the beginning of 2002. The electron-detection threshold is presumed to be at a level of

50 keV. The sensitivity to be achieved in this experiment will crucially depend on the level of the detector background.

Large xenon chamber (ITEP)

A time-projection chamber filled with liquid xenon whose total mass will be 750 kg is being presently developed at ITEP [38]. A scintillation flash arising in xenon upon antineutrino scattering on an electron is fixed by photodetectors specifying the instant at which ionization electrons begin to drift along the electric field aligned with the chamber axis. After that, the electrons are taken away into the gas phase, where their energy and their X and Y coordinates are measured. In the total volume occupied by xenon, the central part containing 150 kg of it will serve as a target proper for antineutrinos, while the remaining xenon, that which surrounds the target, will play the role of a passive and an active shielding.

The threshold for scattering-event detection is planned to be set at a level not exceeding 100 keV. According to the estimate of the authors of the project, a sensitivity in the range $(3–5) \times 10^{-11}\mu_B$ will be achieved in the reactor-electron-antineutrino flux of $\bar{\nu}_e$ $2 \times 10^{13}/\text{cm}^2$ s.

At present, a detector prototype containing 150 kg of xenon is being tested (A.G. Dolgolenko, private communication).

Toward ultralow energies

As the threshold for recoil-electron detection is decreased, events associated with scattering due to magnetic interaction are concentrated in ever narrower energy intervals (see Table 3). Not only does this localization of magnetic-scattering events reduce the background that is generated by events of scattering due to weak interaction and which is correlated with the reactor operation, but it also diminishes the relative contribution to these intervals from the intrinsic detector background, which is the main obstacle to advances toward the region of small magnetic moments.

Semiconductor ionization germanium detectors make it possible to explore the region of energies much lower than those investigated in the Bugey and Krasnoyarsk experiments. By using a HPGe crystal of mass about 2 kg at the Gran Sasso laboratory, which is situated at a depth of 3200 mwe, the Heidelberg–Moscow collaboration demonstrated the possibility of achieving, in the range 11–30 keV, the background spectral density at a level of 0.1/(keV kg d) [39]. To the best of my knowledge, this is the best result in the region of low energies.

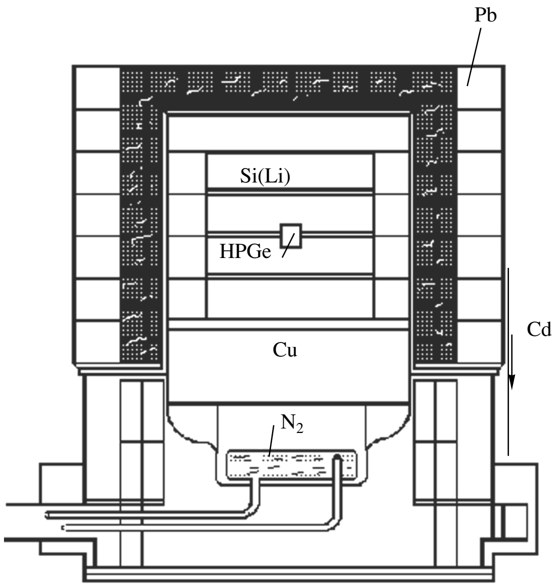

Fig. 13. Layout of the multicrystal detector for $\bar{\nu}_e e$ scattering in Krasnoyarsk (central part).

The spectrometer GEMMA, which employs a germanium crystal of mass 2 kg and a system of active and passive shielding, has been created and is being tested at ITEP ([40] and A.S. Starostin, private communication). It is expected that, at a detection threshold of about 3 keV and a 20 mwe depth of deployment, the spectrometer background will not exceed 0.3/(keV kg d). A cryostat makes it possible to increase the germanium mass up to 6 kg. It is planned that the spectrometer will be installed at one of the reactors of the atomic power plant in Kalinin. According to the estimate of the authors of the project, the sensitivity to the value of μ_ν there will be about $3 \times 10^{-11}\mu_B$ in a flux of $2 \times 10^{13}\bar{\nu}_e/\text{s}$ over two years of data accumulation.

At present, low-background detectors are being developed for measuring much lower energies (see [41] and references therein). These are, first of all, a silicon cryogenic detector that employs the effect of ionization-to-heat transition, which was discovered at JINR in the 1980s, and, then, a germanium detector involving an internal amplification of ionization signals (avalanche germanium detector, also known as AGD). Employment of such detectors will further expand the possibilities for seeking the neutrino magnetic moment. However, advances down the scale of electron energies measured in reactor experiments are hampered by the emergence of a new form of correlated background, that which is associated with recoil nuclei from elastic neutrino–nucleus scattering. Here, at the threshold of the absolutely unexplored region, we conclude the section devoted to describing searches for the antineutrino magnetic moments in reactor experiments.

CONCLUSION

Reactor experiments make it possible to explore the masses of the neutrinos and their mixing in the region of small mass parameters not presently accessible to accelerator experiments. The CHOOZ experiment established definitively that the $\nu_e \to \nu_x$ channel is not dominant in the oscillations of atmospheric neutrinos. KamLAND may become the first experiment that will employ terrestrial neutrino sources and which will discover the phenomenon of oscillations, determine the contributions of the masses m_1 and m_2 to the electron neutrino, and find a solution to the solar-neutrino problem. The Kr2Det experiment, which is characterized by a high sensitivity to small mixing angles, will probably be able to reveal the contribution of the mass m_3 to the electron neutrino or to set a more stringent limit on its value. These investigations rely on unprecedented improvements in methods for detecting the inverse-beta-decay reaction.

Searches for the neutrino magnetic moment that are being performed at the reactors in Bugey and Krasnoyarsk, an experiment that will employ a large xenon chamber and which is being prepared at ITEP, and a foreseen breakthrough into the region of low and ultralow recoil-electron energies will presumably permit going beyond the constraint $\mu_\nu \le 2 \times 10^{-10}\mu_{\rm B}$, which could not have been strengthened for the three past years, and expanding the range of searches toward a value of $\mu_\nu \sim 10^{-11}\mu_{\rm B}$.

The metrological basis of these investigations has become firmer. In particular, the features of the flux and of the spectrum of reactor electron antineutrinos are being refined, and a simple recipe has been found that makes it possible to determine the cross sections for the inelastic scattering of reactor electron antineutrinos on atomic electrons.

ACKNOWLEDGMENTS

I am grateful to E. Akhmedov, S. Bilenky, A. Smirnov, P. Vogel, and S. Fayans for valuable consultations on the theoretical aspects of this study and to L. Bogdanova, A. Dolgolenko, Yu. Kamyshkov, Dy H. Koang, Yu. Kozlov, V. Kopeikin, V. Martemyanov, A. Piepke, L. Popeko, V. Sinev, M. Skorokhatov, and A. Starostin for discussions on the experiments described in this article.

This work was supported by the Russian Foundation for Basic Research (project nos. 00-02-16035, 00-15-96708).

REFERENCES

1. CHOOZ Collab. (M. Apollonio *et al.*), Phys. Lett. B **420**, 397 (1998); **466**, 415 (1999).
2. F. Boehm *et al.*, Phys. Rev. D **62**, 072002 (2000); Phys. Rev. Lett. **84**, 3764 (2000); Y.-F. Wang, L. Miller, and G. Gratta, Phys. Rev. D **62**, 013012 (2000).
3. L. Mikaelyan, Nucl. Phys. B (Proc. Suppl.) **87**, 284 (2000); **91**, 120 (2000); L. A. Mikaelyan and V. V. Sinev, Yad. Fiz. **63**, 1077 (2000) [Phys. At. Nucl. **63**, 1002 (2000)].
4. J. Busenitz, Yad. Fiz. **63**, 1068 (2000) [Phys. At. Nucl. **63**, 993 (2000)]; A. Piepke, Nucl. Phys. B (Proc. Suppl.) **91**, 99 (2000); V. Barger, D. Marfatia, and B. Wood, hep-ph/0112125.
5. B. M. Pontekorvo, Zh. Éksp. Teor. Fiz. **33**, 549 (1957) [Sov. Phys. JETP **6**, 429 (1958)]; Zh. Éksp. Teor. Fiz. **34**, 247 (1958) [Sov. Phys. JETP **7**, 172 (1958)]; Zh. Éksp. Teor. Fiz. **53**, 1717 (1967) [Sov. Phys. JETP **26**, 984 (1958)]; V. Gribov and B. Pontecorvo, Phys. Lett. B **28B**, 493 (1969); S. M. Bilenky and B. Pontecorvo, Phys. Rep. **41**, 225 (1978).
6. S. S. Gershteĭn, E. P. Kuznetsov, and V. A. Ryabov, Usp. Fiz. Nauk **167**, 811 (1997) [Phys. Usp. **40**, 773 (1997)].
7. Yu. V. Kozlov, V. P. Martem'yanov, and K. N. Mukhin, Usp. Fiz. Nauk **167**, 849 (1997) [Phys. Usp. **40**, 807 (1997)].
8. M. B. Voloshin, M. I. Vysotskiĭ, and L. B. Okun', Zh. Éksp. Teor. Fiz. **91**, 754 (1986) [Sov. Phys. JETP **64**, 446 (1986)].
9. E. Kh. Akhmedov, Yad. Fiz. **48**, 599 (1988) [Sov. J. Nucl. Phys. **48**, 382 (1988)]; C.-S. Lim and W. J. Marciano, Phys. Rev. D **37**, 1368 (1988); E. Akhmedov, hep-ph/9705451.
10. L. I. Dorman, Yad. Fiz. **63**, 1059, 1064 (2000) [Phys. At. Nucl. **63**, 984, 989 (2000)]; D. Oakley *et al.*, Astrophys. J. Lett. **437**, L63 (1994).
11. A. I. Derbin, A. V. Chernyĭ, L. A. Popeko, *et al.*, Pis'ma Zh. Éksp. Teor. Fiz. **57**, 754 (1993) [JETP Lett. **57**, 768 (1993)].
12. G. S. Vidyakin, V. N. Vyrodov, I. I. Gurevich, *et al.*, Pis'ma Zh. Éksp. Teor. Fiz. **55**, 212 (1992) [JETP Lett. **55**, 206 (1992)].
13. A. V. Derbin, Yad. Fiz. **57**, 236 (1994) [Phys. At. Nucl. **57**, 222 (1994)].
14. P. Vogel, Phys. Rev. D **29**, 1918 (1984); S. A. Fayans, Yad. Fiz. **42**, 929 (1985) [Sov. J. Nucl. Phys. **42**, 590 (1985)].
15. L. A. Mikaelyan, in *Proceedings of International Conference NEUTRINO'77, Baksan, 1977* (Nauka, Moscow, 1978), Vol. 2, p. 383; A. A. Borovoĭ, Yu. L. Dobrynin, and V. I. Kopeĭkin, Yad. Fiz. **25**, 264 (1977) [Sov. J. Nucl. Phys. **25**, 144 (1977)]; V. I. Kopeĭkin, Yad. Fiz. **32**, 1507 (1980) [Sov. J. Nucl. Phys. **32**, 780 (1980)].
16. K. Schreckenbach *et al.*, Phys. Lett. B **160B**, 325 (1985); A. Hahn *et al.*, Phys. Lett. B **218**, 355 (1989).
17. P. Vogel *et al.*, Phys. Rev. C **24**, 1543 (1981).

18. V. N. Vyrodov *et al.*, Pis'ma Zh. Éksp. Teor. Fiz. **61**, 161 (1995) [JETP Lett. **61**, 163 (1995)]; Y. Declay *et al.*, Phys. Lett. B **338**, 383 (1994).
19. V. I. Kopeĭkin, L. A. Mikaélyan, and V. V. Sinev, Yad. Fiz. **64**, 914 (2001) [Phys. At. Nucl. **64**, 849 (2001)].
20. K. S. Hirata *et al.*, Phys. Lett. B **280**, 146 (1992); R. Becker-Szendy *et al.*, Phys. Rev. D **46**, 3720 (1992).
21. H. Sobel, Nucl. Phys. B (Proc. Suppl.) **91**, 127 (2001).
22. G. Fogli *et al.*, Nucl. Phys. B (Proc. Suppl.) **87**, 239 (2000); **91**, 167 (2001).
23. J. N. Bahcall, P. L. Krastev, and A. Yu. Smirnov, Phys. Rev. D **58**, 096016 (1998); V. Berezinsky, Nucl. Phys. B (Proc. Suppl.) **80**, 17 (2000).
24. J. N. Bahcall, P. L. Krastev, and A. Yu. Smirnov, Phys. Rev. D **60**, 093001 (1999).
25. LSND Collab. (C. Athanassopoulos *et al.*), Phys. Rev. Lett. **77**, 3082 (1996); **81**, 1774 (1998).
26. S. M. Bilenky, C. Guinti, and W. Grimus, Eur. Phys. J. C **1**, 247 (1998); V. Barger *et al.*, Phys. Lett. B **489**, 345 (2000).
27. O. L. G. Peres and A. Yu. Smirnov, Nucl. Phys. B **599**, 3 (2001).
28. L. A. Mikaélyan and V. V. Sinev, Yad. Fiz. **62**, 2177 (1999) [Phys. At. Nucl. **62**, 2008 (1999)].
29. E. A. Akhmedov, G. Bianko, and M. Rebelo, Phys. Rev. Lett. **84**, 3535 (2000).
30. G. Marx and N. Menyhard, Ungar. Akad. Wiss. (Budapest, 1960); M. A. Markov, *Neutrino* (Nauka, Moscow, 1964), p. 132.
31. H. Bethe, Proc. Cambridge Philos. Soc. **35**, 108 (1935); G. V. Domogatski and D. K. Nadyozhin, Yad. Fiz. **12**, 1233 (1970) [Sov. J. Nucl. Phys. **12**, 678 (1970)].
32. A. M. Bakalyarov, V. I. Kopeĭkin, and L. A. Mikaélyan, Yad. Fiz. **59**, 1225 (1996) [Phys. At. Nucl. **59**, 1171 (1996)]; V. I. Kopeĭkin, L. A. Mikaélyan, and V. V. Sinev, Yad. Fiz. **60**, 230 (1997) [Phys. At. Nucl. **60**, 172 (1997)].
33. V. I. Kopeĭkin, L. A. Mikaélyan, and V. V. Sinev, Yad. Fiz. **61**, 2222 (1998) [Phys. At. Nucl. **61**, 2109 (1998)]; **63**, 1087 (2000) [Phys. At. Nucl. **63**, 1012 (2000)].
34. V. I. Kopeĭkin, L. A. Mikaélyan, V. V. Sinev, and S. A. Fayans, Yad. Fiz. **60**, 2032 (1997) [Phys. At. Nucl. **60**, 1859 (1997)]; S. A. Fayans, L. A. Mikaelyan, and V. V. Sinev, Yad. Fiz. **64**, 1551 (2001) [Phys. At. Nucl. **64**, 1475 (2001)].
35. F. Reines, H. Gurr, and H. Sobel, Phys. Rev. Lett. **37**, 315 (1976).
36. C. Broggini, Nucl. Phys. B (Proc. Suppl.) **91**, 105 (2000); MUNU Collab. Proposal, ISN 92115, LNGS 92/27 (1992).
37. Yu. V. Kozlov *et al.*, Nucl. Phys. B (Proc. Suppl.) **87**, 514 (2000).
38. M. Baldo-Ceolin *et al.*, in *Proceedings of WEIN'92,* Ed. by Ts. D. Vylov (World Sci., Singapore, 1993), p. 753.
39. M. Beck *et al.*, Phys. Lett. B **336**, 141 (1994).
40. A. G. Beda, E. V. Deimidova, A. S. Starostin, and M. B. Voloshin, Yad. Fiz. **61**, 72 (1998) [Phys. At. Nucl. **61**, 66 (1998)].
41. B. S. Neganov, V. N. Trofimov, A. A. Yukhimchuk, and L. N. Bogdanova, Yad. Fiz. **64**, 308 (2001) [Phys. At. Nucl. **64**, 261 (2001)]; A. S. Starostin and A. G. Beda, Yad. Fiz. **63**, 1370 (2000) [Phys. At. Nucl. **63**, 1297 (2000)].

Translated by A. Isaakyan

Physics of Atomic Nuclei, Vol. 65, No. 7, 2002, pp. 1188–1197. From Yadernaya Fizika, Vol. 65, No. 7, 2002, pp. 1220–1229.
Original English Text Copyright © 2002 by Zelevinsky.

90th ANNIVERSARY OF I.I. GUREVICH'S BIRTHDAY

Nuclear Physics and Ideas of Quantum Chaos*

V. G. Zelevinsky

Department of Physics and Astronomy and National Superconducting Cyclotron Laboratory,
Michigan State University, East Lansing, MI 48824-1321 USA

Received November 13, 2001

Abstract—The field nowadays called "many-body quantum chaos" was started in 1939 with the article by I.I. Gurevich studying the regularities of nuclear spectra. The field has been extensively developed recently, both mathematically and in application to mesoscopic systems and quantum fields. We argue that nuclear physics and the theory of quantum chaos are mutually beneficial. Many ideas of quantum chaos grew up from the factual material of nuclear physics; this enrichment still continues to take place. On the other hand, many phenomena in nuclear structure and reactions, as well as the general problem of statistical physics of finite strongly interacting systems, can be understood much deeper with the help of ideas and methods borrowed from the field of quantum chaos. A brief review of the selected topics related to the recent development is presented.

1. WHAT IS QUANTUM CHAOS?

According to conventional wisdom, quantum chaos does not exist. One can speak only about quantum signatures of classical chaos [1]. The latter is well understood, at least with respect to one- or few-body problems. The driving force of classical chaos is the instability of phase-space trajectories against small changes of initial conditions. This instability leads to the exponential divergence of close trajectories, dynamical unpredictability, and the need for a statistical approach based on the ergodic covering of an energy surface. In a quantum world, one cannot define infinitesimally close trajectories in phase space. Formally, in a closed quantum system, we deal with the linear integrable dynamics of components of a wave function, in fact the dynamics of phases. The only possible question then is that of evidence of classical chaos that still remains in an underlying quantum system.

However, the opposite point of view is also possible. The transition to the classical limit, $\hbar \to 0$, and the long time evolution, $t \to \infty$, are noncommutative [2]. There exists a critical time t^* beyond which quantum spreading overshadows the classical divergence of trajectories. Following this logic, one can say that classical chaos is only a transient phenomenon, although typical times t^* in many cases can be extremely large. Below, I would prefer an unorthodox viewpoint and discuss phenomena that can be attributed to quantum chaos with no explicit referral to a classical limit.

2. ONE- AND MANY-BODY QUANTUM CHAOS

In a self-sustaining many-body quantum system, such as a complex nucleus, one is usually far from the classical domain. Important concepts as interference of states, mixing, tunneling, isospin, parity, and so on have no classical analogs. Only at the mean-field level [3] can one hope to use periodic orbits or Lyapunov exponents and find a similarity to well-studied problems of billiards (or microwave cavities) and Rydberg atoms [4]. This area can be naturally termed one-body chaos.

For a many-body system, our main interest will be located in the regions of relatively high excitation energies, where, even in the mean-field approximation, the combinatorics of noninteracting particles form a very high level density. Then, the residual interactions prove to be effectively strong. Switching on the interaction from zero to the actual strength λ (in a finite system, this can be done continuously), we get the many-body energy terms $E_\alpha(\lambda)$. Let us consider a class of eigenstates $|\alpha\rangle$ with fixed values of exact constants of the motion, such as the total angular momentum J and its projection M in a finite system. Depending on the approximation used for the Hamiltonian $H(\lambda)$, isospin and parity can also be preserved. The flow of energy levels as a function of λ looks "turbulent" because of multiple level crossings [5, 6]. Within a given symmetry class, all crossings are avoided. Near the crossing point, the levels repel each other, and the wave functions of colliding states are fully mixed. After a few collisions, the original configurations of independent particles

---

*This article was submitted by the author in English.

lose their identity, and the eigenstates acquire a very complicated nature [7, 8, 5].

The emerging picture can be considered at different scales. With a poor resolution, one has to operate with statistical notions (level density, temperature, average single-particle occupancies, strength functions, and spreading widths). This is a traditional picture of a compound nucleus. However, in mesoscopic systems (complex atoms, molecules, atomic clusters, solid-state microdevices), a complementary view is possible. Such systems are sufficiently complex to make a statistical description meaningful. At the same time, one can still analyze, theoretically and experimentally, individual quantum states. Neutron resonances in complex nuclei reveal a situation where a single nearly stationary compound wave function can be studied experimentally [9, 10]. It is not accidental that the fundamental relation between spectral characteristics of a quantum systems and the ideas of chaos was first demonstrated just with the help of data on neutron resonances [11]. And one of the brightest manifestations of quantum chaos—a striking enhancement of weak interactions—was found in the same area (see below).

Looking through a magnifying glass, one can study local fluctuations and correlations of individual energy levels and wave functions in a nucleus in the same way as for a single particle in a quantum billiard, although the driving force for stochastization is the interparticle interaction rather than the shape of the billiard or symmetry (more precisely, its absence) of the mean field. A picture combining different viewpoints arises gradually from what can be loosely called many-body quantum chaos.

As a working definition of complete quantum chaos, one can choose random-matrix theory (RMT) [9, 12, 13], in particular, a Gaussian orthogonal ensemble (GOE) or ensembles of banded random matrices [14]. The GOE extracts the most general local properties of chaotic spectra and wave functions that depend only on the symmetry class of the Hamiltonian. Physically, this means the averaging over all Hamiltonians of a given class, the next step of generalization after averaging over many close microscopic states that is performed in the statistical Gibbs ensembles. Typical GOE matrices have uncorrelated independent normally distributed matrix elements that allow coupling between any two configurations and look qualitatively the same in any orthogonal basis. Banded random matrices, which are more appropriate for two-body interactions, assume a physically motivated ordering of basis states and contain, in such a basis, coupling between closely located states.

Such definitions are independent of the existence of the classical limit. If it can be reached, it becomes possible, reversing the standard wording, to look for manifestations of underlying quantum chaos in the semiclassical region of parameters. Complex nuclei and atoms provide a perfect example of many-body quantum chaos [15, 16, 5, 8, 17]. Below, I give examples, mostly dictated by personal interest, of cross-fertilizing between nuclear physics and quantum chaos; the references are incomplete being chosen almost “at random.”

3. MANY-BODY HAMILTONIAN

An actual system is described by a single deterministic Hamiltonian. In practice, we are usually limited by a mean field and two-body residual interactions. Typically, the Hamiltonian matrix has a quasibanded structure in the natural mean-field basis, and the nonzero off-diagonal elements are distributed [8, 5] like $\propto |H|^q \exp(-\mathrm{const} \cdot |H|)$ with a parameter q on the order of unity rather than according to the Gaussian law required by the GOE limit. This generic distribution, valid also in the interacting-boson model of nuclear collective motion, has not yet been understood, although one can make plausible conjectures [5]. Another major difference compared to the GOE matrix comes from the limitations set by the two-body character of the interaction. The matrix is sparse since many configurations are not coupled by a single-step process, and the same many-body matrix elements are in fact repeated many times in the matrix because a given two-body collision may happen for several different states of the spectator part of the system.

In spite of the non-Gaussian, basis-dependent, sparse, and strongly correlated matrix, the properties of local correlations and fluctuations of eigenvalues and eigenfunctions prove to be rather close to those of the GOE. The spectral statistics are insensitive to the exact distribution of the matrix elements. Many results for fixed realistic Hamiltonians agree with the GOE predictions; owing to this, it is indeed possible to take the GOE limit as a physical definition of quantum chaos. To take into account correlations between the many-body matrix elements due to the two-body character of the forces [18], one can introduce random ensembles different from the GOE [12, 18–20].

4. SPECTRAL STATISTICS

For a long time, the studies of chaotic quantum systems were limited to the local level statistics. The first analysis of the nearest level spacing distribution $P(s)$ was performed by I.I. Gurevich more than 60 years ago [21] by using the spectroscopic data on heavy nuclei available at that time. Random-matrix theory was developed [22, 23] mainly with the input from nuclear and atomic spectroscopy [24, 25]. The generic nature of the GOE spectra was conjectured [26] on the basis of data on neutron resonances.

Although the theoretical question of the onset of chaos is still debatable [27], it is clear that, similar to gas equilibration by collisions, multiple level crossings rapidly mix the wave functions as soon as the coupling between many-body states becomes comparable to their spacing. This process is nonuniform since the density of states increases exponentially with excitation energy due to the combinatorics of energy sharing between simple configurations [9, 28].

The properties of spectral statistics that are typically used include the nearest level spacing distribution $P(s)$ and the spectral rigidity $\Delta(L)$ (or the variance of the level number over some spectral interval). In a regular (integrable) system, we expect the Poisson nearest level spacing distribution, $P(s) = e^{-s}$, where the spacings s are normalized to the average local spacings. This distribution, similar to that of uncorrelated radioactive decays in time, was for the first time used for nuclear spectra in the above-mentioned paper by Gurevich [21]. Later Gurevich and Pevzner showed [29] that, superimposing few-level sequences for different sets of exact quantum numbers, which are not mixed by the Hamiltonian, one rapidly comes to the Poisson distribution. The Wigner distribution $P(s) = (\pi/2)s\exp[-(\pi/4)s^2]$ corresponds to a single family of states (identical exact quantum numbers) that repel each other at short distances because of mixing and, as a result, display a more or less ordered ladder, a kind of an aperiodic crystal. The spectral rigidity $\Delta(L)$ measures average deviations from this periodicity for the spectral fragments including L adjacent levels. These fluctuations grow linearly with L for regular systems, but the level repulsion in the chaotic case reduces them to a weak logarithmic growth.

Because of the fast stochastization of pure mean-field configurations of independent particles by the residual interaction, $P(s)$, $\Delta(L)$, and more detailed characteristics such as the level-curvature distribution [6] converge to the GOE predictions even at an interaction strength λ of about 0.2–0.3 of the realistic value for nuclei [5]. Although the pairing, being the most coherent part of the nuclear residual interaction, by itself would lead [30] only to a moderate degree of chaoticity in highly excited states, it changes significantly the level density. As a result, the observed chaotization of nuclear spectra [31, 32] is alleviated by the compression of two-quasiparticle states above the threshold of Cooper pair breaking.

In spite of the fact that the study of the spectral statistics in realistic and model systems was the favorite subject of many authors, there are still unresolved questions. Below, I list few examples. (i) We do not know for sure what the actual path of the Poisson-to-Wigner transition is as a function of parameters [2, 5]. Several possible scenarios were suggested, and the answer may be not universal. It is hard to check numerically, with a good precision, the small-s region, since, even in large-scale shell-model calculations, level statistics at small s are not sufficient. (ii) Another, even harder, problem is related to the exact knowledge of the behavior of the realistic $P(s)$ at very small spacings. A quadratic rather than linear behavior would be an indication of the presence of terms in the Hamiltonian [24] that are not invariant under time ($\mathcal{T}$) inversion (in this case, it is impossible to select a pure real basis, and the presence of complex mixing matrix elements makes the level degeneracy much less probable, leading to the quadratic repulsion at short distances). It is quite remarkable that one can look for the most fundamental symmetries in nature by studying seemingly irrelevant average features of spectra. Of course, this is possible just because, here, one can get rid of all accidental properties of the system, leaving only basic symmetries. However, because of definite smallness (or absence) of $\mathcal{T}$ violation in strong nuclear forces, a practical search is difficult, requiring very rich statistics [33]. (iii) In spite of the historic role of neutron resonances in heavy nuclei for defining the paradigm of RMT, the quality of available open data is not satisfactory. For instance, there is still a controversial situation with respect to K mixing [34]: we do not know whether this geometric property, the axial symmetry of the mean field, is destroyed at energies around the neutron threshold.

5. CHAOTIC WAVE FUNCTIONS

The structure of the stationary states continues to evolve as a function of the interaction strength λ long after spectral statistics have reached the RMT limit. For completely chaotic dynamics in a Hilbert space of dimension N, one expects that generic wave functions can be represented by unit vectors randomly covering the surface of an N-dimensional sphere.

The complexity of the wave function can be quantified by the moments of the amplitudes C^{α}_{k} of individual eigenstates $|\alpha\rangle = \sum_k C^{\alpha}_{k}|k\rangle$ in a suitable "unperturbed" basis $|k\rangle$ or by information (Shannon) entropy [2, 35, 5], calculated in terms of the weights $w^{\alpha}_{k} = |C^{\alpha}_{k}|^2$ according to $I_{\alpha} = -\sum_k w^{\alpha}_{k}\ln w^{\alpha}_{k}$. Information entropy measures the number N_{α} of significant simple components $|k\rangle$ of the eigenstate $|\alpha\rangle$ and therefore characterizes delocalization with respect to the basis $|k\rangle$, so that $l_\alpha = \exp(I_\alpha)$ shows the delocalization length. A fully delocalized function would have $l \to N$, the space dimension. Because of the orthogonality constraints, the average value for the GOE limit, when the amplitudes C_k^α are distributed normally, is $\bar{l}_\alpha = 0.48\,N$.

As can be seen from shell-model calculations [5], l_α of the eigenstates regularly increases with level density toward the GOE limit (but it does not reach this limit for a realistic self-consistent interaction strength). Both lowest and highest (in energy) states have reduced complexity. This can be understood with the aid of perturbation theory by starting with a noninteracting system and by switching on the interaction. Even in the second order, the ground state acquires a coherent mixing pushing its energy down. The reduced local level density hinders further mixing, which leaves information entropy at a relatively low value, although even the ground state in shell-model calculations, and from the electron scattering data, is noticeably different from the simple Fermi occupation. The fourth moment of amplitudes, $\sum_k |C_k^\alpha|^4$, the so-called inverse participation ratio, can be used for a complementary analysis. It is more sensitive to large components of the wave function, whereas information entropy emphasizes the presence of small components.

Empirically, the distribution functions of the amplitudes can be probed by transition probabilities. Thus, the neutronic decay of a neutron resonance singles out the component of the complex wave function for the simple configuration *ground state of the target nucleus + slow neutron in the continuum*. The distribution of neutron widths is indeed close to the Porter–Thomas (PT) distribution [24, 9]; this immediately follows from the Gaussian distribution of the amplitudes C_k^α. At lower excitation energies, the deviations from the PT distribution are still considerable [36]. A shell-model analysis [5] shows the presence of correlations in the wave functions, while the spectral statistics agree well with RMT. An interesting example, with possible astrophysical implications, is given [37] by Gamow–Teller strengths, which display a regular trend to growth with excitation energy that cannot be explained for purely chaotic wave functions, but which reflects the gross features of nuclear interactions. Assuming the PT distribution of the multipole strength and Wigner distribution of spacings for states invisible in an experiment with an insufficient resolution, one can perform a statistical analysis and recover the missing strength [38].

With the length l_α, or the corresponding number N_α of principal components, taken as a measure for the degree of complexity, a method for estimating the matrix elements of simple, say, one-body, operators in the region of chaotic dynamics was developed [10, 39]. Since typical components of a generic wave function in the chaotic region of complexity N have a magnitude $|C| \simeq 1/\sqrt{N}$, it is easy to show that matrix elements between a simple state and a chaotic state of complexity N, as well as matrix elements between two complex states with approximately the same degree of complexity, are scaled as $N^{-1/2}$. This gives a useful way to classify various processes. Specifically, one can see that a perturbation that mixes chaotic states at a high level density $\rho = 1/D$ is statistically enhanced by a factor $N^{1/2}$ in relation to the mixing by the same perturbation of simple states at a typical spacing of about ND. The statistical enhancement works as an amplifier of weak interactions, causing large effects of parity nonconservation in polarized neutron scattering [40] and neutron-induced fission [41]. In the last case, the independence of the parity-violating fragment asymmetry of the final observables [42], such as the mass distribution or kinetic energy distribution, confirms that the mixing occurred at the stage of a "hot" compound nucleus.

The information entropy is representation-dependent. In fact, it characterizes the degree of mixing of basis states and therefore reflects the interrelation between the eigenbasis and the reference basis. There are attempts at finding invariant measures for the degree of complexity. A useful tool is given by the correlational (von Neumann) entropy defined [43] through the response of the system to external noise. If a random parameter η with a certain distribution function is introduced in the Hamiltonian, $H \to H(\eta)$, one can consider a given energy term $E_\alpha(\eta)$ and construct the density matrix for this level $|\alpha\rangle$ by averaging the wave-function components over η, $\rho^\alpha_{kk'} = \overline{C_k^\alpha C_{k'}^{\alpha *}}$. Here, the phases of the components and, therefore, correlations are taken into account. The invariant von Neumann entropy is defined in a standard way as $S_\alpha = -\mathrm{tr}\{\rho^\alpha \ln(\rho^\alpha)\}$. One can start with a pure function, when the density matrix is the projection operator and has one eigenvalue equal to unity, while all other eigenvalues are zeros; the entropy S of a pure state vanishes. Addressing random noise, one finds that each order of perturbation theory brings in one new nonzero eigenvalue, increasing the value of entropy [43]. Thus, we measure, in a sense, the number of mixed exciton classes instead of the number of components. But the global behavior of S_α along the spectrum is similar to that of the information entropy I_α if the noise is reasonably weak in order to not destroy the system. The correlational entropy is very sensitive to the regions of parameter space where the mean field undergoes strong changes, an analog of macroscopic phase transitions [44].

6. STRENGTH FUNCTIONS

A high information entropy does not prove the chaotic character of wave functions. The function can be coherent, as in the case of collective excitations. However, the statistical weight of collective states is low. They are seen as an excess of an amplitude for a specific simple excitation mode in a given energy region. The concentration of the collective strength in some energy range resembles the phenomenon of scars [45] studied in one-body chaos. The eigenstates $|\alpha\rangle$ are "scarred" by a simple mode $|k\rangle$ of the same symmetry. A convenient tool for such studies is a strength function of a simple mode $|k\rangle$, $F_k(E) = \sum_\alpha w_k^\alpha \delta(E - E_\alpha)$. The strength function (local density of states in condensed matter physics) can be defined in the same way for any simple state $|k\rangle$ regardless of its collectivity. This important concept connects experimental data, which do not resolve dense individual states, with the ideas of quantum chaos.

The fragmentation patterns of individual states are very different, but averaging over a few neighboring states reveals [8, 5, 46] a generic shape of the strength function in the region of chaotic dynamics. Corresponding theory, going back to Wigner [47], can be formulated in a language close to that of quantum chaos [48, 49]. Two physically different limits are distinguished by the ratio of the spreading width Γ to the energy interval Δ of coupling of the original simple state to the chaotic background. The interval Δ is on the order of the energy range of doorway states that serve as an entrance step for the process of stochastization (the bandwidth in the banded random-matrix model).

As far as $\Gamma/\Delta \ll 1$, the standard model of the strength function [9] leads to the Breit–Wigner (BW) shape and the golden rule $\Gamma = 2\pi\langle V^2\rangle/D$ in terms of the average coupling intensity $\langle V^2\rangle$ and the background level spacing D. This expression alone shows [50, 46] the stability of Γ with respect to the process of stochastization: it is invariant under N scaling. Therefore, the spreading width is expected to be saturated as a function of excitation energy. This is clearly seen for isobaric analog resonances [51]. The situation is more complicated for dipole giant resonances (in fact, families of states built on different fluctuating shapes of the mean field [52]). If $\Gamma/\Delta \geq 1$ ("strong coupling"), the standard model does not work; the shape is different from BW; and the spreading width is close [46] to 2σ, where σ is the energy dispersion of the original state. Therefore, Γ can be evaluated in both limits without a full diagonalization of the Hamiltonian. The standard quadratic dependence on the interaction strength λ converts into the linear one at strong coupling, and the behavior $\Gamma(\lambda)$ can be parametrized [46] as $\Gamma(\lambda) = a\lambda^2/(1 + b\lambda)$ with the parameters a and b predicted from the level density and the average energy dispersion.

7. MULTIPLE GIANT RESONANCES

A bright example of application is given by multiple giant resonances (GR) observed in nuclei. Although nuclear GRs are analogs of zero sound in a Fermi liquid, there is a crucial physical difference. In a macroscopic liquid, the energy $\hbar\omega$ of a single sound quantum is always small in relation to temperature T, and the wave is a classical packet of many quanta. In the case of GRs, the situation is opposite, $\hbar\omega/T \gg 1$, and a new interesting question arises: What is the width Γ_n of the pure n-quantum state? Simple arguments based on the standard model of strength functions predict $\Gamma_n/\Gamma_1 = n$, whereas experiments show a narrower width of $\Gamma_2/\Gamma_1 \approx 1.5$. This narrowing is related to the deviations from the standard model and BW shape [53, 54], which are amplified in the convolution of the strength function for multiple sequential excitations. The resulting strength functions is similar to the central limit theorem, close to the Gaussian, in which case widths are added in quadrature. This is in fact the same as the transition from a quadratic to a linear dependence of $\Gamma(\lambda)$; as a result, $\Gamma_n/\Gamma_1 \to \sqrt{n}$.

8. EXPONENTIAL CONVERGENCE

The topic of the localization of eigenstates in Hilbert space recently attracted great attention [55, 56, 20], but the conclusions drawn are contradictory. Shell-model studies [46] show that the remote wings of the strength function of a generic state in the region of high level density decrease exponentially with the distance from the energy centroid, similarly to the tails of the wave functions of spatially localized states in disordered solids. There are also theoretical arguments that relate the exponential wings to the deviations from the exponential time-decay law at short times after the creation of a nonstationary simple state.

Considering the practical problem of diagonalizing a large Hamiltonian matrix with chaotic eigenstates, one can translate [57] the presence of an exponential tail of the strength function into exponentially small contributions of remote basis states to a time-independent wave function. The range of strong contributions is given by the above-mentioned estimate $\Gamma \approx 2\sigma$. Therefore, large shell-model matrices can be truncated [58], including, in the primary diagonalization, configurations with centroids closer than, say, 3σ. Such a truncation already gives, as a rule, a good estimate for the eigenvalue and a high overlap with the exact eigenvector. After few steps of extending the matrix size by including the next configurations, the rest of the matrix can be taken effectively into account by an exponential extrapolation [57]. This procedure was successfully tested and compared with an exact diagonalization. The exponential convergence is a useful practical tool; it works especially well for collective states. Recently, it was used to calculate masses of astrophysically interesting nuclei in the fp shell [59].

9. CHAOS AND THERMAL EQUILIBRIUM

The degree of complexity of chaotic wave functions, measured, for example, by the information entropy, proves to be a smooth monotonically increasing (in practical shell-model calculations—to the middle of the spectrum) function of the excitation energy. Here, one can bridge the gap between the "static" GOE limit (no spectral evolution, all eigenfunctions equally complex), suitable only for describing local fluctuative properties, and the realistic physics of many-body systems; again, the nucleus provides an appropriate testing ground. The information entropy I_α, or the localization length l_α, define the "comoving" GOE frame. Owing to smooth changes along the spectrum, such measures of complexity acquire the properties of thermodynamic variables, and one can introduce the related temperature scale [60, 5].

However, as discussed earlier, these measures of the degree of complexity of individual wave functions depend on the basis. In usual statistical mechanics, the canonical ensemble is determined with the aid of the density matrix $\mathcal{D}_{kl} = \overline{C_k^* C_l}$ with averaging over the states of the environment (heat bath). The thermal entropy $S_{\rm th} = -{\rm tr}\,(\mathcal{D} \ln \mathcal{D})$ is basis-invariant. A closed finite system, such as a nucleus, is described by particle variables, where the role of a heat bath is played [60, 5] by residual interactions (for a nucleus, one can imagine averaging over meson or subnucleon degrees of freedom). In the basis that separates, in an optimal way, regular (mean-field) and incoherent (collision) aspects, the information entropy properly reflects the chaotic features of dynamics. The mean-field basis is therefore singled out, as can be seen from the alternative derivation of the mean-field equations [61] with the aid of the explicit assumption of the chaotic properties of intermediate states in exact operator equations of motion. The density matrix $\mathcal{D}$, averaged over a few individual eigenstates $|\alpha\rangle$, becomes diagonal in the mean-field basis without any external decoherence. Thus, in such a self-consistent basis, the information entropy is equivalent to the basis-independent thermal entropy [60].

These conclusions can be valid only if the macroscopic properties of neighboring eigenfunctions are similar. Only in that case will the coarse-grained observables not depend, after a short phase decoherence time, on the exact population of individual eigenstates within a small energy interval, whereas this independence is necessary to make a microcanonical description meaningful. The similarity of adjacent functions [62] is achieved by chaotic mixing. We arrive at a modified paradigm of the statistical mechanics of closed systems where quantum chaos plays a decisive role, uniformly mixing wave functions of approximately the same energy.

10. FERMI LIQUID DESCRIPTION

Average single-particle occupation numbers for mean-field orbitals determine the response of the system to external fields. Analyses of nuclear and atomic eigenfunctions in the chaotic domain invariably show that the occupancies found for individual states are smooth functions along the spectrum that are uniquely related to the degree of complexity. Even for a relatively small particle number, they tend to approach the Fermi–Dirac distribution [5, 49]. One can develop arguments [27] showing the mechanism of this evolution in terms of the strength functions of simple configurations. This extends Fermi liquid theory beyond the region of its conventional validity to excitation energies where the lifetime of quasiparticles is short. Again, chaotic mixing averages out accidental features of eigenfunctions, revealing regular trends of occupancies. It now becomes possible to use another thermodynamic scale, namely, that which is defined by the single-particle entropy of a Fermi gas [60, 5]. For a self-consistent choice of mean-field orbitals, this scale is virtually equivalent [5] to those mentioned above, microcanonical thermal or based on the information entropy. A significant difference may arise at a very low excitation energy, where even the ground state should be characterized by a nonzero single-particle temperature [61].

11. GEOMETRIC CHAOTICITY

Finite many-body systems allow one to study an aspect of quantum chaos that was almost ignored previously. Apart from energy, the total angular momentum $\mathbf{J}$ of a finite system is conserved. Chaotic mixing respects rotational invariance and occurs separately in each block of states with a given value of J. However, the fact that dynamics is governed by the same two-body Hamiltonian inevitably induces correlations between blocks. The signatures of these correlations can be sought experimentally—for example, as the similarity of mixing for close values of J and, consequently, as a chance of the existence of compound rotational bands [63], in which case a significant transition strength of a compound state is directed to its single counterpart at a lower J value, instead of being chaotically fragmented between different final states. A similar effect may occur in consecutive pair transfers between the corresponding states of neighboring nuclei (pairing rotation).

Within each shell-model partition of a sufficiently high dimension, the orthogonality of different states with the same J based on the same mean-field configuration requires fairly complicated schemes of vector coupling of individual particle spins to the total spin $\mathbf{J}$. This implies a certain degree of geometric chaoticity, which develops even in a noninteracting system and leads to a specific J dependence of the level density and to a very complex structure of correct linear combinations of m-scheme Slater determinants. For this reason, almost all JT-projected states within a shell-model partition have close values of the energy variance σ, which was instrumental for the use of exponential convergence. The random spin coupling proceeds similarly to a random walk and can be considered in a statistical manner [28]. In dynamical problems, such as anharmonic couplings of soft vibrational modes, dissipative effects, or large-amplitude collective motions in general, the conservation of angular momentum is also associated with geometric chaoticity of the response of incoherent excitations to such collective motions. It is possible to base new nonperturbative approximate methods on geometric chaoticity by using diagrammatic techniques [64] analogous to those developed for disordered solids [65] or random matrices [12, 13].

12. ORDER FROM RANDOM INTERACTIONS

The recent development revealed new and rather unexpected features of random interactions. It was discovered [19, 66] that some habitual features of nuclear spectra, such as the predominance of the ground-state spin $J_0 = 0$ in even–even nuclei, which is usually attributed to the strong attractive pairing correlations of nucleons, are preserved up to some extent for two-body interactions taken at random (but still rotationally invariant). In fact, conclusions of this type are quite insensitive to a specific choice of random ensemble for the interaction. If matrix elements of the interaction independently take positive and negative signs in each two-body channel, the probability f_0 for the ground state of a system with an even particle number to have the total spin $J_0 = 0$ is much higher than the statistical fraction of $J = 0$ states in the whole Hilbert space; typically, f_0 reaches a value around 60–70%. This phenomenon was recently discussed by many authors, but the proposed explanations either failed or just reformulated this finding in different terms without shedding light on the underlying physical mechanism.

As was shown in [67, 68], the predominance of $J_0 = 0$ in the ground state for a random rotationally invariant shell-model Hamiltonian is determined, at least partly, by the geometry of a finite Fermi system and is therefore very stable with respect to the variations of the Hamiltonian or random ensemble (or both). The deep reason is related to the spontaneous violation of time-reversal invariance by a ground state with $J_0 \neq 0$. An explicit breaking of $\mathcal{T}$ symmetry by an imaginary random interaction [69] does not help since the effects expressed in terms of odd powers of the imaginary part anyway are averaged out in a random ensemble. However, spontaneous breaking occurs owing to the degeneracy of the ground state in the magnetic quantum number $M = J_z$. The symmetry is restored by the rotation of the orientation as a Goldstone mode.

We consider an aligned state $M = J$, limiting ourselves, for the sake of simplicity, to the case of a single-j level. Applying statistical arguments, we find the single-particle occupation numbers n_m for the most probable many-body state under the constraints on the total particle number $N = \sum_m n_m$ and the spin projection $M = \sum_m m n_m$. This leads to the Fermi–Dirac distribution with the corresponding Lagrange multipliers of the chemical potential and "magnetic field," or rather cranking frequency around the symmetry axis. The expectation value of the random Hamiltonian for such a distribution of particles gives, on average, an yrast line with a random sign of the effective moment of inertia. We conclude that, in this approximation, the ground state is expected to have either zero spin, $J_0 = 0$, or the maximum possible spin, $J = J_{\max}$, with the probability of 50% each. In fact, additional dynamical and kinematical effects (bosonic properties of fermionic pairs, correlations between the occupation numbers n_m, the uniqueness of the maximum spin state, and so on) increase f_0 and reduce $f_{J_{\max}}$ in relation to the zero-order result of 50%, although the probability of $J = J_{\max}$ remains enhanced as a rule.

The analysis of ground-state wave functions [67, 59] shows that, in contrast to the earlier statements of [19, 66], these states do not carry significant collectivity and agree with the random distribution of components in the basis of noninteracting shell-model states. In the same basis, the information entropy of the eigenstates generated by a random interaction is at the GOE level, except for very few edge states. Small effective pairing effects emerge for the ground state because of off-diagonal mixing matrix elements, which are not averaged out in the second order. This leads to the overwhelming fraction of the ground-state spin $J_0 = 0$ in a system of randomly interacting fermions on many spin-$1/2$ levels where off-diagonal processes prevail.

13. CONTINUUM EFFECTS

We discussed the chaotic dynamics of complicated many-body states as if they were genuinely stable. In reality, all excited states are quasistationary and have a finite lifetime. Nuclear excited states emit gamma rays, nucleons, or heavier fragments. We can say that the system is open, and these states are coupled to a continuum and can be seen as resonances in some reactions. Does this fact change their chaotic properties? Until now, continuum effects [70] have not been studied with the same degree of detalization as chaotic properties of an idealized discrete spectrum. However, they require particular attention, especially as nuclear physics moves from the valley of stability to short-lived and loosely bound nuclei, where coupling to a continuum may be important even at rather low excitation energies.

At a low level density, the widths of quasistationary states are small and the levels do not overlap. Here, the characteristic width-to-spacing ratio $\kappa = \Gamma/D$ is small, and the spectrum looks like a comb of well-isolated narrow resonances. However, even in this case, the nearest level spacing distribution is modified [71, 72] at tiny spacings $s < \Gamma$, where the levels cease to repel each other, and $P(s) \to \text{const} \neq 0$. In other words, with an extremely high resolution, one can notice the energy uncertainty due to a finite lifetime. Assuming the GOE-type chaotic internal dynamics and uncorrelated decay amplitudes of intrinsic states, one can predict [73, 71] the distribution of the complex energies $\mathcal{E} = E - (i/2)\Gamma$ and the poles of the scattering matrix in the complex plane. Up to now, these predictions have been tested only in numerical simulations because of the lack of empirical data of a good quality.

As the overlap of resonances increases, high-order effects of continuum coupling become strong and lead to the effective interaction of intrinsic states through common decay channels. This interaction is energy-dependent and non-Hermitian. The anti-Hermitian part comes from the singularities of the effective propagator corresponding to the decay channels that are open at a given energy. The general form of this part is dictated by unitarity [74, 71] and can be represented in the factorized form $W_{\alpha\alpha'} = \sum_c A^c_\alpha A^{c*}_{\alpha'}$ in terms of the energy-dependent amplitudes A^c_α for decay from intrinsic states $|\alpha\rangle$ to the open channels c. At a certain value of the overlap parameter κ, a phase transition occurs with a sharp redistribution of the widths [71]. The number of states that is equal to the number of open channels accumulates a large fraction of the total summed width of all interacting states, making the remaining states short-lived. This can be interpreted as the "self-organization" [75] of intrinsic dynamics by a strong coupling through a continuum. Formally, we deal with the analog of superradiance in optics [76], where a specific state in a system of atoms coupled through the common radiation field acquires a radiation width much larger than that of an individual atom. From the "outside" point of view in a nuclear reaction experiment, one will see very narrow compound states on the smooth background of fast direct processes. Narrow resonances of this type are experimentally known, for example, in Δ–nucleus systems [77, 78]. Very rich physics of collective motion in an open system with chaotic intrinsic interactions [70, 79–81] still waits to be studied. Open quantum dots should reveal similar effects.

Many-body chaos in finite strongly interacting quantum systems; the new approach to the thermodynamics and statistical mechanics of small objects; the interplay of collectivity, random interactions, and geometry; the decay of chaotic systems; and other exciting topics form a fresh and intriguing field for future studies and applications, from details of nuclear spectra to the stability of quantum computers.

ACKNOWLEDGMENTS

My interest in quantum chaos and its manifestations in nuclear physics was induced by repeated discussions with I.I. Gurevich who was an "open" referee for the review article [82] devoted to the 100th anniversary of Niels Bohr. I am grateful to O. Bohigas whose objections were helpful for formulating my viewpoint.

This work was supported in part by the Nobel Foundation and the US National Science Foundation (grant nos. 96-05207 and 00-70911).

REFERENCES

1. F. Haake, *Quantum Signatures of Chaos* (Springer-Verlag, New York, 1991).
2. F. M. Izrailev, Phys. Rep. **196**, 299 (1990).
3. M. Brack and R. K. Bhaduri, *Semiclassical Physics* (Addison-Wesley, Reading, 1987).
4. M. S. Gutzwiller, *Chaos in Quantum and Classical Mechanics* (Springer-Verlag, 1990).
5. V. Zelevinsky, B. A. Brown, N. Frazier, and M. Horoi, Phys. Rep. **276**, 85 (1996).
6. D. Kusnezov, B. A. Brown, and V. Zelevinsky, Phys. Lett. B **385**, 5 (1996).
7. S. Åberg, Prog. Part. Nucl. Phys. **28**, 11 (1992).

8. V. V. Flambaum, A. A. Gribakina, G. F. Gribakin, and M. G. Kozlov, Phys. Rev. A **50**, 267 (1994).
9. Å. Bohr and B. Mottelson, *Nuclear Structure*, Vol. 1: *Single-Particle Motion* (Benjamin, New York, 1969).
10. O. P. Sushkov and V. V. Flambaum, Usp. Fiz. Nauk **136**, 3 (1982) [Sov. Phys. Usp. **25**, 1 (1982)]; V. V. Flambaum and O. P. Sushkov, Nucl. Phys. A **412**, 13 (1984).
11. O. Bohigas, M. J. Giannoni, and C. Schmit, Phys. Rev. Lett. **52**, 1 (1984).
12. T. A. Brody *et al.*, Rev. Mod. Phys. **53**, 385 (1981).
13. T. Guhr, A. Müller-Groeling, and H. A. Weidenmüller, Phys. Rep. **299**, 189 (1998).
14. Y. V. Fyodorov *et al.*, Phys. Rev. Lett. **76**, 1603 (1996).
15. O. Bohigas and H. A. Weidenmüller, Annu. Rev. Nucl. Part. Sci. **38**, 421 (1988).
16. Y. Alhassid and A. Novoselsky, Phys. Rev. C **45**, 1677 (1992).
17. V. Zelevinsky, Annu. Rev. Part. Sci. **46**, 237 (1996).
18. V. V. Flambaum, G. F. Gribakin, and F. M. Izrailev, Phys. Rev. E **53**, 5729 (1996).
19. C. W. Johnson, G. F. Bertsch, and D. J. Dean, Phys. Rev. Lett. **80**, 2749 (1998).
20. L. Benet, T. Rupp, and H. A. Weidenmüller, Phys. Rev. Lett. **87**, 010601 (2001).
21. I. I. Gurevich, Zh. Éksp. Teor. Fiz. **9**, 1283 (1939).
22. F. J. Dyson, J. Math. Phys. (N.Y.) **3**, 140 (1962); **3**, 157 (1962); **3**, 166 (1962).
23. M. L. Mehta, *Random Matrices* (Academic, New York, 1990).
24. *Statistical Theories of Spectra: Fluctuations,* Ed. by C. E. Porter (Academic, New York, 1965).
25. N. Rosenzweig and C. E. Porter, Phys. Rev. **120**, 1698 (1960).
26. R. Haq, A. Pandey, and O. Bohigas, Phys. Rev. Lett. **48**, 1086 (1982).
27. V. V. Flambaum and F. M. Izrailev, Phys. Rev. E **55**, R13 (1997); **56**, 5144 (1997).
28. T. Ericson, Adv. Phys. **9**, 425 (1960).
29. I. I. Gurevich and M. I. Pevzner, Nucl. Phys. **2**, 575 (1957).
30. A. Volya, B. A. Brown, and V. Zelevinsky, Phys. Rev. C (in press).
31. J. D. Garrett, J. Q. Robinson, A. J. Foglia, and H. Q. Jin, Phys. Lett. B **392**, 24 (1997).
32. S. Raman *et al.*, Phys. Rev. C **43**, 521 (1991); A. A. Adams *et al.*, Phys. Lett. B **392**, 1 (1997).
33. J. B. French *et al.*, Phys. Rev. Lett. **54**, 2313 (1985); **58**, 2400 (1987).
34. J. Rekstad *et al.*, Phys. Rev. C **47**, 2621 (1993).
35. V. Zelevinsky, M. Horoi, and B. A. Brown, Phys. Lett. B **350**, 141 (1995).
36. A. A. Adams, G. E. Mitchell, and J. G. Shriner, Phys. Lett. B **422**, 13 (1998).
37. N. Frazier, B. A. Brown, D. J. Millener, and V. Zelevinsky, Phys. Lett. B **414**, 7 (1997).
38. G. Kilgus *et al.*, Z. Phys. A **326**, 41 (1987).
39. V. V. Flambaum and G. F. Gribakin, Prog. Part. Nucl. Phys. **35**, 423 (1995).
40. V. P. Alfimenkov *et al.*, Nucl. Phys. A **398**, 93 (1983); C. M. Frankle *et al.*, Phys. Rev. Lett. **67**, 564 (1991); L. Y. Lowie *et al.*, Phys. Rev. C **59**, 1119 (1999).
41. G. V. Danilyan, B. D. Vodennikov, V. P. Dronyaev, *et al.*, Pis'ma Zh. Éksp. Teor. Fiz. **26**, 197 (1977) [JETP Lett. **26**, 186 (1977)].
42. G. A. Petrov, Nucl. Phys. A **502**, 297 (1989).
43. V. V. Sokolov, B. A. Brown, and V. Zelevinsky, Phys. Rev. E **58**, 56 (1998).
44. P. Cejnar, V. Zelevinsky, and V. V. Sokolov, Phys. Rev. E **63**, 036127 (2001).
45. E. J. Heller, Phys. Rev. Lett. **53**, 1515 (1984).
46. N. Frazier, B. A. Brown, and V. Zelevinsky, Phys. Rev. C **54**, 1665 (1996).
47. E. P. Wigner, Ann. Math. **62**, 548 (1955).
48. B. Lauritzen, P. F. Bortignon, R. A. Broglia, and V. G. Zelevinsky, Phys. Rev. Lett. **74**, 5190 (1995).
49. V. V. Flambaum, F. M. Izrailev, and G. Casati, Phys. Rev. E **54**, 2136 (1996).
50. H. L. Harney, A. Richter, and H. A. Weidenmüller, Rev. Mod. Phys. **58**, 607 (1986).
51. J. Reiter and H. L. Harney, Z. Phys. A **337**, 121 (1990).
52. D. Kusnezov, Y. Alhassid, and K. A. Snover, Nucl. Phys. A **649**, 193c (1999).
53. C. A. Bertulani and V. G. Zelevinsky, Phys. Rev. Lett. **71**, 967 (1993); Nucl. Phys. A **568**, 931 (1994).
54. C. H. Lewenkopf and V.G. Zelevinsky, Nucl. Phys. A **569**, 183c (1994).
55. B. L. Altshuler, Y. Gefen, A. Kamenev, and L. S. Levitov, Phys. Rev. Lett. **78**, 2803 (1997).
56. X. Leyronas, J. Tworzydlo, and C. W. J. Beenakker, Phys. Rev. Lett. **82**, 4894 (1999).
57. M. Horoi, A. Volya, and V. Zelevinsky, Phys. Rev. Lett. **82**, 2064 (1999).
58. M. Horoi, B. A. Brown, and V. Zelevinsky, Phys. Rev. C **50**, R2274 (1994).
59. M. Horoi, B. A. Brown, and V. Zelevinsky, Phys. Rev. C **65**, 027303 (2002).
60. M. Horoi, B. A. Brown, and V. Zelevinsky, Phys. Rev. Lett. **74**, 5194 (1995).
61. V. G. Zelevinsky, Nucl. Phys. A **555**, 109 (1993).
62. I. C. Percival, J. Phys. B **6**, L229 (1973).
63. T. Døssing *et al.*, Phys. Rep. **268**, 1 (1996).
64. S. T. Belyaev and V. G. Zelevinsky, Yad. Fiz. **2**, 615 (1966) [Sov. J. Nucl. Phys. **2**, 442 (1966)].
65. S. F. Edwards, Philos. Mag. **3**, 1020 (1958).
66. C. W. Johnson, G. F. Bertsch, D. J. Dean, and I. Talmi, Phys. Rev. C **61**, 014311 (2000).
67. D. Mulhall, A. Volya, and V. Zelevinsky, Phys. Rev. Lett. **85**, 4016 (2000); Nucl. Phys. A **682**, 229c (2001).
68. V. G. Zelevinsky, D. Mulhall, and A. Volya, Yad. Fiz. **64**, 579 (2001) [Phys. At. Nucl. **64**, 525 (2001)].
69. R. Bijker, A. Frank, and S. Pittel, Phys. Rev. C **60**, 021302 (1999).
70. V. V. Sokolov and V. G. Zelevinsky, Ann. Phys. (N.Y.) **216**, 323 (1992).
71. V. V. Sokolov and V. G. Zelevinsky, Phys. Lett. B **202**, 10 (1988); Nucl. Phys. A **504**, 562 (1989).

72. S. Mizutori and V. G. Zelevinsky, Z. Phys. A **346**, 1 (1993).
73. N. Ulla, J. Math. Phys. (N.Y.) **10**, 2099 (1969).
74. C. Mahaux and H. A. Weidenmüller, *Shell-Model Approach to Nuclear Reactions* (North-Holland, Amsterdam, 1969).
75. I. Rotter, Rep. Prog. Phys. **54**, 635 (1991).
76. R. H. Dicke, Phys. Rev. **93**, 99 (1954).
77. P. Bartsch *et al.*, Eur. Phys. J. A **4**, 209 (1999).
78. N. Auerbach and V. Zelevinsky, Phys. Rev. C **65**, 034601 (2002).
79. V. V. Sokolov and V. G. Zelevinsky, Fizika (Zagreb) **22**, 303 (1990).
80. V. V. Sokolov, I. Rotter, D. V. Savin, and M. Müller, Phys. Rev. C **56**, 1031 (1997); **56**, 1044 (1997).
81. V. V. Sokolov and V. Zelevinsky, Phys. Rev. C **56**, 311 (1997).
82. S. T. Belyaev and V. G. Zelevinsky, Usp. Fiz. Nauk **147**, 210 (1985) [Sov. Phys. Usp. **28**, 854 (1985)].

Physics of Atomic Nuclei, Vol. 65, No. 7, 2002, pp. 1198–1218. From Yadernaya Fizika, Vol. 65, No. 7, 2002, pp. 1230–1250.
Original English Text Copyright © 2002 by Pavlichenkov.

90th ANNIVERSARY OF I.I. GUREVICH'S BIRTHDAY

Superfluid-to-Normal Phase Transition and Extreme Regularity of Superdeformed Bands*

I. M. Pavlichenkov
Russian Research Centre Kurchatov Institute, pl. Kurchatova 1, Moscow, 123182 Russia

Received November 14, 2001

Abstract—We derive an exact semiclassical expression for the second inertial parameter $\mathcal{B}$ for superfluid and normal phases. Interpolation between these limiting values shows that the function $\mathcal{B}(I)$ changes sign at the spin I_c that is critical for the rotational spectrum. The quantity $\mathcal{B}$ proves to be a sensitive measure of the change in static pairing correlations. The superfluid-to-normal transition reveals itself in a specific variation of the ratio $\mathcal{B}/\mathcal{A}$ versus the spin I with a plateau characteristic of the normal phase. We find this dependence to be universal for normal deformed and superdeformed bands. A long plateau with a small value of $\mathcal{B}/\mathcal{A} \sim A^{-8/3}$ explains the extreme regularity of superdeformed bands. *© 2002 MAIK "Nauka/Interperiodica".*

1. INTRODUCTION

Recently, phase transitions in mesoscopic systems have been the subject of intense discussions in nuclear and solid-state physics. Isai Isidorovich Gurevich was the first to employ (in 1939) the concept of a temperature phase transition in nuclear studies [1]. His prediction was based on the observation that the level density of resonance states formed by thermal-neutron capture is an unsteady function of the atomic mass number with a maximum in rare-earth nuclei.

The problem of a rotation-induced transition from a superfluid to a normal phase in nuclei has been a foremost theme in high-spin spectroscopy since Mottelson and Valatin [2] predicted a pairing collapse in rapidly rotating nuclei. This effect can be understood by analogy with a superconductor in a magnetic field. In a deformed nucleus, a Cooper pair is formed by two nucleons with opposite projections of single-particle angular momenta. Being time-noninvariant (as a magnetic field), the Coriolis force in a rotating nucleus acts on both nucleons in opposite directions and tries to decrease the spatial overlap of these time-reversal states. The Coriolis force increases in proportion to the spin of a band. Therefore, at some critical spin, one may expect that all pairs are broken and pairing correlations disappear completely. This phenomenon can be observed by the crossing of the ground-state superfluid band with the band based on the normal state. Thus, the rigid-body moment of inertia corresponding to the second band appears to be an obvious signature of the pairing phase transition.

However, this regime of the transition to the normal phase is not realized in nuclei because they are finite systems with a shell structure and a small number of nucleons involved in pairing correlations. The Coriolis force in a rotating nucleus is proportional to the single-particle angular momentum j of a nucleon. Thus, the Coriolis antipairing effect is the strongest for nucleons occupying the states of subshells with the largest j. In the vicinity of the Fermi surface, these so-called intruder orbitals arise from the $j = \mathcal{N} + 1/2$ subshell, where $\mathcal{N}$ is the principal quantum number of the above shell. Therefore, they are distinguished from other states of the partially filled shell by parity. At normal deformations (ND), intruder states retain their quantum number j, while, at superdeformations (SD), the j-subshell notation becomes less appropriate because of mixing. Initially, the Coriolis force breaks only that Cooper pair which belongs to intruder orbitals, whereas the rest of the pairs remain correlated. The band built on such a two-quasiparticle excitation (the rotationally aligned band) is characterized, due to the blocking effect, by appreciably smaller pairing correlations than the ground-state band. Having the largest moment of inertia, the former crosses the ground-state band and becomes the yrast band. The relevant phenomenon is known as backbending. The subsequent breaking of correlated pairs and their alignment make the internal structure of the yrast band nonhomogeneous and the transition to the normal phase configuration-dependent.

The standard definition of the phase transition is based on the mean-field approximation, in which

---

*This article was submitted by the author in English.

different phases are distinguished by an order parameter, i.e., the static pairing gap Δ. However, the mean-field approach to nuclear pairing correlations faces a fundamental problem of quantum fluctuations, which become quite strong for finite systems. The fluctuating part $\delta\Delta$ (dynamical pairing correlations) of the order parameter is commensurate with Δ in the transition region. Fluctuations smear out a sharp phase transition and make it a difficult issue to find an experimental signature of the superfluid-to-normal phase transition in rotational bands. For example, the dependence of the kinematical [$\mathfrak{J}^{(1)}$] or the dynamical [$\mathfrak{J}^{(2)}$] moment of inertia on the spin I is not a definitive indicator of a phase transition. Usually, experimental evidence of the pairing phase transitions has been discussed in terms of the relative excitation spectrum. As was shown in [3], the disappearance of static pairing leads to a change in the excitation spectrum, from a quasiparticle to a particle–hole spectrum. Unfortunately, the application of this criterion to ND bands [3–5] shows that this method is not free from ambiguities.

Meanwhile, it is well known that the change in the internal structure of a system manifests itself in the modification of its collective excitations. Examples for finite quantum systems are numerous. A classical one is the transition from deformed to spherical nuclei. In this case, the rotational–vibrational spectrum transforms into a purely vibrational one. Analysis of bifurcations in rotational spectra [6] shows an intimate connection between internal and rotational motions. For example, angular-momentum alignment in a band (a change in the coupling scheme) is observed as an increase in the energy signature splitting [7].

The transition we study is more delicate. Let us consider the simplest rotational sequence having the parity and signature $(\pi\alpha) = (+0)$. The relevant energy spectrum can be parametrized as

$$E(I) = \mathcal{A}I(I+1) + \mathcal{B}I^2(I+1)^2, \tag{1.1}$$

where $\mathcal{A} = \hbar^2/2\mathfrak{J}^{(1)}$ and $\mathcal{B}$ are the first two inertial parameters. The spectrum in (1.1) undergoes a noticeable modification if, for example, the second inertial parameter changes sign at some spin I_c. For $I < I_c$, the spectrum is compressed in relation to the rigid-rotor spectrum because $\mathcal{B}$ is negative for low-I states. However, the spectrum becomes extended for $I > I_c$. The effect can be visualized by using the I dependence of the ratio $\mathcal{B}/\mathcal{A}$. The main objective of the present study is to analyze this dependence.

The parameters $\mathcal{A}$ and $\mathcal{B}$ are determined by the γ-ray transition energies $E_\gamma(I) = E(I+2) - E(I)$ as follows:

$$\mathcal{A}(I) = \frac{1}{4(2I+5)} \times \left[\frac{I^2+7I+13}{2I+3}E_\gamma(I) - \frac{I^2+3I+3}{2I+7}E_\gamma(I+2)\right],$$

$$\mathcal{B}(I) = \frac{1}{8(2I+5)}\left[\frac{E_\gamma(I+2)}{2I+7} - \frac{E_\gamma(I)}{2I+3}\right]. \tag{1.2}$$

The coefficient $\mathcal{B}$ characterizes the nonadiabatic properties of a band and is very sensitive to its internal structure. It also realizes the relationship between kinematical and dynamical moments of inertia. Using the well-known expressions for these quantities (see, for example, [8]) and the last formula (1.2), we get

$$\mathcal{B} = \frac{\hbar^2}{2(2I+3)(2I+7)}\left[\frac{1}{\mathfrak{J}^{(2)}} - \frac{2I}{(2I+5)\mathfrak{J}^{(1)}}\right]. \tag{1.3}$$

Thus, the parameter $\mathcal{B}(I)$ is proportional to the difference $\mathfrak{J}^{(1)} - \mathfrak{J}^{(2)}$ in the high-I limit. The ratio $\mathcal{B}/\mathcal{A}$ also determines the convergence radius of the rotational-energy expansion in terms of $I(I+1)$ [9]. A faster convergence is obtained with the Harris formula

$$E(\omega) = E_0 + \frac{1}{2}\alpha\omega^2 + \frac{3}{4}\beta\omega^4 + \ldots, \tag{1.4}$$

which is based on the fourth-order cranking expansion with

$$\alpha = \frac{1}{\omega}\mathrm{tr}(j_x\rho^{(1)}), \quad \beta = \frac{1}{\omega^3}\mathrm{tr}(j_x\rho^{(3)}), \tag{1.5}$$

where $\rho^{(n)}$ is the nth correction to the nucleus density matrix; j_x is the projection of the single-particle angular-momentum operator onto the rotational axis x, which is perpendicular to the symmetry axis z; and ω is the rotational frequency. The latter depends on the angular momentum of the system and is determined by

$$\hbar\sqrt{I(I+1)} = \alpha\omega + \beta\omega^3 + \ldots. \tag{1.6}$$

It follows from Eqs. (1.1), (1.4), and (1.6) that

$$\alpha = \frac{\hbar^2}{2\mathcal{A}}, \quad \beta = -\frac{\hbar^4\mathcal{B}}{4\mathcal{A}^4}. \tag{1.7}$$

The problem of microscopically calculating the parameter $\mathcal{B}$ for ND nuclei attracted considerable attention (see the review article [10] and references therein). It was shown that this quantity receives contributions from four types of nonadiabatic effects:

(i) perturbation of quasiparticle motion by rotation (quasiparticle alignment),

(ii) attenuation of pairing correlations by the Coriolis force (Coriolis antipairing effect),

(iii) a change in the deformation of a nuclear self-consistent field (centrifugal stretching effect),

(iv) vibration–rotation interaction.

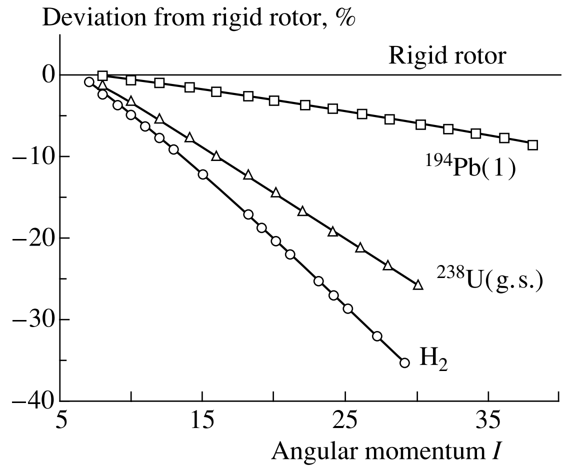

Fig. 1. Relative deviation of energies E in the SD band ^{194}Pb(1), the ground-state band of ^{238}U and the ground-state vibrational band of the H_2 molecule. The deviation was calculated by the formula $(E - E_{\rm rig})/E_{\rm rig}$, where $E_{\rm rig} = \mathcal{A}I(I+1)$, the parameters $\mathcal{A}$ being found from the energies $E_\gamma(4)$ of the $6 \to 4$ transitions. The experimental data were taken from [8, 14].

The first attempt at estimating $\mathcal{B}$ was made by the present author together with Grin' [11]. The Green's function formulation of the Hartree–Fock–Bogoliubov (HFB) method was used to find the expansion in (1.4) for an axially deformed oscillator potential as a self-consistent field. It was shown that the first and the second effect yield $\mathcal{B}/\mathcal{A} \sim A^{-4/3}$, while the centrifugal stretching contribution is $A^{2/3}$ times smaller for well-deformed nuclei.[1)] In the subsequent study [12], I found that the vibration–rotation contribution to the parameter $\mathcal{B}$ has the same $A^{2/3}$ fraction of the main effects. These results were confirmed by the calculations of Marshalek [13] with the more realistic Nilsson potential.

Thus, the first two effects are dominant for well-deformed nuclei. Quasiparticle alignment depends strongly on pairing correlations because the pairing force tries to bind pairs of particles in time-reversal states, reducing the ability of nucleons to carry an angular momentum. Therefore, the parameter $\mathcal{B}$ is very sensitive to the variation in pairing correlations along a band.

One of the amazing features of SD bands is the extreme regularity of their rotational spectra. To demonstrate this feature, the rotational spectra of different axial systems are compared in Fig. 1 with their rigid-rotor counterparts. This comparison shows that the SD band ^{194}Pb(1) is more regular than the ND band of ^{238}U and even the band of the simplest H_2 molecule [14]. Having the ratio $\mathcal{B}/\mathcal{A} \sim 10^{-5}$, the ^{194}Pb(1) band is not a champion among SD bands. For ^{152}Dy(1), the ratio is of the order of 10^{-6}, and this is 1000 times smaller than the above estimate $\mathcal{B}/\mathcal{A} \sim A^{-4/3}$. Thus, an SD nucleus is the best quantum rotor known in nature. Although numerous theoretical calculations (see, e.g., [15–18]) successfully reproduce the measured intraband γ-ray energies, the underlying microscopic mechanism of this phenomenon has yet to be well understood.

In this study, we will reveal an interconnection between the extreme regularity and the transition from the superfluid to the normal phase. The key to our theoretical approach lies in calculating the second inertial parameter. In comparison with ND bands, there are two features of pairing correlations in SD bands that prevent us from using the results of previous theoretical calculations of the parameter $\mathcal{B}$ for superdeformation. First, because of the large shell gap stabilizing the SD minimum, the static pairing field Δ is small and can be commensurate with its fluctuation $\delta\Delta$. A qualitative conclusion concerning the role of the static and dynamical pairing in SD bands is presented in [19]. Second, since intruder single-particle states, which are unavailable at normal deformations, appear near the Fermi surface in the case of superdeformations, it is necessary to go beyond the commonly used monopole pairing force [20]. The gauge-invariant pairing interaction expands the correlation space and stabilizes the pairing field. The coordinate-dependent (nonuniform) pairing is also crucial for the conservation of a nucleon current in a rotating nucleus [21].

To avoid calculating the parameter $\mathcal{B}$ in the transition region, where pairing fluctuations play an important role, an interpolation between $\mathcal{B}_s$ and $\mathcal{B}_n$ is used. The former is associated with the superfluid phase (where $\Delta \gg \delta\Delta$), while the latter is related to the normal phase ($\Delta = 0$). Thus, pairing fluctuations are unessential for these regions, and we can use the mean-field approach. In calculating $\mathcal{B}_s$, the nonuniform pairing induced by rotation is taken into account by using the method of [11]. It should be noted that the quantity $\mathcal{B}_s$ found in that study is inapplicable to superdeformation.

This article is organized as follows. In Section 2, the basic equations of the cranked HFB theory are presented within the Green's function method. The spinor form of the Gor'kov equations is used to simplify calculations in higher orders of perturbation theory. In Section 3, an exact expression for the second inertial parameter in the superfluid phase is derived by means of this technique in the semiclassical approximation. The result is valid for an arbitrary nuclear mean field. The exact analytic expression for $\mathcal{B}_s$ is

---

[1)] We use the estimate $\mathcal{A} \sim \varepsilon_{\rm F} A^{-5/3}$, where $\varepsilon_{\rm F}$ is the Fermi energy and A is the mass number.

obtained in Section 4 in an axially deformed oscillator potential. In that section, we also consider some limiting cases for this quantity. Of special interest is the limit of noninteracting nucleons. It is shown that the relevant parameter $\mathcal{B}_n$ is positive and is smaller than $\mathcal{B}_s$. A comparison with available experimental data for SD and ND bands is presented in Section 5. Section 6 concludes and summarizes the article. Preliminary results of this study were published in [22, 23].

2. GREEN'S FUNCTION FORMALISM IN THE CRANKING HARTREE–FOCK–BOGOLIUBOV METHOD

2.1. Cranked Gor'kov Equations

Our consideration is based on the shell-model Hamiltonian consisting of the cranked one-body term

$$h_\omega(\mathbf{r}) = -\frac{\mathbf{p}^2}{2M} + U(\mathbf{r}) - \boldsymbol{\omega}\cdot\boldsymbol{\ell}, \qquad (2.1)$$
$$\boldsymbol{\omega}\{\omega, 0, 0\}$$

(where $\mathbf{p}$ and M are the nucleon momentum and mass, respectively) and the residual short-range interaction, which is specified by the two-body delta-function interaction

$$v(\mathbf{r}, \mathbf{r}') = -g\delta(\mathbf{r} - \mathbf{r}'), \quad g > 0. \qquad (2.2)$$

For the sake of simplicity, we neglect spin in the cranking term and consider only the orbital part $\boldsymbol{\ell}$ of the angular momentum $\mathbf{j}$. We will also neglect the weak dependence of the self-consistent deformed potential U on rotation (centrifugal stretching effect).

In the coordinate representation, the Gor'kov equations [24] have the form

$$\begin{gathered}[\varepsilon - h_\omega(\mathbf{r}) + \varepsilon_{\mathrm{F}}]G(\mathbf{r}, \mathbf{r}', \varepsilon) \\ + \tilde{\Delta}(\mathbf{r})F^+(\mathbf{r}, \mathbf{r}', \varepsilon) = \delta(\mathbf{r} - \mathbf{r}'), \\ [\varepsilon + h^+_\omega(\mathbf{r}) - \varepsilon_{\mathrm{F}}]F^+(\mathbf{r}, \mathbf{r}', \varepsilon) \\ + \tilde{\Delta}^+(\mathbf{r})G(\mathbf{r}, \mathbf{r}', \varepsilon) = 0, \\ \tilde{\Delta}^*(\mathbf{r}) = g\oint\limits_C \frac{d\varepsilon}{2\pi i}F^+(\mathbf{r}, \mathbf{r}, \varepsilon).\end{gathered} \qquad (2.3)$$

The functions $G(\mathbf{r}, \mathbf{r}', \varepsilon)$ and $F^+(\mathbf{r}, \mathbf{r}', \varepsilon)$ are the Fourier transforms of the Green's functions

$$\begin{gathered}G(\mathbf{r}, \mathbf{r}', t - t') = -i(\Phi_N|T\{\psi(\mathbf{r}, t)\psi^+(\mathbf{r}', t)\}|\Phi_N), \\ F^+(\mathbf{r}, \mathbf{r}', t - t') \qquad (2.4) \\ = -i(\Phi_{N+2}|T\{\psi^+(\mathbf{r}, t)\psi^+(\mathbf{r}', t)\}|\Phi_N)e^{-2i\varepsilon_{\mathrm{F}}t},\end{gathered}$$

where Φ_N and Φ_{N+2} are the eigenfunctions of the ground state of a system of N and $N + 2$ interacting particles, ψ^+ and ψ are creation and annihilation operators in the Heisenberg representation, T is the time-ordering operator, and ε_{F} is the Fermi energy (the chemical potential of the system). The contour C consists of the real axis and an infinite semicircle in the upper half-plane.

2.2. Properties

In deriving Eqs. (2.3), the particle-number-nonconserving approximation was used. In the spirit of the mean-field approach, we neglect the difference between the functions Φ_N and Φ_{N+2}. Thus, the Gor'kov equations describe a system with broken gauge symmetry associated with the particle number. However, the average particle number is fixed. This is achieved by adding the term $-\varepsilon_{\mathrm{F}}\hat{N}$ to the Hamiltonian. The Lagrange multiplier ε_{F} is determined by the equation

$$N = \int d\mathbf{r}\oint\limits_C \frac{d\varepsilon}{2\pi i}G(\mathbf{r}, \mathbf{r}, \varepsilon). \qquad (2.5)$$

Equations (2.3) are also noninvariant under the more general gauge transformation (local Galilean transformation [25])

$$\psi(\mathbf{r}, t) \to \psi(\mathbf{r}, t)e^{i\phi(\mathbf{r})}, \qquad (2.6)$$

where $\phi(\mathbf{r})$ is an arbitrary function of the space coordinates. The quickest way to show this is to introduce the vector potential $\mathbf{A} = [\boldsymbol{\omega}\times\mathbf{r}]/2$ that allows us to rewrite the Coriolis term $V = -\boldsymbol{\omega}\cdot\boldsymbol{\ell}$ in the form $-2\mathbf{p}\cdot\mathbf{A}$. It is seen that the Hamiltonian in (2.1) lacks the term $2M\mathbf{A}^2$, which is absolutely necessary for the gauge invariance of Eqs. (2.3). However, since the two-body interaction (2.2) is invariant under the Galilean transformation, the conservation of the nucleon current is ensured.

The current density is expressed in terms of the Green's function G as [26]

$$\mathbf{j}(\mathbf{r}) = \lim_{\mathbf{r}'\to\mathbf{r}}\oint\limits_C \frac{d\varepsilon}{2\pi i} \qquad (2.7)$$
$$\times\left\{\frac{i\hbar}{2M}(\nabla_{\mathbf{r}} - \nabla_{\mathbf{r}'}) - [\boldsymbol{\omega}\times\mathbf{r}]\right\}G(\mathbf{r}, \mathbf{r}', \varepsilon).$$

With this definition, we find

$$\operatorname{div}\mathbf{j}(\mathbf{r}) = \lim_{\mathbf{r}'\to\mathbf{r}}\oint\limits_C \frac{d\varepsilon}{2\pi\hbar} \qquad (2.8)$$
$$\times[h_\omega(\mathbf{r}) - h^+_\omega(\mathbf{r}')]G(\mathbf{r}, \mathbf{r}', \varepsilon).$$

Using the first of Eq. (2.3) and their complex conjugate

$$\begin{gathered}[\varepsilon - h^+_\omega(\mathbf{r}') + \varepsilon_F]G(\mathbf{r}, \mathbf{r}', \varepsilon) \qquad (2.9) \\ + \tilde{\Delta}^*(\mathbf{r}')F(\mathbf{r}, \mathbf{r}', \varepsilon) = \delta(\mathbf{r} - \mathbf{r}'),\end{gathered}$$

we finally obtain

$$\operatorname{div}\mathbf{j}(\mathbf{r}) = \oint\limits_C \frac{d\varepsilon}{2\pi\hbar} \qquad (2.10)$$
$$\times[\tilde{\Delta}(\mathbf{r})F^+(\mathbf{r}, \mathbf{r}, \varepsilon) - \tilde{\Delta}^*(\mathbf{r})F(\mathbf{r}, \mathbf{r}, \varepsilon)].$$

The right-hand side of this equality vanishes by virtue of the third Gor'kov equation. Because the latter is derived under the assumption of a delta-function interaction, we should conclude that the form of a two-body interaction is of importance for obtaining current conservation. In particular, the commonly used monopole pairing interaction is not invariant under the transformation of (2.6). Therefore, it does not conserve the current density in a rotating nucleus. The case of an arbitrary pairing interaction is considered in [25].

2.3. Matrix Form of the Gor'kov Equations

The two-dimensional form of the Gor'kov equations is very convenient to use in our calculations. Let us introduce the second pair of Green's functions $G^+(\mathbf{r},\mathbf{r}',\varepsilon)$ and $F(\mathbf{r},\mathbf{r}',\varepsilon)$. It can easily be proven [11] that the four equations for these functions can be written in the matrix form

$$\begin{pmatrix} \tilde{\Delta}^* & \varepsilon + h_\omega^+ - \varepsilon_\mathrm{F} \\ \varepsilon - h_\omega + \varepsilon_\mathrm{F} & \tilde{\Delta} \end{pmatrix} \begin{pmatrix} F & G \\ G^+ & F^+ \end{pmatrix} = \hat{1}\delta(\mathbf{r}-\mathbf{r}'). \tag{2.11}$$

The operator h_ω involves the real (h) and the imaginary (V) part. The former is the Hamiltonian of the deformed mean field, whereas the latter stands for the cranking term, $V = -\omega\ell_x$. Separating the quantity $\tilde{\Delta}$ into real and imaginary parts,

$$\tilde{\Delta} = \Delta + \bar{\Delta}, \quad \tilde{\Delta}^* = \Delta - \bar{\Delta}, \tag{2.12}$$

we can rewrite Eq. (2.11) in the compact form

$$(i\hat{p} + \Delta - \hat{\sigma}_1 V - \hat{\sigma}_3\bar{\Delta}) \times \hat{G}(\mathbf{r},\mathbf{r}',p) = \delta(\mathbf{r}-\mathbf{r}'), \tag{2.13}$$

where $\hat{G}$ is the matrix of the functions G and F involved in Eq. (2.11), $\hat{p} = \hat{\sigma}_1 p + \hat{\sigma}_2(h - \varepsilon_F)$, $\hat{\sigma}_\alpha$ are the Pauli matrices, and $p = -i\varepsilon$. We omit the identity matrices before the terms involving Δ and $\delta(\mathbf{r}-\mathbf{r}')$. The functions G and F can be written as traces of $\hat{G}$ in the following way:[2)]

$$G(\mathbf{r},\mathbf{r}',\varepsilon) = \frac{1}{2}\mathrm{Sp}\{(\hat{\sigma}_1 - i\hat{\sigma}_2)\hat{G}(\mathbf{r},\mathbf{r}',p)\},$$

$$F(\mathbf{r},\mathbf{r}',\varepsilon) = \frac{1}{2}\mathrm{Sp}\{(1+\hat{\sigma}_3)\hat{G}(\mathbf{r},\mathbf{r}',p)\}. \tag{2.14}$$

Therefore, the equation for $\tilde{\Delta}(\mathbf{r})$ is

$$\tilde{\Delta}(\mathbf{r}) = g\int\limits_{C'} \frac{dp}{4\pi}\mathrm{Sp}\{(1+\hat{\sigma}_3)\hat{G}(\mathbf{r},\mathbf{r},p)\}, \tag{2.15}$$

and the one-particle density matrix of the system is given by the expression

$$\rho(\mathbf{r}) = \int\limits_{C'} \frac{dp}{4\pi}\mathrm{Sp}\{(\hat{\sigma}_1 - i\hat{\sigma}_2)\hat{G}(\mathbf{r},\mathbf{r},p)\}, \tag{2.16}$$

where the contour C' is obtained from C by rotation through an angle of 90°.

2.4. Perturbation Theory

We use the Green's function method to calculate the parameter $\mathcal{B}$. As follows from Eqs. (1.5) and (1.7), this requires perturbation theory of third order in the cranking term V. According to [13], a considerable computational effort is needed to produce the result into a tractable form. The matrix representation of the Gor'kov equations allows us to elaborate on the elegant form of perturbation theory that considerably simplifies the calculations.

We now proceed to treat Eq. (2.13) by the method of successive approximations. Considering V as a weak perturbation, we expand the Green's function and the self-consistent quantities $\tilde{\Delta}$ and ε_F in the powers of a small parameter:

$$\hat{G} = \hat{G}_0 + \hat{G}_1 + \hat{G}_2 + \hat{G}_3 + \ldots,$$
$$\tilde{\Delta} = \Delta^{(0)} + \bar{\Delta}^{(1)} + \Delta^{(2)} + \bar{\Delta}^{(3)} + \ldots, \tag{2.17}$$
$$\varepsilon_\mathrm{F} = \varepsilon_\mathrm{F}^{(0)} + \varepsilon_\mathrm{F}^{(2)} + \ldots.$$

The nth-order corrections to the last two quantities are determined by Eqs. (2.15) and (2.5), respectively. Since $V = -V^*$, the corrections of odd order to $\tilde{\Delta}$ are purely imaginary and those of even order are real. The effect of the second-order correction to ε_F makes a negligible contribution to the second inertial parameter [13]. Thus, we will use the zero-order approximation for this quantity.

It is natural to work in the basis of the eigenfunctions of the Hamiltonian in (2.1) without the cranking term,

$$(h - \varepsilon_\mathrm{F})\varphi_\nu(\mathbf{r}) = p_\nu\varphi_\nu(\mathbf{r}), \tag{2.18}$$

where p_ν is the energy ε_ν of the single-particle state ν relative to the Fermi energy, $p_\nu = \varepsilon_\nu - \varepsilon_\mathrm{F}$. In this basis, the nth correction to the Green's function has the form

$$\hat{G}_n(\mathbf{r},\mathbf{r}',p) = \sum_{\nu\nu'} \hat{G}^{(n)}_{\nu\nu'}(p)\varphi_\nu(\mathbf{r})\varphi^*_{\nu'}(\mathbf{r}'). \tag{2.19}$$

First of all, we solve the unperturbed Eq. (2.13),

$$(i\hat{p} + \Delta)\hat{G}_0(\mathbf{r},\mathbf{r}',p) = \delta(\mathbf{r}-\mathbf{r}'), \tag{2.20}$$

[2)] We use the symbol tr in the space of single-particle states of the Hamiltonian h, the symbol Sp in the spinor space, and Tr in the combined space.

with the constant pairing gap $\Delta^{(0)} = \Delta$. Substituting Eq. (2.19) into (2.20), one finds

$$\hat{G}^{(0)}_{\nu\nu'}(\mathbf{p}_\nu) = -\frac{i\hat{p}_\nu - \Delta}{\mathbf{p}_\nu^2 + \Delta^2}\delta_{\nu\nu'}, \quad (2.21)$$

where $\mathbf{p}_\nu(p, p_\nu)$ is the two-dimensional vector and $\hat{p}_\nu = \hat{\sigma}_1 p + \hat{\sigma}_2 p_\nu$. The gap Eq. (2.15) takes the simple form

$$1 = g\sum_\nu \frac{1}{2E_\nu}|\varphi_\nu(\mathbf{r})|^2, \quad E_\nu = \sqrt{p_\nu^2 + \Delta^2}. \quad (2.22)$$

This equation has the solution $\Delta = \text{const}$ for the self-consistent potential with a flat bottom. In deriving Eq. (2.22), as well as in subsequent calculations, it is essential to compute the traces of the products of the Pauli matrices. We can readily see that the trace of an odd number of matrices $\hat{\sigma}_1$ and $\hat{\sigma}_2$ vanishes and that the product of an even number is given by the expressions

$$\frac{1}{2}\mathrm{Sp}(\hat{\sigma}_\alpha\hat{\sigma}_\beta) = \delta_{\alpha\beta}, \quad (2.23)$$

$$\frac{1}{2}\mathrm{Sp}(\hat{\sigma}_\alpha\hat{\sigma}_\beta\hat{\sigma}_\gamma\hat{\sigma}_\delta) = \delta_{\alpha\beta}\delta_{\gamma\delta} - \varepsilon_{\alpha\beta}\varepsilon_{\gamma\delta}, \ \ldots,$$

where $\hat{\varepsilon} = i\hat{\sigma}_2$ is a fully antisymmetric matrix.

In the first order, Eq. (2.13) involves the two perturbing terms V and $\bar{\Delta}^{(1)}$:

$$(i\hat{p} + \Delta)\hat{G}_1(\mathbf{r}, \mathbf{r}', p) \quad (2.24)$$
$$= [\hat{\sigma}_1 V + \hat{\sigma}_3\bar{\Delta}^{(1)}]\hat{G}_0(\mathbf{r}, \mathbf{r}', p).$$

This equation has the obvious solution

$$\hat{G}_1(\mathbf{r}, \mathbf{r}', p) \quad (2.25)$$
$$= \int \hat{G}_0(\mathbf{r}, \mathbf{q}, p)\hat{W}(\mathbf{q})\hat{G}_0(\mathbf{q}, \mathbf{r}', p)d\mathbf{q},$$

where the operator

$$\hat{W} = \hat{\sigma}_1 V + \hat{\sigma}_3\bar{\Delta}^{(1)} \quad (2.26)$$

is introduced in order to represent the corrections to the unperturbed Green's function in the simple symbolic form

$$\hat{G}_1 = \hat{G}_0\hat{W}\hat{G}_0,$$
$$\hat{G}_2 = \hat{G}_0\hat{W}\hat{G}_0\hat{W}\hat{G}_0 - \hat{G}_0\Delta^{(2)}\hat{G}_0,$$
$$\hat{G}_3 = \hat{G}_0\hat{W}\hat{G}_0\hat{W}\hat{G}_0\hat{W}\hat{G}_0 \quad (2.27)$$
$$- \hat{G}_0\hat{W}\hat{G}_0\Delta^{(2)}\hat{G}_0 - \hat{G}_0\Delta^{(2)}\hat{G}_0\hat{W}\hat{G}_0$$
$$+ \hat{G}_0\hat{\sigma}_3\bar{\Delta}^{(3)}\hat{G}_0.$$

Here, integration with respect to the intermediate coordinates $\mathbf{q}$ is implied. Using these formulas, one can prove by straightforward calculations the identities

$$\int\limits_{C'} \frac{dp}{2\pi}\mathrm{Sp}\{\hat{G}_{2i+1}(\mathbf{r}, \mathbf{r}', p)\} = 0,$$

$$\int\limits_{C'} \frac{dp}{2\pi}\mathrm{Sp}\{\hat{\sigma}_1\hat{G}_{2i}(\mathbf{r}, \mathbf{r}', p)\} = 0, \quad (2.28)$$

$$\int\limits_{C'} \frac{dp}{2\pi}\mathrm{Sp}\{\hat{\sigma}_2\hat{G}_{2i+1}(\mathbf{r}, \mathbf{r}', p)\} = 0,$$

$$\int\limits_{C'} \frac{dp}{2\pi}\mathrm{Sp}\{\hat{\sigma}_3\hat{G}_{2i}(\mathbf{r}, \mathbf{r}', p)\} = 0.$$

In order to find a self-consistent solution, we have to show how $\tilde{\Delta}^{(n)}$ is obtained from $\hat{G}_n$ by using the equation

$$\tilde{\Delta}^{(n)}(\mathbf{r}) = g\int\limits_{C'} \frac{dp}{4\pi}\mathrm{Sp}\{(1 + \hat{\sigma}_3)\hat{G}_n(\mathbf{r}, \mathbf{r}, p)\}. \quad (2.29)$$

We will consider the unperturbed pairing gap Δ as a parameter of the theory. This allows us to eliminate the interaction constant g. Multiplying the zero-order Eq. (2.22) by $\tilde{\Delta}^{(n)}(\mathbf{r})$, we write the result in the symmetric form

$$\Delta\tilde{\Delta}^{(n)}(\mathbf{r}) = g\int\limits_{C'} \frac{dp}{8\pi}\mathrm{Sp}[\hat{G}_0(\mathbf{r}, \mathbf{r}, p), \tilde{\Delta}^{(n)}(\mathbf{r})]_+, \quad (2.30)$$

where $[\ldots]_+$ is the anticommutator of the corresponding operators. With this ansatz and (2.29), the integral equation for even-order corrections is given by

$$\int\limits_{C'} \frac{dp}{2\pi}\mathrm{Sp}\{2\Delta\hat{G}_{2i}(\mathbf{r}, \mathbf{r}, p) \quad (2.31)$$
$$- [\hat{G}_0(\mathbf{r}, \mathbf{r}, p), \Delta^{(2i)}(\mathbf{r})]_+\} = 0,$$

while that for odd-order ones has the form

$$\int\limits_{C'} \frac{dp}{2\pi}\mathrm{Sp}\{2\Delta\hat{\sigma}_3\hat{G}_{2i+1}(\mathbf{r}, \mathbf{r}, p) \quad (2.32)$$
$$- [\hat{G}_0(\mathbf{r}, \mathbf{r}, p), \bar{\Delta}^{(2i+1)}(\mathbf{r})]_+\} = 0.$$

Similarly, eliminating g from the equations for $\bar{\Delta}^{(n)}$ and $\Delta^{(n-1)}$ (n is odd) in the form of (2.29) yields

$$\int\limits_{C'} \frac{dp}{2\pi}\mathrm{Sp}\{\bar{\Delta}^{(n)}(\mathbf{r})\hat{G}_{n-1}(\mathbf{r}, \mathbf{r}, p) \quad (2.33)$$
$$- \Delta^{(n-1)}(\mathbf{r})\hat{\sigma}_3\hat{G}_n(\mathbf{r}, \mathbf{r}, p)\} = 0.$$

In the same manner, with additional integration with respect to $\mathbf{r}$, we can obtain

$$\int\limits_{C'} \frac{dp}{2\pi}\mathrm{Tr}\{\bar{\Delta}^{(n)}\hat{\sigma}_3\hat{G}_{n-2}(p) \quad (2.34)$$
$$- \bar{\Delta}^{(n-2)}\hat{\sigma}_3\hat{G}_n(p)\} = 0.$$

Here, Tr refers to spinor and to single-particle spaces simultaneously.

The solution to the HFB equations that is represented in the form of successive approximations by formulas (2.21), (2.22), (2.27), (2.31), and (2.32) takes into consideration nonuniform pairing correlations induced by rotation. Nonuniform pairing originates in higher orders of perturbation theory, while a nonrotating system is approximated by a constant pairing field. In spite of an apparent eclecticism, our solution does not violate the current-density conservation, $\mathrm{div}\mathbf{j} = 0$. This is obvious in the zero-order approximation. In even orders of perturbation theory, $\mathrm{div}\mathbf{j}^{(2i)}$ vanishes by virtue of the first and the fourth identity in (2.28). Odd corrections to the quantity in (2.10) can be recast into the form

$$\begin{aligned}&\mathrm{div}\mathbf{j}^{(2i+1)}(\mathbf{r}) \\ &= \sum_{l=0}^{i} \int\limits_{C'} \frac{dp}{2\pi} \mathrm{Sp}\{\bar{\Delta}^{(2l+1)}(\mathbf{r})\hat{G}_{2i-2l}(\mathbf{r},\mathbf{r},p) \\ &\quad - \Delta^{(2l)}\hat{\sigma}_3\hat{G}_{2i-2l+1}(\mathbf{r},\mathbf{r},p)\},\end{aligned} \tag{2.35}$$

which vanishes by virtue of Eq. (2.33). Thus, we have found a consistent solution that is certainly more general than the initially supposed one. It can be used for an arbitrary single-particle potential without danger of arriving at a contradiction (see also [21]). We will use this solution to calculate the second inertial parameter.

Finally, the following identities are useful in the calculations:

$$\begin{aligned}&2\Delta \int\limits_{C'} \frac{dp}{2\pi} \mathrm{Tr}\{\Delta^{(2i)}\hat{G}_{2i}(p)\} \\ &= \int\limits_{C'} \frac{dp}{2\pi} \mathrm{Tr}\{\Delta^{(2i)}[\Delta^{(2i)}, \hat{G}_0(p)]_+\},\end{aligned} \tag{2.36}$$

$$\begin{aligned}&2\Delta \int\limits_{C'} \frac{dp}{2\pi} \mathrm{Tr}\{\bar{\Delta}^{(2i+1)}\hat{\sigma}_3\hat{G}_{2i+1}(p)\} \\ &= \int\limits_{C'} \frac{dp}{2\pi} \mathrm{Tr}\{\bar{\Delta}^{(2i+1)}[\bar{\Delta}^{(2i+1)}, \hat{G}_0(p)]_+\}.\end{aligned} \tag{2.37}$$

These identities are obtained by multiplying Eqs. (2.31) and (2.32) by $\Delta^{(2i)}(\mathbf{r})$ and $\bar{\Delta}^{(2i+1)}(\mathbf{r})$, respectively, and performing an integration with respect to $\mathbf{r}$.

3. CALCULATION OF THE SECOND INERTIAL PARAMETER

3.1. General Expression

As follows from Eq. (1.7), the derivation of the parameter $\mathcal{B}$ reduces to calculating β. This quantity is convenient to deal with. The third-order correction to the density matrix can be obtained from Eqs. (2.16) and (2.27). If we take into account the third equation in (2.28), substitute

$$\hat{\sigma}_1\ell_x = -\frac{1}{\omega}(W - \hat{\sigma}_3\Delta^{(1)}), \tag{3.1}$$

and use the identity in (2.34) with $n = 3$, we find, after some simple algebra, that

$$\begin{aligned}\beta_s &= \frac{1}{\omega^3}\mathrm{tr}\{\ell_x\rho^{(3)}\} = -\frac{1}{\omega^4}\int\limits_{C'} \frac{dp}{4\pi} \mathrm{Tr}\{\hat{W}\hat{G}_3(p)\} \\ &\quad + \frac{1}{\omega^4}\int\limits_{C'} \frac{dp}{4\pi} \mathrm{Tr}\{\Delta^{(3)}\hat{\sigma}_3\hat{G}_1(p)\},\end{aligned} \tag{3.2}$$

where the subscript s means that the relevant quantity refers to the superfluid state. Here and below, we will use $\Delta^{(2i+1)}$ $(i = 0, 1)$ instead of $\bar{\Delta}^{(2i+1)}$. Fortunately, the terms involving $\Delta^{(3)}$ are eliminated from (3.2) after inserting expression (2.27) for $\hat{G}_3$. The resulting formula involves only the corrections $\Delta^{(1)}$ and $\Delta^{(2)}$. It is convenient to transform the terms with $\Delta^{(2)}$ into a quadratic form in this quantity. Referring to the definition of the function $\hat{G}_2$ from Eqs. (2.27), we find that the term involving $\Delta^{(2)}$ becomes

$$\begin{aligned}&\int\limits_{C'} \frac{dp}{2\pi} \mathrm{Tr}\{\Delta^{(2)}\hat{G}_0(p)\hat{W}\hat{G}_0(p)\hat{W}\hat{G}_0(p)\} \\ &= \int\limits_{C'} \frac{dp}{2\pi} \mathrm{Tr}\{\Delta^{(2)}\hat{G}_2(p)\} \\ &\quad - \int\limits_{C'} \frac{dp}{2\pi} \mathrm{Tr}\{\Delta^{(2)}\hat{G}_0(p)\Delta^{(2)}\hat{G}_0(p)\}.\end{aligned} \tag{3.3}$$

With the help of identity (2.36), it is easy to show that the first term on the right-hand side also transforms into a bilinear form of $\Delta^{(2)}$. Combining this result with (3.2), we obtain the final expression for the parameter β_s:

$$\begin{aligned}\beta_s &= -\frac{1}{\omega^4}\int\limits_{C'} \frac{dp}{4\pi} \mathrm{Tr}\{\hat{W}\hat{G}_0(p)\hat{W}\hat{G}_0(p) \\ &\quad \times \hat{W}\hat{G}_0(p)\hat{W}\hat{G}_0(p)\} + \frac{1}{\omega^4\Delta}\int\limits_{C'} \frac{dp}{4\pi} \\ &\quad \times \mathrm{Tr}\{2\Delta\Delta^{(2)}\hat{G}_0(p)\Delta^{(2)}\hat{G}_0(p) + \Delta^{(2)}[\hat{G}_0(p), \Delta^{(2)}]_+\}.\end{aligned} \tag{3.4}$$

This is an exact formula for calculating the second inertial parameter. The first term describes the joint effect of the Coriolis force and the nonuniform pairing field $\Delta^{(1)}(\mathbf{r})$ on independent quasiparticle motion. In the limit of a monopole pairing interaction, which corresponds to a uniform pairing field ($\Delta^{(1)} = 0$), this agrees with the term $\mathcal{B}_c$ found by Marshalek [13]. The second term arises only because of the modification of pairing. In the limit of uniform pairing, this term describes the Coriolis antipairing effect (see Appendix A).

3.2. Semiclassical Approximation

To proceed further, we should find the first- and second-order corrections to the pairing field. As is shown in Appendix A, the corresponding integral equations have the solutions

$$\Delta^{(1)}(\mathbf{r}) = -\frac{i\hbar\omega}{2\Delta} D_1 \dot{\ell}_x, \quad \Delta^{(2)}(\mathbf{r}) = \frac{\hbar^2\omega^2}{4\Delta^3} D_2 \dot{\ell}_x^2, \tag{3.5}$$

where D_1 and D_2 are the amplitudes that are found in a self-consistent way. In order to learn more about nonuniform pairing, we suppose that the self-consistent potential of a deformed nucleus has the form

$$U(\rho) = U\left(\frac{x^2+y^2}{a^2} + \frac{z^2}{b^2}\right), \tag{3.6}$$

where a and b are the semiaxes of a nuclear spheroid. Then, we obtain

$$\dot{\ell}_x = y\frac{\partial U}{\partial z} - z\frac{\partial U}{\partial y} = \frac{b^2 - a^2}{a^2 b^2} yzU'(\rho). \tag{3.7}$$

Thus, the rotation-induced pairing field is a function of only the spatial coordinates. In the first order in rotation, the nonuniform pairing field is proportional to the spherical harmonic $Y_{2\pm1}$. This was a motivation for introducing quadrupole pairing (see [27] and references therein). The second correction $\Delta^{(2)}$ shows, however, that higher multipoles are also involved in nonuniform pairing.

Using the expression for $\Delta^{(1)}$ and the obvious formula for matrix elements $\hbar\dot{\ell}^x_{\nu\nu'} = i(p_\nu - p_{\nu'})\ell^x_{\nu\nu'}$, we can represent each of 16 sums in the first term of Eq. (3.4) in the general form

$$\sum \ell^x_{12}\ell^x_{23}\ell^x_{34}\ell^x_{41} \int\limits_{C'} \frac{dp}{2\pi} \tag{3.8}$$
$$\times \frac{\mathcal{Q}_4(p; p_1, p_2, p_3, p_4)}{(\mathbf{p}_1^2 + \Delta^2)(\mathbf{p}_2^2 + \Delta^2)(\mathbf{p}_3^2 + \Delta^2)(\mathbf{p}_4^2 + \Delta^2)},$$

where the summation indices 1, 2, 3, and 4 refer to the single-particle states ν with the energy p_ν of the Schrödinger equation (2.18) and $\mathcal{Q}_4$ is a polynomial of the fourth power in (p, p_ν) and D_1, which derives from the calculation of the trace of the product of the Pauli matrices and the factors $(i\hat{p}_\nu - \Delta)$.

To evaluate this sum, we use the method proposed by Migdal [21]. Let us first note that, for the fixed state 1, the indices 2, 3, and 4 take only a few values permitted by the selection rules for the matrix elements of the operator ℓ_x. After integration with respect to p, we obtain a function of the variables $p_1, \ldots, p_4$. Considered as a function of the variable p_1, it has, for fixed differences $p_1 - p_2$, $p_1 - p_3$, and $p_1 - p_4$, a sharp maximum at the Fermi surface with a width $\sim\Delta$. Since the average level spacing for ND nuclei, $\delta\varepsilon \sim \varepsilon_\mathrm{F}/A$, is very small in relation to $\Delta \sim \varepsilon_\mathrm{F}/A^{2/3}$, a large number ($\sim A^{1/3}$) of levels fall within the interval Δ. For this reason, we can make, with a semiclassical accuracy, the following substitution in the sum (3.8):

$$\int\limits_{C'} \frac{dp}{2\pi} \frac{\mathcal{Q}_4(p; p_1, p_2, p_3, p_4)}{(\mathbf{p}_1^2 + \Delta^2)(\mathbf{p}_2^2 + \Delta^2)(\mathbf{p}_3^2 + \Delta^2)(\mathbf{p}_4^2 + \Delta^2)}$$
$$\to \delta(\varepsilon_1 - \varepsilon_\mathrm{F}) \int \frac{d\mathbf{p}_1}{2\pi} \tag{3.9}$$
$$\times \frac{\mathcal{Q}_4(p; p_1, p_2, p_3, p_4)}{(\mathbf{p}_1^2 + \Delta^2)(\mathbf{p}_2^2 + \Delta^2)(\mathbf{p}_3^2 + \Delta^2)(\mathbf{p}_4^2 + \Delta^2)}.$$

Similarly, the second term in Eq. (3.4) can be approximated by the expression

$$\frac{1}{\omega^4} \sum |\Delta^{(2)}_{12}|^2 \int \frac{d\mathbf{p}_1}{4\pi} \tag{3.10}$$
$$\times \frac{(p_1 - p_2)^2 + 4\Delta^2}{(\mathbf{p}_1^2 + \Delta^2)(\mathbf{p}_2^2 + \Delta^2)} \delta(\varepsilon_1 - \varepsilon_\mathrm{F}).$$

In calculating these integrals ($d\mathbf{p}_1 = dp\,dp_1$), it is convenient to use the method of Feynman covariant integration [28] because a good convergence of the integrals allows integration with respect to p_1 to be extended over the region from $-\infty$ to ∞. The details of the calculations are given in Appendix B. The integral in (3.9) depends on three independent differences $p_1 - p_2$, $p_1 - p_3$, and $p_1 - p_4$. To represent the final result of the semiclassical approximation in a symmetric form, we introduce six energy differences $p_{\nu\nu'} = p_\nu - p_{\nu'}$, $\nu < \nu'$. Collecting all the integrals of the first and second terms in (3.4), we find

$$\beta_s = \frac{1}{4\Delta^2} \sum \ell^x_{12}\ell^x_{23}\ell^x_{34}\ell^x_{41} \tag{3.11}$$
$$\times F(x_{12}, x_{23}, x_{34}, x_{41}; x_{13}, x_{24}) \delta(\varepsilon_1 - \varepsilon_\mathrm{F}),$$

where the δ function means that summation over the state 1 is replaced, according to the semiclassical approximation, by integration with respect to its quantum numbers.

The function F, which depends on six dimensionless differences $x_{\nu\nu'} = (\varepsilon_\nu - \varepsilon_{\nu'})/2\Delta$, is broken down into two parts:

$$F = f(x_{12}, x_{23}, x_{34}, x_{41}; x_{13}, x_{24}) \tag{3.12}$$

$$+ 8D_2^2 x_{12}x_{23}x_{34}x_{41}h(x_{13}).$$

The first one is relevant to the first term in Eq. (3.4). It is convenient to represent this function in the form

$$f = -(1 + \hat{P}_1 + \hat{P}_2 + \hat{P}_3)G + (1 + \hat{P}_1)H, \quad (3.13)$$

where

$$G = \frac{g(x_{12})}{x_{13}x_{23}x_{24}x_{41}} \{(1 - D_1 x_{12}^2) \quad (3.14)$$
$$\times \left[1 + x_{12}^2 + x_{23}x_{41} - D_1[x_{23}^2(1 - x_{12}x_{24})\right.$$
$$+ x_{41}^2(1 + x_{12}x_{13})] - D_1^2 x_{23}x_{34}x_{41}(x_{23} + x_{41})$$
$$\left. - D_1^3 x_{12}x_{23}^2 x_{34}x_{41}^2\right] - D_1(x_{34} - D_1 x_{12}x_{23}x_{41})$$
$$\times (x_{34} + x_{12}x_{13}x_{24} - D_1 x_{12}x_{23}x_{41})\}$$

and

$$H = \frac{h(x_{13})}{x_{12}x_{23}x_{34}x_{41}} \quad (3.15)$$
$$\times \left[1 - D_1(x_{12}^2 + x_{23}^2 + x_{34}^2 + x_{41}^2)\right.$$
$$\left. + D_1^2(x_{12}x_{41} + x_{23}x_{34})^2\right].$$

Here, the functions

$$g(x) = \frac{\operatorname{arg\,sinh} x}{x\sqrt{1 + x^2}}, \quad h(x) = (1 + x^2)g(x) \quad (3.16)$$

are associated with the Migdal moment of inertia [21]. The amplitudes D_1 and D_2 of the nonuniform pairing field are determined by Eqs. (A.4) and (A.8), respectively. The operator $\hat{P}_i$ permutes the indices ν of single-particle states in all dimensionless differences on which the functions G and H depend. Applying this operator to $x_{\nu\nu'}$, we get

$$\hat{P}_i x_{\nu,\nu'} = x_{\nu+i,\nu'+i}, \quad (3.17)$$

subject to $\nu \bmod 4 = \nu$. It is easy to prove the following symmetry properties of the function F:

$$\hat{P}_1 F = \hat{P}_2 F = \hat{P}_3 F = F,$$

$$F(x_{12}, x_{41}, x_{34}, x_{23}; -x_{24}, -x_{13}) \quad (3.18)$$
$$= F(x_{12}, x_{23}, x_{34}, x_{41}; x_{13}, x_{24}).$$

The above formulas give the semiclassical expression for the second inertial parameter in the superfluid phase. The solution takes into account the effect of rotation on Cooper pairs in a gauge-invariant form. The result is expressed entirely in terms of matrix elements and corresponding energy differences, provided that the constant pairing gap Δ is fixed for a nonrotating nucleus. It is valid for an arbitrary nuclear mean field with a stable deformation. This allows one to study the interplay between rotation, pairing correlations, and mean-field deformations in ND and SD bands.

We first estimate the quantity β_s and find the small parameter of perturbation theory we used. To get an estimate of β_s for ND bands, we observe that the matrix element $\ell^x_{\nu\nu'}$ has two types of $\nu \to \nu'$ transitions:

(i) transitions within the $\mathcal{N}$ shell (close transitions), for which the energy differences are $p_{\nu\nu'} = d_1 \sim \varepsilon_{\mathrm{F}} A^{-2/3}$ and the maximum value L of the matrix element $\ell^x_{\nu\nu'}$ is related to a transition between states of a j shell;

(ii) transitions between shells with major quantum numbers $\mathcal{N}$ and $\mathcal{N} \pm 2$ (distant transitions) with $p_{\nu\nu'} = d_2 \sim \varepsilon_{\mathrm{F}} A^{-1/3}$ and $\ell^x_{\nu\nu'} \sim LA^{-1/3}$.

For state 1, there are three groups of terms in the sum on the right-hand side of (3.11), which are classified according to different combinations of close and distant transitions in the product of the four matrix elements $\ell^x_{\nu\nu'}$. Those involving four close transitions have all dimensionless differences $x_{\nu\nu'} \sim 1$ and, consequently, $F \sim 1$.[3] Thus, the contribution of these terms to the sum in (3.11) is of order L^4. For terms with four distant transitions ($x_{\nu\nu'} \sim A^{1/3}$), we have $F \sim A^{4/3}$. However, this large factor is compensated by the product of small matrix elements $\ell^x_{\nu\nu'}$. The same compensation occurs in the remaining terms with two close and two distant transitions, for which $F \sim A^{2/3}$. Therefore, the contributions of all terms in the sum (3.11) being considered are of the same order L^4, and we can make the following estimation:

$$\beta_s \sim \frac{1}{4\Delta^2} \sum \ell^x_{12}\ell^x_{23}\ell^x_{34}\ell^x_{41}\delta(\varepsilon_1 - \varepsilon_{\mathrm{F}})$$
$$= \frac{1}{4\Delta^2} \sum_1 (\ell_x^4)_{11}\delta(\varepsilon_1 - \varepsilon_{\mathrm{F}}). \quad (3.19)$$

A calculation of the last sum within the Thomas–Fermi approximation gives

$$\beta_s \sim \frac{3M}{20\Delta^2} \int n(\mathbf{r}) p_{\mathrm{F}}^2(\mathbf{r})(y^2 + z^2)^2 d\mathbf{r}. \quad (3.20)$$

In this calculation we used the procedure described in [21], which includes averaging over the directions of the nucleon momentum and the utilization of the ansatz

$$\sum_1 \varphi_1^*(\mathbf{r})\varphi_1(\mathbf{r})\delta(\varepsilon_1 - \varepsilon_{\mathrm{F}}) = \frac{3M}{p_{\mathrm{F}}^2(\mathbf{r})} n(\mathbf{r}), \quad (3.21)$$

where $n(\mathbf{r}) = Cp_{\mathrm{F}}^3(\mathbf{r})$ ($C = \mathrm{const}$) is the nucleon density and $p_{\mathrm{F}}(\mathbf{r}) = \sqrt{2M[\varepsilon_{\mathrm{F}} - U(\mathbf{r})]}$. Comparing (3.20) with the rigid-body moment of inertia

$$\mathfrak{I}_{\mathrm{rig}} = \int n(\mathbf{r})(y^2 + z^2) d\mathbf{r}, \quad (3.22)$$

---

[3] The necessary estimate for the amplitudes of the uniform pairing field, $D_1 \sim D_2 \sim [\ln(d_2/\Delta)]^{-1} \sim 1$, can be obtained from Eqs. (A.4) and (A.8).

we obtain $\beta_s \sim \Im_{\rm rig}(p_{\rm F}R/\Delta)^2 \sim \Im_{\rm rig}(\hbar j_{\rm F}/\Delta)^2$, where R is the rms radius of a nucleus and $p_{\rm F}$ and $j_{\rm F} \sim A^{1/3}$ are, respectively, the mean momentum and the mean angular momentum of a nucleon at the Fermi surface. Thus, the parameter β_s is of order $\hbar^4 A^{11/3}/\varepsilon_{\rm F}^3$. With these results, we can get, from (1.4), the perturbation parameter, $\beta_s\omega^2/\alpha \sim (\hbar\omega j_{\rm F}/\Delta)^2$. The application of perturbation theory implies that this value is small; i.e., the Coriolis interaction is smaller than the two-quasiparticle excitation energy. One can say that perturbation theory is valid for adiabatic rotation. It is clear from Eq. (1.7) that $\mathcal{B}_s \sim \varepsilon_{\rm F}A^{-3}$ and $\mathcal{B}_s/\mathcal{A} \sim A^{-4/3}$. The above estimates refer to ND nuclei in the ground state, where pairing correlations are reasonably strong, $\Delta \sim \varepsilon_{\rm F}A^{-2/3}$.

4. MODEL OF AN ANISOTROPIC OSCILLATOR POTENTIAL

In order to obtain quantitative results, we model the actual self-consistent nuclear field as the axially deformed oscillator potential with frequencies ω_z along the symmetry axis and ω_x in the perpendicular plane:

$$U_{\rm osc}(\mathbf{r}) = \frac{M}{2}[\omega_x^2(x^2+y^2)+\omega_z^2 z^2]. \qquad (4.1)$$

The use of this simplified model is justified by the possibility of deriving an exact analytic expression for the parameter β_s. It is also known that the model reproduces the experimental values of the rotational constants $\mathcal{A}$ and $\mathcal{B}$ for ND bands. Therefore, we can expect that the model would provide useful insights into the rotational regime at superdeformation.

In an anisotropic oscillator potential, the matrix element $\ell^x_{\nu\nu'}$ is nonzero for four transitions. Two close transitions have the energy differences $d_1 = \pm\hbar(\omega_x - \omega_z)$, whereas the distant ones have $d_2 = \pm\hbar(\omega_x + \omega_z)$. The corresponding dimensionless parameters are

$$\nu_{1,2} = \frac{\hbar(\omega_x \mp \omega_z)}{2\Delta} = \frac{k \mp 1}{2\xi k^{2/3}}, \quad \xi = \frac{\Delta}{\hbar\omega_0}, \qquad (4.2)$$

where $\hbar\omega_0 = 41A^{-1/3}$ MeV. Hereafter, we use the axis or the frequency ratio $k = b/a = \omega_x/\omega_z$ and the volume-conservation condition $\omega_x^2\omega_z = \omega_0^3$. It is also convenient to substitute the operator ℓ_x with its time derivative

$$\dot{\ell}_x = M(\omega_x^2 - \omega_z^2)yz, \qquad (4.3)$$

which obey the same selection rules.

For fixed state 1, the sum in (3.11) involves six terms with four close transitions, six terms with four distant transitions, and 24 terms with two close and two distant transitions. The products of four matrix elements are equal to a semiclassical precision for all 36 terms of the sum, $\dot{\ell}^x_{12}\dot{\ell}^x_{23}\dot{\ell}^x_{34}\dot{\ell}^x_{41} \approx \frac{1}{36}(\dot{\ell}_x^4)_{11}$. Summation of all these terms gives

$$\beta_s = \frac{\hbar^4\Phi_n(\nu_1,\nu_2)}{18(2\Delta)^6\nu_1^4}\sum_1(\dot{\ell}_x^4)_{11}\delta(\varepsilon_1 - \varepsilon_{\rm F}). \qquad (4.4)$$

The function Φ_n is the sum of the functions F corresponding to all 36 combinations of the close and distant transitions. The sum can be simplified by using the symmetry properties (3.18). It is convenient to represent the resulting function in the form

$$\Phi_n(\nu_1,\nu_2) = \mathcal{F}(\nu_1,\nu_2) + 2D_2^2\mathcal{H}(\nu_1,\nu_2), \qquad (4.5)$$

where

$$\begin{aligned}\mathcal{F}(\nu_1,\nu_2) = {} & f(\nu_1,-\nu_1,\nu_1,-\nu_1;0,0) \qquad (4.6)\\ & + 2f(\nu_1,\nu_1,-\nu_1,-\nu_1;2\nu_1,0)\\ & + 2(\nu_1/\nu_2)^2[2f(\nu_1,\nu_2,-\nu_2,-\nu_1;\nu_1+\nu_2,0)\\ & + 2f(\nu_1,-\nu_2,\nu_2,-\nu_1;\nu_1-\nu_2,0)\\ & + f(\nu_1,\nu_2,-\nu_1,-\nu_2;\nu_1+\nu_2,-\nu_1+\nu_2)\\ & + f(\nu_1,-\nu_2,-\nu_1,\nu_2;\nu_1-\nu_2,-\nu_1-\nu_2)]\\ & + (\nu_1/\nu_2)^4[f(\nu_2,-\nu_2,\nu_2,-\nu_2;0,0)\\ & + 2f(\nu_2,\nu_2,-\nu_2,-\nu_2;2\nu_2,0)],\end{aligned}$$

and the amplitude D_1, the amplitude D_2, and the functions $\mathcal{H}$ are determined by Eqs. (A.5), (A.11), and (A.12), respectively. The two terms in (4.5) describe the two distinct effects of the Coriolis force: the rotation–quasiparticle interaction and the modification of pairing.

In the Thomas–Fermi approximation, according to the ansatz in (3.21); we have

$$\begin{aligned}&\sum_1(\dot{\ell}_x^4)_{11}\delta(\varepsilon_1 - \varepsilon_{\rm F}) \qquad (4.7)\\ &= 3CM\int \dot{\ell}_x^4(\mathbf{r})\sqrt{2M[\varepsilon_{\rm F} - U_{\rm osc}(\mathbf{r})]}d\mathbf{r}.\end{aligned}$$

Combining the result of integration with expression (3.22) for the rigid-body moment of inertia and the expression

$$\begin{aligned}\rho_{\rm F} &= \int d\mathbf{r}\sum_1\varphi_1^*(\mathbf{r})\varphi_1(\mathbf{r})\delta(\varepsilon_1 - \varepsilon_{\rm F}) \qquad (4.8)\\ &= 3CM\int\sqrt{2M[\varepsilon_{\rm F} - U_{\rm osc}(\mathbf{r})]}d\mathbf{r}\end{aligned}$$

for the mean level density near the Fermi surface, we obtain

$$\begin{aligned}&\sum_1(\dot{\ell}_x^4)_{11}\delta(\varepsilon_1 - \varepsilon_{\rm F}) \qquad (4.9)\\ &= \frac{18(\omega_x - \omega_z)^4(1+k)^4}{5\rho_{\rm F}(1+k^2)^2}\Im_{\rm rig}^2.\end{aligned}$$

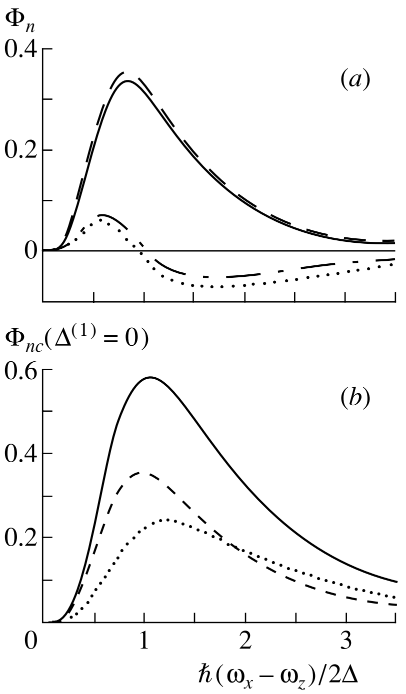

Fig. 2. Comparison of the functions relevant to the second inertial parameter for ND bands. Part (a) displays the functions Φ_n (4.5) (solid curve) and Φ_{nc} (4.11) (dashed curve) and their parts, the functions $\mathcal{F}$ (4.6) (dotted curve) and $\mathcal{F}_c$ (4.12) (dash-dotted curve), which describe the effect of rotation–quasiparticle interaction. Part (b) is for the limit of close transitions. There, the function Φ_{nc} (solid curve) and its constituents $\mathcal{F}_c$ (dashed curve) and $2D_2^2\mathcal{H}_c$ (dotted curve) are shown for $\Delta^{(1)} = 0$. The dimensionless quantity ν_1 corresponding to the close transitions is plotted along the abscissa, while that for the distant ones is fixed by the representative value $\nu_2 = 10$ for all plots.

In the case of a normal deformation, the quantity k is close to unity and, consequently, $\nu_2 \gg \nu_1$. Substituting (4.9) into (4.4) and using the above approximations, we get, for ND bands,

$$\beta_s(\mathrm{ND}) = \frac{\Im^2_{\mathrm{rig}}\Phi_{nc}(\nu_1, \nu_2)}{5\rho_{\mathrm{F}}\Delta^2}. \qquad (4.10)$$

The function Φ_{nc} approximates Φ_n in "the close-transition limit":

$$\Phi_{nc}(\nu_1, \nu_2) = \mathcal{F}_c(\nu_1, \nu_2) + 2D_2^2\mathcal{H}_c(\nu_2), \qquad (4.11)$$

where

$$\mathcal{F}_c(\nu_1, \nu_2) = f(\nu_1, -\nu_1, \nu_1, -\nu_1; 0, 0) + 2f(\nu_1, \nu_1, -\nu_1, -\nu_1; 2\nu_1, 0). \qquad (4.12)$$

The function Φ_{nc} depends on ν_2 only through the amplitudes D_1 and D_2, and the function

$$\mathcal{H}_c(\nu_2) = 8 + 8\ln 2\nu_2 + \ln 4\nu_2. \qquad (4.13)$$

The level density near the Fermi surface can be obtained by combining (4.8) with the number of nucleons $A = \int n(\mathbf{r})d\mathbf{r}$. The result, $\rho_{\mathrm{F}} = 3A/\varepsilon_{\mathrm{F}}$, depends on the Fermi energy, which is found from the volume-conservation condition $a^2b = R^3$. Expression (4.10) was obtained in [11].

Figure 2a shows that Φ_{nc} approximates the exact function Φ_n very well. It also shows that the contribution of the rotation–quasiparticle interaction is small in relation to that of the pairing modification. This result is explained by the interference of two effects: the Coriolis force and the nonuniform pairing field $\Delta^{(1)}$. Neglecting the latter results in the commensurate contributions of the two terms in Eq. (4.11) as is seen from Fig. 2b. This result is consistent with the Marshalek calculations [13].

For superdeformed nuclei, the parameters ν_1 and ν_2 are both large, $\sim A^{1/3}$. Thus, we should expect a decrease in β_s. It is convenient to rewrite Eq. (4.4) by introducing, according to (4.2), the parameters ξ and k instead of ν_1 and ν_2. We express the sum in (4.7) in terms of the rigid-body moment of inertia and the number of nucleons A:

$$\sum_1 (\dot{\ell}_x^4)_{11}\delta(\varepsilon_1 - \varepsilon_F) \qquad (4.14)$$
$$= \frac{24(\omega_x - \omega_z)^4 k^{2/3}(1+k)^4}{5(1+k^2)^3 A^2}\omega_0^2\Im^3_{\mathrm{rig}}.$$

Now, we have

$$\beta_s(\mathrm{SD}) = \frac{k^{2/3}(1+k)^4}{15\hbar^2(1+k^2)^3A^2}\Im^3_{\mathrm{rig}}\Phi(\xi, k), \qquad (4.15)$$
$$\xi^2\Phi(\xi, k) = \Phi_n(\nu_1, \nu_2).$$

The function Φ, along with its limiting case of the uniform pairing, is shown in Fig. 3. It can be seen that nonuniform pairing reduced the quantity $\beta_s(\mathrm{SD})$ even more than $\beta_s(\mathrm{ND})$.

Taking $k = 2$ and $\Delta = 0.5$ MeV ($\xi = 0.065$) as representative parameters for SD bands, we find from Fig. 3 that $\Phi \sim 1$. This yields the following estimate: $\beta_s(\mathrm{SD}) \sim \hbar^4(A/\varepsilon_{\mathrm{F}})^3 \sim \beta_s(\mathrm{ND})A^{-2/3}$ and $\mathcal{B}/\mathcal{A} \sim A^{-2}$. The last estimate is correct for SD bands in the $A \sim 190$ mass region, where $\mathcal{B}/\mathcal{A} \sim 10^{-5}$. Yet, it overestimates the experimental value for ^{84}Zr(1) ($\sim 10^{-5}$) and for ^{144}Gd(1) and ^{152}Dy(1) ($\sim 10^{-6}$). The last two bands have the smallest value of this ratio among all SD mass regions. Thus, a high deformation and nonuniform pairing do not solve the problem of the SD band regularity.

4.1. Limiting Cases

The limiting cases that are of greatest interest to us are those of strong pairing, uncorrelated nucleons, and extremely large deformations. The limit of small deformations was considered in [11].

For a very strong pairing ($\Delta \gg \hbar\omega_0$), the size of the Cooper pair, $R\hbar\omega_0/\Delta$, becomes much less than the nuclear radius R. The rotation of such a nucleus is described by the hydrodynamic equations of an ideal liquid [9], according to which the second inertial parameter vanishes. In the ensuing analysis, nonuniform pairing is a key aspect. For strong pairing, the quantities $\Delta^{(1)}$ and $\Delta^{(2)}$ are proportional to Δ because, as follows from Eqs. (A.4) and (A.8), $D_1 \sim \Delta^2$ and $D_2 \sim \Delta^4$. Therefore, this limit is instructive since it allows one to check the solution of the integral equation for $\Delta^{(2)}$.[4)]

In the strong-pairing limit, the parameters ν_1 and ν_2 are small. It is possible to simplify the function F by expanding $g(x_{\nu\nu'})$ and $h(x_{\nu\nu'})$ in power series in $x_{\nu\nu'}$ and then by approximating it, with the required accuracy, by

$$F = \mathcal{P}_2 + D_1\mathcal{P}_4 + D_1^2\mathcal{P}_4 + D_1^3\mathcal{P}_6 + D_1^4\mathcal{P}_8, \quad (4.16)$$

where $\mathcal{P}_n$ is a polynomial of nth degree in $x_{\nu\nu'}$. Using this function and performing a calculation similar to that which resulted in obtaining Φ_n, we find the limiting value

$$\lim_{\Delta\to\infty} \Phi_n(\nu_1, \nu_2) = -\frac{64}{3}\left(\frac{\omega_x - \omega_z}{\omega_x + \omega_z}\right)^2. \quad (4.17)$$

Combining this result with Eqs. (4.4) and (4.14), we arrive at

$$\beta_s \sim -\frac{\mathfrak{I}^3_{\text{rig}}}{(\hbar A)^2}\left(\frac{b^2 - a^2}{b^2 + a^2}\right)^2 \left(\frac{\hbar\omega_0}{\Delta}\right)^2. \quad (4.18)$$

Thus, the parameter β_s vanishes in the strong-pairing limit.

The rotation of a very elongated nucleus with $k = b/a \gg 1$ exhibits some interesting physics. For this limit, the parameters ν_1 and ν_2 are approximately given by

$$\nu_1 = \nu \pm \delta\nu, \quad \nu = \frac{\omega_x}{2\Delta}, \quad \delta\nu = \frac{\omega_z}{2\Delta}, \quad (4.19)$$

where $\nu \gg 1$ and $\delta\nu/\nu = a/b \ll 1$. Nonuniform pairing is important in this case as well, because the small amplitude $D_1 \approx 1/\nu^2$ is compensated by a large value of ν^2. As a result, the kinematical moment of inertia, which is the sum of the standard cranking-model term and the Migdal one, is close to the rigid-body value:

$$\mathfrak{I}^{(1)} = \mathfrak{I}_{\text{rig}}\left[1 - \left(\frac{a}{b}\right)^2 \frac{10}{\nu^2}\ln 2\nu\right]. \quad (4.20)$$

In the zeroth approximation $\nu_1 = \nu_2$, the function (4.5) vanishes, $\Phi_n(\nu, \nu) = 0$. The next term of its expansion in $\delta\nu$ gives an estimate of the second inertial parameter, $\beta_s \sim (a/b)^2$. We can say that a strongly elongated nucleus in the superfluid phase has the rotational regime that is close to a rigid-body rotation. The deviation from this regime is of order $(a/b)^2$. The physical interpretation of this phenomenon is straightforward: all nucleons of a needle-shaped nucleus with exclusion of the small sphere of radius a at its center are involved in rotational motion.

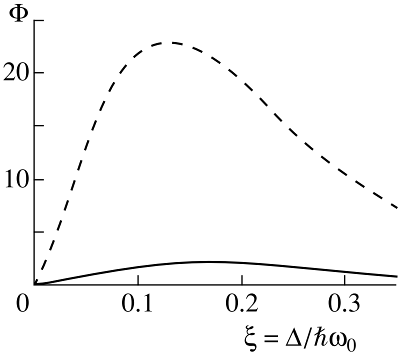

Fig. 3. Plot of the function Φ, to which the second inertial parameter for SD bands is proportional [see Eq. (4.15)], against the dimensionless quantity ξ for the axis ratio $b/a = 2$. The solid and dashed curves correspond to the exact value and the limit of uniform pairing, respectively. The abscissa scale must be multiplied by a factor of approximately 7.7 for nuclei in the $A \sim 150$ mass region in order to obtain the gap energy in MeV.

Let us now consider the normal phase. The right-hand side of Eq. (3.11) vanishes in the limiting case of $\Delta = 0$. This result is an artifact of the semiclassical approximation used in deriving expression (3.11). The correct formula obtained from Eq. (3.4) with the limiting values of the Bogoliubov amplitudes ($u_\nu = 0$ and $v_\nu = 1$ for $\rho_\nu = 1$ and $u_\nu = 1$ and $v_\nu = 0$ for $\rho_\nu = 0$, where ρ_ν is the nucleon occupation numbers) is

$$\beta_n^{(\text{sp})} = -\sum \ell^x_{12}\ell^x_{23}\ell^x_{34}\ell^x_{41} \quad (4.21)$$

$$\times \sum_{i=0}^{3} \hat{P}_i \left\{\frac{\rho_1}{(\varepsilon_1 - \varepsilon_2)(\varepsilon_1 - \varepsilon_3)(\varepsilon_1 - \varepsilon_4)}\right\}.$$

This expression describes the effect of the Coriolis force on single-particle motion. It will be shown in the next section that the cancellation of the leading terms in the sum on the right-hand side of (4.21) substantially reduces this quantity in relation to β_s.

[4)] The solution for $\Delta^{(1)}$ was verified in [21] by obtaining the hydrodynamic moment of inertia.

4.2. Second Inertial Parameter for Uncorrelated Nucleons

In this subsection, we estimate the parameter β in the normal phase. In view of the cancellation mentioned above, we have to take into account the centrifugal-stretching effect, which appears to be on the same order of magnitude as (4.21). As in the case of a superfluid phase, we will use the Green's function technique.5) Our starting point is the equations in the Hartree approximation,6)

$$[\varepsilon - h_\omega(\mathbf{r}) - \mathcal{V}(\mathbf{r})]G(\mathbf{r}, \mathbf{r}', \varepsilon) = \delta(\mathbf{r} - \mathbf{r}'), \quad (4.22)$$

where h_ω is the cranked single-particle Hamiltonian (2.1) with the oscillator potential (4.1) and

$$\mathcal{V}(\mathbf{r}) = \int d\mathbf{q} v_q(\mathbf{r}, \mathbf{q}) \oint\limits_C \frac{d\varepsilon}{2\pi i} G(\mathbf{q}, \mathbf{q}, \varepsilon) \quad (4.23)$$

is the self-consistent potential. We assume that the two-body residual interaction v_q is an effective quadrupole one,

$$v_q(\mathbf{r}, \mathbf{r}_1) = -\frac{\chi}{2}\sum_\mu (-1)^\mu q_{2\mu}(\mathbf{r}'') q_{2-\mu}(\mathbf{r}_1''), \quad (4.24)$$

where the quadrupole moment $q_{2\mu}$ is defined in terms of the doubly stretched coordinates

$$\mathbf{r}'' = \mathbf{i}\frac{\omega_x}{\omega_0}x + \mathbf{j}\frac{\omega_y}{\omega_0}y + \mathbf{k}\frac{\omega_z}{\omega_0}z. \quad (4.25)$$

The interaction strength χ is determined in a self-consistent way as follows:

$$\chi = \frac{4\pi\omega_0^2 M}{5\mathrm{tr}\{(\mathbf{r}'')^2\rho\}}. \quad (4.26)$$

This interaction provides a full self-consistency for deformed nuclei [29].

As usual, we proceed to treat the cranking term V by perturbation theory, expanding the Green's function and the self-consistent potential in the series

$$\begin{gathered} G = G_0 + G_1 + G_2 + G_3 + \ldots, \quad (4.27) \\ \mathcal{V} = \mathcal{V}^{(0)} + \mathcal{V}^{(1)} + \mathcal{V}^{(2)} + \mathcal{V}^{(3)} + \ldots. \end{gathered}$$

The unperturbed Green's function is

$$G_0(\mathbf{r}, \mathbf{r}_1, \varepsilon) = \sum_\nu G_\nu(\varepsilon)\varphi_\nu(\mathbf{r})\varphi_\nu^*(\mathbf{r}_1), \quad (4.28)$$

$$G_\nu(\varepsilon) = \frac{1}{\varepsilon - \varepsilon_\nu + i\delta(1 - 2\rho_\nu)},$$

with $\delta \to +0$. The occupation numbers ρ_ν refer to a nonrotating nucleus. We may note that, under the self-consistent condition

$$\omega_x\Sigma_x = \omega_x\Sigma_y = \omega_z\Sigma_z, \quad (4.29)$$

$$\Sigma_{x,y,z} = \sum_\nu (n_{x,y,z} + 1/2)_\nu \rho_\nu$$

(n_x, n_y, n_z are the oscillator quantum numbers), $\mathcal{V}^{(0)} = 0$. Thus, the average potential is modified only by rotation.

There are no odd corrections to the self-consistent potential, $\mathcal{V}^{(2i+1)} = 0$, because of the different symmetry properties of the operators $q_{2\mu}$ and ℓ_x under the time reversal. Consequently, the third-order correction to the Green's function is expressed as

$$\begin{aligned} G_3 &= G_0VG_0VG_0VG_0 \quad (4.30) \\ &+ G_0VG_0\mathcal{V}^{(2)}G_0 + G_0\mathcal{V}^{(2)}G_0VG_0. \end{aligned}$$

The first term generates the interaction of rotation with single-particle motion. It yields the quantity $\beta_n^{(\mathrm{sp})}$ (4.21). The last two terms are responsible for the centrifugal-stretching effect, which is described by the expression

$$\begin{aligned} \beta_n^{(\mathrm{str})} &= -\frac{2}{\omega^4} \quad (4.31) \\ &\times \oint\limits_C \frac{d\varepsilon}{2\pi i}\mathrm{tr}\{\mathcal{V}^{(2)}G_0(\varepsilon)VG_0(\varepsilon)VG_0(\varepsilon)\}, \end{aligned}$$

where the correction to the mean potential $\mathcal{V}^{(2)}$ is obtained from the equation

$$\begin{aligned} \mathcal{V}^{(2)}(\mathbf{r}) &= -\chi\sum_\mu (-1)^\mu q_{2-\mu}(\mathbf{r}) \oint\limits_C \frac{d\varepsilon}{2\pi i} \quad (4.32) \\ &\times \mathrm{tr}\{q_{2\mu}[G_0(\varepsilon)VG_0(\varepsilon)VG_0(\varepsilon) + G_0(\varepsilon)\mathcal{V}^{(2)}G_0(\varepsilon)]\}. \end{aligned}$$

This equation has the solution

$$\mathcal{V}^{(2)}(\mathbf{r}) = -\omega^2 \sum_\mu \frac{\chi}{1 + \chi\sigma_\mu}(-1)^\mu Q_{2\mu}^{(2)} q_{2-\mu}(\mathbf{r}), \quad (4.33)$$

where

$$\sigma_\mu = \sum_{1,2} |(q_{2\mu})_{12}|^2 \frac{\rho_1 - \rho_2}{\varepsilon_1 - \varepsilon_2}, \quad (4.34)$$

$$Q_{2\mu}^{(2)} = \oint\limits_C \frac{d\varepsilon}{2\pi i}\mathrm{tr}\{q_{2\mu}G_0(\varepsilon)\ell_x G_0(\varepsilon)\ell_x G_0(\varepsilon)\}.$$

The last quantity is the second correction to the nuclear quadrupole moment due to rotation. Its explicit form is

$$Q_{2\mu}^{(2)} = \sum (q_{2\mu})_{12}\ell_{23}^x\ell_{31}^x \quad (4.35)$$

---

5) There is an alternative method based on minimizing the energy of the system in the rotating reference frame as a function of the oscillator frequencies ω_x, ω_y, and ω_z and the rotational frequency ω under the constraint of a constant volume. For fixed occupations of single-particle states, this method gives the same result as that obtained below.

6) This approximation is adequate to a separable two-body interaction that we will use.

$$\times \sum_{i=0}^{2} \hat{P}_i \left\{ \frac{\rho_1}{(\varepsilon_1 - \varepsilon_2)(\varepsilon_1 - \varepsilon_3)} \right\},$$

where the permutation of indices $\nu = 1,\ 2,\ 3$ by the operator $\hat{P}_i$ is subject to the rule $\nu \mathrm{mod} 3 = \nu$. It is obvious that nonzero corrections have the $\mu = 0, \pm 2$ components. The denominator in the sum on the right-hand side of (4.33) renormalizes the interaction strength. A straightforward calculation of σ_μ and the use of Eq. (4.26) with the zero-order density matrix ρ gives $\chi/(1 + \chi\sigma_\mu) = 2\chi$. Combining (4.31) with (4.33), we have

$$\beta_n^{(\mathrm{str})} = \frac{16\pi M^2 \omega_0^2}{15\hbar\omega_z \Sigma_z} \sum_{\mu=0,\pm 2} Q_{2\mu}^{(2)} Q_{2-\mu}^{(2)}. \tag{4.36}$$

We can now calculate two contributions to the parameter β_n by performing summation over the quantum numbers n_x, n_y, and n_z. The anisotropic oscillator potential allows us to find an exact solution to the problem. At first, we find the corrections to the quadrupole moments

$$Q_{20}^{(2)} = \sqrt{\frac{5}{64\pi}} \tag{4.37}$$

$$\times \frac{\hbar\Sigma_z}{M\omega_0^2\omega_z(k^2 - 1)}(2k^4 - 15k^2 + 1),$$

$$Q_{2\pm 2}^{(2)} = \sqrt{\frac{5}{128\pi}} \frac{\hbar\Sigma_z(1 - 5k^2)}{M\omega_0^2\omega_z k^2(k^2 - 1)}.$$

By using (4.36), we then obtain the contribution of the centrifugal stretching effect:

$$\beta_n^{(\mathrm{str})} = \frac{\hbar\Sigma_z}{3\omega_z^3 k^4(k^2 - 1)^2} \tag{4.38}$$

$$\times (k^8 - 15k^6 + 76k^4 - 15k^2 + 1).$$

Finally, after some fairly tedious calculations of the sum in (4.21), we get

$$\beta_n^{(\mathrm{sp})} = \frac{\hbar\Sigma_z}{2\omega_z^3 k^4(k^2 - 1)^2} \tag{4.39}$$

$$\times (k^8 - 10k^6 - 14k^4 - 10k^2 + 1).$$

Adding the last two quantities gives us the parameter β in the normal phase. We have

$$\beta_n = \frac{5\Im_{\mathrm{rig}}}{6\omega_0^2} \frac{k^4 - 10k^2 + 1}{k^{2/3}(k^2 + 1)} \tag{4.40}$$

if we use the following formula for the rigid-body moment of inertia:

$$\Im_{\mathrm{rig}} = \frac{\hbar\Sigma_z}{\omega_z k^2}(k^2 + 1). \tag{4.41}$$

The parameter β_n is substantially reduced in relation to β_s, $\beta_n \sim \hbar^4 A^{7/3}/\varepsilon_{\mathrm{F}}^3 \sim \beta_s(\mathrm{SD})A^{-2/3}$. This can be explained by the cancellation of the main terms in the sums in (4.21) and (4.35). That is precisely why the corresponding quantities $\beta_n^{(\mathrm{sp})}$ and $Q_{2\mu}^{(2)}$ are proportional to Σ_z. This result is predictable because the Hamiltonian h_ω for an anisotropic harmonic oscillator can be diagonalized exactly [30]. Its eigenstates are characterized by the number of rotating bosons. To find $\beta_n^{(\mathrm{sp})}$ and $Q_{2\mu}^{(2)}$, we must calculate first the expectation values of the operators ℓ_x and $Q_{2\mu}$ in this rotating basis. Then, these quantities must be expanded in powers of ω. Because these operators are represented by quadratic forms in rotating bosons, their expectation values and, therefore, all the terms of the series are proportional to the linear combination of Σ_x, Σ_y, and Σ_z.

Another special feature of the solution in (4.40) is that $\beta_n < 0$ for prolate nuclei with $1 < b/a < 3.15$, whereas β_s is always positive. The formal reason behind this effect is a negative value of $\beta_n^{(\mathrm{sp})}$ and the inequality $|\beta_n^{(\mathrm{sp})}| > \beta_n^{(\mathrm{str})} > 0$, which is satisfied for the deformations indicated above. In the superfluid phase, the term responsible for the rotation–quasiparticle interaction may also be negative, but it never exceeds the contribution of the pair-modification effect (see Fig. 2*a*).

5. ANALYSIS OF EXPERIMENTAL DATA

We have shown in the preceding section that the second inertial parameter $\mathcal{B}$ is negative in the superfluid phase and is positive in the normal phase. The two limiting cases allow us to reconstruct the dependence $\mathcal{B}(I)$ for the parametrization (1.1) of a rotational sequence with $(\pi\alpha) = (+0)$. Comparing formulas (4.10) or (4.15) with (4.40), we conclude that the ratio $\mathcal{B}/\mathcal{A}$ must change sign with increasing spin I in a band and approach its limiting value $\mathcal{B}_n/\mathcal{A}_n \sim A^{-8/3}$ for high I.

The limiting ratio for an actual nucleus can be obtained from Eqs. (4.40) and (4.41) if we suppose that the root-mean-square radius and the deformation are exactly the same for the neutron (ν) and for the proton (π) system. The first condition implies that the oscillator frequencies of the neutron and proton potentials satisfy the relation $\omega_{0\tau} = \omega_0(2A_\tau/A)$ ($\tau = \pi, \nu$ and A_τ is the number of nucleons of a given type). The second condition results in the identical ratio of the frequencies along the principal axes for both potentials:

$$\omega_{x\tau} : \omega_{y\tau} : \omega_{z\tau} = m : m : l. \tag{5.1}$$

For the integers m and l, the states with the same number of quanta $\mathcal{N}_{ml} = m(n_x + n_y) + ln_z$ form a deformed shell. Assuming that, for a given number of nucleons A_τ, all $\mathcal{N}_{ml}$ shells are filled, one can express the sum $\Sigma_{z\tau}$ in the form

$$\omega_{z\tau}\Sigma_{z\tau} = \omega_{0\tau}(\Sigma_{x\tau}\Sigma_{y\tau}\Sigma_{z\tau})^{1/3} = \omega_{0\tau}\left(\frac{A_\tau^4}{32}\right)^{1/3}. \quad (5.2)$$

The above formulas allow us to derive the ratio $\mathcal{B}/\mathcal{A}$ for a nucleus consisting of Z protons and N neutrons in the normal state:

$$\frac{\mathcal{B}_n}{\mathcal{A}_n} = -3.205\frac{(k^4 - 10k^2 + 1)k^{2/3}}{(k^2+1)^3 A^{8/3}} \times \left[\left(\frac{Z}{A}\right)^{1/3} + \left(\frac{N}{A}\right)^{1/3}\right]. \quad (5.3)$$

This result holds for a nucleus with an arbitrary deformation $k = b/a = m/l$.

We first concentrate on SD bands. Most of them are not connected to lower lying states of known excitation energy, spin, and parity. Thus, their exit spins I_0 are unknown. A tentative spin assignment is used to take advantage of formulas (1.2) to find the experimental ratio $\mathcal{B}/\mathcal{A}$. To analyze this quantity, we will take into account two basic ingredients: shell gaps, which stabilize the shape, and intruder orbitals involved in alignment. The nucleon-configuration assignment of a band is generally based only on the behavior of the dynamical moment of inertia and the quadrupole moment in a given band. The last quantity,

$$Q_0 = (6.05 \times 10^{-3})A^{2/3}\frac{k^2-1}{k^{2/3}}eb, \quad (5.4)$$

remains remarkably constant as a function of spin within a band. This proves that the deformation k remains virtually unchanged as I increases. We use the experimentally observed value of Q_0 to find the axis ratio b/a, which is required for calculating the quantity in (5.3).

The ratios $\mathcal{B}/\mathcal{A}$ extracted from the measured energy of γ transitions in the four SD bands of the $A = 150$ mass region are shown in Fig. 4. The parity and the signature of these bands are assumed to be $(+, 0)$. We also use the adopted spins for their lowest levels. The ^{152}Dy(1) band belongs to the doubly magic nucleus with the $Z = 66$ proton and the $N = 86$ neutron gaps in single-particle spectra at the same deformation [31]. The gaps decrease the level density and considerably reduce neutron and proton pairing correlations. There is no direct experimental indication of pairing correlations in this band. Theoretical calculations show [32] that their inclusion leads to a better description of the kinematical and dynamical moments of inertia, pairing correlations being more important in the low-spin part. The plot shows that there are two distinct regions in the variation of the ratio $\mathcal{B}/\mathcal{A}$ versus I. The lower part of the band exhibits a sharp increase in this quantity. It then changes sign at the spin value of $I_c = 36$ and approaches the plateau value of (5.3) at the top of the band. This behavior of the ratio apparently shows that static pairing correlations of neutrons and protons are quenched simultaneously. This fact also proves that most of the band belongs to the normal phase.

The band ^{144}Gd(1) is one of the few examples of SD bands that exhibits backbending. The $\pi 6^2$ pair alignment opens up the $Z = 64$ proton-shell gap at the same deformation as the $N = 80$ neutron-shell gap. Thus, we see that, above the backbending, this band becomes similar to the doubly magic ^{152}Dy(1), except that the gap $Z = 64$ is less pronounced than that at $Z = 66$. In addition, the $N = 80$ neutron gap is somewhat smaller than $N = 86$. These factors enhance the level density and favor pairing correlations. As can be seen in Fig. 4, the behavior of $\mathcal{B}/\mathcal{A}$ for this band in the low-I region is the same as that for ^{152}Dy(1) if we scale the axis of ordinates by a factor of 2. Accordingly, the critical value is somewhat larger, $I_c = 38$.

The features observed at low spins in the dynamical moment of inertia of the ^{150}Gd(1) band were explained in terms of the consecutive alignments of the $\nu 7^2$ and $\pi 6^2$ pairs [31]. For the $\pi 6^2 \nu 7^2$ configuration, all levels below the $Z = 64$ and $N = 86$ shell gaps are occupied. The former is found at a slightly smaller deformation than the latter. This factor diminishes the neutron gap and enhances neutron pairing. The Woods–Saxon [31] and the relativistic mean-field [33] calculations demonstrate that static proton and neutron pairing exist at low spins, $I < 48$ ($\hbar\omega < 0.55$ MeV). In addition, the full self-consistent HFB calculations with the particle-number projection [33] show that the effect of pairing on the moments of inertia in ^{150}Gd(1) is about twice as important as in ^{152}Dy(1). It is apparent from Fig. 4 that static pairing correlations in the ^{150}Gd(1) band are stronger than in ^{144}Gd(1). One should expect still stronger pairing correlations in the newly discovered prolate deformed band ^{154}Er(2) [34], since the proton Fermi level at $Z = 68$ lies in the region of a high level density above the $Z = 66$ gap. The experimental dependence for $\mathcal{B}/\mathcal{A}$ in Fig. 4 is consistent with this prediction. It is seen that this ratio does not exceed the value of -5×10^{-6} and does not show a plateau.[7)] The bump seen at $I = 44$ ($\omega = 0.57$ MeV) can be attributed to the alignment of a pair of $i_{13/2}$ protons in agreement

---

[7)] It is worth mentioning that the nonaxial band ^{154}Er(1) demonstrates the dependence of $\mathcal{B}/\mathcal{A}$ with the critical spin $I_c = 31$ and a long plateau.

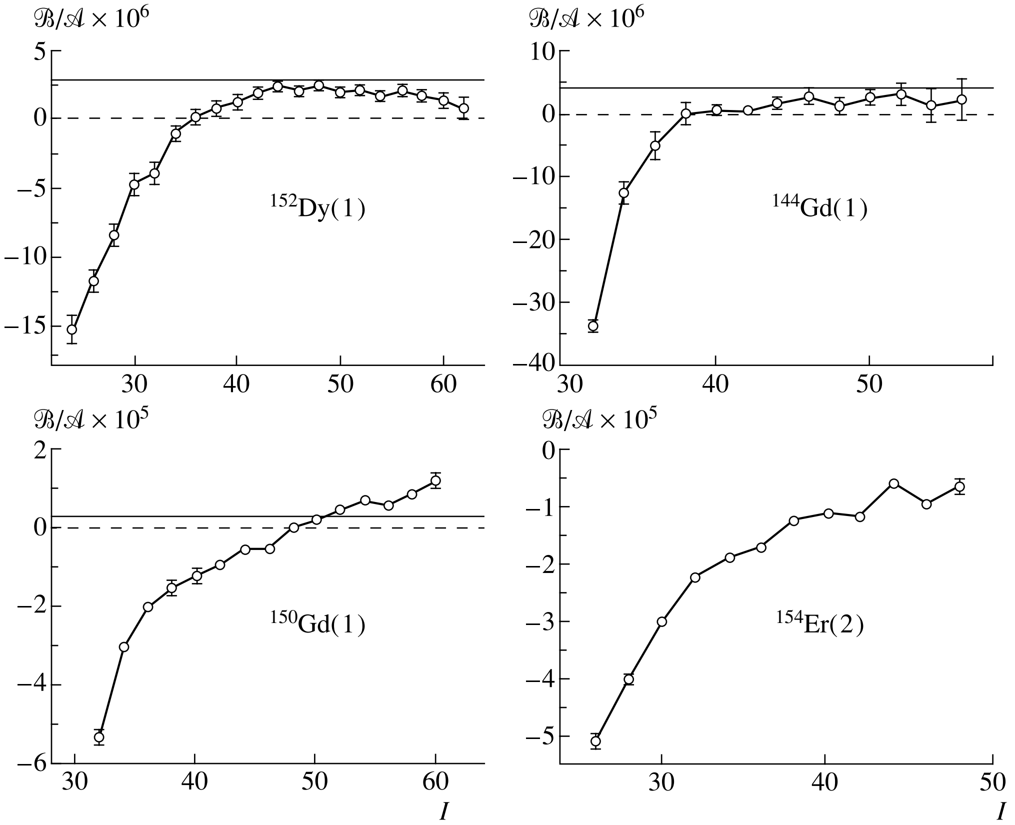

Fig. 4. Ratio $\mathcal{B}/\mathcal{A}$ versus spin for some SD bands of the $A = 150$ region. Expressions (1.2) are used to extract this ratio from experimental data taken from [8, 34]. The error bars (if they are greater than symbol sizes) include only the uncertainties in the γ-ray energies. The uncertainties in the spin assignment are immaterial for all bands [with the exception of ^{152}Dy(1)], since the spin variation in $2\hbar$ would merely shift the curves along the abscissa. The experimental points for the ^{144}Gd(1) band are shown above the $\pi i_{13/2}$ backbending. The solid straight line represents the ratio $\mathcal{B}_n/\mathcal{A}_n$ (5.3) for the normal phase with the deformation b/a found from the quadrupole moment (5.4).

with the calculations of [31]. Thus, the plots of Fig. 4 show the correlation of the spin dependence of the ratio $\mathcal{B}/\mathcal{A}$ with the level density near the Fermi surface: the higher the level density, the stronger the pairing correlations and the less pronounced the plateau.

The highly deformed (HD) bands in the $A = 190$ mass region are related to the $Z = 80$ and $N = 112$ shell gaps. The majority of these bands have similar values of $\mathfrak{I}^{(2)}$, which exhibits a smooth rise as a function of the rotation frequency. This rise is attributed to a gradual alignment, in the presence of static pairing correlations, of $i_{13/2}$ protons and $j_{15/2}$ neutrons. The calculations with pairing are able to reproduce the general trend seen in experiments. The ^{194}Hg(1) and ^{194}Pb(1) bands are of crucial importance because their spins, parities, and excitation energies are known [35, 36]. The plots of Fig. 5 for these bands demonstrate the gradual rise of the ratio $\mathcal{B}/\mathcal{A}$, which confirms the presence of static pairing correlations.

We now consider ND bands. There are several bands of Er, Yb, and Hf isotopes in which the static neutron-pairing gaps are predicted to collapse. However, the proton system still has strong pairing correlations. Accordingly, plot of $\mathcal{B}/\mathcal{A}$ versus I for these bands exhibits a sharp rise, but it does not approach a plateau. The yrast band of ^{84}Zr is an exception. Because, in this nucleus, protons and neutrons occupy similar orbitals near the Fermi surface, quasiparticle alignments and the elimination of pairing gaps occur at similar spins. In addition, the deformed shell gaps at $Z = N = 38$ and the low moment of inertia favor a transition to the normal phase. The combination of these factors makes the pairing properties of the ND band of ^{84}Zr similar to those of SD bands in the $A = 150$ mass region. The ratios $\mathcal{B}/\mathcal{A}$ determined for the ND and SD bands of this nucleus from the data of [37] and [38], respectively, are shown in Fig. 6 versus the spin I. In the SD band ^{84}Zr(1), static pairing correlations are quenched completely because of a high rotation frequency. This inference is supported by the coincidence of experimental points with the $\mathcal{B}_n/\mathcal{A}_n$ plateau. It also becomes apparent from this

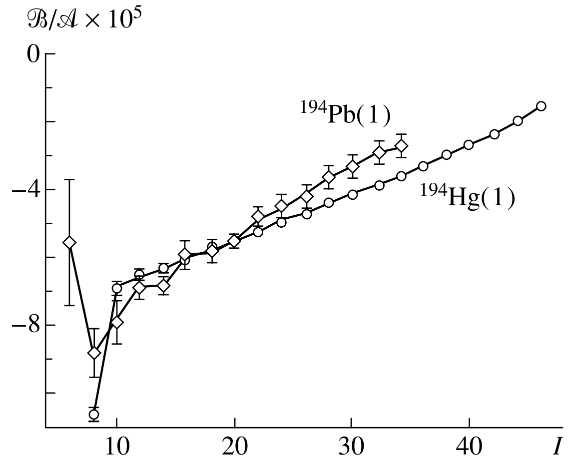

Fig. 5. As in Fig. 4, but for the two HD bands of the $A = 190$ region. Experimental data were taken from [8, 35, 36].

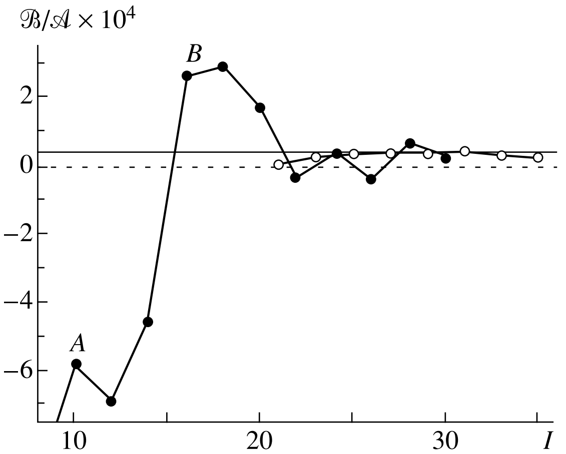

Fig. 6. Ratio $\mathcal{B}/\mathcal{A}$ versus spin for the (solid circles) yrast ND band and the (open circles) SD band of ^{84}Zr. Experimental data were taken from [37, 38]. The solid straight line represents the ratio $\mathcal{B}_n/\mathcal{A}_n$ (5.3) relevant to the deformation of the SD band.

figure that, at high spins, the experimental ratio for the ND band reaches the same plateau. The difference in the limiting value of $\mathcal{B}_n/\mathcal{A}_n$ due to the difference in deformations ($\beta = 0.43$ and 0.55 for the ND and SD bands, respectively) is insignificant. The low-spin part ($I < 18$) of the ND band is compatible with the transition nature of the γ-soft nucleus: small β and a noticeable triaxiality. The alignment of the two $g_{9/2}$ quasiprotons and the subsequent alignment of the two $g_{9/2}$ quasineutrons are clearly seen in Fig. 6 as the humps A and B. Beyond the second alignment, a striking change in deformation occurs in the interval $I = 18$–22 of spins. After the spin $I = 24$, the rotational behavior is compatible with the rigid rotation of a HD axially symmetric nucleus [37].

The characteristic behavior of the ratio $\mathcal{B}/\mathcal{A}$ with the critical spin I_c and the pronounced plateau has also been found in the SD bands of the $A = 150$ nuclei having configurations different from $(+, 0)$. The SD bands ^{152}Tb(2) [the $\pi[301]1/2$ hole in the ^{152}Dy SD core] and ^{153}Ho(3) [the ^{152}Dy SD core coupled to the $\pi[523]7/2$ orbital] show a dependence of $\mathcal{B}/\mathcal{A}$ similar to that of the ^{152}Dy(1) band. The pair of identical bands ^{150}Gd(2) and ^{151}Tb(1) have a dependence similar to that in ^{150}Gd(1). All these bands have somewhat higher values of $\mathcal{B}/\mathcal{A}$ in the low-I region than their $(+, 0)$ counterparts. This proves that an odd nucleon or a particle–hole excitation reduces pairing correlations because of the blocking effect. This phenomenon is characteristic of the static-pairing regime [19]. Superdeformed bands from different mass regions, ^{132}Ce(1), ^{133}Ce(1), and ^{60}Zn(1), exhibit the same behavior of $\mathcal{B}/\mathcal{A}$. A strong configuration-dependent effect is observed in bands where an odd neutron is placed in the $j_{15/2}$ intruder orbitals. For such bands, the ratio $\mathcal{B}/\mathcal{A}$ is positive for all spins. Examples include the bands ^{149}Gd(1) (configuration $\pi 6^2 \nu 7^1$), ^{151}Dy(1) ($\pi 6^4 \nu 7^1$), and ^{153}Dy(1) ($\pi 6^4 \nu 7^3$). A single-particle degree of freedom seems to destroy the typical behavior of the ratio $\mathcal{B}/\mathcal{A}$. More efforts are needed to explain this interesting feature.

These numerous examples prove the universality of the transition from the superfluid to the normal phase for SD and ND bands. This universality can be represented, according to [6], by the effective rotational Hamiltonian,

$$H_{\text{eff}} = a\mathbf{I}^2 + (I/I_c - 1)b\mathbf{I}^4 + c\mathbf{I}^6, \qquad (5.5)$$

which describes the states of the $(+, 0)$ band in the transition region. The parameters a, b, and c and the critical spin I_c are the subjects of a microscopic theory that has to take into account static, dynamical, and uniform pairing. Incorporating the critical spin, which can be found from the experimental plot of $\mathcal{B}/\mathcal{A}$ versus I, this concept of the superfluid-to-normal transition is free from ambiguities characteristic of the approach based on a change in the single-particle spectra [4, 5].

Using the results of our analysis, we can now explain why some SD bands have extremely regular rotational spectra. Figure 4 shows that the most part of the ^{152}Dy(1) and ^{144}Gd(1) bands belongs to the plateau with the inertial-parameter ratio $\mathcal{B}/\mathcal{A} \sim 10^{-6}$, and so does the whole of the SD band ^{84}Zr(1), for which this ratio is $\sim 10^{-5}$. The plateau is a manifestation of the normal phase with the anomalously small ratio (5.3), $\mathcal{B}_n/\mathcal{A}_n \sim A^{-8/3}$. The above values for the SD bands agree with this estimate. Therefore, the extreme regularity is explained by the quenching of static pairing correlations in the lower parts of these bands. On the contrary, the transition in the yrast band of ^{84}Zr occurs in its upper part. Accordingly, the top of the band has the same properties. It is important to note that the bands in which the proton and neutron pairing gaps are present [^{154}Er(2) and all the SD bands in the $A = 190$ mass region] and that the ND bands with proton pairing alone [^{168}Yb(yr) and ^{186}Hf(yr)] are regular to a lesser extent.

We would like to mention yet another feature that requires a further investigation. The down-sloping of the dependence of $\mathcal{B}/\mathcal{A}$ is observed at the top of ^{152}Dy(1), ^{84}Zr(1), and other SD bands with extremely high spins. Because the quantity $\mathcal{B}_n/\mathcal{A}_n$ is a decreasing function of the deformation k, it would be natural to explain this feature by an increase in the nuclear elongation because of the enormous centrifugal stretching at the end of these bands.

6. CONCLUSION

Despite the vast amount of data collected and various theoretical interpretations suggested, a detailed understanding of many properties of SD bands has yet to be achieved. Pairing correlations are just one example of such properties. The presence of static pairing in SD and ND bands is usually established by studying the behavior of the dynamical moment of inertia $\mathfrak{I}^{(2)}$ as a function of the rotation frequency ω. A band crossing associated with a quasiparticle alignment leads to an impressive decrease in $\mathfrak{I}^{(2)}$ with ω or a hump in this dependence. This gives an indication that static pairing correlations are present in that part of a band where such irregularities occur.

In this article, the investigation of pairing correlations is based on the spin dependence of the second inertial parameter $\mathcal{B}$. This quantity, which is proportional to the difference $\mathfrak{I}^{(1)} - \mathfrak{I}^{(2)}$ in the high-I limit, proved to be a more sensitive measure of the change in pairing correlations than $\mathfrak{I}^{(2)}$. The new method requires spin–signature assignments of the band states. However, it gives more definite information about the superfluid-to-normal transition in a band. The most important results obtained in this study can be summarized as follows:

(i) The exact semiclassical expression for the second inertial parameter in the superfluid phase has been found by taking into account the effect of rotation on Cooper pairs in a gauge-invariant form. The presence of nonuniform pairing reduces the nonadiabatic effect of rotation. Its influence increases strongly in the case of superdeformation. Nonuniform pairing allows one to find correctly interesting physical limits for the second inertial parameter.

(ii) The limit of zero static pairing is of special interest. It permits the function $\mathcal{B}(I)$ to be reconstructed by means of interpolation between the values of $\mathcal{B}$ in the superfluid and normal phases. Anisotropic-oscillator-model calculations show that there are two distinct regions in the variation of the ratio $\mathcal{B}/\mathcal{A}$ with I. The lower part of a band is characterized by a gradual decrease in pairing. Accordingly, being negative, the ratio $\mathcal{B}/\mathcal{A}$ exhibits a sharp increase. It then changes sign at the spin value of I_c and approaches the positive value characteristic of the normal phase. The critical point I_c, $\mathcal{B}(I_c) = 0$, is a signature of a superfluid-to-normal transition. The transition manifests itself in the modification of the rotational spectrum of a band.

(iii) The experimental spin dependence of $\mathcal{B}/\mathcal{A}$ is in agreement with the theoretical prediction and demonstrates the universality of the transition to the normal state. This agreement is not a trivial fact because our calculations are based on the simplest model of a nuclear potential and do not take into account pairing fluctuations in the normal phase. Nevertheless, the agreement is not accidental because the universal dependence of $\mathcal{B}/\mathcal{A}$ on I has been observed for a large number of SD bands and some ND ones.

(iv) The universal spin dependence of $\mathcal{B}/\mathcal{A}$ explains the extreme regularity of some SD bands. The characteristic feature of this dependence is a pronounced plateau in the upper part of an SD band ($I > I_c$) corresponding to the normal phase. The calculated ratio in this part of a band is extremely small, $\mathcal{B}/\mathcal{A} \sim A^{-8/3}$. Thus, the closer the critical point I_c to the exit spin I_0, the more regular its rotational spectrum. Spectacular examples are provided by the ^{144}Gd(1) and ^{152}Dy(1) bands having $\mathcal{B}/\mathcal{A} \sim 10^{-6}$.

(v) Some new features have been observed in the upper parts of SD bands. The investigation of this region, which is free from pairing correlations, is extremely important for our understanding of the microscopic structure at the superdeformed minimum.

ACKNOWLEDGMENTS

This work was supported in part by the Russian Foundation for Basic Research, project no. 00-15-96590.

APPENDIX A

Solving the Integral Equations for the Nonuniform Pairing Field

The effect of rotation on pairing correlations is described by the first, $\Delta^{(1)}(\mathbf{r})$, and the second, $\Delta^{(2)}(\mathbf{r})$, corrections to the pairing field, which enter into Eq. (3.4). We have seen in Section 2 that the integral equations that have to be solved are of the general form (2.31) and (2.32) for even and odd corrections, respectively. It is convenient to introduce, in these equations, the operator $\dot{\ell}_x$ that is a function of only the spatial coordinates.

We begin considering the equation for $\Delta^{(1)}$. Using the relation $\hbar\dot{\ell}^x_{12} = i(p_1 - p_2)\ell^x_{12}$, we find from (2.32) for $i = 0$ that

$$\sum_{1,2} \int\limits_{C'} \frac{dp}{2\pi} \frac{1}{(\mathbf{p}_1^2 + \Delta^2)(\mathbf{p}_2^2 + \Delta^2)} \tag{A.1}$$
$$\times [2i\Delta\hbar\omega\dot{\ell}^x_{12} + (p_1 - p_2)^2\Delta^{(1)}_{12}]\varphi_1(\mathbf{r})\varphi_2^*(\mathbf{r}') = 0.$$

The equation is satisfied if we assume that

$$\Delta^{(1)}(\mathbf{r}) = -i\frac{\hbar\omega}{2\Delta}D_1\dot{\ell}_x, \tag{A.2}$$

where the amplitude D_1 is determined upon substituting (A.2) into Eq. (A.1) and performing integration with respect to $\mathbf{r}$:

$$D_1 = 4\Delta^2 \sum_{1,2} |\dot{\ell}^x_{12}|^2 \int\limits_{C'} \frac{dp}{2\pi} \tag{A.3}$$
$$\times \frac{1}{(\mathbf{p}_1^2 + \Delta^2)(\mathbf{p}_2^2 + \Delta^2)} \Bigg/ \left[\sum_{1,2} |\dot{\ell}^x_{12}|^2\right.$$
$$\left.\times \int\limits_{C'} \frac{dp}{2\pi} \frac{(p_1 - p_2)^2}{(\mathbf{p}_1^2 + \Delta^2)(\mathbf{p}_2^2 + \Delta^2)}\right].$$

The solution reduces to

$$D_1 = \frac{\sum_{1,2} |\dot{\ell}^x_{12}|^2 g(x_{12})\delta(\varepsilon_1 - \varepsilon_\mathrm{F})}{\sum_{1,2} |\dot{\ell}^x_{12}|^2 x_{12}^2 g(x_{12})\delta(\varepsilon_1 - \varepsilon_\mathrm{F})} \tag{A.4}$$

in the semiclassical approximation. Summation over the state 1 is to be understood as integration with respect to its quantum numbers. For an anisotropic-oscillator potential, the amplitude can be expressed in the simple analytic form

$$D_1 = \frac{g(\nu_1) + g(\nu_2)}{\nu_1^2 g(\nu_1) + \nu_2^2 g(\nu_2)}. \tag{A.5}$$

The function $g(x)$ and the parameters ν_1 and ν_2 are determined by Eqs. (3.16) and (4.2), respectively.

Upon introducing $\dot{\ell}_x$, the equation for $\Delta^{(2)}(\mathbf{r})$ becomes

$$\sum_{1,2,3} \left[2\hbar^2\omega^2\dot{\ell}^x_{12}\dot{\ell}^x_{23} \int\limits_{C'} \frac{dp}{2\pi}\right. \tag{A.6}$$
$$\times \frac{\mathcal{Q}_3(p; p_1, p_2, p_3)}{(\mathbf{p}_1^2 + \Delta^2)(\mathbf{p}_2^2 + \Delta^2)(\mathbf{p}_3^2 + \Delta^2)} - \Delta^{(2)}_{12}\delta_{23}$$
$$\left.\times \int\limits_{C'} \frac{dp}{2\pi} \frac{(p_1 - p_2)^2 + 4\Delta^2}{(\mathbf{p}_1^2 + \Delta^2)(\mathbf{p}_2^2 + \Delta^2)}\right] \varphi_1(\mathbf{r})\varphi_2^*(\mathbf{r}') = 0,$$

where the polynomial function $\mathcal{Q}_3$ of third degree in (p, p_ν) also depends on the amplitude D_1. We try to solve this equation by making the substitution

$$\Delta^{(2)}(\mathbf{r}) = \frac{\hbar^2\omega^2}{4\Delta^3}D_2\dot{\ell}_x^2. \tag{A.7}$$

Applying the same procedure as before, one can find the amplitude D_2 in the semiclassical approximation; that is,

$$D_2 \tag{A.8}$$
$$= \frac{\sum_{1,2,3} \dot{\ell}^x_{12}\dot{\ell}^x_{23}(\dot{\ell}^2_x)_{31}\phi(x_{12}, x_{13}, x_{23})\delta(\varepsilon_1 - \varepsilon_\mathrm{F})}{\sum_{1,2} |(\dot{\ell}^2_x)_{12}|^2 h(x_{12})\delta(\varepsilon_1 - \varepsilon_\mathrm{F})},$$

where the function $h(x)$ is determined by (3.16) and ϕ has the form

$$\phi(x, y, z) = \frac{1}{2x^2y^2z^2} \tag{A.9}$$
$$\times [-xy(1 - D_1x^2)(1 + xy - D_1z^2)g(x)$$
$$+ y^2(1 - D_1x^2 - D_1z^2)h(y)$$
$$- yz(1 - D_1z^2)(1 + yz - D_1x^2)g(z)].$$

Their symmetry properties are

$$\phi(z, y, x) = \phi(x, y, z), \tag{A.10}$$
$$\phi(-x, -y, -z) = \phi(x, y, z).$$

In the oscillator potential, the sum over states 2 and 3 in the numerator of (A.8) comprises 16 terms, including four with two close transitions, four with two distant transitions, and eight terms with one close and one distant transitions. Performing summation in the semiclassical approximation in the numerator and in the denominator of (A.8), we find

$$D_2 = [4\phi(\nu_1, \nu_1 - \nu_2, -\nu_2) \tag{A.11}$$
$$+ 4\phi(\nu_1, \nu_1 + \nu_2, \nu_2) + \phi(\nu_1, 2\nu_1, \nu_1)$$
$$+ \phi(\nu_2, 2\nu_2, \nu_2) + 4\phi(\nu_1, 0, -\nu_1)$$
$$+ 4\phi(\nu_2, 0, -\nu_2)]\mathcal{H}^{-1}(\nu_1, \nu_2),$$

where

$$\mathcal{H}(\nu_1, \nu_2) = 8 + 4h(\nu_1 - \nu_2) \tag{A.12}$$
$$+ 4h(\nu_1 + \nu_2) + h(2\nu_1) + h(2\nu_2).$$

For the monopole pairing interaction, the pairing field is uniform and the first correction $\Delta^{(1)}$ vanishes. The coordinate-independent solution for the correction $\Delta^{(2)}$ can be found from Eq. (A.6) after averaging over $\mathbf{r}$. The resulting expression may be written in terms of the kinematical moment of inertia,

$$\Delta^{(2)} = \frac{\omega^2}{2\rho_\mathrm{F}}\frac{\partial\mathfrak{J}^{(1)}}{\partial\Delta}, \tag{A.13}$$

$$\mathfrak{I}^{(1)} = \sum_{1,2} |\ell_{12}^x|^2[1-g(x_{12})]\delta(\varepsilon_1-\varepsilon_{\mathrm{F}}),$$

in agreement with the result obtained by Marshalek [13]. From the theoretical viewpoint, this solution is not correct because it violates current conservation.

APPENDIX B

Calculation of Integrals

In this appendix, we give a brief outline of the technique used in calculating the integrals that are necessary for obtaining the function F (3.12) and for solving the integral equations (A.1) and (A.6). All the relevant integrals can be evaluated exactly by the method proposed by Feynman in QED [28]. The method is based on the identity

$$\frac{1}{a_1a_2\ldots a_n} = (n-1)!\int\limits_0^1 dt_1\int\limits_0^{t_1} dt_2\ldots \tag{A.14}$$

$$\int\limits_0^{t_{n-2}} \frac{dt_{n-1}}{[a_1t_{n-1}+a_2(t_{n-2}-t_{n-1})+\ldots+a_n(1-t_1)]^n},$$

which is proved by a direct calculation.

The simplest integral is that which is involved in the sum in (3.10). It is evaluated by using (A.14) as

$$J_1 = \int \frac{d\mathbf{p}_1}{2\pi}\frac{1}{(\mathbf{p}_1^2+\Delta^2)(\mathbf{p}_2^2+\Delta^2)} \tag{A.15}$$

$$= \int\limits_0^1 dt\int\frac{d\mathbf{p}_1}{2\pi}\frac{1}{[\mathbf{p}_1^2+p_{12}^2Q(t)]^2}$$

$$= \frac{1}{2p_{12}^2}\int\limits_0^1\frac{dt}{Q(t)} = \frac{1}{2\Delta^2}g\left(\frac{p_{12}}{2\Delta}\right),$$

where

$$Q(t) = -t^2+t+\delta^2, \quad \delta = \Delta/p_{12}, \quad p_{12} = p_1-p_2.$$

Four integrals appear in the first sum of Eq. (A.6). All those are of the same type. As an example, we consider the term proportional to the square of the amplitude D_1. The relevant integral is

$$J_2 = \Delta\int\frac{d\mathbf{p}_1}{2\pi} \tag{A.16}$$

$$\times\frac{\mathcal{Q}_2(p;p_1,p_2,p_3)}{(\mathbf{p}_1^2+\Delta^2)(\mathbf{p}_2^2+\Delta^2)(\mathbf{p}_3^2+\Delta^2)}$$

$$= \Delta\int\limits_0^1 dt_1\int\limits_0^{t_1} dt_2\int\frac{d\mathbf{p}_1}{2\pi}$$

$$\times\frac{\mathcal{Q}_2(p;p_1+(t_1-t_2)p_{12}+(1-t_1)p_{13})}{[\mathbf{p}_1^2+p_{13}^2Q(t_1,t_2)]^3},$$

where $\mathcal{Q}_2 = p^2+p_1p_2-p_1p_3+p_2p_3+\Delta^2$,

$$Q(t_1,t_2) = -[(1-c^2)t_1+c^2t_2-1]^2$$
$$-(1-c^2)t_1-c^2t_2+1+\delta^2,$$

and $c = p_{12}/p_{13}$. By making the substitutions $u_1 = (1-c)t_1+ct_2$ and $u_2 = t_2$, we find after integration with respect to $\mathbf{p}_1$ that

$$J_2 = \frac{\Delta}{2p_{13}p_{23}} \tag{A.17}$$

$$\times\left\{\int\limits_0^{1-c} du_1\int\limits_0^{u_1} du_2 + \int\limits_{1-c}^{1} du_1\int\limits_{(u_1-1+c)/c}^{u_1} du_2\right\}$$

$$\times\frac{(1-c)u_1-cu_2-1+c-2\delta^2}{[cu_2+Q_1(u_1)]^2},$$

where $Q_1(u_1) = -u_1^2+(1-c)u_1+\delta^2$. A straightforward calculation of these integrals gives

$$J_2 = \frac{1}{2\Delta x_{13}}[x_{12}g(x_{12})+x_{23}g(x_{23})]. \tag{A.18}$$

Finally, let us consider the integral in (3.9). It is evaluated in the same manner as the preceding ones. Upon using the identity in (A.14) and performing integration with respect to $\mathbf{p}_1$, the substitutions $t_1 = [u_1-(d-c)u_2-cu_3]/(1-d)$, $t_2 = u_2$, and $t_3 = u_3$, where $c = p_{12}/p_{14}$ and $d = p_{13}/p_{14}$, leads to four triple integrals that can be taken without a problem.

REFERENCES

1. I. I. Gurevich, Zh. Éksp. Teor. Fiz. **9**, 1283 (1939).
2. B. R. Mottelson and J. G. Valatin, Phys. Rev. Lett. **5**, 511 (1960).
3. Y. R. Shimizu *et al.*, Rev. Mod. Phys. **61**, 131 (1989).
4. J. D. Garrett, G. B. Hagemann, and B. Herskind, Annu. Rev. Nucl. Part. Sci. **36**, 419 (1986).
5. J. R. B. Oliveira *et al.*, Phys. Rev. C **47**, R926 (1993).
6. I. M. Pavlichenkov, Phys. Rep. **226**, 175 (1993).
7. I. M. Pavlichenkov, Zh. Éksp. Teor. Fiz. **96**, 404 (1989) [Sov. Phys. JETP **69**, 227 (1989)].
8. B. Singh, R. B. Firestone, and S. Y. Frank Chy, Nucl. Data Sheets **78**, 1 (1996).
9. A. Bohr and B. R. Mottelson, *Nuclear Structure*, Vol. 2: *Nuclear Deformations* (Benjamin, New York, 1975).
10. I. N. Mihailov, K. Neergård, V. V. Pashkevich, and S. Frauendorf, Fiz. Élem. Chastits At. Yadra **8**, 1338 (1977) [Sov. J. Part. Nucl. **8**, 550 (1977)].
11. Yu. T. Grin' and I. M. Pavlichenkov, Zh. Éksp. Teor. Fiz. **43**, 465 (1962) [Sov. Phys. JETP **16**, 333 (1963)].
12. I. M. Pavlichenkov, Nucl. Phys. **55**, 225 (1964).
13. E. R. Marshalek, Phys. Rev. **158**, 993 (1967).

14. I. Dabrowski, Can. J. Phys. **62**, 1639 (1984).
15. W. Satuła and R. Wyss, Phys. Rev. C **50**, 2888 (1994).
16. J. Dobaczewski and J. Dudek, Phys. Rev. C **52**, 1827 (1995).
17. P.-H. Heenen *et al.*, Nucl. Phys. A **598**, 169 (1996).
18. Y. Sun *et al.*, Phys. Rev. Lett. **78**, 2321 (1997).
19. Y. R. Shimizu, Nucl. Phys. A **520**, 477c (1990).
20. I. Hamamoto and W. Nazarewicz, Phys. Rev. C **49**, 2489 (1994).
21. A. B. Migdal, Nucl. Phys. **13**, 655 (1959).
22. I. M. Pavlichenkov, Pis'ma Zh. Éksp. Teor. Fiz. **71**, 8 (2000) [JETP Lett. **71**, 4 (2000)].
23. I. M. Pavlichenkov, Yad. Fiz. **64**, 1168 (2001) [Phys. At. Nucl. **64**, 1095 (2001)].
24. L. P. Gor'kov, Zh. Éksp. Teor. Fiz. **36**, 1918 (1959) [Sov. Phys. JETP **9**, 1364 (1959)].
25. S. T. Belyaev, Yad. Fiz. **4**, 936 (1966) [Sov. J. Nucl. Phys. **4**, 671 (1966)].
26. A. A. Abrikosov, L. P. Gor'kov, and I. E. Dzyaloshinski, *Methods of Quantum Field Theory in Statistical Physics* (Fizmatgiz, Moscow, 1962; Prentice-Hall, Englewood Cliffs, 1963).
27. K. Mühlhans, M. Diebel, K. Neergård, and U. Mosel, Phys. Lett. B **120B**, 44 (1983).
28. R. P. Feynman, Phys. Rev. **76**, 769 (1949).
29. H. Sakamoto and T. Kishimoto, Nucl. Phys. A **501**, 205 (1989).
30. P. Ring and P. Schuck, *The Nuclear Many-Body Problem* (Springer-Verlag, New York, 1980).
31. W. Nazarewicz, R. Wyss, and A. Johnson, Nucl. Phys. A **503**, 285 (1989).
32. N. El Aouad *et al.*, Nucl. Phys. A **676**, 155 (2000).
33. A. V. Afanasjev, G. A. Lalazissis, and P. Ring, Nucl. Phys. A **634**, 393 (1998).
34. K. Lagergren *et al.*, Phys. Rev. Lett. **87**, 022502 (2001).
35. G. Hackman *et al.*, Phys. Rev. Lett. **79**, 4100 (1997).
36. K. Hauschild *et al.*, Phys. Rev. C **55**, 2819 (1997).
37. H. G. Price *et al.*, Phys. Rev. Lett. **51**, 1842 (1983).
38. H.-Q. Jin *et al.*, Phys. Rev. Lett. **75**, 1471 (1995).

Physics of Atomic Nuclei, Vol. 65, No. 7, 2002, pp. 1219–1221. From Yadernaya Fizika, Vol. 65, No. 7, 2002, pp. 1251–1254.

90th ANNIVERSARY OF I.I. GUREVICH'S BIRTHDAY

Neutrino-Induced Deuteron Disintegration in an Experiment at the Krasnoyarsk Nuclear Reactor*

**Yu. V. Kozlov , S. V. Khaltourtsev, I. N. Machulin , A. V. Martemyanov,
V. P. Martemyanov , A. A. Sabelnikov, V. G. Tarasenkov , E. V. Turbin, and V. N. Vyrodov****

Russian Research Centre Kurchatov Institute, pl. Kurchatova 1, Moscow, 123182 Russia

Received November 15, 2001

Abstract—The results of studying antineutrino interactions with deuterons (CCD and NCD reactions) and hydrogen (CCP) at the Krasnoyarsk underground reactor with the Deuteron detector are presented. The cross sections for NCD and CCD were measured with a precision of 9%. For CCP, the precision is 3%: $\sigma^{\rm NCD}_{\rm expt} = (3.35 \pm 0.31) \times 10^{-44}$ cm^2/fission ^{235}U, $\sigma^{\rm CCD}_{\rm expt} = (1.08 \pm 0.09) \times 10^{-44}$ cm^2/fission ^{235}U, and $\sigma^{\rm CCP}_{\rm expt} = (6.39 \pm 0.19) \times 10^{-43}$ cm^2/fission ^{235}U. The precision of the experimental results is close to the theoretical one and is in good agreement with other experiments. The limit on the parameters of antineutrino oscillations into the sterile state was obtained: $\Delta m^2 \le 4.7 \times 10^{-2}$ eV^2 for $\sin^2(2\theta) = 1.0$ (68% C.L.). A comparison of the measured and theoretical cross section gives us the neutron–neutron scattering length of $a_{nn}(S) = -17 \pm 6$ fm in the approach of zero momentum transfers. The weak neutral current constant is in good agreement with the prediction of the Standard Model: $G^{\rm NC}_A = G^{\rm CC}_A/0.932 \pm 0.056$. © *2002 MAIK "Nauka/Interperiodica"*.

INTRODUCTION

This article presents the results of experiments carried out at the neutrino underground laboratory of the Krasnoyarsk nuclear plant.

The interaction of antineutrinos ($\bar{\nu}_e$) with a deuteron occurs via two channels, neutral current on a deuteron (NCD) and charged current on a deuteron (CCD):

$$\bar{\nu}_e + d \to p + n + \bar{\nu}'_e \text{ (NCD)}, \quad (1)$$

$$\bar{\nu}_e + d \to n + n + e^+ \text{ (CCD)}. \quad (2)$$

These reactions were investigated in the experiments reported in [1–4] and studied theoretically by Gaponov [5].

The study of these reactions can give information about (a) weak constants for charged and neutral currents, (b) the neutron–neutron scattering length, and (c) neutrino oscillations.

DETECTOR DESIGN

The modernized detector Deuteron (for details, see [6]) is situated at an underground laboratory at a distance of 34.0 m from the reactor; the neutrino flux is about a few units of 10^{12} $\bar{\nu}$/cm^2.

The target volume is 513 l of $D_2O(H_2O)$ placed in a stainless tank, which is surrounded by 30 cm of Teflon for neutron reflection, 0.1 cm of Cd, 8 cm of steel shots, 20 cm of graphite, and 16 cm of boron polyethylene ($CH_2 + 3\%B$) for gamma and neutron shielding. The whole installation is pierced to make 169 holes (81 holes pass through the tank and Teflon; the others pass through Teflon only). These holes house 169 proportional ^{3}He neutron counters with a reduced intrinsic alpha background. These counters are used to detect neutrons. They are located in a square lattice with a side of 10 cm. The active shielding covering the main assembly is against cosmic muons.

The efficiency of the detector was calculated by using Monte Carlo (MC) method both for the inverse beta-decay reaction and for the antineutrino–deuteron reaction. The calculations were also performed for a ^{252}Cf source, and this result was checked experimentally. The difference (less than 1%) between the results of the calculation and experimental data shows a good reliability of MC calculations. To make the MC calculation more confident, a special calibration procedure was employed. Using a ^{238}Pu–Li neutron source, which has a neutron spectrum that is very close to the one from CCD and NCD reactions, we measured the spatial distribution inside the tank. From this distribution and from the measured efficiency at the center of the detector, one

---

[*] This article was submitted by the authors in English.

[**] e-mail: `vyrodov@dnuc.polyn.kiae.su`

Table 1

Parameters	Target	
	H_2O	D_2O
Efficiency of one-neutron detection by tank counters only, %	27.5 ± 0.3	56.2 ± 0.1
Efficiency of double-neutron detection by all counters, %	9.9 ± 0.1	41.7 ± 0.1
Neutron lifetime, μs	138 ± 2	203 ± 2

Table 2

	$\sigma \times 10^{44}$, cm^2/fission	
	NCD	CCD
Experiment for the actual mixture of the ^{235}U, ^{249}Pu, ^{238}U fuel	3.38 ± 0.31	1.09 ± 0.09
Experiment corrected for ^{235}U	3.35 ± 0.31	1.08 ± 0.09
Theory for the actual mixture of the ^{235}U, ^{249}Pu, ^{238}U* fuel	3.20 ± 0.16	1.09 ± 0.06
Theory for ^{235}U*	3.17 ± 0.16	1.08 ± 0.06
Theory for ^{235}U**	3.16 ± 0.16	1.12 ± 0.06
Ratio (expt./theory)*	1.06 ± 0.11	1.0 ± 0.10

* Schreckenbach [7] antineutrino spectrum, Kubodera antineutrino–deuteron cross section [8].

** These are theoretical values of the cross sections from the article of Gaponov and Vladimirov [5] for the Schreckenbach [7] reactor antineutrino spectrum.

can obtain the experimental efficiency for NCD and CCD reactions. The neutron efficiency, the neutron lifetime, and the measured efficiency for D_2O and H_2O targets are shown in Table 1. Special attention was given to the correlated background for the NCD channel from the antineutrino interaction with a proton (H_2 atoms), because the cross section for this process is relatively large. The construction of the detector allowed us to decrease the efficiency of neutron detection from a boron polyethylene up to 0.003% (0.25 event/d). We estimate the correlated background ($N_{\rm cor}$) at 0.69 event/d due to the concentration of H_2O (0.15%) in heavy water.

H_2O TARGET

The reaction of inverse beta decay on a proton,

$$\bar{\nu}_e + p \to n + e^+ \text{ (CCP)}, \qquad (3)$$

is used to check and improve some parameters of the detector. In this case, the detector was filled with water (H_2O). The exposure time is 115×10^5 s or about 133 d. Four sets of measurement under different background condition were made. As a result, the CCP cross section was found to be

$$\sigma^{\rm CCP}_{\rm expt} = (6.39 \pm 0.19) \times 10^{-43} \text{ cm}^2/\text{fission } ^{235}\text{U}.$$

This result is in good agreement with the theoretical cross section of $V-A$ theory. The ratio is (68% C.L.)

$$R = \frac{\sigma^{\rm CCP}_{\rm expt}}{\sigma_{V-A}(^{235}\text{U})} = 1.00 \pm 0.04.$$

Table 3

$a_{nn}(S)$, fm	$\langle\sigma^{\rm CCD}\rangle \times 10^{44}$, cm^2/fission
-16.6	1.077
-17.0	1.084
-18.5	1.112
$-23.7 (= a_{np})$	1.179

D_2O TARGET

From the beginning of 1997 to February 2001, experimental data were collected for 718.4 days during the reactor operating period and for 208 days during the reactor shutdown period. Fourteen sets of measurements were performed. Different sets mean different experimental conditions (some improvement of the VETO system, increasing passive shielding, or changing some counters). Taking into account both the "wall" effect and time rejection for double-neutron events and for amplitude selection, we have the following neutron-detection efficiencies:

$$\varepsilon_2^{\rm CCD} = 0.354 \pm 0.003,$$
$$\varepsilon_1^{\rm NCD} = 0.514 \pm 0.005.$$

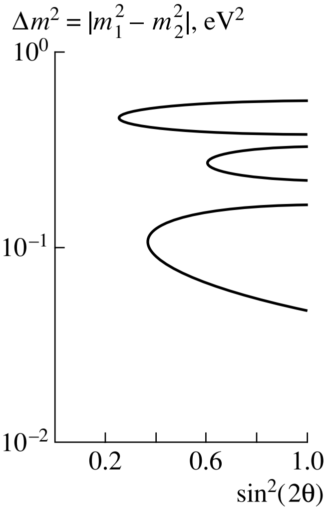

Limit on the neutrino oscillation parameters.

As a result, the experimental counting rate was (event per 10^5 s)

$$\mathrm{N}^{\mathrm{NCD}} = 20.0 \pm 1.8, \qquad (4)$$

$$\mathrm{N}^{\mathrm{CCD}} = 4.45 \pm 0.36. \qquad (5)$$

Using information about the thermal reactor power, the efficiency of the detector, and the distance between detector and the reactor, one can obtain the cross section for both reactions:

$$\sigma_{\mathrm{expt}}^{\mathrm{NCD}} = (3.35 \pm 0.31) \times 10^{-44}\ \mathrm{cm}^2/\text{fission } {}^{235}\mathrm{U},$$

$$\sigma_{\mathrm{expt}}^{\mathrm{CCD}} = (1.08 \pm 0.09) \times 10^{-44}\ \mathrm{cm}^2/\text{fission } {}^{235}\mathrm{U}.$$

These results are in good agreement with the theory (Table 2).

nn SCATTERING LENGTH

The theoretical calculations of the CCD cross section for various values of the neutron–neutron scattering length (in the approach of zero momentum transfers) are presented in Table 3. A comparison of the measured and predicted values gives $a_{nn}(S) = -17 \pm 6$ fm, which is one standard deviation greater than $a_{np}(S)$.

NEUTRAL WEAK CONSTANT

From the experimental ratio $(\sigma_{\mathrm{expt}}^{\mathrm{CCD}}/\sigma_{\mathrm{expt}}^{\mathrm{NCD}})$, which is proportional to

$$(G_A^{\mathrm{NC}}/G_A^{\mathrm{CC}})^2 = (\cos\Theta_C)^{-2},$$

it is easy to obtain the experimental value of G_A^{NC}. The weak-neutral-current constant is in good agreement with the prediction of the Standard Model:

$$G_A^{\mathrm{NC}} = G_A^{\mathrm{CC}}/0.932 \pm 0.056.$$

NEUTRINO OSCILLATIONS

The experimental data for NCD and CCD give the unique possibility of obtaining a limit on the parameters Δm^2 and $\sin^2(2\theta)$ of neutrino oscillations into the sterile state by using the ratio-of-ratios construction

$$R = \frac{\sigma_{\mathrm{expt}}^{\mathrm{CCD}}/\sigma_{\mathrm{expt}}^{\mathrm{NCD}}}{\sigma_{\mathrm{theor}}^{\mathrm{CCD}}/\sigma_{\mathrm{theor}}^{\mathrm{NCD}}} = 0.95 \pm 0.11.$$

This is possible because the thresholds of the CCD and NCD reactions are different (4.0 and 2.2 MeV, respectively), and the NCD reaction is more sensitive to oscillations of a neutrino with a lower energy, because it has a lower threshold of the reaction. The limit on the parameters of reactor-antineutrino oscillations into the sterile state is presented in the figure. The values of the parameters Δm^2 and $\sin^2(2\theta)$ to the right of the curves are excluded. For the maximum mixing angle of the neutrinos states,

$$\sin^2(2\theta) = 1,$$

the following limit was obtained:

$$\Delta m^2 \le 4.7 \times 10^{-2}\ \mathrm{eV}^2\ (68\%\ \mathrm{C.L.}).$$

ACKNOWLEDGMENTS

We would like to thank the staff of the Krasnoyarsk reactor for permanent help, S.T. Belayev and Yu.V. Gaponov for stimulating discussions, and the theory group headed by E.A. Gomin for the adaptation of the MC program to neutrino purposes.

This work was supported by the Russian Foundation for Basic Research (project nos. 99-15-96640, 98-02-16313, and 00-15-96708).

REFERENCES

1. E. Pasierb *et al.*, Phys. Rev. Lett. **43**, 96 (1979).
2. Yu. V. Kozlov *et al.*, Pis'ma Zh. Éksp. Teor. Fiz. **51**, 216 (1990) [JETP Lett. **51**, 245 (1990)].
3. Yu. Vershinsky *et al.*, Pis'ma Zh. Éksp. Teor. Fiz. **53**, 466 (1991) [JETP Lett. **53**, 489 (1991)].
4. S. P. Riley *et al.*, Phys. Rev. C **59**, 3 (1999).
5. Yu. V. Gaponov *et al.*, Yad. Fiz. **49**, 902 (1989) [Sov. J. Nucl. Phys. **49**, 560 (1989)].
6. V. N. Vyrodov *et al.*, Yad. Fiz. **61**, 844 (1998) [Phys. At. Nucl. **61**, 760 (1998)].
7. K. Schreckenbach *et al.*, Phys. Lett. B **160B**, 325 (1985); **218**, 365 (1989).
8. K. Kubodera *et al.*, Int. J. Mod. Phys. E **3**, 101 (1994).

Physics of Atomic Nuclei, Vol. 65, No. 7, 2002, pp. 1222–1227. Translated from Yadernaya Fizika, Vol. 65, No. 7, 2002, pp. 1255–1260.
Original Russian Text Copyright © 2002 by Anashkin, Aulchenko, Akhmetshin, Banzarov, Barkov, Baru, Bashtovoy, Bondarev, Bondar, Bragin, Gabyshev, Gorbachev, Grebeniuk, Grigoriev, Dhawan, Zverev, Ignatov, Kazanin, Karpov, Koop, Krokovny, Kuzmin, Kurdadze, Logashenko, Lukin, Lysenko, Mikhailov, Nesterenko, Okhapkin, Polunin, Popov, Roberts, Root, Ruban, Ryskulov, Sibidanov, Sidorov, Skrinsky, Smakhtin, Snopkov, Solodov, Stepanov, Sukhanov, Thompson, Fedotovich, Khazin, Hughes, Chernyak, Shamov, Shatunov, Shwartz, Eidelman, Yudin.

90th ANNIVERSARY OF I.I. GUREVICH'S BIRTHDAY

Measurement of the Cross Section for the Process $e^+e^- \to K^0_L K^0_S$ in the Energy Range $2E = 1.05$–1.38 GeV with the CMD-2 Detector at VEPP-2M

E. V. Anashkin[1], V. M. Aulchenko[1),2)], R. R. Akhmetshin[1], V. Sh. Banzarov[1], L. M. Barkov[1),2)], S. E. Baru[1], N. S. Bashtovoy[1], D. V. Bondarev[1], A. E. Bondar[1),2)], A. V. Bragin[1], N. I. Gabyshev[1], D. A. Gorbachev[1),2)], A. A. Grebeniuk[1], D. N. Grigoriev[1),2)], S. K. Dhawan[3], S. G. Zverev[1], F. V. Ignatov[1),2)], V. F. Kazanin[1], S. V. Karpov[1], I. A. Koop[1),2)], P. P. Krokovny[1),2)], A. S. Kuzmin[1),2)], L. M. Kurdadze[1], I. B. Logashenko[1], P. A. Lukin[1)*], A. P. Lysenko[1], K. Yu. Mikhailov[1], I. N. Nesterenko[1], V. S. Okhapkin[1], A. A. Polunin[1], A. S. Popov[1], B. L. Roberts[4], N. I. Root[1], A. A. Ruban[1], N. M. Ryskulov[1], A. L. Sibidanov[1], V. A. Sidorov[1], A. N. Skrinsky[1], V. P. Smakhtin[1], I. G. Snopkov[1], E. P. Solodov[1),2)], P. Yu. Stepanov[1], A. I. Sukhanov[1], J. A. Thompson[5], G. V. Fedotovich[1),2)], B. I. Khazin[1),2)], W. V. Hughes[3], D. V. Chernyak[1], A. G. Shamov[1], Yu. M. Shatunov[1], B. A. Shwartz[1),2)], S. I. Eidelman[1),2)], and Yu. V. Yudin[1]

Received February 4, 2002

Abstract—The cross section for the process $e^+e^- \to K^0_L K^0_S$ is measured by using approximately 1000 events recorded by the CMD-2 detector at the VEPP-2M collider in the energy range from 1.05 to 1.38 GeV. © *2002 MAIK "Nauka/Interperiodica"*.

Dedicated to Isai Isidorovich Gurevich—
Teacher and marvelous man

1. INTRODUCTION

Investigation of the process $e^+e^- \to K^0_L K^0_S$ provides important information about the internal structure of kaons. Moreover, measurement of the $e^+e^- \to K^0_L K^0_S$ cross section in the energy region above the ϕ meson makes it possible to study the excited states of the $\rho(770)$, $\omega(782)$, and $\phi(1020)$ mesons [1]. Finally, the cross section for the process $e^+e^- \to K^0_L K^0_S$ is used in calculating the contribution of vacuum polarization by hadrons to the muon anomalous magnetic moment $(g-2)_\mu$ [2].

The $e^+e^- \to K^0_L K^0_S$ cross section in the region above the ϕ meson was measured in [1, 3, 4] with a poor statistical accuracy, the systematic error in those experiments being as large as a value of about 20%. Considerable advances in this realm were made in the experiment of M. Achasov *et al.* [5], who employed the SND detector [6] at the VEPP-2M collider [7]. That study was based on the integrated luminosity of 6.3 pb^{-1}; the systematic error in the measured cross section was 10% in the energy region around $2E \approx$ 1040 MeV and 15% in the region of $E_{\mathrm{c.m.}}$ around 1380 MeV.

Here, we present the results obtained by investigating the process $e^+e^- \to K^0_L K^0_S$ in the energy range 1050–1380 MeV with the CMD-2 detector [8] at the VEPP-2 collider. This investigation was based on the integrated luminosity of 5.8 pb^{-1}; the systematic error in the measured cross section was 5% in the energy range 1050–1090 MeV and 10% at energies around 1380 MeV.

2. KMD-2 DETECTOR

The CMD-2 detector is described in detail in [8]. Figure 1 shows schematically the longitudinal and the transverse section of the detector.

---

[1] Budker Institute of Nuclear Physics, Siberian Division, Russian Academy of Sciences, pr. Akademika Lavrent'eva 11, Novosibirsk, 630090 Russia.

[2] Novosibirsk State University, ul. Pirogova 2, Novosibirsk, 630090 Russia.

[3] Yale University, 219 Prospect St., 554 JWG, Box 6666 New Haven, CT 06511 USA.

[4] Boston University, 590 Commonwealth Ave., Boston, MA 02215, USA.

[5] University of Pittsburgh, 3941 O'Hara St., Pittsburgh, PA 15260, USA.

[*] e-mail: `p.a.lukin@inp.nsk.su`

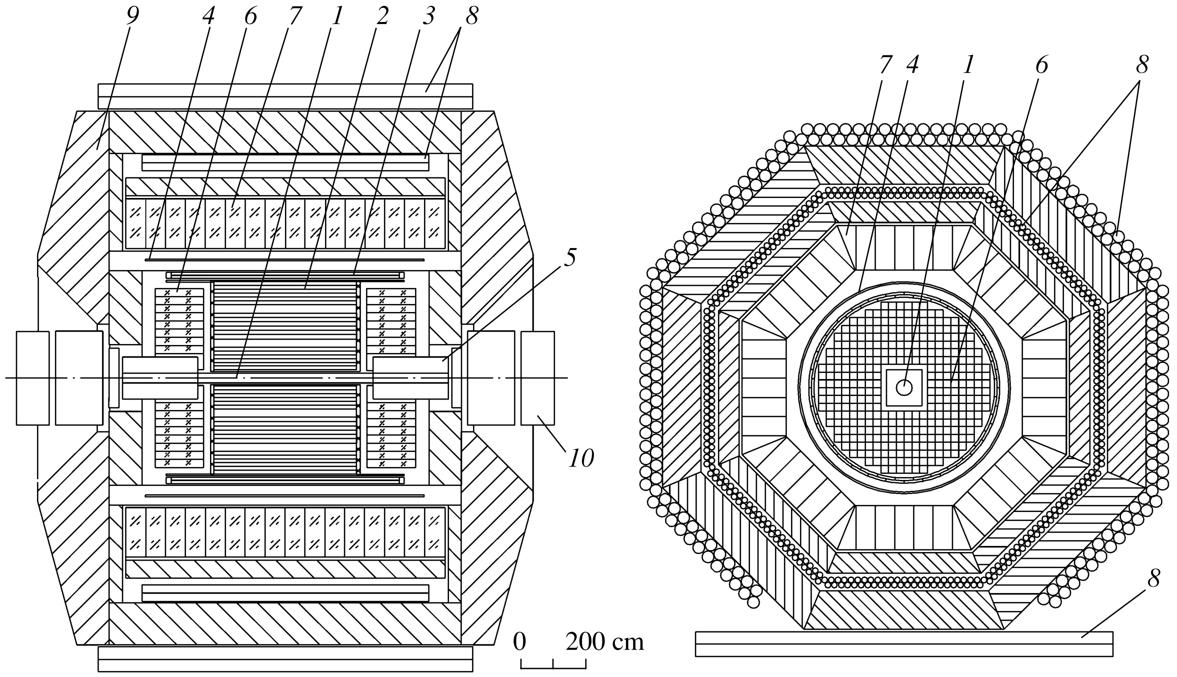

Fig. 1. Longitudinal and transverse sections of the CMD-2 detector: (*1*) vacuum chamber, (*2*) drift chamber, (*3*) Z chamber, (*4*) main superconducting solenoid, (*5*) compensating solenoid, (*6*) endface calorimeter based on BGO, (*7*) cylindrical calorimeter based on CsI, (*8*) flight system, (*9*) magnet yoke, and (*10*) quadrupole lenses.

The tracking system of the detector consists of a cylindrical drift chamber (*2*) [9, 10] surrounding the point of beam crossing. A proportional Z chamber (*3*) [11, 12] positioned behind the drift chamber is used to measure precisely the polar angles of particle tracks; it is also used in the trigger. Both chambers are placed within a thin ($0.38X_0$) superconducting solenoid (*4*) [13] generating a field of strength 1 T. A cylindrical electromagnetic calorimeter (*7*) [14] based on CsI crystals and a muon flight system (*8*) [15] are arranged behind the solenoid outside the magnetic field. An endface electromagnetic calorimeter (*6*) [16] based on BGO crystals, which is also placed within the solenoid, renders the detector virtually impenetrable to photons emitted from the beam-crossing point.

3. DATA ANALYSIS

The detector records the process $e^+e^- \to K_L^0K_S^0$ by the decay of a short-lived kaon into a pair of charged pions.

We selected candidate events according to the following criteria:

(i) An event contains two tracks issuing from the vertex closest to the beam that are associated with particles of opposite electric charges. The particle momenta in an event satisfy the condition $p_{\min}(E_{\text{beam}}) - 20.0\ \text{MeV}/c < p_{1,2} < p_{\max}(E_{\text{beam}}) + 20.0\ \text{MeV}/c$, where $p_{\min}$ and $p_{\max}$ are, respectively, the minimum and the maximum kinematically possible momenta of pions in the decay $K_S^0 \to \pi^+\pi^-$ at the beam energy E_{beam}.

(ii) The maximum ionization loss of particles in the drift chamber satisfies the condition $\max(dE/dx_1, dE/dx_2) < 2.2(dE/dx)_{\text{MIP}}$, where $(dE/dx)_{\text{MIP}}$ stands for the ionization loss of minimally ionizing particles. In this way, we suppress events of the process $e^+e^- \to K^+K^-$ and events of the beam background. Figure 2*a* presents the $\max(dE/dx_1, dE/dx_2)$ distribution of experimental events versus the invariant mass of two tracks under the assumption that the tracks are associated with pions. The horizontal line indicates the value chosen for the selection criterion. It is clear from the figure that the condition leaves useful events, significantly suppressing the background.

(iii) The spatial angle between the tracks satisfies the condition $\psi > 0.5$, while the angle that characterizes the deflection of the tracks from collinearity in the R–φ plane is within the interval $0.2 < |\pi - |\varphi_1 - \varphi_2|| < 3.0$. In this way, we suppress events involving collinear particles.

(iv) The value of the coordinate Z of the vertex is within the range $|Z_{\text{vrtx}}| < 7.0$ cm, while the distance from the vertex to the beam axis in the R–φ plane satisfies the condition $0.07 < R_{\text{vrtx}} < 1.3$ cm. In this way, we suppress background events of nuclear

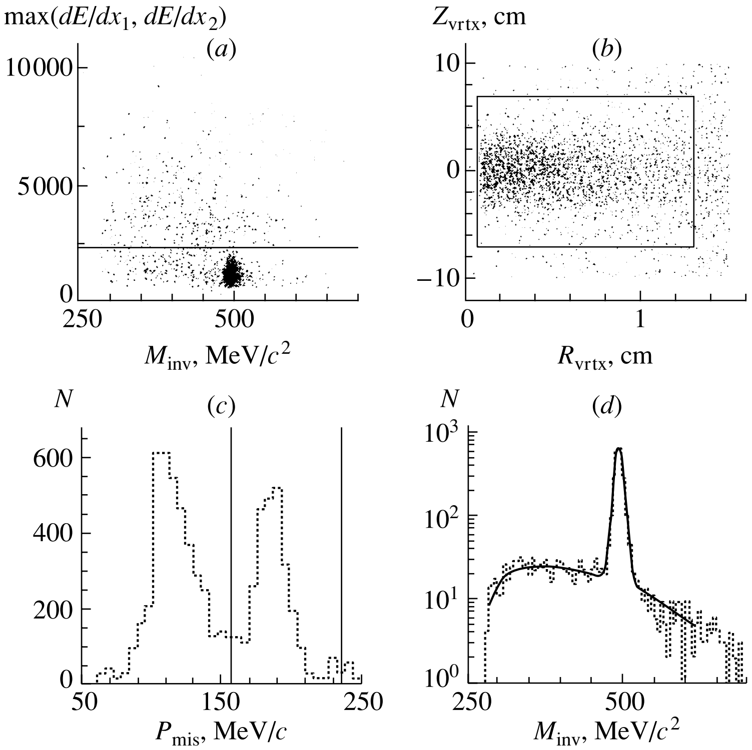

Fig. 2. Experimental distributions used to isolate $e^+e^- \to K_L^0 K_S^0$ events: (a) ionization loss of particles versus the invariant mass of two tracks, (b) z coordinate of the vertex versus the distance from the vertex to the beam axis in the R–φ plane, (c) number of events versus the missing momentum, (d) distribution of events with respect to the invariant mass of two tracks.

interaction between the particles involved and the vacuum-chamber material and events where there are tracks originating from the beam-crossing point. Figure 2b shows the Z_{vrtx} distribution of experimental events versus of the distance R_{vrtx} from the vertex to the beam axis in R–φ plane. The lines correspond to the selection criteria based on these parameters.

It is worth noting that, in the energy region above the ϕ meson, the production of a $K_L^0 K_S^0$ pair is often accompanied by the emission of a hard radiative photon ("return to the ϕ-meson resonance"). Figure 2c shows the distribution of experimental events with respect to the missing momentum defined as

$$P_{\text{mis}} = -(p_1 + p_2),$$

where p_1 and p_2 is the pion momenta from the decay of a K_S^0 meson. The left peak corresponds to events involving the emission of a high-energy photon, while the right peak corresponds to photonless events (for the beam energy of $E_{\text{beam}} = 535$ MeV). In this study, events featuring return to the resonance were eliminated from the analysis by subjecting the missing mass P_{mis} to the selection criterion

$$\sqrt{E_{\text{beam}}^2 - m_{K^0}^2} - 39.0\ \text{MeV}/c < P_{\text{mis}}$$
$$< \sqrt{E_{\text{beam}}^2 - m_{K^0}^2} + 39.0\ \text{MeV}/c$$

(shown in Fig. 2c by vertical lines), where 39.0 MeV corresponds to the experimental missing-mass resolution multiplied by a factor of 5.

The number of the events associated with the sought effect was estimated in fitting the distributions over the invariant mass of two tracks at the vertex. For the approximating function, we took the sum of two Gaussian functions having equal mean values and equal number N of events associated with the effect and a smooth function that described the background pedestal. The pedestal was due primarily to events involving particle scattering by the vacuum-chamber material. In order to determine the parameters of the function that described the distribution of background events, we combined data at a few energy points and used the values obtained in fitting these combinations to determine the number of events at each individual energy value. In the same way, we determined the widths of both Gaussian functions that described the events associated with the effect. Figure 2d presents an example of such a combination in the energy range 1050–1190 MeV.

Upon applying the above selection criteria and subtracting the background, we obtained 948 ± 33 $K_L^0 K_S^0$ events.

At each individual energy point the cross section for the production of a neutral kaon pair was evaluated by the formula

$$\sigma = \frac{N}{\varepsilon_{\text{rec}}\varepsilon_{\text{trig}}\varepsilon_{\text{geom}}L(1+\delta_{\text{rad}})}, \qquad (1)$$

where N is the number of events; ε_{rec} is the event-reconstruction efficiency; $\varepsilon_{\text{trig}}$ is the trigger efficiency; $\varepsilon_{\text{geom}}$ is the geometric efficiency; L is the integrated luminosity, which was determined from the events of large-angle e^+e^- scattering by using the procedure described in [17]; and $(1+\delta_{\text{rad}})$ is the radiative correction to the process $e^+e^- \to K_L^0K_S^0$ due to photon emission by incident particles {this correction was calculated by formulas from [18]; on average, the result was $(1+\delta_{\text{rad}}) \approx 0.92$}.

The trigger and the event-reconstruction efficiency were determined from experimental data by means of the procedure described in [19], while the geometric efficiency was deduced from a Monte Carlo simulation of relevant events. The energy-averaged event-reconstruction, trigger, and geometric efficiencies were found to be

$$\varepsilon_{\text{rec}} = 0.955 \pm 0.018,$$
$$\varepsilon_{\text{trig}} = 0.981 \pm 0.004,$$
$$\varepsilon_{\text{geom}} = 0.130 \pm 0.001.$$

The procedure described in [20] was used here to determine the beam energy at each individual point from the magnetic field in the bending magnets of the collider. The systematic error in the energy value was estimated on the basis of the results obtained in [17] from an analysis of the long-term stability of the beam energy. In this way, it was found that $\Delta E/E = 4 \times 10^{-4}$. The table presents the number of events and the cross section for the process $e^+e^- \to K_L^0K_S^0$ at each individual energy value.

In Fig. 3, closed circles represent the results of our analysis for the energy dependence of the cross section in the energy range $E_{\text{c.m.}} = 1050$–1380 MeV. The data on the cross section in the energy range 1000–1040 MeV were taken from [21]. For the sake of comparison, experimental data from [3–5] are also displayed in Fig. 3. It can be seen that the results of the present analysis are in satisfactory agreement with the results of previous measurements.

The data on the cross section that were obtained from our analysis and data from [21] were fitted on the basis of the vector-dominance model (VDM) [22] with allowance for the contributions from the $\rho(770)$, $\omega(782)$, and $\phi(1020)$ mesons. The explicit form of the approximating expression was

$$\sigma(s) = \sigma_0 \frac{q^3(s)}{q^3(m_\phi^2)} \frac{m_\phi^7 \Gamma_\phi^2}{s^{5/2}} \left| -A_\rho + \frac{1}{3}A_\omega + A_\phi \right|^2, \quad (2)$$

Number of events and cross section for the process $e^+e^- \to K_L^0K_S^0$ at each individual energy value (the first error in the cross section values is statistical, while the second one is systematic)

$\sqrt{s}$, MeV	N	σ, nb
1050.0	310.9 ± 17.8	$17.44 \pm 2.05 \pm 0.85$
1060.0	124.1 ± 11.3	$11.61 \pm 1.07 \pm 0.57$
1070.0	76.1 ± 8.9	$7.10 \pm 0.84 \pm 0.35$
1080.0	39.3 ± 6.6	$5.27 \pm 0.89 \pm 0.26$
1090.0	53.0 ± 7.5	$5.08 \pm 0.73 \pm 0.25$
1100.0	29.0 ± 5.5	$4.23 \pm 0.80 \pm 0.21$
1110.0	33.5 ± 6.1	$3.49 \pm 0.64 \pm 0.29$
1120.0	$18.2^{+4.9}_{-4.2}$	$2.75^{+0.74}_{-0.63} \pm 0.23$
1130.0	$14.7^{+4.2}_{-3.6}$	$2.20^{+0.63}_{-0.54} \pm 0.18$
1140.0	$25.5^{+5.7}_{-5.0}$	$2.74^{+0.61}_{-0.54} \pm 0.23$
1150.0	$17.8^{+4.8}_{-4.1}$	$2.71^{+0.73}_{-0.62} \pm 0.22$
1160.0	$17.2^{+4.8}_{-4.1}$	$1.54^{+0.43}_{-0.37} \pm 0.13$
1170.0	$13.9^{+4.2}_{-3.5}$	$1.96^{+0.59}_{-0.49} \pm 0.16$
1180.0	$15.1^{+4.6}_{-3.9}$	$1.39^{+0.42}_{-0.36} \pm 0.12$
1190.0	$20.9^{+5.3}_{-4.6}$	$1.68^{+0.43}_{-0.37} \pm 0.14$
1204.6	$19.7^{+5.6}_{-4.9}$	$0.84^{+0.24}_{-0.21} \pm 0.07$
1225.0	$26.9^{+6.0}_{-5.3}$	$1.11^{+0.25}_{-0.22} \pm 0.11$
1250.6	$21.3^{+5.7}_{-5.3}$	$0.56^{+0.15}_{-0.14} \pm 0.05$
1275.0	$18.7^{+5.8}_{-5.0}$	$0.54^{+0.17}_{-0.14} \pm 0.05$
1295.8	$20.2^{+6.0}_{-5.2}$	$0.48^{+0.14}_{-0.12} \pm 0.05$
1325.3	$11.2^{+6.2}_{-5.4}$	$0.18^{+0.10}_{-0.09} \pm 0.02$
1368.3	$20.7^{+6.6}_{-5.9}$	$0.25^{+0.08}_{-0.07} \pm 0.02$

where σ_0 is the cross section at the peak of the $\phi(1020)$ meson, $q(s) = (s/4 - m_{K^0}^2)^{1/2}$ is the neutral-kaon momentum, and $A_V = 1/(s - m_V^2 + i\sqrt{s}\Gamma_V(s))$ is the amplitude of the vector meson V. The energy dependence of the width of the vector meson V was taken to be identical to that in [23]. The masses and widths of all resonances were borrowed from [24].

The fitted value of the cross section at the $\phi(1020)$-meson peak [parameter in the approximating expression (2)] proved to be

$$\sigma_0(\phi \to K_L^0K_S^0) = 1376 \pm 6 \pm 23 \text{ nb}, \qquad (3)$$

which is in good agreement with the result of the analysis performed in [21]. The fitted curve is shown in Fig. 3. It can be seen that, in the energy region above 1130 MeV, the experimental points lie above the predictions of the VDM allowing for the contributions of the $\rho(770)$, $\omega(782)$, and $\phi(1020)$ mesons. The observed excess can be due to the contributions of

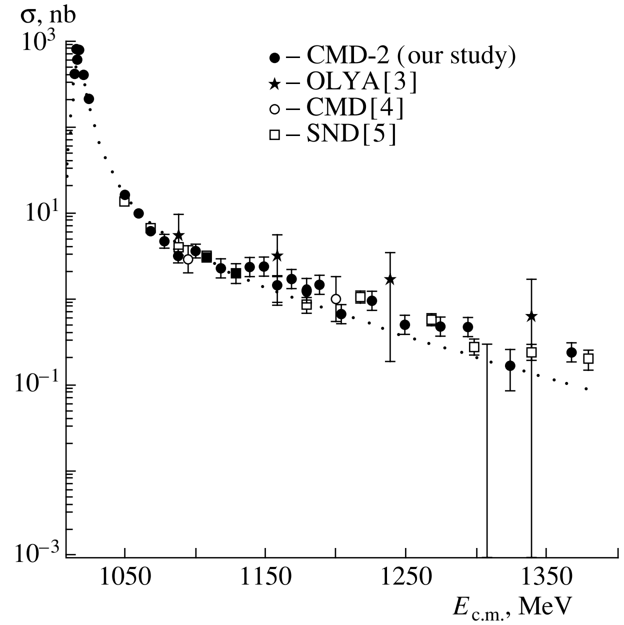

Fig. 3. Energy dependence of the cross section for the process $e^+e^- \to K_L^0K_S^0$ in the energy range $E_{\text{c.m.}} =$ 1000–1380 MeV according to data from various experiments. The approximating curve follows the prediction of the vector-dominance model with allowance for the contributions from the $\rho(770)$, $\omega(782)$, and $\phi(1020)$ mesons.

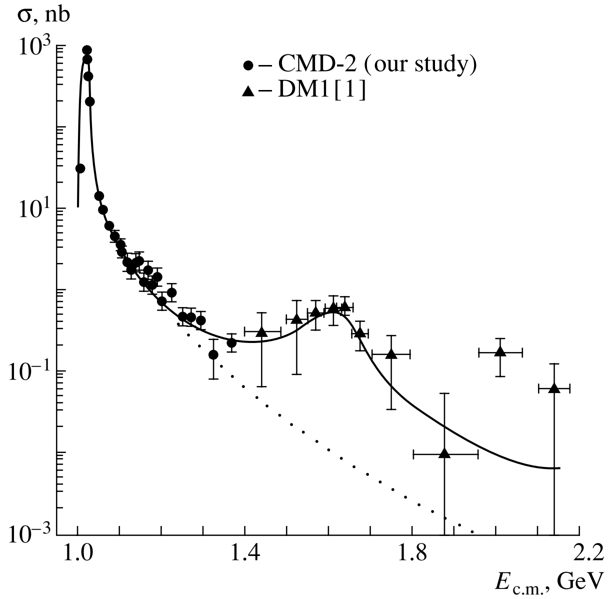

Fig. 4. Experimental data along with the predictions of the vector-dominance model allowing for the contributions (solid curve) from the $\rho(770)$, $\omega(782)$, $\phi(1020)$, and X mesons and (dotted curve) only from the $\rho(770)$, $\omega(782)$, and $\phi(1020)$ mesons.

vector mesons heavier than 1.4 GeV. This assumption is supported by the results obtained by investigating the process $e^+e^- \to K_L^0K_S^0$ in the energy interval 1.4–2.18 GeV with the DM1 detector [1], which are shown in Fig. 4 (triangles). The circles in this figure represent the cross-section values obtained in the present study. In order to describe the resonance behavior of the cross section in the energy region around $E_{\text{c.m.}} \sim 1.6$ GeV, we added the amplitude

$$A_X = \frac{\dfrac{M_X^3\Gamma_X}{m_\phi^3\Gamma_\phi}\sqrt{\dfrac{\sigma_X^0 q^3(m_\phi^2)M_X}{\sigma_0 q^3(M_X^2)m_\phi}}}{s - M_X^2 + i\sqrt{s}\Gamma_X}e^{i\delta_X}$$

to the amplitudes of the light vector mesons and fitted the parameters σ_X^0, M_X, Γ_X, and δ_X and the cross section at the peak of the ϕ meson. For the parameters of the additional resonance, this yielded the values

$$\sigma_X^0 = 0.78 \pm 0.23 \text{ nb},$$
$$M_X = 1624 \pm 18 \text{ MeV}/c^2,$$
$$\Gamma_X = 128 \pm 40 \text{ MeV},$$
$$\delta_X = (160 \pm 42)^\circ.$$

Upon taking into account the contribution from the additional resonance, the cross section at the peak of the ϕ meson changed from 1376 to 1375 nb—that is, by 0.07%, which corresponds to the estimate of the systematic error associated with the model dependence of the cross section from [21]. The solid curve in Fig. 4 represents the results of fitting. For the sake of comparison, the VDM prediction allowing only for the contributions from $\rho(770)$, $\omega(782)$, and $\phi(1020)$ is also displayed in Fig. 4 (dotted curve). It can be seen that the description of the data is improved upon adding the amplitude A_X to the contributions of the light vector mesons. As a candidate for resonances contributing to the cross section in this energy region, we can indicate, for example, $\phi(1680)$. However, a comprehensive description of process dynamics will require much more data in the energy region above 1.4 GeV and a simultaneous analysis of different channels of e^+e^- annihilation. This will become possible upon the commissioning of the VEPP-2000 collider, which is now being constructed at the Budker Institute of Nuclear Physics (Siberian Division, Russian Academy of Sciences, Novosibirsk).

With increasing energy, the systematic error in measuring the cross section grows from 4.9% at $E_{\text{c.m.}} = 1050$–1100 MeV to 9.6% at $E_{\text{c.m.}} =$ 1270–1380 MeV. The main contribution to the systematic error (from 4.0 to 9.2%) comes from the systematic uncertainty in background subtraction and the uncertainty associated with the choice of selection criteria. The systematic error in estimating the detection efficiency is 1.9%.

The systematic error in the luminosity (it is equal to 2%) was performed in [17]. Procedures for estimating other contributions to the systematic error in measuring the cross section are described in [19].

4. CONCLUSION

By analyzing 948 ± 33 events of the process $e^+e^- \to K_L^0K_S^0$, we have determined the cross section for the production of a neutral-kaon pair in the energy range $E_{\text{c.m.}} = 1050{-}1380$ MeV. We have shown that the energy dependence of the cross section in the energy region $E_{\text{c.m.}} > 1130$ MeV cannot be described on the basis of the VDM allowing only for the contributions from the $\rho(770)$, $\omega(782)$, and $\phi(1020)$ mesons.

ACKNOWLEDGMENTS

We are grateful to the personnel of the VEPP-2M collider for ensuring the operability of the facility during the experiment and to technicians of the CMD-2 detector for bringing the detector into operation, adjusting it, and maintaining its high performance.

This work was supported by the INTAS 99-00037, DOE DEF0291ER40646, Integration A0100, NSF PHY-9722600, and NSF PHY-0100468 grants and by the Russian Foundation for Basic Research (project nos. 98-02-17851 and 02-02-16162a).

REFERENCES

1. F. Mane *et al.*, Phys. Lett. B **99B**, 261 (1981).
2. T. Kinoshita *et al.*, Phys. Rev. D **31**, 2108 (1985).
3. P. M. Ivanov *et al.*, Pis'ma Zh. Éksp. Teor. Fiz. **36**, 91 (1982) [JETP Lett. **36**, 112 (1982)].
4. E. P. Solodov, Doctoral Dissertation in Physics and Mathematics (Inst. Yad. Fiz., Novosibirsk, 1984).
5. M. N. Achasov *et al.*, in *Proceedings of the International Workshop on e^+e^- Collisions from ϕ to J/ψ, Novosibirsk, 1999,* Ed. by G. Fedotovich and S. Redin (Budker Inst. of Nuclear Physics, Novosibirsk, 2000), p. 196.
6. M. N. Achasov *et al.*, Nucl. Instrum. Methods Phys. Res. A **449**, 125 (2000).
7. A. N. Skrinsky, in *Proceedings of the Workshop DAΦNE'95, Frascati, 1995;* Frascati Phys. Ser. **4**, 3 (1995).
8. G. A. Aksenov *et al.*, Preprint No. 85-118, IYaF (Budker Inst. of Nuclear Physics, Novosibirsk, 1985); E. V. Anashkin *et al.*, ICFA Instrum. Bull. **5**, 18 (1988).
9. E. V. Anashkin *et al.*, Nucl. Instrum. Methods Phys. Res. A **283**, 752 (1989).
10. F. V. Ignatov *et al.*, Preprint No. 99-64, IYaF (Budker Inst. of Nuclear Physics, Novosibirsk, 1999).
11. E. V. Anashkin *et al.*, Nucl. Instrum. Methods Phys. Res. A **323**, 179 (1992).
12. E. V. Anashkin *et al.*, Preprint No. 99-84, IYaF (Budker Inst. of Nuclear Physics, Novosibirsk, 1999).
13. L. M. Barkov *et al.*, in *Proceedings of the 5th International Conference on Instrumentation for Colliding Beam Physics, Novosibirsk, 1990,* Ed. by E. Solodov (World Sci., Singapore, 1991), p. 480.
14. V. M. Aulchenko *et al.*, Nucl. Instrum. Methods Phys. Res. A **336**, 53 (1993).
15. V. M. Aulchenko *et al.*, Nucl. Instrum. Methods Phys. Res. A **265**, 137 (1988).
16. R. R. Akhmetshin *et al.*, Nucl. Instrum. Methods Phys. Res. A **453**, 249 (2000).
17. R. R. Akhmetshin *et al.*, Preprint No. 99-11, IYaF (Budker Inst. of Nuclear Physics, Novosibirsk, 1999).
18. É. A. Kuraev and V. S. Fadin, Yad. Fiz. **41**, 733 (1985) [Sov. J. Nucl. Phys. **41**, 466 (1985)].
19. E. V. Anashkin *et al.*, Preprint No. 2001-58, IYaF (Budker Inst. of Nuclear Physics, Novosibirsk, 2001).
20. A. P. Lysenko *et al.*, Nucl. Instrum. Methods Phys. Res. A **359**, 419 (1995).
21. R. R. Akhmetshin *et al.*, Phys. Lett. B **466**, 385 (1999); **508**, 217 (2001).
22. R. P. Feynman, *Photon–Hadron Interactions* (Benjamin, Reading, 1972; Nauka, Moscow, 1975).
23. R. R. Akhmetshin *et al.*, Phys. Lett. B **434**, 426 (1998).
24. D. E. Groom *et al.*, Eur. Phys. J. C **15**, 7 (2000).

Translated by M. Kobrinsky

Physics of Atomic Nuclei, Vol. 65, No. 7, 2002, pp. 1228–1235. Translated from Yadernaya Fizika, Vol. 65, No. 7, 2002, pp. 1261–1268.
Original Russian Text Copyright © 2002 by Vasiliev.

90th ANNIVERSARY OF I.I. GUREVICH'S BIRTHDAY

Neutron-Spin Dynamics in Elastic Scattering on Lead

V. V. Vasiliev
*Institute of Theoretical and Experimental Physics,
Bol'shaya Cheremushkinskaya ul. 25, Moscow, 117259 Russia*

Received October 26, 2001

Abstract—Experiments are considered that are devoted to studying neutron-spin dynamics (that is, neutron-spin rotation) in the resonance elastic scattering of polarized neutrons on nuclei of lead isotopes and on their natural mixture. It is shown that the effect measured traditionally includes a true spin rotation upon the transmission through a sample and some addition associated with the instrumental error of the method. An estimate of this error and its validation, which were used, for the first time, to determine the effect on ^{204}Pb, are given. Some measures to refine and expand relevant experimental procedure are proposed with the aim of performing a more thorough and a more diversified investigation of elastic neutron scattering on a nucleus. A program of investigations for all lead isotopes is outlined. Such investigations are of importance in connection with the possible existence of a previously unknown negative-energy P-wave neutron resonance in neutron capture by a ^{204}Pb nucleus. © *2002 MAIK "Nauka/Interperiodica"*.

1. INTRODUCTION

While a student at the Moscow Engineering Physics Institute, I had the privilege of attending the lectures of Isai Isidorovich Gurevich in experimental nuclear physics. Later on, the monograph *The Physics of Low-Energy Neutrons* by I.I. Gurevich and L.V. Tarasov was the first book recommended to me by Yu.G. Abov, who supervised my work at the Institute of Theoretical and Experimental Physics as a graduate student of the fifth year. As my involvement in the activities associated with the production of ultracold neutrons and their application in nuclear-physics experiments deepened with the passage of time, I became a witness of the profound interest that Gurevich showed in this topic at seminars held at the Kurchatov Institute of Atomic Energy. Being, in recent years, a member of a group that has been conducting experiments aimed at discovering the effect of neutron-spin rotation in elastic neutron scattering on lead nuclei, I was surprised and pleased to learn that, in the monograph *Neutron Physics* by I.I. Gurevich and V.P. Protasov, there is the chapter named "Coherent Parity Violation." Thus, we can see that Gurevich became a teacher for the community of specialists in neutron physics, an explicit one for a few of them who were lucky to have this privilege and an implicit one for others, much more numerous members of this community. Like no one other, he could show them the beauty of the physical experiment.

Believing myself to be one of the numerous implicit disciples of Gurevich and the admirers of his talent, I took the responsibility of participating in this commemorative issue on their behalf.

In this article, we will consider resonance elastic neutron scattering on nuclei of lead isotopes with special emphasis on neutron-spin dynamics. In doing this, use is extensively made here of a vast body of experimental data accumulated so far in one very specific region. By this, I mean data from experiments devoted to studying the rotation of the spins of neutrons longitudinally polarized with respect to their momentum that undergo scattering on unpolarized lead nuclei. For the sake of completeness and for convenience of the reader not directly involved in research into this specific realm, we will follow the approach adopted in the well-known monographs [1, 2], which are characterized by the clarity of the presentation and by a wide coverage of the topic, and include a brief account of the relevant experimental procedure [3] in our consideration. We also demonstrate the structure of the measured effect and reveal the explicit contribution of the instrumental uncertainty. By considering the example of the latest measurements [4, 5], we discuss a method for estimating it. Additionally, the most recent experimental results are presented, and, after their brief analysis, the possible ways to solve some of the problems of this method are proposed.

2. STRUCTURE OF THE MEASURED EFFECT AND RESULT OBTAINED ON THE ^{204}Pb NUCLEUS

In substantiating experiments aimed at measuring spin rotation, it is common practice to consider (see, for example, [2]), the neutron-helicity dependence of the amplitude for neutron interaction with a nucleus. As was indicated by Michel as far back as 1964 [6],

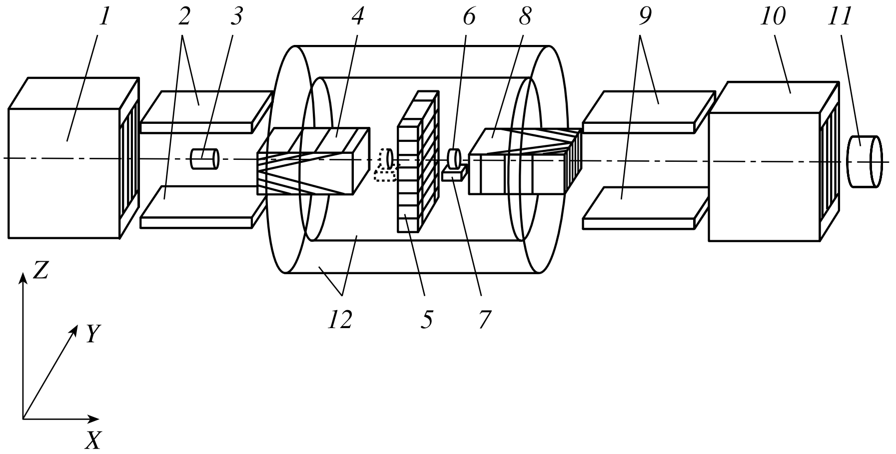

Fig. 1. Layout of the experimental facility for observing neutron-spin rotation: (*1*) neutron polarizer, (*2*) guiding magnet, (*3*) bismuth filter, (*4*) input coil (current-carrying "foil"), (*5*) π coil, (*6*) sample, (*7*) sample holder, (*8*) backward (output) coil, (*9*) guiding magnet, (*10*) analyzer, (*11*) neutron detector (^{6}Li-glass + phototube), and (*12*) magnetic screen.

a coherent effect that is caused by parity-violating weak interaction could manifest itself as the effect of neutron-spin rotation in a transversely polarized neutron beam owing to the fact that neutron waves characterized by opposite signs of the helicity $(\mathbf{s}\cdot\mathbf{p})$, where $\mathbf{s}$ and $\mathbf{p}$ are the neutron spin and the neutron momentum, respectively, have different refraction factors n_+ and n_-. The reason is that, in the Hamiltonian for neutron–nucleus interaction, there is a weak-interaction component, which depends on the direction of the neutron spin. If the neutron beam used is polarized orthogonally to the momentum, the spin wave function in the direction of the momentum $p = \hbar k$ can be represented as the spinor $\frac{1}{\sqrt{2}}\begin{pmatrix}1\\1\end{pmatrix}$. Upon the passage through a sample of length l, neutron waves of opposite polarizations acquire the different phases $\Delta\Phi_\pm = kln_\pm$, which are proportional to the sample length. Thus, the spinor components acquire different phases, whence it follows that, upon traversing the sample, the spinor in question can be represented in the form

$$\frac{1}{\sqrt{2}}\exp(ikn_+l)\begin{pmatrix}1\\e^{-i\varphi}\end{pmatrix},$$

where $\varphi = kl\mathrm{Re}(n_+ - n_-)$ and k is the neutron wave number. The above expression for the spinor corresponds to a spin that is rotated about the momentum through the angle φ.

The angle of neutron-spin rotation is measured with the aid of the facility schematically shown in Fig. 1. All explanations are given in the caption under the figure. The simplified scheme of the relevant experiment is depicted in Fig. 2. This scheme demonstrates that, if the primary beam is polarized transversely with respect to the momentum directed along the Z axis, the beam polarization along the Y axis measures the spin-rotation angle. The so-called π coil is tuned in such a way that, being switched on, it rotates a horizontal spin through an angle of π.

In fact, three pairs of neutron-detector counts at each of the two sample positions (see Fig. 2) are measured for the π coil switched on positively, switched off, and switched on negatively (a rotation through an angle of π in the opposite direction):

$$FN_+^{P+}, FN_-^{P+}, FN_+^{P0}, FN_-^{P0}, FN_+^{P-}, FN_-^{P-};$$

$$BN_+^{P+}, BN_-^{P+}, BN_+^{P0}, BN_-^{P0}, BN_+^{P-}, BN_-^{P-}.$$

Here, F and B denote the positions of the sample (forward and backward, respectively), which is moved from one position to the other, while the superscripts $P+$, $P0$, and $P-$ denote the regimes of the π coil, with the signs $+$, $-$, and 0 indicating, respectively, the field directions and the regime where the field is switched off. The signs in the subscripts indicate the direction of the field of the output coil *8*, the plus (minus) sign corresponding to the spin direction along (against) the field direction. Relative quantities of the form $A = (N_+ - N_-)/(N_+ + N_-)$ are composed of the aforementioned six pairs of values and are associated with asymmetries of the angles; that is,

$$\Psi_F^+ \equiv FA^{P+}, \quad \Psi_B^+ \equiv BA^{P+}, \quad \Psi_F^- \equiv FA^{P-},$$
$$\Psi_B^- \equiv BA^{P-}, \quad \Psi_F^0 \equiv FA^{P0}, \quad \Psi_B^0 \equiv BA^{P0}.$$

The angle Φ_{PNC}, which is due to the parity-nonconserving effect (or, more conservatively, an angle that is associated with neutron transmission through the sample) and the angles of spin rotation by magnetic

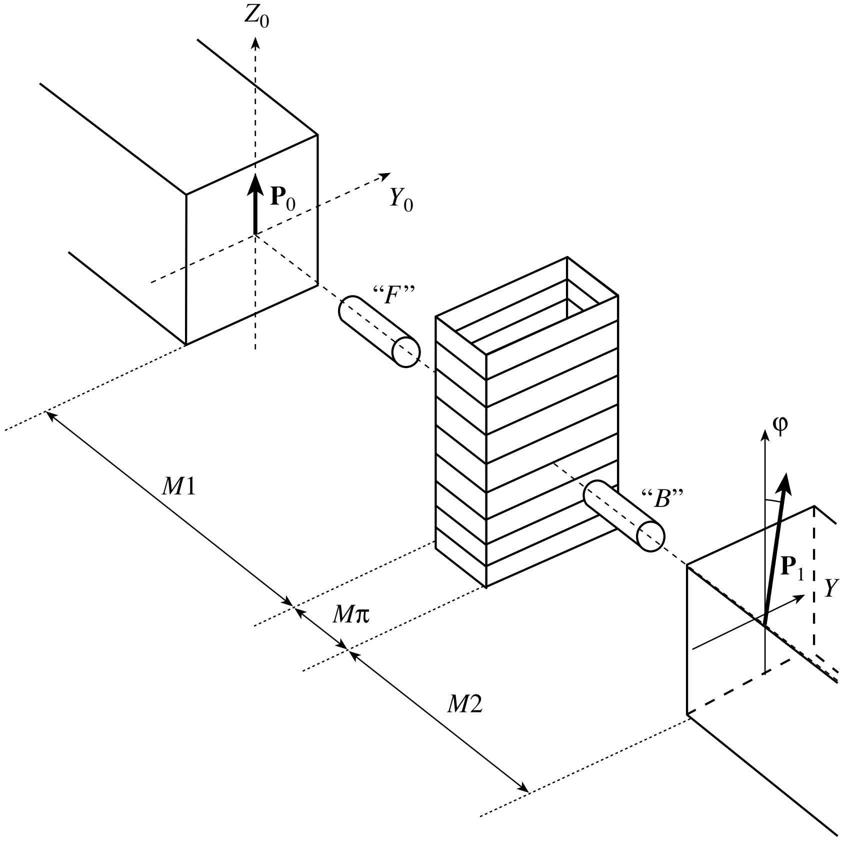

Fig. 2. Simplified schematic representation of the experiment described in this article.

fields, as well as the contributions of angles that are caused by instrumental effects, can be included in the measured asymmetries (angles) by means of the relations

$$\Psi_F^+ = -\Phi_{\mathrm{PNC}} - \Phi_{M1} + \Phi_{M2} + \Phi_\pi, \qquad (1a)$$

$$\Psi_B^+ = +\Phi_{\mathrm{PNC}} - \Phi_{M1} + \Phi_{M2} + \Phi_\pi + 2(\delta_2 - \delta_1) + 2\delta_\pi, \qquad (1b)$$

$$\Psi_F^0 = +\Phi_{\mathrm{PNC}} + \Phi_{M1} + \Phi_{M2}, \qquad (2a)$$

$$\Psi_B^0 = +\Phi_{\mathrm{PNC}} + \Phi_{M1} + \Phi_{M2} + 2(\delta_1 + \delta_2), \qquad (2b)$$

$$\Psi_F^- = -\Phi_{\mathrm{PNC}} - \Phi_{M1} + \Phi_{M2} - \Phi_\pi, \qquad (3a)$$

$$\Psi_B^- = +\Phi_{\mathrm{PNC}} - \Phi_{M1} + \Phi_{M2} - \Phi_\pi + 2(\delta_2 - \delta_1) - 2\delta_\pi, \qquad (3b)$$

where Φ_{M1} and Φ_{M2} are the angles of spin rotation caused by the residual magnetic fields, respectively, in front of ($M1$ zone) and behind ($M2$ zone) the π coil (see Fig. 2), and Φ_π is an angle that is due to the irremovable longitudinal field of the π coil.

The angles $2\delta_1$ and $2\delta_2$ were introduced by the authors of [5] in the analysis of experiments belonging to the type being discussed. Here, we define these angles as follows:

The angle $2\delta_1$ is the additional angle that arises in the $M1$ zone because of moving the sample to the backward position (concurrently, the effective neutron trajectory is shifted somewhat, with the result that, at the corresponding segments of the shifted trajectory, the effective magnetic field differs slightly from the field for the forward position).

The angle $2\delta_2$ is an additional angle that arises in the $M2$ zone for the same reasons.

The angle $2\delta_\pi$ is the additional angle in the π zone.

Another reason for introducing the additional angle $2\delta_2$ is the same nonequivalence of the positions, but, this time, from the point of view of the sample length; that is, the inaccuracy of the mechanical system for moving the sample from one position to the other may result in that the sample proves to be inclined at a very small angle with respect to the beam axis. At the different positions, these angles are different, which can make a direct contribution to the effect because of the resulting distinctions between the effective lengths of the sample. This is especially important in the case of a short sample. It should be emphasized that we are dealing here with relative effects on the order of 10^{-5}.

The possible inaccuracy in the relative 90° orientation of the input and the output coil is included in Φ_{M2}.

In the eventual form, Eqs. (1a)–(3b) reduce to the so-called π numbers; that is,

$$\pi^+ = (\Psi_B^+ - \Psi_F^+)/2 = +\Phi_{\text{PNC}} + (\delta_2 - \delta_1) + \delta_\pi, \tag{4a}$$

$$\pi^0 = (\Psi_B^0 - \Psi_F^0)/2 = (\delta_1 + \delta_2), \tag{4b}$$

$$\pi^- = (\Psi_B^- - \Psi_F^-)/2 = +\Phi_{\text{PNC}} + (\delta_2 - \delta_1) - \delta_\pi. \tag{4c}$$

Further, it is obvious that the quantity

$$\begin{aligned}\pi^{\text{sum}} &= ((\Psi_B^+ - \Psi_F^+)/2 + (\Psi_B^- - \Psi_F^-)/2)/2 \\ &= \Phi_{\text{PNC}} + (\delta_2 - \delta_1)\end{aligned} \tag{5}$$

is the closest to the effect associated with the sample.

The quantity $(\delta_2 - \delta_1)$ is a manifest instrumental uncertainty.

The statement that, upon averaging over a large number of cycles, this difference vanishes to the required precision—that is, $\langle \delta_2 - \delta_1 \rangle = 0$—has not been confirmed. If, on the other hand, the sum $\langle (\delta_1 + \delta_2) \rangle$ vanishes, this does not generally imply that $\langle \delta_2 - \delta_1 \rangle = 0$. The case of $\delta_1 = \delta_2$, whenever possible, requires justification—that is, a dedicated measurement at a higher level of precision. It is also obvious that available data are insufficient for determining Φ_{PNC} from the set of Eqs. (1a)–(3b). In the case where the effect is measured on the ^{204}Pb isotope, a possible way out can be an additional measurement on a sample that is known from the point of view of the effect and which has the same dimensions—for example, on a sample from natural lead. However, each reinstallment of the sample would lead to a change in the aforementioned instrumental uncertainty. One can hardly take this circumstance into account; moreover, it is impossible to implement this reinstallment with the required frequency because of a long-term (about 120 s) measuring cycle on an individual sample.

Nonetheless, there exists a method for estimating the difference $(\delta_2 - \delta_1)$ on the basis of available data [5]. This method was first used in [5] with a qualification, but without giving a validation. This will be done here. In order to characterize the distinction between the neutron-spin-rotation angles that is due to the displacement of the sample, one can introduce the ratios $k_1 = \delta_1/\Phi_{M1}$ and $k_2 = \delta_2/\Phi_{M2}$ for the $M1$ and $M2$ zones. For a first approximation, one can assume that the strength of the longitudinal field increases quadratically with increasing distance from some axis at which it is minimal. We then have $k_{1,2} \sim \Delta r_{1,2}/r_{1,2}$, where $\Delta r_{1,2}$ characterizes the shift of the trajectory and $r_{1,2}$ is the distance from this axis. Since the aforementioned shift of the trajectory can be considered to be parallel, so that the relevant trajectories are similar, we can set $k_1 = k_2 = \bar{k}$. It follows that $k_{1,2} \approx \bar{k}$, where $\bar{k} = (\delta_1 + \delta_2)/(\Phi_{M1} + \Phi_{M2})$. This might have been expected in the present case, since the π coil is situated at the center of the cylindrical screen of the magnetic shield and since the neutron-beam axis coincides with the screen axis.

In any case, the question of how the residual longitudinal magnetic field is distributed along the trajectories being investigated must be additionally explored in each series of measurements versus external conditions. Some proposal along these lines will be given below.

Since the relation $\Phi_{\text{PNC}} \ll \Phi_{M1} + \Phi_{M2}$ holds, which has become clear upon a preliminary treatment of data from the latest series of measurements for a ^{204}Pb sample, but which is not inevitably so in general, we can determine the ratio $\bar{k} = (\delta_2 + \delta_1)/(\Phi_{M1} + \Phi_{M2})$ from (1a) and (4b); that is,

$$\bar{k} \approx \pi^0/\Psi_F^0. \tag{6}$$

The next step consists in calculating δ_2 and δ_1 on the basis of (1a)–(3b):

$$\delta_1 = \frac{\bar{k}}{1 + 2\bar{k}}[\Psi_B^0/2 - (\Psi_B^+ + \Psi_B^-)/4], \tag{7}$$

$$\delta_2 = \bar{k}[\Psi_F^0/2 + (\Psi_F^+ + \Psi_F^-)/4]. \tag{8}$$

This estimate of δ_1 and δ_2 fully takes advantage of information obtained experimentally and highlights the relationship between π^0 and the instrumental uncertainty. The difference $(\delta_2 - \delta_1)$ can be computed in each run of the measurements. Therefore, the linear regression π^{sum} as a function of $(\delta_2 - \delta_1)$ according to Eq. (5) will yield the result for the sought quantity Φ_{PNC} upon an interpolation to the point $(\delta_2 - \delta_1) = 0$.

For the ^{204}Pb isotope, this procedure yielded the result reported in [5]. Upon rescaling to a 100% content of the isotope in question, this result translates into the specific effect of $\Delta\Phi_{\text{PNC}} = (8 \pm 2) \times 10^{-5}$ rad/cm. For the sake of comparison, we note that the effect obtained without taking into account the difference $(\delta_2 - \delta_1)$ is greater by about 25%, the error in it being somewhat less (10%).

Comparison of the results for different lead isotopes

Isotope (composition)	$\Delta\Phi_{\mathrm{PNC}}$, rad/cm	References
Pb (natural mixture)	$(2.24 \pm 0.33) \times 10^{-6}$	[7]
Pb (natural mixture)	$(3.53 \pm 0.79) \times 10^{-6}$	[8]
^{206}Pb	not measured	
^{207}Pb	$< 4.3 \times 10^{-6}$	[8]
^{208}Pb	not measured	
^{204}Pb	$(8 \pm 2) \times 10^{-5}$	[5]
1.4% ^{204}Pb (upon rescaling to a natural composition)	$< 2 \times 10^{-6}$	

3. BRIEF ANALYSIS OF DATA ON NEUTRON-SPIN ROTATION IN NEUTRON SCATTERING ON LEAD

For the sake of comparison, the results obtained for neutron-spin rotation in experiments with the measured lead isotopes and with natural lead are given in the table. From these data, it can be seen that the achieved accuracy is insufficient for drawing the conclusion that the effect on the ^{204}Pb isotope [4, 5] fully accounts for the result obtained for a natural mixture of lead isotopes, but that this cannot be ruled out at a 90% confidence level. On the other hand, the contribution of systematic errors of the $(\delta_2 - \delta_1)$ type was disregarded in earlier measurements, and this could lead to an exaggerated result. It should be emphasized that the revealed structure of the effect is inherent in the facility used and, more generally, in the method as it is (not in the last run exclusively). It is necessary to perform such an analysis not only for the experiment with ^{204}Pb but also for all the preceding experiments. Thus, the present method for measuring the angle of neutron-spin rotation and the facility implementing the method require a further refinement for improving the accuracy and reliability of results.

In considering the content of the natural mixture of lead isotopes and the available experimental results, it becomes obvious that these data are insufficient for drawing a definitive conclusion on the origin of the effect. The ^{206}Pb and ^{208}Pb isotopes were rejected. If, for some reason or another, the expected effect on the ^{208}Pb isotope is close to zero—for example, two orders of magnitude less than the effect obtained with a natural mixture of lead isotopes—this should be corroborated experimentally. Such an experiment with a "zero" result will provide a "zero" sample, which is acutely needed for calibrating the facility.

4. REFINEMENT OF THE PROCEDURE

The strengthening and improvement of the magnetic shielding in the region where samples are displaced and where the π coil is arranged is a minimal requirement on the facility [4, 5].

In imposing more stringent requirements on the stability of external conditions and in order to reduce the instrumental error, it is worthwhile to consider modifications that could be introduced in the facility without abandoning the basic approach to a determination of the effect. The existing instrumental error, which was comprehensively explored and taken into account in [5], stems to a considerable extent from the distinction between the positions of the sample in front of and behind the π coil, but it also receives contributions associated with an insufficient reliability of the system of tie-rods, springs, and guide bars along which the sample holder moves (taken together, this leads to variable shifts in this system).

It seems that the accuracy can be improved by using a scheme where the sample is permanently at rest in between two π coils. It should be recalled that the current through a π coil is tuned in such a way that, upon passing through the region of this coil, a horizontally oriented neutron spin (the horizontal component of the polarization) is rotated through an angle of π.

We denote by $M1$, $M2$, and $M3$ the residual magnetic fields, respectively, in front of, in between, and behind the π coils. Since any magnetic shielding leaves small or very small magnetic fields, their presence can mimic the spin-rotation effect on the sample. We denote by Φ_{M1}, Φ_{M2}, and Φ_{M3} the spin-rotation angles due to precession in these fields. Any π coil, however correct and accurate its design, implementation, and arrangement would be, generates a longitudinal magnetic field. We denote it by $\Phi_{\pi1}$ for the first coil and by $\Phi_{\pi2}$ for second coil.

Using the superposition principle, one can obtain an expression for the angle through which the spin of a neutron that traverses two differently connected coils and the sample (playing the role of a target) in between them is rotated. We denote the resulting angle by $\Psi(+,-)$ for the positive polarity of the first coil and the negative polarity of the second coil; when one of the coils is switched off, there appears a symbol 0 at the corresponding position. Further, we also employ a more complicated combination of simultaneously connected coils; that is, $\Psi S = (\Psi(+,+) + \Psi(-,-))/2$. We have

$$\Psi(0,0) = +\Phi_{M1} + \Phi_{M2} + \Phi_{\mathrm{PNC}} + \Phi_{M3}, \quad (9a)$$

$$\Psi(+,0) = -\Phi_{M1} + \Phi_{\pi1} + \Phi_{M2} + \Phi_{\mathrm{PNC}} + \Phi_{M3}, \quad (9b)$$

$$\Psi(-,0) = -\Phi_{M1} - \Phi_{\pi 1} + \Phi_{M2} + \Phi_{\rm PNC} + \Phi_{M3}, \tag{9c}$$

$$\Psi(0,+) = -\Phi_{M1} - \Phi_{M2} - \Phi_{\rm PNC} + \Phi_{\pi 2} + \Phi_{M3}, \tag{9d}$$

$$\Psi(0,-) = -\Phi_{M1} - \Phi_{M2} - \Phi_{\rm PNC} - \Phi_{\pi 2} + \Phi_{M3}, \tag{9e}$$

$$\Psi {\rm S} = +\Phi_{M1} - \Phi_{M2} - \Phi_{\rm PNC} + \Phi_{M3}. \tag{9f}$$

From this set of equations, it can be seen that it is impossible to compute the angles Φ_{M2} and $\Phi_{\rm PNC}$ individually. It is precisely for the purpose of separating these quantities that the sample is displaced from one position to the other in the traditional facility. In the new scheme, it is necessary to perform an experiment without a sample. It can easily be seen that

$$\Phi_{M2} + \Phi_{\rm PNC} = (\Psi(+,0) - \Psi(0,+) + \Psi(-,0) - \Psi(0,-))/4 \equiv A(1). \tag{10}$$

We then have $\Phi_{\rm PNC} = A(1) - A(0)$, where $A(0)$ corresponds to a measurement without a sample and $A(1)$ is the relevant quantity in the measurement where the sample is present. Thus, an experiment involving the "sample—no-sample" sequence is inevitable. Obviously, the best situation is that where $A(0)/A(1) \ll 1$, in which case the experiment without a sample will be merely a test one. When, however, we are dealing with effects at a level of 10^{-6}, the condition $A(0)/A(1) \ll 1$ can hardly be guaranteed at the stage of creating the facility to be used.

It seems that an experiment employing two π coils and a sample placed in one position is clearer. At least, the link between the effect and the sample will become more obvious. Moreover, the result obtained from a measurement according to the "sample—no-sample" sequence directly determines $\Phi_{\rm PNC}$ without any addition caused by magnetic fields, provided that the external magnetic conditions are steady-state. Within the proposed configuration, one can employ a more precise mechanism for installing, replacing, or displacing a sample—for example, a turret-type or a drum-type precision mechanism.

The following argument can be the only objection to performing an experiment of the "sample—no-sample" type. The effective neutron trajectory between the coils in the presence of a sample may differ somewhat from the trajectory in the absence of a sample. This implies that the magnetic fields $M2_{\rm sample}$ and $M2_{\text{no-sample}}$ may be different. Here, we are dealing with distinctions on the order of 10^{-6}–10^{-5} between the angles of precession.

If the source of this field is within the facility proper, the transverse field gradient can be measured with this precision by shifting the facility by a few hundredths of a millimeter. The point is that, as can in fact be seen from expression (10), a polarized neutron beam is used, in this case, as a means for measuring weak magnetic fields. More precisely, the effective magnetic field is measured, in the classical scheme, over the flight base from the polarizer to the π coil and from the π coil to the analyzer. With the aid of two π coils, the regions over which the magnetic fields are averaged are localized more precisely; at the same time, the average values of the magnetic induction over the gaps determined by the positions of the π coils can be measured, provided that the spectrum of neutrons is known or provided that the degree of beam monochromaticity is sufficiently high. Moreover, the distribution of the longitudinal magnetic field along the trajectory in the absence of a sample (or in the presence of a sample if its cross-sectional area is much larger than that of the beam) can be measured by displacing the two paired π coils along the neutron beam or, as has already been said, across the beam. By scanning, in this way, the magnetic field along the longitudinal and along the transverse direction, one can obtain its distribution, choose a right position for the sample, and minimize the instrumental uncertainty.

In the proposed scheme, the magnetic field is measured over a finite segment owing to the use of two π coils; that is, the magnetic field is integrated in the expression for the spin-rotation angle over a less extended segment.

Thus, we can see that, in assessing the efficiency of a multilayer external screen, a polarized neutron beam measures a very low magnetic field.

As was discussed in Section 3, it would be optimal to measure the magnetic field $M2_{\rm sample}$ by using a calibration sample that is close in density to the sample used in the actual experiment and which is identical to it in the technology of fabrication. In measuring, for example, the parity-odd neutron-spin-rotation effect on ^{204}Pb, one can take, for a calibration sample, that which is of the same dimensions as the sample being actually explored and which was prepared from natural lead according to the same technology of casting and rolling or, say that which contains about 100% ^{208}Pb if the prediction of zero effect for doubly magic nuclei comes true. Since the effect on natural lead is known to a sufficiently high precision, the effect due to spurious precession can also be calculated by determining the total effect on the basis of Eqs. (9a)–(9f).

These are advantages of an experiment in which the sample used occupies a single position. By extending the problem to be addressed, it is possible, however, to make use of yet another advantage offered by the new experimental scheme.

5. OTHER EFFECTS OF P-ODD ASYMMETRY IN (n, n') REACTIONS

A theoretical substantiation of the neutron-spin-rotation effect in resonance elastic scattering [9–11] employs the most general arguments concerning the density of P- and S-wave neutron resonances, their spacings, the relationships between theirs widths, etc. Therefore, it is legitimate to assume that enhancement effects are operative for all spatial effects associated with neutron emission.

On the other hand, the emergence of asymmetry (parity-violation effect) is theoretically explained in [10, 11] by the mechanism according to which neutron capture by the target nucleus with the formation of a compound state is accompanied, owing to the universal weak interaction, by the transformation of an S-wave neutron into a P-wave one [10]. This hypothesis does not rule out the possibility of the emission of a P-wave neutron whose spin projection is opposite to the projection of the primary-neutron spin. If this is indeed so, the effect of birefringence and the effect asymmetric polarization may be superimposed in experiments as a neutron undergoes a transition through the compound state. Either effect can be interpreted as neutron-spin rotation. In general, this conclusion calls for an experimental verification. The possibility of the interplay of the two effects has not yet been subjected to experimental tests in a transversely polarized beam.

In this connection, it would be worthwhile to conduct an experiment aimed at observing the polarization of the scattered wave. For example, the polarization of the beam halo formed owing to forward scattering at small angles could be measured with the aid of the same traditional facility. In performing such an experiment, it is sufficient to ensure that only the beam halo arising because of scattering would arrive at the analyzer and to measure its polarization separately from the polarization of the beam propagating without scattering. In that case, the sample used is also at rest in the beam or is removed from the beam. The ratio of the polarization of the beam scattered on the sample to the polarization of the beam propagating directly in the absence of a sample, $PR = P^{\text{sample}}/P^{\text{no-sample}}$ could be a measured quantity. It should be recalled that we imply here the projection of the polarization onto the y axis.

An observation of the asymmetry of neutron emission from the compound nucleus with respect to the direction of the captured-neutron spin could be another possibility for extending the range of parity-violation effects. In all probability, one can assume that a dynamical enhancement of a weak single-particle effect of parity violation will lead to asymmetries at a level of 10^{-5}–10^{-4} in this case as well.

It is advisable to measure a few parameters that characterize the parity-violation process in (n, n') reactions.

First, this is the relative asymmetry of neutrons that are emitted along and against the original direction of the spin of the neutron captured in the compound nucleus. It is quite conceivable that neutron emission from the compound nucleus is characterized by right–left asymmetry, or, to state it otherwise, the amplitude of compound-nucleus decay depends on the pseudoscalar quantity $\mathbf{p}' \cdot \mathbf{s}$, where $\mathbf{p}'$ is the momentum of the emitted (scattered) neutron and $\mathbf{s}$ is the primary-neutron spin. In general, this relationship between the parameters of the initial and the final state in the expression for the weak-interaction-process amplitude is quite conventional.

In order to verify the above hypothesis, it is sufficient to place two detectors of sufficient area on the two sides (along and against the spin) of a transversely polarized beam. By detecting neutrons emitted by the nucleus in the direction that is orthogonal to the primary-beam momentum and which is parallel to the primary-neutron spin conceptually, this is in line with the approach adopted in the first experiments devoted to searches for parity violation in (n, γ) reactions [12], it is possible to measure the asymmetry of the emission of resonantly scattered neutrons with respect to the spin of primary-beam particles. It can be conjectured that all the arguments put forth in the aforementioned theoretical studies in favor of the enhancement of P-odd effects remain in force for (n, n') reactions as well, with the exception of the accumulation of the effect in response to an increase in the sample length.

Second, it is possible to measure the polarization of neutrons emitted orthogonally to the momentum–spin plane in the direction of the primary momentum—that is, to measure the polarization P_X of neutrons emitted along and against the direction of the y axis in the coordinate frame depicted in Fig. 2.

Third, it is interesting to measure, with a high precision, the angular distribution of neutrons emitted by a compound nucleus and to verify whether this distribution is compatible with the presumed mixing of the S and P waves. The one-position scheme is preferable for such experiments as well.

Thus, the total scheme of the experimental facility to be used must include, in addition to the aforementioned system for measuring the spin-rotation angle, the system of detectors arranged crosswise in order to record neutrons emitted by the sample. One pair of detectors would record neutrons emitted by the sample along and against the direction of the spin of the incident (captured) neutron. The second pair of detectors, which is equipped with analyzers, would measure neutron counts in the orthogonal direction and the neutron polarization P_X (in order to measure the "background" and its polarization). Test experiments are obvious in the present case.

6. CONCLUSION

The development of studies aimed at observing the rotation of the spin of neutrons incident on lead isotopes led to the theoretical prediction of a subthreshold neutron resonance of the P-wave character in neutron capture by a ^{204}Pb nucleus [10]. At the same time, an analysis of relevant experimental data made it possible to conclude that there is an instrumental uncertainty in the structure of the effect and that it is possible to assess this uncertainty quantitatively and to take it into account. In this situation, it becomes necessary to refine the procedure further in order to improve its accuracy and to draw more definitive conclusions on the origin of the P-odd effect on a natural mixture of lead isotopes. In addition, it is desirable to perform experiments that would quantify the effect arising on samples enriched in the ^{206}Pb and ^{208}Pb isotopes. This information would become a necessary test for corroborating the crucial role of the ^{204}Pb isotope.

On the other hand, the experimental method for measuring spin rotation requires including new approaches in order to eliminate conventional sources of systematic effects. In particular, it is proposed to use a one-position method of measurements, which enables a more straightforward interpretation of the observed effect and a more clear-cut determination of the contribution from the possible systematic error. Moreover, the one-position procedure can be extended to studying all facets of the parity-violation phenomenon in (n, n') reactions proceeding through the formation of a compound nucleus. Among other things, it is worthwhile to analyze and to verify experimentally the presumed effect of the asymmetry of compound-nucleus decay through neutron emission. Obviously, this effect is not associated with spin rotation. However, it is possible to organize measurements in such a way that these two effects, which are so distinct, will be recorded simultaneously.

ACKNOWLEDGMENTS

I am grateful to R. Golub, P.A. Krupchitsky, and I.L. Karpikhin for detailed discussions on the results of the latest experiments and on the problem of the instrumental uncertainty. I am also indebted to O.N. Ermakov for enlightening discussions that were devoted to the special features of the experimental facility and which preceded the experiment with a ^{204}Pb target. Special thanks are due to Yu.G. Abov for his attention to this study and interest in it.

REFERENCES

1. I. I. Gurevich and L. V. Tarasov, *Low-Energy Neutron Physics* (Nauka, Moscow, 1965; North-Holland, Amsterdam, 1968).
2. I. I. Gurevich and V. P. Protasov, *Neutron Physics* (Énergoatomizdat, Moscow, 1997), p. 265.
3. P. A. Krupchitsky, *Fundamental Investigations with Polarized Slow Neutrons* (Énergoatomizdat, Moscow, 1985; Springer-Verlag, New York, 1987).
4. O. N. Ermakov *et al.*, in *Proceedings of the 8th International Seminar on the Interaction of Neutrons with Nuclei "Neutron Spectroscopy, Nuclear Structure, and Related Topics," Dubna 2000,* E3-2000-192, p. 377.
5. R. Golub *et al.*, in *Proceedings of the 9th International Seminar on the Interaction of Neutrons with Nuclei "Neutron Spectroscopy, Nuclear Structure, and Related Topics," Dubna 2001,* E3-2001-192, p. 33.
6. F. Curtis Michel, Phys. Rev. B **133**, 329 (1964).
7. B. Heckel *et al.*, Phys. Lett. B **119B**, 298 (1982).
8. V. P. Bolotsky *et al.*, Yad. Fiz. **59**, 1873 (1996) [Phys. At. Nucl. **59**, 1808 (1996)].
9. O. P. Sushkov and V. V. Flambaum, Pis'ma Zh. Éksp. Teor. Fiz. **32**, 377 (1980) [JETP Lett. **32**, 352 (1980)].
10. G. A. Lobov, Yad. Fiz. **63**, 1465 (2000) [Phys. At. Nucl. **63**, 1387 (2000)].
11. V. E. Bunakov, Fiz. Élem. Chastits At. Yadra **26**, 286 (1995) [Phys. Part. Nucl. **26**, 115 (1995)].
12. Yu. G. Abov, P. A. Krupchitsky, and Yu. A. Oratovsky, Phys. Lett. **12**, 25 (1964).

Translated by A. Isaakyan

Physics of Atomic Nuclei, Vol. 65, No. 7, 2002, pp. 1236–1242. Translated from Yadernaya Fizika, Vol. 65, No. 7, 2002, pp. 1269–1275.

90th ANNIVERSARY OF I.I. GUREVICH'S BIRTHDAY

Special Features of the Radiative Capture of Ultracold Neutrons by Thin and Thick Layers of Matter

T. Ya. Tudorovskiy and A. L. Barabanov

Russian Research Centre Kurchatov Institute, pl. Kurchatova 1, Moscow, 123182 Russia

Received December 19, 2001

Abstract—The radiative capture of ultracold neutrons traversing thin and thick homogeneous layers of matter is analyzed. The applicability range of the formulas for the probabilities of reflection, transmission, and capture in thick layers (under certain conditions, they admit a simple interpretation—it is often quoted in the literature—that is based on the effective capture cross section, which is in inverse proportion to the velocity of a neutron in matter) is investigated, along with the conditions under which there arises the effective capture cross section. *© 2002 MAIK "Nauka/Interperiodica".*

1. INTRODUCTION

Radiative capture is one of the channels through which ultracold neutrons (UCN) can escape from matter traps employed for their storage. In order to reduce such losses, the trap walls are usually manufactured from weakly absorbing substances. The opposite case—that of UCN reflection from a surface of a strongly absorbing medium—was first considered by Gurevich and Nemirovsky [1].

Direct observations of radiative UCN capture by the nuclei of medium atoms were performed quite recently by the methods of (n,γ) spectroscopy (see [2, 3]). In those experiments, the contributions of different nuclei to neutron capture are separated by the energy of emitted γ rays. Investigation of UCN transmission through matter layers is less informative in this sense—not only are such experiments unable to distinguish between captures by different nuclear species, but they also give no way to separate radiative capture proper from other channels of losses (for example, from inelastic scattering). Only in special cases—such as that in [4], where the authors investigated the transmission of UCNs through layers of matter containing strongly absorbing Gd nuclei—does radiative capture obviously dominate over other processes that lead to the removal of neutrons from the beam entering the layer.

From the theoretical point of view, radiative capture is rather a simple phenomenon, in contrast to, say, inelastic scattering (for more details on inelastic scattering, see, for example, [5]). For this reason, experimental results on radiative capture must admit a simple interpretation. Indeed, it was found in [2] for UCN interaction with stainless steel that the γ-ray yield exceeds considerably the estimates obtained under the assumption that various atoms entering into the composition of a sample are distributed uniformly over its volume. This result was interpreted as an indication of a significant nonuniformity of distribution of steel elements over the steel volume. Discrepancies between theoretical and experimental results were observed in [4] as well. In that case, however, the reasons behind the discrepancies have yet to be clarified: only some plausible hypotheses were discussed in [4] and in the comment given in [6]. In the present study, we also indicate some features of radiative capture that seem to have been disregarded in [4].

Experiments studying radiative UCN capture are of great interest precisely because of their clarity from the theoretical point of view. Let us consider, by way example, the problem of inelastic UCN scattering for UCN interaction with matter. In all probability, this is the phenomenon that is responsible for anomalous neutron losses [7], which are being widely discussed at present, and for the recently discovered effects of small heating and cooling of UCNs in matter traps (see, for example, [8]). Data on radiative capture can furnish quantitative information that concerns the structure of surface layers and the concentration of impurities and which is of importance for estimating inelastic scattering. In particular, the detection of γ rays emitted upon neutron capture by protons—this was done in [9]—will make it possible to assess the content of hydrogen at the surface of the trap walls and, hence, to establish more reliably the role of hydrogen in inelastic UCN scattering.

In the simplest way, radiative capture is taken into account in terms of the imaginary part of the potential representing UCN interaction with matter (see, for example, [10, 11]), this imaginary part being in direct proportion to the imaginary part of the neutron–nucleus scattering length. The total number of neu-

1063-7788/02/6507-1236$22.00 © 2002 MAIK "Nauka/Interperiodica"

trons absorbed in matter is determined by the total neutron flux through any closed surface surrounding the sample. For a planar homogeneous layer, the problem is solved straightforwardly. At a small thickness of a layer, the number of absorbed neutrons quickly oscillates as a function of the incident-neutron energy exceeding the real part of the potential, these oscillations being due to the interference of waves multiply reflected from the inner surfaces of the layers. At large thicknesses, one can neglect this interference and sum, instead of amplitudes, the probabilities of capture from a primary beam, a singly reflected beam, a doubly reflected beam, and so on [12]. In this case, the quantum-mechanical problem of neutron interaction with matter that is represented by a specific potential cannot be solved completely. Relevant calculations involve, first, the probabilities of particle transmission and reflection at the boundary of a half-space filled with matter and, second, the cross section for capture by one nucleus, this cross section being assumed to be in inverse proportion to the neutron velocity in matter rather than in a vacuum.

This procedure for calculating the probability of neutron transmission through a matter layer seems reasonable, the results of such calculations being, as a rule, in good agreement with experimental data. This is apparently not so only for data reported in the aforementioned article of Rauch *et al.* [4], who investigated the propagation of UCNs through strongly absorbing layers. But even if there were no such exception, it would be of great interest, in our opinion, to give a consistent validation of the procedure formulated above. We were unable to find such a validation in the literature. From our point of view, this is all the more important since, in a consistent quantum-mechanical approach, the probability of radiative neutron capture in matter is determined by the sum of the probabilities of capture on individual nuclei. But these probabilities are proportional to the "true" cross sections for capture by an individual nucleus—that is, to the cross sections that are inversely proportional to the neutron velocity in a vacuum. It would be intriguing to trace the way in which the true cross sections for capture transform into effective cross sections that are inversely proportional to the neutron velocity in matter.

It is also of interest to investigate the probability of neutron capture in a planar layer in addition to the usually explored problem of neutron transmission through a layer. With the aid of (n,γ) spectroscopy, the capture probability can be measured directly by the γ-ray yield. At the same time, the interpretation of the transmission probability can be hindered by the paucity of experimental data under the conditions where reflection from the layer is not monitored or where inelastic scattering is significant, along with capture.

Here, we do not consider inelastic-scattering effects, assuming all nuclei of matter to be at rest. The potential of UCN interaction with matter can be represented as

$$U(\mathbf{r}) = U'(\mathbf{r}) + iU'' = \frac{2\pi\hbar^2}{m}\sum_{\nu} n_\nu(\mathbf{r})\beta_\nu, \quad (1)$$

where m is the neutron mass, $n_\nu(\mathbf{r})$ is the concentration of nuclei of matter that belong to the ν species, and $\beta_\nu = \beta'_\nu + i\beta''_\nu$ is the coherent scattering length for neutron interaction with a nucleus of the ν species. The imaginary part β'' of the coherent scattering length is negative; therefore, the imaginary part U'' of the potential is also negative according to (1).

2. RADIATIVE-CAPTURE PROBABILITY

The probability of radiative neutron capture in matter can be calculated by two equivalent methods.

The first method follows from the definition of the flux. Let us enclose the sample under investigation by an arbitrary surface $\partial\Omega$, which is the boundary of some region Ω. The number of particles accumulated within this surface per unit time is given by

$$\frac{dN_c}{dt} = -\oint_{\partial\Omega} \mathbf{j}\,d\mathbf{s}, \quad (2)$$

where

$$\mathbf{j} = \frac{\hbar}{2mi}(\psi^*\nabla\psi - \psi\nabla\psi^*) \quad (3)$$

is the flux density-vector and $d\mathbf{s}$ is an outward oriented area element of the surface $\partial\Omega$. By definition, the cross section for radiative capture is

$$\sigma_c = \frac{dN_c/dt}{j_0} = -\frac{1}{j_0}\oint_{\partial\Omega} \mathbf{j}\,d\mathbf{s}, \quad (4)$$

where j_0 is the density of the incident-particle flux. Everywhere below, we will assume that $j_0 = \hbar k/m$—that is, the wave function for incident particles has the form $\psi_0 = \exp(i\mathbf{k}\cdot\mathbf{r})$, where $\mathbf{k}$ is the neutron wave vector in a vacuum.

A transformation of formula (4) will lead us to the second method for calculating the capture cross section. In the time-independent case, the following continuity condition can easily be obtained from the Schrödinger equation with the complex-valued potential (1):

$$|\psi|^2 U'' = \frac{\hbar}{2}\,\mathrm{div}\,\mathbf{j}. \quad (5)$$

By transforming the surface integral appearing in (4) into a volume integral and by using formulas (1) and (5), we find

$$\sigma_c = -\sum_{\nu} \int\limits_{V} \frac{4\pi}{k} \beta''_{\nu} |\psi(\mathbf{r})|^2 n_{\nu}(\mathbf{r}) dV. \qquad (6)$$

Integration in (6) is performed over the sample volume V.

This expression for the cross section describing radiative neutron capture by matter can be recast into the form

$$\sigma_c = \sum_{\nu} \int_V \sigma_{\nu}^{(1)} |\psi(\mathbf{r})|^2 n_{\nu}(\mathbf{r}) dV, \qquad (7)$$

where

$$\sigma_{\nu}^{(1)} = -\frac{4\pi}{k} \beta''_{\nu} \qquad (8)$$

is the true cross section for neutron capture by a single isolated nucleus (see, for example, [11]) and $n_{\nu}(\mathbf{r})dV$ is the number of nuclei in the volume dV. Formula (7) has a clear physical meaning: the total capture cross section is obtained by summing, over all nuclei, the products of the cross section for capture by an individual nucleus and the quantity $|\psi(\mathbf{r})|^2$, which is proportional to the probability of finding a neutron near this nucleus. It is natural to refer to the method of calculating the radiative-capture cross section according to (6) and (7) as the method of summation over nuclei.

The radiative-capture probability (coefficient of losses) is expressed in terms of the capture cross section as

$$w_c = \frac{\sigma_c}{S_{\perp}}, \qquad (9)$$

where $S_{\perp}$ is the cross-sectional area of the sample in a beam of incident neutrons.

3. HOMOGENEOUS HALF-SPACE AND HOMOGENEOUS PLANAR LAYER

Let us consider the simplest case, that of neutron capture in a homogeneous half-space. Suppose that a particle is incident from a vacuum ($x < 0$) on the half-space $x > 0$ filled with matter. The particle wave function has the form

$$\psi_{\mathbf{k}}(\mathbf{r}) = e^{i\mathbf{k}_{\parallel} \cdot \mathbf{r}_{\parallel}} \times \begin{cases} e^{ik_{\perp}x} + re^{-ik_{\perp}x}, & x < 0, \\ te^{i\bar{k}x}, & x > 0, \end{cases} \qquad (10)$$

where $\mathbf{k}$ is the wave vector in a vacuum and $\mathbf{k}_{\parallel}$ and $k_{\perp}$ are its components that are, respectively, parallel and orthogonal to the boundary of the half-space. The normal component $\bar{k}$ of the neutron wave vector in matter is given by

$$\bar{k} = \sqrt{k_{\perp}^2 - u_0}, \qquad u_0 = \frac{2mU}{\hbar^2}. \qquad (11)$$

The amplitudes r and t can be derived from the matching conditions at the boundary $x = 0$:

$$r = \frac{k_{\perp} - \bar{k}}{k_{\perp} + \bar{k}}, \qquad t = \frac{2k_{\perp}}{k_{\perp} + \bar{k}}. \qquad (12)$$

The quantities

$$R = |r|^2, \qquad T = 1 - |r|^2 \qquad (13)$$

determine, respectively, the probability of reflection from the boundary of the half-space and the probability of penetration into the half-space.

Since $U = U' + iU''$, the quantities $u_0 = u'_0 + iu''_0$ and $\bar{k} = \bar{k}' + i\bar{k}''$ also have a real and an imaginary part. By squaring the first formula in (11) and by isolating, on the left- and on the right-hand side, the imaginary parts, we derive the useful relation

$$2\bar{k}'\bar{k}'' = -u''_0. \qquad (14)$$

We also note that, at any $k_{\perp} > 0$, the quantities $\bar{k}'$ and $\bar{k}''$ are positive and are determined by the formulas

$$\bar{k}'^2 = \frac{1}{2}\left(\sqrt{(k_{\perp}^2 - u'_0)^2 + u''^2_0} + (k_{\perp}^2 - u'_0)\right), \qquad (15)$$

$$\bar{k}''^2 = \frac{1}{2}\left(\sqrt{(k_{\perp}^2 - u'_0)^2 + u''^2_0} - (k_{\perp}^2 - u'_0)\right). \qquad (16)$$

Following the first (standard) method for calculating the capture probability, we write the total flux through an arbitrary plane $x = x_0 < 0$ bounding the half-space as

$$\int \mathbf{j}d\mathbf{s} = -S\frac{\hbar k_{\perp}}{m}\left(1 - |r|^2\right). \qquad (17)$$

Here, we assume that the area of the plane surface separating matter from a vacuum, albeit being very large (such that we can use the concept of a half-space), is finite and is equal to S. We neglect boundary effects. Substituting our result into (4) and (9) and considering that $S_{\perp} = Sk_{\perp}/k$, we arrive at the well-known relation

$$w_c = 1 - |r|^2. \qquad (18)$$

In this case, the absorption probability coincides with the probability T of penetration into the half-space.

Let us now trace the procedure of summation over nuclei. In accordance with (6) and (10), we have

$$\sigma_c = -S\sum_{\nu} \frac{2\pi n_{\nu} \beta''_{\nu} |t|^2}{k\bar{k}''}. \qquad (19)$$

Isolating the term $u_0'' = 4\pi \sum_\nu n_\nu \beta_\nu''$ on the right-hand side and using Eq. (14), we recast the cross section into the form

$$\sigma_c = S \frac{\bar{k}'|t|^2}{k} = \frac{S k_\perp}{k}\left(1 - |r|^2\right). \tag{20}$$

Again, formula (18) follows from here in accordance with (9). It should be emphasized that, for each individual nucleus, we have used the true capture cross section, which is inversely proportional to the neutron velocity in a vacuum.

Let us now calculate the radiative-capture probability for the case where UCNs traverse a homogeneous planar matter layer of thickness a. In this case, the neutron wave function has the form

$$\psi_{\mathbf{k}}(\mathbf{r}) = e^{i\mathbf{k}_\parallel \cdot \mathbf{r}_\parallel} \tag{21}$$

$$\times \begin{cases} e^{ik_\perp x} + b e^{-ik_\perp x}, & x < -a/2, \\ f e^{i\bar{k}x} + g e^{-i\bar{k}x}, & -a/2 < x < a/2, \\ c e^{ik_\perp x}, & x > a/2, \end{cases}$$

where the quantities $\mathbf{k}_\parallel$, $k_\perp$, and $\bar{k}$ are defined in the same way as in (10). The amplitudes b, c, f, and g are determined from the conditions of matching at the boundaries of the layer and are given by

$$b = e^{-ik_\perp a} \frac{r(1-\gamma^2)}{1 - r^2\gamma^2}, \quad c = e^{-ik_\perp a} \frac{\gamma(1-r^2)}{1 - r^2\gamma^2}, \tag{22}$$

$$f = e^{-ik_\perp a/2} \frac{t\gamma^{1/2}}{1 - r^2\gamma^2}, \quad g = -r\gamma f, \tag{23}$$

where

$$\gamma = e^{i\bar{k}a} = |\gamma| e^{i\bar{k}'a}, \quad |\gamma| = e^{-\bar{k}''a}. \tag{24}$$

At a sufficiently large value of the layer thickness a, the parameter γ is always small in magnitude for a subbarrier neutron ($k_\perp^2 < u_0'$). For an above-barrier neutron, two cases are possible, that of strong absorption ($\bar{k}''a \gg 1$) and that of weak absorption ($\bar{k}''a \ll 1$). In the former case, the parameter γ is again small in magnitude, while, in the latter case, the parameter γ oscillates as a function of the neutron energy, the frequency of these oscillations becoming higher with increasing layer thickness a.

We note that, in calculating the capture probability by the first method—that is, in terms of the neutron fluxes beyond the layer—one needs the explicit expressions (22) for the amplitudes b and c. At the same time, the method of summation over nuclei employs the wave function that describes neutrons within the layer and which is completely determined by the amplitudes f and g (23). Of course, the results are identical. The first method is, however, clearer. Within it, we obtain

$$w_c = 1 - \rho - \tau, \tag{25}$$

where

$$\rho = |b|^2 = \frac{|r|^2 |1-\gamma^2|^2}{|1 - r^2\gamma^2|^2} \tag{26}$$

is the probability of reflection from the layer and

$$\tau = |c|^2 = \frac{|\gamma|^2 |1-r^2|^2}{|1 - r^2\gamma^2|^2} \tag{27}$$

is the probability of transmission through it.

If the parameter γ is small in magnitude, the quantities ρ, τ, and w_c are smooth functions of the incident-neutron energy. In the limit $|\gamma| \to 0$, we return to the case of a half-space,

$$\rho \to R, \qquad \tau \to 0, \qquad w_c \to T. \tag{28}$$

We repeat that this case corresponds to subbarrier neutrons at a sufficiently large layer thickness and to above-barrier neutrons at a very strong absorption in the layer ($\bar{k}''a \gg 1$). The fact that the reflection of subbarrier neutrons is not small even at a very strong absorption in matter was emphasized in [1].

But if a neutron is in the above-barrier region ($k_\perp^2 > u_0'$) and if the product $\bar{k}''a$ is not overly large, the parameter γ and the quantities ρ, τ, and w_c, together with it, oscillate as functions of the neutron energy. As the neutron energy grows above the barrier, the amplitudes of these oscillations decrease because of the reduction of r.

4. THICK HOMOGENEOUS LAYER

Of particular interest is the case where a neutron is in the above-barrier region and where oscillations are well pronounced, but where the layer thickness a is so large that high-frequency oscillations cannot be experimentally resolved. A great many experiments studying neutron transmission through layers were performed precisely for such a relationship between the parameters. It is intuitively clear that the above oscillations arise because of the interference between waves multiply reflected from the inner boundaries of the layer. Hence, the smoothing of oscillations corresponds to the disregard of the interference. In this case, the probabilities of reflection, transmission, and capture can be calculated by means of a mere summation of the relevant probabilities [12].

Let us denote by α the probability that a neutron traversing a layer is captured by none of matter nuclei. We note that the probability of neutron reflection from the inner boundary of a half-space can be obtained from formulas (12) and (13) by means of the substitutions $k_\perp \to \bar{k}$ and $\bar{k} \to k_\perp$. But this implies that the probability in question coincides with the probability R of reflection from the outer boundary of the half-space. Accordingly, the probability of escape from the half-space, $T = 1 - R$, is equal to the probability of penetration into the half-space. For the probability of reflection from the layer, we then obtain

$$\rho' = R + T(\alpha R\alpha)T + T(\alpha R\alpha)(R\alpha R\alpha)T \tag{29}$$
$$+ \ldots = R\left(1 + \frac{\alpha^2 T^2}{1 - \alpha^2 R^2}\right).$$

In the same manner, the probability of transmission through the layer is given by

$$\tau' = T\alpha T + T\alpha(R\alpha R\alpha)T + \ldots = \frac{\alpha T^2}{1 - \alpha^2 R^2}. \tag{30}$$

The capture probability is calculated either from (25) or directly:

$$w'_c = T(1 - \alpha) + T(\alpha R)(1 - \alpha) \tag{31}$$
$$+ \ldots = \frac{T(1 - \alpha)}{1 - \alpha R}.$$

For the quantity α, it is natural to use the representation

$$\alpha = e^{-n\sigma_{\text{eff}}^{(1)} a}, \tag{32}$$

where $n = \sum_\nu n_\nu$ is the total concentration of nuclei in the sample being considered and $\sigma_{\text{eff}}^{(1)}$ is the effective cross section for the capture of a neutron by one nucleus.

At the same time, formulas (25)–(27) determine the exact expressions for the oscillating probabilities of reflection, transmission, and capture in the layer. The smoothing of the oscillations can be performed as follows. The oscillations of the transmission probability τ are determined by the factor

$$\frac{1}{|1 - r^2\gamma^2|^2} \tag{33}$$
$$= \sum_{l,m=0}^{\infty} r^{2l}(r^*)^{2m}|\gamma|^{2l+2m} e^{2i(l-m)\bar{k}'a}.$$

The smoothed (averaged with respect to oscillations) part of this expression is determined by the sum of $m = l$ terms; that is,

$$\left\langle \frac{1}{|1 - r^2\gamma^2|^2} \right\rangle = \frac{1}{1 - |r\gamma|^4}. \tag{34}$$

The averaging of the factor

$$\left\langle \frac{\gamma^2}{|1 - r^2\gamma^2|^2} \right\rangle = \frac{(r^*)^2|\gamma|^4}{1 - |r\gamma|^4}, \tag{35}$$

which appears in the expression for the reflection probability ρ, can be performed in a similar way. For the averaged quantities $\langle\rho\rangle$ and $\langle\tau\rangle$, we obtain

$$\langle\rho\rangle = \frac{|r|^2\left(1 + |\gamma|^4 - 2|\gamma|^4\mathrm{Re}(r^2)\right)}{1 - |r\gamma|^4}, \tag{36}$$
$$\langle\tau\rangle = \frac{|\gamma|^2|1 - r^2|^2}{1 - |r\gamma|^4}.$$

These formulas can be identically recast into the form

$$\langle\rho\rangle = R\left(1 + \frac{|\gamma|^4 T^2}{1 - |\gamma|^4 R^2}(1 + A)\right), \tag{37}$$
$$\langle\tau\rangle = \frac{|\gamma|^2 T^2}{1 - |\gamma|^4 R^2}(1 + A),$$

where

$$A \equiv \frac{2\left(|r|^2 - \mathrm{Re}(r^2)\right)}{(1 - |r|^2)^2} = \frac{\bar{k}''^2}{\bar{k}'^2}. \tag{38}$$

Suppose that the energy of an above-barrier neutron is much larger that the imaginary part of the potential; that is, $(k_\perp^2 - u'_0) \gg |u''_0|$. We then have $A \ll 1$, and the averaged reflection and transmission probabilities become

$$\langle\rho\rangle = R\left(1 + \frac{|\gamma|^4 T^2}{1 - |\gamma|^4 R^2}\right), \tag{39}$$
$$\langle\tau\rangle = \frac{|\gamma|^2 T^2}{1 - |\gamma|^4 R^2}.$$

Comparing these expressions with (29) and (30), we obtain

$$\alpha = |\gamma|^2 = e^{-2\bar{k}''a}. \tag{40}$$

Further, we compare this result with (32) and employ Eq. (14). In this way, we find that the effective cross section for capture on one nucleus can be represented in the form

$$\sigma_{\text{eff}}^{(1)} = -\frac{4\pi\langle\beta''\rangle}{\bar{k}'}, \qquad \langle\beta''\rangle = \frac{\sum_\nu n_\nu \beta''_\nu}{n}. \tag{41}$$

Thus, we conclude that, if $(k_\perp^2 - u'_0) \gg |u''_0|$, the effective cross section is indeed inversely proportional to the real part of the neutron wave vector in a medium—that is, to the group velocity of the neutron wave in matter. It is for these values of $k_\perp^2$ that the approximate equality $\bar{k}' \simeq \sqrt{k_\perp^2 - u'_0}$ follows from (15).

It should be noted that, in the small region $0 \leq k_\perp^2 - u'_0 \leq |u''_0|$ of the above-barrier neutron energies, the wave number $\bar{k}'$ can no longer be considered as a quantity that is proportional to the neutron velocity in matter. Strictly at the barrier top—that is, at $k_\perp^2 = u'_0$—we have $\bar{k}' = \sqrt{|u''_0|/2}$ in accordance with

(15). In this case, the effective cross section (41) for capture does not go to infinity, as would occur if it were inversely proportional to the neutron velocity in a medium; instead, this cross section takes some finite value referred to in [1] as a saturation value. Strictly speaking, this saturation should not be taken too literally. It occurs only if $u_0' = 0$, so that, in the limit $k_\perp \to 0$, we have

$$\sigma_{\text{eff}}^{(1)} \to \sigma_{\text{eff,max}}^{(1)} = 2\sqrt{\frac{2\pi|\langle\beta''\rangle|}{n}}. \qquad (42)$$

This is precisely the case that was considered in [1] {formula (42) coincides with formula (18) from [1]}. But if $u_0' > 0$, it turns out that, upon the transition of $k_\perp^2$ to the region of subbarrier values ($k_\perp^2 < u_0'$), the quantity $\bar{k}'$ continues decreasing according to the law [see (14)–(16)]

$$\bar{k}' = \frac{|u_0''|}{2\bar{k}''}, \qquad \bar{k}'' \simeq \sqrt{u_0' - k_\perp^2} \gg \sqrt{|u_0''|}, \qquad (43)$$

while the effective cross section accordingly continues growing. It is obvious, however, that this growth is not at all associated with radiative capture. A decrease in the factor $\alpha = |\gamma|^2$, which is determined by formulas (32) and (40), is due to the usual subbarrier suppression of the wave function.

We also note that, immediately above the barrier—that is, in the region $0 \le k_\perp^2 - u_0' \le |u_0''|$, the factor A (38) is on the order of unity, which increases the transmission probability $\langle\tau\rangle$ (37) in relation to that which is expected on the basis of relations (30) and (39). A treatment of experimental results without taking into account this fact may lead to underestimating the effective capture cross section. It is interesting to note that this occurred in the experiment reported in [4]: as the incident-neutron velocity was reduced down to a value close to the critical one (that is, corresponding to the barrier top), the effective capture cross section as extracted from the transmission probability according to (30) and (32) proved to be smaller than that which is predicted by extrapolating formula (41) to the region of low velocities.

It is intriguing that next to nothing changes for the probability $\langle\rho\rangle$ (37) of reflection from a thick layer upon taking into account the factor A. At sufficiently high above-barrier energies, the factor A does indeed tend to zero. At the same time, $\alpha = |\gamma|^2 \to 0$ near the barrier if $|u_0''|a^2 \gg 1$, so that we have $\langle\rho\rangle \to R$.

In conclusion, we present a formula for the quantity obtained by averaging, over oscillations, the probability of neutron capture in a layer:

$$\langle w_c\rangle = 1 - \langle\rho\rangle - \langle\tau\rangle \qquad (44)$$
$$= \frac{T(1-\alpha)}{1-\alpha R} - A\frac{\alpha T^2}{1-\alpha R}.$$

In just the same way as in the case of the probability of reflection, the inclusion of an additional term that is proportional to the factor A does not give anything for a thick layer if $|u_0''|a^2 \gg 1$. High above the barrier, we have $A \to 0$, while, near the barrier top, $\alpha = |\gamma|^2 \to 0$, so that $\langle w_c\rangle \to T$.

The results obtained by numerically calculating the capture probabilities for weakly and strongly absorbing substances are presented in [13]. These results provide an illustration of the above considerations on well-resolved oscillations for thin and unresolved oscillations for thick layers.

5. CONCLUSION

This study has been devoted to analyzing the radiative capture of UCNs traversing a homogeneous layer of matter. The exact expressions for the probabilities of the reflection, transmission, and capture of neutrons in a layer oscillate as functions of the neutron energy if this energy exceeds the real part of the potential describing the UCN interaction with matter. For thick layers, these oscillations are so frequent that they cannot be resolved experimentally. Therefore, the actually measured quantities appear to be the result of averaging over these oscillations.

It has been shown that the expressions obtained for the reflection, transmission, and capture probabilities from exact formulas by averaging over oscillations admit a simple interpretation in terms of the elementary probabilities R, T, and α, which is often discussed in the literature. Here, R and T are the probabilities of, respectively, reflection and transmission through the layer boundary, while α is the probability of transmission through the layer matter. The quantity α is expressed in terms of the effective cross section for neutron capture by one nucleus, this cross section being in inverse proportion to the neutron velocity in matter.

It should be emphasized that the effective capture cross section differs from the true capture cross section (8) appearing in the exact formula for the probability calculated for capture in matter by the method of summation over nuclei. The effective capture cross section appears only in analyzing observables in experiments employing thick layers and only in the above-barrier region (we note that only in the above-barrier region can we use the notion of the neutron velocity in matter). In the case of thin layers and subbarrier energies, the notion of an effective capture cross section inversely proportional to the neutron velocity in matter is meaningless.

We have also demonstrated that, in the region where the neutron energy exceeds only slightly the barrier height, the approximate formulas for the reflection, transmission, and capture probabilities should be treated with caution, because, near the barrier top, the generally omitted corrections to these formulas may become significant. This especially concerns the probability of transmission through a thick layer, since this probability vanishes very fast as the energy of the neutron incident on the layer decreases below the barrier height. The corrections growing in response to the same change in the incident-neutron energy can cause a considerable deviation of the transmission probability from the result obtained for it by a mere extrapolation from the above-barrier region.

ACKNOWLEDGMENTS

This work was supported by the Russian Foundation for Basic Research (project no. 00-15-96590).

REFERENCES

1. I. I. Gurevich and P. É. Nemirovskiĭ, Zh. Éksp. Teor. Fiz. **41**, 1175 (1961) [Sov. Phys. JETP **14**, 838 (1962)].
2. S. S. Arzumanov, L. N. Bondarenko, E. I. Korobkina, *et al.*, Pis'ma Zh. Éksp. Teor. Fiz. **65**, 3 (1997) [JETP Lett. **65**, 1 (1997)].
3. S. Arzumanov, L. Bondarenko, P. Geltenbort, *et al.*, Nucl. Instrum. Methods Phys. Res. A **440**, 690 (2000).
4. H. Rauch, M. Zawisky, Ch. Stellmach, and P. Geltenbort, Phys. Rev. Lett. **83**, 4955 (1999).
5. A. L. Barabanov and S. T. Belyaev, Eur. Phys. J. B **15**, 59 (2000).
6. J. Felber, R. Gahler, and R. Golub, Phys. Rev. Lett. **85**, 5667 (2000).
7. V. P. Alfimenkov, V. V. Nesvizhevskiĭ, A. P. Serebrov, *et al.*, Pis'ma Zh. Éksp. Teor. Fiz. **55**, 92 (1992) [JETP Lett. **55**, 84 (1992)].
8. A. V. Strelkov, V. V. Nesvizhevski, P. Geltenbort, *et al.*, Nucl. Instrum. Methods Phys. Res. A **440**, 695 (2000).
9. S. Arzumanov, S. Belyaev, L. Bondarenko, *et al.*, in *Proceedings of the 9th International Seminar on the Interaction of Neutrons with Nuclei,* Preprint No. E3-2001-192, OIYaI (Joint Inst. for Nuclear Research, Dubna, 2001), p. 397.
10. V. K. Ignatovich, *Physics of Ultracold Neutrons* (Nauka, Moscow, 1986).
11. A. L. Barabanov and S. T. Belyaev, Yad. Fiz. **62**, 824 (1999) [Phys. At. Nucl. **62**, 769 (1999)].
12. A. Steyerl, Nucl. Instrum. Methods **101**, 295 (1972).
13. T. Ya. Tudorovskiy and A. L. Barabanov, in *Proceedings of the 9th International Seminar on the Interaction of Neutrons with Nuclei,* Preprint No. E3-2001-192, OIYaI (Joint Inst. for Nuclear Research, Dubna, 2001), p. 425.

Translated by A. Isaakyan

Physics of Atomic Nuclei, Vol. 65, No. 7, 2002, pp. 1243–1258. Translated from Yadernaya Fizika, Vol. 65, No. 7, 2002, pp. 1276–1291.

90th ANNIVERSARY OF I.I. GUREVICH'S BIRTHDAY

Local-Potential Approximation for the Brueckner G Matrix and Problem of Optimally Choosing Model Subspace

M. Baldo[1], **U. Lombardo**[1], **E. E. Saperstein, and M. V. Zverev**

Russian Research Centre Kurchatov Institute, pl. Kurchatova 1, Moscow, 123182 Russia

Received June 4, 2001

Abstract—The validity of the local-potential approximation, which was proposed previously for the singlet-pairing problem in semi-infinite nuclear matter, is investigated in the Bethe–Goldstone equation for the Brueckner G matrix. For this purpose, use is made of the method developed earlier for solving this equation for a planar slab of nuclear matter in the case of a separable form of NN interaction. The $^1S_0$ singlet and the $^3S_1+{}^3D_1$ triplet channel are considered. The complete two-particle Hilbert space is split into a model and the complementary subspace that are separated by an energy E_0. The two-particle propagator is calculated precisely in the first subspace, and the local-potential approximation is used in the second subspace. With an eye to subsequently employing the G matrix to calculate the Landau–Migdal amplitude, the total two-particle energy is fixed at $E = 2\mu$, where μ is the chemical potential of the system under consideration. Specific numerical calculations are performed at $\mu = -8$ MeV. The applicability of the local-potential approximation is investigated versus the cutoff energy E_0. It is shown that, in either channel being considered, the accuracy of the local-potential approximation is rather high for $E_0 \geq 10$ MeV. *© 2002 MAIK "Nauka/Interperiodica".*

1. INTRODUCTION

The microscopic theory of nuclear matter on the basis of the Brueckner approach (see, for example, the monographs [1, 2]) made considerable advances, which were associated both with solving more precisely the Bethe–Goldstone equation, underlying Brueckner theory, and with taking into account various corrections to this approach [3, 4]. At the same time, the applications of the Brueckner method to finite nuclei were considered predominantly in the standard local-density approximation.

This approximation is fairly accurate in calculating the volume properties of nuclei, but it is absolutely inappropriate for describing their surface region, where the density $\rho(r)$ takes values at which nuclear matter is unstable. In particular, the scalar–isoscalar Landau–Migdal amplitude f sharply changes in this region from a strong attraction beyond a nucleus to a virtually zero value in its interior [5]. At the surface, there is therefore a region of ρ values at which the Pomeranchuk stability condition is violated within the local-density approximation [5, 6]. Since, within the self-consistent theory of finite Fermi systems [7, 8], it is the amplitude f that is responsible for the formation of the main (central) part of the self-consistent field in a nucleus, it is necessary to go beyond the local-density approximation in order to construct a consistent microscopic theory of nuclei.

In the past few years, a microscopic approach in nuclear theory has been developed on the basis of solving the Bethe–Goldstone equation and similar equations of many-body theory without resorting to the local-density approximation. The particular problem of microscopically calculating, within Brueckner theory, the effective pairing interaction $\mathcal{V}_{\text{eff}}$ in the $^1S_0$ channel for the semi-infinite nuclear matter was considered in [9, 10]. The effective interaction was calculated for the case that is standard for nuclear physics and which corresponds to the choice of model subspace including all two-particle states formed on the basis of single-particle states λ of negative energy ε_λ. In doing this, use was made of a separable representation of the NN potential—namely, the separable form [11, 12] of the Paris potential [13] (previously, this form was tested in calculations within the Brueckner method for infinite nuclear matter [14, 15]). The effective pairing interaction obeys an equation whose form is very close to that of the Bethe–Goldstone equation. The use of a separable NN potential made it possible to solve, by means of the technique of a mixed coordinate–momentum representation, this equation in a semi-infinite system directly without resort to any additional approximations. However, this required rather cumbersome calculations. In order to simplify the calculations, a

---

[1] Istituto Nazionale di Fisica Nucleare, Sezione di Catania, Corso Italia 57, I-95129 Catania, Italy.

new form of local approximations was found in [9, 10]. This form, called the local-potential approximation, proved to be rather accurate everywhere, including the surface region. The local-potential approximation is applied to calculating the two-particle propagator that appears in the equation for the effective interaction and which is determined in the subspace complementary to the model subspace being considered. The local-potential approximation consists in replacing the exact Bethe–Goldstone propagator in a given nonhomogeneous system by a combination of propagators for infinite nuclear matter that correspond to various values of the depth of the self-consistent mean field. Namely, the propagator taken at a fixed value of the half-sum $\mathbf{R} = (\mathbf{R}_{12} + \mathbf{R}_{34})/2$ of the c.m. coordinates of two nucleons prior to and after an interaction event is set to the propagator for infinite nuclear matter placed in the constant-depth potential $V_0 = V(\mathbf{R})$. A comparison of a direct calculation of $\mathcal{V}_{\text{eff}}$ and the results obtained within the local-potential approximation revealed [9, 10] that, even in the surface region, the accuracy of this approximation is not poorer than a few percent. The technique of the mixed representation and the method of the local-potential approximation can be straightforwardly extended to the more realistic case of a planar slab [16–18], and it is precisely the case that will be considered in this study.

The Landau–Migdal amplitude $\mathcal{F}$, which determines the effective interaction of quasiparticles near the Fermi surface, is a basic ingredient of the phenomenological theory of finite Fermi systems. Within Brueckner theory, it can be represented as

$$\mathcal{F}(\mathbf{r}_1, \mathbf{r}_2, \mathbf{r}_3, \mathbf{r}_4) = \sqrt{Z(\mathbf{r}_1)Z(\mathbf{r}_2)Z(\mathbf{r}_3)Z(\mathbf{r}_4)} \quad (1)$$
$$G(\mathbf{r}_1, \mathbf{r}_2, \mathbf{r}_3, \mathbf{r}_4; E = 2\mu),$$

where $Z(\mathbf{r})$ is a coordinate-dependent renormalization factor in the Green's function and the G matrix is determined by solving the Bethe–Goldstone equation. From the computational point of view, the problem of calculating the amplitude $\mathcal{F}$ on the basis of Eq. (1) is much more involved than the problem of determining the effective pairing interaction. First of all, we must consider at least one additional channel, the ${}^3S_1$ triplet channel, which is coupled to the ${}^3D_1$ channel and for which the calculations are more complicated than for the ${}^1S_0$ singlet channel. But the most serious complication stems from the need for taking into account nonvanishing values of the total-momentum projection $P_\perp$ onto the planar-slab plane—one can obviously set $P_\perp = 0$ in the problem of pairing, but, in calculating the amplitude $\mathcal{F}$ on the basis of expression (1), there arises an integral with respect to $P_\perp$ over the region $P_\perp \le 2k_{\text{F}}$, where k_{F} is the Fermi momentum within the planar slab. Although it is possible, in principle, to construct a direct numerical solution to the problem, this would require very cumbersome calculations because of the complications listed above. Therefore, the need for a sufficiently accurate approximate method for calculating the G matrix is even more acute here than in the problem of pairing. For this purpose, it is natural to analyze the local-potential approximation, which considerably simplifies relevant calculations and which yielded precise results in the close problem of microscopically calculating $\mathcal{V}_{\text{eff}}$. In the case of the ${}^1S_0$ channel, the accuracy of the local-potential approximation in solving the Bethe–Goldstone equation for the G matrix is nearly identical to that in calculating the effective pairing interaction. Indeed, the effects of superfluidity in the complementary subspace were disregarded in [9, 10], as is usually done in the pairing problem. This having been done, the corresponding two-particle propagators in this subspace—and it is the subspace where the local-potential approximation is used—coincide for the two problems being considered. As to the triplet channel, it is not obvious in advance whether the local-potential approximation is applicable to this case, and it is the main objective of the present study to explore precisely this question.

In the case of the Bethe–Goldstone equation, it does not seem that there is any gain from introducing an effective interaction. Upon splitting the full Hilbert space S into a model subspace S_0 and the complementary subspace S', $S = S_0 + S'$, it is more natural to use the local-potential approximation in the subspace S' directly for the propagator. In accordance with this splitting, the two-particle propagator A in the Bethe–Goldstone equation is also represented as the sum $A = A_0 + A'$. The propagator in the model subspace, A_0, must be calculated precisely, while the second term A' is assumed to be evaluated within the local-potential approximation. It is obvious that, in the propagator, quantum effects and effects of finite dimensions are due to the contribution of single-particle states near the Fermi surface. In the propagator A, contribution is enhanced owing to the smallness of the corresponding energy denominators. The contributions in question induce long-range terms in A, and it is therefore necessary to take them into account precisely. On the contrary, the contribution of any individual term from states occurring far off the Fermi surface is small and only the sum of a large number of such terms is significant. They induce short-range terms in A, and one can try to use some forms of local approximations—in particular, the local-potential approximation—in order to calculate the contribution of these terms. It is obvious that the applicability of the local-potential approximation must depend on the choice of model space S_0. The vaster the subspace S_0, the greater the number of dangerous terms that are taken precisely into account and, hence, the higher the accuracy of the local-potential approximation. We use this simple physical idea to establish the criterion of applicability of the local-potential approximation. We will consider a sequence of model subspaces $S_0(E_0)$ depending on the cutoff energy E_0 and including all single-particle states of energies $\varepsilon_\lambda < E_0$. We note that the model subspace the we used previously in the problem of pairing corresponds to $E_0 = 0$. The accuracy of the local-potential approximation must become higher with increasing cutoff energy E_0. We will deem that the local-potential approximation is workable from the cutoff-energy value E_0 if a further increase in E_0 would not change the G matrix within a preset accuracy.

The ensuing exposition is organized as follows. In Section 2, we present the Bethe–Goldstone equation for a planar slab of nuclear matter in the case of separable NN forces. In Section 3, we consider the splitting of the full Hilbert space into the model subspace characterized by a cutoff energy E_0 and the complementary subspace. At a fixed value of E_0, we introduce the local-potential approximation in order to calculate the Bethe–Goldstone propagator in the complementary subspace. In Section 4, we analyze the accuracy of the local-potential approximation directly in calculating the Bethe–Goldstone propagators versus E_0. In Section 5, we explore the applicability of the local-potential approximation in solving the Bethe–Goldstone equation for the G matrix in the $^1S_0$ singlet channel at the same values of E_0. In Section 6, a similar analysis is performed for the $^3S_1 + {}^3D_1$ triplet channel. Section 7 contains general conclusions and a brief summary.

2. BETHE–GOLDSTONE EQUATION IN PLANAR-SLAB GEOMETRY

We consider the Bethe–Goldstone equation for a planar nuclear-matter slab of thickness $2L$ in a one-dimensional potential well $V(x)$ symmetric with respect to the point $x = 0$. This system is fairly simple, but it represents a rather realistic model of heavy nuclei. A specific form of the potential $V(x)$ is immaterial for general relations. The use of a separable form of a realistic NN potential is an approximation that significantly simplifies the problem and makes it possible to reduce the Bethe–Goldstone equation to a set of one-dimensional integral equations. A method for solving the Bethe–Goldstone equation for such a model was developed in [18] by applying the technique of a mixed coordinate–momentum representation. Here, we will employ this method; therefore, we present the majority of the equations in a condensed symbolic form, referring the interested reader for details to [18]. Only some relations that are necessary for understanding the results of the calculations will be given in an expanded form.

As was mentioned in the Introduction, we will use below the G matrix to calculate the Landau–Migdal amplitude, which describes the effective quasiparticle interaction near the Fermi surface. From the outset, we will therefore consider the Bethe–Goldstone equation corresponding to the interaction of two nucleons at the Fermi surface—that is, at the energies $\varepsilon_\lambda = \mu$, where μ is the chemical potential of the system under consideration. In the symbolic form, this equation can be written as

$$G(E) = \mathcal{V} + \mathcal{V}A(E)G(E), \qquad (2)$$

where $\mathcal{V}$ is the free NN potential, $E = 2\mu$, and A is the Bethe–Goldstone propagator. The propagator is determined by the integral of the product $(\mathcal{G}^p(E/2+\varepsilon)\mathcal{G}^p(E/2-\varepsilon))$ of two particle components of the single-particle Green's function with respect to the relative energy ε. It is well known from [1, 2] that the propagator A in the Bethe–Goldstone equation does not involve the contribution $(\mathcal{G}^h\mathcal{G}^h)$ from the hole components of the Green's functions.

The Bethe–Goldstone equation with realistic NN potentials is characterized by a poor convergence of relevant integrals with respect to intermediate momenta because of the presence of a strong repulsive core in these potentials. In order to improve the convergence, it is useful to renormalize Eq. (2) with the aid of the T matrix taken for free NN scattering off the mass shell at the negative energy $E = 2\mu$. The T matrix obeys the Lippmann–Schwinger equation

$$T(E) = \mathcal{V} + \mathcal{V}A^{\mathrm{fr}}(E)T(E), \qquad (3)$$

where $A^{\mathrm{fr}}(E)$ is the propagator for two free nucleons whose total energy is E.

The renormalized Bethe–Goldstone equation has the form

$$G = T + T(A - A^{\mathrm{fr}})G. \qquad (4)$$

As in [18], we use the separable version introduced in [11, 12] for the Paris NN potential [13]. For the $^1S_0$ channel, it has the (3×3) form

$$\mathcal{V}(\mathbf{k}, \mathbf{k}') = \sum_{i,j=1}^{3} \lambda_{ij} g_i(k^2) g_j(k'^2). \qquad (5)$$

For the $^3S_1 + {}^3D_1$ triplet channel, there is a similar 4×4 expansion, where the form factors g_i become operators in orbital-angular-momentum space. We can formally employ the form (5) with the substitution

$g_i(k^2) \to \hat{g}_i(k^2)$, where the column $\hat{g}_i$ has two components,

$$\hat{g}_i(k^2) = \begin{pmatrix} g_i^{L=0}(k^2) \\ g_i^{L=2}(k^2) \end{pmatrix}, \tag{6}$$

with L being the relative orbital angular momentum in the c.m. frame.

Now, we consider the $S = 0$ singlet channel in more detail.

The separable form (5) of the NN potential in Eqs. (2) and (3) leads to similar expansions for the G matrix,

$$G(k_\perp^2, k_\perp'^2, \mathbf{P}_\perp; x_1, x_2, x_3, x_4; E) \tag{7}$$
$$= \sum_{ij} G_{ij}(X, X'; E, \mathbf{P}_\perp) g_i(k_\perp^2, x) g_j(k_\perp'^2, x'),$$

and for the T matrix,

$$T(k_\perp^2, k_\perp'^2, \mathbf{P}_\perp; x_1, x_2, x_3, x_4; E) \tag{8}$$
$$= \sum_{ij} T_{ij}(X-X'; E, \mathbf{P}_\perp) g_i(k_\perp^2, x) g_j(k_\perp'^2, x').$$

Here, we have introduced the form factor $g_i(k_\perp^2, x)$ in the mixed representation. This form factor is defined as the inverse Fourier transform of the quantity $g_i(k_\perp^2 + k_x^2)$ in the variable k_x; the corresponding analytic expressions can be found in [9] for the singlet and in [17] for the triplet channel. In expressions (7) and (8), use has been made of the obvious notation for the c.m. coordinates and for the relative coordinates in the x-axis direction. Of course, the coefficients T_{ij} in the T-matrix expansion depend only on the difference $t = X - X'$ of the c.m. coordinates. In the direction orthogonal to the x axis, we have introduced the total and the relative momentum (($\mathbf{P}_\perp$) and ($\mathbf{k}_\perp$), respectively).

The substitution of expansions (7) and (8) into Eq. (4) leads to the set of the one-dimensional integral equations

$$G_{ij}(X, X'; E, \mathbf{P}_\perp) = T_{ij}(X-X'; E, \mathbf{P}_\perp) \tag{9}$$
$$+ \sum_{lm} \int dX_1 dX_2 T_{il}(X - X_1; E, \mathbf{P}_\perp)$$
$$\times \delta B_{lm}(X_1, X_2; E, \mathbf{P}_\perp) G_{mj}(X_2, X'; E, \mathbf{P}_\perp),$$

where

$$\delta B_{lm} = B_{lm} - B_{lm}^{\mathrm{fr}} \tag{10}$$

is the difference of the convolution B_{lm} of the two-particle propagator A with the form factors g_l and g_m and the analogous convolution B_{lm}^{fr} for the free propagator A^{fr}. The explicit expression for B_{lm} has the form

$$B_{lm}(X, X'; E, \mathbf{P}_\perp) \tag{11}$$
$$= \sum_{nn'} \int \frac{d\mathbf{k}_\perp}{(2\pi)^2} \frac{(1 - n_\lambda)(1 - n_{\lambda'})}{E - P_\perp^2/4m - \varepsilon_n - \varepsilon_{n'} - k_\perp^2/m}$$
$$\times g_{nn'}^l(k_\perp^2, X)\, g_{n'n}^m(k_\perp^2, X').$$

Here, we have used the following condensed notation: $\lambda = (n, \mathbf{p}_\perp)$, $\lambda' = (n', \mathbf{p}'_\perp)$, $\mathbf{p}_\perp = \mathbf{P}_\perp/2 + \mathbf{k}_\perp$, $\mathbf{p}'_\perp = \mathbf{P}_\perp/2 - \mathbf{k}_\perp$, and $n_\lambda = \theta(\mu - \varepsilon_\lambda)$, where $\varepsilon_\lambda = \varepsilon_n + p_\perp^2/2m$, ε_n standing for the eigenenergies of the one-dimensional Schrödinger equation in a given potential $V(x)$. The corresponding eigenfunctions $y_n(x)$ (they are chosen to be real-valued) appear in the matrix elements of the form factors; that is,

$$g_{n,n'}^l(k_\perp^2, X) \tag{12}$$
$$= \int dx\, g_l(k_\perp^2, x_{12})\, y_n(X + x/2) y_{n'}(X - x/2).$$

We note that, in fact, the symbolic sum over nn' in (11) includes both actual summation over discrete states and integration over the continuous spectrum with the standard substitution $\sum_n \to \int dp/2\pi$.

In the singlet channel, the Bethe–Goldstone equation for the G matrix coincides with the equation for the effective pairing interaction [9, 10]. Owing to this, it can be solved by the methods developed in [9, 10]. In particular, it is convenient to single out the delta-function-like (in the variables X and X') Born term $\mathcal{V}$ in the G matrix; that is,

$$G = \mathcal{V} + \delta G. \tag{13}$$

From (2), it can straightforwardly be found that the correlation part δG of the total G matrix satisfies the equation

$$\delta G = \mathcal{V} A \mathcal{V} + \mathcal{V} A \delta G. \tag{14}$$

The Born term must similarly be isolated in the T matrix:

$$T = \mathcal{V} + \delta T. \tag{15}$$

As a result, the renormalized Bethe–Goldstone Eq. (4) takes the form

$$\delta G = F + T(A - A^{\mathrm{fr}})\delta G, \tag{16}$$

where the nonhomogeneous term can be represented as

$$F = \delta T + T(A - A^{\mathrm{fr}})\mathcal{V}. \tag{17}$$

For Eqs. (16) and (17), the explicit form similar to (9) is quite obvious. For the planar-slab geometry being considered, the procedure for numerically solving Eq. (16) can be simplified by using parity conversation under the inversion $x \to -x$. The set of single-particle eigenfunctions y_n can be broken down into the subset of even and the subset of odd eigenfunctions (y_n^+ and y_n^-, respectively). In the equations under consideration, the two-particle propagator therefore appears to be the sum

$$A = A^+ + A^- \tag{18}$$

of even and odd components. The first term A^+ arises from those terms of the sum in (11) that involve (λ, λ') states of the same parity, while the second term A^- arises from opposite-parity states. Since the NN potential $\mathcal{V}$ conserves parity, the propagators A^+ and A^- are not mixed in the integral term of the Bethe–Goldstone equation. Therefore, the correlation part of the G matrix is also the sum of even and odd components,

$$\delta G = \delta G^+ + \delta G^-, \tag{19}$$

the equations for which decouple

$$\delta G^\pi = \mathcal{V} A^\pi \mathcal{V} + \mathcal{V} A^\pi \delta G^\pi, \tag{20}$$

with $\pi = +, -$.

It is obvious that the integral Eqs. (20) can be reduced to a form that involves only positive x, whereby the relevant calculations are considerably reduced. These equations must be solved for both values of π, whereupon the total G matrix can be found from relations (13) and (19).

Upon the substitution $g_i(k^2) \to \hat{g}_i(k^2)$, all of the equations given above remain formally valid for the $S = 1$ triplet channel. As a matter of fact, it is the convolution integral (11) where the most pronounced changes occur. For the triplet channel, it takes the form

$$B_{lm}^{S=1}(X, X'; E, \mathbf{P}_\perp) = \sum_{nn'} \int \frac{d\mathbf{k}_\perp}{(2\pi)^2} \frac{(1 - n_\lambda)(1 - n_{\lambda'})}{E - P_\perp^2/4m - \varepsilon_n - \varepsilon_{n'} - k_\perp^2/m} \tag{21}$$
$$\times \left(g_{nn'}^{(0)l}(k_\perp^2, X)\, g_{n'n}^{(0)m}(k_\perp^2, X') + g_{nn'}^{(2)l}(k_\perp^2, X)\, g_{n'n}^{(2)m}(k_\perp^2, X') \right).$$

We also note that, now, all multipole expansions of the form (7) or (8) involve 2×2 matrices. By way of example, we present explicitly the components of such an expansion for the G matrix. We have

$$G^{LL'}(k_\perp^2, k_\perp'^2, \mathbf{P}_\perp; x_1, x_2, x_3, x_4; E) \tag{22}$$
$$= \sum_{ij} G_{ij}(X, X'; E, \mathbf{P}_\perp) g_i^{(L)}(k_\perp^2, x) g_j^{(L')}(k_\perp'^2, x'),$$

where L and L' are equal to 0 or 2.

3. CHOICE OF MODEL SPACE AND LOCAL-POTENTIAL APPROXIMATION FOR THE BETHE–GOLDSTONE PROPAGATOR

The most serious computational problems in solving the Bethe–Goldstone equation for inhomogeneous systems arise in calculating the propagators given by (11) and (21). It is precisely in order to simplify this calculation that the full Hilbert space S is split into a model subspace $S_0(E_0)$ and the complementary subspace $S'(E_0)$ $[S = S_0 + S']$, the local-potential approximation being further used in the complementary subspace. We briefly present arguments in favor of the use of this approximation. The subspace $S_0(E_0)$ includes all two-particle (λ, λ') states, where the single-particle energies ε_λ and $\varepsilon_{\lambda'}$ are both small: $\varepsilon_\lambda, \varepsilon_{\lambda'} < E_0$.[2] In the complementary subspace $S'(E_0)$, at least one of these energies is large: $\max(\varepsilon_\lambda, \varepsilon_{\lambda'}) > E_0$. In the case of the model subspace, the contribution of each individual two-particle (λ, λ') state to the sum in (11) or in (21) is enhanced in relation to the analogous contribution of states from the complementary subspace owing to the smallness of the energy denominator.

By an individual state, we mean here fixed values of n and n' and a narrow interval of integration with respect to the variable $k_\perp$. Such individual contributions induce long-range components of the propagators A in the Bethe–Goldstone equation [18]. These components decrease slowly with increasing distance between the points X and X', so that they must be calculated precisely in the finite system being considered. On the contrary, no individual (λ, λ') state is insignificant by itself in the case of the complementary subspace. Only the sum of a large number of such states, which corresponds to integration over a wide interval of $k_\perp$, contributes noticeably to A. The corresponding components of the Bethe–Goldstone propagator have pronounced maxima at close values of the nucleon coordinates and are determined primarily by

---

[2] As a matter of fact, it is the differences $\varepsilon_\lambda - \mu$ and $\varepsilon_{\lambda'} - \mu$ appearing in the denominators of the propagators in (11) and (21) that are small at the total energy equal to $E = 2\mu$.

the local properties of the system under consideration [17]. Therefore, it is reasonable to use some version of local approximations in calculating these components. In the case of the Bethe–Goldstone equation, the use of the local-potential approximation seems more natural than the use of the local-density approximation, since the Bethe–Goldstone propagator in the vicinity of a given point X is determined directly by the potential well $V(X)$ rather than by the density $\rho(X)$. At the same time, there is no simple local relation between $\rho(X)$ and $V(X)$ in the surface region.

The partition of the Hilbert space, $S = S_0 + S'$, leads to the representation of the Bethe–Goldstone propagator as the sum

$$A = A_0 + A', \tag{23}$$

where the term A_0 involves all (λ, λ') states that belong to the model subspace, while A' involves all of the remaining states. In accordance with the above qualitative analysis, we calculate the propagator A_0 for the model subspace precisely and use the local-potential approximation for the residual term A'. It is obvious that the accuracy of the local-potential approximation becomes higher as the model subspace S_0 is expanded. Indeed, the local-potential approximation is obviously exact in the limit $E_0 \to \infty$, since all integrals in (11) and (21) converge. We will say that the local-potential approximation has the required accuracy at some value of E_0 if the G matrix does not change in response to a further increase in E_0.

Basically, the scheme of applying the local-potential approximation is the same for both channels being considered and is very close to that used in the pairing problem, which was studied in [9, 10], where use was made of the model subspace corresponding to the choice of $E_0 = 0$. At fixed values of the c.m. coordinates X_{12} and X_{34}, the convolution integral in (11) for $S = 0$ [or in (21) for $S = 1$] is replaced by the corresponding integral for nuclear matter placed in a potential well of constant depth equal to $V_0 = V(X)$, where $X = (X_{12} + X_{34})/2$, the latter integral being dependent only on the difference $t = X_{12} - X_{34}$ of the c.m. coordinates; that is,

$$\begin{aligned} &B^{\mathrm{LPA}}_{lm}(X_{12}, X_{34}; E, \mathbf{P}_\perp) \\ &= B^{\mathrm{inf}}_{lm}(V[X], t; E, \mathbf{P}_\perp). \end{aligned} \tag{24}$$

In our specific calculations, we used the Woods–Saxon potential having the depth of $V_0 = 50$ MeV, the diffuseness of $d = 0.65$ fm, and the half-width of $L = 8$ fm, which are typical of heavy nuclei. In order to calculate the propagators in the local-potential approximation at fixed values of the chemical potential μ, the transverse momentum $\mathbf{P}_\perp$, and the cutoff energy E_0, we took the sequence of the potential depths $V_n = \delta V \cdot (n-1)$ with the step of $\delta V = 2$ MeV in depth. For this set of V_n, we calculated the basis array of the propagators $B^{\mathrm{inf}}_{lm}([V_n], t; E = 2\mu, \mathbf{P}_\perp)$ for nuclear matter. For a fixed coordinate mesh X_k, the elements $B^{\mathrm{LPA}}_{lm}(X_i, X_k)$ of the propagator matrix in the local-potential approximation were determined as follows. First, we found the depth of the Woods–Saxon potential well, $V(X_0 = (X_i + X_k)/2)$. At fixed $t = |X_i - X_k|$, we then constructed the propagator in the local-potential approximation by means of linear interpolation between two neighboring values $B^{\mathrm{inf}}_{lm}([V_n], t; E, \mathbf{P}_\perp)$ and $B^{\mathrm{inf}}_{lm}([V_{n+1}], t; E, \mathbf{P}_\perp)$ under the condition that the inequality $V_n < V(X_0) < V_{n+1}$ is satisfied. By definition, the convolution integral B^{fr}_{lm} for the free propagator A^{fr} coincides with $B^{\mathrm{inf}}_{lm}([V_1 = 0], t; E, \mathbf{P}_\perp)$. A more detailed description of the computational procedure based on the local-potential approximation is given in [9, 10, 18].

4. ANALYSIS OF THE ACCURACY OF THE LOCAL-POTENTIAL APPROXIMATION FOR BETHE–GOLDSTONE PROPAGATORS

The total transverse momentum $P_\perp$ appears as a parameter in the general Bethe–Goldstone equations for a planar slab that were considered above. As has already been mentioned, the dangerous terms in the propagators [more precisely, the convolution integrals in (11) and (21)] that belong to the model subspace and which must be treated precisely arise because of the smallness of the corresponding energy denominators in the sums on the right-hand sides of Eqs. (11) and (21). It is obvious that they become more dangerous as the quantity $P_\perp$ decreases. It follows that the case of $P_\perp = 0$ is the most critical from the point of view of applicability of the local-potential approximation. For this reason, we will investigate precisely this case, which is the least favorable for the application of the local-potential approximation. We restrict our consideration to the single chemical-potential value of $\mu = -8$ MeV, which is characteristic of β-stable nuclei. Thus, we set $E = -16$ MeV and $P_\perp = 0$ (below, these parameters will be omitted, as a rule) in all the equations of the preceding section.

As was mentioned above, Eq. (20) is solved in practice at a fixed parity π, in which case this equation involves the propagator A^π whose parity π is also fixed. As a matter of fact, we are dealing with a renormalized analog of Eq. (20) [according to (16)], where there appears the difference (10) of the convolutions of the exact $[B_{lm}(X, X')]$ and the free $[B^{\mathrm{fr}}_{lm}(X - X')]$ propagator. This difference is more convenient for a

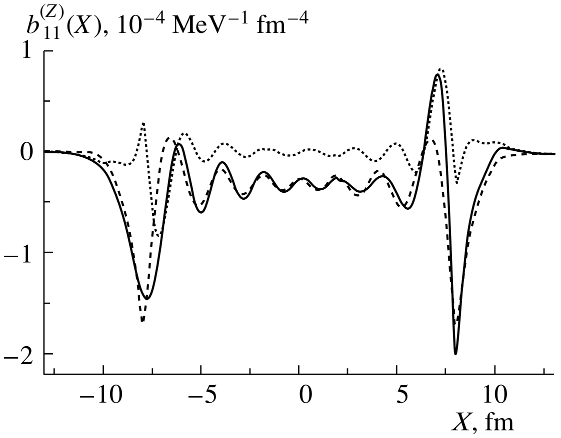

Fig. 1. Even (dashed curve) and odd (dotted curve) profile functions for the component $b_{11}^{(Z)}(X)$ in the singlet channel at $Z = 8$ fm. The solid curve represents their sum.

graphical analysis as well, because very sharp maxima that are present in each individual convolution at the coinciding points $X = X'$ are compensated in it.

Let us begin our analysis by considering the $S = 0$ singlet channel. The general idea of the properties of the propagator can be inferred from the profile functions

$$b_{lm}^{(Z)}(X) = \delta B_{lm}(X, X' = Z). \tag{25}$$

As will be shown below, the profile functions exhibit the most characteristic behavior if the variable Z is taken near the planar-slab surface. By way of example, the even $[b^+(X)]$ and the odd $[b^-(X)]$ profile functions, along with their sum $b(X) = b^+(X) + b^-(X)$, are depicted in Fig. 1 for the $lm = 11$ components at $Z = 8$ fm. The calculations were performed for the model subspace corresponding to $E_0 = 0$. The functions b^+ and b^- both have pronounced maxima at $X = Z$. Obviously, they have the identical (in absolute value) maxima at $X = -Z$. It is interesting to note that the total profile function $b(X)$ has a pronounced maximum at $X = -Z$, although its magnitude is somewhat less than the magnitude of the main maximum at $X = Z$. Such behavior of the propagator for a finite system at large $|X - Z|$ has nothing in common with the asymptotic reduction of the propagator for an infinite system at large $|X - Z|$ [18]. In a finite system, the long-range interaction is a purely quantum effect that is associated with the contribution of states belonging to the model subspace.

We have calculated the propagators for a few values of the cutoff energy ($E_0 = 0, 10, 20$ MeV) and analyzed the dependence of the results on this parameter. From Fig. 1, we can see that, although there are considerable numerical distinctions between the even

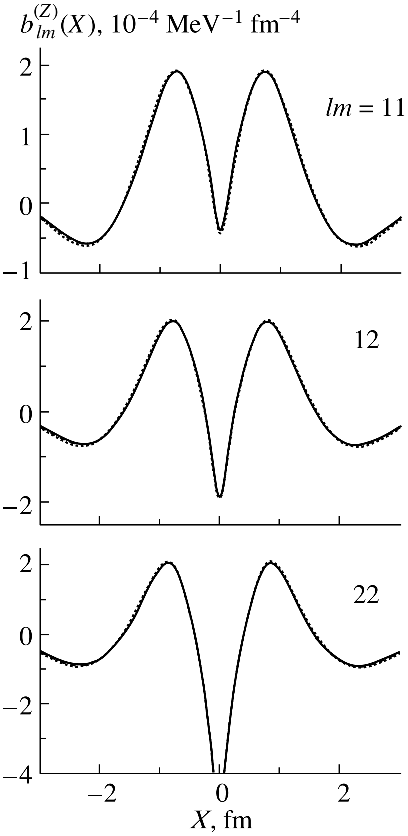

Fig. 2. Even profile functions for the propagators $b_{lm}^{(Z)}(X)$ in the singlet channel at $Z = 0$ for $E_0 =$ (dotted curves) 0, (dashed curves) 10, and (solid curves) 20 MeV.

and the odd profile functions, they display qualitatively similar types of behavior: they have pronounced maxima at $X = Z$ and oscillate, decreasing in magnitude with increasing $|X-Z|$. In order to avoid encumbering the article with unnecessary details, we therefore present only the even profile functions $b_{lm}^{(Z)}(X)$ of the propagators at $Z = 0$ and $Z = 8$ fm and only at three "main" values $lm = 11, 12, 22$.[3] These functions are shown in Figs. 2 and 3.

For the purposes of a quantitative comparison of the values of the propagator at different values of E_0, it is useful to compute, in addition, the zeroth moments of the difference propagator,

$$\bar{b}_{lm}(X) = \int\limits_{-\infty}^{\infty} dt\, \delta B_{lm}(X, X + t). \tag{26}$$

They are presented in Fig. 4 for the same three values of lm. An analysis of Figs. 2–4 reveals that the

---

[3] It was shown in [16, 17] and will be discussed in Section 5 that, in the singlet channel, the components carrying the subscript 3 are virtually insignificant.

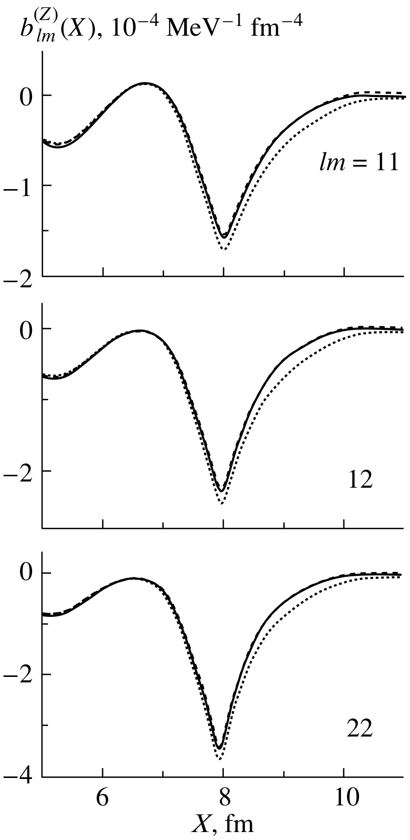

Fig. 3. As in Fig. 2, but for $Z = 8$ fm.

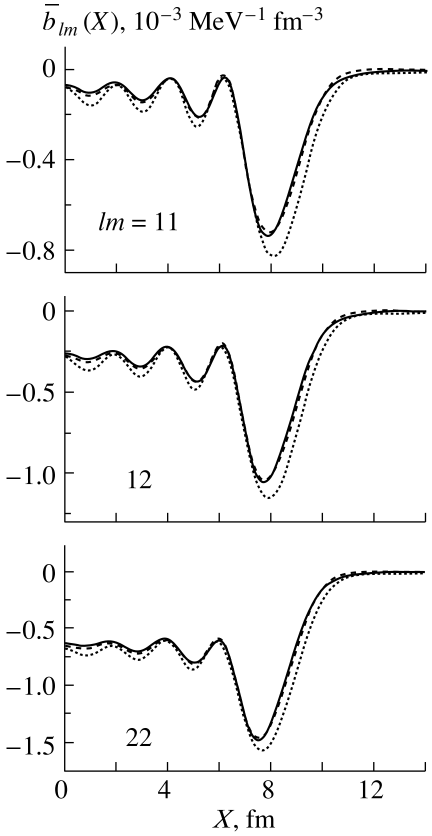

Fig. 4. Zeroth moments $\bar{b}_{lm}(X)$ of the difference propagators at $E_0 = 0$, 10, and 20 MeV (the notation for the curves is identical to that in Fig. 2).

variations in the propagator are insignificant even in response to increasing E_0 from 0 to 10 MeV; as E_0 is increased further up to 20 MeV, they become nearly negligible. We can conclude that, for the singlet channel, the local-potential approximation can reliably be used from $E_0 = 10$ MeV, but it must be fairly accurate even at $E_0 = 0$. We note that all these conclusions are also valid for odd profile functions and for "small" components carrying the subscript 3. A more definitive conclusion on the degree of accuracy of the local-potential approximation could be drawn from an analysis of the G matrix (see next section).

Let us now proceed to consider the $S = 1$ triplet channel. It will be shown in Section 6 that almost all components of the propagator (there are now ten of them) are equally important in this case. Nevertheless, we restrict ourselves to some typical components in order to avoid encumbering the presentation. A few profile functions (as before, only the even components and at the same values of E_0 as in the singlet case) are shown in Figs. 5 and 6. For $Z = 0$, we present only two components since, for all of the remaining components, the situation is analogous: the distinctions between all three curves corresponding to the different values of E_0 are negligible. In the case of $Z = 8$ fm, the situation is more complicated—along with the components for which the effect of E_0 on the profile function is also very small, there are such for which the distinctions between the three curves are significant. In Fig. 6, there are examples of both the former and the latter. It can be seen, however, that, in the worst case ($lm = 23$), where the distinction between the profile functions at $E_0 = 0$ and 10 MeV is large, the further increase in the cutoff energy up to $E_0 = 20$ MeV leads to only an insignificant change in $b(X)$. We also note that even such noticeable variations in the propagator with increasing E_0 are strongly leveled out in calculating the zeroth moments, which are given in Fig. 7 for five values of lm, yet another "bad" value of $lm = 22$ being added here. An analysis of the curves in Figs. 5–7 shows that, just as in the singlet channel, one may hope for a high precision of the local-potential approximation at the cutoff energy E_0 of 10 to 20 MeV. At the same time, the applicability of the local-potential approximation at $E_0 = 0$ is questionable, in contrast to what we have had in the singlet case. As in the case of the singlet channel, only upon analyzing the G matrix, which is directly related to physical observables of interest, can one draw definitive conclusions on the degree of pre-

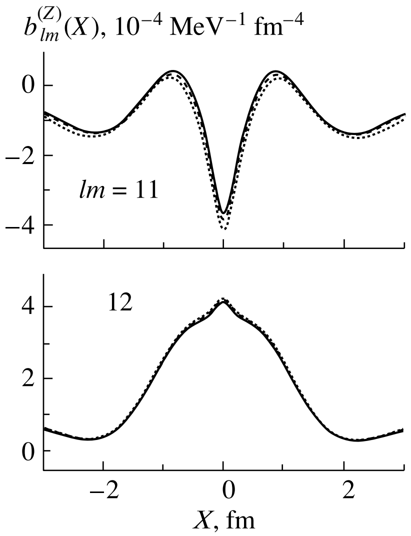

Fig. 5. As in Fig. 2, but for the triplet channel.

cision of the local-potential approximation. Indeed, the variation of the propagator in response to changes in E_0 can either grow or decrease in solving Eq. (14) for the correlation part of the G matrix. As will be seen below, it is rather the latter that occurs. An analysis of the G matrix in the triplet channel is presented in Section 6.

5. LOCAL-POTENTIAL APPROXIMATION FOR THE *G* MATRIX IN THE SINGLET CHANNEL

As was noted above, the Bethe–Goldstone Eq. (14) for the correlation part of the G matrix decouples in parity $\pi = +, -$. Therefore, we consider Eq. (20), which is written for a preset value of π and which is defined only for positive x. Upon finding the convolution integrals (11) and the analogous integrals for the free propagator A^{fr}, the kernel of Eq. (16) and the nonhomogeneous term (17) can be determined by means of straightforward integration. Further, we obtain a set of integral equations for six independent components $\delta G_{ij}^{\pi}(X, X')$ [analogous to those in (9)]; these equations can be solved numerically [9, 17]. Finally, the total correlation part of the G matrix with the components $\delta G_{ij}(X, X')$ is derived from (19), while the total G matrix having the components $G_{ij}(X, X')$ is found from (13). They differ by a trivial delta-function term:

$$\delta G_{ij}(X, X') = G_{ij}(X, X') - \lambda_{ij}\delta(X - X'). \quad (27)$$

Since the observables of interest involve the total G matrix rather than its even or odd components individually, it is natural to analyze precisely this matrix and not its even components, as was done

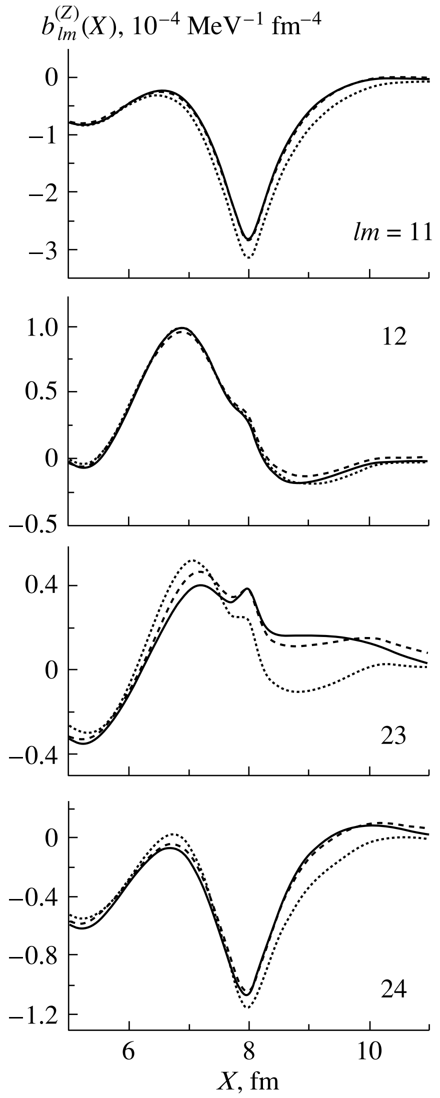

Fig. 6. As in Fig. 2, but at $Z = 8$ fm for the triplet channel.

in the case of the propagators. As to the delta-function term (27), its removal makes the G matrix more convenient for a graphical representation and analysis. For this reason, we will usually consider the correlation part of the G matrix rather than its total form. Prior to proceeding to analyze the results of the calculations, we would like to make yet another comment. Following [9, 10], we changed the original normalization [11, 12] of the expansion in (5) in such a way as to ensure fulfillment of the equality $g_i(0) = 1$. In this case, the absolute values of the coefficients λ_{ij} provide direct information about the strength of the corresponding terms in the NN potential. They are as follows (in GeV fm^3): $\lambda_{11} = -3.659, \lambda_{12} = 2.169, \lambda_{22} = -1.485,\ \ \lambda_{13} = -0.0236, \lambda_{23} = 0.0576$, and $\lambda_{33} = 0.0172$. As we can see, the strength of the “large” components, which involve only the

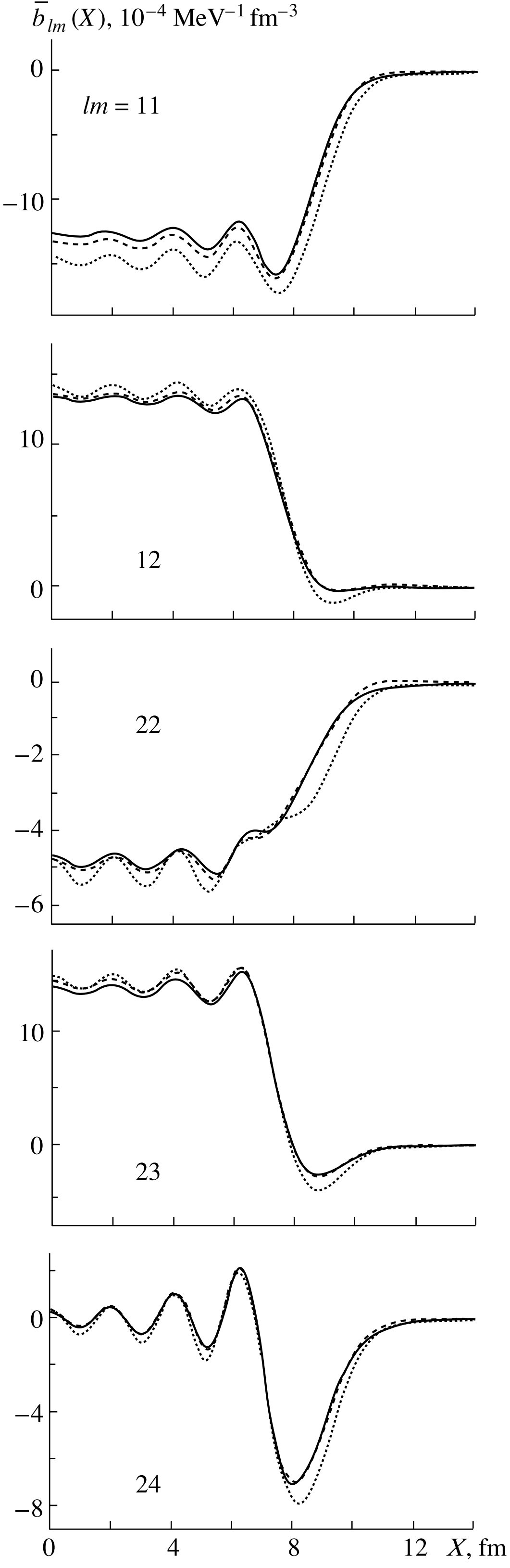

Fig. 7. As in Fig. 4, but for the triplet channel.

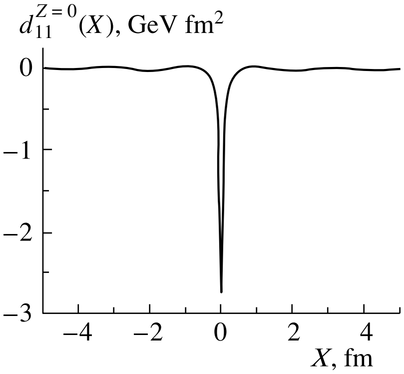

Fig. 8. Profile function $d_{11}^{Z=0}(X)$ in the singlet channel at $E_0 = 0$.

subscripts $i = 1, 2$, is two orders of magnitude greater than the strength of the "small" components, which carry the superscript $i = 3$. The small components are significant only at high momenta that implicitly appear in the Bethe–Goldstone equation or in the Lippmann–Schwinger equation because a relatively large value of the form factor $g_3(k^2)$ partly compensates for the smallness of these components. Indeed, this form factor grows with increasing k, while the first two form factors decrease [11]. In calculating the Landau–Migdal amplitude and other observable nuclear features, there appear G-matrix elements at relatively low momenta of $k \simeq k_\mathrm{F}$. In this case, the contribution of the small components is negligible. In a qualitative analysis, we therefore focus on the large components, but, of course, we take into account all λ_{ik} terms in our calculations.

We have calculated the G matrix for the same values of the cutoff energy as above ($E_0 = 0, 10, 20$ MeV) and analyzed the dependence of the G matrix on this parameter. To present the results, we depict, as was done in analyzing the propagators, the profile functions for the correlation term in the G matrix,

$$d_{ij}^{(Z)}(X) = \delta G_{ij}(X, X' = Z). \tag{28}$$

By way of example, the profile function $d_{11}^{Z=0}(X)$ is displayed in Fig. 8 for the case of the model subspace corresponding to the cutoff energy of $E_0 = 0$. We can see that, even upon the removal of the delta-function Born term from the G matrix, the remaining part has a sharp peak at the point $X = Z$. On the same scale, the analogous curves obtained at $E_0 = 10$ and 20 MeV will be virtually indistinguishable from the curves plotted for $E_0 = 0$. In order to make the distinctions visible, one must magnify the scale, cutting off, if necessary, the central maximum. For the $ij = 11, 12, 22$ "large" components, the profile functions magnified in this way are given in Fig. 9 for $Z = 0$ and

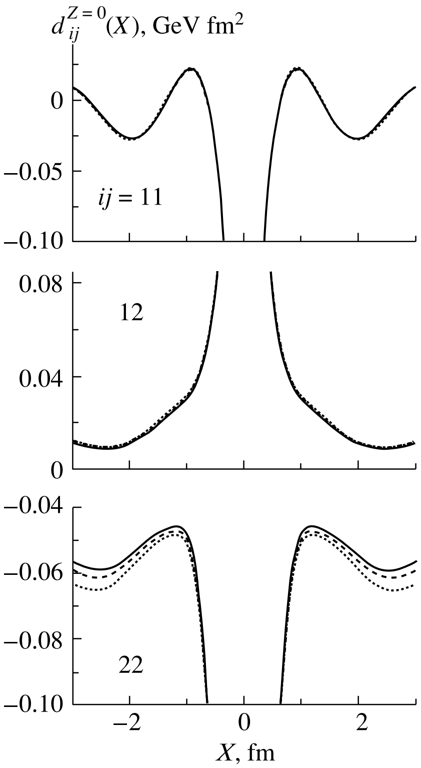

Fig. 9. Profile functions $d_{ij}^{Z=0}(X)$ in the singlet channel at $E_0 =$ (dotted curves) 0, (dashed curves) 10, and (solid curves) 20 MeV.

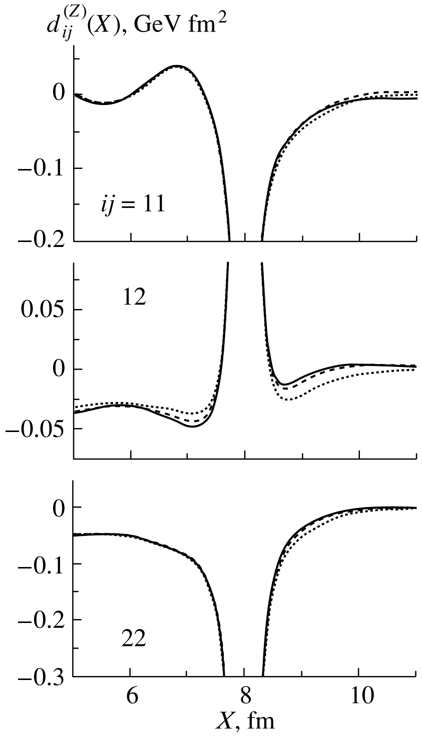

Fig. 10. As in Fig. 9, but for $Z = 8$ fm.

in Fig. 10 for $Z = 8$ fm. We can see that even the distinction between the curves obtained at $E_0 = 0$ and at 10 MeV is rather small. As to distinctions between the shapes of the profile functions at $E_0 = 10$ MeV and $E_0 = 20$ MeV, they are virtually nonexistent.

In order to analyze the E_0 dependence of the G matrix at a more quantitative level, it is reasonable to calculate, as in the case of the propagators, its zeroth moments

$$\bar{G}_{ij}(X) = \int_{-\infty}^{\infty} dt\, G_{ij}(X, X+t). \qquad (29)$$

Since it is obvious that the contribution of the delta-function term to the integral in (29) is independent of E_0, it is reasonable to calculate the zeroth moment of the total G matrix rather than that of its correlated part. Although the absolute variation of two such moments in response to a variation in E_0 will be identical, the relative variation is more informative in the former case, because it is precisely the total G matrix that appears in physical observables. The zeroth moments (29) calculated at various values of E_0 are shown in Fig. 11 for the same large components and, as an example, for one of the small components, $ij = 13$. We can see that there is an insignificant distinction of about a few percent between the curves computed at $E_0 = 0$ and at 10 MeV; as before, the further increase in E_0 from 10 to 20 MeV exerts virtually no effect on the results. This is so not only for large but also for small components.

In order to characterize the G matrix in the $^1S_0$ channel on average, we introduce (as was done for the effective pairing interaction in [9, 10]) the quantity

$$\langle G_\mathrm{F}\rangle_{S=0}(X) = \sum_{ij} \bar{G}_{ij}(X)\, g_i(k_\mathrm{F}^2(X))\, g_j(k_\mathrm{F}^2(X)), \qquad (30)$$

where the local Fermi momentum is $k_\mathrm{F}(X) = \sqrt{2m(\mu - V(X))}$ in the classically allowed region—that is, at $\mu - V(X) > 0$—and $k_\mathrm{F}(X) = 0$ beyond this region. The quantity introduced in Eq. (30) has the meaning of the intensity of the G matrix averaged near the Fermi surface. An average of this kind arises in calculating the Landau–Migdal amplitude in terms of the Brueckner G matrix if we consistently use, in doing this, the local-potential approximation [18]. Here, one comment is in order. Although the profile functions $d_{ij}^{(Z)}(X)$ have a sharp maximum at the point $X = Z$, the long-range tails, which are hardly visible in Fig. 8, also make a noticeable contribution to the zeroth moments in (29).[4] These terms in the

---

[4] This contribution depends on ij and, as a rule, does not exceed 10–20%.

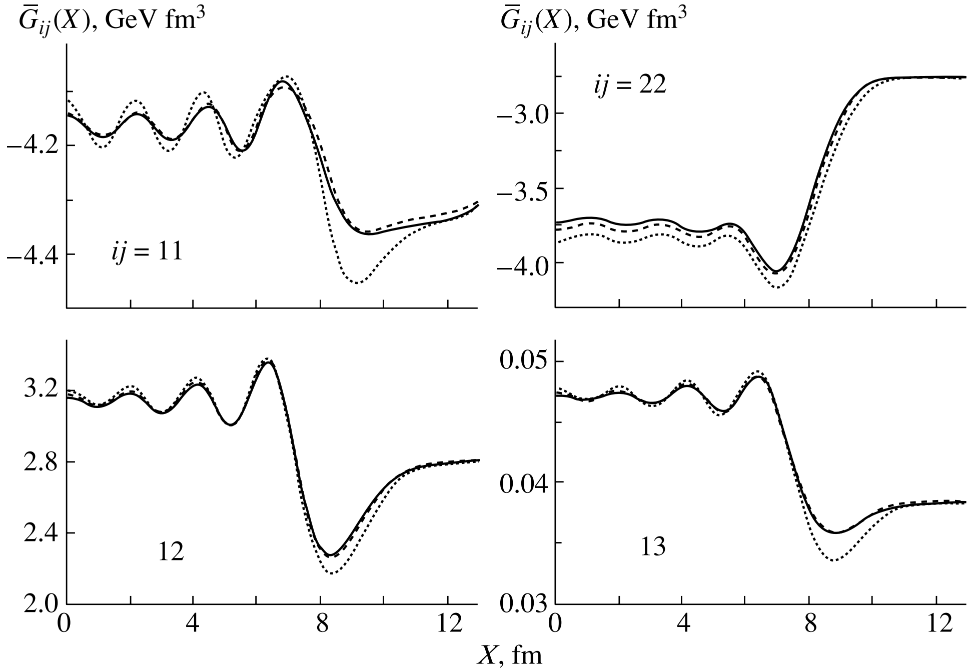

Fig. 11. Zeroth moments $\bar{G}_{ij}(X)$ in the singlet channel at E_0 = (dotted curves) 0, (dashed curves) 10, and (solid curves) 20 MeV.

G matrix arise owing to the contribution of states near the Fermi surface, and their contribution to the integral in (29) was analyzed for the case of $E_0 = 0$ in [18]. Since the Landau–Migdal amplitude is assumed to be a local function of the coordinates [5], it is natural, in calculating it, to cut off the G-matrix tails being considered. In [18], we proposed a recipe for averaging the G matrix near the Fermi surface [see Eq. (30)] by using the zeroth moments subjected to a cutoff that are determined by an integral that has the same form as in (29), but which is taken within finite integration limits: $|t| < t_c$, where $t_c = 3$ fm. It goes without saying that, in investigating the applicability of the local-potential approximation, it is absolutely immaterial which kind of zeroth moment is used in the definition of the averaged G matrix (30). Nevertheless, we will use the same recipe as in [18], since it seems more physically justified. The quantity obtained by averaging the G matrix in the $^1S_0$ channel according to this recipe is presented in Fig. 12 for the above three values of the cutoff energy E_0, along with the off-mass-shell T matrix averaged in the same manner, that is,

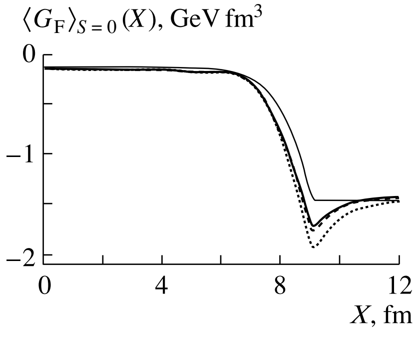

Fig. 12. Quantity $\langle G_{\rm F}\rangle_{S=0}(X)$ obtained by averaging, near the Fermi surface, the G matrix in the singlet channel at E_0 = (dotted curve) 0, (dashed curve) 10, and (solid curve) 20 MeV and the T matrix averaged near the Fermi surface (thin solid curve).

$$\langle T_{\rm F}\rangle_{S=0}(X) = \sum_{ij} \bar{T}_{ij}(E = 2\mu)\, g_i(k_{\rm F}^2(X))\, g_j(k_{\rm F}^2(X)), \tag{31}$$

where the zeroth moments $\bar{T}_{ij}$ of the T-matrix components are defined in a way similar to that in (29). Of course, their values do not depend on X. In the case of the T matrix, the cutoff introduced at $t_c = 3$ fm induces virtually no changes in the zeroth moments, but, here, we also use the recipe with a cutoff for the sake of uniformity.

Again, the distinction between the averaged G matrices at $E_0 = 10$ and at 20 MeV is negligible. They both differ only slightly from the G matrix at $E_0 = 0$ everywhere, with the exception of the surface region. It should be noted that the averaged G matrix differs insignificantly from the T matrix. This property

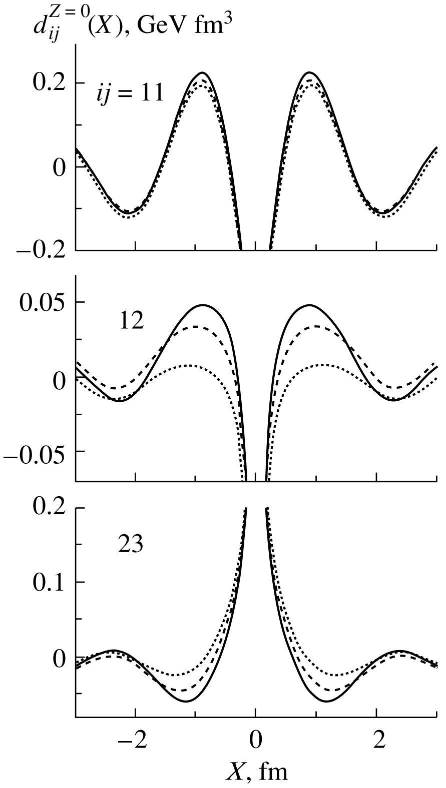

Fig. 13. As in Fig. 9, but for the triplet channel.

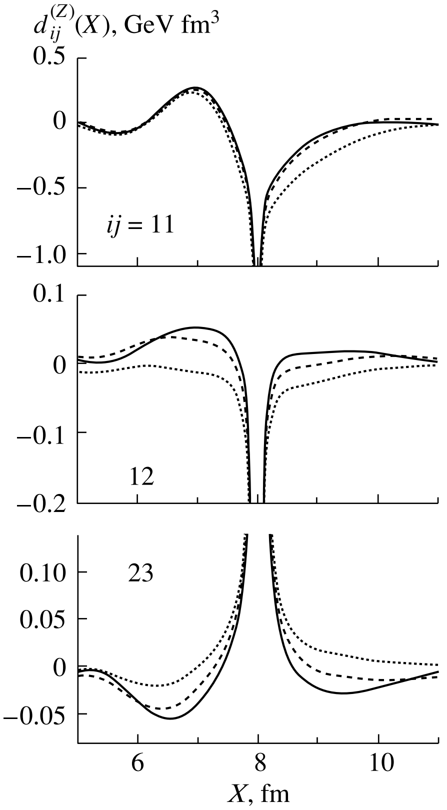

Fig. 14. As in Fig. 9, but at $Z = 8$ fm for the triplet channel.

was previously discovered in [16, 17] for the effective pairing interaction in the $^1S_0$ channel.

An analysis of Figs. 9–12 leads to the conclusion that, in the $S = 0$ singlet channel, the local-potential approximation works well for $E_0 = 10$–20 MeV. Moreover, this approximation is accurate at $E_0 = 0$ to within a few percent. The last statement is consistent with the results of the analysis performed in [9, 10], where the local-potential approximation was considered for the first time in calculating the effective pairing interaction in the $^1S_0$ channel.

6. LOCAL-POTENTIAL APPROXIMATION FOR THE G MATRIX IN THE TRIPLET CHANNEL

By and large, the computational scheme for the $^3S_1 + {^3D_1}$ triplet channel is similar to that outlined above for the singlet channel. However, specific calculations become more cumbersome. For example, there arise ten independent components $G_{ij}(X, X')$ of the G matrix and, respectively, ten integral equations of the type in (9) for them instead of six equations in the singlet case. Apart from this, the evaluation of the integral in (21)—the convolution of the propagator with the form factors—is more involved than in the singlet case. For this reason, the problem of simplifying the calculations is more acute here than in the singlet channel.

In contrast to the singlet case, it is difficult here to break down multipole terms into large and small ones. As in the singlet channel, we have changed the original normalization [11] of the expansion coefficients in (5) and (6) in such a way as to ensure fulfillment of the equality $g_i^{L=0}(0) = 1$ [we note that the second components of all form factors issue from zero: $g_i^{L=2}(0) = 0$]. The renormalized coefficients regain the absolute meaning of the intensity of the corresponding terms in the NN potential. They have the following values (in GeV fm^3 units): $\lambda_{11} = -1.618$, $\lambda_{12} = -1.296$, $\lambda_{13} = 0.8921$, $\lambda_{14} = 0.04271$, $\lambda_{22} = 0.7848$, $\lambda_{23} = 1.394$, $\lambda_{24} = -0.786$, $\lambda_{33} = -0.745$, $\lambda_{34} = -0.5723$, and $\lambda_{44} = 1.865$. We can see that, although these coefficients show wide variations, only one of them—namely, λ_{14}—is two orders of magnitude smaller than the maximum ones. For this reason, almost all terms make commensurate contributions to observables. In order to avoid encumbering the presentation with a large number of figures, we chose, as was done in analyzing the propagators, a few typical components in order to illustrate the results of the calculations.

The profile functions and the zeroth moments are presented in Figs. 13–15. The distinctions between

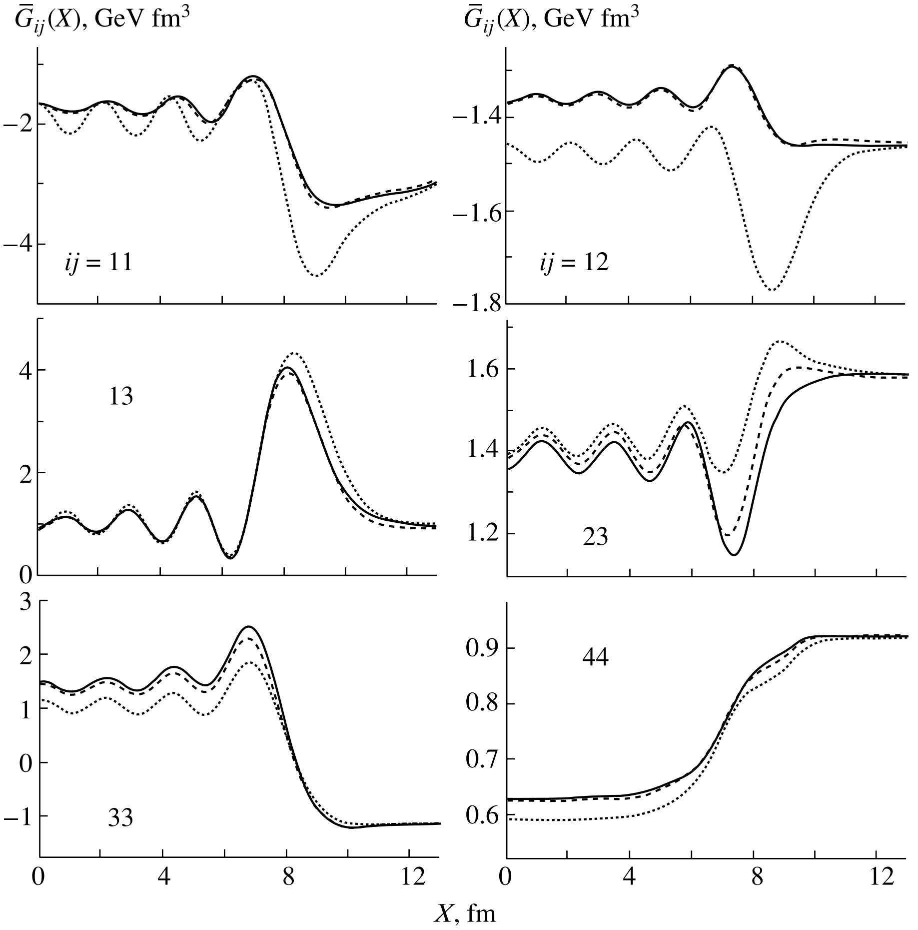

Fig. 15. As in Fig. 11, but for the triplet channel.

all curves for the cutoff-energy values of $E_0 = 0$ and 10 MeV become more pronounced in relation to the singlet channel, especially in the surface region. At the same time, a further increase in E_0 up to 20 MeV leads to virtually no changes in the G matrix—the maximum distinctions between the corresponding curves at $E_0 = 10$ and at 20 MeV are about a few percent. Again, we can therefore conclude that the local-potential approximation has a sufficient accuracy if the model subspace is chosen to correspond to cutoff-energy (E_0) values of 10 to 20 MeV. In contrast to the singlet case, the accuracy of the local-potential approximation is not high, however, for $E_0 = 0$. This fact can be understood rather easily if we consider that, in the surface region, the G matrix asymptotically goes over into the free off-mass-shell T matrix. The latter has a pole at low energies, which is virtual in the singlet channel and is real in the triplet case. In order to describe correctly the behavior of the G matrix near the pole of the T matrix, it is necessary to take into account, to a fairly high precision, the contribution of single-particle states of low energy, including states that belong to the continuous spectrum. Therefore, such states must be included in the model subspace S_0. This occurs at cutoff energies of $E_0 \geq 10$ MeV; however, the situation is different at $E_0 = 0$. In principle, this argument refers to both channels being considered, but the energy $E = 2\mu = -16$ MeV, at which we calculate the G matrix, is noticeably closer to the pole of the T matrix in the triplet than in the singlet case. Hence, the effect being considered is stronger in the triplet case. A comparison of the profile functions for the G matrix in the triplet channel with the corresponding profile functions for the propagators (see Figs. 5 and 6) shows that the local-potential approximation is more accurate for the G matrix than for the propagators. In other words, integration of the propagators in Eq. (14) somewhat levels out, as we assumed, their variations caused by changes in E_0.

Let us now proceed to consider the G matrix averaged near the Fermi surface in the triplet channel. In contrast to the singlet case, it is now a 2×2 matrix in the space of the total orbital angular momentum L;

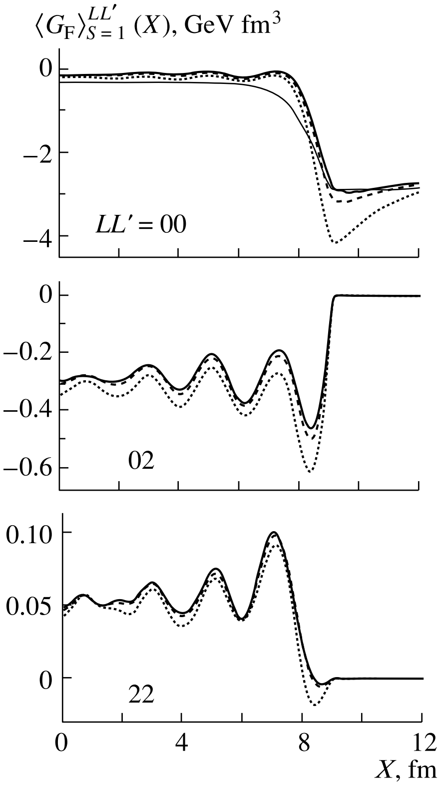

Fig. 16. As in Fig. 12, but for the triplet channel.

that is,

$$\langle G_{\rm F}\rangle^{LL'}_{S=1}(X) \tag{32}$$
$$= \sum_{ij} \bar{G}^{S=1}_{ij}(X)\, g_i^{(L)}(k_{\rm F}^2(X))\, g_j^{(L')}(k_{\rm F}^2(X)),$$

where $L, L' = 0, 2$. Just as in the singlet case, the quantity $\bar{G}_{ij}$ in (32) stands for the zeroth moment subjected to a cutoff. In Fig. 16, the components of this matrix are presented at all three values of the cutoff energy E_0. As can be seen from this figure, the component $\langle G_{\rm F}\rangle^{00}_{S=1}$ is considerably larger than all the remaining components, especially in the surface region, because the form factor $g_i^{(2)}$ vanishes in the classically forbidden region,. Again, all components of the averaged G matrix at $E_0 = 10$ MeV nearly coincide with the corresponding components at $E_0 = 20$ MeV. At the same time, both these curves differ significantly from the analogous curve calculated at $E_0 = 0$.

7. CONCLUSION

The present article reports on a continuation of a series of studies where a microscopic method for describing finite nuclear systems was developed without using the standard local-density approximation, which is not appropriate for describing the nuclear surface. In considering the problem of microscopically calculating the effective pairing interaction in the $^1S_0$ channel for semi-infinite nuclear matter, an alternative version of a local approximation, the local-potential approximation, was proposed previously in [9, 10]. For the pairing problem, this approximation proved to be sufficiently precise everywhere, including the surface region. In the present study, we have investigated the applicability of the local-potential approximation in solving the Bethe–Goldstone equation for the Brueckner G matrix. We have employed the method developed in [18] for solving the Bethe–Goldstone equation for a planar slab of nuclear matter. The method is based on the technique of the mixed coordinate–momentum representation for the case of a separable NN potential. As in [9, 10, 18], we have relied on the separable representation [11, 12] of the Paris potential. In such a system, the Bethe–Goldstone equation is solved for the G matrix in the two channels (the $^1S_0$ singlet and the $^3S_1 + {}^3D_1$ triplet channel) that make a dominant contribution in calculating the Landau–Migdal amplitude on the basis of Eq. (1) [18].

The full Hilbert space is split into two subspaces separated by a cutoff energy E_0. The model subspace $S_0(E_0)$ includes all two-particle states in which both single-particle energies ε_λ and $\varepsilon_{\lambda'}$ are less than this cutoff energy E_0. The contribution of such individual states to the propagator for the Bethe–Goldstone equation is enhanced owing to the smallness of the energy denominator; therefore, it must be calculated precisely. In the complementary subspace $S'(E_0)$, at least one of these energies is greater than E_0, so that all the energy denominators in the Bethe–Goldstone propagator are large. Therefore, the contribution of each individual state to this propagator is negligible—only the sum of a large number of such states may be of importance. It is proposed to use the local-potential approximation for the corresponding part of the Bethe–Goldstone propagator. A priori, it is obvious that the higher the energy E_0, the higher the accuracy of the local-potential approximation, since the approximation becomes exact in the limit of infinitely large E_0. This fact is used to establish the criterion of applicability of the local-potential approximation: the approximation is taken to be justified at a given value of E_0 if a further increase in E_0 leads to virtually no changes in the G matrix. A qualitative analysis has revealed that the conditions of applicability of the local-potential approximation become more favorable with increasing total transverse momentum $P_\perp$, which is a parameter in the Bethe–Goldstone equation for the planar slab. Therefore, the analysis in the present study has been performed only for the most dangerous case of $P_\perp = 0$.

For the two channels being considered, the G matrix has been computed at a few values of the cutoff energy E_0. It has appeared that, in response to changes in E_0 from $E_0 = 10$ to 20 MeV, the properties of the G matrix vary by not more than a few percent for each of the above channels. Thereby, it has been demonstrated that the local-potential approximation can be used to calculate the Brueckner G matrix at $E_0 \geq 10$ MeV. In the singlet channel, the conditions of applicability of the local-potential approximation are somewhat more favorable, and the accuracy of this approximation is rather high even at $E_0 = 0$. The last result is in accord with the conclusion drawn in [9, 10], where the local-potential approximation was investigated in solving the problem of singlet pairing in semi-infinite nuclear matter. At the same time, the accuracy of the local-potential approximation in the triplet channel is not high at $E_0 = 0$.

In this study, we have performed our analysis for the single chemical-potential value of $\mu = -8$ MeV, which is typical of β-stable nuclei. For nuclei near the nucleon-stability boundary, which are characterized by small values of μ, the conditions of applicability of the local-potential approximation are somewhat less favorable. It should be noted that nuclei from this region cannot be considered as isosymmetric systems. In particular, it must be considered that $\mu_n \neq \mu_p$—specifically, the chemical potential of one of the subsystems (as a rule, μ_n) vanishes at the stability boundary, while the chemical potential of the other subsystem (μ_p) remains on the same order of magnitude as in stable nuclei. In the triplet channel, which corresponds to the isospin of $T = 1$, the G matrix will then depend on the energy $E = \mu_n + \mu_p$, which is close to that considered here. As to the singlet case, it is necessary to consider the pp and the nn channel individually. In the former case, it is the energy $E = 2\mu_p$ that appears in the G matrix, whence we conclude that the results of the above analysis remain valid. Only in the two-neutron channel is the energy $E = 2\mu_n$ appearing in the G matrix close to zero, and the applicability of the local-potential approximation must in principle be explored anew. Estimations have shown that the accuracy of the local-potential approximation is fairly high at $E_0 = 10$–20 MeV in the last case inclusive, but it is of course illegitimate to employ this approximation at $E_0 = 0$.

ACKNOWLEDGMENTS

This work was supported in part by the Russian Foundation for Basic Research (project nos. 00-02-17319 and 00-15-96590).

REFERENCES

1. H. A. Bethe, Annu. Rev. Nucl. Sci. **21**, 93 (1971).
2. P. Ring and P. Schuck, *The Nuclear Many-Body Problem* (Springer-Verlag, Berlin, 1980).
3. J. Wambach, T. L. Ainsworth, and D. Pines, Nucl. Phys. A **555**, 128 (1993).
4. H.-J. Schulze, J. Cugnon, A. Lejeune, *et al.*, Phys. Lett. B **375**, 1 (1996).
5. A. B. Migdal, *Theory of Finite Fermi Systems and Applications to Atomic Nuclei* (Nauka, Moscow, 1965; Interscience, New York, 1967).
6. A. A. Abrikosov, L. P. Gor'kov, and I. E. Dzyaloshinskii, *Methods of Quantum Field Theory in Statistical Physics* (Fizmatgiz, Moscow, 1962; Prentice-Hall, Englewood Cliffs, 1963).
7. A. B. Migdal, *Theory of Finite Fermi Systems and Properties to Atomic Nuclei*, 2nd ed., (Nauka, Moscow, 1983).
8. V. A. Khodel and E. E. Saperstein, Phys. Rep. **92**, 183 (1982).
9. M. Baldo, U. Lombardo, E. E. Saperstein, and M. V. Zverev, Yad. Fiz. **60**, 1206 (1997) [Phys. At. Nucl. **60**, 1081 (1997)].
10. M. Baldo, U. Lombardo, E. E. Saperstein, and M. V. Zverev, Nucl. Phys. A **628**, 503 (1998).
11. J. Haidenbauer and W. Plessas, Phys. Rev. C **30**, 1822 (1984).
12. J. Haidenbauer and W. Plessas, Phys. Rev. C **32**, 1424 (1985).
13. M. Lacombe, B. Loiseaux, J. M. Richard, *et al.*, Phys. Rev. C **21**, 861 (1980).
14. M. Baldo, J. Cugnon, A. Lejeune, and U. Lombardo, Nucl. Phys. A **515**, 409 (1990).
15. M. Baldo, I. Bombaci, G. Giansiracusa, and U. Lombardo, Nucl. Phys. A **545**, 741 (1992).
16. M. Baldo, U. Lombardo, E. E. Saperstein, and M. V. Zverev, Phys. Lett. B **477**, 410 (2000).
17. M. Baldo, U. Lombardo, E. E. Saperstein, and M. V. Zverev, Yad. Fiz. **63**, 1454 (2000) [Phys. At. Nucl. **63**, 1377 (2000)].
18. M. Baldo, U. Lombardo, E. E. Saperstein, and M. V. Zverev, Yad. Fiz. **64**, 247 (2001) [Phys. At. Nucl. **64**, 203 (2001)].

Translated by A. Isaakyan

Physics of Atomic Nuclei, Vol. 65, No. 7, 2002, pp. 1259–1270. From Yadernaya Fizika, Vol. 65, No. 7, 2002, pp. 1292–1304.

90th ANNIVERSARY OF I.I. GUREVICH'S BIRTHDAY

Nonthermal Radiation from Black Holes*

I. B. Khriplovich**

Budker Institute of Nuclear Physics, Siberian Division, Russian Academy of Sciences,
pr. Akademika Lavrent'eva 11, Novosibirsk, 630090 Russia,
and Novosibirsk State University, ul. Pirogova 2, Novosibirsk, 630090 Russia

Received September 27, 2001; in final form, November 15, 2001

Abstract—We consider particle production by charged and rotating black holes. A simple derivation is presented for the leading term ($n = 1$) in the Schwinger formula for pair creation by a constant electric field. The same approach is then applied to charged-particle production by a charged black hole. The effect is due to the tunneling of created particles through an effective Dirac gap. Nonthermal radiation from a rotating black hole can also be explained in an analogous way. In the leading semiclassical approximation, this approach is applicable to bosons as well. © *2002 MAIK "Nauka/Interperiodica"*.

Dedicated to the memory
of Isai Isidorovich Gurevich, a remarkable
physicist and marvelous personality

1. INTRODUCTION

Particle production by charged (Reissner–Nordstrem) and rotating (Kerr) black holes was predicted simultaneously with or even somewhat earlier than famous thermal radiation. Although the problems of nonthermal particle creation are rather old, there are some aspects of them that were elucidated only recently. These aspects are discussed in the present article.

The problem of particle production by the electric field of a black hole was repeatedly discussed [1–7]. The probability of this process was estimated in [1–6] by using, in some way or another, the result obtained previously [8–10] for the case of an electric field constant over the entire space. This approximation might look quite natural with regard to sufficiently large black holes, for which the gravitational radius significantly exceeds the Compton wavelength of the particle, $\lambda = 1/m$. (We use the system of units where $\hbar = 1$ and $c = 1$; the Newtonian gravitational constant k is written explicitly.) However, it will be demonstrated below that, in fact, the constant-field approximation is generally inadequate to the present problem and does not reflect some of its significant features. A consistent semiclassical solution to the problem was given in [11].

The investigation of particle production by Kerr black holes started with the prediction [12, 13] of the amplification of an electromagnetic wave upon the reflection from a rotating black hole, so-called superradiation. The effect was studied in detail in [14, 15] for electromagnetic and gravitational waves. It looks rather obvious that, if the amplification of a wave upon reflection is possible, then its generation by a rotating black hole is also possible. Indeed, a direct calculation [16] demonstrated that the nonthermal radiation under discussion does exist, and not only for bosons, photons and gravitons, but also for neutrinos. The last result looks rather mysterious since there is no superradiation for fermions.

In [17], nonthermal radiation from Kerr black holes was considered from another point of view: as tunneling of quanta being created through the Dirac gap. Certainly, this approach by itself can be valid only for fermions. It is clear, however, that, in the leading semiclassical approximation, the production of fermions and bosons is described by the same, apart from the statistical weight, relations.

Let us note that, in [18], an analogous mechanism was considered in order to describe friction experienced by a body rotating in a superfluid liquid at $T = 0$: the quantum tunneling of quasiparticles to the region where their energy in the rotating frame is negative.

2. RADIATION FROM CHARGED BLACK HOLES

2.1. Particle Production by Constant Electric Field

It is convenient to start the discussion just from the problem of particle production by a constant electric field. We restrict ourselves to the consideration of the production of electrons and positrons, primarily because the probability of the emission of these

---

[*] This article was submitted by the author in English.

[**] e-mail: `khriplovich@inp.nsk.su`

1063-7788/02/6507-1259$22.00 © 2002 MAIK "Nauka/Interperiodica"

Fig. 1. Dirac gap.

lightest charged particles is the maximum. Moreover, the picture of the Dirac sea allows one, in the case of fermions, to dispense with the second-quantization formalism, with the result that the consideration becomes most transparent. To calculate the main, exponential dependence of the effect, it is sufficient to restrict oneself to a simple approach due to [8] (see also [19, 20]). In the potential $-eEz$ of a constant electric field E, the usual Dirac gap (Fig. 1) tilts (see Fig. 2). As a result, a particle of negative energy in the absence of a field can now tunnel through the gap (see the horizontal dashed line in Fig. 2) and go to infinity as a usual particle. The hole created in this way is nothing but an antiparticle. The exponential factor in the probability of particle creation obviously depends on the action only within the barrier. This action does not change under a shift of the dashed line in Fig. 2, up or down, i.e., under a shift by $\Delta\mathcal{E}$ of the energy $\mathcal{E}$ of the created particle. Being obviously an integral of the motion, $\mathcal{E}$ is also the energy of the initial particle of the Dirac sea. If we set, for instance, $\mathcal{E} = -m$, so that the particle enters the barrier at $z = 0$, the squared four-dimensional momentum

$$(\mathcal{E} - e\phi)^2 - p^2 = m^2$$

becomes

$$(-m + eEz)^2 - p^2 = m^2.$$

For the time being, we assume that the transverse particle-momentum component $\mathbf{p}_\perp = (p_x, p_y)$, which is also an integral of the motion, is equal to zero. Within the barrier, the modulus of the momentum $p(z) = p_z(z)$ is

$$|p(z)| = \sqrt{m^2 - (m - eEz)^2}.$$

The action within the barrier is

$$S = \int\limits_0^{2m/eE} dz|p(z)| = \frac{\pi m^2}{2eE}.$$

Finally, the exponential factor in the probability W is [8]

$$W \sim \exp(-2S) \sim \exp(-\pi m^2/eE). \quad (1)$$

One can easily take into account, in the exponent in (1), the transverse momentum $\mathbf{p}_\perp$. This integral of the motion will clearly enter into all the preceding formulas only in the combination $m^2 + p_\perp^2$. Therefore, expression (1) requires, in this case, the substitution $m^2 \to m^2 + p_\perp^2$, changing thus to

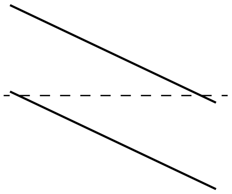

Fig. 2. Dirac gap in electric field.

$$W \sim \exp[-\pi(m^2 + p_\perp^2)/eE]. \quad (2)$$

Let us now calculate the preexponential factor in the probability of particle creation, as was done in [21]. The exponential in (2) is the probability that a particle of the Dirac sea approaching the potential barrier from the left (see Fig. 2) will tunnel through it to the right, thus becoming a real electron. To obtain the total number of pairs created per unit volume per unit time, the exponential in (2) should be multiplied by the current density of the particles of the Dirac sea,

$$j_z = \rho v_z. \quad (3)$$

For the velocity, we use the general relation

$$v_z = \frac{\partial\mathcal{E}}{\partial p}$$

(the subscript z on the longitudinal momentum p is again omitted here and below). The particle density is as usual

$$\rho = 2\frac{d^2p_\perp dp}{(2\pi)^3}, \quad (4)$$

the factor of 2 being due to two possible orientations of the electron spin.

For a fixed coordinate z and fixed $\mathbf{p}_\perp$, we have the identity

$$\frac{\partial\mathcal{E}}{\partial p}dp = d\mathcal{E}. \quad (5)$$

On the other hand, it is obvious that the interval $d\mathcal{E}$ of energies of tunneling particles is directly related to the interval dz of longitudinal coordinates of the points where the particles enter the barrier: $d\mathcal{E} = eEdz$ (apart from an immaterial sign). Being interested in the probability per unit volume, in general, and per unit longitudinal distance, in particular, we should delete the thus arising factor dz in calculating the effect. Thus, the total number of pairs created per unit volume per unit time is

$$W_{1/2} = 2eE\int\frac{d^2p_\perp}{(2\pi)^3}\exp[-\pi(m^2 + p_\perp^2)/eE]. \quad (6)$$

Now, a trivial integration with respect to the transverse momenta yields the final result

$$W_{l/2} = \frac{e^2E^2}{4\pi^3}\exp(-\pi m^2/eE). \qquad (7)$$

The quantity W in the above formulas is equipped with the subscript $1/2$ to indicate that the result refers to particles of spin one-half. Obviously, the notion of the Dirac sea and, hence, the above derivation by itself do not apply to boson-pair creation. However, in the semiclassical approximation, the creation rate for particles of spin zero is almost the same. The only difference is that, since these particles do not have two polarization states, the rate is two times smaller than that in (7):

$$W_0 = \frac{e^2E^2}{8\pi^3}\exp(-\pi m^2/eE). \qquad (8)$$

The corresponding exact results for a constant electric field are [10]

$$W_{1/2} = \frac{e^2E^2}{4\pi^3}\sum_{n=1}^{\infty}\frac{1}{n^2}\exp(-n\pi m^2/eE), \qquad (9)$$

$$W_0 = \frac{e^2E^2}{8\pi^3}\sum_{n=1}^{\infty}\frac{(-1)^{n-1}}{n^2}\exp(-n\pi m^2/eE). \qquad (10)$$

Obviously, the inclusion of higher terms, with $n \geq 2$, in the sums in (9) and (10) is meaningful only for very strong electric fields, for $eE \sim m^2$. For smaller fields, when $eE \ll m^2$, the simple formulas (7) and (8) are correct quantitatively.

The above straightforward derivation clearly explains some important properties of the phenomenon. First of all, the action within the barrier does not change under a shift of the dashed line in Fig. 2, up or down. Owing to this property alone, expressions (1) and (7) are independent of the energy of created particles. Then, for the external field to be considered as a constant one, it should change weakly along the path within the barrier. Obviously, the length of this path, $l \sim m/eE$, differs significantly from the Compton wavelength $\lambda = 1/m$ of the particle. The ratio l/λ is on the same order of magnitude as the action S within the barrier; therefore, it should be large for the semiclassical approximation to be applicable at all.

The case of a constant electric field has one more special feature. The same criterion of the semiclassical approximation, $l/\lambda \gg 1$, also means that the tilt of the Dirac gap is very small. Therefore, the vicinity of the turning point, where the classical picture is inapplicable, is anomalously large in the (formally) classically accessible region. That is why the formation length for electron–positron pairs is, in this case, not m/eE, as one may expect naively, but a much larger quantity, $m/eE(m^2/eE)^{1/2}$, as was demonstrated by direct calculations in [21, 22].

2.2. Particle Production by Charged Black Holes: Exponential Dependence

It is clear now that, generally speaking, the constant-field approximation is not applicable to the problem of radiation from a charged black hole and that the probability of particle production in this problem is strongly energy-dependent. The explicit form of this dependence will be found below.

We begin solving the problem by calculating the action within the barrier. The metric of a charged black hole is well known to be

$$ds^2 = f dt^2 - f^{-1}dr^2 - r^2(d\theta^2 + \sin^2\theta d\phi^2), \qquad (11)$$

where

$$f = 1 - \frac{2kM}{r} + \frac{kQ^2}{r^2}, \qquad (12)$$

M and Q being, respectively, the mass and charge of the black hole. The equation for the particle 4-momentum in these coordinates is

$$f^{-1}\left(\varepsilon - \frac{eQ}{r}\right)^2 - fp^2 - \frac{l^2}{r^2} = m^2. \qquad (13)$$

Here, ε and p are, respectively, the energy and the radial momentum of the particle. We assume that the particle charge e is of the same sign as the charge of the hole Q, assigning the charge $-e$ to the antiparticle.

Clearly, the action within the barrier is minimal for the vanishing orbital angular momentum l. It is therefore rather evident (and will be demonstrated below explicitly) that, after summation over l, it is precisely the s state that defines the exponential in the total probability of the process. Therefore, we restrict ourselves, for the moment, to the case of a purely radial motion. The equation for the Dirac gap for $l = 0$ is

$$\varepsilon_{\pm}(r) = \frac{eQ}{r} \pm m\sqrt{f}, \qquad (14)$$

which is presented in Fig. 3. It is known [23] that, at the horizon of a black hole, for $r = r_+ = kM + \sqrt{k^2M^2 - kQ^2}$, the gap vanishes. Then, as r is increased, the lower boundary $\varepsilon_-(r)$ of the gap decreases monotonically, tending asymptotically to $-m$. In general, the upper branch $\varepsilon_+(r)$ first increases and then decreases, tending asymptotically to m.

It is clear from Fig. 3 that those particles of the Dirac sea whose coordinate r exceeds the gravitational radius r_+ and whose energy ε belongs to the interval $\varepsilon_-(r) > \varepsilon > m$ tunnel through the gap to infinity. In other words, a black hole loses its charge

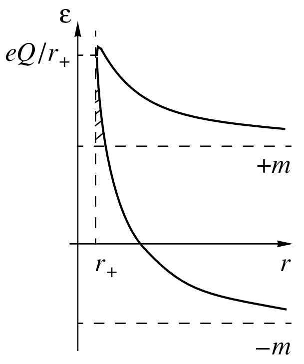

Fig. 3. Dirac gap for a nonextremal black hole.

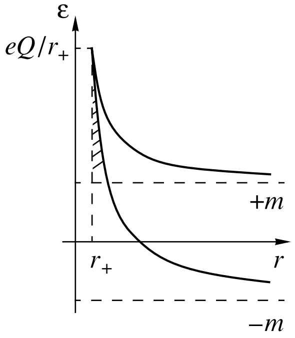

Fig. 4. Dirac gap for extremal black hole.

because of the discussed effect, by emitting particles with the same sign of the charge e as the sign of Q. Clearly, the phenomenon takes place only under the condition

$$\frac{eQ}{r_+} > m. \tag{15}$$

For an extremal black hole, with $Q^2 = kM^2$, the Dirac gap looks somewhat different (see Fig. 4): when Q^2 tends to kM^2, the location of the maximum of the curve $\varepsilon_+(r)$ tends to r_+, and the value of the maximum tends to eQ/r_+. It is obvious, however, that this does not change the situation qualitatively. Thus, although an extremal black hole has zero Hawking temperature and, accordingly, gives no thermal radiation, it still creates charged particles owing to the above effect.

In the general case of $Q^2 \leq kM^2$, the doubled action within the barrier entering into the exponential for the radiation probability is

$$2|S| = 2\int_{r_1}^{r_2} dr|p(r,\varepsilon)| \tag{16}$$

$$= 2\int_{r_1}^{r_2} \frac{drr}{r^2 - 2kMr + kQ^2}$$

$$\times \sqrt{-p_0^2 r^2 + 2(\varepsilon eQ - km^2 M)r - (e^2 - km^2)Q^2}.$$

Here, $p_0 = \sqrt{\varepsilon^2 - m^2}$ is the momentum of the emitted particle at infinity and the turning points $r_{1,2}$ are as usual the roots of the quadratic polynomial in the radicand; we are interested in the energy interval $m \leq E \leq eQ/r_+$. Of course, the integral can be found explicitly, although this requires somewhat tedious calculations. However, the result is sufficiently simple:

$$2|S| = 2\pi \frac{m^2}{(\varepsilon + p_0)p_0}[eQ - (\varepsilon - p_0)kM]. \tag{17}$$

(Previously, this exponent was obtained in [7] from the solution to the Klein–Gordon equation in the Reissner–Nordstrem metric.) Certainly, expression (17), as distinct from the exponent in formula (1), depends on energy quite significantly.

Let us note that the action within the barrier does not vanish even for the limiting value of the energy $\varepsilon_m = eQ/r_+$. For a nonextremal black hole, it is clear already from Fig. 3. For an extremal black hole, this fact is not so obvious. However, due to the singularity in $|p(r,\varepsilon)|$, the action within the barrier is finite for $\varepsilon = \varepsilon_m = eQ/r_+$ for an extremal black hole as well. In this case, the exponential factor in the probability is

$$\exp[-\pi(\sqrt{k}m/e)kmM]. \tag{18}$$

Due to the extreme smallness of the ratio

$$\frac{\sqrt{k}m}{e} \sim 10^{-21}, \tag{19}$$

the exponent here is large only for a very heavy black hole, with a mass M exceeding that of the Sun by more than five orders of magnitude. Since the total probability, integrated over energy, is dominated by the energy region $\varepsilon \sim \varepsilon_m$, the semiclassical approach is applicable in the case of extremal black holes only for these very heavy objects. Let us also note that, for particles emitted by an extremal black hole, typical values of the ratio ε/m are very large:

$$\frac{\varepsilon}{m} \sim \frac{\varepsilon_m}{m} = \frac{eQ}{kmM} = \frac{e}{\sqrt{k}m} \sim 10^{21}.$$

In other words, an extremal black hole mainly radiates highly ultrarelativistic particles in any case.

Let us return to nonextremal holes. In the nonrelativistic limit, where $eQ/r_+ \to m$ and, accordingly, the particle velocity tends to zero ($v \to 0$), the exponential is of course very small:

$$\exp(-2\pi kmM/v). \tag{20}$$

Therefore, we will consider mainly the ultrarelativistic limit, where the exponential is

$$\exp[-\pi(m^2/e^2)eQ]. \tag{21}$$

Of course, the energies $\varepsilon \sim \varepsilon_m \sim eQ/kM$ are also significant here, so that the ultrarelativistic limit corresponds to the condition

$$eQ > kmM. \tag{22}$$

But then the semiclassical result (21) is applicable (i.e., the action within the barrier is large) only under the condition

$$kmM > 1. \tag{23}$$

This last condition means that the gravitational radius of the black hole ($r_+ \sim kM$) is much larger than the Compton wavelength of the electron ($1/m$). In other words, the result in (21) refers to macroscopic black holes. Combining (22) with (23), we arrive at one more condition for the applicability of formula (21):

$$eQ \gg 1. \tag{24}$$

We shall return to this relation later.

Let us note that, in [4], the action within the barrier was calculated under the same assumptions as formula (21). However, the result presented in [4], $2|S| = \pi m^2 r_+^2/eQ$, is totally independent of energy [and corresponds to formula (2), which refers to the case of a constant electric field]. Obviously, this cannot be correct for the integral under discussion in the general case of $\varepsilon \neq \varepsilon_m$.

2.3. Particle Production by Charged Black Holes: Preexponential Factor

Now, the radiation intensity is conveniently calculated in the following way. For $r \to \infty$, the radial current density of free particles in the energy interval $d\varepsilon$ is

$$j_r(\varepsilon, l)d\varepsilon = 2\sum \frac{d^3p}{(2\pi)^3}\frac{\partial \varepsilon}{\partial p_r} \tag{25}$$

$$= 2\sum_l \frac{2\pi(2l+1)dp_r}{(2\pi)^3 r^2}\frac{\partial \varepsilon}{\partial p_r}.$$

Summation over the directions of the angular momentum reduces in fact to multiplication by the number $2l+1$ of possible projections of the orbital angular momentum **l** onto the z axis and to integration with respect to the azimuthal angle of the vector **l** (this gives 2π). By means of the identity

$$\frac{\partial \varepsilon}{\partial p_r}dp_r = d\varepsilon,$$

we eventually find that the total flux of free particles for $r \to \infty$ is

$$4\pi r^2 j_r(\varepsilon, l) = \frac{2(2l+1)}{\pi}. \tag{26}$$

One can easily see that, in our problem, the total flux of radiated particles differs from the last expression only by the barrier-penetration factor. Thus, the number of particles emitted per unit time is

$$\frac{dN}{dt} = \frac{2}{\pi}\int d\varepsilon \sum_l (2l + l)\exp[-2|S(\varepsilon, l)|]. \tag{27}$$

In the most interesting, ultrarelativistic, case, dN/dt can be calculated explicitly. Let us consider the expression for the momentum in the region within the barrier for $l \neq 0$:

$$|p(\varepsilon, l, r)| = f^{-1}\sqrt{\left(m^2 + \frac{l^2}{r^2}\right)f + \left(\varepsilon - \frac{eQ}{r}\right)^2}. \tag{28}$$

The main contribution to the integral with respect to energies in formula (27) comes from the region $\varepsilon \to \varepsilon_m$. In this region, the functions $f(r)$ and $\varepsilon - eQ/r$ entering into expression (28) are small and change quickly. As to the quantity

$$\mu^2(r, l) = m^2 + l^2/r^2, \tag{29}$$

one can substitute in it for r its average value, which lies between the turning points r_1 and r_2. In the limit $\varepsilon \to \varepsilon_m$, which is discussed here, the near turning point obviously coincides with the horizon radius, $r_1 = r_+$. The expression for the distant turning point in this limit is

$$r_2 = r_+\left[1 + \frac{2\mu^2}{\varepsilon^2 - \mu^2}\frac{\sqrt{k^2M^2 - kQ^2}}{r_+}\right]. \tag{30}$$

Assuming that, for estimates, one can set $r \sim r_+$ in formula (29), one can easily show that the correction to 1 in the square brackets is bounded by the ratio $l^2/(eQ)^2$. Assuming that this ratio is small (we will see below that this assumption is self-consistent), we arrive at the conclusion that $r_2 \approx r_+$; hence, μ^2 can be considered to be independent of r: $\mu^2(r, l) \approx m^2 + l^2/r_+^2$. As a result, we obtain

$$2|S(\varepsilon, l)| = \pi eQ\left(\frac{m^2}{\varepsilon^2} + \frac{l^2}{r_+^2\varepsilon^2}\right). \tag{31}$$

Now, we easily find

$$dN/dt = m\left(\frac{eQ}{\pi m r_+}\right)^3 \exp(-\pi m^2 r_+^2/eQ). \tag{32}$$

Let us note that the range of orbital angular momenta contributing to the total probability (32), is effectively bounded by the condition $l^2 \lesssim eQ$. Since $eQ \gg 1$, this condition allows one to go over from summation over l in formula (27) to integration. On the other hand, this condition justifies the approximation $\mu^2(r, l) \approx m^2 + l^2/r_+^2$ used.

2.4. Applicability of the Semiclassical Approximation

However, up to now, we have not considered one more condition necessary for the derivation of formula (32). We mean the applicability of the semiclassical approximation to the left of the barrier, for $r_+ \le r \le r_1$. This condition has the usual form

$$\frac{d}{dr}\frac{1}{p(r)} < 1. \tag{33}$$

In other words, the minimum size of the initial wave packet should not exceed the distance from the horizon to the turning point. Using the estimate

$$p(r) \sim \frac{r_+(eQ - \varepsilon r_+)}{(r - r_+)(r - r_-)}$$

for the momentum in the most important region, one can check that, for an extremal black hole, the condition in (33) is valid owing to the constraint $eQ \gg 1$. In a nonextremal case, for $r_+ - r_- \sim r_+$, the situation is different: the condition in (33) reduces to

$$\varepsilon < \frac{eQ - 1}{r_+} \sim \frac{eQ}{r_+}. \tag{34}$$

Thus, for a nonextremal black hole, the condition of the semiclassical approximation does not hold in the most important region $\varepsilon \to \varepsilon_m$. Nevertheless, the semiclassical result (32) remains true qualitatively, apart from a numerical factor in the preexponential.

Some comments on the radiation of light charged black holes, for which $kmM < 1$—i.e., for which the gravitational radius is less than the Compton wavelength of the electron—are in order now. In this case, the first part,

$$\varepsilon < \frac{eQ - 1}{r_+},$$

of inequality (34), which guarantees the localization of the initial wave packet in the region of a strong field, means, in particular, that

$$eQ = Z\alpha > 1 \tag{35}$$

(we have introduced here $Z = Q/e$). It is well known (see, e.g., [24, 25]) that the vacuum for a pointlike charge with $Z\alpha > 1$ is unstable, so that such an object loses its charge by emitting charged particles. It is quite natural that, for a black hole whose gravitational radius is smaller than the Compton wavelength of the electron, the condition of emitting a charge is the same as in the pure QED. {Let us note that 1 on the right-hand side of (35) should not be taken too literally: even in QED, where the instability condition for the vacuum of spin-1/2 particles is just $Z\alpha > 1$ for a pointlike nucleus, for a finite-size nucleus, it changes [24, 25] to become $Z\alpha > 1.24$. On the other hand, the instability condition is $Z\alpha > 1/2$ for the vacuum of scalar particles in the field of a pointlike nucleus [26, 27].} As was mentioned above, for a light black hole, with $kmM < 1$, the condition $eQ > 1$ being discussed leads to a small action within the barrier and to the inapplicability of the semiclassical approximation used in the present article. The problem of the radiation from a charged black hole with $kmM < 1$ was investigated numerically in [28].

2.5. Discussion of Previous Results: Comparison with the Hawking Radiation

The exponential

$$\exp(-\pi m^2 r_+^2/eQ)$$

in our formula (32) coincides with the expression arising from formula (1), which refers to a constant electric field E if one substitutes for this field its value Q/r_+^2 at the black hole horizon. An approach based on formulas for a constant electric field was used in [1–6]. Thus, our result for the main, exponential dependence of the probability integrated with respect to energies coincides with the corresponding result of those articles. Moreover, our final formula (32) agrees with the corresponding result of [6], apart from an overall factor of 1/2. (This difference is of no interest by itself: it was noted above that, for a nonextremal black hole, the semiclassical approximation cannot guarantee an exact value of the overall numerical factor.)

As to the corresponding result of [7] [see formula (36) in [7]], the exponential therein is $\exp[-4\pi(kmM)^2/eQ]$ instead of $\exp(-\pi m^2 r_+^2/eQ)$, and the preexponential factor is proportional to $(eQ)^2/kM$ instead of $m(eQ/mr_+)^3$.

We believe that our analysis of the phenomenon, which demonstrates its significant distinctions from particle production by a constant external field, is useful. First of all, it follows from this analysis that the probability of particle production by a charged black hole has an absolutely nontrivial energy spectrum. Then, in no way are real particles produced by a charged black hole over the entire space: for a given energy ε, they are radiated by a spherical surface of radius $r_2(\varepsilon)$, this surface being close to the horizon for the maximum energy. {It follows from this, for instance, that the derivation of the aforementioned result of [6] for dN/dt has no physical grounds: this derivation reduces to substituting $E = Q/r^2$ into the Schwinger formula (7), obtained for a constant field, with subsequent integration over the entire space outside the horizon.}

Let us now compare the radiation intensity I due to the effect discussed with the intensity $I_{\rm H}$ of Hawking thermal radiation. Introducing additional weight ε in the integrand on the right-hand side of (27), we obtain

$$I = \pi m^2 \left(\frac{eQ}{\pi m r_+}\right)^4 \exp(-\pi m^2 r_+^2/eQ). \quad (36)$$

As to the Hawking intensity, the simplest way to estimate it is to use dimensional arguments—that is, just to divide the Hawking temperature

$$T_{\rm H} = \frac{r_+ - r_-}{4\pi r_+^2}$$

by a typical classical time of the problem, r_+. Thus, we have

$$I_{\rm H} \sim \frac{l}{4\pi r_+^2}. \quad (37)$$

A more accurate result for I_H differs from this estimate by a small numerical factor of about 2×10^{-2}, but one can neglect this distinction for qualitative estimates. The intensities in (36) and (37) become equal for

$$eQ \sim \frac{\pi}{6}\frac{(mr_+)^2}{\ln mr_+} \sim \frac{\pi}{6}\frac{(kmM)^2}{\ln kmM}. \quad (38)$$

{One cannot agree with the condition $eQ \sim 1/(4\pi)$ for the equality of these intensities, derived in [6] from the comparison of $\varepsilon_m = eQ/r_+$ with $T_{\rm H} = (r_+ - r_-)/(4\pi r_+)$.}

2.6. Change in the Horizon Area

To conclude this section, we consider the change in the horizon surface of a black hole and, hence, in its entropy due to the nonthermal radiation being discussed. To this end, it is convenient to introduce, as in [29], the so-called irreducible mass M_0 of a black hole:

$$2M_0 = M + \sqrt{M^2 - Q^2}; \quad (39)$$

here and below, we set $k = 1$. This relation can also be conveniently rewritten as

$$M = M_0 + \frac{Q^2}{4M_0}. \quad (40)$$

Obviously, $r_+ = 2M_0$, so that the horizon surface and the black hole entropy are proportional to M_0^2.

When a charged particle is emitted, the charge of a black hole changes by $\Delta Q = -e$ and its mass changes by $\Delta M = -eQ/r_+ + \xi$, where ξ is the deviation of the particle energy from the maximum one. Using relation (40), one can easily see that, as the result of the radiation, the irreducible mass M_0 and, hence, the horizon surface and entropy of a nonextremal black hole do not change if the particle energy is the maximum, eQ/r_+. In other words, such a process, which is the most probable one, is adiabatic. For $\xi > 0$, the irreducible mass, horizon surface, and entropy increase.

As usual, an extremal black hole, with $M = Q = 2M_0$, is a specific case. Here, for the maximum energy of an emitted particle, $\varepsilon_m = e$, we have $\Delta M = \Delta Q = -e$, so that the black hole remains extremal after radiation. In this case, $\Delta M_0 = -e/2$; i.e., the irreducible mass and the horizon surface decrease. In the more general case of $\Delta M = -e + \xi$, the irreducible mass changes as

$$\Delta M_0 = -\frac{e-\xi}{2} + \sqrt{\left(M_0 - \frac{e}{2} + \frac{\xi}{4}\right)\xi}. \quad (41)$$

It is clear that, in the case of an extremal black hole of large mass, the square root dominates this expression even for a small deviation ξ of the emitted energy from the maximum one, so that the horizon surface increases.

3. RADIATION FROM ROTATING BLACK HOLES

3.1. Scalar Field

We will start the discussion of radiation from rotating black holes with a problem that is of methodological rather than of direct physical interest, with the radiation of scalar massless particles.

The semiclassical solution to the problem started from the Hamilton–Jacobi equations for the motion of a massless particle in a Kerr field (see, for instance, [30]):

$$\left(\frac{\partial S_r(r)}{\partial r}\right)^2 = -\frac{\kappa^2}{\Delta} + \frac{[(r^2+a^2)\varepsilon - a l_z]^2}{\Delta^2}, \quad (42)$$

$$\left(\frac{\partial S_\theta(\theta)}{\partial \theta}\right)^2 = \kappa^2 - \left(a\varepsilon\sin\theta - \frac{l_z}{\sin\theta}\right)^2. \quad (43)$$

Here, $S_r(r)$ and $S_\theta(\theta)$ are the radial and angular actions, respectively;

$$\Delta = r^2 - r_g r + a^2; \quad r_g = 2kM;$$

$\mathbf{a} = \mathbf{J}/M$ is the angular momentum of the black hole in units of its mass M; and l_z is the projection of the particle angular momentum onto $\mathbf{a}$.

In the spherically symmetric limit $a \to \infty$, the constant κ^2 of the separation of variables is equal to

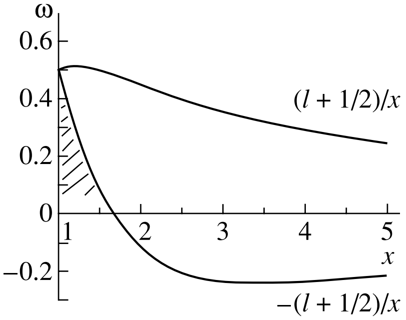

Fig. 5. Gap for $l = 1$.

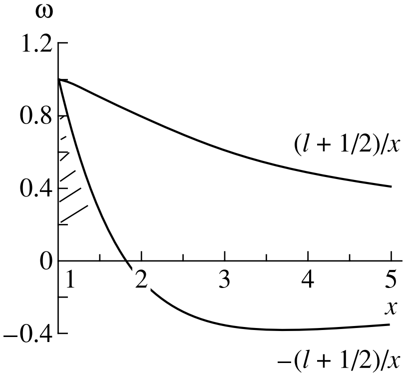

Fig. 6. Gap for $l > 1$.

the particle angular momentum squared $\mathbf{l}^2$ [$l(l+1)$ in quantum mechanics]. The influence of black-hole rotation—i.e., of the finite a—upon κ^2 is taken into account by means of perturbation theory applied to Eq. (43). The result is [14]

$$\kappa^2 = l(l+1) - 2\omega\alpha l_z + \frac{2}{3}\omega^2\alpha^2\left[1 + \frac{3l_z^2 - l(l+1)}{(2l-1)(2l+3)}\right]. \qquad (44)$$

Here and below, we use the dimensionless variables $\omega = \varepsilon kM$, $x = r/kM$, and $\alpha = a/kM$. Let us recall that, in the semiclassical approximation, one must make the substitution

$$l(l+1) \to (l+1/2)^2.$$

It should also be noted that, in the exact quantum-mechanical problem, the reduction of the radial wave equation to the canonical form

$$R'' + p^2(r)R = 0$$

results in that the expression for $p^2(r)$ develops additional [in relation to the right-hand side of Eq. (42)] nonclassical terms that should be, strictly speaking, included for $l \simeq 1$. For the sake of simplicity, however, we neglect here and below these nonclassical corrections to $p^2(r)$, which should not have a qualitative effect on the results obtained.

The dependence of the classically inaccessible region, where the radial momentum squared p^2 is negative, on the distance x is presented for various angular momenta in Figs. 5 and 6. At the horizon, the gap vanishes [23]. For $r \to \infty$, the boundaries of the classically inaccessible region behave as $\pm(l+1/2)/r$. In other words, the centrifugal term for massless particles plays, in a sense, the role of a mass squared. Let us note that, for $l > 1$, both branches of the equation $p^2(r) = 0$ are descending, but, for $l = 1$, one branch near the horizon grows, while the other descends. Thus, the radiation mechanism consists in tunneling, i.e., in the escape of particles from the dashed region to infinity.

One should note the analogy between the emission of charged particles by a charged black hole and the effect discussed. In the first case, the radiation is due to Coulomb repulsion, while, in the second case, it is due to the repulsive interaction between the angular momenta of the particle and black hole [31].

The action within the barrier for the radial Eq. (42) is

$$|S_r| = \int dx \sqrt{\frac{k^2}{(x-1)^2} - \frac{[\omega(x^2+1) - l_z]^2}{(x-1)^4}}, \qquad (45)$$

where the integral is taken between two turning points. For the sake of simplicity, we confine ourselves, for the time being, to the case of an extremal black hole, $a = kM$. Let us note that, due to a singular dependence of p on x, the action within the barrier does not vanish at $l > 1$ even for the maximum energy $\omega = l_z/2$. So much the more, it remains finite at $l = 1$ (compare Figs. 5 and 6).

The repulsive interaction is proportional to the projection l_z of the particle angular momentum and enters into the tunneling probability in the exponent, but the barrier depends on the orbital angular momentum l itself. Therefore, the main contribution to the effect will obviously come from particles with l_z close to l. A numerical calculation demonstrates that the contribution of the $l_z \neq l$ states can be neglected completely. Moreover, since the action within the barrier decreases with growing energy, the main contribution to the effect comes from particles with energies close to a maximum.

Unfortunately, an analytic calculation of the action within the barrier is hardly possible even for an extremal black hole. In order to get a qualitative idea of the effect, we will therefore use a simplified expression for κ^2:

$$\kappa^2 = l^2 + l - 2\omega l + \omega^2. \qquad (46)$$

[The results of a more accurate numerical calculation with expression (44) will be presented below.]

In this approximation, one can obtain a simple analytic formula for the action within the barrier for all angular momenta but $l = 1$. Let us assume that $\omega = (1-\delta)l/2$ with $\delta \ll 1$; just this range of energies dominates the radiation. Then, the turning points of interest to us, which are situated to the right of the horizon, are

$$x_{1,2} = 1 + \frac{2\delta}{2 \pm \sqrt{1+4/l}}. \qquad (47)$$

Now, one easily finds

$$|S_{\text{an}}| = \frac{\pi l}{2}\left(2 - \sqrt{3 - \frac{4}{l}}\right). \qquad (48)$$

One can see from this equation that the term l (following l^2) in formula (46) is quite important even for large angular momenta: it generates the terms $4/l$ in formulas (47) and (48), thus enhancing $|S|$ for $l \gg 1$ by $\pi/\sqrt{3}$. Correspondingly, the transmission factor $D = \exp(-2|S|)$ becomes about 40 times smaller. Let us note that even the transition in κ^2 from $l(l+1)$ to $(l+1/2)^2$ makes the effect considerably smaller for l commensurate with unity; however, this suppression dies out for large angular momenta.

It follows from formula (48) that the action within the barrier is large; it increases monotonically with l, starting from $|S| = \pi$ for $l = 2$. As to $l = 1$, one can see, by comparing Figs. 5 and 6, that, here, the barrier is wider than for $l = 2$; therefore, the action should be larger. Indeed, the numerical calculation of the action within the barrier, $|S|$, with κ^2 given by formula (44) confirms these estimates. Its results are presented in Table 1, where, for the sake of comparison, we also present the analytic estimates $|S_{\text{an}}|$ with formula (46). By the way, this comparison demonstrates that the approximate analytic formula (46) works very well. The numbers presented in Table 1 refer to an extremal black hole and the maximum energy of emitted particles. It is clear, however, that the transition to nonextremal black holes, lower energies, and larger l will result in the growth of the action within the barrier. Since, here, it proves to be always considerably larger than unity, the use of the semiclassical approximation within the barrier is quite reasonable.

Let us check now whether it applies to the left of the barrier. Here, near the horizon, one can neglect, in the expression for the momentum p, the term associated with the centrifugal barrier, so that condition (33) becomes

$$\frac{d}{dx}\frac{1}{p(x)} \approx \frac{d}{dx}\frac{(x-1)^2}{\omega(x^2+\alpha^2) - \alpha l}. \qquad (49)$$

Table 1. Action within the barrier for scalar particles

l	$\lvert S\rvert$	$\lvert S_{\text{an}}\rvert$
1	3.45	
2	3.15	3.14
3	3.33	3.34

One can easily see that, for not very large l, which are of importance in our case, this expression is commensurate with unity and condition (49) does not hold. Despite this circumstance and despite the disregard of the nonclassical corrections to $p^2(x)$ that were mentioned above, the results of the semiclassical calculation, which are presented below, should be correct at least qualitatively.

Let us return to the calculation of the radiation intensity. The line of reasoning used previously demonstrates that, here, the total flux of free particles for $r \to \infty$ is

$$4\pi r^2 j_r(\varepsilon, l) = 4\pi r^2 \sum_{l_z} \frac{2\pi}{(2\pi)^3 r^2} \to \frac{1}{\pi}. \qquad (50)$$

Again, the total flux of radiated particles differs from this expression only by the barrier-penetration factor. Thus, in our semiclassical approximation, the loss of mass by a black hole per unit time is given by

$$\frac{dM}{dt} = -\frac{1}{\pi}\sum_{l=1}^{\infty}\int_{0}^{\varepsilon_{\max}} \varepsilon \exp(-2|S(\varepsilon, l)|)d\varepsilon. \qquad (51)$$

Here, the maximum energy of radiated quanta is

$$\varepsilon_{\max} = \frac{al}{r_h^2 + a^2}, \qquad (52)$$

where $r_h = km + \sqrt{k^2M^2 - a^2}$ is the radius of the horizon of a Kerr black hole. The analogous expression for the loss of the angular momentum is

$$\frac{dJ}{dt} = -\frac{1}{\pi}\sum_{l=1}^{\infty}\int_{0}^{\varepsilon_{\max}} l \exp(-2|S(\varepsilon, l)|)d\varepsilon. \qquad (53)$$

The results obtained by numerically calculating, with formulas (51) and (53), the loss by a black hole of its mass and angular momentum for various values of the rotation parameter α are presented in Table 2. We present here and below, for spinning particles, the results of calculations only for sufficiently rapid rotation, $\alpha \approx 1$. The point is that, as α decreases further, not only the thermal radiation grows fast, but the effect discussed decreases faster. For smaller α, this effect becomes much smaller than the thermal one; therefore, its consideration there does not make much sense.

Table 2. Loss of mass (in units of $10^{-3}\,\pi M^2$) and angular momentum (in units of $10^{-3}\,\pi M$) due to the radiation of scalar particles

α	$\lvert dM/dt\rvert$	$\lvert dJ/dt\rvert$
0.999	2.6	6.4
0.9	0.19	0.77

As one can see from Table 2, the rate of loss of the angular momentum is higher, in comparable units, than the rate of loss of mass. In fact, this follows immediately from expression (52). From this expression alone, one can see that, even for the maximum possible energy, the ratio of the corresponding numbers is 2 : 1. The actual ratios are even larger. Hence, an important conclusion follows: extremal black holes do not exist. Even if an extremal hole is formed somehow, it loses the extremality immediately in the process of radiation.

3.2. Radiation of Photons and Gravitons

We begin investigating the radiation of real particles with an electromagnetic field. A photon has two modes of opposite parities: a so-called electric mode, with $l = j \pm 1$, and a magnetic one, with $l = j$ [19]. It follows from the duality invariance that the radiation intensities for these two modes are equal. Thus, one can confine oneself to solving the problem for a magnetic mode and then just double the result.

One can demonstrate that the situation with gravitational waves is analogous. Again, there are two modes that, because of special duality, contribute equally to the radiation, and $l = j$ for one of these modes.

For a $l = j$ mode, the radial equation in the semiclassical approximation is obviously the same as for the scalar field, but with a different value of κ^2. This can also be demonstrated by proceeding from the so-called Teukolsky equation [32] [by neglecting again nonclassical corrections to $p^2(r)$]. The corresponding eigenvalues of the angular equation for particles of spin s, found again in perturbation theory, are [14]

$$\begin{aligned}\kappa^2 &= j(j+1) + \frac{1}{4} - 2\alpha\omega j_z - \frac{2\alpha\omega j_z s}{j(j+1)} \\ &+ \alpha^2\omega^2\left\{\frac{2}{3}\left[1 + \frac{3j_z^2 - j(j+1)}{(2j-1)(2j+3)}\right]\right. \\ &- \frac{2s^2}{j(j+1)}\,\frac{3j_z^2 - j(j+1)}{(2j-1)(2j+3)} \\ &+ 2s^2\left[\frac{(j^2-s^2)(j^2-j_z^2)}{j^2(2j-1)(2j+1)}\right. \\ &\left.\left. - \frac{((j+1)^2-j_z^2)((j+1)^2-s^2)}{(j+1)^3(2j+1)(2j+3)}\right]\right\}. \end{aligned} \tag{54}$$

In this expression, we have included the term 1/4, which is necessary for the correct semiclassical description. Let us note that, as follows from the consideration of the helicity of a massless particle, the restriction $j \geq s$ holds. Accordingly, $j \geq 1$ for a photon and $j \geq 2$ for a graviton. As well as in the scalar case, the main contribution to the radiation comes from the states with the maximum projection of the angular momentum, $j_z = j$.

Table 3. Action within the barrier for photons and gravitons

	$s=1$		$s=2$	
j	1	2	2	3
$\lvert S\rvert$	1.84	2.17	1.0	1.7

Table 4. Loss of mass (in units of $10^{-3}\,\pi M^2$) and angular momentum (in units of $10^{-3}\,\pi M$) due to the radiation of photons and gravitons

	$s=1$		$s=2$	
α	$\lvert dM/dt\rvert$	$\lvert dJ/dt\rvert$	$\lvert dM/dt\rvert$	$\lvert dJ/dt\rvert$
0.999	16.5 (9.6)	39 (24)	66 (228)	148 (549)
0.9	0.72 (2.26)	2.8 (8.2)	0.58 (12.9)	2 (48)

Let us first discuss whether the semiclassical approximation is applicable here. As to the situation to the left of the barrier, it does not differ qualitatively from the scalar case. The situation within the barrier is different. As one can see from Eq. (54), the presence of spin makes κ^2 smaller and, accordingly, makes smaller the centrifugal repulsion. As a result, the barrier and the action within it both decrease. This qualitative argument is confirmed by a numerical calculation of $|S|$ for photons and gravitons with the maximum projection of the angular momentum $j_z = j$ and maximum energy for the case of an extremal black hole (see Table 3). Therefore, one should expect in the present case that the accuracy of semiclassical results is lower than in the scalar case.

The semiclassical formulas for electromagnetic and gravitational radiation differ formally from the corresponding scalar formulas (51) and (53) only by the extra factor of 2, which reflects the existence of two modes. The results of this calculation are presented in Table 4, where, for the sake of comparison, we indicate, in parentheses, the results of the complete quantum-mechanical calculation [16] which also takes into account thermal radiation.

It is clear from Table 4 that, even for $\alpha = 0.999$, in which case the thermal radiation is negligibly small, our semiclassical calculation agrees only qualitatively with the complete calculation. This is quite natural if one recalls that the semiclassical action in the present problem exceeds unity not by much, if at all. This explanation is supported by the fact that, for a photon, where $|S|$ is considerably larger (see Table 3), the semiclassical calculation agrees better with the complete calculation.

3.3. Radiation of Neutrinos

Let us at last consider the radiation of neutrinos by a rotating black hole, which are massless particles of spin 1/2. The wave function of a two-component neutrino is written as (see, for instance [16])

$$\psi = \exp(-i\varepsilon t + ij_z\phi)\begin{pmatrix} R_1 & S_1 \\ R_2 & S_2 \end{pmatrix}. \tag{55}$$

It is of importance that the wave equations for a neutrino in the Kerr metrics also admit the separation of variables [32]. The radial equations in dimensionless variables are

$$\frac{dR_1}{dx} - i\frac{\omega(x^2+\alpha^2) - j_z\alpha}{\Delta}R_1 = \frac{\kappa}{\sqrt{\Delta}}R_2, \tag{56}$$

$$\frac{dR_2}{dx} + i\frac{\omega(x^2+\alpha^2) - j_z\alpha}{\Delta}R_2 = \frac{\kappa}{\sqrt{\Delta}}R_1.$$

The angular equations are

$$\frac{dS_1}{d\theta} + \left(\omega\alpha\sin\theta - \frac{j_z}{\sin\theta}\right)S_1 = \kappa S_2, \tag{57}$$

$$\frac{dS_2}{d\theta} - \left(\omega\alpha\sin\theta - \frac{j_z}{\sin\theta}\right)S_2 = -\kappa S_1.$$

For κ^2, the same formula (54) holds, but now of course with $s = 1/2$. Just as for bosons, it is sufficient in practice to consider $j_z = j$ states.

It is important that R_1 corresponds at infinity, for $x \to \infty$, and at the horizon, for $x \to 1$, to a wave traveling to the right and that R_2 corresponds for $x \to \infty$ and for $x \to 1$ to a wave traveling to the left. [For this classification, it is convenient to use the so-called "tortoise" coordinate $\xi(x)$; $\xi \approx x \to +\infty$ for $x \to \infty$, and $\xi \approx \ln(x-1) \to -\infty$ for $x \to 1$.] It is therefore quite natural that, here, the radial current density is

$$j_r = |R_1|^2 - |R_2|^2.$$

We are interested in the barrier-penetration factor for the state that is an outgoing wave at infinity. For a neutrino or an antineutrino, such a state has a fixed helicity, but it does not have a definite parity. Meanwhile, the potential barrier depends, roughly speaking, on the orbital angular momentum in our problem; therefore, it is much more transparent to $l = j - 1/2$ states than to $l = j + 1/2$ states. (These states of given l have definite parity and are superpositions of a neutrino and an antineutrino.) Moreover, at $l = j - 1/2$ for small j, which make the main contribution to the radiation, the action has no imaginary part at all or its imaginary part is small, so that our above approach is inapplicable. Therefore, we will solve numerically the exact problem of neutrino radiation.

Table 5. Loss of mass (in units of $10^{-3}\ \pi M^2$) and angular momentum (in units of $10^{-3}\ \pi M$) due to the radiation of neutrinos

α	$\lvert dM/dt\rvert$	$\lvert dJ/dt\rvert$
0.99	4.4 (2.1)	11 (5.65)
0.9	0.7 (1)	2.7 (3.25)

Technically, it is convenient to find the reflection coefficient R in the problem of neutrino scattering off a black hole and then use the obvious relation for the transmission coefficient D:

$$D = 1 - R.$$

Here, the expressions for the loss of mass and angular momentum by a black hole are

$$\frac{dM}{dt} = -\frac{1}{\pi}\sum_{j=1/2}^{\infty}\int_0^{\varepsilon_{\max}} \varepsilon D(\varepsilon, j)d\varepsilon; \tag{58}$$

$$\frac{dJ}{dt} = -\frac{1}{\pi}\sum_{j=1/2}^{\infty}\int_0^{\varepsilon_{\max}} jD(\varepsilon, j)d\varepsilon; \tag{59}$$

$$\varepsilon_{\max} = \frac{aj}{r_h^2 + a^2}. \tag{60}$$

The results obtained by numerically solving the system of radial Eqs. (56) are given in Table 5. In parentheses, we present the results of [16], which include the Hawking radiation contribution. For a black hole close to an extremal one, at $\alpha = 0.99$, where the thermal radiation is virtually absent, our results are about twice as large as previous ones.

ACKNOWLEDGMENTS

I am extremely grateful to R.V. Korkin, with whom I obtained the results concerning radiation from Kerr black holes.

This work was supported in part by the Russian Foundation for Basic Research (project no. 01-02-16898 and project no. 00-15-96811 for Leading Scientific Schools), by the Ministry of Education of the Russian Federation (grant no. E00-3.3-148), and by the Federal Program Integration-2001.

REFERENCES

1. M. A. Markov and V. P. Frolov, Teor. Mat. Fiz. **3**, 3 (1970).
2. W. T. Zaumen, Nature **247**, 531 (1974).
3. B. Carter, Phys. Rev. Lett. **33**, 558 (1974).
4. G. W. Gibbons, Commun. Math. Phys. **44**, 245 (1975).
5. T. Damour and R. Ruffini, Phys. Rev. Lett. **35**, 463 (1975).
6. I. D. Novikov and A. A. Starobinsky, Zh. Éksp. Teor. Fiz. **78**, 3 (1980) [Sov. Phys. JETP **51**, 1 (1980)].
7. I. M. Ternov, A. B. Gaina, and G. A. Chizhov, Yad. Fiz. **44**, 533 (1986) [Sov. J. Nucl. Phys. **44**, 343 (1986)].
8. F. Sauter, Z. Phys. **69**, 742 (1931).
9. W. Heisenberg and H. Euler, Z. Phys. **98**, 714 (1936).
10. J. Schwinger, Phys. Rev. **82**, 664 (1951).
11. I. B. Khriplovich, Zh. Éksp. Teor. Fiz. **115**, 1539 (1999) [JETP **88**, 845 (1999)]; gr-qc/9812060.
12. Ya. B. Zel'dovich, Pis'ma Zh. Éksp. Teor. Fiz. **14**, 270 (1971) [JETP Lett. **14**, 180 (1971)]; Zh. Éksp. Teor. Fiz. **62**, 2076 (1972) [Sov. Phys. JETP **35**, 1085 (1972)].
13. C. W. Misner, Bull. Am. Phys. Soc. **17**, 472 (1972).
14. A. A. Starobinsky, Zh. Éksp. Teor. Fiz. **64**, 48 (1973) [Sov. Phys. JETP **37**, 28 (1973)]; A. A. Starobinsky and S. M. Churilov, Zh. Éksp. Teor. Fiz. **65**, 3 (1973) [Sov. Phys. JETP **38**, 1 (1974)].
15. J. D. Bekenstein and M. Schiffer, Phys. Rev. D **58**, 064014 (1998).
16. D. N. Page, Phys. Rev. D **14**, 3260 (1976).
17. R. V. Korkin and I. B. Khriplovich, Zh. Éksp. Teor. Fiz. **121**, 531 (2002) [JETP **94**, 453 (2002)]; gr-qc/0107101.
18. A. Calogeracos and G. E. Volovik, Pis'ma Zh. Éksp. Teor. Fiz. **69**, 257 (1999) [JETP Lett. **69**, 281 (1999)]; cond-mat/9901163.
19. V. B. Berestetskiĭ, E. M. Lifshitz, and L. P. Pitaevskiĭ, *Quantum Electrodynamics* (Nauka, Moscow, 1980; Pergamon, Oxford, 1982).
20. W. Greiner and J. Reinhardt, *Quantum Electrodynamics* (Springer-Verlag, Berlin, 1994).
21. A. I. Nikishov, in *Quantum Electrodynamics of Phenomena in Intense Fields* (Nauka, Moscow, 1979); Tr. Fiz. Inst. Akad. Nauk SSSR **111**, 1 (1979).
22. A. I. Nikishov, Zh. Éksp. Teor. Fiz. **57**, 1210 (1969) [Sov. Phys. JETP **30**, 660 (1970)].
23. N. Deruelle and R. Ruffini, Phys. Lett. B **52B**, 437 (1974).
24. Ya. B. Zel'dovich and V. S. Popov, Usp. Fiz. Nauk **105**, 403 (1971) [Sov. Phys. Usp. **14**, 673 (1972)].
25. A. B. Migdal, Usp. Fiz. Nauk **123**, 369 (1977) [Sov. Phys. Usp. **20**, 879 (1977)].
26. A. Sommerfeld, *Wave Mechanics* (Dutton, New York, 1930).
27. H. Bethe, *Intermediate Quantum Mechanics* (Benjamin, New York, 1964).
28. D. N. Page, Phys. Rev. D **16**, 2402 (1977).
29. D. Christodoulou, Phys. Rev. Lett. **25**, 1596 (1970); D. Christodoulou and R. Ruffini, Phys. Rev. D **4**, 3552 (1971).
30. L. D. Landau and E. M. Lifshitz, *The Classical Theory of Fields* (Nauka, Moscow, 1973; Pergamon, Oxford, 1975).
31. W. G. Unruh, Phys. Rev. D **10**, 3194 (1974).
32. S. A. Teukolsky, Phys. Rev. Lett. **29**, 1114 (1972).

Physics of Atomic Nuclei, Vol. 65, No. 7, 2002, pp. 1271–1272. Translated from Yadernaya Fizika, Vol. 65, No. 7, 2002, pp. 1304–1305.
Original Russian Text Copyright © 2002 by Gurevich.

90th ANNIVERSARY OF I.I. GUREVICH'S BIRTHDAY

Some Odd Bits for I.I. Gurevich's Biography

A. I. Gurevich

Received November 21, 2001

After graduating from Leningrad State University, I.I. Gurevich came to work at the Radium Institute. Soon after the start of the Great Patriotic War, the institute was evacuated to Kazan. There, Gurevich was recruited for the Soviet atomic project, headed by I.V. Kurchatov. By that time, Gurevich had carried out a number of research studies in neutron physics. While in Kazan, he defended his doctoral dissertation in that field. Along with Ya.B. Zeldovich, I.Ya. Pomeranchuk, and Yu.B. Khariton, Gurevich developed in the Soviet Union the theory of neutron moderation, without which nuclear reactors would have been impossible. He continued his studies in neutron physics in subsequent years too.

At the end of the war, when the LIPAN, or the USSR Laboratory of Measuring Instruments (later to become the Kurchatov Institute of Atomic Energy and, presently, the Russian Research Centre Kurchatov Institute) was already in place, Gurevich came back to Leningrad for a few months. There, he married Tat'yana Borisovna Stroeva, whom he had known since the 1930s and loved to the end of his life. They moved to Moscow on May 9, 1945, Victory Day. It was, of course, pure coincidence, yet somehow symbolic.

The Moscow district of Shchukino, the Kurchatov institute's location, was a suburb at that time; it was not until 1947 that it became part of the city. It inherited its name from a local village. The neighborhood included a military camp, barracks, huts, dachas, etc. There were also a few apartment houses owned by the Ministry of Defense and some other government departments, e.g., the Gamaleya Institute of Microbiology and Epidemiology, which had been there since before the war.

Many employees of the LIPAN lived on its premises. Isai Isidorovich and Tat'yana Borisovna were given an apartment in the institute's main building; afterward, of course, such apartments were converted into service rooms. It was there that their eldest son, Aleksandr (the present writer) was born. As there was no physical distance between home and work, and also by virtue of his hospitality, Isai Isidorovich customarily brought home in the evening one colleague or another. Tat'yana Borisovna usually had no objections, but there were occasions when there was nothing in the way of food at home, for those were hard times. Our housemaid was particularly displeased. (It should be noted that security regulations notwithstanding, institute employees were allowed to hire domestic help, who, after clearance by security services, received a pass to the institute territory.) I believe that Isai Isidorovich was visited more frequently than most of his colleagues.

Starting in 1947, LIPAN employees began to move to new houses outside the institute premises. At that time, Isai Isidorovich became one of Kurchatov's deputies and received an apartment in the first new building. L.A. Artsimovich, S.Yu. Luk'yanov, M.S. Kozodaev, and L.M. Nemenov moved into apartments in the same section. At a later date, two-story cottages were built nearby, and Gurevich was offered one, but he refused for fear that housekeeping concerns would divert him from science. After the move, Isai Isidorovich and Tat'yana Borisovna had their youngest son, Mikhail. Isai Isidorovich lived in that apartment to the end of his life, and Tat'yana Borisovna and Mikhail, together with his wife, are still living there.

The standard of living of LIPAN employees was by far above the Moscow average, let alone the country. But then, they worked at full stretch, as the saying goes. Their families' way of life somewhat resembled that of prerevolutionary intelligentsia. They all knew and visited each other, and were very inventive in their joint celebrations. Here, Isai Isidorovich was irreplaceable, being a rare wag. However, he could go too far in making fun of someone, and then his wife Tat'yana took him to task. He adored her, calling her fondly "Tse-eM," a Russian abbreviation standing for the "hub of the universe."

In the first postwar decade, many LIPAN employees spent even summers together. For several consecutive years, many of them, including Gurevich, rented a summer cottage in the village of Stepanovka near Moscow and, later on, in the famous Nikolina Gora. That isolated community survived until the late 1950s. By the 1960s, there had been built numerous apartment houses in the vicinity, most of which had no relation either to the Kurchatov Institute or any other nuclear physics institutes. Shchukino became just another Moscow district.

1063-7788/02/6507-1271$22.00 © 2002 MAIK "Nauka/Interperiodica"

In 1955, Gurevich resigned his office, only keeping for himself a research sector, in order to get rid of administrative duties and dedicate himself fully to science. Thereafter, in addition to neutron physics, he was engaged in the physics of positive muons and muonium. He discovered the two-frequency precession of muonium. Gurevich also obtained important results in K^0-meson oscillations and researched other elementary particles.

My brother Mikhail, who was psychologically closer to Isai Isidorovich than I was, is better qualified to describe him as a personality.

Translated by E. Azgal'dov

Physics of Atomic Nuclei, Vol. 65, No. 7, 2002, pp. 1273–1274. Translated from Yadernaya Fizika, Vol. 65, No. 7, 2002, pp. 1306–1308.
Original Russian Text Copyright © 2002 by Gurevich.

90th ANNIVERSARY OF I.I. GUREVICH'S BIRTHDAY

Toward I.I. Gurevich's Psychological Portrait

M. I. Gurevich

Received November 21, 2001

Remembrances of a member of the family of any outstanding person always have a serious flaw—the point of observation is too close, so that trivial details tend to obscure key traits; you cannot see the forest for the trees. Fully realizing this danger, I shall not try to make a complete description of my father's personality and shall limit myself to several aspects.

One of his chief properties was that he managed to preserve many traits of a child, if not of a preschool age, at least not a year older than 10, i.e., a harmonious personality open to the world. Here are a few illustrative examples.

It is common knowledge that a son of an outstanding father will usually be somewhat suppressed by his powerful personality; Freud's relations with his son are a classical example. I have witnessed this phenomenon among my friends. Yet, I never experienced anything like this myself, even though I am not a particularly strong character. The reason is that my father, like a harmonious child, in his association with people did not play the absurd game of who is the smartest. He simply did not bother about it—what he was after was new ideas and impressions, which he soaked in with complete trust in the world that generated them. The keyword here is the world, not any particular source of information, for father was neither a fool nor an overly naive person.

His perception of the new was like a child's in yet another respect—there was no self-interest in it, not only in a narrow pecuniary sense, but also in the sense of "personality development," "enrichment with achievements of world culture," etc.

His interest in the world, which he maintained even in his latter years, when he was very ill, I would call curiosity in its best, childish sense, rather than inquisitiveness, because the latter term carries some snobbish differentiation of "high" and "low" information.

This is not to say, of course, that father's curiosity was omnivorous—he was more interested in some fields than others, while still others did not interest him at all—but this division was not speculative, superficial, for it sprang from his very being and was in full harmony with his personality.

For example, father took little interest in individuals as such—he was more absorbed in ideas and their destinies; therefore, his interest in people was rather selective, and many quite worthy men bored him.

His natural way of perception of the world was mirrored in his reading—from works on general questions of world view to adventure novels.

One cannot say that father did not change with age. Somewhere after turning 70, he began to give more thought to philosophy, religion, and generally universal questions of human life, but his harmonious perception was unchanged.

It would be in order to mention his attitude to the game. Among all the people of his generation I have known, he was perhaps the most capable of apprehending Johann Heusinga's view of the game as the driving force of human progress. Being a man of his time, he did not, of course, put scientific study on the same plane with games, but he treated games rather seriously and liked playing them. He played chess, Erudite, mahjongg, and other board games. He was a permanent member of a company of vint players, which was organized by A.M. Andriyanov. (It is to be regretted that this Russian game, beloved by many luminaries of Russian culture, has completely gone to seed and been ousted by bridge.)

Speaking of the gaming aspects of science, it should be noted that they are usually interpreted as exclusively agonistic (competitive). This, to my mind, is a big fallacy, which stems from the unconscious substitution of "competitive game" for "game." It may be that there cannot be a game in sport that is not competitive, but the games children play are not necessarily competitive, at any rate, not zero-sum ones. In science, the most important gaming element is not to be the first to say "mew," but the joint solving of riddles. To participate in "free scientific gabbing," so necessary for the progress of science, one must be quick to take an interest in a problem and make an active contribution to attempted solutions. It comes natural to a child but by no means always so to an adult. Well, I have not known anyone better equipped for "scientific gabbing" than my father. I even regard myself as rather spoilt by my opportunity of many years to have had such a person to talk to.

1063-7788/02/6507-1273$22.00 © 2002 MAIK "Nauka/Interperiodica"

My father's attitude to the issue of superiority was yet another proof of his integrity. It is not as if he was quite indifferent to how people saw him, but father only set store by those evaluative parameters of his personality he himself had chosen: I play these games, but I do not and will not play those. For instance, while he had his driver's license, he did not like driving, and was not in the least concerned about his skill in that area.

The last, and perhaps the most important, thing that must be mentioned is that my father had the capacity for being joyful—not to be merry at all times, but to feel those small joys of life that so often are left unnoticed. He could become animated even when he was in a hospital, where he suffered very much. Father used to say, "Happiness is enjoying going to work and enjoying going home."

The second thing I wanted to speak about is my father's intuition. It was extremely powerful, and he could hear it. On several occasions, I was amazed at the accuracy of his forecasts and estimates in matters where he seemed to be relatively incompetent. Yet, the strength of his intuition surpassed his ability to hear it, or at least to be aware of his hearing. Not infrequently, he tried to rationalize his vision, and that rationalization could yield in accuracy to his vision.

In the 1940s and the early 1950s, one of my father's important functions in the atomic project was to coordinate experimental and theoretical work. Though I have no right to pass final judgment, I can suppose that this function could only be performed by someone with a rich rather than narrowly directed intuition.

Here, I should like to note once again the absence of narrowness, which was not merely intuitive but also conscious—my father was very annoyed by any kind of fanaticism. Yet, we are all human, and I have an a propos anecdote to tell. One day, my father complained that I had not chosen to become a pure mathematician or physicist, to which I replied, "Your father was an engineer and your uncles too. Are you sure they were more stupid than you?" Father was silent for a while, then admitted that I had him there.

Translated by E. Azgal'dov

Physics of Atomic Nuclei, Vol. 65, No. 7, 2002, p. 1275. Translated from Yadernaya Fizika, Vol. 65, No. 7, 2002, p. 1308.
Original Russian Text Copyright © 2002 by Okun.

90th ANNIVERSARY OF I.I. GUREVICH'S BIRTHDAY

Uncle Sanya

L. B. Okun

Institute of Theoretical and Experimental Physics,
Bol'shaya Cheremushkinskaya ul. 25, Moscow, 117218 Russia

Received November 19, 2001

I saw Isai Isidorovich Gurevich for the first time in the fall of 1951, when he started to deliver a year's course of lectures to us, fifth-year students at the Moscow Mechanical Institute, which was to become the Moscow Engineering Physics Institute (MEPhI). He introduced us to the foundations of theoretical nuclear physics; the subject was codified in our timetable as Course no. 7, for the Moscow Mechanical Institute belonged to the Ministry of Medium Machine Building and was thus secret.

Isai Isidorovich was so easy-tempered and benevolent and so lucid and detailed in his lectures that each of his listeners has kept most pleasant memories of him. When I found myself at the Institute of Theoretical and Experimental Physics in 1954, I realized that not only his students were warmly disposed toward Isai Isidorovich, but so were all the collaborators of I.Ya. Pomeranchuk, who lovingly called him Uncle Sanya behind his back.

Various episodes come back to memory.

In the fall of 1956, I went by train to Tbilisi to attend a conference on cosmic rays. It was nighttime when I finally reached my hotel, where I discovered that they had accommodated me in the same room with Isai Isidorovich. He met me in his sleeping pajamas and said, "There is no plug in the bathtub. Use my shaving-brush instead it and take a bath after your long travel." It was at that conference that we first heard about the work of Lee and Yang on parity nonconservation. Precision measurements of parity nonconservation in muon decay were to become the main focus of activity of Gurevich and his team for many subsequent years.

In September 1957, Gurevich was allowed to attend a conference in Padua and Venice. On the night before his departure, I brought to his place my report, "Some Comments on the Composite Model of Elementary Particles," where I generalized the Sakata model and applied it to weak interactions. Isai Isidorovich put my paper in his suitcase and read it in Italy on my behalf. It was published in the conference proceedings.

From 1968, when Gurevich was elected to corresponding membership to the USSR Academy of Sciences, we regularly met at meetings and sessions of the Department of Nuclear Physics. We often spoke on the phone. Nearly always, he started the conversation with a flowery Oriental greeting, "I kiss the footprints of the fleas of my master's dog." Very rarely, I had the opportunity of taking over these "footprints of the fleas."

In the late 1960s, I organized annual sessions of the Department of Nuclear Physics at MEPhI during the winter vacation. In a few years' time, I was able to convince Gurevich to head the organizing committee of these sessions.

Gurevich often fell sick in the 1980s. Igor' Kobzarev and I visited him at the hospital, after he had had a pacemaker implanted. On that occasion, he talked much of poetry and gave us a photocopy of Georgii Ivanov's poems that had just appeared in a periodical.

I remember my visit, by train and on a bicycle, to the summer cottage that his wife and he rented in Snegiri near Moscow. We had made arrangements for that visit in advance: lunch and a kind and intelligent host were waiting for me. At the end of the day, Isai Isidorovich saw me off to the field road...

Translated by E. Azgal'dov

Physics of Atomic Nuclei, Vol. 65, No. 7, 2002, pp. 1276–1281. Translated from Yadernaya Fizika, Vol. 65, No. 7, 2002, pp. 1309–1314.
Original Russian Text Copyright © 2002 by Gavrin, Gorbachev, Ibragimova, Cleveland.

NUCLEI
Experiment

Rate of Germanium-Isotope Production by Background Processes in the SAGE Experiment

V. N. Gavrin, V. V. Gorbachev, T. V. Ibragimova, and B. T. Cleveland[1)]

Institute for Nuclear Research, Russian Academy of Sciences,
pr. Shestidesyatiletiya Oktyabrya 7a, Moscow, 117312 Russia

Received June 25, 2001

Abstract—Data on a direct determination of systematic uncertainties caused by the background production of germanium isotopes in the radiochemical SAGE experiment measuring the solar-neutrino flux are analyzed. The result obtained for the rate of ^{68}Ge production is $6.5(1 \pm 1.0)$ times greater than the expected one; the rate of ^{69}Ge production does not exceed preliminary estimates. The above result for ^{68}Ge corresponds to the systematic uncertainty that is caused by the interaction of cosmic-ray muons and which is equal to 5.8% (4.5 SNU) at a solar-neutrino-capture rate of 77.0 SNU. An experiment is proposed that would test the effect of cosmic-ray muon influence on the SAGE systematic uncertainty and which would be performed at the location of the underground scintillation telescope facilities of the Baksan Neutrino Observatory (Institute for Nuclear Research, Russian Academy of Sciences). © *2002 MAIK "Nauka/Interperiodica".*

1. INTRODUCTION

The possibility of directly determining systematic uncertainties is attractive in any experiment. In this article, we describe a determination of some systematic uncertainties in the radiochemical SAGE experiment.

Since 1990, the Russian–American (previously, Soviet–American) gallium experiment (SAGE) has been measuring the solar-neutrino-capture rate in about 60 tons of liquid metal gallium. Neutrinos interact with the ^{71}Ga isotope of the target through the inverse-beta-decay reaction: $^{71}\mathrm{Ga}(\nu_e, e^-)^{71}\mathrm{Ge}$. By using a special chemical procedure, product ^{71}Ge atoms are extracted from the target at the end of each exposure run (1–1.5 months); are transformed into a gaseous state of GeH_4 (germane); and are placed into a proportional counter, where the decay of these atoms is observed for 5 to 6 months. A detailed description of the experiment, including an account of the chemical procedures used to extract germanium from the gallium target, counting of ^{71}Ge decays, and data analysis, is presented in [1, 2].

The eleven years of observation resulted in obtaining the solar-neutrino-capture rate of $77.0^{+7.1}_{-6.9}$ SNU[2)]—that is, about 60% of 129 SNU predicted by the standard solar model for a gallium target [3, 4]. The discrepancy between the observed and expected neutrino fluxes is widely known as the solar-neutrino problem. In this connection, accuracy in measuring the neutrino flux is of great importance, and it is the need for precisely estimating the errors in such measurements that motivated the present study.

The ^{71}Ge isotope, whose production rate is used to determine the solar-neutrino flux, can also be generated in a gallium target under the effect of cosmic rays and environmental radioactivity. Together with ^{71}Ge, other germanium isotopes—^{68}Ge and ^{69}Ge—are produced in a gallium target. The known relations between the rates of production of the three isotopes in various processes make it possible to determine the ^{71}Ge background production rate by measuring ^{68}Ge and ^{69}Ge [5]. A long period over which the SAGE measurements have been performed enables us to determine the systematic uncertainty associated with the background production of the germanium isotopes directly on the basis of searches for ^{68}Ge and ^{69}Ge events in analyzing the accumulated experimental data of solar-neutrino measurements.

For this purpose, we will first briefly consider the system counting ^{71}Ge decays and discuss the possibilities for extracting ^{68}Ge and ^{69}Ge events from the total data sample. Having determined the efficiency of the procedures used to seek germanium events, we apply these procedures to the accumulated data and

---

[1)] University of Washington, Box 351560, Seattle, WA 98195-1560, USA.

[2)] 1 SNU is one neutrino-capture event per 10^{36} target atoms per second.

obtain the sought rate of germanium-isotope production in the gallium target.

2. SYSTEM COUNTING ^{71}Ge DECAYS

The decay of ^{71}Ge ($T_{1/2} = 11.4$ days) proceeds via electron capture with the emission of 10.4-, 1.2-, and 0.1-keV Auger electrons (K, L, and M modes, respectively). Short tracks of these electrons in the counter gas result in a fast rise time of the proportional-counter pulses—such events are referred to as pointlike ones, in contrast to extended events associated with long tracks.

The system counting ^{71}Ge decays indicates the time of pulse arrival; a digital oscilloscope records the shape of each pulse, and this shape is used to assess, in the off-line mode, the energy and the pulse rise time. An active shield based on a NaI crystal selects pulses accompanied by γ emission. The dynamical range of energy measurements between 0.3 and 16 keV enables us to record the K and L decays of ^{71}Ge. Thus, events that are candidates for ^{71}Ge decay are selected according to three signatures: (1) the pulse height falls within the K- and L-peak windows, (2) the pulse rise time is short (pointlike event), and (3) there is no accompanying γ emission.

After counting ^{71}Ge decays in the proportional counter for 5 to 6 months, the time analysis of selected events is performed: by using the maximum-likelihood method, ^{71}Ge decays are separated from background pulses, recorded at a constant rate, by an excess of the counting rate at the beginning of the counting time [6].

Figure 1 shows the schemes of ^{68}Ge and ^{69}Ge decays. In the case of ^{68}Ge, the counter records two decays: ^{68}Ge decay ($T_{1/2} = 271$ d) is indistinguishable from ^{71}Ge decay, and the subsequent decay of ^{68}Ga ($T_{1/2} = 68.3$ min) occurs via the emission of a β^+ particle in 90% of events and via electron capture in 10% of events. As to ^{69}Ge ($T_{1/2} = 39.1$ h), it decays via electron capture (64%) or by β^+ mode (36%) to excitation levels of ^{69}Ga, the pulses from these decays being accompanied by γ emission of various energies.

3. ^{68}Ge PRODUCTION RATE

3.1. Selection of ^{68}Ge Events

In the SAGE gallium target, nuclei of the ^{68}Ge isotope are produced predominantly by the interactions of cosmic-ray muons. The ^{68}Ge production rate obtained by means of calculations and indirect experiments [5, 7, 8] is given in [1]. This rate is equal to 0.026 ± 0.015 ^{68}Ge atoms per day in 60 tons of gallium. We will compare the results of our analysis with this value.

Candidate events for ^{68}Ge decay were selected by a pulse pair. The first pulse was selected according to the criteria of a ^{71}Ge event, while the second pulse was selected according to its coincidence with the 1022-keV γ line. Figure 2 shows the energy spectrum of events that were recorded in the NaI crystal in coincidence with proportional-counter pulses during measurements with the counter containing a large amount of ^{68}Ge introduced in the counter gas. The 1022-keV line corresponds to recording two annihilation photons in the NaI detector. Figure 2 also shows the spectrum of pulses in NaI that were coincident with counter pulses and which were accumulated in solar-neutrino measurements from August 1996 to December 2000. The analysis of both spectra presented in that figure permits one to select the energy range for NaI over which the probability of random coincidences is minimal, with the detection efficiency being sufficiently high for events corresponding to ^{68}Ge. About 50% of ^{68}Ge decays counted by the NaI detector and 10% of events from the coincidence spectrum for the solar measurements fall within this range.

We used two methods for restricting the time interval Δt between the pulses of the pair. In the first method, $\Delta t < 2T_{1/2}(^{68}\mathrm{Ga}) = 137$ min. In this case, the effect, which is the number of ^{68}Ge decays, is estimated as the difference of the number of recorded pulse pairs and the expected mean number of random coincidences. In the second method, $\Delta t < 1$ d. In this case, we used the time analysis similar to that of ^{71}Ge pulses—that is, the maximum-likelihood method for ^{68}Ga decay at a constant background of random coincidences. There, the background of random coincidences is not averaged over all measurements, but it is associated with an individual measurement. If the results obtained by the two methods agree, this will suggest that, in selecting ^{68}Ge candidates, the background is entirely due to random coincidences.

3.2. Efficiency of Selection of ^{68}Ge Events

The number n_c of recorded ^{68}Ge events is related to the number n_0 of ^{68}Ge atoms produced in the target by the equation $n_c = n_0\varepsilon$. The efficiency ε is the product of the efficiency of germanium extraction from the target after the solar exposure ($\varepsilon_{\rm ext} \sim 0.9$), the efficiency of counting ^{71}Ge decays in the proportional counter ($\varepsilon_{\rm cnt} \sim 0.6$), the probability of ^{68}Ge decay within the actual time of counting ($\varepsilon_t \sim 0.23$), the probability of ^{68}Ga decay within the time interval Δt (see subsection 3.1) ($\varepsilon_\tau = 0.75$ for $\Delta t = 137$ min

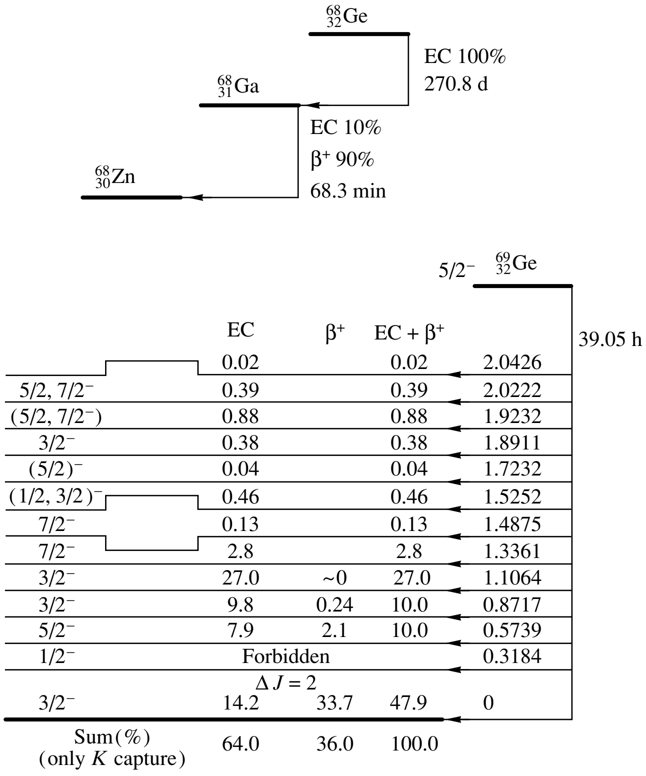

Fig. 1. Decay scheme of germanium isotopes [7].

and 1.0 for $\Delta t = 1$ d), and the efficiency of recording ^{68}Ga decays (ε_g); that is, $\varepsilon = \varepsilon_{\text{ext}}\varepsilon_{\text{cnt}}\varepsilon_t\varepsilon_\tau\varepsilon_g$. In turn, the efficiency of recording ^{68}Ga decays, ε_g, is the product of the probability of recording a β^+ particle in the proportional counter and the probability of recording two annihilation photons within the energy range chosen for NaI. The former probability is $\varepsilon_\beta \sim 0.65$, because the decay occurs at the counter wall and because, of half of the particles going to the wall, 30% return into the gas volume. The latter probability is $\varepsilon_\gamma \sim 0.90 \cdot 0.95 \cdot 0.50 \sim 0.4$; here, we have considered that β^+ particles are emitted in 90% of ^{68}Ga decays, that the probability of detection of at least one photon by the NaI detector is 0.95, and that 50% of events coinciding with NaI signals fall within the chosen energy range. Therefore, the total efficiency of the procedure for seeking ^{68}Ge events is ε about ~2.7%.

Thus, we conclude that, if N ^{68}Ge events were‘ found in k solar runs, then the ^{68}Ge production rate per target-mass unit is (we assume that this rate is constant)

$$\dot{n} = \lambda N / \sum_{i=1}^{k} (1 - e^{-\lambda\theta_i}) m_i \varepsilon_i,$$

where λ is the ^{68}Ge-decay constant, $(1 - e^{-\lambda\theta_i})$ is the “saturation factor” (the fraction of the ^{68}Ge atoms accumulated in the target over the exposure time θ_i), m_i is the gallium mass used in the ith exposure, and ε_i is the efficiency ε of the ith measurement.

3.3. Random Coincidences

The number of random coincidences that can be observed if use is made of the above method for identifying the ^{68}Ge events depends on the rate of counting pulses in the proportional counter that are coincident with NaI signals and on the number of pulses selected according to the ^{71}Ge criteria.

For a single event selected according to the ^{71}Ge criteria, the probability of random coincidences is $P = 1 - e^{-a}$, where $a = \Lambda\Delta t$ is the Poisson distribution parameter, Λ being the mean rate of counting pulses coinciding with the NaI signals within the chosen energy range. In our measurements, $\Lambda = 0.06 \pm 0.01$ d^{-1} and $P = 5.5 \times 10^{-3}$ for $\Delta t = 137$ min.

3.4. Results

For the present analysis, we can use the data accumulated since August 1996. Within this period, the gain has not changed in the NaI channel; therefore, we can use fixed boundaries of the energy range chosen in the NaI for selecting ^{68}Ga events.

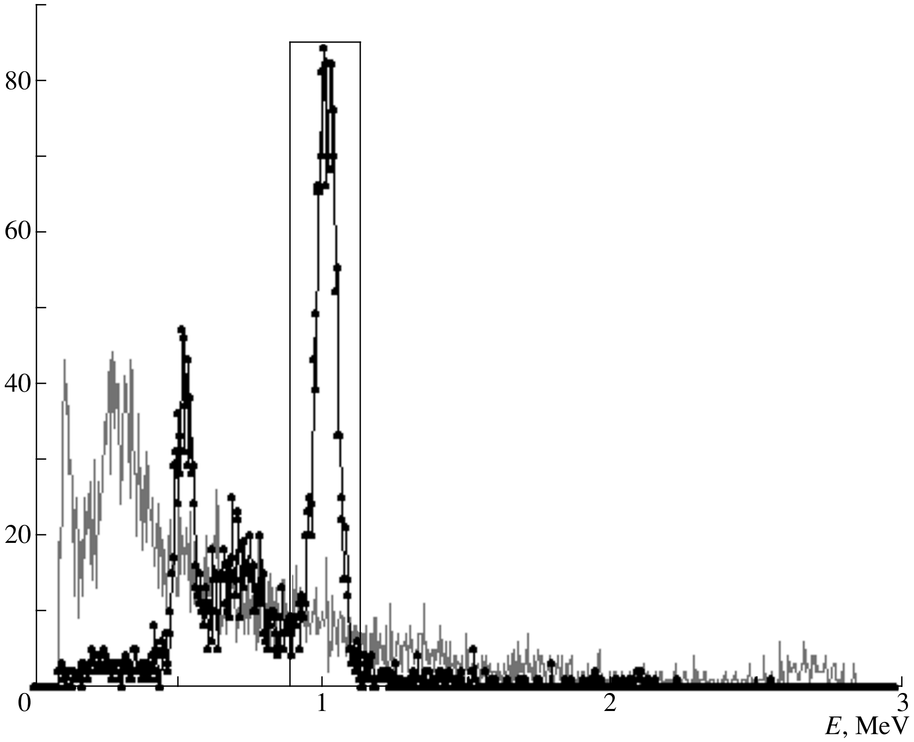

Fig. 2. Spectra of events in the NaI detector that are coincident with proportional-counter pulses. The dark line with points represents the spectrum of ^{68}Ge decays; the gray line corresponds to the spectrum of events accumulated in solar runs. The vertical rectangle shows the boundaries within which ^{68}Ge events were selected.

To avoid uncertainties in estimating the efficiencies, we eliminated tail portions of duration Δt from all actual-time intervals of counting in determining the first pulse in a pair of ^{68}Ge events. In 32 solar runs, nine pair pulses for ^{68}Ge were found under the aforementioned conditions for $\Delta t = 137$ min. At the expected mean number of random coincidences that is equal to 4.5 ± 0.1, $4.5(= 9 - 4.5)$ events should be associated with ^{68}Ge decay. This value corresponds to the ^{68}Ge production rate of $0.17(1 \pm 0.82)$ d^{-1} in the 60-t gallium target (we obtained the total uncertainty by combining squares of the individual relative uncertainties). This rate is $6.5(1 \pm 1.0)$ times higher than the expected one.

In an alternative data processing with $\Delta t = 1$ d, the time analysis associated $4.7^{+3.6}_{-3.1}$ events of 55 pair events with ^{68}Ge decay; this result agrees with that obtained in processing mean values.

The natural radioactive series of uranium and thorium can be a source of pair events that we associate with ^{68}Ge decay. Among decay pairs, we sought those in which the second events were accompanied by γ emission with $E_\gamma > 850$ keV (in this case, it was possible to detect photons within the energy range chosen for NaI). Our analysis revealed that the radioactive series cannot explain the result obtained above.

We also analyzed data obtained in counting so-called secondary extractions (these are test extractions that are periodically performed after germanium extraction from the gallium reactors upon the completion of a solar exposure). The amount of germanium resulting from the secondary extraction is about 20–30 times less than that in primary ones. The ^{68}Ge isotope was not found in secondary extraction.

Thus, the results of our analysis suggest that the observed events are associated with ^{68}Ge decay. However, an approximation of the time intervals between the pulses in the observed pairs yielded a decay curve characterized by a half-life of (27^{+30}_{-12}) min, which is nearly one-half as great as that of ^{68}Ge.

4. ^{69}Ge PRODUCTION RATE

4.1. Selection of ^{69}Ge *Events*

According to the estimates from [1, 5], the production of ^{69}Ge in the SAGE gallium target is due to the effect of solar neutrinos (5.8 SNU, which corresponds to the ^{69}Ge production rate of 0.156 ^{69}Ge atoms per day in the 60-t target), cosmic-ray muons (0.036

^{69}Ge atoms per day), and the neutron and α activity of surrounding materials (0.015 ^{69}Ge atoms per day). The total ^{69}Ge production rate from all sources is 0.21 ^{69}Ge atoms per day in 60 tons of gallium.

In order to single out pulses associated with ^{69}Ge decay, we used a method based on the coincidence of the electron-capture mode of ^{69}Ge decay and the 1106-keV γ line. Proportional-counter pulses were selected by the pulse height and by the rise time in accordance with the selection criteria for ^{71}Ge. The time analysis based on the maximum-likelihood method was applied to the selected events—that is, those of ^{69}Ge decay ($T_{1/2} = 39.1$ h) with a constant background-counting rate.

4.2. *Efficiency of Selection of* ^{69}Ge *Events*

The ^{69}Ge production rate in the 60-t gallium target is $\dot{n} = \lambda(n_i/\varepsilon_i)(60/m_i)$, where λ is the ^{69}Ge decay constant, n_i is the number of ^{69}Ge decays that was measured in the ith run, ε_i is the efficiency of recording ^{69}Ge decays, and m_i is the gallium mass used in the ith measurement. In turn, the efficiency of recording ^{69}Ge decays is, just like that for ^{68}Ge, the product of the efficiency of germanium extraction from the target after a solar exposure ($\varepsilon_{\mathrm{ext}} \sim 0.9$), the efficiency of counting ^{71}Ge decays in the proportional counter ($\varepsilon_{\mathrm{cnt}} \sim 0.6$), the probability of ^{69}Ge decay within the actual counting time ($\varepsilon_\tau \sim 0.5$), and the probabilities of the emission of 1106-keV photons and their recording in the NaI detector ($\varepsilon_n \sim 0.27 \times 0.67 = 0.18$). Therefore, we have $\varepsilon = \varepsilon_{\mathrm{ext}}\varepsilon_{\mathrm{cnt}}\varepsilon_n\varepsilon_\tau(1 - e^{-\lambda\theta})$. At an exposure time of $\theta \sim 30$ d, the saturation factor $(1 - e^{-\lambda\theta})$ is equal to unity. Thus, the total efficiency of recording ^{69}Ge atoms is about 5%.

4.3. *Results*

For our analysis, we have used the same data as those for determining the ^{68}Ge production rate—that is, data accumulated from August 1996 to December 2000. Nineteen pulses corresponding to the ^{69}Ge selection were found in 32 solar measurements. On the basis of the time analysis, all selected pulses were associated with the uniformly distributed background. The ^{69}Ge production rate in the 60-t gallium target is $\leq$0.49 ^{69}Ge atoms per day at a 68% confidence level.

This constraint does not rule out the possibility that the rate of production of this isotope under the effect of cosmic-ray muons can be higher than the predicted one; this is suggested by the analysis of ^{68}Ge events.

5. POSSIBILITY OF TEST MEASUREMENTS: AN EXPERIMENT AT THE UNDERGROUND SCINTILLATION TELESCOPE

The results of the analysis of solar-run measurements aimed at determining the rate of germanium-isotope production in a gallium target demonstrate that we may underestimate the background associated with the interactions of cosmic-ray muons. The estimated amount of ^{68}Ge complies with the ^{71}Ge production rate of 0.08 ^{71}Ge atoms per day in the muon-induced reactions—that is, 5.8% (4.5 SNU) of the measured neutrino-capture rate of 77 SNU. Moreover, the time analysis aimed at identifying ^{71}Ge decays against a constant background associates up to 10% of ^{68}Ge decays with ^{71}Ge decays, and this leads to an additional systematic overestimation of the measured solar neutrino flux; it can reach approximately 0.1 pulse (^{71}Ge)/run over a 30-d exposure at a production rate of 0.17 ^{68}Ge atoms per day (that is, up to 2% of the measured value).

The result of the above analysis has a large statistical uncertainty. In order to assess the effect of cosmic-ray muons on the measured solar-neutrino flux to a high precision, it is reasonable to perform an additional direct experiment that would study the muon effect on gallium measurements.

The Baksan Neutrino Observatory (BNO) provides quite favorable conditions for such an experiment. The underground scintillation telescope (UST) and the gallium–germanium neutrino telescope (GGNT), which is the location of the SAGE experiment, belong to the complex of the underground low-background BNO laboratories of the Institute for Nuclear Research (Russian Academy of Sciences). The UST depth is sufficient for eliminating all components of cosmic rays, with the exception of muons. The muon flux at UST was measured to a high precision and is equal to 4.35×10^{-6} (cm^2 s)$^{-1}$ [9]; that is, it is about 1000 times greater than that in the GGNT chamber $\{3.03(1 \pm 0.03) \times 10^{-9}$ (cm^2 s)$^{-1}\}$ [10]). While the ^{68}Ge production rate is 0.026 ^{68}Ge atoms per day in 60 tons of gallium in GGNT, its expected value in UST is $0.026(4.35 \times 10^{-6})/(3.03 \times 10^{-9})(145/381)^{0.73} = 18.4$ ^{68}Ge atoms per day. It has been considered here that muon interactions are proportional to the mean muon energy raised to the power 0.73 [11]; the mean muon energy is 145 GeV in UST and 381 GeV in GGNT. Thus, we can see that, by using only part of the gallium (for instance, 7 t), the ^{68}Ge production rate in muon interactions can be measured at UST to a precision of 10% in the course of two six-month exposures.

6. CONCLUSION

The above analysis of the data from solar measurements has revealed that the ^{68}Ge production rate in the SAGE gallium target exceeds the value obtained in indirect experiments and preliminary calculations by a factor of $6.5(1 \pm 1.0)$. According to the data from the solar-run analysis, the ^{69}Ge production rate is consistent with preliminary estimates. These results demonstrate that an error in estimating the systematic uncertainty in measurements of solar muon flux may arise because of the possible underestimation of the effect of cosmic-ray muons. In this connection, it is desirable to perform direct measurements of the rate of germanium-isotope production at a higher muon flux. Two six-month exposures of 7 t of gallium in the UST of the BNO would make it possible to measure the ^{68}Ge production rate to a precision better than 10%.

ACKNOWLEDGMENTS

We are grateful to J.N. Abdurashitov, A.V. Kalikhov, and other members of the SAGE collaboration for stimulating discussions on the problems considered in this article. We are also indebted to G.T. Zatsepin for enlightening discussions.

REFERENCES

1. J. N. Abdurashitov *et al.*, Phys. Rev. C **60**, 055801 (1999).
2. V. N. Gavrin, Nucl. Phys. B (Proc. Suppl.) **91**, 36 (2000).
3. J. N. Bahcall, S. Basu, and M. N. Pinsonneault, Phys. Lett. B **433**, 1 (1998).
4. S. Turck-Chieze, Nucl. Phys. B (Proc. Suppl.) **91**, 73 (2001).
5. Yu. I. Zakharov, Candidate's Dissertation in Physics and Mathematics (Inst. Yad. Issled. Akad. Nauk SSSR, Moscow, 1987).
6. B. T. Cleveland, Nucl. Instrum. Methods Phys. Res. **214**, 451 (1983).
7. M. Cribier, B. Pichard, J. Rich, *et al.*, Astropart. Phys. **6**, 1351 (1997).
8. J. N. Bahcall, B. T. Cleveland, R. Davis, Jr., *et al.*, Phys. Rev. Lett. **40**, 1351 (1978).
9. V. I. Gurentsov, Preprint No. P-0379, IYaI AN SSSR (Institute for Nuclear Research, USSR Academy of Sciences, Moscow, 1984).
10. V. N. Kornoukhov, Candidate's Dissertation in Physics and Mathematics (Inst. Yad. Issled. Ross. Akad. Nauk, Moscow, 1998).
11. O. G. Ryazhskaya and G. T. Zatsepin, in *Proceedings of the 9th International Conference on Cosmic Rays, London, 1965* (Inst. of Physics, London, 1965), Vol. 2, p. 987.

Translated by E. Kozlovskiĭ

Physics of Atomic Nuclei, Vol. 65, No. 7, 2002, pp. 1282–1287. Translated from Yadernaya Fizika, Vol. 65, No. 7, 2002, pp. 1315–1320.
Original Russian Text Copyright © 2002 by Galanina, Zelenskaya.

NUCLEI
Experiment

Manifestations of a Dineutron Cluster in Elastic $\alpha\,^6$He Scattering

L. I. Galanina and N. S. Zelenskaya[*]

Institute of Nuclear Physics, Moscow State University, Vorob'evy gory, Moscow, 119899 Russia

Received March 16, 2001; in final form, September 4, 2001

Abstract—A consistent theoretical analysis of elastic α^6He scattering is performed with allowance for the correction associated with the exchange of a dineutron cluster. It is shown that the inclusion of the exchange mechanism, along with that of potential scattering, makes it possible to reproduce the measured cross section over the entire range of the ^{6}He scattering angle. Concurrently, one can also obtain information about the spatial distribution of the dineutron cluster and the α particle in the ground state of the ^{6}He nucleus. © *2002 MAIK "Nauka/Interperiodica".*

1. INTRODUCTION

Investigation of light neutron-rich nuclei in the reactions with radioactive beams has recently become one of the topical problems in contemporary nuclear physics. Extensive searches for hydrogen and lithium isotopes involving a large neutron excess (about 4 to 5 neutrons) and a detailed exploration of their spectroscopy were performed in [1, 2]. Some shapes of the spatial distribution of nucleons in neutron-rich nuclei were determined in the experiments reported in [1], which were based on some sophisticated correlation methods. However, even the simplest nuclei involving only two extra neutrons have not yet received adequate study, either from the point of view of their spectroscopy or from the point of view of the topology of the spatial arrangement of the neutrons and the remaining virtual cluster. The arrangement of the deuteron with respect to the α-particle cluster in the ^{6}Li nucleus was investigated theoretically in [3, 4] on the basis of microscopic models allowing for the lowest two values of the relative orbital angular momentum ($\Lambda = 0, 2$) in the α–d system (the states associated with these values of the orbital angular momentum were specified differently in [3] and in [4]: Kukulin *et al.* [3] used the principal quantum number $N = 2$ of two $1p$ nucleons in the three-body model, whereas Zhukov *et al.* [4], who relied on the method of K harmonics, took into account not only $K_{\rm min}$ but also $K_{\rm min} + 2$). Allowance for two values of Λ enhances the number of admissible topologies of the ^{6}Li nucleus; as a result, a whole series of configurations involving a nonstandard arrangement of the proton and the neutron with respect to the α particle becomes possible (borromean nuclei, in terms of the authors of [4]), apart from the conventional αd cluster configuration. As to the ^{6}He nucleus, detailed microscopic calculations for it were performed in [5]. These calculations predict that the ^{6}He wave function has two strongly different spatial components. The first corresponds to the configurations where there are two closely spaced neutrons whose center of mass lies at a considerable distance from the α particle (dineutron cluster). The second is characterized by cigar shape, with the distance between the neutrons being large and the distance between the center of mass of the two neutrons and the α particle being small.

The existence of a dineutron configuration in the ^{6}He nucleus may have a pronounced effect on elastic α^6He scattering—in particular, at large scattering angles. Indeed, the cross section for elastic backward scattering must develop maxima upon taking into account cluster exchange (see [6]). Elastic α^6He scattering for angles of up to 160° was studied experimentally in Dubna by using a beam of 15-MeV ^{6}He ions. According to [7], a satisfactory description of data from that experiment can be obtained under the assumption that the ^{6}He nucleus has a dineutron cluster configuration.

Recently, experimental groups from Leiden and Brussels Universities [8] obtained new data on the differential cross sections for elastic α^6He scattering at moderate energies up to the largest angles. Here, we analyze these data within the microscopic approach proposed in [6]. This approach is based on taking into account, along with potential scattering, exchange processes associated with the dissociation of the ^{6}He nucleus. In contrast to [6], however, we consider here exchange processes within the three-body problem, applying the DWBA with finite-range interactions (DWBAFR) [9]. In the case of elastic scattering, the amplitude of exchange processes can be considered as the simplest many-body (more precisely,

---

[*] e-mail: `wg2@anna19.npi.msu.su`

three-body) correction to the optical-model potential. It is rather difficult to substantiate this statement rigorously, but, if one is dealing with reactions like that being considered, which involve strongly absorbing particles and many open channels, the introduction of exchange processes as a correction to potential scattering seems reasonable. Moreover, the unitarity of the total S matrix, which is determined both by elastic scattering and by exchange processes, offers an independent check upon the validity of our concept.

The ensuing exposition is organized as follows. In Section 2, we present general formulas for calculating the amplitudes for the elastic scattering of particles with allowance for exchange processes. The matrix element for exchange processes is computed by the distorted wave method for finite-range interaction [9], the basic formulas of the method being simplified by using the identity of the input and the output channel of the reaction being considered. The calculated angular distributions of elastically scattered ^{6}He ions and the structure of the wave function for the relative motion of the α cluster and the center of mass of the dineutron are discussed in Section 3. The respective reflection coefficients (the absolute value of the S matrix) are presented in Section 4, where they are also compared with the predictions of various phenomenological models.

2. CALCULATION OF THE ELASTIC-SCATTERING AMPLITUDE

The well-known optical model provides a conventional approach to describing elastic scattering of composite particles. The distorted wave of the relative motion of scattered particles is expanded in partial waves of orbital angular momentum L, which are determined from the Schrödinger equation with a phenomenological optical potential. However, this approach gives no way to derive the angular distribution over the entire range of scattering angles; in particular, it cannot reproduce maxima in the cross section for backward scattering. This is because potential scattering does not exhaust processes contributing to the elastic scattering of composite particles, especially at large scattering angles. It is necessary to take into account various inelastic processes—in particular, exchange processes associated with the dissociation of the target nucleus into two fragments. In this case, the total amplitude for the elastic scattering of composite particles x and A is expressed in terms of the amplitude $f_{\rm opt}(\theta)$ for optical-potential scattering and the exchange correction $\Delta f(\theta)$ as

$$f(\theta) = f_{\rm C}(\theta) + \frac{1}{2ik}\sum_{L=0}^{\infty}(2L+1)e^{2i\sigma_L} \quad (1)$$

$$\times (S_L^{\rm opt} + a_L - 1)P_L(\cos\theta),$$

where θ is the scattering angle; k is the wave vector of the relative motion of particles x and A; $P_L(\cos\theta)$ are Legendre polynomials; $f_{\rm C}(\theta)$ and σ_L are, respectively, the Coulomb amplitude and phase shift; $S_L^{\rm opt}$ are the S-matrix elements for potential scattering in the optical model,

$$f_{\rm opt}(\theta) = f_{\rm C}(\theta) + \frac{1}{2ik}\sum_{L=0}^{\infty}(2L+1)e^{2i\sigma_L} \quad (2)$$

$$\times (S_L^{\rm opt} - 1)P_L(\cos\theta);$$

and the coefficients a_L, which depend only on L, determine the contribution of exchange processes to the total S matrix. The coefficients a_L are defined as the coefficients in the expansion of the exchange correction $\Delta f(\theta)$ in a series in Legendre polynomials; the exchange correction is related to the matrix element M_{if} for the exchange process by the equation

$$\Delta f(\theta) = -\frac{\mu_{xA}}{2\pi h^2}M_{if}, \quad (3)$$

where μ_{xA} is the reduced mass of the colliding particles.

The matrix element M_{if} for dineutron exchange is calculated here by the distorted-wave method for finite-range interaction [9].

Within this method, our nuclear reaction is considered in the three-body approximation and, in the case of elastic scattering, proceeds as follows:

$$x + A \to x + (C + x') \quad (4)$$

$$\to x' + (x + C) \to x' + A, \quad x' = x.$$

It should be noted that, usually, one must perform summation over spin variables characterizing intermediate states (difference of particle spins, total spin in each isolated channel, spin transfer, etc.). In the case of elastic scattering, however, these spin variables vanish because of the identity of the initial and final states.

Let us denote the spin, the orbital angular momentum, the total angular momentum, and its projection of particle $A(x)$ by $S_{A(x)}$, $L_{A(x)}$, $J_{A(x)}$, and $M_{A(x)}$, respectively. In the case of elastic scattering, the matrix element for exchange processes is then calculated by the formula

$$M_{if} = \sum_{M_A}(-1)^{J_x+M_x}\sum_{\Lambda}\Theta^{\Lambda}_{J_A}\beta_{\Lambda}, \quad (5)$$

where Λ is the orbital angular momentum in the decay vertices and $\Theta^{\Lambda}_{J_A}$ is the structure factor related to the reduced width $\Theta^{A\to C+x}_{\Lambda L_A S_A}$ by the equation

$$\Theta^{\Lambda}_{J_A} = \frac{1}{\sqrt{2J_x+1}}\sum_{L_A S_A}(-1)^{\Lambda+L_A-S_A+J_A} \quad (6)$$

Optical-potential parameters for elastic α^6He scattering

U_R, MeV	R_V, fm	a_V, fm	W, MeV	WD, MeV	R_W, fm	A_W, fm	R_C, fm
200	1.3	0.6	10	0	2	0.6	1.4

$$\times \frac{1}{\sqrt{2\Lambda+1}}(\Theta^{A\to C+x}_{\Lambda L_A S_A})^2.$$

The kinematical integral β_Λ is expressed in terms of the form factor $F^L_\Lambda(r,r')$ and the distorted waves $\chi^{\rm in}_L(kr)$ and $\chi^{\rm out}_L(kr')$ in the input and output channels as

$$\beta_\Lambda = \frac{4\sqrt{2}\pi}{k^2}\sum_L(-1)^L P_L(\cos\theta)(2L+1) \quad (7)$$
$$\times \int \chi^{\rm in}_L(kr)F^L_\Lambda(r,r')\chi^{\rm out}_L(kr')rr'drdr'.$$

For the invariant form factor, we use the standard definition

$$F^L_\Lambda = \frac{1}{\sqrt{(2L+1)(2\Lambda+1)}}\sum_{\mu,m}(-1)^\mu I_L, \quad (8)$$
$$I_L = \int \Psi^2_{\Lambda\mu}(\mathbf{r})VY_{Lm}(\mathbf{r})Y_{Lm}(\mathbf{r}')d\Omega_{\mathbf{r}}d\Omega_{\mathbf{r}'},$$

where $\Psi_{\Lambda\mu}(\mathbf{r})$ is the wave function describing the relative motion of clusters x and C in nucleus A with the orbital angular momentum Λ (the invariant form factor depends on the squared wave function, because the decay vertices for elastic scattering are identical) and V is the potential of xC interaction.

Formulas (5)–(8) arise upon applying the DWBAFR to the particular case of the elastic channel where $A = B$ and $x = y$ and where the orbital-angular-momentum transfer is $l = 0$.

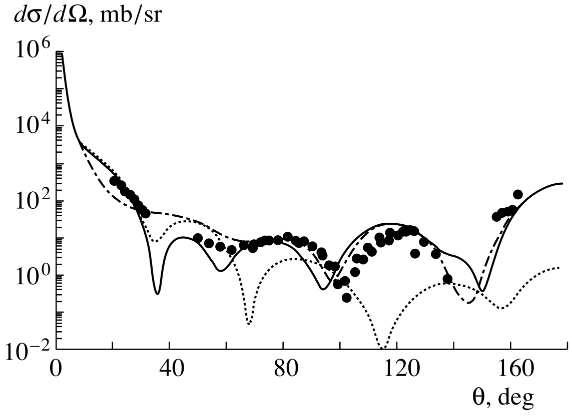

Fig. 1. Differential cross section for elastic α^6He scattering: (solid curve) total differential cross section, (dotted curve) cross section in the optical model, (dash-dotted curve) dineutron-exchange cross section, and (points) experimental cross section from [8].

A comparison of formula (3) with (5)–(8) makes it possible to derive explicit expressions for the coefficients a_L,

$$a_L \approx (-1)^L(2L+1)\Theta^\Lambda_{J_A}I_L\beta_\Lambda(\cos\theta), \quad (9)$$

which determine the exchange correction to the scattering amplitude.

3. COMPUTATION OF ANGULAR DISTRIBUTIONS FOR ELASTIC α^6He SCATTERING

We have performed calculations for the elastic scattering of an α particle by a ^{6}He nucleus at $E_{\rm lab} = 19.6$ MeV ($E_{\rm c.m.} = 11.6$ MeV), taking into account exchange corrections calculated by formulas (1)–(9). The total differential cross section for elastic scattering, the differential cross section for potential scattering, and the contribution of the exchange correction to the differential cross section are shown in Fig. 1 (solid, dashed, and dash-dotted curves, respectively). The parameters of the optical potential taken here in the standard Woods–Saxon form that were used in our calculations are presented in the table.

It should be noted that the optical potential ensuring the best fit to the experimental data with allowance for the exchange correction is expected to differ from the analogous optical potential in the case of potential scattering, because the latter takes these corrections into account implicitly. In general, the calculated cross sections are stable to variations in the optical-potential parameters. The angular distributions show the highest sensitivity to variations in the depth and the radius of the real part of the potential [provided that $U_R R^n_V = {\rm const}$, $R_V = r_V A^{1/3}$, $n = 2$ (continuous ambiguity)].

As can be seen from Fig. 1, the angular distribution in the range from 0° to 60° is controlled by potential scattering. At larger angles, the contribution of dineutron exchange becomes dominant. These mechanisms interfere either constructively or destructively (approximately at 70°).

Our calculation of the contribution of exchange processes to the cross section for elastic α^6He scattering made it possible to extract the ground-state wave function for the relative motion of the dineutron and α-particle cluster in the ^{6}He nucleus. As

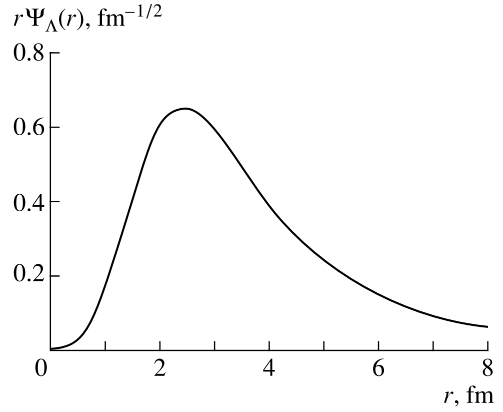

Fig. 2. Probability density $r\Psi_\Lambda(r)$ for the ^{6}He wave function versus r in the alpha–dineutron channel at $\Lambda = 0$.

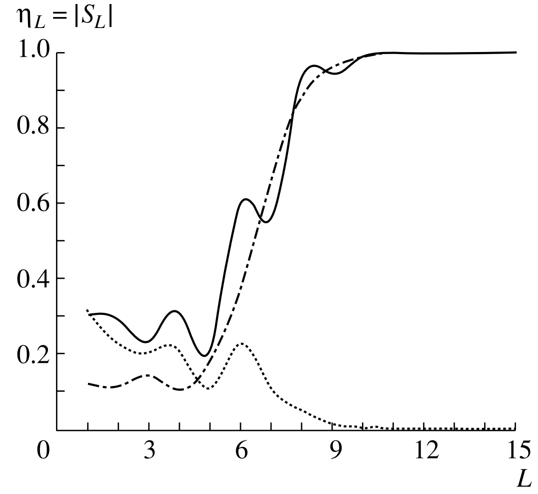

Fig. 3. Coefficient of reflection $\eta_L = |S_L|$ as a function of L for elastic α^6He scattering: (solid curve) total η_L, (dotted curve) η_L^{opt}, and (dash-dotted curve) exchange correction a_L.

was shown in [5], the nucleus ^{6}He can be in either of two states having different topologies. These are that which is associated with the dineutron configuration proper ($R_{\alpha,2n} = 4$ fm, $R_{n,n} = 1$ fm), which makes a substantial contribution to the ground-state wave function, and that which is associated with a cigar configuration ($R_{\alpha,2n} = 1$ fm, $R_{n,n} = 4$ fm), which plays an important role in the excited state of the ^{6}He nucleus and in the elastic scattering of these ions at high energies (about 100 MeV). The geometric configuration of the sought wave function was determined by using the WDP procedure [10] to fit the depth of the potential for preassigned values of the binding energy of the ^{6}He nucleus, the number of nodes of the wave function, and the geometric parameters of the potential $U(r) = 1/(1 + \exp(r - r_0)/a)$ of the alpha–dineutron interaction.

The quantity $r\Psi_\Lambda(r)$ characterizing the relative motion of the dineutron and the α particle in the $\Lambda = 0$ wave is shown in Fig. 2 at $r_0 = 2.7$ fm and $a = 0.7$ fm. It can be seen that the calculated value of $R_{\alpha,2n}$ is about 4 fm; that is, the dineutron structure of the ^{6}He nucleus is realized in elastic α^6He scattering at moderate energies.

4. BEHAVIOR OF THE S MATRIX FOR ELASTIC α^6He SCATTERING AT THE NUCLEAR PERIPHERY

Thus, the dineutron configuration of the wave function with $R_{\alpha,2n} = 4$ fm is realized in elastic α^6He scattering at moderate energies of ^{6}He ions. In other words, dineutron exchange occurs at the nuclear periphery, thereby reducing the absorption of this cluster at the nuclear surface. There are phenomenological approaches where such a reduction of absorption is introduced in one model-dependent way or another. By way of example, we indicate that, in the Regge pole model, the growth of the cross section at large scattering angles is ensured by introducing a resonance dependence of the S matrix on L at $L = L_{\mathrm{cr}}$. In the potential approach, singularities in the S matrix are obtained by modifying optical potentials. For example, the imaginary part of the optical potential in the model where this imaginary part depends on L is chosen in the form

$$W(L) = W[1 + \exp(L - L_0)/\Delta L]^{-1}.$$

This choice of potential reflects the fact that heavy ions of high L cannot be captured by the target nucleus, so that absorption must decrease with increasing L. The reduction of absorption in the model with an L-split potential is ensured by sign-alternating corrections to the optical potential. The phases of these corrections are $(-1)^L$, which coincide with the phases of Legendre polynomials at an angle of 180° in expansion (1), giving rise to a sharp growth of the cross section as the scattering angle tends to 180°.

All phenomenological models give a nonmonotonic dependence of the S matrix on L in the surface region of the nucleus. Such a nonmonotonic dependence is reproduced upon taking into account exchange processes.

Indeed, exchange processes proceed through projectile interaction with individual clusters of the target nucleus. For this reason, the overlap of the bound-cluster and projectile wave functions is small both in the interior of the nucleus and at large distances. As a consequence, the exchange correction to the S matrix has a maximum (or maxima) in the surface region of the nucleus. The dependence of the total S matrix on L also becomes nonmonotonic; that is, the

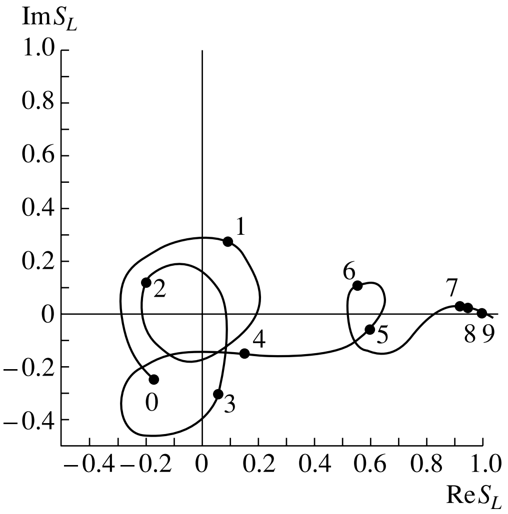

Fig. 4. Argand plot (dependence of the imaginary part of the S matrix on its real part) for elastic α^6He scattering. The numbers on the curve are the values of the orbital angular momentum.

introduction of the exchange correction is equivalent to employing the Regge pole model.

The nonmonotonic, resonance, dependence of the total S matrix on L is conveniently illustrated in Fig. 3, which displays the reflection coefficients $\eta_L = |S_L|$ and η_L^{opt} and the exchange corrections $|a_L|$ versus L, and in Fig. 4 by the Argand plot for the real and imaginary part of the S matrix [11]. Each loop on the Argand plot corresponds to an extremum of the S matrix for a given value of L.

As can be seen from Figs. 3 and 4, the exchange correction gives rise to a nonmonotonic dependence of the S matrix on L both at small values of L and at the boundary of the nucleus, where $L \simeq 6$. The total reflection coefficient approaches unity more steeply than the reflection coefficient in the potential model. It is natural to assume that this is due to the use of the phenomenological model featuring an L-dependent imaginary part of the optical potential.

From (9), it follows that the sign of the corrections a_L coincides with the sign of $(-1)^L$; that is, the phenomenological model with an L-split potential can be reproduced by adding the exchange correction to the S matrix.

Thus, the inclusion of the exchange correction to potential scattering makes it possible to obtain, within a unified theoretical approach, a detailed description of the behavior of the reflection coefficients postulated in various phenomenological models.

Moreover, none of the phenomenological models can yield such rich information about the behavior of the S matrix near the surface of the nucleus (and thereby about the behavior of the cross section at large angles) as the microscopic approach that takes into account exchange processes does.

CONCLUSION

It has been shown that the inclusion of the dineutron-exchange correction in studying elastic α^6He scattering makes it possible to match the theoretical cross section with the experimental data over the entire range of ^{6}He scattering angles. Moreover, this has enabled us to estimate the mean distance $R_{\alpha,2n}$ between the virtual dineutron cluster and the α particle in the ground state of the ^{6}He nucleus.

The behavior of the S matrix in the surface region of the nucleus permits an independent derivation of $R_{\alpha,2n}$. At c.m. energies of up to 20 MeV, the boundary value of $L \simeq 5$ corresponds to $R_{\alpha,2n} \simeq 4$ fm, which agrees well with microscopic computations of the wave function for this nucleus in the dineutron configuration.

That the virtual dineutron has appeared as a rather stable configuration of the ^{6}He nucleus in reactions with other particles of moderate energies is of course unexpectable. Experimental data from [12] show that the momentum distribution of the neutron that has escaped scattering on the target nucleus in the ^{6}He + ^{12}C fragmentation reaction at high energies (0.8 GeV/nucleon) corresponds to a cigar configuration of the ^{6}He nucleus [5]. In other words, different configurations of this nucleus manifest themselves differently, depending on the energy of the system. This fact indicates that the wave functions for $A = 6$ are rather complicated and that it is necessary to study them comprehensively in order to reveal the existence of dineutron configurations in the neutron-rich nuclei with a neutron excess greater than three.

ACKNOWLEDGMENTS

This work was supported in part by the Russian Foundation for Basic Research (project no. 01-02-16196) and the program “Russian Universities.”

REFERENCES

1. A. A. Korsheninnikov, Yad. Fiz. **52**, 1304 (1990) [Sov. J. Nucl. Phys. **52**, 827 (1990)]; A. A. Korcheninnikov and T. Kobayashi, Nucl. Phys. A **567**, 97 (1994); A. A. Korcheninnikov, K. Yochida, D. V. Aleksandrov, *et al.*, Phys. Lett. B **316**, 38 (1993); **326**, 31 (1994); **343**, 53 (1995); Phys. Rev. C **53**, 537 (1996).
2. M. G. Gornov, Yu. B. Gurov, and V. A. Pechkurov, Phys. Rev. Lett. **81**, 4325 (1998).
3. V. I. Kukulin, V. M. Krasnopol’skiĭ, M. A. Miselkhi, and V. T. Voronchev, Yad. Fiz. **34**, 21 (1981) [Sov. J. Nucl. Phys. **34**, 11 (1981)].

4. M. V. Zhukov, B. D. Danilin, D. V. Fedorov, *et al.*, Phys. Rep. **231**, 151 (1993).
5. V. I. Kukulin, V. M. Krasnopol'sky, V. T. Voronchev, and P. V. Sazonov, Nucl. Phys. A **453**, 365 (1986); B. V. Danilin and M. V. Zhukov, Yad. Fiz. **56** (4), 67 (1993) [Phys. At. Nucl. **56**, 460 (1993)].
6. N. S. Zelenskaya, I. B. Teplov, and T. A. Yushchenko, Yad. Fiz. **33**, 1183 (1981) [Sov. J. Nucl. Phys. **33**, 628 (1981)].
7. G. M. Ter-Akopian, A. M. Odin, A. S. Fomichev, *et al.*, in *Proceedings of the 47th Conference on Nuclear Spectroscopy and Nuclear Structure, St. Petersburg, 1998,* p. 203.
8. R. Raabe, A. Piechaczek, A. Andreev, *et al.*, Phys. Lett. B **458**, 1 (1999).
9. N. S. Zelenskaya and I. B. Teplov, *Exchange Processes in Nuclear Reactions* (Mosk. Gos. Univ., Moscow, 1985); N. S. Zelenskaya and A. K. Morzabaev, Yad. Fiz. **43**, 879 (1986) [Sov. J. Nucl. Phys. **43**, 559 (1986)].
10. N. Austern, Phys. Rev. B **136**, 1743 (1964)
11. K. W. McVoy, Phys. Rev. C **3**, 1104 (1971).
12. T. Kobayashi, Nucl. Phys. A **553**, 465 (1993).

Translated by R. Rogalev

Physics of Atomic Nuclei, Vol. 65, No. 7, 2002, pp. 1288–1301. Translated from Yadernaya Fizika, Vol. 65, No. 7, 2002, pp. 1321–1334.
Original Russian Text Copyright © 2002 by Lukyanov, Permyakov, Chubov.

Description of Elastic Heavy-Ion Scattering within the Glauber–Sitenko Approach

V. K. Lukyanov[*], **V. P. Permyakov, and Yu. V. Chubov**

Joint Institute for Nuclear Research, Dubna, Moscow oblast, 141980 Russia

Received March 27, 2001; in final form, June 6, 2001

Abstract—Analytic expressions for the amplitudes of elastic nucleus–nucleus scattering for various collision regimes are derived within the Glauber–Sitenko approach. The procedure used to do this employs an extended optical potential of the Woods–Saxon type and takes into account the deflection of trajectories by a strong Coulomb field. A comparison of the analytically calculated cross sections with numerical results and experimental data shows that the approach in question can be successfully used in the energy range from 10 to 100 MeV per nucleon. It is demonstrated that, for a preset potential, it is possible to find angular ranges dominated by specific patterns of scattering, such as classical or rainbow scattering and Fresnel or Fraunhofer diffraction. *© 2002 MAIK "Nauka/Interperiodica".*

1. INTRODUCTION

The character of heavy-ion scattering by nuclei is associated, to a considerable extent, with the special features of the potential at its periphery, where a strong, but weakly changing, Coulomb potential and, on the contrary, the sharply changing, potential of nuclear forces both play a significant role. It is of importance here that use is made of extended optical potentials of the Woods–Saxon type, which have a large interaction range. It should be noted that, at present, there exist efficient codes for computing differential cross sections for scattering. However, it is advisable to consider problems associated with the physical pattern of processes on the basis of analytic methods for calculating and analyzing relevant amplitudes. Such methods make it possible to understand why the character of angular distributions changes with increasing scattering angles, how angular distributions depend on energy and on the set of colliding nuclei, what one can expect from changes in the input parameters of the problem being studied, etc. Such approaches were developed primarily for diffraction scattering models, where fits to the experimental data were constructed by varying the parameters of the scattering S matrix whose form was preassigned phenomenologically (see [1–4]). The angular distributions of elastically scattered nuclei were interpreted in terms of the physical language borrowed from the description of optical interference and diffraction.

At the same time, actual analyses of experimental data are based, most frequently, on the potential approach where optical potentials are preset phenomenologically or where their real part is calculated as the folding of nuclear-matter-density distributions and effective nucleon–nucleon forces. In addition, allowances are made there for exchange effects, for the density dependence of NN forces, and for some other relevant phenomena [5–8]. In relation to the diffraction approach, the potential approach provides a more profound physical basis for understanding both the scattering mechanism proper and the manifestations of the special features of nuclear structure—for example, the neutron and the proton halo at the far periphery of some light nuclei and the excess of neutrons near the nuclear surface.

In this connection, it is of interest to develop analytic methods for calculating amplitudes namely within the potential approach both for a qualitative investigation of the scattering pattern and for quantitative calculations aimed at reproducing precise numerical solutions for the same potential. For this purpose, we consider here heavy-ion scattering at rather high energies of about 10 to 100 MeV per nucleon, in which case the following conditions are satisfied: $E \gg V$, where E is the collision energy and V is the interaction potential, and the wavelength is much smaller than the characteristic parameters of the potential, such as its range R and the thickness a of its surface layer. Under these conditions, one can adopt, for a basis, the eikonal Glauber–Sitenko approach [9, 10], where we have, at our disposal, an explicit analytic expression for the amplitude of scattering at small angles of $\vartheta < \sqrt{2/kR}$ (k is the collision momentum). This approach is widely applied

---

[*] e-mail: `lukyanov@thsun1.jinr.ru`

to hadron–nucleus scattering, where Gaussian distributions are usually chosen for the potential or for the target-nucleus density. Integration in the phase along the straight-line trajectory of the motion can then be performed explicitly, and one can sometimes obtain an explicit expression even for the amplitude. As to nucleus–nucleus scattering, a microscopic approach was developed for it in [11–14] on the basis of a generalization of the Glauber–Sitenko theory for multiple diffractive scattering. The optical approximation, which is a simplified version of this approach, leads to the eikonal phase in the form of a folding integral of the product of the two-dimensional densities of nucleons in colliding nuclei and the Fourier transform of the amplitude for nucleon–nucleon scattering. This amplitude is known from experimental data as a complex-valued function of the momentum transfer. From the phase constructed in this way, one can in principle obtain the complex potential of nucleus–nucleus interaction by applying the inverse Fourier transformation (see, for example, [15]). However, it is difficult to implement this procedure in practice. For this, it is necessary, above all, to obtain an explicit expression for the eikonal phase, but this has been achieved so far only for Gaussian density distributions or for density distributions expanded in series in Gaussian functions (see, for example, [16, 17]). There is in addition the problem of taking into account the distortion of the straight-line trajectory of the motion within the Glauber–Sitenko approach. For heavy-ion scattering, where the role of the periphery is significant, Gaussian functions unfortunately do not ensure the required level of precision, and one has to use, for potentials and densities, more realistic forms that have exponential behavior near the nuclear surface.

Thus, phenomenological optical potentials or, as was stated above, complex-valued potentials whose real part is calculated by the folding method and whose imaginary part is specified phenomenologically (see, for example, [18]) have still been traditionally used to describe quantitatively heavy-ion scattering. Since the range of such nucleus–nucleus potentials, which is equal to the sum of the radii of colliding nuclei, is large, their shapes belong to the extended type of Woods–Saxon potentials. For these, however, no explicit form of the eikonal phase was found until recently, which prevented the development of analytic methods for calculating scattering amplitudes. And only in [19] was an approximated expression for the eikonal phase obtained for the symmetrized Woods–Saxon potential. This expression faithfully reproduces the behavior of the phase determined by means of a numerical integration, making it possible, owing to this, to obtain differential cross sections that comply with the results of precise calculations. In turn, the availability of an explicit expression for the eikonal phase in the case of a realistic nuclear potential enables one to adapt known asymptotic methods for estimating rapidly oscillating integrals to the specific problem of calculating the amplitudes for nucleus–nucleus scattering. This was the objective of the present study, where, within the Glauber–Sitenko approach, we obtain explicit expressions for the amplitudes corresponding to various regimes of heavy-ion scattering in certain angular intervals. We take into account and discuss effects of the Coulomb distortion of the trajectory of the motion, whereby we expand the applicability range of the approach. The accuracy of the analytic estimates obtained here is tested by direct computer calculations of relevant angular distributions. A comparison with experimental data is also performed.

2. THE METHOD

In the Glauber–Sitenko approach, the scattering amplitude has the form [9, 10]

$$f(q) = -ik \int\limits_0^\infty J_0(qb) \left[e^{i\chi(b)} - 1\right] bdb, \tag{1}$$

where $q = 2k\sin(\vartheta/2)$ is the momentum transfer, ϑ is the scattering angle, the eikonal phase is given by

$$\chi(b) = -\frac{k}{2E} \int\limits_{-\infty}^{\infty} V(\sqrt{b^2+z^2})\, dz, \tag{2}$$

and b is the impact parameter. The interaction potential includes the nuclear and the Coulomb term:

$$V(r) = V_N(r) + V_{\mathrm{C}}(r). \tag{3}$$

As usual, the nuclear potential is taken in the form of the optical Woods–Saxon potential

$$V_N(r) = (V_0 + iW_0)u_{\mathrm{F}}(r), \tag{4}$$

$$u_{\mathrm{F}}(r) = \left(1 + \exp\frac{r-R}{a}\right)^{-1}.$$

The Coulomb potential is chosen in the traditional form

$$V_{\mathrm{C}}(r) = \frac{V_B}{2}\left(3 - \frac{r^2}{R_{\mathrm{C}}^2}\right)\Theta(R_{\mathrm{C}} - r) + \frac{V_B}{r}R_{\mathrm{C}}\Theta(r - R_{\mathrm{C}}), \tag{5}$$

$$V_B = \frac{Z_1 Z_2 e^2}{R_{\mathrm{C}}},$$

which corresponds to the interaction of the charge $Z_1 e$ with the charge $Z_2 e$ uniformly distributed over a sphere of radius R_{C}.

By virtue of the condition $kb \gg 1$, the integral in amplitude (1) strongly oscillates. This enables us to use asymptotic methods for estimating it. In doing this, the Bessel function is replaced by its asymptotic expression $J_0(x) = \sqrt{2/\pi x}\cos(x - \pi/4)$ ($x \gg 1$). Additionally, it is sufficient to take into account only the first term in (1) in considering scattering at angles $\vartheta \neq 0$. We then have

$$f(q) = f_{(+)} - f_{(-)}, \tag{6}$$

$$f_{(\pm)} = -\frac{1}{4\sin(\vartheta/2)}\sqrt{\frac{q}{\pi}}(1 \pm i)t_{(\pm)},$$

$$t_{(\pm)} = \int\limits_0^\infty \sqrt{b}db\exp[ig_{(\pm)}(b)], \tag{7}$$

$$g_{(\pm)}(b) = \pm qb + \chi(b), \quad \chi(b) = \chi_N(b) + \chi_{\mathrm{C}}(b), \tag{8}$$

where $\chi_N(b)$ and $\chi_{\mathrm{C}}(b)$ are, respectively, the nuclear and the Coulomb phase shift, which are computed by formula (2) with the corresponding potentials (4) and (5). The amplitudes $f_{(-)}$ and $f_{(+)}$ are referred to as the far-side and the near-side amplitude, respectively; in the semiclassical limit, they are associated with trajectories that have passed the near side and the far side of the scatterer, respectively.

Methods for computing integrals involving quickly oscillating functions in the integrands—such as the pole, the saddle-point, and the stationary-phase method—require the assumed phases $\chi(b)$ in an explicit analytic form. The phase shifts $\chi(b)$ [see Eq. (2)] are also the integrals of the potential along the straight-line trajectory of the motion of nuclei. For the Coulomb potential, the phase shift in question is calculable explicitly [20]. The result is

$$\chi_{\mathrm{C}}(b) = \frac{\eta}{R_{\mathrm{C}}}\left\{\left[-\frac{8}{3}\xi + \frac{2b^2}{3R_{\mathrm{C}}^2}\xi \right.\right. \tag{9}$$
$$\left. + 2R_{\mathrm{C}}\ln(k(R_{\mathrm{C}} + \xi))\right]\Theta(R_{\mathrm{C}} - b)$$
$$\left. + 2R_{\mathrm{C}}\ln(kb)\Theta(b - R_{\mathrm{C}})\right\},$$

where $\xi = \sqrt{R_{\mathrm{C}}^2 - b^2}$ and $\eta = Z_1Z_2e^2k/2E$ is the Sommerfeld parameter. As to the nuclear Woods–Saxon potential (4), it is hardly possible to obtain the analytic expression for the phase shift χ_N in this potential. In order to solve this problem anyway, one can approximate the potential by the sum of Gaussian functions, fitting the corresponding parameters in the sum (see, for example, [16]). The profile integral in the phase shift (2) is then taken explicitly. This method is inconvenient because, for each new set of the parameters of the Woods–Saxon potential, the adjusted potential must be fitted anew. But if, one fits a Gaussian potential to reproduce only the exponential tail of the Woods–Saxon potential [17], which plays the main role in nucleus–nucleus scattering, this would lead to a sharp distinction between its normalization and the normalization of the corresponding Fermi function, $\int_0^\infty u_{\mathrm{F}}(r)dr \simeq R$ [21].

An alternative method for calculating the profile integral in (2) was proposed in [19]. This method is based on an approximate separability of the variables b and z in the integrand. The distribution function of the potential was taken in the more realistic form of the symmetrized Fermi function

$$u_{\mathrm{SF}}(r) = \frac{\sinh C}{\cosh C + \cosh(r/a)}, \quad C = R/a, \tag{10}$$

which coincides with u_{F} in the region $r > 0$ for extended nuclei, when $R \gg a$. In contrast to the function u_{F}, its first derivative vanishes at $r = 0$, owing to which it is more convenient in analytic calculations than the Fermi function [21]. The above method made it possible to find that the eikonal phase for scattering in the field of the symmetrized Woods–Saxon potential can be represented in the explicit analytic form [19]

$$\chi_N(b) = -kR\frac{V_0 + iW_0}{E}P(1, C)u_{\mathrm{SF}}(b), \tag{11}$$

where

$$P(1, C) = \frac{1}{C}\left[2.489453 + 0.34597C - 0.0046C^2\right].$$

In the peripheral region of the potential, $b \sim R$, expression (11) for $5 \leq C \leq 20$ faithfully reproduces the behavior of the phase shift obtained by means of numerical integration in expression (2). Moreover, a comparison revealed [19] that the elastic-scattering differential cross section calculated with the phase shift found numerically and that calculated with the phase shift in the form (11) agree well over the entire range of applicability of the Glauber–Sitenko approach.

Below, we develop approximate methods for computing scattering amplitudes using the analytic expressions (9) and (11) for the phase shifts. In the case of nucleus–nucleus scattering considered here, we have $qb \simeq qR \gg 1$, which makes it possible to use the asymptotic stationary-phase method. For this purpose, the exponents $g_{(\pm)}$ in (7) must be expanded in Taylor series in the vicinity of the saddle points b_{s_n}, which determine the regions that make the main contribution to the integral. We then have

$$g_{(\pm)}(b) = g_{(\pm)}(b_{s_n}) + g'_{(\pm)}(b_{s_n})(b - b_{s_n}) \tag{12}$$

Parameters of the potentials used to describe the elastic scattering of ^{17}O on ^{208}Pb, ^{120}Sn, ^{90}Zr, and ^{60}Ni [24, 25] and the scattering of ^{32}S on ^{27}Al [26]

Reaction	$E_{\mathrm{c.m.}}$, MeV	V_0, MeV	W_0, MeV	R, fm	a, fm	R_{C}, fm
$^{17}\mathrm{O} + {}^{208}\mathrm{Pb}$	1327	50	47.1	9.286	0.727	10.196
$^{17}\mathrm{O} + {}^{120}\mathrm{Sn}$	1257	50	45.0	8.171	0.706	9.0
$^{17}\mathrm{O} + {}^{90}\mathrm{Zr}$	1207	50	37.1	7.666	0.697	8.463
$^{17}\mathrm{O} + {}^{60}\mathrm{Ni}$	1118	50	39.5	6.823	0.754	7.783
$^{32}\mathrm{S} + {}^{27}\mathrm{Al}$	55	100	48.76	7.428	0.5	7.428

$$+\frac{g''_{(\pm)}(b_{s_n})}{2}(b-b_{s_n})^2+\ldots.$$

From the condition requiring the vanishing of the first derivatives, $g'_{(\pm)}(b_{s_n})=0$, we derive the following equations for the saddle points:

$$\pm q+\chi'_N(b_{s_n})+\chi'_{\mathrm{C}}(b_{s_n})=0. \qquad (13)$$

At $W_0=0$,[1] solving Eq. (13) leads to a real-valued function $q=q(b)$. In general, it appears that the solution to the equation for $g_{(+)}$ yields a stationary point that lies off the interval of integration. In (6), the term $f_{(+)}$ can therefore be disregarded, whereupon the scattering amplitude $f(q)$ is determined by the term $f_{(-)}$ exclusively. For it, the corresponding equation in (13) gives two solutions—that is, two saddle points b_{s_1} and b_{s_2}. If they are widely spaced,[2] their contributions to $f_{(-)}$ can be considered to be independent. Substituting expression (12) with $g'_{(-)}(b_{s_n})=0$ into (7), taking the slowly varying factor $\sqrt{b}$ at the saddle point outside the integral sign, and making the limits of integration on the left and on the right of b_{s_n} tend to infinity, we can evaluate the integral in (7) explicitly, whereupon the amplitude assumes the form

$$f_{(-)}=-\frac{1}{4\sin(\vartheta/2)}\sqrt{\frac{q}{\pi}}(1-i)\sum_{n=1,2}t_{(-),n}, \qquad (14)$$

where

$$t_{(-),n}=\sqrt{b_{s_n}}\sqrt{\frac{2\pi}{g''_{(-)}(b_{s_n})}}\exp[i(g_{(-)}(b_{s_n})+\pi/4)]. \qquad (15)$$

Figure 1 shows the behavior of the saddle points—that is, the deflection function $q=q(b)$—versus the impact parameter for ^{17}O scattering on ^{208}Pb at $E_{\mathrm{c.m.}}=1327$ MeV. (The parameters of the potential are given in the table.) The dash-dotted curve represents its behavior for the Coulomb scattering of pointlike charges, in which case the phase shift is $\chi_{\mathrm{C}}=2\eta\ln(kb)$. The dotted curve shows the small deflection that arises if the charge Z_1e is scattered in the field of the charge Z_2e uniformly distributed over a sphere of radius R_{C} [see Eq. (5)]. The long-dashed curve corresponds to a numerical solution to Eq. (13) for the case where the Coulomb and the nuclear potential are taken into account and where the corresponding phase shifts χ_{C} and χ_N are given by expressions (9) and (11). This curve

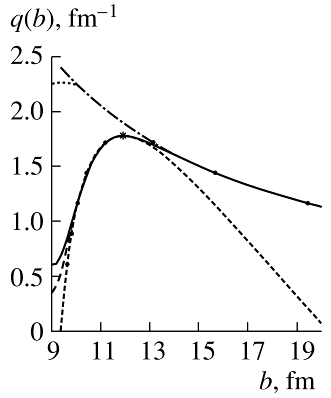

Fig. 1. Impact-parameter dependence of the deflection function constructed on the basis of the eikonal phase for $^{17}\mathrm{O}+{}^{208}\mathrm{Pb}$ scattering ($E_{\mathrm{c.m.}}=1327$ MeV). The parameters of the potential are presented in the table, and the eikonal phases are taken in the form (9) and (11). A detailed description of the figure is given in the main body of the text.

---

[1] In the final expressions given below, we will replace V_0 by V_0+iW_0, which is correct for $W_0\ll V_0$. In the peripheral region, $b\sim R_1+R_2$, and the region of classical scattering angles, $\vartheta<|V|/E$, this leads to a modest renormalization of the particle flux by the factor $(1-W_0/4E)$ (see, for example, [22]). For the more general case of complex-valued variables, the stationary-phase method was developed in [23] for the diffractive-scattering model.

[2] These two points are first-order saddle points because $g''_{(-)}(b_{s_n})\neq 0$.

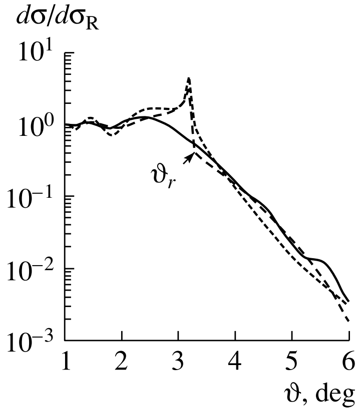

Fig. 2. Ratio of the differential cross sections $d\sigma$ for elastic scattering in the ^{17}O + ^{208}Pb reaction at $E_{\text{c.m.}} = 1327$ MeV to the corresponding Rutherford cross section $d\sigma_{\text{R}}$. The parameters of the potential are the same as in Fig. 1. The solid curve represents the results of precise numerical calculations with $W_0 \neq 0$. The dashed curves were computed by the stationary-phase method (short dashes) without ($W_0 = 0$) and (long dashes) with ($W_0 \neq 0$) allowance for absorption.

nearly coincides with the solid curve obtained if, instead of the total Coulomb phase shift (9), its asymptotic part $\chi_{\text{C}} = 2\eta \ln(kb)$, which coincides with the phase shift for the scattering of pointlike charges, is used for all values of b. This feature is peculiar to precisely nucleus—nucleus scattering. The replacement of the total Coulomb phase shift by the simpler phase shift for pointlike charges considerably simplifies the ensuing analytic calculations. By and large, we can see from Fig. 1 that the deflection function $q(b)$ has a characteristic maximum $q_{\max} \equiv q_r = q(b_r)$ in the interaction-surface region, which is precisely the region that determines the main features of the scattering pattern. In this region, it is convenient to represent the impact-parameter dependence of the classical momentum transfer, $q(b)$, in the logarithmic-parabola form [27]

$$q = q_r - \rho \left[\ln \frac{b - b_1}{b_r - b_1} \right]^2, \qquad (16)$$

where the parameters b_r, q_r, b_1, and ρ are determined by fitting this parabola to the exact curve $q(b)$ obtained, for example, by numerically solving Eq. (13). It is of paramount importance to ensure the highest possible degree of precision in this fitting. For example, methodological calculations show that an error of about 0.5 fm in determining the position of b_r leads to an order of magnitude change in the cross section. Under such conditions, it is also important to retain the necessary precision in deriving the explicit dependence of the parabola parameters on the input geometric and strength parameters of the nucleus—nucleus potential. For this purpose, we developed a method where the derivative of the function $q(b)$ was first approximated by a polynomial of third degree in the region of its maximum, whereupon its roots yielded explicit solutions for b_r, q_r, b_1, and ρ (see Appendix). In this way, we completely determined the parabola in (16) and two solutions for the saddle points from it in turn. The results are

$$b_{s_1} = b_1 + (b_r - b_1) \exp\left\{ -\sqrt{(q_r - q)/\rho} \right\}, \qquad (17)$$
$$b_{s_2} = b_1 + (b_r - b_1) \exp\left\{ +\sqrt{(q_r - q)/\rho} \right\}.$$

This approximation of the function $q(b)$ by a logarithmic parabola is shown in Fig. 1 by short dashes. We note that the parameter b_1 in formula (16) stands for the point at which the curve representing the deflection momentum $q(b)$ intersects the b axis on the left, while the quantities b_r and q_r are the coordinates of the points corresponding to the limiting value of the classical momentum transfer (large asterisk in Fig. 1). One can see that the parabola faithfully reproduces the region of the maximum and the left wing of the deflection function calculated numerically (it is the region where the saddle points b_{s_1} lie). On the right, the true function $q(b)$ is well approximated by the saddle-point curve $2\eta/q$ for the Coulomb phase shift corresponding to pointlike charges. Thus, the behavior of the true deflection-momentum function is simulated by choosing

$$b_{s_1} = b_1 + (b_r - b_1) \exp\left\{ -\sqrt{(q_r - q)/\rho} \right\}, \quad b < b_r,$$
$$b_{s_2} = 2\eta/q, \quad b > b_r. \qquad (18)$$

In Fig. 1, the positions of these points are indicated by asterisks.

3. CLASSICAL AND QUANTUM REGIONS OF SCATTERING

At angles in the region $\vartheta < \vartheta_r$ ($q < q_r$), scattering occurs in the classically allowed region. Here, at every angle 9, there are two trajectories of the motion that are associated with the different impact parameters b_{s_1} and b_{s_2}. In Fig. 2, the results obtained by numerically calculating the ratio of the elastic-scattering cross section to the Rutherford cross section, $d\sigma/d\sigma_{\text{R}}$, are compared to the results of our analytic calculations.[3)] The amplitude $f(q)$ is determined by formulas (6) and (15). Absorption is taken into account via changing the real potential by the complex one in the final expression for the amplitude. It can

---

[3)] In these calculations and everywhere below, we take into account the Coulomb distortion of the trajectory. In Section 6, these effects will be discussed separately.

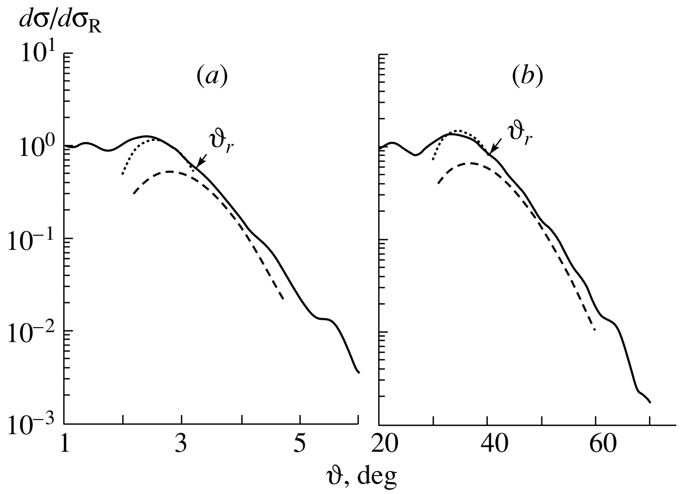

Fig. 3. Cross-section ratio $d\sigma/d\sigma_{\rm R}$ in the rainbow-angle region for (a) ^{17}O + ^{208}Pb scattering at $E_{\rm c.m.} = 1327$ MeV and (b) ^{32}S + ^{27}Al scattering at $E_{\rm c.m.} = 55$ MeV: (solid curves) results of the exact numerical calculation at $W_0 \neq 0$, (dashed curves) results of the calculations by the stationary-phase method by using (20), and (dotted curve) results for the case of two closely lying points on the basis of (22). The parameters of the potentials are quoted in the table.

be seen that the results of our analytic calculations comply well with the numerical results. This is not so in the region of angles close to ϑ_r, which corresponds to an extremum of the deflection-momentum function $q(b)$. In the limit $\vartheta \to \vartheta_r$, the cross section tends to infinity since the second derivative $g''_{(-)}(b_r)$ in the denominator on the right-hand of (15) vanishes.

Oscillations of the cross-section ratio $d\sigma/d\sigma_{\rm R}$ about unity occur because of the interference between the nuclear and the Coulomb amplitude, which are determined by the different saddle points b_{s_1} and b_{s_2}. They have the different phase shifts $g_{(-)}(b_{s_1})$ and $g_{(-)}(b_{s_2})$, respectively, with the result that the squared modulus of the amplitude,

$$|f(q)|^2 = |f[b_{s_1}(q)]|^2 + |f[b_{s_2}(q)]|^2 + \frac{2k^2}{q^2}\sqrt{\frac{q\pi b_{s_1} b_{s_2}}{g''_{(-)}(b_{s_1}) g''_{(-)}(b_{s_2})}} \times \cos[g_{(-)}(b_{s_1}) - g_{(-)}(b_{s_2})],$$

involves an oscillating interference term. At small angles $\vartheta < \vartheta_r \simeq |V|/E$, the nuclear amplitude $f[b_{s_1}(q)]$ is always small compared to the strong Coulomb amplitude and thus manifests itself only through the interference. For $\vartheta \to 0$, the oscillations are completely suppressed by Rutherford scattering. The inclusion of nonzero W_0 leads to the absorption of particles, with the natural result that the oscillations are smoothed. This scattering pattern corresponds to Fresnel diffraction at the edge of a screen in optics.

As the saddle points b_{s_1} and b_{s_2} approach the point b_r, which fixes the limiting classical angle, $\vartheta \simeq \vartheta_r$, the regions around the points $b \simeq b_{s_1}$ and $b \simeq b_{s_2}$, which make a dominant contribution to the corresponding part of the amplitude, begin to overlap. In this case, the estimation of the integrals in (15) near b_r and the assumption that their contributions to the amplitude in (12) are independent both become meaningless. The problem can be resolved either by adding the next terms in the expansion (12) of the phase shift $g_{(-)}(b)$ or by modifying the stationary-phase method, for example, as was proposed in [28]. In the next section, this case will be considered in detail.

The behavior of the amplitude for angles $\vartheta > \vartheta_r$, which are far off the classical-scattering region, can be understood on the basis of qualitative arguments by using the same parametrization of $q(b)$ employed in the region of classical angles. For $q > q_r$, we obtain $\sqrt{q_r - q} = i\sqrt{q - q_r}$ from (17). Here, only the saddle point b_{s_1}, which determines the exponential decay of the amplitude $f_{(-)} \sim \exp -(q{\rm Im} b_{s_1})$ and the corresponding scattering cross section (see dashed curves in the region $\vartheta > \vartheta_r$ in Fig. 2), remains physically justified. This behavior is also corroborated by numerical calculations (solid curve). It is typical and is observed experimentally.

4. REGION OF THE COULOMB RAINBOW (RAINBOW SCATTERING)

Let us consider the angular region around ϑ_r. Here, experimental data display a broad maximum in the angular distribution for scattering, which, by analogy with a rainbow arising in nature because of the interference between the refracted and the reflected ray of light in a water drop, is referred to as

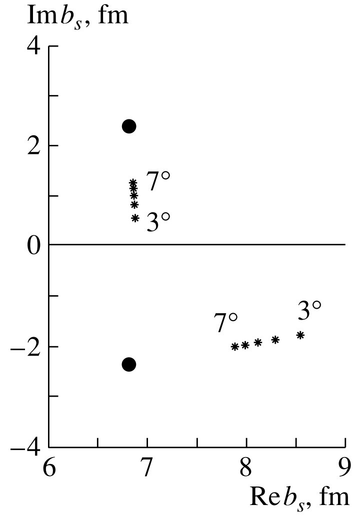

Fig. 4. Motion of the saddle points in the complex plane of b as the angle ϑ grows from 3° to 7° for $^{17}\mathrm{O} + {}^{60}\mathrm{Ni}$ scattering. The parameters of the potential are quoted in the table. The closed circles correspond to the poles $r_1^{\pm} = R \pm i\pi a$, while the asterisks represent the results of the calculations by the approximate formulas (31) and (35).

rainbow scattering. In our case, this is the interference of two amplitudes associated with two saddle points on the right and on the left of b_r and which are associated with two close trajectories passing near the limiting classical trajectory of the motion. Thus, we consider the mechanism of scattering in the region $\vartheta_r \simeq |V_{\max}(r \simeq R_{\mathrm{C}})|/E$, where the saddle points b_{s_1} and b_{s_2} merge (Fig. 1), and there arises a higher order saddle point.

In order to obtain the scattering amplitude in this region, we first expand the function $g_{(-)}$ in a power series near the rainbow point $b \sim b_r$. Since $g''_{(-)}(b_r) = 0$, we must retain the third-order terms in this expansion. Considering that $g'_{(-)}(b_r) = -q + q_r$ and $g^{(3)}_{(-)}(b_r) = \chi^{(3)}(b_r)$, we arrive at

$$g_{(-)}(b) = -qb_r + \chi(b_r) \tag{19}$$
$$- (q - q_r)(b - b_r) + \frac{\chi^{(3)}(b_r)}{6}(b - b_r)^3 + \dots .$$

In this case, the result that the stationary-phase method yields for the integral in (7) is

$$t_{(-)} = 2\pi \left[\frac{2}{\chi^{(3)}(b_r)}\right]^{1/3} \sqrt{b_r} \tag{20}$$
$$\times \exp[ig_{(-)}(b_r)]\mathrm{Ai}(\sigma),$$

where the Airy function is defined as

$$\mathrm{Ai}(\sigma) = \frac{1}{2\pi}\int\limits_{-\infty}^{\infty} \exp[i(\sigma z + z^3/3)]dz, \tag{21}$$

$$\sigma = (q - q_r)\left[\frac{-2}{\chi^{(3)}(b_r)}\right]^{1/3}.$$

This approximation is traditionally used in diffraction models. As in the case of Fresnel diffraction, rainbow scattering is determined exclusively by the near-side component $f_{(-)}$ of the amplitude. Because of the characteristic behavior of the Airy function, oscillations of the cross section are observed on the illuminated side ($\vartheta < \vartheta_r$), decaying fast as we move apart from the angle ϑ_r; on the dark side ($\vartheta > \vartheta_r$), the cross section decreases fast. The maximum of the angular distribution occurs on the illuminated side and corresponds to the maximum of the Airy function (wave rainbow), where $\sigma = -1$. In this case, the limiting angle ϑ_r determines the position of the classical (geometric) rainbow.

In Fig. 3, the results of the numerical and analytic calculations of the cross section for scattering near the rainbow angle are compared both at high (Fig. 3*a*) and at low (Fig. 3*b*) energies for various pairs of interacting nuclei. We can see that the calculation within the stationary-phase method in the traditional Airy approximation as specified by Eq. (20) (dashed curves) is unable to describe satisfactorily nucleus–nucleus scattering. In either case, the curve obtained from the analytic calculations passes significantly lower than that computed numerically. In all probability, the reason is that the expansion (19) of the function $g_{(-)}$ to the third-order terms is insufficient. By way of example, we indicate that, in the case of scattering of $^{17}\mathrm{O}$ on $^{208}\mathrm{Pb}$ (Fig. 3*a*), the results obtained on the basis of the expansion of $g_{(-)}$ in the form (19) agree with the results of the numerical calculations only in the region $b = b_r \pm 0.5$ fm—this corresponds to scattering in a very narrow angular interval. The inclusion of absorption by means of the substitution of $V_0 + iW_0$ for V_0 leads to a still greater discrepancy.

In order to obtain an adequate description of rainbow nucleus–nucleus scattering, we invoked the method applied to the case where two saddle points are closely spaced [28]. Its special feature is that the phase shift $g_{(\pm)}(b)$ in (7) is expanded not in the vicinity of the second-order stationary point but in the vicinity of the midpoint between b_{s_1} and b_{s_2}, which, in the limiting case, goes over into a higher order point. Evaluating the integral in (7) by this method, we obtain

$$t_{(-)} = \pi\sigma^{1/4}\left(h_1\sqrt{b_{s_1}} + h_2\sqrt{b_{s_2}}\right)e^{ia_0}\mathrm{Ai}(\sigma), \tag{22}$$

where

$$h_{1,2} = \sqrt{\frac{\mp 2}{g''_{(-)}(b_{s_{1,2}})}}, \tag{23}$$

$$a_0 = \frac{1}{2}\left[g_{(-)}(b_{s_1}) + g_{(-)}(b_{s_2})\right],$$

$$\sigma = \left[\frac{3}{4}(g_{(-)}(b_{s_1}) - g_{(-)}(b_{s_2}))\right]^{2/3}.$$

For $b_{s_1} \to b_{s_2}$, we have $g''_{(-)}(b_{s_{1,2}}) \to 0$. In this limiting case, we arrive at

$$h_1 = h_2 = \left[\frac{-2}{g^{(3)}_{(-)}(b_r)}\right]^{1/3}, \quad b_{s_1} = b_{s_2} = b_r.$$

For the saddle point $b_{s_2} \sim b_r$, one should take the expression for it from (17).

The cross sections calculated by (22) are shown in Fig. 3 by the dotted curves. It is seen that they are in a good agreement with the cross sections computed numerically on the left of the limiting classical angle ϑ_r up to the region of angles where the wave rainbow forms the maximum of the cross-section ratio $d\sigma/d\sigma_{\mathrm{R}}$. It was shown above that, at larger and at smaller angles with respect to the specific rainbow angular interval, the cross section can be interpreted in terms of Fresnel diffraction.

5. PATTERN OF FRAUNHOFER SCATTERING

Let us dwell at some length on the behavior of the cross section for elastic scattering at angles $\vartheta > \vartheta_r$—that is, in the region forbidden for classical scattering. We have seen that the Fresnel pattern describes well the classical region and that, for $\vartheta > \vartheta_r$, the cross section decreases exponentially. However, experiments often yield patterns where, against the background of the general exponential decrease, there arise oscillations of the cross section, which are characteristic of Fraunhofer diffraction in optics. The use of an optical potential that has both a real and an imaginary part makes it possible to explain many subtle details in the behavior of the cross section in this angular region. The fact that, both for the near-side ($f_{(-)}$) and for the far-side ($f_{(+)}$) component of the total amplitude $f(q)$, there are now stationary points b_{s_n} falling within the integration interval ($\mathrm{Re}\, b_{s_n} > 0$) is a new theoretical aspect. These points are shifted to the complex plane of the impact parameter b to the region where there occur the poles $r_p^{\pm}(\epsilon) = \pm R + \epsilon i\pi a(2p-1)$ ($p = 1, 2, 3\ldots$, $\epsilon = \pm 1$) of the nuclear-phase-shift function $u_{\mathrm{SF}}(b)$. Previously, an attempt was made in [29] to determine the explicit form of the profile integral $\int_{-\infty}^{\infty} u_{\mathrm{F}}(\sqrt{b^2+z^2})dz$ (which involves the Fermi function in the integrand) in the phase shift (2) through continuing into the complex plane. The result was expressed in terms of the sum of the residues at the poles of the Fermi function, $r_p^{\pm} = R \pm i\pi a(2p-1)$ ($p = 1, 2, 3\ldots$). In the limit $b \to 0$, this sum yielded, however, zero instead of the true value $\simeq 2R$. Eventually, an ansatz was proposed in the form

$$\chi_N(b) = -kR\frac{V_0 + iW_0}{E} \times \left[1 - i\pi\frac{a}{R}\sum_p\left(\frac{r_p^+}{\lambda_p^{(+)}} + \frac{r_p^-}{\lambda_p^{(-)}}\right)\right], \tag{24}$$

where $\lambda_p^{(\pm)} = \sqrt{(r_p^{\pm})^2 - b^2}$ and the condition $\mathrm{Im}\,\lambda_p^{(\pm)} \geq 0$ must be satisfied. A numerical test revealed that, even if a few hundred terms are retained in the sum, this approximation does not ensure the required accuracy on the real axis in the region $b > R$; however, it faithfully reproduces the behavior of the profile integral in the complex plane near the poles that are the closest to the real axis of b. The last circumstance can be used in deriving asymptotic estimates for the amplitudes in the case where the saddle points are complex-valued and are situated in the region of the extrema of the phase shift—here, these are poles of $\chi_N(b)$. In our case, the main contribution to the amplitude at $q \gg q_r$ comes from the saddle points near two poles closest to the real axis, the inclusion of each next pair introducing a lower order correction, proportional to $\exp(-\pi a q)$. Within a more consistent procedure, one would avoid discarding $p \geq 1$ poles in (24), in contrast to what was done, for example, in [30], and simulate the total contribution of the remaining terms of the sum in the region of the poles $r_1^{\pm} = R \pm i\pi a$ by a smooth function $\Delta(b)$ [31]. It is this modified two-pole approximation that is used here for the nuclear phase shift:

$$\chi_N(b) = -kR\frac{V_0 + iW_0}{E} \times \left[1 - i\pi\frac{a}{R}\left(\frac{r_1^+}{\lambda_1^{(+)}} + \frac{r_1^-}{\lambda_1^{(-)}}\right) + \frac{\Delta(b)}{2R}\right]. \tag{25}$$

The expression for the correcting function $\Delta(b) = \Delta_R(b) + i\Delta_I(b)$, where $b = b_1 + ib_2$, is presented in [31]. For the Coulomb phase shift, we take, as previously, the asymptotic value $2\eta\ln(kb)$.

In seeking stationary points in the region where the phase shift changes sharply, we can neglect small contributions from the derivatives of the smooth functions $\chi_{\mathrm{C}}(b)$ and $\Delta(b)$. Since the saddle points occurring in the first and the second quadrant of the com-

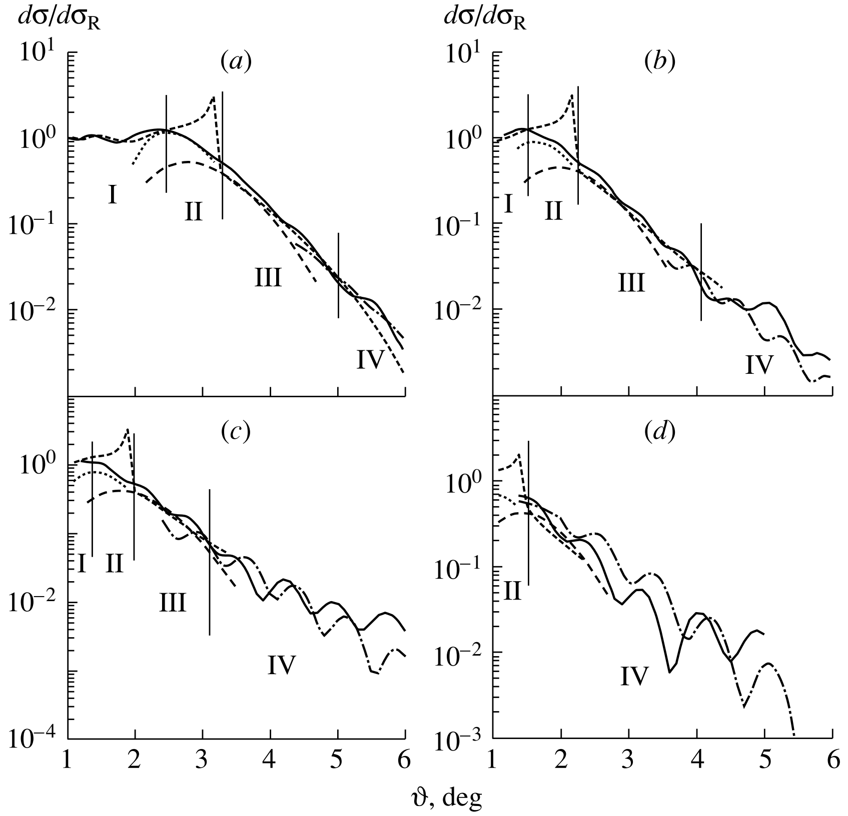

Fig. 5. Regions where various scattering mechanisms are operative for the examples of elastic ^{17}O scattering on (*a*) ^{208}Pb ($E_{\text{c.m.}} = 1327$ MeV), (*b*) ^{120}Sn ($E_{\text{c.m.}} = 1257$ MeV), (*c*) ^{90}Zr ($E_{\text{c.m.}} = 1207$ MeV), and (*d*) ^{60}Ni ($E_{\text{c.m.}} = 1118$ MeV): (I) Fresnel diffraction pattern of scattering, (II) region of rainbow scattering, (III) region where the near amplitude contributes at $\vartheta > \vartheta_r$, and (IV) region of Fraunhofer scattering. The solid curves correspond to a precise numerical calculation, while the remaining curves were calculated within the stationary-phase method by (short dashes) formula (15), (long dashes) formula (20), and (dotted curves) formula (22). The dash-dotted curves are described in the main body of the text (see Section 5). The parameters of the potentials are quoted in the table.

plex plane of b are associated with the near-side and the far-side amplitudes, we can retain, in the saddle-point equation, only the first term in parentheses in (25) for $f_{(+)}$ and the second term for $f_{(-)}$ (see [32]). Thus, we generalized the approach developed in [30] for hadron–nucleus scattering, where only one pole in the first quadrant was taken into account. Now, the saddle-point equation has the form

$$g'_{(\pm)}(b) = \pm q + \bar{\alpha}\frac{r_1^{\pm}\, b}{\left(\lambda_1^{(\pm)}\right)^3} = 0, \tag{26}$$

where

$$\bar{\alpha} = -\pi a k \frac{|W_0| - i|V_0|}{E} = |\alpha| e^{i\beta_\alpha}, \tag{27}$$

$$\beta_\alpha = 2\pi - \arcsin\frac{1}{\sqrt{1 + (W_0/V_0)^2}}. \tag{28}$$

For the sake of convenience, we use the representation

$$r_1^{\pm} = R \pm i\pi a = |r^{\pm}|\, e^{i\beta_r^{(\pm)}}, \tag{29}$$

$$\beta_r^{(+)} = \arcsin\frac{\pi a}{\sqrt{\pi^2 a^2 + R^2}} \simeq \frac{\pi a}{R}, \tag{30}$$
$$\beta_r^{(-)} = 2\pi - \beta_r^{(+)}.$$

According to the method proposed in [30], we seek solutions to Eq. (26) near the poles $r_1^{\pm}$ in the form

$$b_s^{(\pm)} = r_1^{\pm} + \delta^{(\pm)}. \tag{31}$$

By using the condition $|\delta^{(\pm)}| \ll |r_1^{\pm}|$, we can then reduce Eq. (26) to a cubic equation for the quantity $\lambda^{(\pm)}$ and find its roots,

$$\lambda_n^{(\pm)} = |\lambda|\, e^{i\beta_\lambda^{(\pm)}}, \quad |\lambda| = \left[\frac{|\alpha||r^{\pm}|^2}{q}\right]^{1/3}, \tag{32}$$

$$\beta_\lambda^{(\pm)} = \frac{\pi}{3}\left[2n + \frac{1}{2} \pm \frac{1}{2}\right] + \frac{1}{3}\beta_\alpha + \frac{2}{3}\beta_r^{(\pm)}, \tag{33}$$

for which $\mathrm{Im}\,\lambda_n^{(\pm)} \geq 0$ and solutions $b_s^{(\pm)}$ fall within quadrants I and IV [32]. By using the condition $|\delta^{(\pm)}| \ll |r_1^{\pm}|$, we now obtain

$$\lambda_n^{(\pm)} = \sqrt{(r_1^{\pm} + b_{s_n}^{(\pm)})(r_1^{\pm} - b_{s_n}^{(\pm)})} \simeq \sqrt{-2r_1^{\pm}\delta_n^{(\pm)}} \tag{34}$$

and, from (32), then derive the final expression

$$\delta_n^{(\pm)} = -\frac{1}{2}\frac{|\lambda|^2}{|r_1^{(\pm)}|}e^{i\beta_\delta^{(\pm)}}, \tag{35}$$

$$\beta_\delta^{(\pm)} = \frac{2}{3}\pi(2n+1) + \frac{2}{3}\beta_\alpha \pm \frac{1}{3}\beta_r^{(+)}.$$

The behavior of the saddle points in the complex plane of b, which were obtained on the basis of the approximate formulas (31) and (35), is illustrated in Fig. 4. The sum of the near and the far amplitude calculated by using these points determines the Fraunhofer-type diffraction pattern of the scattering. It is discussed in detail below (see Section 6).

6. DISCUSSION OF RESULTS. INCLUSION OF THE COULOMB DISTORTION OF TRAJECTORY

For the example of elastic ^{17}O scattering on ^{208}Pb, ^{120}Sn, ^{90}Zr, and ^{60}Ni, we show in Fig. 5 that different scattering mechanisms operate in different regions of the angular distribution.

For $\vartheta < \vartheta_r$ (regions I and II), the scattering process is determined by the sum of two near-side amplitudes and each of them, at the same momentum transfer, is specified by its own impact parameter (b_{s_1} and b_{s_2}). Thus, there are two trajectories in the range of action of the Coulomb potential and the tail of the nuclear potential that provide scattering at the same angle ϑ. At very small angles, the contribution of the nuclear trajectory is insignificant because of the strong absorption of particles at small b_{s_1}. In this case, the scattering process is determined primarily by the second, Coulomb, trajectory characterized by a large impact parameter b_{s_2}, in which case the ratio $d\sigma/d\sigma_{\mathrm{R}}$ is close to unity. As the angle ϑ increases, the saddle points on the "nuclear" slope $q(b_{s_1})$ are shifted to the region of larger b values at the periphery of the tail of the nuclear potential, where absorption is weak and where the role of its real part, which is responsible for refraction, becomes more important. As a result, the interference pattern of the angular distribution in region I becomes more pronounced. It is common practice to associate it with Fresnel diffraction.

The existence of the limiting scattering angle ϑ_r, near which the classical trajectories are bunched, is a feature peculiar to the angular distribution in region II. Just for this reason, one can draw an analogy with the optical interference of the refracted and the once reflected rays of light in a water drop (rainbow scattering).

For $\vartheta < \vartheta_r$, it is possible to distinguish clearly regions I and II and to determine the point at which the analytic expressions for the corresponding scattering amplitudes are matched. For example, one can see from Fig. 5 that, in region I, the results of the calculation of classical scattering by formula (15) (short dashes) is in good agreement with the precise numerical integration of the initial amplitude (1) (solid curves) up to angles at which a broad maximum begins to manifest itself. Further, up to the limiting classical scattering angle (region II), the exact numerical results are reproduced by formula (22) for rainbow scattering (dotted curves). The positions of the maxima in the angular distributions of $d\sigma/d\sigma_{\mathrm{R}}$ correspond to the maximum of the function $\mathrm{Ai}(\sigma)$ in expression (22) at $\sigma = -1$. If $\sigma < -1$ at a given angle ϑ, one should take expression (20) for the amplitude; otherwise, it is necessary to use formula (22). It should be noted that the results of the calculation by the traditional formula (20) for rainbow scattering (long dashes) are much lower and are at odds with the results of numerical computations. The classically allowed region of scattering shrinks for the interaction of lighter nuclei at the same energy.

In the quantum region of scattering ($\vartheta > \vartheta_r$), the stationary points occur in the complex plane. The experimental cross sections for $\vartheta > \vartheta_r$ typically show an exponential decrease without oscillations (region III) or with oscillations (region IV). In the first case (region III), only the near-side amplitude featuring a single complex stationary point b_{s_1} [expression (17) for $q > q_r$] makes a leading contribution to the amplitude (short dashes). In region IV, the oscillations of the cross section are due to the summation of the near-side and the far-side amplitude of Fraunhofer scattering (dash-dotted curve). In calculating these amplitudes, the saddle points were determined in the complex plane with allowance for absorption. Here, in contrast to the classical region, the choice of the matching point is rather arbitrary. In this study, the solutions corresponding to regions III and IV go over to each other at their intersection point closest to ϑ_r on the right. It should be noted that, as the ratio of the Coulomb barrier to the collision energy, V_B/E, decreases, the Fraunhofer character of scattering in the quantum region becomes ever more pronounced.

Let us consider the problem of the Coulomb distortion of the trajectory. Under the effect of strong Coulomb repulsion, the trajectory of heavy ions is

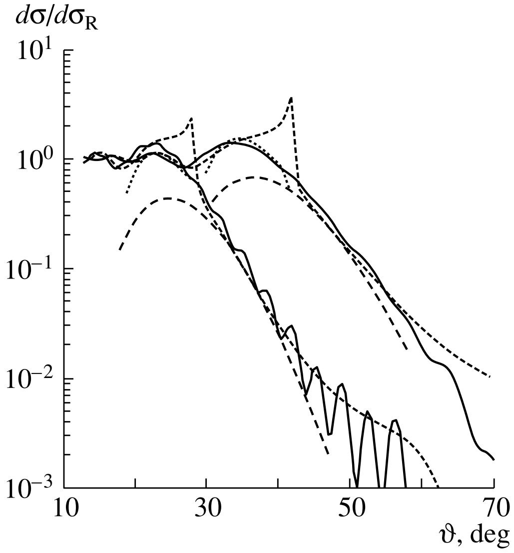

Fig. 6. Effect of the Coulomb deflection of the trajectory for the example of ^{32}S scattering on ^{27}Al at $E_{\text{c.m.}} =$ 55 MeV: (left curves) results of the calculation without deflection ($a_c = 0$) and (right curves) results of the calculation with allowance for deflection ($a_c \neq 0$). The curves were calculated under the same assumptions as in Fig. 5.

strongly deflected from a straight line, and this noticeably affects the behavior of the cross section. The distortion in question can be taken into account [24] if, from the outset, we replace, in the nuclear phase shift (2), the impact parameter b by the distance b_c of closest approach of nuclei; that is,

$$\chi_N(b) \to \chi_N(b_c), \quad b_c = a_c + \sqrt{b^2 + a_c^2}, \qquad (36)$$

where $a_c = \eta/k$ is the half-distance of closest approach in the Coulomb field $Z_1Z_2e^2/r$ for a head-on collision. It is obvious that the substitution $b \to b_c$ complicates the form of the corresponding derivatives of χ_N with respect to b; however, it is possible, even after this, to derive explicit expressions for the limiting classical momentum transfer $q_{\max} \equiv q_r$ and for the stationary points.

In Fig. 6, we present the results of the (solid curves) numerical and (dashed and dotted curves) analytic calculations of the ratio $d\sigma/d\sigma_R$ for elastic ^{32}S scattering on ^{27}Al at $E_{\text{c.m.}} = 55$ MeV. The curves on the left and on the right of the figure were calculated, respectively, without ($a_c = 0$) and with ($a_c \neq 0$) allowance for the Coulomb distortion of the trajectory. It can be seen that the distortion strongly shifts the pattern of the angular distribution, the results of the analytic calculations being in good agreement with the numerical results. As was mentioned above, the cross section is very sensitive to the position of the maximum in the deflection-momentum function. Even if a_c is small, it is of crucial importance to determine precisely the quantities q_r and b_r now with allowance for the Coulomb deflection in the original phase shift χ_N.

In considering Fraunhofer scattering, we have seen that the stationary points b_s are complex-valued. In this case, the distortion was taken into account by making, for b_s in the nuclear phase in the final expression for the amplitude, the substitution

$$b_s \to \tilde{b}_s = a_c + \sqrt{b_s^2 + a_c^2}. \qquad (37)$$

Experience gained in our calculations reveals that this substitution must be made for Coulomb barrier values of $V_B > 0.04E$.

In Fig. 7, the results of the calculations by the analytic formulas are compared with experimental data from [25] (asterisks). The curves corresponding to different scattering mechanisms are matched at their intersection points. The Coulomb distortion of the trajectory is taken into account according to the scheme outlined above. It can be seen that the calculations reproduce the observed pattern of the differential cross sections, reflecting the main features of their behavior in different regions of the scattering angle. Small shifts of the theoretical curves with respect to the experimental data are obviously associated with the need for refining the mechanism of taking into account the distortion of the trajectories due to both the Coulomb and the nuclear field, especially in the region of Fraunhofer diffraction, where the analysis is performed in the complex plane of the impact parameter.

By and large, we can conclude that the Glauber–Sitenko approximation is quite applicable to analyzing nucleus–nucleus collisions at energies from 10 to 100 MeV per nucleon. The region of its applicability in the scattering angles expands owing to the Coulomb shift of the trajectory of the motion of a projectile ion by $\vartheta_c \simeq |V_{\max}(r \sim R)|/E$. Thus, there appear the classical and the quantum scattering-angle region, $\vartheta < \vartheta_c$ and $\vartheta_c < \vartheta < \vartheta_c + \sqrt{2/kR}$, which are separated by a boundary whose choice involves some degree of arbitrariness and which display their own special interference and diffraction features. The use of an explicit form of the eikonal phase for the extended optical Woods–Saxon potential makes it possible to develop asymptotic methods for calculating eikonal amplitudes in this energy region and to describe the pattern of nucleus–nucleus scattering in terms of the diffraction models. It turned out that both the computational methods and the scattering amplitudes obtained within these methods are highly sensitive to the behavior of the potential in a rather narrow region of its periphery. Taking into account these special features, we have been able not only to understand the scattering mechanism at a qualitative level but also

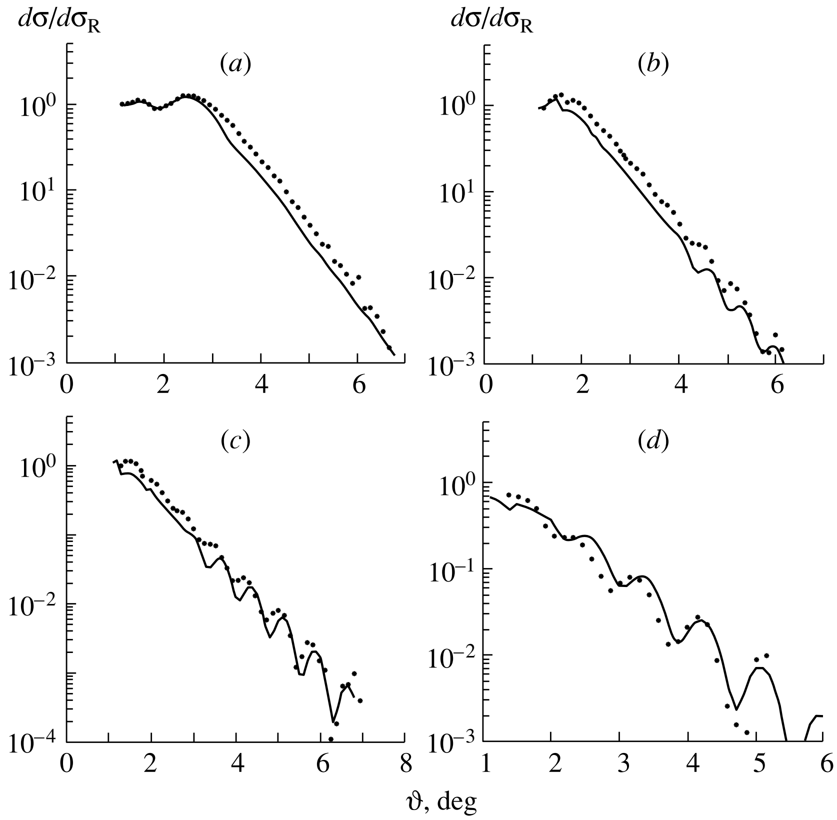

Fig. 7. Results of analytic calculations of the ratio $d\sigma/d\sigma_R$ along with experimental data for elastic ^{17}O scattering on (a) ^{208}Pb ($E_{\rm c.m.} = 1327$ MeV), (b) ^{120}Sn ($E_{\rm c.m.} = 1257$ MeV), (c) ^{90}Zr ($E_{\rm c.m.} = 1207$ MeV), and (d) ^{60}Ni ($E_{\rm c.m.} = 1118$ MeV). The experimental data (asterisks) were borrowed from [25]. The curves represent the results of the analytic calculations performed for the cross sections associated with the effect of various scattering mechanisms and matched in accordance with the partition into the regions in Fig. 5. The parameters of the potentials are identical to those in Fig. 5.

to describe quantitatively the main regularities in the differential cross sections measured experimentally.

ACKNOWLEDGMENTS

The work of V.K. Lukyanov and Yu.V. Chubov was supported by the Russian Foundation for Basic Research (project no. 00-15-96737).

APPENDIX

Coefficients in the Logarithmic Parabola in Terms of the Input Parameters of the Reaction

According to (13), the deflection-momentum function has the form

$$q = \chi'_N + \chi'_{\rm C}. \tag{A.1}$$

Substituting χ_N from (11) and $\chi_{\rm C} = 2\eta\ln(kb)$ into (A.1), we obtain

$$q = \frac{2\eta}{b} + \gamma_N \cdot 2RP(1, C)u'_{\rm SF}(b), \tag{A.2}$$

where $\gamma_n = -\dfrac{k}{2E}(V_0 + iW_0)$. From this equation, it is impossible to find the explicit dependence $b = b(q)$, which determines stationary points. For this reason, the right-hand side of (A.2) is approximated by the logarithmic parabola (16) $q = q_r - \rho\left[\ln\dfrac{b - b_1}{b_r - b_1}\right]^2$ in the region near the maximum of the deflection-momentum function ($q_{\rm max} = q_r = q(b_r)$). In this approximation, stationary points are found in the explicit form (17). In constructing the above approximation, it is necessary to determine the position of the maximum to a high precision; that is, q_r and b_r are the main parameters of the logarithmic parabola. To do this, we proceed in the following way: at the point b_r, the derivative of expression (A.2) vanishes, which yields the equation

$$-\frac{2\eta}{b_r^2} + \gamma_N \cdot 2RP(1, C)u''_{\rm SF}(b) = 0. \tag{A.3}$$

The most appropriate way to solve this equation explicitly is to reduce it to a cubic equation. The cubic equation has at least one real solution, and it is the solution that determines the position of the maximum. In the case of three real roots, that which is the closest to nuclear-potential range R from the right will be the required root b_r.

In order to obtain the coefficients in the polynomial of third degree whose graph passes through the zero of expression (A.3), four points x_n $(n = 0, 1, 2, 3)$ at the nuclear-potential tail in the region where the maximum of $q(b)$ is formed are chosen as follows:[4)]

$$u_{\mathrm{F}}(x_0) = 0.005, \quad u_{\mathrm{F}}(x_1) = 0.01, \quad u_{\mathrm{F}}(x_2) = 0.02, \quad u_{\mathrm{F}}(x_3) = 0.05. \tag{A.4}$$

It is straightforward to express these points in terms of the geometric parameters of the potential; that is,

$$x_0 = R + a\ln 199, \quad x_1 = R + a\ln 99, \quad x_2 = R + a\ln 49, \quad x_3 = R + a\ln 19. \tag{A.5}$$

Between the points in (A.5), we construct an interpolating Newton polynomial [33]:

$$\begin{aligned}\phi(b) = \phi(x_0) + (b - x_0)\phi(x_0, x_1) \\ + (b - x_0)(b - x_1)\phi(x_0, x_1, x_2) \\ + (b - x_0)(b - x_1)(b - x_2)\phi(x_0, x_1, x_2, x_3),\end{aligned} \tag{A.6}$$

where $\phi(x_n)$ stands for the values of expression (A.3) at the points x_n, and $\phi(x_0, ..., x_n)$ are divided differences of nth order that are given by

$$\phi(x_0, x_1) = \frac{\phi(x_0) - \phi(x_1)}{x_0 - x_1},$$

$$\phi(x_0, x_1, x_2) = \frac{\phi(x_0, x_1) - \phi(x_1, x_2)}{x_0 - x_2},$$

$$\phi(x_0, x_1, x_2, x_3) = \frac{\phi(x_0, x_1, x_2) - \phi(x_1, x_2, x_3)}{x_0 - x_3}.$$

Removing the parentheses in (A.6) and collecting the coefficients at the same powers of b, we obtain a cubic equation whose real-valued solution determines b_r, while q_r is obtained by direct substitution of b_r into (A.2).

In order to determine b_1, we approximate the function $q(b)$ by a parabola with the vertex at the point (b_r, q_r); that is, $q(b) = q_r - A(b - b_r)^2$. From the requirement that the parabola pass through a point (for example, x_3) on the left branch of $q(b)$, we find the coefficient A. We then have $b_1 = b_r - \sqrt{q_r/A}$.

The coefficient ρ is determined from the condition requiring that the logarithmic parabola be coincident with the function $q(b)$ (A.2) at an arbitrary point of the interval $[b_1; b_r]$. We choose it to be $(b_1 + b_r)/2$.

The proposed method disregards the deflection of the trajectory under the effect of the Coulomb field. This effect can be taken into account if we again use the condition in (A.4), but now for the function $u_{\mathrm{F}}(\tilde{x})$, where $\tilde{x} = a_c + \sqrt{x^2 + a_c^2}$. We note that the substitution of $\tilde{x}$ for x in (A.1) leads to more cumbersome expressions for the derivatives in (A.2) and (A.3), but this does not change the above scheme for deriving b_r, q_r, b_1, and ρ.

REFERENCES

1. M. S. Hussein and K. W. McVoy, Prog. Part. Nucl. Phys. **12**, 103 (1984).
2. W. E. Frahn, *Diffractive Processes in Nuclear Physics* (Clarendon, Oxford, 1985).
3. E. V. Inopin and A. V. Shebeko, *Diffractive Interaction of Hadrons with Nuclei* (Naukova Dumka, Kiev, 1987), p. 154.
4. A. I. Akhiezer, Yu. A. Berezhnoĭ, and V. V. Pilipenko, Fiz. Élem. Chastits At. Yadra **31**, 458 (2000).
5. G. R. Satchler and W. G. Love, Phys. Rep. **55**, 183 (1979).
6. Dao Tien Khoa and O. M. Knyaz'kov, Fiz. Élem. Chastits At. Yadra **21**, 1456 (1990) [Sov. J. Part. Nucl. **21**, 623 (1990)].
7. Dao Tien Khoa, G. R. Satchler, and W. von Oertzen, Phys. Lett. B **358**, 14 (1995).
8. O. M. Knyaz'kov, I. N. Kukhtina, and S. A. Fayans, Fiz. Élem. Chastits At. Yadra **28**, 1061 (1997) [Phys. Part. Nucl. **28**, 418 (1997)].
9. R. J. Glauber, *Lectures in Theoretical Physics* (Interscience, New York, 1959), p. 315.
10. A. G. Sitenko, Ukr. Fiz. Zh. **4**, 152 (1959).
11. W. Czyž and L. C. Maximon, Ann. Phys. (N.Y.) **52**, 59 (1969).
12. J. Formánec, Nucl. Phys. B **12**, 441 (1969).
13. V. Franko and A. Tekou, Phys. Rev. C **16**, 658 (1977).
14. K. G. Boreskov and A. B. Kaĭdalov, Yad. Fiz. **48**, 575 (1988) [Sov. J. Nucl. Phys. **48**, 367 (1988)].
15. R. da Silveira and Ch. Leclercq-Willain, J. Phys. G **13**, 149 (1987).
16. O. D. Dalkarov and V. A. Karmanov, Nucl. Phys. A **445**, 579 (1985).
17. P. J. Karol, Phys. Rev. C **11**, 1203 (1975).
18. A. A. Ogloblin *et al.*, Phys. Rev. C **62**, 044601 (2000).
19. V. K. Lukyanov and E. V. Zemlyanaya, J. Phys. G **26**, 357 (2000).
20. G. Faldt, Phys. Rev. D **2**, 846 (1970).
21. M. Grypeos, C. Koutroulos, V. Lukyanov, and V. Shebeko, J. Phys. G **24**, 1913 (1998).
22. V. K. Luk'yanov, Yad. Fiz. **58**, 1955 (1995) [Phys. At. Nucl. **58**, 1848 (1995)].
23. N. Rowley and C. Marty, Nucl. Phys. A **266**, 494 (1976).
24. A. Vitturi and F. Zardi, Phys. Rev. C **38**, 2086 (1988).
25. R. Liguori Neto *et al.*, Nucl. Phys. A **560**, 733 (1993).
26. D. J. Garrett *et al.*, Phys. Rev. C **12**, 489 (1975).

[4)] For the explicit determination of the points to be as simple as is possible, we use here u_{F} instead of u_{SF}, since these functions coincide at real $b > 0$.

27. K. W. Ford and J. A. Wheeler, Ann. Phys. (N.Y.) **7**, 287 (1959).
28. L. B. Felsen, and N. Marcuvitz, *Radiation and Scattering of Waves* (Prentice-Hall, Englewood Cliffs, 1973; Mir, Moscow, 1978), Vol. 1, Chap. 4.
29. J. R. Shepard and E. Rost, Phys. Rev. C **25**, 2660 (1982).
30. R. D. Amado, J. P. Dedonder, and F. Lenz, Phys. Rev. C **21**, 647 (1980).
31. V. K. Luk'yanov, V. P. Permyakov, and Yu. V. Chubov, Izv. Akad. Nauk, Ser. Fiz. **63**, 53 (1999).
32. A. V. Embulaev, E. V. Zemlyanaya, V. K. Luk'yanov, *et al.*, Izv. Akad. Nauk, Ser. Fiz. **62**, 2136 (1998).
33. N. N. Kalitkin, *Numerical Methods* (Nauka, Moscow, 1978).

Translated by A. Isaakyan

Physics of Atomic Nuclei, Vol. 65, No. 7, 2002, pp. 1302–1306. From Yadernaya Fizika, Vol. 65, No. 7, 2002, pp. 1335–1339.

ELEMENTARY PARTICLES AND FIELDS
Experiment

Search for Axions Emitted in Nuclear Magnetic Transitions[*]

A. V. Derbin[**], A. I. Egorov, I. A. Mitropolsky,
V. N. Muratova, S. V. Bakhlanov, and L. M. Tukhkonen

Petersburg Nuclear Physics Institute, Russian Academy of Sciences, Gatchina, 188350 Russia

Received April 11, 2001; in final form, July 11, 2001

Abstract—Searches for invisible axions emitted in the electromagnetic transitions of isomeric nuclei are continued. It is found experimentally that the probability of axion emission in an $M1$ transition in ^{125m}Te is less than 8.5×10^{-6} (90% C.L.). *© 2002 MAIK "Nauka/Interperiodica".*

Theoretical models of the invisible axion with an arbitrary scale of symmetry breaking up to the Planck mass serve as a basis for experimental searches for a pseudoscalar particle that interacts weakly with matter and whose mass ranges from 10^{-12} eV to tens of keV [1–5]. Although the limits on the axion mass that were obtained from astrophysical estimates [6, 7] span almost the entire scale of possible masses, direct laboratory experiments give an upper limit of 6 keV for the axion mass [8]. Models that include the interactions of particles from a mirror world found a new window for the axion mass (~ 1 MeV) that is not excluded by astrophysical data [9].

A new possibility for axion searches is opened up by the method of missing γ ray in nuclear magnetic transitions [10, 11]. Assume an "ideal" detector that detects the energy of all photons and electrons arising from the decay of a nucleus. In this case, the energy spectrum must consist of one peak only with the shape defined by the response function. Meanwhile the invisible axion leaves the detector without interactions. Therefore, this emission will be accompanied by a shift of the total energy spectrum by an amount equal to the transition energy. A study of magnetic transitions in isomeric nuclei is preferable [11] because there is no uncertainty associated with the emission of a neutrino for nuclei undergoing β and electron-capture decay.

In the present study, we continued measuring the energy spectrum of photons and electrons arising from the decay of the ^{125m}Te nucleus. This isomeric nucleus undergoes 109.3-keV $M4$ γ transitions and 35.5-keV $M1$ γ transitions [12]. For the latter, there is a small admixture of an $E2$ transition ($E2/M1 = 0.029$). An excited tellurium nucleus interacts with an atomic shell, each decay of a nucleus being accompanied by a cascade of γ and x rays and conversion and Auger electrons. The scheme of ^{125m}Te decay is shown in Fig. 1. The types of particles produced and the energy and probability of appearance per decay are also shown.

As a model of an "ideal" detector, we used two cylindrical planar HPGe detectors butted together at their end gold surfaces. A small hollow 0.5 mm deep and 3 mm in diameter was ground out at the center of the surface of one of the detectors. The ^{125m}Te source was placed in this hollow. This construction was used to measure the energy spectrum of ^{125m}Te decay.

A sample of tellurium of high-radiation-purity grade was specially prepared for this experiment using the method described earlier in [11]. A tin strip of foil with a mass of 0.1 g was irradiated in a reactor for one month in a flux of 10^{13} neutron/(cm^2 s). The process of production of ^{125m}Te is shown below:

$$n + {}^{124}\mathrm{Sn} \rightarrow {}^{125}\mathrm{Sn}(\beta^-, T_{1/2} = 9.7\ \mathrm{d})$$
$$\rightarrow {}^{125}\mathrm{Sb}(\beta^-, T_{1/2} = 2.7\ \mathrm{yr}) \rightarrow {}^{125m}\mathrm{Te}.$$

After radiochemical purification, a drop of sulfuric acid solution was placed in the hollow with gold coating of the HPGe detector. Tellurium was deposited by electrolysis, forming a spot about 3 mm in diameter.

The sensitive volume of each detector was 40 mm in diameter and 7 mm thick. The absorption of the 35-keV γ ray inside this operating volume of the two detectors was more than 10^{-14}. The absorption of the 109-keV γ rays in the detectors was 97%. It increased the background near 100 keV due to the backscattering of γ rays by the detector holder.

Before the deposition of ^{125m}Te on the surface of the germanium detectors, their characteristics were tested in a separate cryostat. The upper limit on the electron energy losses in the gold coating

---

[*] This article was submitted by the authors in English.

[**] e-mail: `derbin@mail.pnpi.spb.ru`

(30 μg/cm^2) and in the insensitive layer of the detector was determined with a ^{207}Bi source. For a 481.7-keV electron incident along the normal, these losses did not exceed 0.2 keV. This indicates that the detector could detect the L-series x rays of tellurium, which have an average energy of 4 keV, with an efficiency of 95%. If it is assumed that the coefficient of the backscattering of electrons from the detector surface is 0.3 for the configuration employed, then it can be expected that the loss of 30-keV electrons as the result of multiple backscattering will not exceed 10^{-5}. Like Auger L electrons, 4-keV conversion electrons are absorbed in the dead layer of the detector and do not contribute to the total energy release.

After tellurium was deposited on one of the detectors, the detector was placed on the beryllium window of a spectrometer with a Si(Li) detector. The x-ray spectrum obtained in the decay of ^{125m}Te was measured with a resolution of 160 eV (Fig. 2) to determine the probability of the emission of Auger L electrons. This value is of fundamental importance for the proposed method because it permits us to distinguish the emission of an axion from the absorption of a photon or an electron in the dead layer of the detector. The probability of absorption in it is higher for a 27-keV x-ray (or 30-keV electron) than for a 35-keV x-ray (or 34-keV electron). At that time, L x rays accompanying such transitions are detected with nearly a 100% efficiency. It will give rise to an additional intensity in the line shifted to higher energies by 4 keV. According to the decay scheme in Fig. 1, two peaks at energies of 104.5 and 108.3 keV and an intensity ratio of 2.9 should be observed in the total spectrum when an axion is emitted in an $M1$ transition. If the losses of energy are associated with the absorption of particles in the dead layer of the detector, the ratio of the intensities of the above peaks will decrease to 2.2. This difference can be a criterion of a positive result of an observation.

After the measurements described above had been performed, the HPGe detectors were placed up against each other in a cryostat and cooled to liquid-nitrogen temperature. The detectors had individual bias voltages of 1200 and 900 V, which were applied to the n^+ contact. The potential of their common p contact was zero. The two detectors had similar spectrometric channels: a preamplifier with a resistive feedback and an uncoiled FET and an amplifier with the shaping time of 2 μs and a 4096-channel ADC. The resolution measured with respect to the 122-keV γ line of ^{57}Co was 1.9 keV. The two channels were summed and the total signal was processed in an additional ADC. The total energy spectrum from both detectors, the total spectra from each detector, and four spectra corresponding to coincidences and anticoincidences of the detectors were stored in the computer memory. The two-dimensional energy spectrum was also stored in order to seek the optimum background-to-effect ratio.

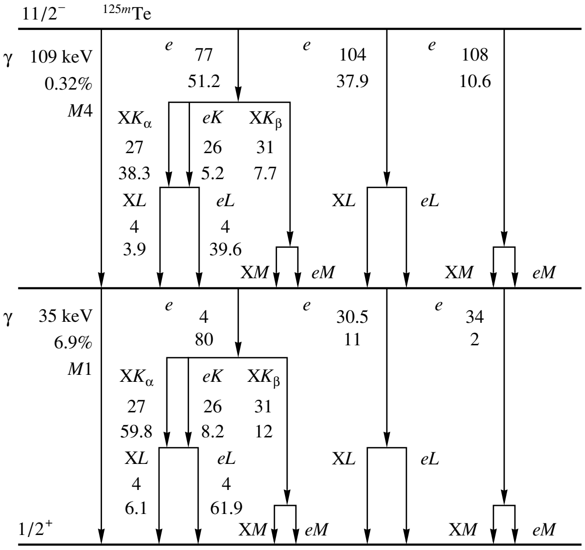

Fig. 1. Main modes of ^{125m}Te decay. Two γ transitions are shown; e are conversion electrons; XK, XL, and XM are characteristic x rays from, respectively, the K, L, and M atomic shells; eK, eL, and eM are Auger electrons. The upper value is the particle energy, while the lower value is the probability of emission per one decay of ^{125m}Te.

A total of 3.5×10^8 decays of ^{125m}Te were detected over 150 h of measurements. A typical spectrum from one detector for one series of measurements is shown in Fig. 3. The spectrum contains 29 peaks corresponding to different modes of ^{125m}Te decay and satellites associated with the escape of germanium x rays from the detector. The numbers *1* and *2* label the two main peaks at energies of 27.4 ($K_{\alpha1,\alpha2}$) and 104.5 keV ($e104$, $e77 + K_\alpha$). Peak *3* corresponds to the monochromatic 77-keV electron line. The resolution of the HPGe detector measured according to this line was 2.1 keV. The shift of the position of the peak as determined according to the energy calibration by x-ray lines of tellurium and germanium was 320 eV. This means that the average energy losses in the insensitive layer of the detector were 700 eV for electrons of energy 30 keV. Lines 4, 5, and 6 are shifted by 12, 8, and 4 keV, respectively, to the left of the total-absorption peak (144.8 keV). This is due to the loss of an x ray, a conversion electron, or an Auger electron.

The total spectrum from the two detectors is shown in Fig. 4. As might have been expected, the maximum of the peak corresponding to the total detected energy is at 132 keV and not at 144.8 keV.

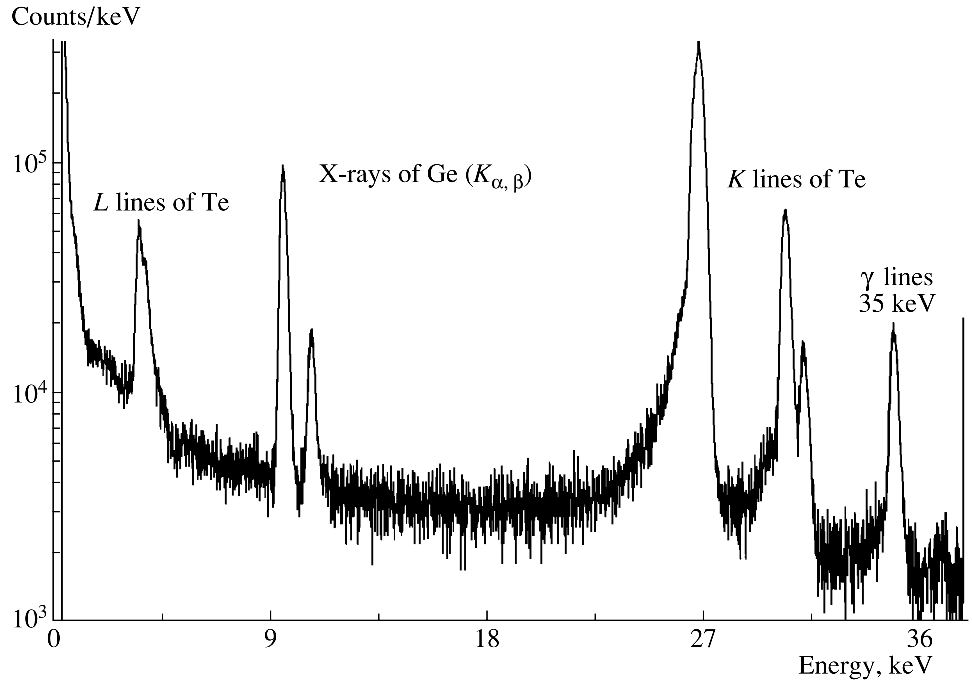

Fig. 2. Spectrum of ^{125m}Te measured by a Si(Li) detector. The value of a channel is 10 eV.

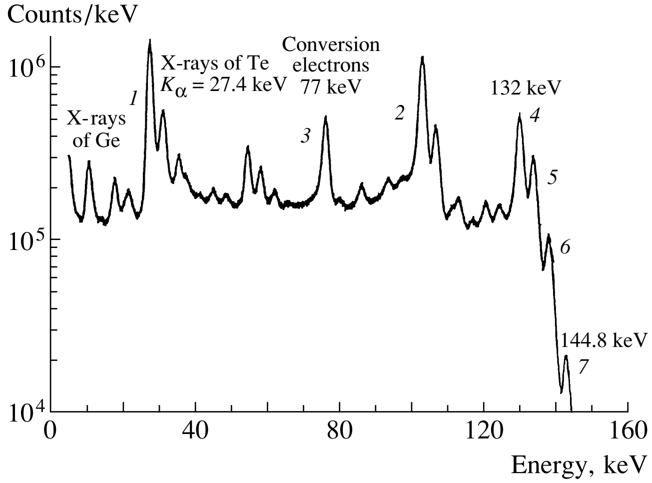

Fig. 3. Spectrum of ^{125m}Te measured by one HPGe detector. There are 29 peaks against two peaks expected for two magnetic transitions in the nucleus.

The energy shift is due to the loss of one or two Auger *L* electrons or one 4-keV conversion electron. Since the resolution for the total spectrum is 1.5 times poorer, the right-hand edge of the peak possesses a profiled shape corresponding to unresolved peaks at energies of 136, 140, and 144 keV. The background level near 104 keV was equal to 3.5×10^5 keV^{-1} and was determined by the tails of the electron lines associated with the multiple reflections of electrons from the surface of the detectors.

The maximum-likelihood method was used to find the intensities of the lines at energies of 104.5 keV and 108.3 keV. The likelihood function was found from the assumption that the number of counts in each channel has a normal distribution and is a sum of an exponential function chosen to describe the background and the response function for the electrons, which is determined from the total spectrum. The response function was represented as a Gaussian peak, whose variance was determined by the resolution of the composite detector, and an exponential tail of area 40%.

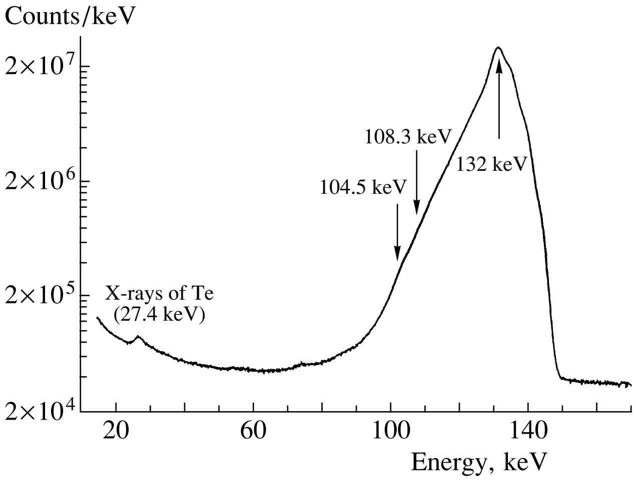

Fig. 4. Spectrum of the total detected energy. Two vertical arrows indicate the positions of the expected peaks in the case of axion emission.

The value obtained for the ratio of the intensity of axion radiation to the total intensity was $I_a/I_\gamma = (4.5 \pm 2.5) \times 10^{-6}$. It corresponds to an upper limit on the probability of axion emission in the $M1$ transition of ^{125m}Te, $I_a/I_\gamma \leq 0.85 \times 10^{-5}$ at the 90% C.L.

Let us compare this result with theoretical estimates. The residual neutron–proton interaction in nuclei featuring two particles of one kind above a magic core and half-filled shell of particles of the other kind leads to the nuclear spectra containing low-lying intruder states in addition to the single-particle states of a spherical nucleus. According to the data from stripping and pickup nuclear reactions, the lowest levels $1/2^+$, $3/2^+$, and $11/2^-$ in ^{125}Te are largely single-particle levels [13]. Their energies can be explained by the presence of a small negative deformation, $\varepsilon \approx -0.1$.

The standard long-wave approximation for pointlike nucleons can be used to determine the probabilities ω_γ and ω_a of nuclear electromagnetic and axion transitions, respectively, in the energy region studied. If the nuclear transition is determined by the change in the state of a single nucleon and if this nucleon is a neutron $[\mu_1(n) = 0]$, the axion transition operator can be related, in the single-particle approximation, to the magnetic transition operator having the same multipolarity by the equation

$$\hat{T}(AL) = 2\frac{g_a^0 - g_a^1}{e\mu_s(n)}\hat{T}(ML), \qquad (1)$$

where g_a^0 and g_a^1 are the isoscalar and the isovector parameter of the axion–nucleon interaction and $\mu_s(n) = -3.827$ is the spin gyromagnetic ratio of the neutron. Taking into account Eq. (1) and the possibility of an admixture of an $E2$ transition, we find that the ratio of the axion- and magnetic-transition probabilities can be represented as

$$\frac{\omega_\mathrm{a}}{\omega_\gamma} = \frac{2(g_\mathrm{a}^0 - g_\mathrm{a}^1)^2 E_\mathrm{a}^3}{(1+\delta^2)e^2\mu_s^2(n)E_\gamma^3}, \qquad (2)$$

where $E_a^2 = E_\gamma^2 - m_a^2$. For the axion–nucleon coupling constants, we employ the values obtained in [14–16]; that is,

$$g_a^0 = -1.77 \times 10^{-5}\frac{m_a}{1\ \mathrm{keV}}(1 + 2.94S),$$
$$g_a^1 = -2.72 \times 10^{-5}\frac{m_a}{1\ \mathrm{keV}}, \quad S = 0.68,$$

where m_a is given in keV units. The dependence of ω_a/ω_γ on m_a reaches a maximum value of 2.8×10^{-6} at $m_a = 22$ keV. Therefore, our theoretical estimate is three times lower than our experimental estimate. For this reason, we cannot set a limit on the axion mass in the range 0–35 keV.

The sensitivity of our method of missing γ ray can be increased. At first, the background near 104 keV must be reduced. The background level is determined mainly by the tails of the electron lines produced by the backscattering of electrons from the surface of the detectors. The thickness of the dead layer of the detector and the thickness and the atomic number of the conducting coating must be decreased. The contribution of natural radioactivity to the background is almost an order of magnitude less, but the use of a passive and active shielding can decrease it further. Increasing the measurement time and improving the resolution by using cooled FET in the preamplifiers open up additional possibilities. All of these measures will make it possible to reach the sensitivity to the axion mass at a level of 1 keV.

ACKNOWLEDGMENTS

This work was supported by the Russian Foundation for Basic Research (project no. 00-02-16-808).

REFERENCES

1. A. R. Zhitnitskiĭ, Yad. Fiz. **31**, 497 (1980) [Sov. J. Nucl. Phys. **31**, 260 (1980)].
2. M. Dine, F. Fishler, and M. Srednicki, Phys. Lett. B **104B**, 199 (1981).
3. M. B. Wise, H. Georgi, and S. Glashow, Phys. Rev. Lett. **47**, 402 (1981).
4. J. E. Kim, Phys. Rev. Lett. **47**, 402 (1981).
5. M. A. Shifman, A. I. Vainstein, and V. I. Zakharov, Nucl. Phys. B **166**, 493 (1980).
6. M. S. Turner, Phys. Rep. **197**, 67 (1990).
7. G. G. Raffelt, Phys. Rep. **198**, 1 (1990).
8. Particle Data Group (R. M. Barnett *et al.*), Phys. Rev. D **54**, 238 (1996).
9. Z. Berezhiani, L. Gianfagna, and M. Giannotti, Phys. Lett. B **500**, 285 (2001).
10. M. Minowa, I. Inoue, T. Asanuma, and M. Imamura, Phys. Rev. Lett. **71**, 4120 (1993).
11. A. V. Derbin, A. I. Egorov, I. A. Mitropol'skii, *et al.*, Pis'ma Zh. Éksp. Teor. Fiz. **65**, 576 (1997) [JETP Lett. **65**, 605 (1997)].
12. C. M. Lederer and V. S. Shirley, *Table of Isotopes* (Wiley, New York, 1978).
13. J. Katakura *et al.*, Nucl. Data Sheets **70**, 217 (1993).
14. D. B. Kaplan, Nucl. Phys. B **260**, 215 (1985).
15. M. Srednicki, Nucl. Phys. B **260**, 689 (1985).
16. W. C. Haxton and K. Y. Lee, Phys. Rev. Lett. **66**, 2557 (1991).

Physics of Atomic Nuclei, Vol. 65, No. 7, 2002, pp. 1307–1312. Translated from Yadernaya Fizika, Vol. 65, No. 7, 2002, pp. 1340–1345.
Original Russian Text Copyright © 2002 by Blinov, Turov, Chadeyeva.

ELEMENTARY PARTICLES AND FIELDS
Experiment

Search for Dibaryon Production in ^{4}Hep Interactions at Intermediate Energies

A. V. Blinov[*], **V. F. Turov, and M. V. Chadeyeva**

Institute of Theoretical and Experimental Physics,
Bol'shaya Cheremushkinskaya ul. 25, Moscow, 117259 Russia

Received June 13, 2001; in final form, September 4, 2001

Abstract—With the aid of the 2-m liquid-hydrogen bubble chamber constructed at the Institute of Theoretical and Experimental Physics (ITEP, Moscow), ^{4}Hep interactions are studied at primary alpha-particle momenta of 2.7 and 5 GeV/c (the respective kinetic energies of primary protons in the ^{4}He rest frame are $T_p = 220$ and 620 MeV). The effective-mass spectra of two nucleons from the reactions $^4\mathrm{He}p \to dppn$ and $^4\mathrm{He}p \to pppnn$ are analyzed. The effective-mass spectrum of the two-proton system produced in the quasielastic-charge-exchange reaction $p^4\mathrm{He} \to n_F(pp)d$ at $T_p = 620$ MeV (here, n_F stands for the fast neutron in the ^{4}He rest frame) shows a narrow peak, which is indicative of the existence of a dibaryon whose mass and width are $M_{2p} = 2008 \pm 13$ MeV and $\Gamma_{2p} = 20 \pm 5$ MeV, respectively. In the mass spectra of the two-proton system from the reactions $p^4\mathrm{He} \to n_F(pp)d$ and $p^4\mathrm{He} \to p_F(pp)(nn)$, narrow threshold peaks are also found at a mass of $M_{2p} \simeq 1878$–1879 MeV. *© 2002 MAIK "Nauka/Interperiodica".*

1. INTRODUCTION

The question of whether dibaryons exist has so far been one of the most intriguing and controversial questions in nuclear physics. This problem has been explored in a great number of theoretical and experimental studies (see, for example, the article of Tatischeff *et al.* [1], who presented a review of modern experiments devoted to searches for dibaryons). The overwhelming majority of indications of the existence of narrow dibaryons (of width $\Gamma \leq 50$ MeV) have been obtained in bubble-chamber experiments. At the same time, the results of some other studies, both those that employ the same experimental procedure [2] and those that invoke electronics (see [1]), show no evidence of the existence of resonances. It should be noted that the majority of experiments seeking dibaryons were performed in studying lepton and hadron interactions with extremely light nuclei (d, ^{3}He,^{4}He).

Previously, systematic searches for dibaryon resonances in ^{3}Hp and ^{3}Hep interactions at intermediate energies were conducted within an ITEP experiment that studied nuclear reactions in few-nucleon systems by means of liquid-hydrogen bubble chambers [3–6]. The mass spectra of NN and $NN\pi$ systems, characterized by various isospin projections were analyzed. In the mass spectra of the pp, pn, nn, $pn\pi^+(n\Delta^{++})$, and $pp\pi^+(p\Delta^{++})$ systems no evidence of dibaryon-resonance production was found in the energy range from 1.88 to 2.5 GeV.

In the present study, we use the 2-m liquid-hydrogen bubble chamber constructed at the Institute of Theoretical and Experimental Physics (ITEP, Moscow) to seek dibaryon production in ^{4}Hep interactions at primary alpha-particle momenta of 2.7 and 5 GeV/c (the respective kinetic energies of primary protons in the ^{4}He rest frame are $T_p = 220$ and 620 MeV). It is worth noting that the first pieces of evidence of narrow-dibaryon production in ^{4}Hep interactions were obtained in experiments where the 1-m liquid-hydrogen bubble chamber installed at the Joint Institute for Nuclear Research (JINR, Dubna) was exposed to the beam of 8.6-GeV/c alpha particles [7].

In what is concerned with searches for dibaryons, ^{4}Hep interactions should obviously be preferred to the interactions of other light nuclei (d, ^{3}H, ^{3}He) with protons, because the internucleon distances are relatively shorter in the ^{4}He nucleus, with the result that the probability of the possible existence of multiquark states with hidden color is higher in this nucleus.

Earlier, narrow peaks were observed in analyzing the mass spectra of two protons in hadron–nucleus and nucleus–nucleus interactions in the mass region near $2m_p$ [8–10]. In [9, 10], they were interpreted as a manifestation of the effect associated with the

---

[*] e-mail: `Blinov@itep.ru`

Cross sections for the reactions $^4\mathrm{He}p \to dppn$ and $^4\mathrm{He}p \to pppnn$ at primary momenta of 2.7 GeV/c ($T_p = 220$ MeV) and 5 GeV/c ($T_p = 620$ MeV)

Momentum, GeV/c	Reaction channel		Number of events		Cross section, mb
2.7	$^4\mathrm{He}p \to dppn$	Direct	2345	3494	21.4 ± 0.4
		Charge exchange	1149		
	$^4\mathrm{He}p \to pppnn$		1620		9.9 ± 0.2
5	$^4\mathrm{He}p \to dppn$	Direct	1894	2567	21.2 ± 0.4
		Charge exchange	673		
	$^4\mathrm{He}p \to pppnn$		1394		11.5 ± 0.3

final-state interaction of protons (so-called Migdal—Watson effect). Data on the mass spectra of the $2p$ system near the threshold (in this region, these data are equivalent to the relative-momentum distribution) can be used to obtain two-proton correlation functions in order to determine the spacetime dimension of the particle-emission region in the nuclear reactions [11—13]. In the present study, we analyze in detail the mass spectra of two protons from $^4\mathrm{He}p$ interactions in the threshold region.

2. DESCRIPTION OF THE EXPERIMENT

The 2-m ITEP liquid-hydrogen bubble chamber was exposed to separated beams of 2.7- and 5-GeV/c ^{4}He nuclei. The chamber was placed in a magnetic field of strength 0.92 T. Background particles in the primary beam (predominantly deuterons) were reliably separated by track ionization. We obtained about 60 000 and 120 000 photographs at 2.7 and 5 GeV/c, respectively, at an average counting intensity of about 5—8 particles per chamber width. The total number of measured interaction events was about 18 000—19 000 for either value of the primary momentum. A more detailed account of the procedures used in the present measurements and in subsequent data processing is given in [14]. It should be noted that our experimental procedure makes it possible to analyze data on the reactions in question under the conditions of 4π coverage.

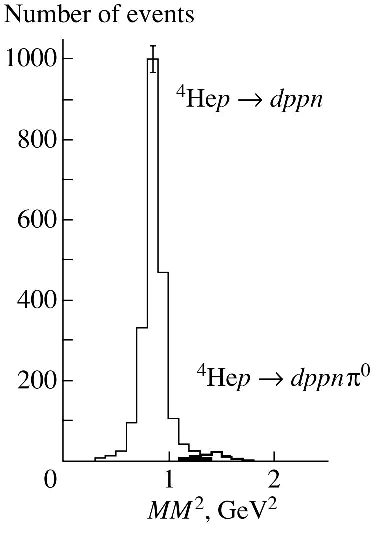

Fig. 1. Distributions in the missing mass squared MM^2 for unbalanced events of the reaction $^4\mathrm{He}p \to dppn$ (thin-line histogram) and for events of the reaction $^4\mathrm{He}p \to dppn\pi^0$ (thick-line histogram) at a momentum of 5 GeV/c. The shaded region corresponds to the overlap of the pionic and the pionless channel.

The total cross section for $^4\mathrm{He}p$ interaction was estimated by using the standard procedure of counting the number of events within a specific chamber volume [14]. This yielded 109.4 ± 1.8 and 121.5 ± 2.9 mb for, respectively, 2.7 and 5 GeV/c (the quoted errors are purely statistical). The systematic error in the absolute normalization of the cross sections amounted to about 3%.

The results presented in this article are based on the analysis of our data on the reactions

$$^4\mathrm{He}p \to dppn, \qquad (1)$$

$$^4\mathrm{He}p \to pppnn. \qquad (2)$$

In order to identify particles in three-prong αp interactions, we applied the standard bubble-chamber-experiment procedure of sampling mass hypotheses with allowance for data on visible ionization of secondary-particle tracks. Events of reaction (1), where there was only one neutral particle in the final state, were subjected to the procedure of kinematical balancing. Events of reaction (2), where there were two neutral particles, were not balanced. It is worth noting that at a primary momentum of 2.7 GeV/c ($T_p = 220$ MeV)—that is, below the threshold for pion production in an elementary NN collision—pion production in $^4\mathrm{He}p$ interaction is almost completely suppressed.

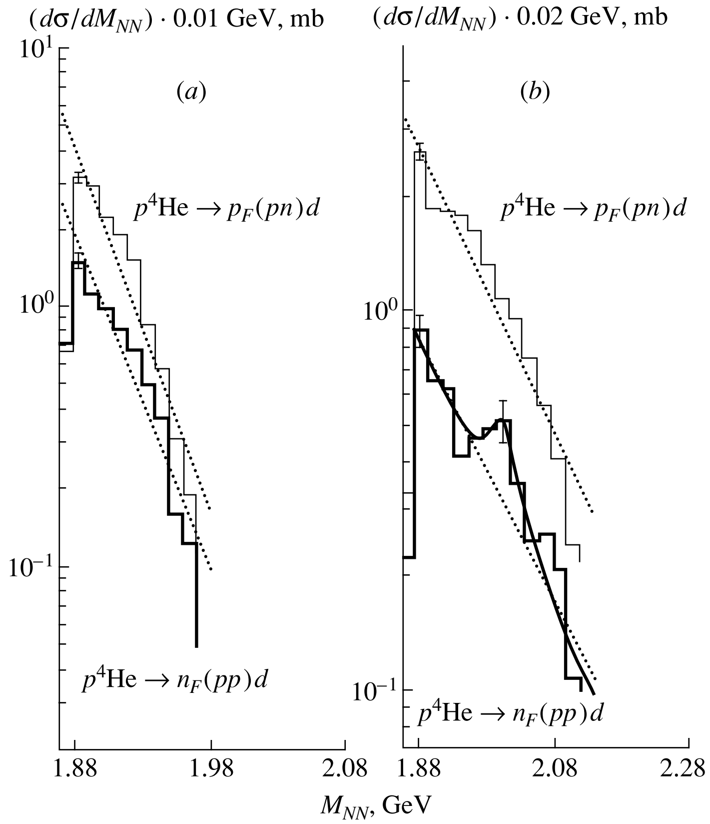

Fig. 2. Effective-mass distributions of two slow nucleons (in the ^{4}He rest frame) for the (thin-line histograms) direct channel of the reaction $p^4\mathrm{He} \to p_F(pn)d$ and (thick-line histograms) quasielastic-charge-exchange channel $p^4\mathrm{He} \to n_F(pp)d$ at $T_p =$ (*a*) 220 and (*b*) 620 MeV [$p_F(n_F)$ is the fast proton (neutron) in the ^{4}He rest frame]: (solid curve in Fig. 2*b*) fit to the experimental data in the interval $1.88 < M_{NN} < 2.12$ GeV in terms of the sum of the exponential background and the Breit–Wigner function with parameters $M_{2p} = 2008 \pm 7$ MeV and $\Gamma_{2p} = 46 \pm 14$ MeV and (dotted straight lines) exponential fit to the experimental data in the intervals (*a*) $1.88 < M_{NN} < 1.97$ GeV and (*b*) $1.88 < M_{NN} < 2.12$ GeV (for the case of the quasielastic-charge-exchange channel at $T_p = 620$ MeV, we fitted the data beyond the interval $1.96 < M_{NN} < 2.06$ GeV).

Figure 1 presents the distributions in the missing mass squared MM^2 for unbalanced events of reaction (1), as well as for events of the reaction $^4\mathrm{He}p \to dppn\pi^0$ at 5-GeV/c momentum that were not subjected to fitting. The distributions correspond to about 80% of the total statistics. The MM^2 distribution for reaction (1) has a Gaussian form with a mean value close to the neutron mass squared $m_n^2 \simeq 0.88$ GeV^2. The region where the channels with and without a neutral pion overlap (shaded region in Fig. 1) contains $\leq$1% of the total number of events of reaction (1). In channel (2) at a momentum of 5 GeV/c, there is obviously an admixture of events associated with the channel $^4\mathrm{He}p \to pppnn\pi^0$ (we estimate it at about 5%).

It is natural to break down the set of events of channel (1) into two classes associated with the fastest secondary nucleons in the ^{4}He rest frame—specifically protons (direct channel) and neutrons (quasielastic charge exchange). The cross sections for the reactions under consideration and the numbers of events in them are given in the table for the above two values of the primary momentum. We note that there is an admixture (about 10%) of events of reaction (1) where the deuteron formed by the pickup mechanism is the fastest particle in the ^{4}He rest frame. In analyzing the effective-mass distributions, such events, where all three secondary nucleons are spectators, are of course taken into account in one class of events or the other.

3. RESULTS AND CONCLUSIONS

Figure 2 displays the effective-mass distributions for two spectator nucleons from (thin-line histograms) the direct channel of the reaction $p^4\mathrm{He} \to p_F(pn)d$ and (thick-line histograms) the quasielastic-charge-exchange channel $p^4\mathrm{He} \to n_F(pp)d$ at $T_p =$ (*a*) 220 and (*b*) 620 MeV [$p_F(n_F)$ means the fast proton (neutron) in the ^{4}He rest frame]. There are no special features in the mass spectra of two spectator

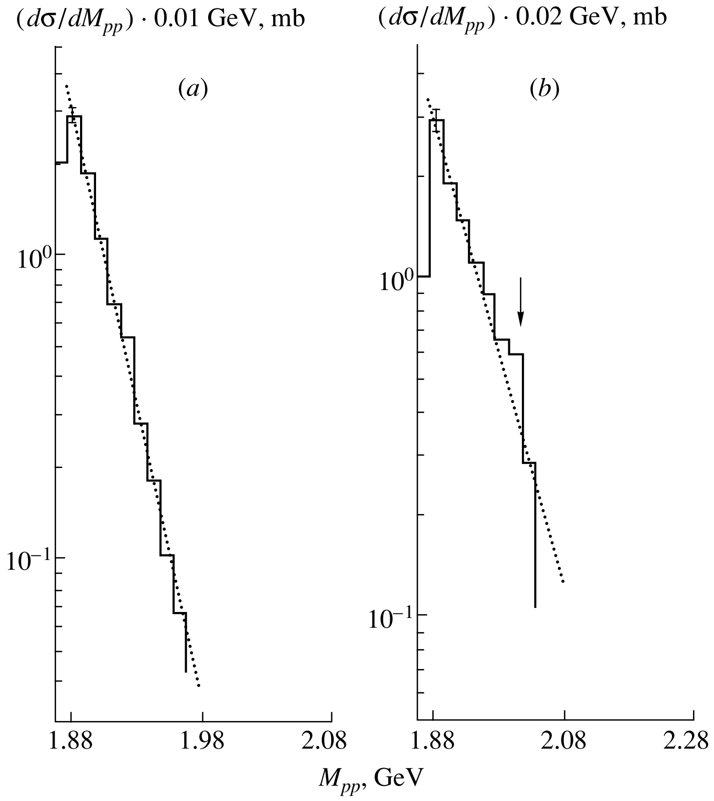

Fig. 3. Effective-mass distribution of two protons from the reaction $p^4\mathrm{He} \to p_F(pp)(nn)$ at (*a*) $T_p = 220$ MeV and (*b*) 620 MeV that are slow in the ^{4}He rest frame (p_F is the fast proton in this reference frame). The dotted lines correspond to an exponential fit to experimental data in the intervals $1.88 < M_{pp} < 1.97$ GeV and $1.88 < M_{pp} < 2.12$ GeV for cases (*a*) and (*b*), respectively.

nucleons from the direct channel of the reaction at considered energies or from the charge-exchange channel at $T_p = 220$ MeV. The dotted lines in Figs. 2*a* and 2*b* represent an exponential fit to the data in the intervals $1.88 < M_{NN} < 1.97$ GeV and $1.88 < M_{NN} < 2.12$ GeV, respectively. The mass spectrum for the charge-exchange channel at $T_p = 620$ MeV exhibits a pronounced peak (at the maximum, the enhancement amounts to 3.1 standard deviations). A fit to the experimental data within the interval $1.88 < M_{NN} < 2.12$ GeV in terms of the sum of an exponential background and the Breit–Wigner function with parameters $M_{2p} = 2008 \pm 7$ MeV and $\Gamma_{2p} = 46 \pm 14$ MeV ($\chi^2/\mathrm{NDF} = 7.6/8$) is shown in Fig. 2*b* by the solid line (in this case, the dotted line in Fig. 2*b* corresponds to an exponential fit to the data beyond the interval $1.96 < M_{NN} < 2.06$ GeV). It should be noted that the purely exponential fit to the experimental dependence over the entire interval under consideration, without including the Breit–Wigner function, yields the value of $\chi^2/\mathrm{NDF} = 21/10$, which is not satisfactory from the statistical point of view.

The basic results of our analysis of the experimental distributions in Fig. 2 are the following.

(i) The position and width of the peak observed in the mass spectrum of the $2p$ system in the present experiment are close to those found earlier in [15] ($M_{2p} = 2007 \pm 15$ MeV, $\Gamma_{2p} = 39 \pm 17$ MeV), as well as to those from other experiments (see [1]).

(ii) A comparative analysis of the mass spectra for the charge-exchange channel at the above two energy values enables us to conclude that the observable peak can be tentatively associated with the excitation of nonnucleonic degrees of freedom in the reaction under consideration (this conclusion is supported, in particular, by the proximity of the position of the observed peak to the summed mass of two free nucleons and the pion) and that it can be hardly interpreted within theoretical models taking into account only nucleonic interaction mechanisms (multiple-scattering model, pole model, etc.).

(iii) If the peak observed in the charge-exchange channel is caused by the excitation of dibaryons of isospin $I = 1$, then it comes as no surprise that similar structures are not observed in the direct channel,

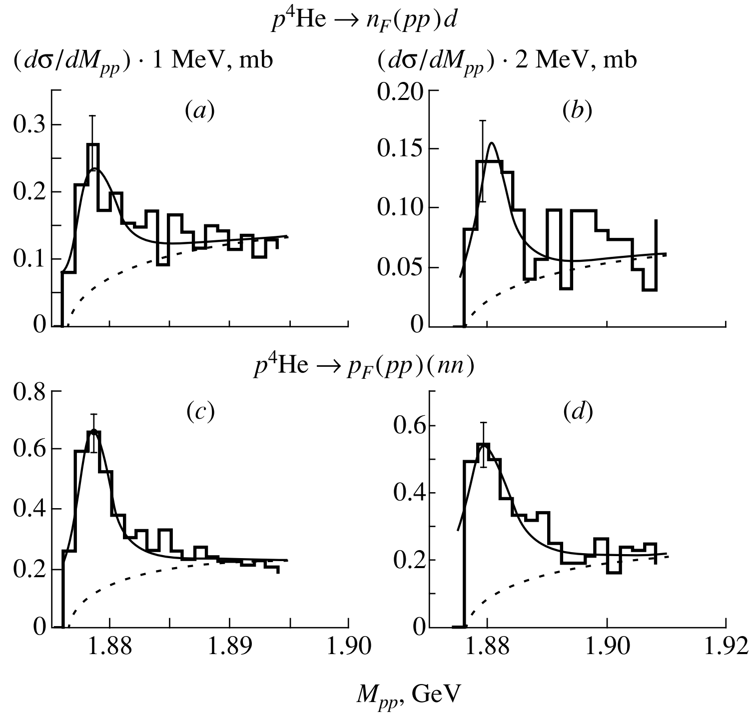

Fig. 4. Effective-mass distributions (near the point $2m_p$) of two protons that originate from the reaction $p^4\mathrm{He} \to n_F(pp)d$ at $T_p =$ (*a*) 220 and (*b*) 620 MeV and from the reaction $p^4\mathrm{He} \to p_F(pp)(nn)$ at $T_p =$ (*c*) 220 and (*d*) 620 MeV and which are slow in the $^4\mathrm{He}$ rest frame. The solid curves represent a fit to the experimental data in terms of the sum of the function $F^{(2)}$ describing the two-body phase space and the Breit–Wigner function. The dotted curves correspond to the pure contribution of the two-body phase space.

since the background conditions in the quasielastic-charge-exchange reaction are more favorable than those in the direct channel. In order to determine the mass and the width of the dibaryon proper in fitting the data, the Breit–Wigner function modified in such a way as to take into account the experimental resolution of the facility was used in the form (see, for example, [15])

$$\mathrm{BW}(M) = \frac{1}{(2\pi)^{1/2}} \tag{3}$$
$$\times \int \frac{\mathrm{BW}(m)}{\sigma(m)} \exp\left[-\frac{(M-m)^2}{2\sigma^2(m)}\right] dm,$$

where $\sigma(m)$ is the experimental error in determining M_{2p}.

As a result, we obtained the following results of the hypothesized dibaryon: the mass is $M_{2p} = 2008 \pm 13$ MeV and the width is $\Gamma_{2p} = 20 \pm 5$ MeV ($\chi^2/\mathrm{NDF} = 7.9/8$), which is in excellent agreement with the values of $M_{2p} = 2009 \pm 15$ MeV and $\Gamma_{2p} = 16 \pm 19$ MeV found in [15]. The cross section for dibaryon production amounts to about 0.45 ± 0.06 mb.

In order to observe similar structures in other channels of $^4\mathrm{He}p$ interaction, we have studied the mass spectra of two nucleons from reaction (2) where the total accumulated statistics is sufficient for analysis. Figure 3 shows the distributions in effective mass of two spectator protons from the reaction $p^4\mathrm{He} \to p_F(pp)(nn)$ at $T_p =$ (*a*) 220 and (*b*) 620 MeV (here, p_F is the fast proton in the $^4\mathrm{He}$ rest frame). There are no any pronounced features in these spectra. A small enhancement of data over the exponential background (dotted lines) at $M_{pp} \sim 2008$ MeV in Fig. 3*b* (indicated by an arrow) is not statistically significant.

In analyzing the mass spectra of the two-proton system from the reaction $p + n \to p + p + \pi^-$ (backward) at 1.98 GeV/c in the mass region close to $2m_p$, a narrow peak was previously observed at a mass value of 1877.5 ± 0.5 MeV, with the width being 2.0 ± 0.5 MeV [10]. For masses close to $2m_p$, Fig. 4 shows the effective-mass distributions of two protons that originate from the reaction $p^4\mathrm{He} \to n_F(pp)d$ at $T_p =$ (*a*) 220 and (*b*) 620 MeV and from the reaction $p^4\mathrm{He} \to p_F(pp)(nn)$ at $T_p =$ (*c*) 220 and (*d*) 620 MeV and which are slow, in each case, in the $^4\mathrm{He}$ rest frame. In the mass interval between 1877 and 1878 MeV, one can see narrow peaks of width 3 to 5 MeV. The solid curves in Fig. 4 represent a fit to the experimental data in terms of the sum of the function $F^{(2)}$ describing the two-body phase space and a function of the Breit–Wigner type. The function $F^{(2)}$ is taken in the form (see, for example, [16])

$$F^{(2)}(m_{2p}) \sim \text{const} \times (m_{2p} - 2m_p)^{1/2}(m_{\max} - m_{2p})^{\alpha}, \quad (4)$$

where $\alpha = 2$ and $m_{\max} = 2.0233$ (2.3304) GeV at $T_p = 220$ (620) MeV for reactions (1) and $\alpha = 7/2$ and $m_{\max} = 2.0211$ (2.3282) GeV at $T_p = 220$ (620) MeV for reaction (2). [The dotted curves correspond to the pure contribution of the two-particle phase space according to Eq. (4).] This fit is only one of the possible descriptions of this structure. In the above form, the best fit to the data in Fig. 4 is obtained at the following peak parameters: $M_{2p} = 1878.8 \pm 0.4$ MeV and $\Gamma_{2p} = 3.7 \pm 1.3$ MeV at $\chi^2/\text{NDF} = 13.2/16$ (see Fig. 4*c*).

As was mentioned above, the observed features in the *pp* mass spectrum near the threshold can be used to determine the spacetime dimension of the emission region in nuclear reactions. We are going to perform such an analysis in a dedicated publication.

In conclusion, we would like to formulate the basic results of the present study.

An analysis of the mass spectra of two spectator protons from the quasielastic-charge-exchange reaction $p^4\text{He} \to n_F(pp)d$ at $T_p = 620$ MeV has revealed a peak that may serve as an indication of the existence of a two-proton resonance of mass $M_{2p} = 2008 \pm 13$ MeV and width $\Gamma_{2p} = 20 \pm 5$ MeV. At the maximum, the enhancement over the background amounts to 3.1 standard deviations. The position and the width of the peak observed in the present experiment are close to those observed earlier in [15] and in some other experiments (see [1]).

In the mass spectra of the $2p$ system from the reactions $p^4\text{He} \to n_F(pp)d$ and $p^4\text{He} \to p_F(pp)(nn)$, we have observed narrow peaks near $M_{2p} = 1878$–1879 MeV. The parameters of these peaks can be used to deduce information about the dimension of the particle-emission region in $^4\text{He}p$ interactions.

ACKNOWLEDGMENTS

We are grateful to V.V. Kulikov, G.A. Leksin, V.V. Smolyankin, and A.V. Stavinskiĭ for correct critical comments and constructive proposals.

REFERENCES

1. B. Tatischeff *et al.*, Phys. Rev. C **59**, 1878 (1999).
2. N. Katayama *et al.*, Nucl. Phys. A **423**, 410 (1984).
3. A. V. Blinov *et al.*, Yad. Fiz. **41**, 1440 (1985) [Sov. J. Nucl. Phys. **41**, 913 (1985)]; Nucl. Phys. A **451**, 701 (1986).
4. S. K. Abdullin *et al.*, Yad. Fiz. **47**, 152 (1988) [Sov. J. Nucl. Phys. **47**, 99 (1988)].
5. A. V. Blinov *et al.*, Yad. Fiz. **47**, 933 (1988) [Sov. J. Nucl. Phys. **47**, 594 (1988)].
6. S. K. Abdullin *et al.*, Yad. Fiz. **48**, 917 (1988) [Sov. J. Nucl. Phys. **48**, 584 (1988)].
7. V. V. Glagolev *et al.*, Preprint No. E1-83-59, OIYaI (Joint Inst. for Nuclear Research, Dubna, 1983); Warsaw–Dubna–Košice–Moscow–Strasburg–Tbilisi Collab. (P. Zelinski *et al.*), Yad. Fiz. **40**, 482 (1984) [Sov. J. Nucl. Phys. **40**, 306 (1984)].
8. T. Siemiarczuk and P. Zielinski, Phys. Lett. B **24B**, 675 (1967).
9. S. A. Azimov *et al.*, Yad. Fiz. **19**, 317 (1974) [Sov. J. Nucl. Phys. **19**, 156 (1974)].
10. B. M. Abramov *et al.*, Yad. Fiz. **57**, 850 (1994) [Phys. At. Nucl. **57**, 797 (1994)].
11. S. E. Koonin, Phys. Lett. B **70B**, 43 (1977).
12. Yu. D. Bayukov *et al.*, Yad. Fiz. **34**, 95 (1981) [Sov. J. Nucl. Phys. **34**, 54 (1981)].
13. V. A. Budilov *et al.*, Phys. Lett. B **243**, 341 (1990).
14. S. K. Abdullin *et al.*, Yad. Fiz. **56** (4), 204 (1993) [Phys. At. Nucl. **56**, 536 (1993)]; Nucl. Phys. A **569**, 753 (1994).
15. Collab. Dubna–Košice–Moscow–Tbilisi (V. V. Glagolev *et al.*), Yad. Fiz. **51**, 736 (1990) [Sov. J. Nucl. Phys. **51**, 467 (1990)].
16. E. Byckling and K. Kajantie, *Particle Kinematics* (Wiley, New York, 1973; Mir, Moscow, 1975).

Translated by O. Chernavskaya

Physics of Atomic Nuclei, Vol. 65, No. 7, 2002, pp. 1313–1318. Translated from Yadernaya Fizika, Vol. 65, No. 7, 2002, pp. 1346–1351.
Original Russian Text Copyright © 2002 by Glushkov, Pravdin, Sleptsov, Sleptsova, Kalmykov.

ELEMENTARY PARTICLES AND FIELDS
Experiment

Zenith-Angle Dependences of $\rho_{s,600}$ and $\rho_{\mu,600}$ in Giant Air Showers

A. V. Glushkov*, M. I. Pravdin, I. E. Sleptsov, V. R. Sleptsova, and N. N. Kalmykov[1]

Institute of Cosmophysical Research and Aeronomy, Yakutsk Research Center, Siberian Division, Russian Academy of Sciences, Yakutsk, 677891 Russia.

Received March 16, 2001; in final form, July 18, 2001

Abstract—Results of a global analysis of data from the Yakutsk array and AGASA are presented. The zenith-angle dependences $\rho_{s,600}(\theta)$ and $\rho_{\mu,600}(\theta)$ of the densities of all charged particles and muons (the threshold energy is $E_\mu \approx 1.0 \cdot \sec\theta$ GeV) at a distance of 600 m from the axis of giant air showers (GAS) of energies $E_0 \geq 10^{19}$ eV are considered. These dependences are compared with the results of the calculations based on the QGSJET model and performed for the case of primary protons. The results of the calculations within this model agree well with data from both arrays at $E_0 \leq 2 \times 10^{18}$ eV, but they are in a glaring contradiction with GAS data. The experiments indicate that the lateral structure of showers changes at $E_0 \geq (3–5) \times 10^{18}$ eV. In all probability this is due to some new processes accompanying their evolution. The neglect of this fact can lead to considerably overestimating the GAS energy (by a factor of 1.5–2.5).

1. INTRODUCTION

Even first observations of extensive air showers (EAS) at the largest world arrays Volcano Ranch (USA) [1], Haverah Park (England) [2], SUGAR (Sydney University Giant Air Shower Recorder) [3], and Yakutsk [4] made it possible to discover giant air showers (GAS) of energies $E_0 > 10^{19}$ eV. After discovering relic radiation, it was shown that the flux of primary protons and nuclei must abruptly decrease at $E_0 > 3 \times 10^{19}$ eV [5, 6] because of their interaction with this radiation. However, the observations of GASs with estimated energies of up to about $(1–3) \times 10^{20}$ eV at various arrays [7–10] contradict this prediction made by Greisen, Zatsepin, and Kuz'min.

In order to investigate the problem of the endpoint of the GAS energy spectrum, arrays are constructed that are larger than those mentioned above. The AGASA (Akeno Giant Air Shower Array) facility of area about 100 km^2 [11] continues operating now and has detected six new GASs with $E_0 > 10^{20}$ eV [12]. Giant arrays having areas of about 1000–5000 km^2 and a spacing between individual detectors of 1–1.5 km [13–15] are being designed and built.

There is no doubt that giant arrays will greatly increase GAS statistics. In our opinion, however, the answer to the question of the endpoint energy of cosmic rays should be sought, first of all, by investigating the structure of GASs in greater detail. Experimental data obtained at the Yakutsk array [16–22] showed that the pattern of shower development in the region $E_0 > (3–5) \times 10^{18}$ eV differs from that at lower energies.

In this study, we display new data on GASs detected at the Yakutsk array over the period from 1974 to 1999. These data are compared with the results of our calculations based on the QGSJET model [23], which reproduces well a vast set of EAS experimental data for $E_0 \leq (2–3) \times 10^{18}$ eV [16–22, 24]. The investigation performed in [25] revealed that, in a sense, this model is the best one in the energy region around 10^6 GeV, because, in analyzing different experimental features of EASs, it leads to the same estimates of the mass composition of cosmic rays in the knee region of the primary energy spectrum. Our results were supplemented with the AGASA experimental data from [26, 27], and this enabled us to get a clearer and a more comprehensive idea of new details in GAS evolution.

2. FEATURES UNDER INVESTIGATION

Below, we consider primarily the zenith-angle dependences $\rho_{\mu,600}(\theta)$ and $\rho_{s,600}(\theta)$ of the densities of muons (the threshold energy is $E_\mu \approx 1.0 \cdot \sec\theta$ GeV) and of all charged particles (electrons and muons, which can be measured by sea-level scintillation detectors) at the distance of $R = 600$ m from the shower core. The parameter $\rho_{s,600}(\theta)$ is of crucial importance because it provides some kind of a measure of the

---

[1] Institute of Nuclear Physics, Moscow State University, Vorob'evy gory, Moscow, 119899 Russia

*e-mail: `a.v.glushkov@ikfia.ysn.ru`

primary-particle energy. At the Yakutsk array (the atmosphere depth is $X_{\rm Y} = 1020$ g/cm^2), E_0 is determined from the relations

$$E_0 = (4.8 \pm 1.6) \times 10^{17}(\rho_{s,600}(0^\circ))^{1.0\pm0.02} \text{ [eV]}, \tag{1}$$

$$\rho_{s,600}(0^\circ) = \rho_{s,600}(\theta)\exp((\sec\theta - 1)X_{\rm Y}/\lambda_\rho) \text{ [m}^{-2}\text{]}, \tag{2}$$

$$\lambda_\rho = (450 \pm 44) + (32 \pm 15)\log(\rho_{s,600}(0^\circ)) \text{ [g/cm}^2\text{]}, \tag{3}$$

which were obtained by the calorimetric method [28, 29]. At the AGASA (the atmosphere depth is $X_{\rm A} = 920$ g/cm^2), this is done on the basis of the relations [26]

$$E_0 = 2.0 \times 10^{17}(\rho_{s,600}(0^\circ))^{1.0} \text{ [eV]}, \tag{4}$$

$$\rho_{s,600}(0^\circ) = \rho_{s,600}(\theta)\exp((\sec\theta - 1)X_{\rm A}/500 + (\sec\theta - 1)^2 X_{\rm A}/594) \text{ [m}^{-2}\text{]}, \tag{5}$$

which were found as an average from various models of EAS evolution.

The experimental data in question are compared with the results of calculations performed within the QGSJET model for the case of primary protons. In these calculations, we set the atmosphere depths to $X_{\rm Y}$ and $X_{\rm A}$ and took into account the actual features of the experiments at the two arrays. The lateral distributions of all charged particles were found as the sum of the densities of $E_e \geq 1.0$ MeV electrons and $E_\mu \geq 0.01$ GeV muons; that is, $\rho_{\rm ch} = \rho_e(\geq 1.0 \text{ MeV}) + \rho_\mu(\geq 0.01 \text{ GeV})$.

3. RESULTS AND DISCUSSION

The analysis of data from the Yakutsk array involves information about showers arriving at zenith angles of $\theta \leq 60^\circ$. The parameters $\rho_{s,600}(\theta)$ and $\rho_{\mu,600}(\theta)$ were found from the average lateral distributions that were constructed as in [21] by dividing the entire set of showers into groups with a step $\Delta\cos\theta = 0.1$, $\Delta\log E_0 = 0.2$ and by averaging the showers within each group individually.

The QGSJET model considered here yields the following dependences for estimating E_0 (in eV) from the parameters $\rho_{\rm ch,600}(0^\circ)$ and $\rho_{\mu,600}(0^\circ)$ in vertical showers:

$$E_0 = 3.48 \times 10^{17}(\rho_{\rm ch,600}(0^\circ))^{1.0\pm0.01}, \tag{6}$$

$$E_0 = 2.4 \times 10^{18}(\rho_{\mu,600}(0^\circ))^{1.08\pm0.01} \tag{7}$$

for the Yakutsk array and

$$E_0 = 2.04 \times 10^{17}(\rho_{\rm ch,600}(0^\circ))^{1.04\pm0.01}, \tag{8}$$

$$E_0 = 2.5 \times 10^{18}(\rho_{\mu,600}(0^\circ))^{1.14\pm0.02} \tag{9}$$

for the AGASA.

It can be seen that, in relation to (6), formula (1) leads to E_0 values overestimated by a factor of about 1.4 and that (4) and (8) are in fairly good agreement with each other. Because the distinction between (1) and (6) requires a dedicated investigation, we have used here relation (6) to calculate E_0 in this study. This approach does not remove the problem of correctly estimating GAS energies as such, but it enables us to consider the experimental data from the two arrays on the basis of a unified model of EAS evolution.

Figure 1 shows the experimental lateral distributions of all charged particles and muons in $E_0 = 2 \times 10^{18}$ eV, $\cos\theta \geq 0.95$ EASs according to the (closed circles) Yakutsk and (open circles) AGASA data. The curves represent the calculated lateral distributions in these showers for the atmosphere depths (solid curves) $X_{\rm Y}$ and (dashed curves) $X_{\rm A}$. It can be seen that the results of the calculations are compatible with the measured lateral distributions for both EAS components.

Figure 2 displays the zenith-angle dependences $\rho_{s,600}(\theta)$ and $\rho_{\mu,600}(\theta)$ for $E_0 = 2 \times 10^{18}$ eV EASs. Here, we present the experimental data (solid circles) and the calculated solid curves referring to the Yakutsk array for (*1*) all charged particles, (*2*) muons, and (*3*) electrons. The experimental values of ρ_e were found as the difference $\rho_e = \rho_s - k(\theta)\rho_\mu(E_\mu \geq 1.0 \cdot \sec\theta \text{ GeV})$. The factor $k(\theta) = 1.25{-}1.4$ was taken from the QGSJET calculations for the passage to the muon density with the threshold energy of $E_\mu \geq 0.01$ GeV. Figure 2 also gives the AGASA experimental data (open circles) for $\rho_{s,600}(\theta)$ that were found in [26] by the equal-intensity-cut method and for $\rho_{\mu,600}(\theta)$ with the threshold energy of $E_\mu \approx 1.0 \cdot \sec\theta$ GeV [30].

Here, there is also satisfactory agreement between the theory and the experiment for all three EAS components. Furthermore, it can be seen that the density $\rho_{\mu,600}(\theta)$ is independent of the atmosphere depth for $\theta \leq 50^\circ$ and is a convenient parameter for estimating E_0 at arrays occurring at different altitudes above sea level.

There is no such agreement for GASs. The Yakutsk data show that the measured densities $\rho_{s,600}(\theta)$ at $E_0 = 10^{19}$ eV are higher than the calculated values by a factor of about 1.25 (Fig. 3*a*). The densities $\rho_{\mu,600}(\theta)$ (dash-dotted curve), which coincide with $\rho_{s,600}(\theta)$ in inclined events ($\theta \geq 52^\circ$), undergo more pronounced changes. In the AGASA data, there is, on the contrary, an indication that the experimental

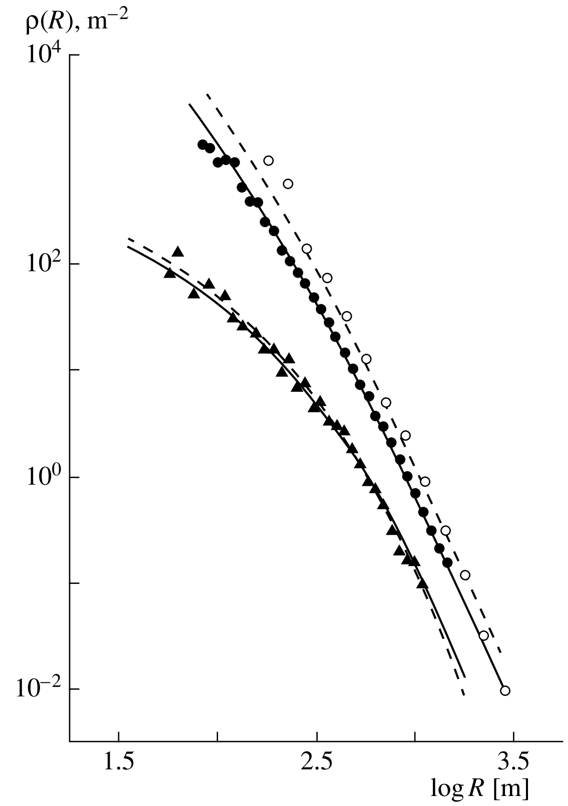

Fig. 1. Average lateral distributions of (●, ○) all charged particles and (▲) muons with a threshold energy of $E_\mu \approx 1.0 \cdot \sec\theta$ GeV in $E_0 = 2 \times 10^{18}$ eV, $\langle\cos\theta\rangle = 0.98$ showers: (●, ▲) Yakutsk data and (○) AGASA data [30]. The solid and dashed curves were calculated on the basis of the QGSJET model for the case of primary protons for, respectively, the Yakutsk array and the AGASA.

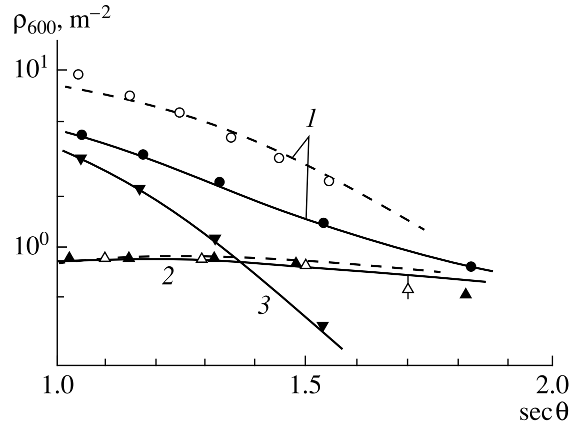

Fig. 2. Density ρ_{600} of (*1*) all charged particles, (*2*) muons, and (*3*) electrons as a function of $\sec\theta$ at $E_0 = 2 \times 10^{18}$ eV according to (●, ▲, ▼) Yakutsk data and AGASA data from (○) [26] and (△) [30]. The solid and dashed curves were calculated according to the QGSJET model for the case of primary protons for the Yakutsk array and the AGASA, respectively.

densities $\rho_{s,600}(\theta)$ are underestimated by a factor of about 1.25 in the zenith-angle range 35°–50°.

The above anomaly in GAS evolution grows fast with increasing energy of primary cosmic rays. This can be clearly seen in Fig. 3*b* for $E_0 = 3 \times 10^{19}$ eV showers. All experimental data totally contradict the predictions of the QGSJET model. This contradiction is not associated with relatively low statistics of events.

In analyzing the data in Fig. 3*b*, there arises the following picture. The trend in the Yakutsk data toward a variation in $\rho_{\mu,600}(\theta)$ (dash-dotted curve *2*) becomes more pronounced, leading to a nearly threefold increase in relation to the results of the calculations at $\theta \geq 35°$. The experimental densities $\rho_{s,600}(\theta)$ in GASs whose axes deviate only slightly from the vertical direction are higher than the calculated ones by a factor of about 1.4 and agree with $\rho_{\mu,600}(\theta)$ for $\theta \geq 45°$. The values of $\rho_{s,600}(\theta)$ that were measured at the AGASA for $\theta \leq 30°$ exceed the results of the calculations by a factor of about 1.4 as well. In more inclined showers, the analogous experimental values decrease fast, lying below the calculated values by a factor of about 1.4 for $\theta \geq 37°$; for $\theta \geq 45°$, they become commensurate with the Yakutsk data.

From this analysis, it follows that, for $\theta \geq 45°$, only $E_\mu \geq 1.5$ GeV muons are detected in these showers at the above distance from the core. Here, there are no softer muons and, the more so, electrons, as was observed in the analogous inclined EASs whose primary energies lie in the region $E_0 \leq 2 \times 10^{18}$ eV (Fig. 2). Not only do the electron-flux densities $\rho_{e,600}(\theta)$ decrease anomalously fast with increasing zenith angle (dash-dotted curves *3* in Fig. 3*b*), but they also exceed the calculated values (solid curve *3*) in the nearly vertical GASs ($\theta \leq 20°$) by a factor of about 1.4.

The above trend is likely to become more pronounced as the GAS energy approaches the limiting value. The disregard of this circumstance and the formal use of relations (1)–(9) may lead to large errors in estimating E_0.

The asterisk in Fig. 3*b* shows the density $\rho_{s,600}(58.7°) \approx \rho_{\mu,600}(58.7°) = 54\ \mathrm{m}^{-2}$ of the largest shower detected at the Yakutsk array [8]. The arrow indicates the rescaling of this density to the vertical direction with the absorption range equal to $\lambda_\rho = 530\ \mathrm{g/cm}^2$ according to (3). According to (1), the energy of this shower is estimated at $E_0 = 1.55 \times 10^{20}$ eV.

In fact, the energy of this GAS is much lower. If we consider that the measured value of $\rho_{s,600}(\theta)$ for $\sec\theta \approx 1.9$ in Fig. 3*b* is greater than the calculated value by a factor of about 2.5 (the corrected density is

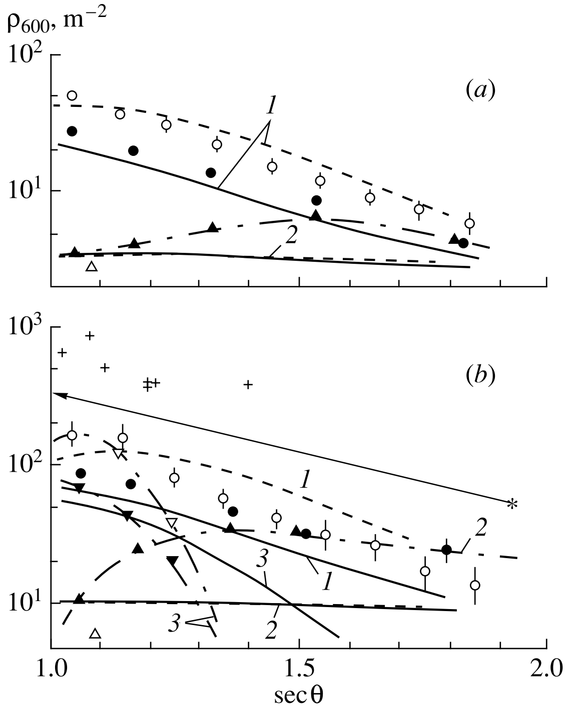

Fig. 3. Density ρ_{600} of (*1*) all charged particles, (*2*) muons, and (*3*) electrons as a function of $\sec\theta$ at (*a*) $E_0 = 10^{19}$ and (*b*) 3×10^{19} eV. In Fig. 3*b*, the closed and open inverted triangles represent the experimental values of $\rho_{e,600} = \rho_{s,600} - k(\theta)\rho_{\mu,600}$, while the asterisk and crosses show $\rho_{s,600}(\theta)$ in $E_0 \geq 10^{20}$ eV showers according to the data of the Yakutsk array and the AGASA [27, 30], respectively. The dash-dotted curves connecting experimental dots were drawn in order to illustrate more clearly their anomalous behavior. The rest of the notation is analogous to that in Fig. 2.

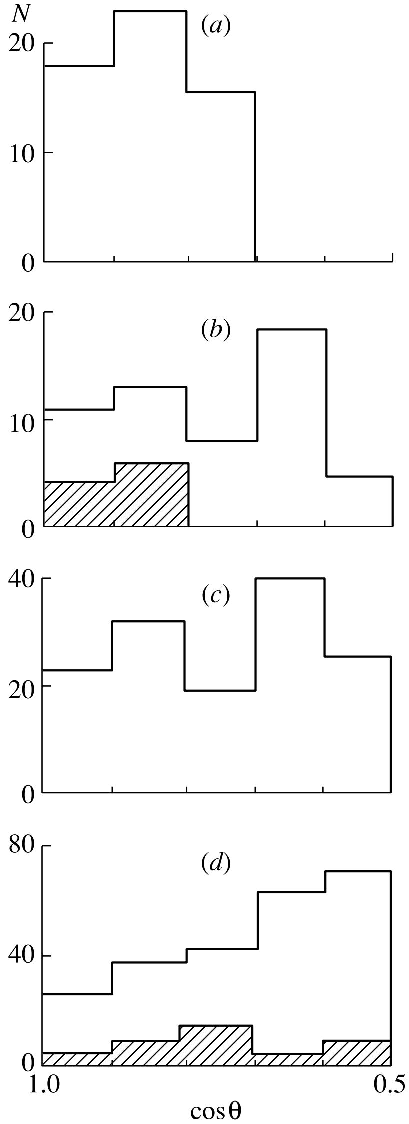

Fig. 4. Zenith-angle distributions of GASs according to (*a*) AGASA [27], (*b*) Volcano Ranch [7], (*c*) Haverah Park [7], and (*d*) SUGAR [31] data. The shaded regions correspond to showers whose axes fall within the array.

$54/2.5 = 21.6$ m^{-2}) and if we rescale this value to the vertical direction according to the theoretical curve *1* ($\rho_{s,600}(0°) = 172$ m^{-2}) and additionally use relation (6), the result will be $E_0 \approx 6 \times 10^{19}$ eV. From the value of $\rho_{\mu,600}(58.7°)$ (the refined value is $54/2.3 = 23.5$ m^{-2}) and relation (7), it follows that $E_0 \approx 5.6 \times 10^{19}$ eV.

The crosses in Fig. 3*b* show the values of $\rho_{s,600}(\theta)$ for seven $E_0 \geq 10^{20}$ eV GASs according to the AGASA data from [27]. It is intriguing that these events are observed for $\sec\theta \leq 1.22$ ($\theta \leq 35°$), where $\rho_{s,600}(\theta)$ has a relative peak (open circles). A nonrandom nature of this distribution is corroborated by the histogram of 48 $E_0 \geq 4 \times 10^{19}$ eV, $\theta \leq 45°$ GASs in Fig. 4*a* from the AGASA data [27]. Events (N) were taken in the intervals $\Delta\cos\theta = 0.1$ and were divided by $\cos\theta$. This representation provides their identical significance within each interval $\Delta\cos\theta$.

We note that $E_0 \geq 10^{19}$ eV GASs at other arrays have similar zenith-angle distributions. Volcano Ranch data from [7] (44 events) are shown in Fig. 4*b*. This array is deployed at an altitude of 834 g/cm^2. The majority of the showers have fallen at its boundary. If only those of them are taken into consideration whose axes are within this array, there remain nine events with $\theta \leq 36°$ (shaded histogram).

Figure 4*c* shows the distribution of 144 Haverah Park GASs [7], which resembles the preceding distribution. The Haverah Park array is located at sea level and employs detectors of a different type (Cherenkov water tanks) that recorded a relatively large contribution of muons in the total detector response. The detectors themselves are much more widely spaced.

It is noteworthy that, for $\theta \leq 45°$, all three arrays yield similar distributions, although event statistics are insufficient everywhere. It can be conjectured that this form of the distributions has a common origin in the anomalous GAS evolution considered above (Fig. 3).

Figure 4*d* displays data from the SUGAR array [31], which detected showers by muons with threshold energy $E_\mu \approx 0.75 \cdot \sec\theta$ GeV. The shaded histogram corresponds to 35 $E_0 \geq 5 \times 10^{19}$ eV events, while the open histogram includes events whose energies fall within the range $1.5 \times 10^{19} \leq E_0 < 5 \times 10^{19}$ eV. Here, we can clearly see the growth of the number of showers with increasing zenith angle. This agrees with our conclusion that the relative contribution of muons to the structural modifications of inclined showers increases.

4. CONCLUSION

From the above and from the results presented in [16–21], there emerges the following picture. In the energy region $E_0 \leq 2 \times 10^{18}$ eV, the experimental data from the Yakutsk array and from the AGASA are compatible with the results calculated on the basis of the QGSJET model for the case of primary protons. For $E_0 \geq (3–5) \times 10^{18}$ eV, EASs evolve in a different way. With increasing energy, their lateral structure changes significantly, and the fraction of muons increases markedly in the inclined events ($\theta > 35°–40°$), as can be seen from Fig. 3. Here, the muon component changes more pronouncedly, which cannot be explained in terms of the QGSJET model; therefore, different concepts of GAS evolution are required.

It can be assumed that this anomaly has a threshold character in energy and that it is caused by new processes of nuclear interactions; this threshold may be at about $(2–3) \times 10^{18}$ eV. Above this energy, cosmic-ray interactions produce exotic secondaries (one or a few of them), which determine entirely a further evolution of GASs.

The above GAS anomalies can be associated not only with changes in the character of nuclear interaction nature but also with a radical change in the composition of primary particles. An analysis of Yakutsk data from [32–35] showed that the directions of the arrival of $E_0 \geq (8–10) \times 10^{18}$ eV EASs have a statistically significant ($\sim 4\sigma$) positive correlation with the Supergalaxy plane. There is no such correlation with the Galaxy plane. In all probability, this supports the hypothesis that cosmic rays of such energies are predominantly of an extragalactic origin and gives grounds to believe that primary particles must be electrically neutral in this case.

It is improbable that these are neutrons. At $E_0 \sim 10^{19}$ eV, their Lorentz factor is about 10^{10}, so that they can travel a distance of about 100 kpc prior to undergoing decay, but this is much smaller than the Supergalaxy size (about 50 Mpc). It is more likely that these are some other stable neutral particles.

We cannot rule out the possibility that these are neutrinos. The calculations performed in [36] show that, under certain conditions of growth of the cross section for neutrino–nucleon interaction ($\sigma_{\nu N}$), the formation of the EASs that are similar to GASs is possible in the region of extremely high energies.

In our opinion, however, the existence of cosmic rays of energy $E_0 \approx 10^{20}$ eV has yet to be proven conclusively. An increase in the number of such events owing to longer exposures of the operating arrays or owing to building arrays of giant areas (about 1000–5000 km^2) and arrays with a detector spacing of 1–1.5 km [13–15] can be irrelevant to solving the problem of GAS endpoint energies. No extrapolations of either experimental dependences or calculated data [available for $E_0 \leq (2–3) \times 10^{18}$ eV] into this region are legitimated. They can lead to large errors in estimating the primary-particle energy. Here, it is necessary to investigate individually the lateral distributions of charged particles and muons at arrays with a detector spacing not larger than 200–300 m.

ACKNOWLEDGMENTS

This study was supported by the Ministry for Science of the Russian Federation within the program of support of the Yakutsk EAS array (no. 01-30) included in "The Inventory of Unique Research and Experimental Facilities of National Significance" and by the Russian Foundation for Basic Research (project no. 00-15-96787 for the support of Leading Scientific Schools).

REFERENCES

1. J. Linsley, Phys. Rev. Lett. **10**, 146 (1963).
2. D. M. Edge, A. C. Evans, H. J. Garmston, *et al.*, J. Phys. A **6**, 1612 (1973).
3. C. J. Bell *et al.*, J. Phys. A **7**, 990 (1974).
4. D. D. Krasilnikov *et al.*, J. Phys. A **7**, 176 (1974).
5. K. Greisen, Phys. Rev. Lett. **16**, 748 (1966).
6. G. T. Zatsepin and V. A. Kuz'min, Pis'ma Zh. Éksp. Teor. Fiz. **4**, 114 (1966) [JETP Lett. **4**, 78 (1966)].
7. *Catalog of Highest Energy Cosmic Rays: Giant Extensive Air Showers* (World Data Center C2 for Cosmic Rays, Japan, 1980), No. 1.
8. N. N. Efimov, T. A. Egorov, A. V. Glushkov, *et al.*, in *Proceedings of International Workshop on Astrophysical Aspects of the Most Energetic Cosmic Rays, Kofu, 1990,* p. 20.

9. N. Hayashida, K. Honda, M. Honda, *et al.*, ICRR Report 324-94-19 (Tokyo, 1994).
10. D. J. Bird, S. C. Corbato, H. Y. Dai, *et al.*, Astrophys. J. **424**, 491 (1994).
11. N. Chiba, K. Hashimoto, N. Hayashida, *et al.*, Nucl. Instrum. Methods Phys. Res. A **311**, 338 (1992).
12. M. Takeda, N. Hayashida, K. Honda, *et al.*, Phys. Rev. Lett. **81**, 1163 (1998).
13. G. B. Khristiansen, Yu. A. Fomin, B. A. Khrenov, *et al.*, Nucl. Phys. B (Proc. Suppl.) **28**, 40 (1992).
14. J. C. Cronin *et al.*, Preprint EHI 92-08 (University of Chicago, Chicago, 1992).
15. M. Teshima, M. Bessho, H. Y. Dai, *et al.*, in *Proceedings of RIKEN: International Workshop on Electromagnetic and Nuclear Cascade Phenomena at High and Extremely High Energies, 1993,* p. 135.
16. A. V. Glushkov, I. T. Makarov, E. S. Nikiforova, *et al.*, Astropart. Phys. **4**, 1274 (1995).
17. A. V. Glushkov, M. I. Pravdin, and I. Ye. Sleptsov, in *Proceedings of the 25th International Conference on Cosmic Rays, Durban, 1997,* Vol. 6, p. 233.
18. A. V. Glushkov, M. I. Pravdin, and I. E. Sleptsov, Pis'ma Zh. Éksp. Teor. Fiz. **67**, 361 (1998) [JETP Lett. **67**, 383 (1998)].
19. A. V. Glushkov, I. T. Makarov, M. I. Pravdin, and I. E. Sleptsov, Izv. Akad. Nauk, Ser. Fiz. **63**, 538 (1999).
20. A. V. Glushkov, I. T. Makarov, M. I. Pravdin, *et al.*, Pis'ma Zh. Éksp. Teor. Fiz. **71**, 145 (2000) [JETP Lett. **71**, 97 (2000)].
21. A. V. Glushkov, M. I. Pravdin, I. E. Sleptsov, *et al.*, Yad. Fiz. **63**, 1557 (2000) [Phys. At. Nucl. **63**, 1477 (2000)].
22. A. V. Glushkov and M. I. Pravdin, Pis'ma Zh. Éksp. Teor. Fiz. **73**, 131 (2001) [JETP Lett. **73**, 115 (2001)].
23. N. N. Kalmykov, G. B. Khristiansen, S. S. Ostapenko, and A. I. Pavlov, in *Proceedings of the 24th International Conference on Cosmic Rays, Roma, 1995,* Vol. 1, p. 123.
24. N. N. Kalmykov *et al.*, Nucl. Phys. B (Proc. Suppl.) **52**, 17 (1997).
25. A. D. Erlykin and A. W. Wolfendale, in *Proceedings 16th ECRS, Alcalá de Henares, 1998,* p. 269.
26. M. Nagano, D. Heck, S. Shinozaki, *et al.*, Preprint No. 6191, FZKA (Karlsruhe, 1998).
27. M. Takeda, N. Hayashida, K. Honda, *et al.*, astro-ph/9902239.
28. A. V. Glushkov, M. N. D'yakonov, T. A. Egorov, *et al.*, Izv. Akad. Nauk, Ser. Fiz. **55**, 713 (1991).
29. N. N. Efimov, N. N. Efremov, A. V. Glushkov, *et al.*, in *Proceedings of the 22nd International Conference on Cosmic Rays, Dublin, 1991,* Vol. 4, p. 335.
30. S. Yoshida, N. Hayashida, K. Honda, *et al.*, J. Phys. G **20**, 651 (1994).
31. *Catalog of Highest Energy Cosmic Rays: Giant Extensive Air Showers* (World Data Center C2 for Cosmic Rays, Japan, 1986), No. 2.
32. A. V. Glushkov and I. E. Sleptsov, Izv. Akad. Nauk, Ser. Fiz. **65**, 437 (2001).
33. A. V. Glushkov and M. I. Pravdin, Zh. Éksp. Teor. Fiz. **119**, 1029 (2001) [JETP **92**, 887 (2001)].
34. A. V. Glushkov and M. I. Pravdin, Pis'ma Astron. Zh. **27**, 577 (2001) [Astron. Lett. **27**, 493 (2001)].
35. A. V. Glushkov, Pis'ma Zh. Éksp. Teor. Fiz. **73**, 355 (2001) [JETP Lett. **73**, 313 (2001)].
36. L. Anchordoqui, H. Golgberg, T. McCauley, *et al.*, hep-ph/0011097.

Translated by V. Bukhanov

Physics of Atomic Nuclei, Vol. 65, No. 7, 2002, pp. 1319–1340. From Yadernaya Fizika, Vol. 65, No. 7, 2002, pp. 1352–1373.

ELEMENTARY PARTICLES AND FIELDS
Theory

Running Electromagnetic-Coupling Constant: Low-Energy Normalization and the Value at M_Z*

A. A. Pivovarov

Institut für Physik, Johannes-Gutenberg-Universität, Standingerweg 7, D-55099 Mainz, Germany,
and Institute for Nuclear Research, Russian Academy of Sciences,
pr. Shestidesyatiletiya Oktyabrya 7a, Moscow, 117312 Russia

Received January 12, 2001; in final form, April 5, 2001

Abstract—A numerical value for the running electromagnetic-coupling constant in the $\overline{MS}$ scheme is calculated at a low-energy normalization scale equal to the τ-lepton mass M_τ. This low-energy boundary value is used for running the electromagnetic coupling to larger scales, where high-precision experimental measurements can be performed. Particular scales of interest are the b-quark mass for studying Υ-resonance physics and the Z-boson mass M_Z for high-precision tests of the Standard Model and for the determination of the Higgs boson mass from radiative corrections. A numerical value of the running electromagnetic-coupling constant at M_Z in the on-shell renormalization scheme is also given.

1. INTRODUCTION

A dimensional regularization of divergent integrals related to Feynman diagrams of perturbation theory (PT) and renormalization by a minimal subtraction of singularities are convenient technical tools for calculations in particle phenomenology [1, 2]. In the leading order of PT, dimensional regularization does not give any decisive computational advantage. However, high-order many-loop PT calculations are rather involved, and, in practice, only the use of a dimensional regularization supplemented with recurrence relations based on the integration-by-part technique [3] allowed one to obtain analytically new theoretical predictions for a number of processes (see, e.g., [4]). Minimal subtraction, being a simple method for renormalizing dimensionally regularized PT diagrams, also provides a natural way to parametrize theoretical calculations in terms of couplings and masses defined in the $\overline{MS}$ scheme [5]. The renormalization in the $\overline{MS}$ scheme is mass-independent, which allows an efficient computation of renormalization-group (RG) functions describing the evolution of $\overline{MS}$ parameters. However, the mass independence of the renormalization procedure is physically inconvenient because the decoupling of heavy particles is not automatic [6]. The physical property of decoupling is restored within an effective-theory approach with an explicit separation of different mass scales such that the parameters of neighboring effective theories (couplings, masses, etc.) should be sewed (matched) near the point where a new scale appears. This machinery, developed up to the three-loop order in PT, allows one to compare theoretical results in the $\overline{MS}$ scheme for a variety of scales with a uniform control over the precision of PT calculations. In particular, this technique allows one to compare theoretical quantities extracted from low-energy data with results of Z-boson-peak analyses within the Standard Model (SM) of particle interactions. The high-precision tests of the SM at the Z-boson peak showed good agreement with theoretical results obtained from low-energy data. For new-physics searches and further tests of the SM at the next level of precision, computations for many observables at the Z-boson peak should be performed with a two-loop accuracy, which presently is an actual calculational task. Because of the computational advantage of dimensional regularization for various many-loop calculations, high-order PT results for theoretical amplitudes at the Z-boson peak tend to be obtained in terms of the $\overline{MS}$-scheme parameters, which are natural quantities emerging from the minimally subtracted dimensionally regularized diagrams. It was found that the use of the running electromagnetic (EM) coupling normalized at M_Z in the $\overline{MS}$ scheme makes PT expansions near the Z-boson peak reliable and corrections small. However, the running EM coupling in the $\overline{MS}$ scheme has no immediate physical meaning, and its numerical value is not well known. At the same time, QED, being an old part of the SM, is well tested at low energies, where the fine-structure constant α is a natural

---

*This article was submitted by the author in English.

interaction parameter defined in a physical manner by subtraction on the photon mass shell. The numerical value of the fine-structure constant is accurate, which would make it a natural reference parameter for high-precision tests of the SM. However, because of a huge numerical difference between the values of the photon and Z-boson masses, the use of the fine-structure constant as an expansion parameter for PT calculations at the Z-boson peak generates large corrections in higher orders. For applications to high-precision tests of the SM with observables near the Z-boson peak [7], one should transform α into a proper high-energy parameter, i.e., into the electromagnetic-coupling constant at a scale of the Z-boson mass M_Z (see, e.g., [8, 9]). Then, large PT corrections are hidden (renormalized) in a numerical value of this new parameter, which is more suitable for describing the Z-boson-peak observables in the PT framework than α. Therefore, a numerical value of the running EM coupling constant at M_Z is a new important number that was chosen for a standard reference parameter [10]. The difference of the numerical value of this parameter and $\alpha^{-1} = 137.036\ldots$ should be theoretically calculated by using the RG technique [11–13]. Because the fine-structure constant is defined at a vanishing momentum, it is an infrared-sensitive quantity and the contribution of strong interactions to its RG evolution cannot be computed perturbatively: the infrared region is a strong-coupling domain that requires a nonperturbative (non-PT) treatment. The contribution of the infrared (IR) region is usually taken into account within a semiphenomenological approximation through a dispersion relation with direct integration of low-energy data. There has been a renewal of interest in a precise determination of the hadronic contribution to the electromagnetic-coupling constant at M_Z over the last years in connection with the constraints on the Higgs boson mass from radiative corrections in the SM [14]. Some recent references giving a state-of-the-art analysis of this contribution are [15–18]. A quasianalytic approach was used in [19], where some references to earlier articles can be found (see also [20, 21]). A thorough data-based analysis is given in [22]. However, a virtual lack of data for energies higher than 15–20 GeV makes it unavoidable to use theoretical formulas in the dispersion relation at high energies. Fortunately, theoretical results necessary for electromagnetic-current correlation functions (the photon vacuum polarization function) are known in high orders of PT and are reliable at high energies because of the property of asymptotic freedom in QCD. Therefore, the real value of dispersion relations is to find a boundary condition for the running EM coupling at a low-energy normalization scale, where data are accurate. If this low-energy normalization scale is sufficiently large for strong interaction PT to be applicable, then the RG can be used to run the initial value to any larger scale with a very high precision. The running of the electromagnetic-coupling constant can be defined in different ways depending on the renormalization procedure chosen. The evolution can be described in both the on-shell and the $\overline{MS}$ schemes: the corresponding β functions are available with a high precision within PT. The recent calculation of the numerical value for the running EM coupling at M_Z with evolution in the $\overline{MS}$ scheme is presented in [23].

In the present study, I calculate a low-energy boundary value for the running EM coupling in the $\overline{MS}$ scheme using almost no experimental data but masses of ground states in the ρ- and φ-meson channels. A necessary IR modification of the light-quark spectrum is determined by consistency with operator-product expansion (OPE). Theoretical parameters of the calculation are the strong-coupling constant $\alpha_s(M_\tau)$, the strange-quark mass $m_s(M_\tau)$, and the gluon and quark vacuum condensates. Numerical values for these parameters accumulate a lot of information about the low-energy data contained in the rate $R(s)$ of e^+e^- annihilation into hadrons. Therefore, the present calculation compresses low-energy data into numerical values of several key theoretical parameters; this allows one to perform an analysis of the IR domain necessary for determining a low-scale boundary value for running the EM coupling. The evolution to larger scales is straightforward and very precise within perturbation theory.

2. BASIC RELATIONS

The relation between the running EM coupling constant $\bar{\alpha}(\mu)$ in the $\overline{MS}$ scheme (μ is the usual normalization point) and the fine-structure constant α are well known and can be obtained by considering the photon vacuum polarization function. The correlation function for the EM currents j_μ^{EM},

$$12\pi^2 i \int \langle T j_\mu^{\mathrm{EM}}(x) j_\nu^{\mathrm{EM}}(0)\rangle e^{iqx} dx = (q_\mu q_\nu - g_{\mu\nu} q^2)\Pi_\#(q^2), \quad (1)$$

is defined with a generic scalar function $\Pi_\#(q^2)$. The particular scalar functions $\Pi(\mu^2, q^2)$ and $\Pi_{\mathrm{os}}(q^2)$ (subscript “os” means “on-shell”) are defined through the correlation function for electromagnetic currents in (1) [and the generic function $\Pi_\#(q^2)$] but with different subtraction procedures to remove ultraviolet divergences. The first function $\Pi(\mu^2, q^2)$ is renormalized in the $\overline{MS}$ scheme, and the second function

$\Pi_{\rm os}(q^2)$ is renormalized by subtraction on the photon mass shell $q^2=0$, which implies a normalization condition $\Pi_{\rm os}(0)=0$. Note that, for the actual calculation of $\Pi_{\rm os}(q^2)$, one can use a dimensional regularization and the $\overline{MS}$ scheme in cases where $\Pi(\mu^2,0)$ has no IR singularities in PT (for instance, for massive quarks):

$$\Pi_{\rm os}(q^2)=\Pi(\mu^2,q^2)-\Pi(\mu^2,0).$$

The relation between the couplings and polarization functions in the different schemes reads

$$\frac{3\pi}{\bar\alpha(\mu^2)}+\Pi(\mu^2,q^2)=\frac{3\pi}{\alpha}+\Pi_{\rm os}(q^2). \qquad (2)$$

In the limit $q^2\to 0$, one finds

$$\frac{3\pi}{\bar\alpha(\mu^2)}+\Pi(\mu^2,0)=\frac{3\pi}{\alpha}. \qquad (3)$$

Equation (2) is related to the Coulomb law for charged particles. For the potential of the EM interaction of two charged leptons, one finds in the $\overline{MS}$ scheme that

$$V(\mathbf{q}^2)=-\frac{4\pi\bar\alpha(\mu^2)}{\mathbf{q}^2}\left[1+\frac{\bar\alpha(\mu^2)}{3\pi}\Pi(\mu^2,\mathbf{q}^2)\right]^{-1}. \qquad (4)$$

This expression is μ-independent because of RG invariance. Being expressed in terms of the fine-structure constant α, the Coulomb potential reads

$$V(\mathbf{q}^2)=-\frac{4\pi\alpha}{\mathbf{q}^2}\left[1+\frac{\alpha}{3\pi}\Pi_{\rm os}(\mathbf{q}^2)\right]^{-1} \qquad (5)$$

with $\Pi_{\rm os}(0)=0$. The limit of long distances,

$$4\pi\alpha=-\lim_{\mathbf{q}^2\to 0}\mathbf{q}^2V(\mathbf{q}^2), \qquad (6)$$

gives the fine-structure constant. In the Coulomb law [Eqs. (4) and (5)], $q=(0,\mathbf{q})$ and $q^2=-\mathbf{q}^2$. This makes q^2 in Eq. (2) essentially Euclidean. We retain the notation $\mathbf{q}^2$ for a positive number to stress the calculation in the Euclidean domain. Equation (3) is just a relation between schemes of a finite renormalization of the EM couplings.

Taking the limit $\mathbf{q}^2\to 0$ in Eq. (2) requires a special analysis for light quarks because of IR singularities. The polarization function $\Pi(\mu^2,0)$ cannot be calculated in PT if strong interactions are included because the light quarks (u, d, s) are essentially massless.

In addition to the $\overline{MS}$ running coupling constant $\bar\alpha(\mu)$, an on-shell running coupling $\alpha_{\rm os}(\mathbf{q}^2)$ can also be used in Z-boson-peak analyses. The on-shell running coupling is defined by the relation

$$\alpha_{\rm os}(\mathbf{q}^2)=\alpha\Big/\left[1+\frac{\alpha}{3\pi}\Pi_{\rm os}(\mathbf{q}^2)\right], \quad \alpha_{\rm os}(0)=\alpha. \qquad (7)$$

The numerical value for the on-shell running coupling $\alpha_{\rm os}(\mathbf{q}^2)$ can be found from Eq. (2) if $\bar\alpha(\mu)$ is known and if $\Pi(\mu^2,\mathbf{q}^2)$ is calculable for a given $\mathbf{q}^2$.

In the present study, I calculate a low-energy boundary condition for the running EM coupling in the $\overline{MS}$ scheme, i.e., the value $\bar\alpha(\mu_0)$ at some μ_0. A convenient numerical value for the low-energy scale μ_0 is the τ-lepton mass M_τ, which is sufficiently large for strong-interaction PT to work, $\mu_0=M_\tau$. The low-energy coupling $\bar\alpha(M_\tau)$ can be evolved to other scales with the RG equation. The particular scales of interest are the b-quark mass m_b for Υ-resonance physics and M_Z for high-precision SM tests and Higgs-boson searches. The RG functions in the $\overline{MS}$ scheme are known with a very high accuracy, which makes the running precise numerically.

3. LOW-ENERGY NORMALIZATION: FORMULAS

In order to determine a numerical value for the running EM coupling $\bar\alpha(\mu_0)$ by using Eq. (3), one has to compute the polarization function $\Pi(\mu_0^2,q^2)$ at $q^2=0$. There are lepton and quark contributions to the EM current (see a note about the W bosons below). Because decoupling is not explicit, one counts only the contributions of particles that are considered to be active for a given scale.

3.1. Leptons

For a lepton l with the pole mass M_l, we retain masses that make $\Pi(\mu^2,0)$ directly computable in low orders of PT, where strong interactions are absent. The matching condition reads

$$\Pi^l(\mu^2,0)=\ln\frac{\mu^2}{M_l^2} \qquad (8)$$
$$+\frac{\bar\alpha(\mu^2)}{\pi}\left(\frac{45}{16}+\frac{3}{4}\ln\frac{\mu^2}{M_l^2}\right)+\mathcal{O}(\bar\alpha^2).$$

Note that $\mathcal{O}(\alpha^2)$ corrections are also available [24], but they are totally negligible numerically for our purposes. With an accuracy of order α, there is no numerical difference between the fine-structure constant α and the running coupling constant $\bar\alpha(\mu^2)$ on the right-hand side of Eq. (8). For numerical estimates, we substitute α. For $\mu=M_l$, the lepton l decouples completely in the leading order (which is the case for the τ lepton). Because the fine-structure constant α is small numerically, we do not resum the expression on the right-hand side of Eq. (8). With an $\mathcal{O}(\alpha)$ accuracy, expression (8) can be used at any μ (see below). In this sense, the matching for leptons can be performed just at any scale of interest with the same accuracy by using the explicit result given in Eq. (8), for instance, at $\mu = M_Z$. To calculate the polarization function for leptons, we use the pole mass M_l, which is well known numerically. Equation (8) gives a leptonic part of the finite renormalization between the running and the fine-structure constant in Eq. (3). In Eq. (8), we neglect strong interactions (quark contributions), which appear in the α^2 order. If strong interactions are included, then one cannot use PT expressions with such a low scale as the electron or muon mass, and the full IR analysis analogous to that done for light quarks (see below) is necessary. Equation (8) solves the lepton part of the normalization condition for the running EM coupling.

3.2. Light Quarks

For the hadronic part of the vacuum polarization function, we first consider the contribution of light quarks. For the light (massless) quarks, the limit $\mathbf{q}^2 \to 0$ in Eq. (2), which is necessary for relating the running EM coupling to the fine-structure constant, cannot be reached in PT. This is, however, an IR problem which is unsolved in QCD within PT. In QCD with massless quarks, the low-energy domain is not described by PT, and PT expressions should be modified for the limit $\mathbf{q}^2 \to 0$ in Eq. (2) to exist. Such a modification must not change an ultraviolet (UV) structure of the correlation functions because RG invariance should be respected. Therefore, it is convenient to perform an IR modification by using dispersion relations, which make contributions of different energy ranges separately. There are three potentially IR-dangerous contributions made by the light quarks u, d, and s. For matching the contributions of light quarks, we work in $n_f = 3$ effective theory, i.e., in QCD with three active light quarks.

A note about the notation is in order. We consider a generic light-quark correlation function normalized at the parton level to unity (as for its asymptotic spectral density). Then, we add necessary factors to take into account the color or the charge structure (or both). Thus, for the u quark, for instance, we have

$$\Pi^u(\mathbf{q}^2) = N_c e_u^2 \Pi^{\text{light}}(\mathbf{q}^2), \tag{9}$$

where $e_u = 2/3$ is a u-quark EM charge and $N_c = 3$ is a number of colors.

For light quarks, the PT part of the correlation function is calculable for large $\mathbf{q}^2$ and, in the $\overline{MS}$ scheme, reads (e.g., [25])

$$\Pi^{\text{light}}(\mu^2, \mathbf{q}^2) = \ln\frac{\mu^2}{\mathbf{q}^2} + \frac{5}{3} \tag{10}$$

$$+ a_s\left(\ln\frac{\mu^2}{\mathbf{q}^2} + \frac{55}{12} - 4\zeta(3)\right)$$

$$+ a_s^2\left(\frac{9}{8}\ln^2\frac{\mu^2}{\mathbf{q}^2} + \left(\frac{299}{24} - 9\zeta(3)\right)\ln\frac{\mu^2}{\mathbf{q}^2} + \frac{34525}{864} - \frac{715}{18}\zeta(3) + \frac{25}{3}\zeta(5)\right),$$

where $a_s = \alpha_s/\pi$. Equation (10) is written for $n_f = 3$ active light quarks with the $n_f = 3$ effective coupling $a_s \equiv a_s^{(3)}(\mu)$. The limit $\mathbf{q}^2 \to 0$ cannot be reached in Eq. (10) because there is no scale for light quarks and because no PT expression like Eq. (8) is available. Because singularities at low momenta are related to IR problems, it suffices to modify only the IR structure of the correlation function $\Pi^{\text{light}}(\mu^2, \mathbf{q}^2)$. It is convenient to modify just the contribution of low-energy states to the correlation function, and this can be done through a dispersion relation. The dispersion relation reads

$$\Pi^{\text{light}}(\mathbf{q}^2) = \int_0^\infty \frac{\rho^{\text{light}}(s)ds}{s + \mathbf{q}^2}, \tag{11}$$

where a dimensional regularization is implied for $\rho^{\text{light}}(s)$. In fact, Eq. (11) can be used for the bare quantities $\Pi^{\text{light}}(\mathbf{q}^2)$ and $\rho^{\text{light}}(s)$. The limit $\mathbf{q}^2 \to 0$ on the right-hand side of Eq. (11) is IR-singular and cannot be reached if the PT expression for the spectral density $\rho^{\text{light}}(s)$ is used. Therefore, one should modify the low-energy behavior of the spectrum, where PT is not applicable. If such a modification is local [has only a finite support in the energy variable s in Eq. (11)], then it does not affect any UV properties (μ^2 dependence) of $\Pi^{\text{light}}(\mu^2, \mathbf{q}^2)$ that are important for the RG. A low-energy modification is inspired by an experiment: at low energies, there is a well-pronounced bound state as the result of strong interaction between quarks. We therefore adopt a model of IR modification according to which the high-energy tail of the integral in Eq. (11) is computed in PT (duality arguments) that retains the RG structure of the result, while, in the low-energy domain, there is a contribution of a single resonance. An IR modification is performed for the contributions of the u, d, and s quarks. The massless u and d quarks interact with photons through the isotopic combinations $I = 1$ (ρ-meson channel) and $I = 0$ (ω-meson channel). For our purposes, these two channels are completely degenerate and are treated simultaneously. The s-quark contribution is considered separately because of its nonvanishing (small) mass m_s.

For a generic light-quark correlation function in the massless PT approximation, one introduces the IR modification

$$\rho^{\text{light}}(s) \to \rho^{\text{light}}_{\text{IRmod}}(s) \tag{12}$$

$$= F_R\delta(s - m_R^2) + \rho^{\text{light}}(s)\theta(s - s_0),$$

where F_R, m_R, and s_0 are IR parameters of the spectrum. Note that they are not necessarily the numbers determined directly from experimental data. Substituting the IR-modified spectrum (12) into Eq. (11), one finds

$$\Pi^{\text{light}}_{\text{IRmod}}(\mu^2,0) = \frac{F_R}{m_R^2} + \ln\frac{\mu^2}{s_0} + \frac{5}{3} \tag{13}$$
$$+ a_s\left(\ln\frac{\mu^2}{s_0} + \frac{55}{12} - 4\zeta(3)\right) + a_s^2\left(\frac{9}{8}\ln^2\frac{\mu^2}{s_0}\right.$$
$$+\left(\frac{299}{24} - 9\zeta(3)\right)\ln\frac{\mu^2}{s_0} + \frac{34525}{864}$$
$$\left. - \frac{715}{18}\zeta(3) + \frac{25}{3}\zeta(5) - \frac{3\pi^2}{8}\right).$$

We identify m_R with the mass of the lowest resonance, which is the only input giving a scale to the problem. The IR-modifying parameters F_R and s_0 are fixed from the quark–hadron duality arguments.

Notice the difference in the a_s^2 order between Eq. (10) and Eq. (13): in Eq. (13), there is the new term $-3\pi^2/8$. This is a so-called π^2 correction (e.g., [26]). It can be rewritten in terms of $\zeta(2) = \pi^2/6$.

To describe the IR structure of the correlation function in the representation given by Eq. (13), we use an OPE with power-law corrections that semiphenomenologically encode information about the low-energy domain of the spectrum through the vacuum condensates of local gauge-invariant operators [27]. The OPE for the light-quark correlation function reads

$$\Pi^{\text{OPE}}(\mu^2, \mathbf{q}^2) = \Pi^{\text{light}}(\mu^2, \mathbf{q}^2) \tag{14}$$
$$+ \frac{\langle\mathcal{O}_4\rangle}{\mathbf{q}^4} + \mathcal{O}\left(\frac{\langle\mathcal{O}_6\rangle}{\mathbf{q}^6}\right).$$

The quantities $\langle\mathcal{O}_{4,6}\rangle$ make the non-PT contributions of dimension-four and dimension-six vacuum condensates. These contributions are UV-soft (they do not change short-distance properties) and are related to the IR modification of the spectrum. For the purposes of fixing the numerical values of the parameters F_R and s_0, which describe the IR modification of the spectrum, one needs only the first two power-law corrections $1/\mathbf{q}^2$ and $1/\mathbf{q}^4$; the coefficient of the $1/\mathbf{q}^2$ correction vanishes because there are no gauge-invariant dimension-two operators in the massless limit. Computing the IR-modified polarization function and comparing it with the OPE expression, we find finite-energy sum rules (FESR) for fixing the parameters F_R and s_0 [28]. The system of sum rules has the form

$$F_R = s_0\left\{1 + a_s + a_s^2\left(\beta_0\ln\frac{\mu^2}{s_0} + k_1 + \beta_0\right)\right\} + \mathcal{O}(a_s^3), \tag{15}$$
$$F_R m_R^2 = \frac{s_0^2}{2}\left\{1 + a_s + a_s^2\left(\beta_0\ln\frac{\mu^2}{s_0} + k_1 + \frac{\beta_0}{2}\right)\right\} - \langle\mathcal{O}_4\rangle + \mathcal{O}(a_s^3),$$

where $\beta_0 = 9/4$ and

$$k_1 = \frac{299}{24} - 9\zeta(3).$$

We treat $\langle\mathcal{O}_4\rangle$ as a small correction and take its coefficient function to be a constant (the total contribution is RG-invariant). Equations (15) fix F_R and s_0 through m_R^2 and $\langle\mathcal{O}_4\rangle$. Using higher order terms in the OPE expansion (for instance, $\langle\mathcal{O}_6\rangle/\mathbf{q}^6$), one can avoid substituting m_R^2 from experimental data because, within the IR modification given in Eq. (12), the IR scale is determined by the dimension-six vacuum condensate $\langle\mathcal{O}_6\rangle$ [28]. We do not do this because the primary purpose of the present analysis is to find the low-scale normalization for the EM coupling and not to describe the spectrum in the low-energy domain. The use of the experimental value for the resonance mass m_R^2 makes the calculation more precise because the numerical value for the $\langle\mathcal{O}_6\rangle$ condensate is not known well (cf. [29]).

The leading-order solution to Eqs. (15) (upon neglecting PT and non-PT corrections) is given by the partonic-model result $s_0 = 2m_R^2$, $F_R = s_0 = 2m_R^2$, which is rather precise. This solution was used to predict masses and residues of the radial excitations of vector mesons within the local-duality approach when the experimental spectrum is approximated by a sequence of infinitely narrow resonances [30]. Such an approximation for the experimental spectrum is justified by theoretical considerations in the large-N_c limit [31] and by the exact solution to two-dimensional QCD [32]. For the experimental spectrum of infinitely narrow resonances, the local-duality approach means the averaging over the energy interval around a single resonance [30]. It is expected to be less precise than the global-duality method in which averaging is performed over the entire spectrum. However, within the global-duality approach, only the total contribution of all hadronic states can be studied, while local duality can be used even for the first few resonances, allowing one to predict characteristics of individual hadronic states.

An accurate treatment of Eqs. (15) gives the solution

$$s_0 = 2m_R^2\left(1+\frac{\beta_0}{2}a_s^2\right)+\frac{\langle\mathcal{O}_4\rangle}{m_R^2}(1-a_s), \tag{16}$$

$$\frac{F_R}{m_R^2} = 2\left\{1+a_s+a_s^2\left(\beta_0\ln\frac{\mu^2}{2m_R^2}+k_1+\frac{3}{2}\beta_0\right)\right\}+\frac{\langle\mathcal{O}_4\rangle}{m_R^4}.$$

In the solution given by Eqs. (16), only linear terms in the non-PT correction $\langle\mathcal{O}_4\rangle$ are retained. This is well justified numerically. The $a_s^2\langle\mathcal{O}_4\rangle$ terms are neglected because the coefficient function for the condensate $\langle\mathcal{O}_4\rangle$ is not known to this precision. In Eq. (13), the scale parameter is s_0, while the system of Eqs. (16) is solved in terms of m_R, which we identify with the resonance mass and take from experimental data. Therefore, we express the PT scale s_0 in terms of m_R according to the solution given by Eqs. (16). The expansion of the log-term in Eq. (13) reads

$$\ln\frac{\mu^2}{s_0} = \ln\frac{\mu^2}{2m_R^2}-\frac{\beta_0}{2}a_s^2-\frac{\langle\mathcal{O}_4\rangle}{2m_R^4}(1-a_s).$$

With these results, one finds an expression for the IR-modified polarization function for light quarks at the origin:

$$\begin{aligned}&\Pi^{\text{light}}_{\text{IRmod}}(\mu^2,0)\\ &=2\left\{1+a_s+a_s^2\left(\beta_0\ln\frac{\mu^2}{2m_R^2}+k_1+\frac{3}{2}\beta_0\right)\right\}+\frac{\langle\mathcal{O}_4\rangle}{m_R^4}\\ &\quad+\ln\frac{\mu^2}{2m_R^2}-\frac{\beta_0}{2}a_s^2-\frac{\langle\mathcal{O}_4\rangle}{2m_R^4}(1-a_s)+\frac{5}{3}\\ &\quad+a_s\left(\ln\frac{\mu^2}{2m_R^2}-\frac{\langle\mathcal{O}_4\rangle}{2m_R^4}+\frac{55}{12}-4\zeta(3)\right)\\ &\quad+a_s^2\left(\frac{9}{8}\ln^2\frac{\mu^2}{2m_R^2}+\left(\frac{299}{24}-9\zeta(3)\right)\ln\frac{\mu^2}{2m_R^2}\right.\\ &\quad\left.+\frac{34525}{864}-\frac{715}{18}\zeta(3)+\frac{25}{3}\zeta(5)-\frac{3\pi^2}{8}\right).\end{aligned}$$

Here, the second line gives the resonance contribution, while the rest is the high-energy tail (continuum contribution), which is computed in PT. Finally, we obtain

$$\begin{aligned}&\Pi^{\text{light}}_{\text{IRmod}}(\mu^2,0) \qquad (17)\\ &=2\left\{1+a_s+a_s^2\left(\beta_0\ln\frac{\mu^2}{2m_R^2}+k_1+\frac{3}{2}\beta_0\right)\right\}+\frac{\langle\mathcal{O}_4\rangle}{m_R^4}\\ &\quad+\ln\frac{\mu^2}{2m_R^2}-\frac{\beta_0}{2}a_s^2+\frac{5}{3}\\ &\quad+a_s\left(\ln\frac{\mu^2}{2m_R^2}+\frac{55}{12}-4\zeta(3)\right)\\ &\quad+a_s^2\left(\frac{\beta_0}{2}\ln^2\frac{\mu^2}{2m_R^2}+k_1\ln\frac{\mu^2}{2m_R^2}\right.\\ &\quad\left.+\frac{34525}{864}-\frac{715}{18}\zeta(3)+\frac{25}{3}\zeta(5)-\frac{3\pi^2}{8}\right).\end{aligned}$$

Equation (17) gives $\Pi^{\text{light}}_{\text{IRmod}}(\mu^2,0)$ as an explicit function of the non-PT scale m_R (to be taken from experiments) and the theoretical quantities a_s and $\langle\mathcal{O}_4\rangle$. The choice of numerical value for a_s is discussed in detail later.

The condensate of dimension-four operators for light quarks is given by

$$\begin{aligned}\langle\mathcal{O}_4\rangle &= \frac{\pi^2}{3}\left(1+\frac{7}{6}a_s\right)\left\langle\frac{\alpha_s}{\pi}G^2\right\rangle \qquad (18)\\ &\quad+2\pi^2\left(1+\frac{1}{3}a_s\right)(m_u+m_d)(\langle\bar{u}u\rangle+\langle\bar{d}d\rangle).\end{aligned}$$

The PT correction to the gluon condensate was computed in [33]. We retain small corrections proportional to the light-quark masses and treat them in the approximation of isotopic symmetry for the light-quark condensates $\langle\bar{u}u\rangle=\langle\bar{d}d\rangle$, which is rather precise for u and d quarks. The quark-condensate part of Eq. (18) is given by the relation of partial conservation of axial current (PCAC) for the π meson,

$$(m_u+m_d)\langle\bar{u}u+\bar{d}d\rangle = -f_\pi^2m_\pi^2.$$

Here, $f_\pi = 133$ MeV is a charged-pion decay constant and $m_\pi = 139.6$ MeV is the charged-pion mass. For the standard numerical value of the gluon condensate, $\langle(\alpha_s/\pi)G^2\rangle = 0.012\ \text{GeV}^4$ [27], and $a_s = 0.1$, one finds

$$\begin{aligned}\langle\mathcal{O}_4\rangle &= \frac{\pi^2}{3}\left(1+\frac{7}{6}a_s\right)\langle\frac{\alpha_s}{\pi}G^2\rangle \qquad (19)\\ &\quad-2\pi^2\left(1+\frac{1}{3}a_s\right)f_\pi^2m_\pi^2 = 0.037\ \text{GeV}^4.\end{aligned}$$

For the most important contribution of u and d quarks (the u-quark contribution is enhanced by a factor of 4 because of its doubled electric charge in relation to the other light quarks), the relation $s_0 = 2m_\rho^2$, where $m_\rho = 768.5$ MeV is the mass of the lowest (ρ-meson) resonance in the nonstrange isotopic $I = 1$ vector channel, is rather precise numerically. The gluon condensate generates a small correction to the basic duality relation for the light quarks, $s_0 = 2m_R^2$. Note that we do not identify F_R with the experimental number available from the analysis of the ρ-meson leptonic width, but we treat it as an IR-modifying parameter that should be fixed from the requirement of consistency with OPE. It is close numerically to its experimental counterpart because it is known that OPE provides a rather accurate description of the low-energy physical spectrum if vacuum condensates are included. In the present study, we stick to a theoretical description of the IR domain and use the lowest resonance mass as the only input for the IR modification. The same is true for the $I = 0$ channel, where the lowest resonance is the ω meson with mass $m_\omega = 781.94$ MeV. We do not distinguish these two channels. We consider the parameters F_R and s_0 as the IR modifiers fixed theoretically through OPE and do not attempt to substitute them from experimental data (using leptonic decay widths for F_R and the shape of the spectrum for s_0).

Note that the IR parameters F_R, m_R, and s_0 of the spectrum are μ-independent. This can be seen explicitly from (15).

The $n_f = 3$ effective theory is valid only up to $\mathbf{q}^2 \sim m_c^2$, and, formally, there are corrections of order $\mathbf{q}^2/m_c^2$ [34]. However, these corrections are small in the case of current correlation functions [35, 36].

For the s quark, there are also corrections due to the strange-quark mass m_s, which change slightly the shape of the spectrum and the consistency equations for the IR modifiers. We consider m_s as an additional IR modifier that does not affect UV properties (renormalization in the $\overline{MS}$ scheme is mass-independent) and treat it as a power-law correction. We write the OPE for the s quark in the form

$$\Pi^{\mathrm{OPE},s}(\mu^2, \mathbf{q}^2) = \Pi^{\mathrm{light}}(\mu^2, \mathbf{q}^2) - \frac{6m_s^2}{\mathbf{q}^2} + \frac{\langle \mathcal{O}_4^s \rangle}{\mathbf{q}^4} + \mathcal{O}\left(\frac{\langle \mathcal{O}_6 \rangle}{\mathbf{q}^6}\right).$$

The system of equations for fixing the parameters F_{Rs} and s_{0s} reads

$$F_{Rs} + 6m_s^2 = s_{0s}\left\{1 + a_s + a_s^2(\beta_0 \ln\frac{\mu^2}{s_{0s}} + k_1 + \beta_0)\right\} + \mathcal{O}(a_s^3), \tag{20}$$
$$F_s m_{Rs}^2 = \frac{s_{0s}^2}{2}\left\{1 + a_s + a_s^2\left(\beta_0 \ln\frac{\mu^2}{s_{0s}} + k_1 + \frac{\beta_0}{2}\right)\right\} - \langle \mathcal{O}_4^s \rangle + \mathcal{O}(a_s^3).$$

Here,

$$\langle \mathcal{O}_4^s \rangle = \frac{\pi^2}{3}\left(1 + \frac{7}{6}a_s\right)\left\langle \frac{\alpha_s}{\pi}G^2 \right\rangle + 8\pi^2\left(1 + \frac{1}{3}a_s\right) m_s \langle \bar{s}s \rangle$$

is a dimension-four contribution in the strange channel. One finds a solution to Eqs. (20) in the form

$$s_{0s} = 2m_{Rs}^2\left(1 + \frac{\beta_0}{2}a_s^2\right) + \frac{\langle \mathcal{O}_4^s \rangle}{m_{Rs}^2}(1 - a_s) - 6m_s^2, \tag{21}$$
$$\frac{F_{Rs}}{m_{Rs}^2} = 2\left\{1 + a_s + a_s^2\left(\beta_0 \ln\frac{\mu^2}{2m_{Rs}^2} + k_1 + \frac{3}{2}\beta_0\right)\right\} + \frac{\langle \mathcal{O}_4^s \rangle}{m_{Rs}^4} - 12\frac{m_s^2}{m_{Rs}^2}.$$

The correction due to m_s^2 is not large. Instead of Eq. (17), one has

$$\Pi_{\mathrm{IRmod}}^{\text{light-}s}(\mu^2, 0) = \Pi_{\mathrm{IRmod}}^{\mathrm{light}}(\mu^2, 0) - 9\frac{m_s^2}{m_{Rs}^2}, \tag{22}$$

and $m_{Rs} = m_\varphi$ and $\langle \mathcal{O}_4^s \rangle$ should be used in the first term of Eq. (22) instead of m_ρ and $\langle \mathcal{O}_4 \rangle$. Here, $m_\varphi = 1019.4$ MeV is the mass of the φ meson, which is the lowest resonance in the strange channel. A numerical value for $\langle \mathcal{O}_4^s \rangle$ is obtained as follows. We use the relation (e.g., [37])

$$\frac{2m_s}{m_u + m_d} = 25.0$$

and the phenomenological result $\langle \bar{s}s \rangle = (0.8 \pm 0.2) \times \langle \bar{u}u \rangle$ [38] to find

$$m_s \langle \bar{s}s \rangle = 12.5 \cdot 0.8 \cdot (m_u + m_d)\langle \bar{u}u \rangle = -5.0 f_\pi^2 m_\pi^2 = -0.0017\ \mathrm{GeV}^4. \tag{23}$$

One could also use the PCAC relation for the K

meson,

$$(m_s + m_u)\langle \bar{s}s + \bar{u}u\rangle = -f_K^2 m_K^2 + \mathcal{O}(m_s^2),$$

with $f_K = 1.17 f_\pi$ and $m_K = 493.7$ MeV. Note that the PCAC relation in the strange channel is valid only up to terms of order m_s^2, which are not completely negligible numerically in relation to the pion case [39]. Therefore, we use the result given in Eq. (23). For the standard value of $\langle(\alpha_s/\pi)G^2\rangle = 0.012$ GeV^4 [27] and $a_s = 0.1$, one finds

$$\langle \mathcal{O}_4^s\rangle = \frac{\pi^2}{3}\left(1 + \frac{7}{6}a_s\right)\left\langle \frac{\alpha_s}{\pi}G^2\right\rangle \tag{24}$$
$$+ 8\pi^2\left(1 + \frac{1}{3}a_s\right)(-5.0 f_\pi^2 m_\pi^2) = -0.0965\ \text{GeV}^4.$$

The correction due to $m_s\langle\bar{s}s\rangle$ is dominant in the dimension-four contribution in the strange case. Because the dimension-four terms represent only small corrections to the leading results for the correlation functions in Eqs. (17) and (22), the precision with which they are calculated suffices for our purposes.

For the absolute value of m_s to be substituted into the m_s^2 correction, we use the results of recent analyses [40] and take $m_s(M_\tau) = 130 \pm 27_{\text{expt}} \pm 9_{\text{theor}}$ MeV. For $m_{Rs} = m_\varphi = 1019.4$ MeV, one finds

$$\frac{m_s^2}{m_\varphi^2} = 0.0163,$$

which is a small expansion parameter that justifies the treatment of the m_s^2 contribution as a small correction.

Note that there are attempts at using the constituent masses for the light quarks and at estimating the polarization functions in the way this is done for leptons or heavy quarks. Apart from being ad hoc (and not supported by experimental data), this IR modification of the light-quark correlation functions contradicts OPE or local duality (or both) over the energy interval between the origin and 1 to 2 GeV.

Thus, Eqs. (13) and (17) represent a semiphenomenological subtraction for the light-quark correlation function at $\mathbf{q}^2 = 0$ based on the IR modification of the spectrum consistent with OPE. Some mismatch with OPE in orders higher than $\mathcal{O}(1/\mathbf{q}^4)$, which is possible because of the simplicity of the IR modification, is neglected. This is justified because we need only the integral characteristics of the spectrum for calculating $\Pi^{\text{light}}_{\text{IRmod}}(\mu^2, 0)$, but we are not interested in the pointwise behavior of the spectral function $\rho^{\text{light}}_{\text{IRmod}}(s)$, which is used as an auxiliary quantity in this particular instance.

3.3. Heavy Quarks

Matching heavy quarks is straightforward and is similar to that of leptons. It is performed within PT. For a heavy quark q with a pole mass $m_q \gg \Lambda_{\text{QCD}}$, one has

$$\Pi^q(\mu^2, 0) = N_c e_q^2 \Pi^{\text{heavy}}(\mu^2, 0),$$

where $\Pi^{\text{heavy}}(\mu^2, 0)$ is a generic contribution of a heavy quark to the vacuum polarization function [41],

$$\Pi^{\text{heavy}}(\mu^2, 0) = \ln\frac{\mu^2}{m_q^2} \tag{25}$$
$$+ e_q^2\frac{\alpha}{\pi}\left(\frac{45}{16} + \frac{3}{4}\ln\frac{\mu^2}{m_q^2}\right) + a_s\left(\frac{15}{4} + \ln\frac{\mu^2}{m_q^2}\right)$$
$$+ a_s^2\left(\frac{41219}{2592} - \frac{917}{1296}n_l + \left(4 + \frac{4}{3}\ln 2 - \frac{2}{3}n_l\right)\zeta(2)\right.$$
$$+ \frac{607}{144}\zeta(3) + \left(\frac{437}{36} - \frac{7}{9}n_l\right)\ln\frac{\mu^2}{m_q^2}$$
$$\left. + \left(\frac{31}{24} - \frac{1}{12}n_l\right)\ln^2\frac{\mu^2}{m_q^2}\right) + \mathcal{O}(\alpha^2, \alpha_s^3).$$

Here, n_l is the number of quarks that are lighter than the heavy one, and $a_s = \alpha_s/\pi$ is the strong-coupling constant in the effective theory with $n_l + 1$ active quarks normalized at the scale μ. The numbers in Eq. (25) are given for the pole mass of the heavy quark. We neglect the (known) EM contribution of order α^2 because it is smaller than the unknown term of order α_s^3. The contribution of order $\alpha\alpha_s$ is also neglected. Equation (25) represents a contribution of the corrected partonic model, i.e., that with a heavy-quark loop in the leading approximation. There is also the contribution of heavy-quark loops to the light-quark vacuum polarization function that should be taken into account in constructing the effective theory with a decoupled heavy quark. This contribution is small. It reads [42]

$$\Pi^{\text{light-heavy}}(\mu^2, 0) = a_s^2 N_c\left(\sum_{i=1}^{n_l} e_i^2\right) \tag{26}$$
$$\times\left(\frac{295}{1296} - \frac{11}{72}\ln\frac{\mu^2}{m_q^2} - \frac{1}{12}\ln^2\frac{\mu^2}{m_q^2}\right).$$

The contribution of the gluonic condensate is neglected (see [23]). Equations (25) and (26) are used for the c and b quarks. Note that these formulas cannot be used for the s quark. Indeed, because of α_s corrections, the PT scale in Eq. (25) is effectively equal to m_q and is too small for PT to be applicable in the case of the strange quark since $m_s \sim \Lambda_{\text{QCD}}$.

4. LOW-ENERGY NORMALIZATION: NUMERICS

In the preceding sections, the contributions of fermions to the photon vacuum polarization function have been presented. We are not going to consider scales larger than M_Z; therefore, bosonic contributions to the EM current and polarization function (namely, W-boson loops) are not taken into account. The above equations describe an effective theory without W bosons, which decouple at energies smaller than M_Z and which should be added separately for the Z-boson-peak tests.

A numerical value of the strong coupling at low energies is rather important for the whole analysis. Estimates of a numerical value for the strong coupling at low scales are usually based on the τ-lepton-decay data. Within the contour-resummation technique [43, 44], the value obtained is $\alpha_s^{(3)}(M_\tau^2) = 0.343 \pm 0.009_{\rm expt}$. Within a renormalization scheme-invariant treatment of [45], a slightly different value of $\alpha_s^{(3)}(M_\tau^2) = 0.318 \pm 0.006_{\rm expt} \pm 0.016_{\rm theor}$ was recently found. The uncertainty is due to the experimental error and due to the truncation of the series, which is estimated within an optimistic scenario that higher order terms of PT are still small and exhibit no explicit asymptotic growth. Even for the optimistic scenario with a reduced theoretical error in relation to the conservative estimates, the theoretical error dominates the total uncertainty of the numerical value for the strong coupling. Note that a numerical value for the strong coupling obtained with the well-known contour-improved techniques is based on a special resummation procedure for treating contributions generated by the running, which does not necessarily improve results, but which definitely changes them in relation to finite-order estimates at the present level of precision. The change is still within the error bars, which makes two procedures for extracting the numerical value for the strong coupling, finite-order PT and contour resummation, consistent. We use the value of $\alpha_s^{(3)}(M_\tau^2) = 0.318 \pm 0.017$ as our basic input for the low-energy strong coupling. The central value of $\alpha_s^{(3)}(M_\tau^2) = 0.318$ corresponds to $\alpha_s^{(5)}(M_Z) = 0.118$ when it is evolved with a four-loop β function and three-loop matching at the m_c and m_b thresholds.

First, we calculate the numerical value of the running EM coupling constant at $\mu = M_\tau$, which is a convenient low-scale normalization point. Note that the numerical value of the c-quark pole mass is rather close to M_τ. In fact, the recent estimate is $m_c = 1.8 \pm 0.2$ GeV, and we take $m_c = M_\tau = 1.777$ GeV as a central value, i.e., $m_c = M_\tau \pm 0.2$ GeV. Thus, the low-energy normalization value $\bar{\alpha}^{(4)}(M_\tau)$ is computed with three active leptons and four active quarks.

4.1. Leptons

The lepton contribution is calculated with lepton masses $M_e = 0.5110$ MeV, $M_\mu = 105.66$ MeV, and $M_\tau = 1777$ MeV [10]. These values are extremely precise; therefore, we use them as exact and assign no errors to them. We neglect the difference between the running EM coupling $\bar{\alpha}$ and fine-structure constant α in corrections [which results in a $\mathcal{O}(\alpha^2)$ shift that is numerically negligible]. We use $\alpha^{-1} = 137.036$. According to Eq. (8), leptons yield

$$\Delta^{\rm lept}(M_\tau^2) = \sum_{l=e,\mu,\tau} \Pi^l(M_\tau^2, 0) \tag{27}$$
$$= \left(1 + \frac{3}{4}\frac{\alpha}{\pi}\right)\left(\ln\frac{M_\tau^2}{M_e^2} + \ln\frac{M_\tau^2}{M_\mu^2} + \ln\frac{M_\tau^2}{M_\tau^2}\right)$$
$$+ \frac{135}{16}\frac{\alpha}{\pi} = 21.953 + 0.058 = 22.011,$$

where the first number is obtained in the limit $\alpha = 0$. The α correction is almost negligible for the normalization at the scale M_τ. Note that the τ lepton makes no logarithmic contribution at the scale $\mu = M_\tau$.

The $\mathcal{O}(\bar{\alpha}^2)$ correction for the lepton contribution in the $\overline{MS}$ scheme is also available [24]. This correction is parametrically small, and there are no unexpectedly large numerical coefficients (in fact, they are also small), which makes the parametric estimate based on the counting of powers of α rather precise. The sum of the contributions of three leptons in the $\bar{\alpha}^2$ order is completely negligible, and we treat the leptonic contribution in Eqs. (8) and (27) as exact.

4.2. Light Quarks

From Eq. (17) with $m_R = m_\rho$ for the u and d quarks and with $m_R = m_\varphi$ for the s quark, one finds for the total light-quark contribution $\Delta^{uds}(M_\tau^2)$ that

$$\Delta^{uds}(M_\tau^2) = \Delta^u(M_\tau^2) + \Delta^d(M_\tau^2) + \Delta^s(M_\tau^2)$$
$$= \Delta^\rho(M_\tau^2) + \Delta^\omega(M_\tau^2) + \Delta^\varphi(M_\tau^2)$$
$$= \frac{4}{3}\Delta^{\rm light}(M_\tau^2) + \frac{1}{3}\Delta^{\rm light}(M_\tau^2) + \frac{1}{3}\Delta^{\rm light-s}(M_\tau^2)$$
$$= \frac{5}{3}\Delta^{\rm light}(M_\tau^2) + \frac{1}{3}\Delta^{\rm light-s}(M_\tau^2)$$
$$= 9.13662 + 5.32853 a_s + 24.9086 a_s^2$$
$$= 9.13662 + 0.53937 + 0.25521 = 9.9312.$$

Because the calculation is explicit, we can give this result in more detail, showing all different contributions:

$$\Delta^{uds}(M_\tau^2) = 9.11165 + 0.539367\left(\frac{a_s}{0.101}\right) \tag{28}$$

$$+ 0.2552\left(\frac{a_s}{0.101}\right)^2 + 0.08865\left(\frac{\langle \mathcal{O}_4\rangle}{0.037\ \mathrm{GeV}^4}\right)$$
$$- 0.0488\left(\frac{m_s}{130\ \mathrm{MeV}}\right)^2 + 0.0149\left(\frac{\langle \mathcal{O}_4^s\rangle}{0.0965\ \mathrm{GeV}^4}\right).$$

The IR part of the spectrum (resonances) and the partonic quark approximation make a dominant contribution. The QCD perturbative corrections and power-law corrections due to m_s and the $\langle \mathcal{O}_4\rangle$ condensates are small. The error is

$$\delta\Delta^{uds}(M_\tau^2) = 10.5\delta a_s + 0.09\frac{\delta\langle \mathcal{O}_4\rangle}{\langle \mathcal{O}_4\rangle} \tag{29}$$
$$- 0.1\frac{\delta m_s}{m_s} - 0.015\frac{\delta\langle \mathcal{O}_4^s\rangle}{\langle \mathcal{O}_4^s\rangle}.$$

The variations $\delta\langle \mathcal{O}_4^s\rangle$ and $\delta\langle \mathcal{O}_4\rangle$ are not completely independent—both quantities contain a variation of the gluon condensate. Also, the error of a_s and that of the gluon condensate are correlated (see, for instance, [46]). In order to estimate the total error of $\Delta^{uds}(M_\tau^2)$ in terms of less correlated quantities, one could rewrite power-law corrections in Eq. (28) in the basis of the gluon and strange quark condensates [47]. Because the correlation is not well established numerically, we neglect the effects of the correlation. We consider the errors of the strong coupling a_s, of the gluon condensate for $\delta\langle \mathcal{O}_4\rangle$, of the strange-quark mass m_s, and of the strange-quark condensate $\langle \bar{s}s\rangle$ for $\delta\langle \mathcal{O}_4^s\rangle$ as independent quantities and use $\delta a_s = 0.017/\pi = 0.0054$, $\delta\langle \mathcal{O}_4\rangle/\langle \mathcal{O}_4\rangle = 1/2$ due to the gluon condensate, and $\delta m_s/m_s = 0.28$, $\delta\langle \mathcal{O}_4^s\rangle/\langle \mathcal{O}_4^s\rangle = 1/4$ due to $\langle \bar{s}s\rangle$. With these (conservative) estimates of uncertainties, one finds

$$\delta\Delta^{uds}(M_\tau^2) = \pm 0.057|_{a_s} \pm 0.045|_{\langle \mathcal{O}_4\rangle}$$
$$\pm 0.028|_{m_s} \pm 0.004|_{\langle \mathcal{O}_4^s\rangle}.$$

The dominant error is due to δa_s. The gluon condensate gives a sizable error because it is enhanced by the charge structure of light (mainly u) quarks and because its uncertainty is taken to be very conservative to compensate for the possible correlation with a_s. The strange channel is suppressed by a factor of 1/3 in the total sum of light-quark contributions, and its specific features only slightly affect the result. The total error for the light-quark contributions added in quadrature reads

$$\delta\Delta^{uds}(M_\tau^2) = \pm 0.078.$$

The final result for the contribution of the light quarks to the low-energy normalization of the running EM coupling is

$$\Delta^{uds}(M_\tau^2) = 9.9312 \pm 0.078. \tag{30}$$

We retain some additional digits at intermediate stages just for computational purposes.

4.3. Contribution of the c Quark

For the c quark, we use Eqs. (25) and (26). The strong-coupling constant in $n_f = 4$ effective theory is found by matching the strong-coupling constant in $n_f = 3$ and $n_f = 4$ effective theories.

Matching at the pole-mass scale m_P for the strong coupling has the form [48]

$$a_s^{(n_l)}(m_P^2) = a_s^{(n_l+1)}(m_P^2) \tag{31}$$
$$\times\left(1 + C_2 a_s^{(n_l+1)}(m_P^2)^2 + C_3 a_s^{(n_l+1)}(m_P^2)^3 + \mathcal{O}(a_s^4)\right),$$

where

$$C_2 = -\frac{7}{24}, \tag{32}$$

$$C_3 = -\frac{80507}{27648}\zeta(3) - \frac{2}{9}\zeta(2)(\ln 2 + 3) \tag{33}$$
$$- \frac{58933}{124416} + \frac{n_l}{9}\left(\zeta(2) + \frac{2479}{3456}\right).$$

We solve (invert) Eq. (31) perturbatively and find the expression

$$a_s^{(n_l+1)}(m_P^2) \tag{34}$$
$$= a_s^{(n_l)}(m_P^2)\left\{1 - C_2 a_s^{(n_l)}(m_P^2)^2 - C_3 a_s^{(n_l)}(m_P^2)^3\right\},$$

which is used to determine the couplings in the neighboring effective theories at their boundary scale that is chosen to be the pole mass of a heavy quark. Matching at $m_c = M_\tau = 1.777$ GeV (we remind the reader that the numerical value of the c-quark mass is chosen to be $m_c = M_\tau \pm 0.2$ GeV) with $\alpha_s^{(3)}(M_\tau^2) = 0.318$ gives $a_s^{(4)}(m_c^2 = M_\tau^2) = 0.102$ or $\alpha_s^{(4)}(m_c^2 = M_\tau^2) = 0.320$. This value for the strong coupling is used in Eq. (25) to calculate the c-quark contribution to the finite renormalization of the EM coupling. Note that, although one computes with $a_s^{(4)}(M_\tau^2)$, it can well be identified numerically with $a_s^{(3)}(M_\tau^2)$: the change due to matching is tiny and is much smaller than the error of $a_s^{(3)}(M_\tau^2)$.

Using Eqs. (25) and (26), one finds

$$\Delta^c(M_\tau^2) = \Pi^c(\mu^2 = M_\tau^2, 0) = 0.00387 \tag{35}$$
$$+ 0.00474 + 0.51001 + 0.32817 = 0.84679,$$

where the first term is a EM contribution, the second one is a loop contribution [Eq. (26)], and the last two terms give the PT expansion of the direct contribution [Eq. (25)]. One sees that the EM and loop contributions are much smaller than the direct contribution. The convergence of PT series for the direct contribution is not fast.

The uncertainty of the c-quark contribution is straightforward to estimate. The main error comes from the uncertainty in the c-quark mass. In the next-to-leading order (NLO), one finds from Eq. (25) that

$$\delta\Delta^c(M_\tau^2) = -\frac{4}{3}(1+a_s)\frac{2\delta m_c}{m_c} \tag{36}$$
$$= -\frac{8}{3}(1+a_s)\frac{\delta m_c}{m_c} = \pm 0.330$$

for $m_c = M_\tau \pm 0.2$ GeV and $a_s = 0.1$. This is a very large uncertainty. The contribution $\Delta^c(M_\tau^2)$ in Eq. (35) is small because the c quark almost decouples, but the uncertainty of $\Delta^c(M_\tau^2)$ is large. The uncertainty is mainly given by the variation of $\ln(M_\tau^2/m_c^2)$ in Eq. (25), which is independent of the absolute value of the contribution. For the central value $m_c = M_\tau$, one would find a vanishing contribution in the leading order, but its uncertainty would remain almost unchanged and equal to 0.330. Also, the c-quark mass is not very large, and the convergence of the PT expansion in Eqs. (25) and (35) is slow.

Note that, in order to estimate the uncertainty of the c-quark contribution, we do not take into account the uncertainty in the coupling a_s. The reason is that the uncertainties in the quark mass m_c and coupling a_s are correlated. Indeed, to the leading order, one can find, from Eq. (25), the uncertainty due to an independent variation of a_s in the form

$$\delta\Pi^{\text{heavy}}(M_\tau^2, 0) = \frac{15}{4}\delta a_s. \tag{37}$$

However, Eq. (25) can be rewritten in terms of the running mass $\bar{m}_c(\mu^2)$. To the first order in a_s, the relation between masses reads

$$m_c = \bar{m}_c(\mu^2)\left\{1 + a_s(\mu^2)\left(\ln\frac{\mu^2}{\bar{m}_c^2(\mu^2)} + \frac{4}{3}\right)\right\}, \tag{38}$$

which leads to the change in Eq. (25):

$$\ln\frac{\mu^2}{m_c^2} + a_s\left(\frac{15}{4} + \ln\frac{\mu^2}{m_c^2}\right)$$
$$\to \ln\frac{\mu^2}{\bar{m}_c^2(\mu^2)} + a_s\left(\frac{13}{12} - \ln\frac{\mu^2}{\bar{m}_c^2(\mu^2)}\right).$$

The NLO result for the polarization function in terms of the running mass now reads

$$\Pi^{\text{heavy}}_{\text{run.mass}}(\mu^2, 0)$$
$$= \ln\frac{\mu^2}{\bar{m}_c^2(\mu^2)} + a_s\left(\frac{13}{12} - \ln\frac{\mu^2}{\bar{m}_c^2(\mu^2)}\right).$$

This expression leads to the uncertainty

$$\delta\Pi^{\text{heavy}}_{\text{run.mass}}(M_\tau^2, 0) = \left(\frac{13}{12} - \ln\frac{M_\tau^2}{\bar{m}_c^2(\mu^2)}\right)\delta a_s,$$

which is smaller numerically than the preceding result given in Eq. (37). The rest of the uncertainty is now in the relation between the pole and running masses given in Eq. (38), which represents a regular change of variables in the finite-order PT and is under a rather strict control. We work with the pole mass and assume that the uncertainty in the polarization function at the origin is saturated by the uncertainty of the pole mass. It is also assumed that the uncertainty in the pole mass is estimated in such a way that it includes the uncertainty in a_s.

4.4. Running EM Coupling at M_τ in $n_f = 4$ Effective Theory

The total finite renormalization between the fine-structure constant and the $\overline{MS}$-scheme EM coupling at M_τ is given by

$$\Delta^{(4)}(M_\tau^2) = \Delta^{\text{lept}}(M_\tau^2) + \Delta^{uds}(M_\tau^2) \tag{39}$$
$$+ \Delta^c(M_\tau^2) = 22.0109 + 9.9312 + 0.8468 = 32.7889,$$

which leads to

$$\frac{3\pi}{\bar{\alpha}^{(4)}(M_\tau^2)} = \frac{3\pi}{\alpha} - \Delta^{(4)}(M_\tau^2) = \frac{3\pi}{\alpha} - 32.7889. \tag{40}$$

The low-energy normalization value for the EM coupling in the $\overline{MS}$ scheme reads

$$\frac{1}{\bar{\alpha}^{(4)}(M_\tau^2)} = 133.557. \tag{41}$$

We now consider the uncertainty in this central value. The lepton contributions are treated as exact ones, so that the number in Eq. (27) has no errors. The errors due to the light quarks are given in Eq. (30). Note that one could reduce the sensitivity of $\Delta^{uds}(M_\tau^2)$ to a_s, whose error dominates the total error in Eq. (30), by taking F_R from experimental data through the leptonic decay width of the ρ meson (and of the ω and φ mesons in other light-quark channels). Then, the resonance contribution F_R/m_R^2 does not depend on a_s. The first duality relation fixes s_0 immediately by using the fact that the power-law correction of order $1/q^2$ is absent in the OPE expression for the correlation function. However, this procedure introduces an experimental error due to the uncertainty in the numerical value of the leptonic decay width of the ρ meson,

$$\Gamma_{ee}^{\rho} = 6.77 \pm 0.32 \text{ keV}.$$

This uncertainty leads to almost the same error for the final quantity $\Delta^{uds}(M_\tau^2)$ as the uncertainty in a_s. This seems natural. Indeed, the strong coupling at low energies is extracted from τ data, in which the ρ-meson contribution constitutes a significant part.

This example shows how the coupling constant encodes information about experimental data. Another point about the use of Γ_{ee}^{ρ} for the lowest resonance contribution is that the consistency with OPE is less strict for such a procedure (no dimension-four operators participate). Still having in mind the possibility of a further improvement of the accuracy through experimental data, we consider our estimate of the error given in Eq. (30) as a rather conservative one.

The uncertainty in the c-quark contribution is given in Eq. (36). Collecting all together, one finds the final prediction

$$\Delta^{(4)}(M_\tau^2) = 32.7889 \pm 0.078_{\rm light} \pm 0.330_c \qquad (42)$$

and

$$\frac{3\pi}{\bar{\alpha}^{(4)}(M_\tau^2)} = \frac{3\pi}{\alpha} - \Delta^{(4)}(M_\tau^2) \qquad (43)$$
$$= \frac{3\pi}{\alpha} - (32.7889 \pm 0.078_{\rm light} \pm 0.330_c).$$

Equation (43) is the main result for the low-energy normalization of the running EM coupling. For the coupling itself, it reads

$$\frac{1}{\bar{\alpha}^{(4)}(M_\tau^2)} = 133.557 \pm 0.0083_{\rm light} \pm 0.0350_c \qquad (44)$$

and

$$\bar{\alpha}^{(4)}(M_\tau^2) = 1.0261\alpha.$$

The value $\bar{\alpha}^{(4)}(M_\tau^2)$ [or, equivalently, $\Delta^{(4)}(M_\tau^2)$] represents the boundary (initial) condition for the evolution of the running EM coupling. With this value known, the EM coupling can be run to other scales. The final goal is $M_Z = 91.187$ GeV, where high-precision tests of the SM are done. As will be seen later, the running itself is very precise numerically and the main uncertainty in the running EM coupling at larger scales is due to the boundary condition [Eq. (44)]. The boundary condition of Eq. (44) has a rather large uncertainty mainly because of the error in the c-quark mass. The uncertainty due to the light-quark contribution is reasonably small. It is dominated by the error in $a_s(M_\tau)$, which is mainly theoretical; i.e., it is associated with the truncation of PT series used to describe τ-lepton decay data. The uncertainty in $a_s(M_\tau)$ can be reduced if some other sources for its determination are used in addition to the τ system. Reducing the uncertainty in c-quark pole mass requires a more accurate treatment of the threshold region of $c\bar{c}$ production, which is a rather challenging problem in QCD.

5. RG EVOLUTION OF THE EM COUPLING IN THE $\overline{MS}$ SCHEME

With the boundary value known at a sufficiently large scale, where the PT expression for the EM β-function is applicable, one can run the EM coupling to larger scales. The final goal is the determination of a numerical value for the EM coupling at M_Z in order to perform high-precision tests of the SM. The running itself (as a functional) is extremely precise because β functions are very well known. The precision of running is affected by the initial value of a_s, which is chosen to be $a_s^{(3)}(M_\tau^2)$, and by the b-quark mass m_b.

5.1. Basic Relations for the RG Evolution

For the evolution between the τ-lepton mass $M_\tau = 1.777$ GeV (numerically, $m_c = M_\tau$) and $M_Z = 91.187$ GeV, the number of active quarks is either four or five and only one threshold at m_b is encountered. The evolution equation (running) is written in the form

$$-\mu^2\frac{d}{d\mu^2}\left(\frac{3\pi}{\bar{\alpha}(\mu^2)}\right) = 3\left(1+\frac{3}{4}\frac{\bar{\alpha}}{\pi}\right) \qquad (45)$$
$$+\left(\frac{10}{3}+\frac{1}{3}\theta_b\right)+\left(\frac{17}{18}+\frac{1}{36}\theta_b\right)\frac{\bar{\alpha}}{\pi}$$
$$-\left(\frac{34}{27}+\frac{1}{27}\theta_b\right)\frac{\bar{\alpha}}{4\pi}a_s + a_s h^{\rm QCD}(a_s),$$

where $h^{\rm QCD}(a_s)$ describes effects of strong interactions. Here, θ_b is a parameter for the b-quark presence, $n_f = 4 + \theta_b$. From M_τ to m_b, one has $n_f = 4$ and $\theta_b = 0$, while, from m_b to M_Z, one has $n_f = 5$ and $\theta_b = 1$. In Eq. (45), the strong coupling $a_s(\mu^2)$ obeys the RG equation

$$\mu^2\frac{d}{d\mu^2}a_s(\mu^2) = \beta(a_s(\mu^2)) + a_s^2\frac{\bar{\alpha}}{8\pi}\left(\sum_q e_q^2\right), \qquad (46)$$

with

$$\beta(a_s) = -a_s^2(\beta_0+\beta_1 a_s \qquad (47)$$
$$+\beta_2 a_s^2+\beta_3 a_s^3)+\mathcal{O}(a_s^6)$$

being the strong-interaction β function. In QCD, one has

$$h^{\rm QCD}(a_s) = \left(\frac{10}{3}+\frac{1}{3}\theta_b\right) \qquad (48)$$
$$\times\left\{1+a_s\left(\frac{287}{144}-\frac{11}{72}\theta_b\right)+a_s^2\left(\frac{38551}{15552}\right.\right.$$
$$\left.\left.-\frac{7595}{7776}\theta_b-\frac{77}{3888}\theta_b^2-\frac{55}{54}\zeta(3)(1+\theta_b)\right)\right\}$$
$$+a_s^2\left(\frac{2}{3}-\frac{1}{3}\theta_b\right)^2\left(\frac{55}{72}-\frac{5}{3}\zeta(3)\right),$$

where the first three lines give the "direct" contribution and the fourth line gives the light-by-light contribution, which is written separately because of its different color structure. This result is obtained from the photon renormalization constant given in [25] and explicitly written in [42, 49]. It was used in [23] to calculate the evolution of the EM coupling constant. Numerically, one finds

$$h^{\mathrm{QCD}}(a_s) = \left(\frac{10}{3} + \frac{1}{3}\theta_b\right) \tag{49}$$
$$\times \left(1 + a_s(1.993 - 0.153\theta_b)\right.$$
$$\left.+ a_s^2(1.26 - 2.20\theta_b - 0.02\theta_b^2)\right)$$
$$+ a_s^2(-0.55 + 0.55\theta_b - 0.14\theta_b^2).$$

The coefficients of the EM β function are small, which makes the convergence of PT series for the evolution rather fast. Equations (45) and (46) should be solved simultaneously. However, the EM coupling $\bar{\alpha}(\mu)$ is small; therefore, we neglect its running in the corrections and substitute there the value numerically equal to the fine-structure constant α. Then, one has to integrate the trajectory of the strong coupling $a_s(\mu)$, which is given by the solution to the RG equation (46). The α correction in the strong-coupling β function is numerically of order a_s^2 and formally should be retained if a_s^4 terms in the β function are retained. However, the main contribution to the running comes from the partonic part of the EM β function in Eq. (45); i.e., it is independent of both EM and strong couplings. Other terms give only small corrections. As for practical calculations, one can do everything numerically; however, it happens that the two-loop running gives almost the same result as an exact treatment. With the two-loop accuracy, integration can be done analytically in a simple form. Indeed, for $\beta(a_s) = -\beta_0 a_s^2 - \beta_1 a_s^3$, one finds

$$\int\limits_{\mu_1^2}^{\mu_2^2} a_s(\xi) d\ln\xi = \frac{1}{\beta_0}\ln\left(\frac{\beta_0/a_s(\mu_2^2) + \beta_1}{\beta_0/a_s(\mu_1^2) + \beta_1}\right), \tag{50}$$

$$\int\limits_{\mu_1^2}^{\mu_2^2} a_s(\xi)^2 \frac{d\xi}{\xi} = -\frac{1}{\beta_1}\ln\left(\frac{\beta_0 + \beta_1 a_s(\mu_2^2)}{\beta_0 + \beta_1 a_s(\mu_1^2)}\right),$$

where the NLO solution for the running coupling $a_s(\mu)$ is given by

$$\ln\left(\frac{\mu^2}{\Lambda^2}\right) = \Phi(a_s) = \int^{a_s} \frac{d\xi}{-\xi^2(\beta_0 + \beta_1\xi)} \tag{51}$$
$$= \frac{1}{a_s\beta_0} + \frac{\beta_1}{\beta_0^2}\ln\left(\frac{a_s\beta_0^2}{\beta_0 + a_s\beta_1}\right).$$

Here, Λ is the usual RG scale of QCD. In the order that is next to the NLO (NNLO), it is also possible to perform integration along the RG trajectory explicitly, but the results are too awkward to be presented here. In fact, the NLO integration as given in Eqs. (50) and (51) is rather precise numerically and can be used for preliminary estimates. However, we avoid any approximation of this sort (cf. [23]) and give numbers for a direct numerical treatment of RG Eqs. (45) and (46) with the four-loop strong-coupling β function from Eq. (47) and the function h^{QCD} from Eq. (48).

The solution to the RG equation can be used for the range of μ where the corresponding effective theory (with a given number of active leptons and quarks) is valid. Because decoupling is not automatic, one should explicitly take into account thresholds.

5.2. Running to m_b

The first scale of interest is m_b, which is relevant to describing the physics of $b\bar{b}$ production near the threshold and accurate data on Υ resonances (note that the real threshold energy is in fact $2m_b$, but the matching is defined at m_b). We use $m_b = 4.8 \pm 0.2$ GeV as determined in [50].

In the approximation where the EM coupling is taken to be constant in the correction, the contribution of leptons is given by

$$\Delta_{\tau b}^{\mathrm{lept}}(m_b^2) = 3\left(1 + \frac{3}{4}\frac{\alpha}{\pi}\right)\ln\frac{m_b^2}{M_\tau^2} \tag{52}$$
$$= 3\left(1 + \frac{3}{4}\frac{\alpha}{\pi}\right)\cdot 1.98738 = 5.9725.$$

The hadronic part is more involved. In the energy range from M_τ to m_b, the number of active quarks is four or $\theta_b = 0$. The partonic part of the quark contribution reads

$$\Delta_{\tau b}^{(0)}(m_b^2) = N_c\sum_q e_q^2\left(1 + e_q^2\frac{3}{4}\frac{\bar{\alpha}}{\pi}\right)\ln\frac{m_b^2}{M_\tau^2} \tag{53}$$
$$= \left(\frac{10}{3} + \frac{17}{18}\frac{\alpha}{\pi}\right)\ln\frac{m_b^2}{M_\tau^2} = 6.62896,$$

where we use $\bar{\alpha} = \alpha$. The result is independent of the strong-coupling constant (the parton-model result without real QCD interaction). The quark part beyond the partonic approximation requires integrating the evolution trajectory of the strong coupling in $n_f = 4$ effective theory. The initial value of the strong coupling is $a_s^{(4)}(M_\tau^2) = 0.102001$, as was obtained from matching at M_τ^2 for the c-quark contribution. In the NLO, one still finds the sizable contribution

$$\Delta_{\tau b}^{(1)}(m_b^2) = \left(\frac{10}{3} - \frac{17}{54}\frac{\alpha}{\pi}\right) I_{\tau b}^{(1)} = 0.54878. \tag{54}$$

The NNLO contribution proportional to a_s^2 in Eq. (45),

$$\Delta_{\tau b}^{(2)}(m_b^2) = \frac{10}{3}\frac{287}{144} I_{\tau b}^{(2)} = 0.091848, \tag{55}$$

and the NNNLO (next to the NNLO) contribution proportional to a_s^3 in Eq. (45),

$$\Delta_{\tau b}^{(3)}(m_b^2) = \left(\frac{200675}{23328} - \frac{335}{81}\zeta(3)\right) I_{\tau b}^{(3)} \tag{56}$$
$$= 3.63085 I_{\tau b}^{(3)} = 0.0042699,$$

give only small corrections. Here, we have

$$I_{\tau b}^{(n)} = \int\limits_{M_\tau^2}^{m_b^2} (a_s^{(4)}(s))^n \frac{ds}{s}.$$

The total correction to the parton-model result (i.e., QCD contribution)

$$\Delta_{\tau b}^{\mathrm{had.cor}}(m_b^2) = \Delta_{\tau b}^{(1)}(m_b^2) + \Delta_{\tau b}^{(2)}(m_b^2) \tag{57}$$
$$+ \Delta_{\tau b}^{(3)}(m_b^2) = 0.644899$$

is much smaller than the leading partonic result $\Delta_{\tau b}^{(0)}(m_b^2)$. For the EM coupling at m_b, one finds

$$\frac{3\pi}{\bar\alpha^{(4)}(m_b^2)} = \frac{3\pi}{\bar\alpha^{(4)}(M_\tau^2)} \tag{58}$$
$$- (5.9725 + 6.6290 + 0.6449)$$
$$= \frac{3\pi}{\bar\alpha^{(4)}(M_\tau^2)} - 13.2464.$$

The lepton and parton contributions dominate. Collecting all together, one finds

$$\frac{3\pi}{\bar\alpha^{(4)}(m_b^2)} = \frac{3\pi}{\bar\alpha^{(4)}(M_\tau^2)} - 13.2464 \tag{59}$$
$$= \frac{3\pi}{\alpha} - (32.7889 + 13.2464) = \frac{3\pi}{\alpha} - 46.0353.$$

And finally, we have

$$\frac{1}{\bar\alpha^{(4)}(m_b^2)} = 132.152 \tag{60}$$

or

$$\bar\alpha^{(4)}(m_b^2) = 1.037\alpha. \tag{61}$$

This number can be used to analyze Υ-resonance physics.

Because decoupling is not explicit in mass-independent renormalization schemes, there is another EM coupling parameter related to the scale m_b. Upon changing the number of active quarks to $n_f = 5$, one obtains

$$\frac{3\pi}{\bar\alpha^{(4)}(m_b^2)} = \frac{3\pi}{\bar\alpha^{(5)}(m_b^2)} + \Pi^{b\mathrm{full}}(\mu^2 = m_b^2, 0). \tag{62}$$

The polarization function $\Pi^{b\mathrm{full}}(\mu^2 = m_b^2, 0)$, which gives a corresponding shift for the EM constant is written in terms of the effective strong-coupling constant $a_s^{(5)}(m_b^2)$. A numerical value for $a_s^{(5)}(m_b^2)$ is obtained through matching the strong coupling at the scale m_b. The running of the coupling $a_s^{(4)}(M_\tau^2) = 0.102$ to $m_b = 4.8$ GeV gives $a_s^{(4)}(m_b^2) = 0.06851$ ($\alpha_s^{(4)}(m_b^2) = 0.2152$). Then, matching at m_b results in $a_s^{(5)}(m_b^2) = 0.06869$. With this number, the result of matching for the EM constant is

$$\Delta^b(m_b^2) = \Pi^{b\mathrm{full}}(\mu^2 = m_b^2, 0) \tag{63}$$
$$= \Pi^{b\mathrm{dir}}(\mu^2 = m_b^2, 0) + \Pi^{b\mathrm{loop}}(\mu^2 = m_b^2, 0)$$
$$= 0.00024_{\mathrm{EM}} + 0.00358_{\mathrm{loop}} + 0.08587$$
$$+ 0.03437 = 0.1241.$$

The EM contribution is totally negligible. The loop contribution is rather small. The PT convergence of the direct contribution is not fast and is similar to the c-quark case. One has

$$\Delta^b(m_b^2) = 0.1241. \tag{64}$$

Finally, the EM couplings of $n_f = 4$ and $n_f = 5$ effective theories in the vicinity of m_b are related by the equation

$$\frac{3\pi}{\bar\alpha^{(5)}(m_b^2)} = \frac{3\pi}{\bar\alpha^{(4)}(m_b^2)} - \Delta^b(m_b^2) \tag{65}$$
$$= \frac{3\pi}{\bar\alpha^{(4)}(m_b^2)} - 0.1241.$$

Explicitly, one finds

$$\bar\alpha^{(5)}(m_b^2) = \frac{1}{132.138} = 1.0001\bar\alpha^{(4)}(m_b^2).$$

This difference can be safely neglected in applications to Υ-resonance physics.

The uncertainty due to m_b is tiny. Indeed, the error in the b-quark mass leads to the uncertainty

$$\delta\Delta^b(m_b^2) = -\frac{1}{3}(1 + a_s^{(5)}(m_b^2))\frac{2\delta m_b}{m_b} \tag{66}$$
$$= -\frac{2}{3}(1 + a_s^{(5)}(m_b^2))\frac{\delta m_b}{m_b} = \pm 0.030.$$

There are two reasons for this smallness in relation to the c-quark case: the electric charge of the b quark, $|e_b|$, is two times smaller than $|e_c|$, and the relative uncertainty in the b-quark mass m_b ($\delta m_b/m_b$) is much smaller than that of the c-quark mass. Note that, because the contribution $\Delta^b(m_b^2)$ itself is small, the relative uncertainty $\delta\Delta^b(m_b^2)/\Delta^b(m_b^2)$ is huge. However, one cannot use it here. Even for $\Delta^b(m_b^2) = 0$, the uncertainty $\delta\Delta^b(m_b^2)$ is basically 0.030.

5.3. Running from m_b to M_Z

In this subsection, we describe the evolution of the EM coupling constant $\bar{\alpha}^{(5)}(m_b^2)$ from $m_b = 4.8$ GeV to $M_Z = 91.187$ GeV. Various contributions according to Eqs. (45) and (48) are the following:

the leptonic contribution

$$\Delta_{bZ}^{\text{lept}} = 3\left(1 + \frac{3}{4}\frac{\alpha}{\pi}\right)\ln\frac{M_Z^2}{m_b^2} = 17.6966; \qquad (67)$$

the leading quark-partonic a_s-independent contribution

$$\Delta_{bZ}^{(0)} = \left(\frac{11}{3} + \frac{35}{36}\frac{\alpha}{\pi}\right)\ln\frac{M_Z^2}{m_b^2} = 21.6048; \qquad (68)$$

the NLO contribution with $a_s^{(5)}(m_b^2) = 0.06869$ as an initial value for the evolution trajectory,

$$\Delta_{bZ}^{(1)} = \left(\frac{11}{3} - \frac{35}{108}\frac{\alpha}{\pi}\right) I_{bZ}^{(1)} = 1.0780; \qquad (69)$$

the NNLO contribution proportional to a_s^2,

$$\Delta_{bZ}^{(2)} = \frac{11}{3}\frac{265}{144} I_{bZ}^{(2)} = 0.10213; \qquad (70)$$

and the NNNLO contribution proportional to a_s^3,

$$\Delta_{bZ}^{(3)} = \left(\frac{257543}{46656} - \frac{620}{81}\zeta(3)\right) I_{bZ}^{(3)} \qquad (71)$$
$$= -3.68089 I_{bZ}^{(3)} = -0.002954.$$

Here, we have

$$I_{bZ}^{(n)} = \int\limits_{m_b^2}^{M_Z^2} (a_s^{(5)}(s))^n \frac{ds}{s}.$$

The total QCD correction to the partonic result

$$\Delta_{bZ}^{\text{had.cor}} = \Delta_{bZ}^{(1)} + \Delta_{bZ}^{(2)} + \Delta_{bZ}^{(3)} = 1.1772 \qquad (72)$$

is small in relation to the leading quark-partonic a_s-independent contribution given in Eq. (68). The total effect of running over the interval from m_b to M_Z,

$$\Delta_{bZ}^{\text{lept}} + \Delta_{bZ}^{(0)} + \Delta_{bZ}^{\text{had.cor}} \qquad (73)$$
$$= 17.6966 + 21.6048 + 1.1772 = 40.479,$$

is dominated by leptons and by the quark-partonic contribution. We find the EM coupling at M_Z expressed in terms of the EM coupling at m_b in the form

$$\frac{3\pi}{\bar{\alpha}^{(5)}(M_Z^2)} = \frac{3\pi}{\bar{\alpha}^{(5)}(m_b^2)} - 40.479. \qquad (74)$$

This equation gives the relation between the running EM couplings necessary for applications in b- and Z-physics.

Table 1. Leptonic contributions

Range	0–M_τ	M_τ–m_b	m_b–M_Z	Total
Δ^{lept}	22.011	5.973	17.697	45.681

Collecting together Eqs. (40), (58), (64), and (74), we find the absolute value of the running EM coupling at M_Z expressed in terms of the fine-structure constant α,

$$\frac{3\pi}{\bar{\alpha}^{(5)}(M_Z^2)} = \frac{3\pi}{\alpha} - 32.7889(\text{match } M_\tau) \qquad (75)$$
$$- 13.2464(\text{run } m_c 2 m_b) - 0.1241(\text{match } m_b)$$
$$- 40.479(\text{run } m_b 2 M_Z) = \frac{3\pi}{\alpha} - 86.6384$$

and

$$\frac{1}{\bar{\alpha}^{(5)}(M_Z^2)} = \frac{1}{\alpha} - 86.6384/(3\pi) \qquad (76)$$
$$= 137.036 - 9.1926 = 127.843.$$

The result can be written as a relation between the running EM coupling and the fine-structure constant:

$$\bar{\alpha}^{(5)}(M_Z^2) = 1.0719\alpha. \qquad (77)$$

This number can be used for a Z-boson-peak analysis.

6. SUMMARY OF THE RESULTS

In this section, we give a brief summary of the calculation, paying attention to uncertainties in the results (see Tables 1–4).

The uncertainty in the low-energy normalization value at the τ mass is given in Eqs. (42)–(44). It is largely dominated by the uncertainty due to the c-quark contribution. Adding uncertainties

$$\delta\Delta^{(4)}(M_\tau^2) = \pm 0.078_{\text{light}} \pm 0.330_c$$

in quadrature, one finds

$$\delta\Delta^{(4)}(M_\tau^2) = \pm 0.339$$

and

$$0.339/(3\pi) = 0.036.$$

Finally, one finds for the low-energy normalization value of the running EM coupling that

$$\frac{1}{\bar{\alpha}^{(4)}(M_\tau^2)} = 133.557 \pm 0.036. \qquad (78)$$

The total error is dominated by the uncertainty due to the c-quark matching contribution, which is mainly given by the uncertainty in the c-quark mass.

Table 2. Matching at various scales

Matching	$\Delta^{uds}(M_\tau)$	$\Delta^{c}(M_\tau)$	$\Delta^{b}(m_b)$
Value	9.9312 ± 0.078	0.8468 ± 0.330	0.1241 ± 0.030

Table 3. Running of powers of a_s

Power	$M_\tau - m_b$	$m_b - M_Z$	Total
$\Delta^{(0)} \sim a_s^0$	6.6290	21.605	28.234
$\Delta^{(1)} \sim a_s^1$	0.5488	1.078	1.627
$\Delta^{(2)} \sim a_s^2$	0.0918	0.102	0.194
$\Delta^{(3)} \sim a_s^3$	0.0043	-0.003	0.001
Total sum	7.2739	22.782	30.056
$\Delta^{\text{had.cor}}$	0.6449	1.177	1.822

Table 4. Quantity $I^{(1)}_{\tau b}$ from Eq. (54) in different orders of the strong β function and with or without the EM contribution to the strong β function

Order	$I^{(1)}_{\tau b}$ with EM	$I^{(1)}_{\tau b}$ without EM
LO	0.169104	0.169100
NLO	0.165542	0.165538
NNLO	0.164938	0.164934
NNNLO	0.164671	0.164667

For the scales m_b and M_Z, the errors due to running, which arise basically because of the uncertainty in the coupling constant a_s, should be included. The running itself is precise because the β functions in Eqs. (45) and (46) are computed up to a high order of PT and because the coupling constant a_s is rather well known. The dominant contribution comes from leptons and partonic quarks and is independent of the genuine QCD interaction (see Tables 1, 3). The EM terms give a tiny correction. Table 4 presents the quantity $\int_{M_\tau^2}^{m_b^2} a_s(s)ds/s$ with running for $a_s(s)$ in different orders and with or without the EM contribution to the strong β function. The inclusion of EM terms slows down the decrease in the strong coupling, and the integrals are slightly larger; still, it is completely negligible numerically. In the leading order, we have the uncertainty in the integrals due to errors in the initial value of the strong coupling,

$$\delta I^{(1)}_{ab} = \frac{L_{ab}}{1 + a_s\beta_0 L_{ab}}\delta a_s \tag{79}$$

with $L_{ab} = \ln(\mu_b^2/\mu_a^2)$. This equation suffices for estimating the error of the QCD contribution to running. The NNLO and NNNLO terms give only small corrections. One can also find the uncertainty in the running by varying the initial value of a_s in the numerical evaluation of the evolution. The results obtained are close numerically to the estimate given in Eq. (79). However, Eq. (79) has an advantage of being analytic and simple, which makes the evaluation of the error more transparent.

At m_b (and M_Z), errors due to running and due to matching the light-quark contribution at M_τ are not independent: both are determined mainly by the uncertainty in a_s. Therefore, these errors should be added linearly.

For the interval from M_τ to m_b one finds from Eq. (79) that

$$\delta\Delta^{\text{had.cor}}_{\tau b}|_{a_s} = 4.56\delta a_s = 0.025,$$

and the total error (with linearly added errors for matching the light-quark contribution at M_τ and running) is

$$\delta\Delta^{(5)}(m_b^2) = \pm(0.078 + 0.025)_{\text{light+run}} \pm 0.330_c$$
$$\pm 0.030_b = \pm 0.103_{\text{light+run}} \pm 0.330_c \pm 0.030_b.$$

Adding independent errors in quadrature, one has

$$\delta\Delta^{(5)}(m_b^2) = \pm 0.347$$

and

$$0.347/(3\pi) = 0.0368.$$

Finally, one finds that the uncertainty for the EM coupling at m_b is

$$\frac{1}{\bar{\alpha}^{(4)}(m_b)} \approx \frac{1}{\bar{\alpha}^{(5)}(m_b)} = \frac{1}{\alpha} - \Delta^{(5)}(m_b^2) \tag{80}$$
$$= 137.036 - (4.89766 \pm 0.0368)$$
$$= 132.138 \pm 0.0368.$$

For the scale M_Z, the error due to running is estimated at

$$\delta\Delta^{\text{had.cor}}_{\tau Z}|_{a_s} = \frac{11}{3}\delta I^{(1)}_{\tau Z}(a_s(m_b^2)) = 13.6\delta a_s = 0.074,$$

which leads to

$$\delta\Delta^{(5)}(M_Z^2) = \pm 0.078_{\text{light}} \pm 0.330_c \pm 0.030_b \tag{81}$$
$$\pm 0.074_{\text{run}} = \pm 0.152_{\text{light+run}} \pm 0.330_c \pm 0.030_b.$$

Adding independent errors in quadrature, one has

$$\delta\Delta^{(5)}(M_Z^2) = \pm 0.3646$$

and

$$0.3646/(3\pi) = 0.0387.$$

These estimates give the error for the coupling at M_Z:

$$\frac{1}{\bar{\alpha}^{(5)}(M_Z^2)} = 127.843 \pm 0.039. \tag{82}$$

Equation (82) is the final result for the running EM coupling at M_Z. However, it cannot be directly compared with the results of the standard analyses because the quantity in Eq. (82) is defined in a different scheme. We consider the uncertainty in Eq. (82) as rather conservative.

7. COMPARISON WITH OTHER SCHEMES

With the number from Eq. (82), one can find the on-shell parameter $\alpha_{\rm os}$ at M_Z using the relation

$$\frac{3\pi}{\alpha_{\rm os}(\mathbf{q}^2)} = \frac{3\pi}{\alpha} + \Pi_{\rm os}(\mathbf{q}^2) \tag{83}$$
$$= \frac{3\pi}{\bar{\alpha}^{(5)}(\mu^2)} + \Pi^{(5)}(\mu^2, \mathbf{q}^2).$$

In addition, one has to compute $\Pi^{(5)}(\mu^2, \mathbf{q}^2)$ in $n_f = 5$ effective theory at the point $q^2 \sim M_Z^2$. We have restored the notation q^2: the new variable q^2 will be used in the Minkowskian domain. In order to compute the leading part of $\Pi^{(5)}(\mu^2, \mathbf{q}^2)$ in the kinematical range $\mu^2 \sim \mathbf{q}^2 \sim M_Z^2$, one can consider all five active quarks (u, d, s, c, b) and all three leptons as massless and use Eq. (10) with the only change because of a different number of active quarks, which is now five instead of three. This change affects only a_s^2 order in Eq. (10) and changes nothing for leptons in the NLO approximation. For light quarks, the generic polarization function is given by

$$\Pi^{\text{light}-n_f}(\mu^2, \mathbf{q}^2) = \ln\frac{\mu^2}{\mathbf{q}^2} + \frac{5}{3} \tag{84}$$
$$+ a_s\left(\ln\frac{\mu^2}{\mathbf{q}^2} + \frac{55}{12} - 4\zeta(3)\right)$$
$$+ a_s^2\left\{\frac{\beta_0(n_f)}{2}\ln^2\frac{\mu^2}{\mathbf{q}^2} + \left(\frac{365}{24} - \frac{11}{12}n_f\right.\right.$$
$$\left. - 4\beta_0(n_f)\zeta(3)\right)\ln\frac{\mu^2}{\mathbf{q}^2} + \frac{41927}{864} - \frac{3701}{1296}n_f$$
$$\left. - \left(\frac{829}{18} - \frac{19}{9}n_f\right)\zeta(3) + \frac{25}{3}\zeta(5)\right\}$$

with $\beta_0(n_f) = (11 - (2/3)n_f)/4$. For a more accurate evaluation of $\Pi^{(5)}(\mu^2, \mathbf{q}^2)$ at the scale M_Z, we retain the leading corrections due to the b- and c-quark masses and the τ-lepton mass and the leading correction due to the t-quark contribution. One finds

$$\Pi^{(5)}(\mu^2, \mathbf{q}^2) = 3\Pi^{\text{light-lept}}(\mu^2, \mathbf{q}^2) \tag{85}$$
$$+ \frac{11}{3}\Pi^{\text{light-quark}}(\mu^2, \mathbf{q}^2) - \left(\frac{1}{3}\right)\frac{6m_b^2}{\mathbf{q}^2}$$
$$- \left(\frac{4}{3}\right)\frac{6m_c^2}{\mathbf{q}^2} - \frac{6M_\tau^2}{\mathbf{q}^2} + \Delta_{(t)}\Pi^{(5)}(\mu^2, \mathbf{q}^2).$$

Note that the power-law correction due to a quark mass is exact up to the a_s^2 order when expressed in terms of the pole mass. The corrections due to the t-quark contribution, $\Delta_{(t)}\Pi^{(5)}(\mu^2, \mathbf{q}^2)$, for the quantity $\Pi^{(5)}(\mu^2, \mathbf{q}^2)$ at $\mathbf{q}^2 \approx M_Z^2$ can be computed as a power series in $\mathbf{q}^2/m_t^2$; the expansion parameter $\mathbf{q}^2/m_t^2$ is small at the point $\mathbf{q}^2 = M_Z^2$ for $m_t = 175$ GeV. Indeed, retaining only the leading term and the first corrections, one has

$$\Delta_{(t)}\Pi^{(5)}(M_Z^2, \mathbf{q}^2) \tag{86}$$
$$= -\frac{4}{15}\frac{\mathbf{q}^2}{m_t^2}\left\{1 + \frac{410}{81}a_s^{(5)}(M_Z^2) - \frac{3}{28}\frac{\mathbf{q}^2}{m_t^2}\right\}.$$

A typical expansion in Eq. (86) reads

$$\Delta_{(t)}\Pi^{(5)}(M_Z^2, M_Z^2) = -0.0724 \tag{87}$$
$$- 0.0138_{a_s} + 0.0021_{M_Z} = -0.0841$$

with the obvious notation indicating the origin of different contributions. We do not take into account bosons, and W-boson loops should be analyzed separately.

To calculate the on-shell coupling $\alpha_{\rm os}(\mathbf{q}^2)$ at the scale M_Z by using Eq. (83), one can use either $\mathbf{q}^2 = M_Z^2$ (Euclidean definition) [51] or $q^2 = -\mathbf{q}^2 = M_Z^2$ with taking the real part of the correlation function (Minkowskian definition). The Minkowskian definition is usually discussed in the literature. Note that we calculate not the e^+e^--scattering amplitude at the total energy M_Z ($q^2 = M_Z^2$), which definitely should be taken at a physical point on the cut in the case of cross-section calculations, but the coupling constant, which parametrizes this amplitude at the scale M_Z. Within the RG approach, the scale of the parameters of an effective theory valid in a given energy range should not coincide with any actual physical value of the energy or momentum squared (see, e.g., [52]).

First, we use the Euclidean definition for the on-shell coupling, which is consistently perturbative and requires computing the correlation function $\Pi^{(5)}(M_Z^2, \mathbf{q}^2)$ in a deep Euclidean domain for $\mathbf{q}^2 = M_Z^2$. Using Eqs. (85) and (86), one finds the expansion

$$\Pi^{(5)}(M_Z^2, M_Z^2) = 11.1111 - 0.03097_{a_s} \tag{88}$$
$$+ 0.00112_{a_s^2} - 0.00168_{\rm EM} - 0.00554_b$$
$$- 0.00304_c - 0.00228_\tau - 0.0841_t$$
$$= 11.0796 - 0.01086_{bc\tau} - 0.0841_t.$$

Note that the EM correction is numerically of order a_s^2. Still, these corrections are very small. From

Eq. (83), we find

$$\frac{3\pi}{\alpha_{\mathrm{os}}(M_Z^2)} = \frac{3\pi}{\bar\alpha^{(5)}(M_Z^2)} + \Pi^{(5)}(M_Z^2, M_Z^2)$$
$$= \frac{3\pi}{\alpha} - 86.6384 + 11.0796 - 0.01086_{bc\tau} - 0.0841_t$$
$$= \frac{3\pi}{\alpha} - 75.5588 - 0.01086_{bc\tau} - 0.0841_t.$$

For the sake of clarity, we retain the contribution of power-law corrections separately for a further comparison with the results in the Minkowskian domain. One has numerically

$$\frac{1}{\alpha_{\mathrm{os}}(M_Z^2)} = \frac{1}{\alpha} - (75.5588 + 0.01086_{bc\tau}$$
$$+ 0.0841_t)/(3\pi) = 137.036 - 8.0271 = 129.009.$$

Because the error estimate in Eq. (82) is not affected by this change of the scheme (overly small and rather precise contributions are added), the final result for the on-shell coupling within the Euclidean definition reads

$$\frac{1}{\alpha_{\mathrm{os}}(M_Z^2)} = 129.009 \pm 0.039. \qquad (89)$$

However, the reference values for the on-shell coupling available in the literature are given in the Minkowskian domain for $q^2 = -\mathbf{q}^2 = M_Z^2$, i.e., for the real part of the correlation function $\Pi^{(5)}(M_Z^2, q^2)$ computed on the physical cut. Within the approximation used, going to the Minkowskian domain of momenta q^2 changes only the term of order a_s^2 and power-law corrections in Eq. (88). Indeed, in Eq. (84), the only term that is numerically affected by the transition to the Minkowskian domain is $\ln^2(\mu^2/\mathbf{q}^2)$, with the following change in relation to the Euclidean result:

$$\mathrm{Re}\left\{\ln^2\left(\frac{\mu^2}{-M_Z^2}\right)\right\} = \ln^2\left(\frac{\mu^2}{M_Z^2}\right) - \pi^2. \qquad (90)$$

Instead of Eq. (88), one finds

$$\mathrm{Re}\left\{\Pi^{(5)}(M_Z^2, -M_Z^2)\right\} \qquad (91)$$
$$= 11.0796 - 0.04893_{\pi^2} + 0.01086_{bc\tau\mathrm{Mink}}$$
$$+ 0.08828_{t\mathrm{Mink}} = 11.1298$$

and

$$\mathrm{Re}\frac{1}{\alpha_{\mathrm{os}}(-M_Z^2)} = 137.036$$
$$- (86.6384 - 11.1298)/(3\pi) = 129.024.$$

The final result for the on-shell coupling with the Minkowskian definition is

$$\mathrm{Re}\frac{1}{\alpha_{\mathrm{os}}(-M_Z^2)} = 129.024 \pm 0.039. \qquad (92)$$

The difference between the central numerical values for the couplings in Eq. (89), which gives the Euclidean definition, and in Eq. (92), which gives the Minkowskian definition, is 0.015. Note that the Euclidean definition was considered in [51], where the numerical difference of about 0.02 from the Minkowskian definition was found from a rather simplified treatment. It is close to the present, more accurate result 0.015. Note that the point M_Z is safe for the PT calculation in the Minkowskian domain for the approximation used (no singularities of the spectrum near this point). At other points, this is not so even in the approximation in which we work. For instance, if the Υ-resonance mass m_Υ is taken as a reference scale, then the Euclidean definition is equally applicable at this point being still perturbative, while the Minkowskian definition faces the problem that the polarization function on the cut is not smooth. A phenomenological approach based on a direct integration of data fails because of the fast change in the spectrum at the location of the Υ resonance, which makes integration with the principal-value prescription for regularizing the singularities ill-defined. A theory-based approach within PT fails at the point m_Υ because PT calculations for the correlation function near the threshold on the physical cut ($m_\Upsilon \sim 2m_b$) are not reliable. Therefore, the Minkowskian definition is not uniformly applicable at any scale.

The result given in Eq. (92) differs from some recent determinations based on the use of experimental data for performing integration over the low-energy region. For the result of [16],

$$\mathrm{Re}\frac{1}{\alpha_{\mathrm{os}}(-M_Z^2)} = 128.925 \pm 0.056, \qquad (93)$$

the number obtained in the present study and given in Eq. (92) almost touches the reference value in Eq. (93) within 1σ (σ is a standard deviation). The results of some other groups are concentrated around the same central value as in Eq. (93) but with much smaller errors. For a further comparison, we use the result

$$\mathrm{Re}\frac{1}{\alpha_{\mathrm{os}}(-M_Z^2)} = 128.927 \pm 0.023, \qquad (94)$$

which was presented in [17].

The difference between the value from Eq. (92) and the reference result in Eq. (94) is $129.024 - 128.927 = 0.097$, which constitutes $(2{-}4)\sigma$ and can be significant. Therefore, we discuss the difference in more detail.

The usual parametrization of the fermionic contributions to the on-shell running EM coupling at M_Z reads

$$\mathrm{Re}\frac{1}{\alpha_{\mathrm{os}}(-M_Z^2)}$$

$$= \frac{1}{\alpha}\left(1 - \Delta\alpha_{\text{lep}} - \Delta\alpha^{(5)}_{\text{had}} - \Delta\alpha_{\text{top}}\right)$$

(note that

$$\text{Re}\left(\frac{1}{\alpha_{\text{os}}(-M_Z^2)}\right) \neq \frac{1}{\text{Re}\alpha_{\text{os}}(-M_Z^2)},$$

although the difference is tiny). The total leptonic contribution to the EM coupling constant at M_Z given in the last column of Table 1 reads

$$\Delta^{\text{lept}}(M_Z^2) = 45.681.$$

The leptonic part of $\Pi^{(5)}(M_Z^2, -M_Z^2)$ reads

$$\text{Re}\left\{\Pi^{(5)\text{lept}}(M_Z^2, -M_Z^2)\right\}$$
$$= 3\text{Re}\left(\Pi^{\text{light-lept}}(M_Z^2, -M_Z^2)\right) + \frac{6M_\tau^2}{M_Z^2}$$
$$= 4.9988 + 0.0023 = 5.0011.$$

The leading-order contribution is equal to five, while the EM and τ-lepton-mass corrections are small. For the total leptonic contribution to the on-shell coupling in the Minkowskian domain, one finds

$$\Delta\alpha_{\text{lept}} = \frac{\alpha}{3\pi}(45.681 - 5.001) = 314.974 \times 10^{-4},$$

which is close to the value

$$\Delta\alpha_{\text{lept}}|_{\text{ref}} = (314.19 + 0.78) \times 10^{-4}$$
$$= 314.97 \times 10^{-4},$$

which is quoted in [17].

For the top contribution in the Minkowskian domain, one finds from Eq. (86) [see also Eq. (91)] that

$$\Delta\alpha_{\text{top}} = \frac{\alpha}{3\pi}(-0.0883) = -0.68 \times 10^{-4},$$

while the value that the authors of [17] obtained, taking more accurately into account higher order corrections, is

$$\Delta\alpha_{\text{top}}|_{\text{ref}} = -0.70 \times 10^{-4}.$$

The difference is small and is neglected. From the numerical value given in Eq. (92), the total contribution of fermions to the shift of the EM coupling is determined to be

$$\Delta\alpha_{\text{lep}} + \Delta\alpha_{\text{top}} + \Delta\alpha^{(5)}_{\text{had}}$$
$$= 1 - \alpha(129.024 \pm 0.039) = 0.0584664 \pm 0.000285.$$

Taking $\Delta\alpha_{\text{lept}}$ and $\Delta\alpha_{\text{top}}$ as exact quantities (no errors), one finds the following numerical value for $\Delta\alpha^{(5)}_{\text{had}}$:

$$\Delta\alpha^{(5)}_{\text{had}} = (0.0584664 \pm 0.000285) - 0.031497 \quad (95)$$
$$+ 0.000068 = (270.37 \pm 2.85) \times 10^{-4}.$$

At the same time, the result of [17] is

$$\Delta\alpha^{(5)}_{\text{had}}\Big|_1 = (277.45 \pm 1.68) \times 10^{-4}, \quad (96)$$

and the number of [16] is

$$\Delta\alpha^{(5)}_{\text{had}}\Big|_2 = (277.6 \pm 4.1) \times 10^{-4}. \quad (97)$$

The difference between the central values given in Eq. (95) and Eqs. (96) and (97) is about $(2–4)\sigma$ depending on the numerical value of the error quoted:

$$277.45 - 270.37 = 7.08 \approx 2.5 \cdot 2.85$$
$$\approx 4.3 \cdot 1.68 \approx 1.7 \cdot 4.1.$$

This difference can be significant. Therefore, we discuss the sensitivity of our prediction in (95) [and of Eq. (82), from which it is uniquely obtained] to the numerical values of the parameters used in the theoretical calculation of the present study. If $m_s = 0$, then the ρ and φ channels should be theoretically degenerate because there is no reason for them to be different. This means that, in addition to annihilating explicit corrections due to m_s^2 in Eq. (22), one should identify m_{Rs} with the resonance in the nonstrange channel, i.e., numerically substitute $m_{Rs} = m_\rho$ into the solution for the IR-modifying parameters in Eqs. (20). With such changes, one finds the result for $\Delta^{uds}(M_\tau^2)$ in the form

$$\Delta^{uds}(M_\tau^2)\,|_{m_s=0} = 10.23, \quad (98)$$

which generates a numerical shift of about 0.3 in the value of $\Delta^{uds}(M_\tau^2)$ in relation to the result for the nonvanishing strange-quark mass in Eq. (30). Note that, if the direct integration of the low-energy data is used, then the full dependence of the results on m_s is lost. Only the PT high-energy tail depends explicitly on m_s, but this dependence is weak. The change in $\Delta\alpha^{(5)}_{\text{had}}$ corresponding to the result in Eq. (98) is

$$\Delta\alpha^{(5)}_{\text{had}}\,|_{m_s=0} - \Delta\alpha^{(5)}_{\text{had}} = 0.3\frac{\alpha}{3\pi}$$
$$= 0.000232 = 2.3 \times 10^{-4}.$$

The use of the numerical value of $m_c = 1.6$ GeV for the c-quark mass instead of $m_c = 1.777$ GeV generates a 0.33 shift in the value of the matching quantity $\Delta^c(M_\tau^2)$, which leads to the following change in $\Delta\alpha^{(5)}_{\text{had}}$:

$$\Delta\alpha^{(5)}_{\text{had}}\Big|_{m_c=1.6} - \Delta\alpha^{(5)}_{\text{had}} = 0.33\frac{\alpha}{3\pi}$$
$$= 0.000256 = 2.6 \times 10^{-4}.$$

Note that this change cannot be found if the contributions of actual charmonium resonances are calculated directly. The total shift of $\Delta\alpha^{(5)}_{\text{had}}$ in relation to Eq. (95)

because of the change in numerical values of the theoretical parameters m_s and m_c reads

$$\Delta\alpha^{(5)}_{\text{had}}\Big|_{m_s=0,m_c=1.6} \tag{99}$$
$$= (270.37 + 2.3 + 2.6 \pm 2.85) \times 10^{-4}$$
$$= (275.27 \pm 2.85) \times 10^{-4}.$$

The change in the numerical value of the strong-coupling constant α_s from $\alpha_s(M_\tau^2) = 0.318$ to $\alpha_s(M_\tau^2) = 0.335$ gives a 0.152 shift in $\Delta^{(5)}(M_Z^2)$ [according to our error estimates in Eq. (81)] to end up with

$$\Delta\alpha^{(5)}_{\text{had}}\Big|_{m_s=0,m_c=1.6,\alpha_s=0.335} \tag{100}$$
$$= (270.37 + 2.3 + 2.6 + 1.2 \pm 2.85) \times 10^{-4}$$
$$= (276.47 \pm 2.85) \times 10^{-4}.$$

This result agrees with other estimates within 1σ. The set of numerical values for the relevant parameters used in Eq. (100) is rather close to the set used to obtain the value in Eq. (95) [$m_s = 130$ MeV, $m_c = 1.777$ GeV, $\alpha_s^{(3)}(M_\tau^2) = 0.318$]. The total shift in $\Delta\alpha^{(5)}_{\text{had}}$ for the new set of parameters in Eq. (100) is larger than the total error given in Eq. (95) because the total error is computed in quadrature, while the change in the spectrum due to $m_s = 0$ (which makes all three light-quark channels degenerate) has not been included in the total error. To distinguish definitively between the results in Eq. (100) and Eq. (95), one needs more precise numerical values of theoretical parameters.

Within the present approach, we use virtually no real data on cross sections, but we rely on the numerical values of a few theoretical parameters which are extracted from such data. These parameters are the strong-coupling constant, the quark masses, and the vacuum condensates. It is generally believed that the actual data can be properly described with these parameters if theoretical formulas are sufficiently accurate. In the case of computing the hadronic contribution to the photon vacuum polarization function in the Euclidean domain, a theoretical description is pretty accurate because PT is applicable and very precise—in fact, the PT results in this area are almost the best ones available among all PT calculations. An additional reason for such a high theoretical precision is that, in order to calculate $\Delta\alpha^{(5)}_{\text{had}}$ in the Euclidean domain, one extracts only very general information encoded in the data—just the integral over the entire spectrum with a smooth weight function and no details of the behavior over specific energy regions. This is the situation where global duality, which is exact by definition (the hadron and quark descriptions are supposed to be exactly equivalent in principle), is applicable and is under a strict control numerically within PT. However, our calculation shows that, at the present level of precision, the result for $\Delta\alpha^{(5)}_{\text{had}}$ is rather sensitive to the numerical values of the parameters m_c and a_s which should be fixed from the data. The uncertainties in these parameters can be reduced both with better data and with better theoretical formulas for extracting numerical values for these parameters from experimental data (especially m_c), while the theoretical framework for calculating the hadronic contribution itself is already very precise. Using the result given in Eq. (95) and the formulas for the radiative corrections to the Weinberg angle from [53] (assuming the Minkowskian definition for the on-shell coupling), we find that the central value of the Higgs boson mass moves from the reference value of $M_H = 100$ GeV for $\Delta\alpha^{(5)}_{\text{had}} = 280.0 \times 10^{-4}$ to $M_H = 191$ GeV for the value of $\Delta\alpha^{(5)}_{\text{had}} = 270.37 \times 10^{-4}$ found in the present study.

8. CONCLUSION

The technique of calculating $\Delta\alpha^{(5)}_{\text{had}}$ within a dimensional regularization and a minimal subtraction is straightforward in PT. It heavily relies on the renormalization group, which is the most powerful tool of modern high-precision analyses in particle phenomenology. Because PT is not applicable only at low energies, one should modify only the IR region of integration for light quarks: a numerical integration of data at energies higher than 2 to 3 GeV is equivalent to the theoretical calculation in PT if both data and theory are properly treated. The present calculation uses virtually no explicit scattering data but the values of the lowest resonance masses for the light-quark vector channels. Other experimental information is encoded through the numerical values of the coupling constant, quark masses, and some vacuum condensates.

The Minkowskian definition of the on-shell coupling constant is deficient and not applicable at some points. Both the $\overline{MS}$ and the on-shell coupling constants in the Euclidean domain can be reliably determined by using theoretical formulas already established in high orders of PT. In view of future high-precision tests of the SM at M_Z and two-loop calculations for observables in this region, it seems that the parametrization of the theory with the running EM coupling in the $\overline{MS}$ scheme is the most promising.

The main uncertainty in the hadronic contribution to the running EM coupling constant at M_Z comes from the error in the numerical value of the c-quark mass m_c. The uncertainty in a_s is less important. Unfortunately, the c-quark mass is a quantity that is very complicated to study. The reason is that its numerical value is close to the strong-interaction scale on the order of the ρ-meson or the proton mass. Therefore, m_c should be treated exactly in theoretical formulas—virtually no simplifying approximation is applicable in the kinematical range of energies of order m_c. The presence of a mass usually makes loop calculations within PT more difficult technically. Near the $c\bar{c}$ production threshold, where the mass is significant and where its numerical value can be reliably extracted from accurate experimental data, the Coulomb interaction is enhanced, which requires taking it into account exactly, while the c-quark mass is too small for nonrelativistic QCD to work well. Finally, non-PT corrections due to the vacuum condensates within OPE are important numerically in this energy range, but they are not well known because they are given by gluonic operators [54]. Although the coefficient functions for the relevant operators up to dimension eight were calculated in [55], the numerical values of their vacuum condensates are poorly known. These reasons make an accurate determination of the c quark mass difficult. The uncertainty related to the contribution of the c quark to the hadronic vacuum polarization is additionally enhanced because of the large electric charge of the c quark. For the b quark, for instance, all the above problems are much less severe. Therefore, c-quark physics plays a significant part in Higgs boson searches through radiative corrections.

ACKNOWLEDGMENTS

I am indebted to K.G. Chetyrkin for discussions on various aspects of many-loop calculations and correspondence. Discussions with F. Jegerlehner, J.G. Körner, J.H. Kühn, and K. Schilcher are gratefully acknowledged.

The work was supported in part by the Russian Foundation for Basic Research (project no. 99-01-00091) and by the Volkswagen Foundation under contract no. I/73611. (Presently, A.A. Pivovarov is an Alexander von Humboldt fellow.)

REFERENCES

1. G. 't Hooft and M. Weltman, Nucl. Phys. B **44**, 189 (1972).
2. G. 't Hooft, Nucl. Phys. B **61**, 455 (1973).
3. K. G. Chetyrkin and F. V. Tkachov, Nucl. Phys. B **192**, 159 (1981); F. V. Tkachov, Phys. Lett. B **100B**, 65 (1981).
4. K. G. Chetyrkin, J. H. Kühn, and A. Kwiatkowski, Phys. Rep. **277**, 189 (1996).
5. W. A. Bardeen, A. J. Buras, D. W. Duke, and T. Muta, Phys. Rev. D **18**, 3998 (1978).
6. T. Appelquist and J. Carazzone, Phys. Rev. D **11**, 2856 (1975).
7. *Precision Tests of the Standard Electroweak Model,* Ed. by P. Langacker (World Sci., Singapore, 1995).
8. D. Bardin *et al.*, *Electroweak Working Group Report,* CERN-95-03A (1997).
9. W. Hollik, J. Phys. G **23**, 1503 (1997).
10. Particle Data Group (C. Caso *et al.*), Eur. Phys. J. C **3**, 1 (1998).
11. E.C.G. Stueckelberg and A. Petermann, Helv. Phys. Acta **26**, 499 (1953).
12. M. Gell-Mann and F. E. Low, Phys. Rev. **95**, 1300 (1954).
13. N. N. Bogolyubov and D. V. Shirkov, Dokl. Akad. Nauk SSSR **103**, 391 (1955); Nuovo Cimento **3**, 845 (1956).
14. J. Gunion *et al.*, *Frontiers in Physics* (Addison-Wesley, Menlo Park, 1990).
15. M. Davier, Nucl. Phys. B (Proc. Suppl.) **76**, 327 (1999); hep-ph/9812370.
16. S. Groote, J. G. Körner, K. Schilcher, and N. F. Nasrallah, Phys. Lett. B **440**, 375 (1998).
17. J. H. Kühn and M. Steinhauser, Phys. Lett. B **437**, 425 (1998).
18. M. Davier and A. Hocker, Phys. Lett. B **435**, 427 (1998).
19. N. V. Krasnikov and R. Rodenberg, Nuovo Cimento A **111**, 217 (1998).
20. V. Novikov, L. Okun, M. Vysotsky, and A. Rozanov, Preprint ITEP-PH-6-97 (Moscow, 1997); hep-ph/9707359.
21. H. Burkhardt and B. Pietrzyk, Phys. Lett. B **356**, 398 (1995).
22. S. Eidelman and F. Jegerlehner, Z. Phys. C **67**, 585 (1995).
23. J. Erler, Phys. Rev. D **59**, 054008 (1999).
24. D. J. Broadhurst, Z. Phys. C **54**, 599 (1992).
25. L. R. Surguladze and M. A. Samuel, Rev. Mod. Phys. **68**, 259 (1996).
26. N. V. Krasnikov and A. A. Pivovarov, Phys. Lett. B **116B**, 168 (1982).
27. M. A. Shifman, A. I. Vainshtein, and V. I. Zakharov, Nucl. Phys. B **147**, 385 (1979).
28. N. V. Krasnikov, A. A. Pivovarov, and N. Tavkhelidze, Pis'ma Zh. Éksp. Teor. Fiz. **36**, 272 (1982) [JETP Lett. **36**, 333 (1982)]; Z. Phys. C **19**, 301 (1983).
29. A. A. Pivovarov, Yad. Fiz. **62**, 2077 (1999) [Phys. At. Nucl. **62**, 1924 (1999)]; hep-ph/9712534.
30. N. V. Krasnikov and A. A. Pivovarov, Phys. Lett. B **112B**, 397 (1982).
31. G. 't Hooft, Nucl. Phys. B **72**, 461 (1974).
32. G. 't Hooft, Nucl. Phys. B **75**, 461 (1974).
33. K. G. Chetyrkin, V. P. Spiridonov, and S. G. Gorishnii, Phys. Lett. B **160B**, 149 (1985).
34. A. A. Pivovarov, Phys. Lett. B **263**, 282 (1991); Yad. Fiz. **54**, 1084 (1991) [Sov. J. Nucl. Phys. **54**, 656 (1991)]; A. A. Penin and A. A. Pivovarov, Phys. Rev. D **49**, 265 (1994).
35. K. G. Chetyrkin, Phys. Lett. B **307**, 169 (1993).

36. S. A. Larin, T. van Ritbergen, and J. A. M. Vermaseren, Nucl. Phys. B **438**, 278 (1995).
37. J. Gasser and H. Leutwyler, Phys. Rep. **87**, 77 (1982).
38. N. V. Krasnikov and A. A. Pivovarov, Nuovo Cimento A **81**, 680 (1984).
39. A. A. Ovchinnikov and A. A. Pivovarov, Phys. Lett. B **163B**, 231 (1985); Yad. Fiz. **48**, 1135 (1988) [Sov. J. Nucl. Phys. **48**, 721 (1988)].
40. K. G. Chetyrkin, J. H. Kühn, and A. A. Pivovarov, Nucl. Phys. B **533**, 473 (1998); J. G. Körner, F. Krajewski, and A. A. Pivovarov, Eur. Phys. J. C **20**, 259 (2001); hep-ph/0003165.
41. K. G. Chetyrkin, J. H. Kühn, and M. Steinhauser, Nucl. Phys. B **505**, 40 (1997).
42. K. G. Chetyrkin, J. H. Kühn, and M. Steinhauser, Nucl. Phys. B **510**, 61 (1998).
43. A. A. Pivovarov, Yad. Fiz. **54**, 1114 (1991) [Sov. J. Nucl. Phys. **54**, 676 (1991)]; Z. Phys. C **53**, 461 (1992); Nuovo Cimento A **105**, 813 (1992).
44. S. Groote, J. G. Körner, and A. A. Pivovarov, Phys. Lett. B **407**, 66 (1997); Mod. Phys. Lett. A **13**, 637 (1998).
45. J. G. Körner, F. Krajewski, and A. A. Pivovarov, Phys. Rev. D **63**, 036001 (2001).
46. N. V. Krasnikov and A. A. Pivovarov, Mod. Phys. Lett. A **11**, 835 (1996); hep-ph/9510207; Yad. Fiz. **64**, 1576 (2001) [Phys. At. Nucl. **64**, 1500 (2001)].
47. A. A. Pivovarov, Yad. Fiz. **52**, 583 (1990) [Sov. J. Nucl. Phys. **52**, 372 (1990)].
48. K. G. Chetyrkin, B. A. Kniehl, and M. Steinhauser, Phys. Rev. Lett. **79**, 2184 (1997).
49. K. G. Chetyrkin, Phys. Lett. B **391**, 402 (1997).
50. J. H. Kühn, A. A. Penin, and A. A. Pivovarov, Nucl. Phys. B **534**, 356 (1998); A. A. Penin and A. A. Pivovarov, Phys. Lett. B **435**, 413 (1998); Nucl. Phys. B **549**, 217 (1999); Phys. Lett. B **443**, 264 (1998).
51. J. G. Körner, A. A. Pivovarov, and K. Schilcher, Eur. Phys. J. C **9**, 551 (1999).
52. J. G. Körner, F. Krajewski, and A. A. Pivovarov, Eur. Phys. J. C **12**, 461 (2000); **14**, 123 (2000).
53. G. D'Agostini and G. Degrassi, Eur. Phys. J. C **10**, 663 (1999).
54. V. A. Novikov *et al.*, Phys. Rep. **41**, 1 (1978).
55. S. N. Nikolaev and A. V. Radyushkin, Phys. Lett. B **124B**, 243 (1983); Nucl. Phys. B **213**, 285 (1983).

Physics of Atomic Nuclei, Vol. 65, No. 7, 2002, pp. 1341–1351. From Yadernaya Fizika, Vol. 65, No. 7, 2002, pp. 1374–1384.
Original English Text Copyright © 2002 by Bityukov, Krasnikov.

ELEMENTARY PARTICLES AND FIELDS
Theory

LHC (CMS) Discovery Potential for Models with Effective Supersymmetry and Nonuniversal Gaugino Masses*

S. I. Bityukov and N. V. Krasnikov[1)]

Institute for High Energy Physics, Protvino, Moscow oblast, 142284 Russia

Received April 5, 2001; in final form, September 10, 2001

Abstract—We investigate squark and gluino pair production at LHC (CMS) with subsequent decays into quarks, leptons, and the lightest supersymmetric particles (LSP) in models with effective supersymmetry, where the third generation of squarks is relatively light, whilst the first two generations of squarks are heavy. We consider the general case of nonuniversal gaugino masses. The visibility of a signal through an excess over Standard Model background in $(n \geq 2)$ jets + $(m \geq 0)$ leptons + E_T^{miss} events depends rather strongly on the relation between the LSP, second-neutralino, gluino, and squark masses and decreases with increasing LSP mass. We find that, for a relatively heavy gluino, it is very difficult to detect a SUSY signal even for light third-generation squarks ($m_{\tilde{q}_3} \leq 1$ TeV) if the LSP mass is close to the third-generation squark mass. *© 2002 MAIK "Nauka/Interperiodica".*

1. INTRODUCTION

One of the large hadron collider (LHC) supergoals is the discovery of supersymmetry. In particular, it is very important to investigate ways to discover strongly interacting superparticles (squarks and gluino). In [1] (see also [2]), the squark and gluino discovery potential of the LHC was investigated within minimal supergravity—the minimal supersymmetric extension of the Standard Model (mSUGRA–MSSM) framework [3], where all sparticle masses are determined mainly by two parameters: m_0 [common squark and slepton mass at Grand Unified theory (GUT) scale] and $m_{1/2}$ (common gaugino mass at the GUT scale). The signature used in investigating squarks and gluino observability at LHC is $(n \geq 2)$ jets + $(m \geq 0)$ leptons + E_T^{miss} events. The conclusion of [1] is that the LHC is able to detect squarks and gluino with masses up to 2–2.5 TeV. In [4], the supersymmetry (SUSY) discovery potential of the LHC was investigated for the case of nonuniversal gaugino masses with universal squark masses for the first, second, and third generations. The conclusion of [4] is that the visibility of a signal by an excess over the Standard Model (SM) background in $(n \geq 2)$ jets + E_T^{miss} events depends rather strongly on the relation between the lightest supersymmetric particle (LSP), gluino, and squark masses and decreases with increasing LSP mass. For a relatively large LSP mass, close to squark or gluino masses, and for $(m_{\tilde{q}}, m_{\tilde{g}}) \geq 1.5$ TeV, the signal is too small to be observable.

In this article, we investigate squark- and gluino-pair production at LHC for the compact muon solenoid (CMS) with subsequent decays into quarks, leptons, and LSP in models with effective supersymmetry [5], where the third generation of squarks is relatively light, while the first two generations of squarks are heavy.[2)] Models with effective supersymmetry solve, in a natural way, problems associated with flavor-changing neutral currents, lepton-flavor violation, the electric dipole moments of the electron and the neutron, and proton decay. In such models, there are two mass scales: the gauginos, higgsinos, and third-generation squarks are rather light (to stabilize the electroweak scale), while the first two generations of squarks and sleptons are heavy, with masses in the range between about 5 and 20 TeV. We investigate the general case where the relation between the gaugino masses is arbitrary. We study the detection of supersymmetry using the classical signature $(n \geq 2, 3, 4)$ jets + $(m \geq 0)$ leptons + E_T^{miss}. We find that the SUSY discovery potential depends rather strongly on the relation between squarks, gluino, LSP, and second-neutralino masses, and it decreases with increasing LSP mass. For relatively heavy gluinos, it would be very difficult or even impossible to detect a SUSY signal even for light third-generation squarks ($m_{\tilde{q}_3} \leq 1$ TeV) if the

---

*This article was submitted by the authors in English.

[1)] Institute for Nuclear Research, Russian Academy of Sciences, pr. Shestidesyatiletiya Oktyabrya 7a, Moscow, 117312 Russia.

[2)] Preliminary results of this study were reported in [6].

LSP mass is close to the third-generation-squark mass. It should be noted that, in [7], the ATLAS detector potential for the discovery of SUGRA–MSSM focusing on effective supersymmetry for $\tan\beta = 10$ and $\mu < 0$ was studied for the signature $n \geq 2$ jets + 1 isolated lepton + E_T^{miss}. In [8], the signature "$2b\ 2W$" resulting from the gluino decay into $\tilde{g} \to 2b + 2W + \ldots$ was used to detect the signal in such models.

2. SPARTICLE DECAYS

The decays of squarks and gluinos depend on the relation between the squark and gluino masses. For $m_{\tilde{q}} > m_{\tilde{g}}$, squarks decay mainly into gluino and quarks,

$$\tilde{q} \to \tilde{g}q,$$

while the gluino decays mainly into a quark–antiquark pair and a gaugino,

$$\tilde{g} \to q\bar{q}\tilde{\chi}_i^0,$$
$$\tilde{g} \to q\bar{q}'\tilde{\chi}_1^{\pm}.$$

For $m_{\tilde{q}} < m_{\tilde{g}}$, the gluino decays mainly into squarks and quarks,

$$\tilde{g} \to \bar{q}\tilde{q}, q\bar{\tilde{q}},$$

whereas the squarks decay mainly into quarks and a gaugino,

$$\tilde{q} \to q\tilde{\chi}_i^0.$$
$$\tilde{q} \to q'\tilde{\chi}_1^{\pm}.$$

The lightest chargino $\tilde{\chi}_1^{\pm}$ has several leptonic decay modes giving a lepton and missing energy:

the three-body decay

$$\tilde{\chi}_1^{\pm} \longrightarrow \tilde{\chi}_1^0 + l^{\pm} + \nu$$

and the two-body decays

$$\begin{aligned}
\tilde{\chi}_1^{\pm} &\longrightarrow \tilde{l}_{L,R}^{\pm} + \nu,\\
&\qquad\quad \lfloor\!\!\longrightarrow \tilde{\chi}_1^0 + l^{\pm}\\
\tilde{\chi}_1^{\pm} &\longrightarrow \tilde{\nu}_L + l^{\pm},\\
&\qquad\quad \lfloor\!\!\longrightarrow \tilde{\chi}_1^0 + \nu\\
\tilde{\chi}_1^{\pm} &\longrightarrow \tilde{\chi}_1^0 + W^{\pm}.\\
&\qquad\qquad\quad \lfloor\!\!\longrightarrow l^{\pm} + \nu
\end{aligned}$$

The leptonic decays of $\tilde{\chi}_2^0$ give two leptons and missing energy:

the three-body decays

$$\begin{aligned}
\tilde{\chi}_2^0 &\longrightarrow \tilde{\chi}_1^0 + l^+l^-,\\
\tilde{\chi}_2^0 &\longrightarrow \tilde{\chi}_1^{\pm} + l^{\mp} + \nu,\\
&\qquad\quad \lfloor\!\!\longrightarrow \tilde{\chi}_1^0 + l^{\pm} + \nu
\end{aligned}$$

and the two-body decay

$$\begin{aligned}
\tilde{\chi}_2^0 &\longrightarrow \tilde{l}_{L,R}^{\pm} + l^{\mp}.\\
&\qquad\quad \lfloor\!\!\longrightarrow \tilde{\chi}_1^0 + l^{\pm}
\end{aligned}$$

As the result of chargino and second neutralino leptonic decays, apart from the classical signature

$$(n \geq 2, 3, 4)\text{ jets} + E_T^{\text{miss}},$$

signatures such as

$$(n \geq 2, 3, 4)\text{ jets} + (m \geq 1)\text{ leptons} + E_T^{\text{miss}}$$

with leptons and jets in the final state arise. As was mentioned above, these signatures were used in [1] to investigate LHC (CMS) potential for squark and gluino discovery within the SUGRA–MSSM model, where the gaugino masses $m_{\tilde{\chi}_1^0}$ and $m_{\tilde{\chi}_2^0}$ are essentially determined by a common gaugino mass $m_{1/2}$, with $m_{\tilde{\chi}_2^0} \approx 0.9m_{1/2}$ and $m_{\tilde{\chi}_1^0} \approx (1/2)m_{1/2}$.

The cross section for the production of strongly interacting superparticles,

$$pp \to \tilde{g}\tilde{g}, \tilde{q}\tilde{g}, \tilde{q}\tilde{q}, \tag{1}$$

depends on the gluino and squark masses. Within the SUGRA–MSSM model, the sparticle masses satisfy the approximate relations

$$m_{\tilde{q}}^2 \approx m_0^2 + 6m_{1/2}^2, \tag{2}$$

$$m_{\tilde{\chi}_1^0} \approx 0.45m_{1/2}, \tag{3}$$

$$m_{\tilde{\chi}_2^0} \approx m_{\tilde{\chi}_1^{\pm}} \approx 2m_{\tilde{\chi}_1^0}, \tag{4}$$

$$m_{\tilde{g}} \approx 2.5m_{1/2}. \tag{5}$$

Despite the simplicity of the SUGRA–MSSM framework, it is a very particular model. The mass formulas for sparticles in the SUGRA–MSSM model are derived under the assumption that, at the GUT scale ($M_{\text{GUT}} \approx 2 \times 10^{16}$ GeV), soft-supersymmetry-breaking terms are universal. However, we can in general expect that the actual sparticle masses can differ in a drastic way from the SUGRA–MSSM sparticle mass pattern for many reasons (see, for instance, [9–13]). It is thus appropriate to investigate the LHC SUSY discovery potential in a model-independent way.

Table 1. Two sets (a and b) of cuts used in the study

Number of cut	E_{T1}	E_{T2}	E_{T3}	E_{T4}	E_T^{miss}
Cuts (a)					
1	40.0	40.0	40.0	40.0	200.0
2	100.0	100.0	100.0	100.0	200.0
3	100.0	150.0	150.0	150.0	200.0
4	50.0	100.0	100.0	100.0	200.0
5	200.0	200.0	200.0	200.0	400.0
6	200.0	300.0	300.0	300.0	400.0
7	100.0	200.0	200.0	200.0	400.0
8	300.0	300.0	300.0	300.0	600.0
9	300.0	450.0	450.0	450.0	600.0
10	150.0	300.0	300.0	300.0	600.0
11	400.0	400.0	400.0	400.0	800.0
12	400.0	600.0	600.0	600.0	800.0
13	200.0	400.0	400.0	400.0	800.0
14	500.0	500.0	500.0	500.0	1000.0
15	500.0	750.0	750.0	750.0	1000.0
16	250.0	500.0	500.0	500.0	1000.0
17	600.0	600.0	600.0	600.0	1200.0
18	600.0	900.0	900.0	900.0	1200.0
19	300.0	600.0	600.0	600.0	1200.0
Cuts (b)					
1	40.0	40.0	40.0	40.0	200.0
2	100.0	125.0	150.0	150.0	200.0
3	166.7	208.3	250.0	250.0	200.0
4	233.3	291.7	350.0	350.0	200.0
5	300.0	375.0	450.0	450.0	200.0
6	100.0	125.0	150.0	150.0	400.0
7	166.7	208.3	250.0	250.0	400.0
8	233.3	291.7	350.0	350.0	400.0
9	300.0	375.0	450.0	450.0	400.0
10	100.0	125.0	150.0	150.0	600.0
11	166.7	208.3	250.0	250.0	600.0
12	233.3	291.7	350.0	350.0	600.0
13	300.0	375.0	450.0	450.0	600.0
14	100.0	125.0	150.0	150.0	800.0
15	166.7	208.3	250.0	250.0	800.0
16	233.3	291.7	350.0	350.0	800.0
17	300.0	375.0	450.0	450.0	800.0
18	100.0	125.0	150.0	150.0	1000.0
19	166.7	208.3	250.0	250.0	1000.0
20	233.3	291.7	350.0	350.0	1000.0
21	300.0	375.0	450.0	450.0	1000.0
22	100.0	125.0	150.0	150.0	1200.0
23	166.7	208.3	250.0	250.0	1200.0
24	233.3	291.7	350.0	350.0	1200.0
25	300.0	375.0	450.0	450.0	1200.0

Note: E is in GeV.

Table 2. The discovery potential of CMS for different values. (Here, +(−) means that signal is detectable (nondetectable). All masses are in GeV. The parameter m_{0_3} is the soft supersymmetry breaking mass of the 3rd-generation squarks. It is equal to squark mass before electroweak symmetry breaking.)

$m_{\tilde\chi_1}, m_{\tilde\chi_2}$	Incl.	No lept.	$l^\pm$	l^+l^-	$l^\pm l^\pm$	$3l$	$m_{\tilde\chi_1}, m_{\tilde\chi_2}$	Incl.	No lept.	$l^\pm$	l^+l^-	$l^\pm l^\pm$	$3l$
$m_{0_3} = 900, m_{\tilde q_{1,2}} = 3800, m_{\tilde g} = 2000, \mu = 1800, \tan\beta = 35, \sigma = 0.067$ pb, $L = 10^4$ pb^{-1}							$m_{0_3} = 700, m_{\tilde q_{1,2}} = 3800, m_{\tilde g} = 2000, \mu = 1800, \tan\beta = 35, \sigma = 0.49$ pb, $L = 10^4$ pb^{-1}						
150, 1800	+	+	−	−	−	−	116, 1800	+	+	−	−	−	−
450, 1800	−	−	−	−	−	−	350, 1800	−	−	−	−	−	−
675, 1800	−	−	−	−	−	−	525, 1800	−	−	−	−	−	−
810, 1800	−	−	−	−	−	−	630, 1800	−	+	−	−	−	−
150, 450	−	−	−	−	−	−	116, 350	+	+	−	−	−	−
150, 675	+	+	−	−	−	−	116, 525	+	+	−	−	−	−
450, 675	−	−	−	−	−	−	350, 525	+	+	−	−	−	−
675, 810	−	−	−	−	−	−	525, 630	−	−	−	−	−	−
$m_{\tilde q_3} = 800, m_{\tilde q_{1,2}} = 3800, m_{\tilde g} = 2000, \mu = 1800, \tan\beta = 5, \sigma = 0.12$ pb, $L = 10^4$ pb^{-1}							$m_{\tilde q_3} = 700, m_{\tilde q_{1,2}} = 1550, m_{\tilde g} = 600, \mu = 1800, \tan\beta = 5, \sigma = 10$ pb, $L = 10^4$ pb^{-1}						
133, 1800	+	+	−	−	−	−	100, 570	+	+	+	+	+	+
400, 1800	−	−	−	−	−	−	300, 570	+	+	−	−	−	−
600, 1800	−	−	−	−	−	−	450, 570	+	+	−	−	−	−
720, 1800	−	−	−	−	−	−	540, 570	+	+	−	−	−	−
133, 266	−	−	−	−	−	−	$m_{0_3} = 700, m_{\tilde q_{1,2}} = 1550, m_{\tilde g} = 600, \mu = 1800, \tan\beta = 35, \sigma = 10$ pb, $L = 10^4$ pb^{-1}						
133, 600	+	−	−	−	−	−	100, 570	+	+	+	−	−	−
400, 720	−	−	−	−	−	−	300, 570	+	+	−	−	−	−
450, 540	−	−	−	−	−	−	450, 570	+	+	−	−	−	−
							540, 570	+	+	−	−	−	−
$m_{0_3} = 800, m_{\tilde q_{1,2}} = 3800, m_{\tilde g} = 2000, \mu = 1800, \tan\beta = 35, \sigma = 0.18$ pb, $L = 10^4$ pb^{-1}							$m_{\tilde q_3} = 600, m_{\tilde q_{1,2}} = 3800, m_{\tilde g} = 2000, \mu = 1800, \tan\beta = 5, \sigma = 0.77$ pb, $L = 10^4$ pb^{-1}						
133, 1800	+	+	−	−	−	−	100, 1800	+	+	−	−	−	−
400, 1800	−	−	−	−	−	−	300, 1800	+	+	−	−	−	−
600, 1800	−	−	−	−	−	−	450, 1800	−	−	−	−	−	−
720, 1800	−	−	−	−	−	−	540, 1800	−	−	−	−	−	−
133, 266	−	−	−	−	−	−	100, 300	+	+	−	−	−	−
133, 600	+	+	−	−	−	−	100, 450	+	+	−	−	−	−
400, 720	−	−	−	−	−	−	300, 450	−	−	−	−	−	−
450, 540	−	−	−	−	−	−	450, 540	−	−	−	−	−	−
$m_{\tilde q_3} = 700, m_{\tilde q_{1,2}} = 3800, m_{\tilde g} = 2000, \mu = 1800, \tan\beta = 5, \sigma = 0.28$ pb, $L = 10^4$ pb^{-1}							$m_{0_3} = 600, m_{\tilde q_{1,2}} = 3800, m_{\tilde g} = 2000, \mu = 1800, \tan\beta = 35, \sigma = 2.1$ pb, $L = 10^4$ pb^{-1}						
116, 1800	+	+	−	−	−	−	100, 1800	+	+	−	−	−	−
350, 1800	−	−	−	−	−	−	300, 1800	−	+	−	−	−	−
525, 1800	−	−	−	−	−	−	450, 1800	−	+	−	−	−	−
630, 1800	−	−	−	−	−	−	540, 1800	−	+	−	−	−	−
116, 350	+	−	−	−	−	−	100, 300	+	+	−	−	+	+
116, 525	+	+	−	−	−	−	100, 450	+	+	−	−	−	−
350, 525	−	−	−	−	−	−	300, 450	−	−	−	−	−	−
525, 630	−	−	−	−	−	−	450, 540	−	−	−	−	−	−

Table 2. (Contd.)

$m_{\tilde\chi_1}, m_{\tilde\chi_2}$	Incl.	No lept.	$l^\pm$	l^+l^-	$l^\pm l^\pm$	$3l$	$m_{\tilde\chi_1}, m_{\tilde\chi_2}$	Incl.	No lept.	$l^\pm$	l^+l^-	$l^\pm l^\pm$	$3l$
$m_{\tilde q_3} = 500, m_{\tilde q_{1,2}} = 3800, m_{\tilde g} = 2000, \mu = 1800,$ $\tan\beta = 5, \sigma = 2.2$ pb, $L = 10^4$ pb^{-1}							$m_{\tilde q_3} = 1000, m_{\tilde q_{1,2}} = 3800, m_{\tilde g} = 1750, \mu = 1800,$ $\tan\beta = 5, \sigma = 0.032$ pb, $L = 10^5$ pb^{-1}						
83, 1800	+	+	−	−	−	−	170, 1800	+	+	−	−	−	−
250, 1800	+	+	−	−	−	−	500, 1800	−	−	−	−	−	−
375, 1800	−	+	−	−	−	−	750, 1800	−	−	−	−	−	−
450, 1800	−	−	−	−	−	−	900, 1800	−	−	−	−	−	−
83, 250	+	+	−	−	−	−	170, 330	+	−	−	−	−	−
83, 375	−	+	−	−	−	−	170, 750	+	−	−	−	−	−
250, 375	−	+	−	−	−	−	500, 900	+	−	−	−	−	−
375, 450	−	+	−	−	−	−	750, 900	−	−	−	−	−	−

$m_{\tilde g} = 3500, m_{\tilde q_{1,2}} = 3800, \mu = 1800, L = 10^5$ pb^{-1}

$m_{\tilde\chi_1}, m_{\tilde\chi_2}$	$\tan\beta$		Incl.	No lept.	$l^\pm$	l^+l^-	$l^\pm l^\pm$	$3l$
166, 1800	5	$m_{\tilde q_3} = 1000$	+	+	−	−	−	−
$m_{\tilde q_3}/6$,1800	5	$m_{\tilde q_3} = 1100$	−	−	−	−	−	−
$m_{\tilde q_3}/6$,1800	5	$m_{\tilde q_3} = 1200$	−	−	−	−	−	−
$m_{0_3}/6$,1800	35	$m_{0_3} = 1000$	+	−	−	−	−	−
$m_{0_3}/6$,1800	35	$m_{0_3} = 1100$	−	−	−	−	−	−
$m_{0_3}/6$,1800	35	$m_{0_3} = 1200$	−	−	−	−	−	−

$m_{\tilde\chi_1}, m_{\tilde\chi_2}$	Incl.	No lept.	$l^\pm$	l^+l^-	$l^\pm l^\pm$	$3l$	$m_{\tilde\chi_1}, m_{\tilde\chi_2}$	Incl.	No lept.	$l^\pm$	l^+l^-	$l^\pm l^\pm$	$3l$
$m_{\tilde q_3} = 1200, m_{\tilde q_{1,2}} = 3800, m_{\tilde g} = 1500, \mu = 1800,$ $\tan\beta = 5, \sigma = 0.017$ pb, $L = 10^5$ pb^{-1}							$m_{\tilde q_3} = 1000, m_{\tilde q_{1,2}} = 3800, m_{\tilde g} = 1500, \mu = 1800,$ $\tan\beta = 5, \sigma = 0.036$ pb, $L = 10^5$ pb^{-1}						
200, 1800	+	+	−	−	−	−	166, 1800	+	+	−	−	−	−
600, 1800	+	−	−	−	−	−	500, 1800	+	+	−	−	−	−
900, 1800	−	−	−	−	−	−	750, 1800	−	−	−	−	−	−
1080, 1800	−	−	−	−	−	−	900, 1800	−	−	−	−	−	−
200, 400	+	−	−	−	−	−	166, 332	+	−	+	−	−	−
200, 600	+	−	−	−	+	−	166, 750	+	+	+	−	+	−
600, 900	+	−	−	−	−	−	500, 900	+	+	−	−	−	−
							750, 900	−	−	−	−	−	−
$m_{0_3} = 1200, m_{\tilde q_{1,2}} = 3800, m_{\tilde g} = 1500, \mu = 1800,$ $\tan\beta = 35, \sigma = 0.018$ pb, $L = 10^5$ pb^{-1}							$m_{\tilde q_3} = 1000, m_{\tilde q_{1,2}} = 3800, m_{\tilde g} = 1250, \mu = 1800,$ $\tan\beta = 5, \sigma = 0.075$ pb, $L = 10^5$ pb^{-1}						
200, 1800	+	+	−	−	−	−	166, 1800	+	+	+	+	+	−
600, 1800	+	−	−	−	−	−	500, 1800	+	+	−	−	+	−
900, 1800	−	−	−	−	−	−	750, 1800	+	−	−	−	+	−
1080, 1800	+	+	−	−	−	−	900, 1800	−	−	−	−	−	−
200, 400	+	−	−	−	−	−	166, 332	+	+	−	−	+	−
200, 600	+	−	+	−	+	−	166, 750	+	+	+	+	+	+
600, 900	+	−	−	−	−	−	500, 900	+	+	−	−	−	−
900, 1080	−	−	−	−	−	−	750, 900	+	+	−	−	+	−
$m_{\tilde q_3} = 1000, m_{\tilde q_{1,2}} = 3800, m_{\tilde g} = 2000, \mu = 1800,$ $\tan\beta = 5, \sigma = 0.027$ pb, $L = 10^5$ pb^{-1}							$m_{0_3} = 1000, m_{\tilde q_{1,2}} = 3800, m_{\tilde g} = 3500, \mu = 1800,$ $\tan\beta = 35, \sigma = 0.030$ pb, $L = 10^5$ pb^{-1}						
170, 1800	+	+	−	−	−	−	166, 1800	+	−	−	−	−	−
500, 1800	−	−	−	−	−	−	500, 1800	−	−	−	−	−	−
750, 1800	−	−	−	−	−	−	750, 1800	−	−	−	−	−	−
900, 1800	−	−	−	−	−	−	850, 1800	−	−	−	−	−	−
170, 330	−	−	−	−	−	−	166, 322	−	−	−	−	−	−
170, 750	+	+	−	−	−	−	166, 750	+	−	−	−	−	−
500, 900	−	−	−	−	−	−	500, 750	−	−	−	−	−	−
750, 900	−	−	−	−	−	−	500, 900	−	−	−	−	−	−
							750, 900	−	−	−	−	−	−

Table 2. (Contd.)

$m_{\tilde\chi_1}, m_{\tilde\chi_2}$	Incl.	No lept.	$l^\pm$	l^+l^-	$l^\pm l^\pm$	$3l$	$m_{\tilde\chi_1}, m_{\tilde\chi_2}$	Incl.	No lept.	$l^\pm$	l^+l^-	$l^\pm l^\pm$	$3l$
$m_{\tilde q_3} = 1000, m_{\tilde q_{1,2}} = 3800, m_{\tilde g} = 2000, \mu = 500, \tan\beta = 5, \sigma = 0.027$ pb, $L = 10^5$ pb^{-1}							$m_{0_3} = 900, m_{\tilde q_{1,2}} = 3800, m_{\tilde g} = 3500, \mu = 1800, \tan\beta = 35, \sigma = 0.071$ pb, $L = 10^5$ pb^{-1}						
170, 1800	+	−	−	+	−	+	150, 1800	+	+	−	−	−	−
500, 1800	−	−	−	−	−	−	450, 1800	−	−	−	−	−	−
750, 1800	−	−	−	−	−	−	675, 1800	−	−	−	−	−	−
900, 1800	−	−	−	−	−	−	750, 1800	−	−	−	−	−	−
170, 330	−	−	−	−	+	+	150, 300	−	−	−	−	+	−
170, 750	+	−	−	−	+	+	150, 675	+	+	−	−	−	−
500, 900	−	−	−	−	−	−	450, 675	−	−	−	−	−	−
750, 900	−	−	−	−	−	−	450, 810	−	−	−	−	−	−
							675, 810	−	−	−	−	−	−
$m_{0_3} = 1000, m_{\tilde q_{1,2}} = 3800, m_{\tilde g} = 2000, \mu = 500, \tan\beta = 35, \sigma = 0.031$ pb, $L = 10^5$ pb^{-1}							$m_{\tilde q_3} = 900, m_{\tilde q_{1,2}} = 3800, m_{\tilde g} = 2000, \mu = 450, \tan\beta = 5, \sigma = 0.057$ pb, $L = 10^5$ pb^{-1}						
170, 1800	+	−	−	−	−	+	150, 1800	+	+	−	+	−	+
500, 1800	−	−	−	−	−	−	450, 1800	−	−	−	+	−	−
750, 1800	−	−	−	−	−	−	675, 1800	−	−	−	−	−	−
900, 1800	−	−	−	−	−	−	810, 1800	−	+	−	−	−	−
170, 330	−	−	−	−	+	+	150, 450	+	−	−	−	+	−
170, 750	+	−	−	−	+	+	150, 675	+	−	−	−	+	+
500, 900	−	−	−	−	−	−	450, 675	−	−	−	−	+	−
750, 900	−	−	−	−	−	−	675, 810	−	−	−	−	+	−
$m_{\tilde q_3} = 1000, m_{\tilde q_{1,2}} = 3800, m_{\tilde g} = 2000, \mu = 800, \tan\beta = 5, \sigma = 0.026$ pb, $L = 10^5$ pb^{-1}							$m_{0_3} = 900, m_{\tilde q_{1,2}} = 3800, m_{\tilde g} = 2000, \mu = 450, \tan\beta = 35, \sigma = 0.063$ pb, $L = 10^5$ pb^{-1}						
170, 1800	+	+	−	−	−	−	150, 1800	+	−	−	+	+	+
500, 1800	−	−	−	−	−	−	450, 1800	−	−	−	−	−	−
750, 1800	−	−	−	−	+	−	675, 1800	+	−	−	−	−	−
900, 1800	−	−	−	−	−	−	810, 1800	−	−	−	−	−	−
170, 330	−	−	−	−	+	−	150, 450	+	−	−	−	+	+
170, 750	+	−	−	−	−	−	150, 675	+	−	−	+	+	+
500, 900	−	−	−	−	−	−	450, 675	−	−	−	−	+	−
750, 900	−	−	−	−	−	−	675, 810	−	−	−	−	−	−
$m_{0_3} = 1000, m_{\tilde q_{1,2}} = 3800, m_{\tilde g} = 2000, \mu = 800, \tan\beta = 35, \sigma = 0.031$ pb, $L = 10^5$ pb^{-1}							$m_{0_3} = 900, m_{\tilde q_{1,2}} = 3800, m_{\tilde g} = 2000, \mu = 2m_{\chi_1^0}, \tan\beta = 35, \sigma = 0.071$ pb, $L = 10^5$ pb^{-1}						
170, 1800	+	+	−	−	−	−	150, 1800	+	+	−	−	+	+
500, 1800	−	−	−	−	−	−	450, 1800	−	−	−	−	−	−
750, 1800	−	−	−	−	−	−	675, 1800	−	−	−	−	−	−
900, 1800	−	−	−	−	−	−	150, 450	+	−	−	−	+	+
170, 330	−	−	−	−	+	+	150, 675	+	+	−	+	+	+
170, 750	+	+	−	−	−	−	450, 675	−	−	−	−	−	−
500, 900	−	−	−	−	−	−	675, 810	−	−	−	−	−	−
750, 900	−	−	−	−	−	−							

Table 2. (Contd.)

$m_{\tilde\chi_1}, m_{\tilde\chi_2}$	Incl.	No lept.	$l^\pm$	l^+l^-	$l^\pm l^\pm$	$3l$
$m_{\tilde q_3} = 800, m_{\tilde q_{1,2}} = 3800, m_{\tilde g} = 2000, \mu = 1800,$ $\tan\beta = 5, \sigma = 0.12$ pb, $L = 10^5$ pb^{-1}						
133, 1800	+	+	−	−	+	−
400, 1800	+	+	−	−	−	−
600, 1800	−	−	−	−	−	−
720, 1800	−	−	−	−	−	−
133, 266	−	−	−	−	+	−
133, 600	+	+	−	−	−	−
400, 720	+	+	−	−	−	−
450, 540	−	−	−	−	−	−
$m_{\tilde q_3} = 800, m_{\tilde q_{1,2}} = 3800, m_{\tilde g} = 1500, \mu = 1800,$ $\tan\beta = 5, \sigma = 0.13$ pb, $L = 10^5$ pb^{-1}						
133, 1800	+	+	+	+	+	+
400, 1800	+	+	−	+	+	+
600, 1800	+	+	−	−	+	+
720, 1800	+	+	−	−	−	−
133, 266	+	+	+	+	+	−
133, 600	+	+	+	+	+	+
$m_{\tilde q_3} = 800, m_{\tilde q_{1,2}} = 3800, m_{\tilde g} = 1000, \mu = 1800,$ $\tan\beta = 5, \sigma = 0.14$ pb, $L = 10^5$ pb^{-1}						
133, 1800	+	+	+	+	+	+
400, 1800	+	+	+	−	+	+
600, 1800	+	+	−	−	+	−
720, 1800	+	+	−	−	+	−
133, 266	+	+	+	+	+	+
133, 600	+	+	+	+	+	+
400, 720	+	+	−	−	+	+
600, 720	+	+	−	−	+	−
$m_{0_3} = 800, m_{\tilde q_{1,2}} = 3800, m_{\tilde g} = 3500, \mu = 1800,$ $\tan\beta = 35, \sigma = 0.18$ pb, $L = 10^5$ pb^{-1}						
133, 1800	+	+	−	−	−	−
400, 1800	−	−	−	−	−	−
600, 1800	−	−	−	−	−	−
720, 1800	+	+	+	−	−	−
133, 266	−	−	−	−	+	+
133, 600	+	+	−	+	+	+
400, 600	−	−	−	−	−	−
400, 720	−	−	−	−	−	−
450, 540	−	−	−	−	+	+
$m_{0_3} = 800, m_{\tilde q_{1,2}} = 3800, m_{\tilde g} = 1000, \mu = 1800,$ $\tan\beta = 35, \sigma = 0.47$ pb, $L = 10^5$ pb^{-1}						
133, 1800	+	+	+	+	+	+
400, 1800	+	+	+	+	+	−
600, 1800	+	+	−	−	+	−
720, 1800	+	+	+	+	+	+
133, 266	+	+	+	+	+	+
133, 600	+	+	+	+	+	+
400, 600	+	+	+	+	+	+
400, 720	+	+	+	+	+	−

$m_{\tilde\chi_1}, m_{\tilde\chi_2}$	Incl.	No lept.	$l^\pm$	l^+l^-	$l^\pm l^\pm$	$3l$
$m_{0_3} = 800, m_{\tilde q_{1,2}} = 3800, m_{\tilde g} = 1500, \mu = 1800,$ $\tan\beta = 35, \sigma = 0.18$ pb, $L = 10^5$ pb^{-1}						
133, 1800	+	+	−	−	+	−
400, 1800	+	+	−	−	−	−
600, 1800	−	−	−	−	+	−
720, 1800	+	+	−	−	−	−
133, 266	+	+	+	+	+	+
133, 600	+	+	+	+	+	+
400, 600	+	+	−	−	+	−
400, 720	+	−	−	+	+	+
600, 720	+	−	−	+	+	+
$m_{0_3} = 800, m_{\tilde q_{1,2}} = 3800, m_{\tilde g} = 2000, \mu = 1800,$ $\tan\beta = 35, \sigma = 0.23$ pb, $L = 10^5$ pb^{-1}						
166, 1800	+	+	−	−	−	−
400, 1800	−	−	−	−	−	+
600, 1800	−	−	−	−	−	−
720, 1800	−	−	−	−	−	−
166, 333	+	+	−	−	−	−
166, 600	+	+	−	−	−	−
400, 600	−	−	−	−	−	−
400, 720	−	−	−	−	−	−
600, 720	−	−	−	−	−	−
$m_{\tilde q_3} = 750, m_{\tilde q_{1,2}} = 3800, m_{\tilde g} = 3500, \mu = 1800,$ $\tan\beta = 5, \sigma = 0.19$ pb, $L = 10^5$ pb^{-1}						
125, 1800	+	+	−	−	+	−
375, 1800	−	+	−	−	+	+
560, 1800	−	−	−	−	−	−
675, 1800	−	−	−	−	−	−
125, 250	−	−	−	−	+	−
125, 560	+	−	−	−	+	+
375, 675	−	−	−	−	−	−
560, 675	−	−	−	−	−	−
$m_{\tilde q_3} = 700, m_{\tilde q_{1,2}} = 3800, m_{\tilde g} = 3500, \mu = 1800,$ $\tan\beta = 5, \sigma = 0.28$ pb, $L = 10^5$ pb^{-1}						
117, 1800	+	+	−	−	−	−
350, 1800	+	+	−	−	−	−
525, 1800	−	−	−	−	−	−
630, 1800	−	−	−	−	−	−
117, 234	−	−	−	+	−	−
117, 525	+	+	−	−	−	−
350, 525	−	−	−	−	−	−
350, 630	−	−	−	−	−	−
525, 630	−	−	−	−	−	−
$m_{0_3} = 650, m_{\tilde g} = 3500, m_{\tilde q_{1,2}} = 3800, \mu = 1800,$ $\tan\beta = 35, \sigma = 0.94$ pb, $L = 10^5$ pb^{-1}						
108, 1800	+	+	−	+	−	−
325, 1800	+	+	+	+	−	−
487, 1800	+	+	+	+	−	−
585, 1800	+	+	+	+	−	−
108, 216	−	−	−	+	+	+
108, 487	+	+	−	+	−	+
487, 585	+	+	+	+	−	+

Table 2. (Contd.)

$m_{\tilde{\chi}_1}, m_{\tilde{\chi}_2}$	Incl.	No lept.	$l^\pm$	l^+l^-	$l^\pm l^\pm$	$3l$	$m_{\tilde{\chi}_1}, m_{\tilde{\chi}_2}$	Incl.	No lept.	$l^\pm$	l^+l^-	$l^\pm l^\pm$	$3l$
$m_{\tilde{q}_3} = 650, m_{\tilde{q}_{1,2}} = 3800, m_{\tilde{g}} = 3500, \mu = 1800, \tan\beta = 5, \sigma = 0.48$ pb, $L = 10^5$ pb^{-1}							$m_{\tilde{q}_3} = 600, m_{\tilde{q}_{1,2}} = 3800, m_{\tilde{g}} = 3500, \mu = 1800, \tan\beta = 5, \sigma = 0.77$ pb, $L = 10^5$ pb^{-1}						
108, 1800	+	+	−	−	−	−	100, 1800	+	+	−	−	−	−
325, 1800	+	+	−	−	−	−	300, 1800	+	+	−	−	−	−
490, 1800	−	−	−	−	−	−	450, 1800	−	+	−	−	−	−
585, 1800	−	−	−	−	−	−	540, 1800	−	−	−	−	−	−
108, 216	+	+	+	+	+	+	100, 200	−	−	−	−	−	−
325, 490	−	−	−	−	−	−	100, 450	+	+	+	−	−	−
325, 585	+	+	−	−	−	−	300, 540	+	+	−	−	−	−
490, 585	−	−	−	−	−	−	450, 540	−	−	−	−	−	−
108, 490	+	+	−	−	−	−	20, 1800	+	+	+	−	−	−

3. SIMULATION OF THE DETECTOR RESPONSE

Our simulations are performed at the particle level with parametrized detector responses based on detailed detector simulations. To be specific, our estimates were obtained for the CMS detector. The fast simulation program CMSJET 4.701 for the CMS detector [14] was used. The main aspects of CMSJET relevant to our study are the following.

Charged particles are tracked in a 4-T magnetic field. A 90% reconstruction efficiency per charged track with transverse momenta of $p_T > 1$ GeV within the pseudorapidity interval $|\eta| < 2.5$ is assumed.

The geometric acceptances for μ and e are $|\eta| < 2.4$ and 2.5, respectively. The lepton momentum is smeared according to parametrizations obtained from full GEANT.[3] For a 10-GeV lepton, the momentum resolution $\Delta p_T/p_T$ is better than 1% over a full η coverage. For a 100-GeV lepton, the resolution becomes about (1–5) × 10^{-2}, depending on η. We assumed a 90% triggering-plus-reconstruction efficiency per lepton within the geometric acceptance of the CMS detector.

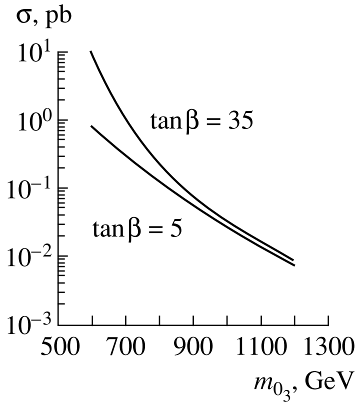

Fig. 1. Dependence of the $pp \to$ squarks, gluino + ... cross section on the third-generation soft-breaking mass m_{0_3} for $m_{\tilde{g}} = 2000$ GeV and $m_{\tilde{q}_{1,2}} = 3800$ GeV and for two values of $\tan\beta$.

The electromagnetic calorimeter of CMS extends up to $|\eta| = 2.61$. There is a pointing crack in the ECAL barrel/endcap transition region between $|\eta| = 1.478$–1.566 (6 ECAL crystals). The hadronic calorimeter covers $|\eta| < 3$. The very forward calorimeter extends from $|\eta| > 3$ to $|\eta| < 5$. Noise terms were simulated with Gaussian distributions, and zero suppression cuts were applied.

The developments of e/γ and hadron showers are taken into account by parametrizing the lateral and longitudinal profiles of the showers. The starting point of a shower is fluctuated according to an exponential law.

For jet reconstruction, we used a modified UA1 Jet Finding Algorithm, with a cone size of $\Delta R = 0.8$ and a 25-GeV transverse energy threshold for jets.

4. BACKGROUNDS AND SUSY KINEMATICS

All SUSY processes with a full particle spectrum, couplings, the production cross section, and decays are generated with ISAJET 7.42, ISASUSY [15]. The Standard Model backgrounds are generated by PYTHIA 5.7 [16]. We used STEQ3L structure functions.

---

[3] Detector Description and Simulation Tools. CERN Program Library Long Writeup W50013, CERN, Geneva, 1993.

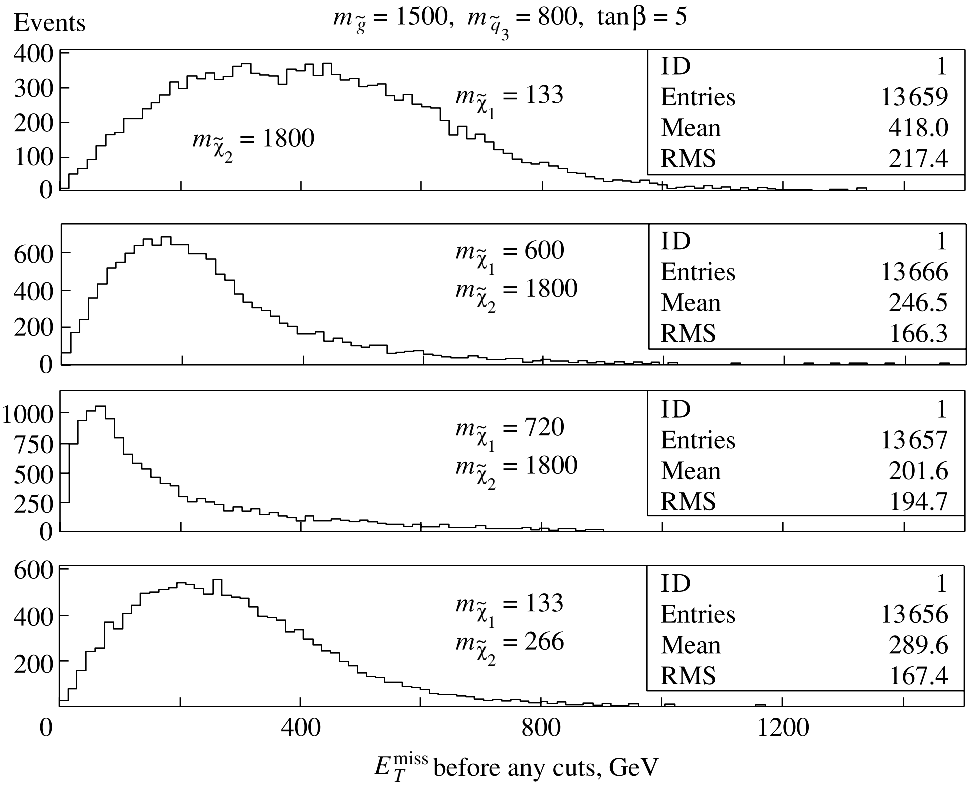

Fig. 2. $E_T^{\rm miss}$ distribution before any cuts on different masses of $\tilde\chi_1^0$ and $\tilde\chi_2^0$.

The following SM processes make the main contribution to the background: $W+$jets, $Z+$jets, $t\bar t$, $WZ, ZZ, b\bar b$, and QCD ($2\to2$) processes.

As was mentioned above, we consider, as signatures, $(n\geq m)$ jets + $(m\geq k)$ isolated leptons + $E_T^{\rm miss}$, where $m=2,3,4$ and $k=0,1,2,3$. Explicitly, we have considered the following signatures:

$$(n\geq m)\text{jets}+E_T^{\rm miss},$$

$$(n\geq m)\text{jets}+E_T^{\rm miss}+\text{ no isolated leptons},$$

$$(n\geq m)\text{jets}+E_T^{\rm miss}+1\text{ isolated lepton},$$

$$(n\geq m)\text{jets}+E_T^{\rm miss}+l^+l^-\text{ pair of isolated leptons},$$

$$(n\geq m)\text{jets}+E_T^{\rm miss}+l^\pm l^\pm\text{ pair of isolated leptons},$$

$$(n\geq m)\text{jets}+E_T^{\rm miss}+3\text{ isolated leptons}.$$

For leptons, we use the cut $P_{lT}\equiv\sqrt{p_{l1}^2+p_{l2}^2}\geq P_{lT_0}=20$ GeV. Our definition of an isolated lepton coincides with the definition used in the CMSJET code [14]. We use two sets of cuts (a and b) for the transverse missing energy $E_T^{\rm miss}$ and transverse jet energy E_{Tk} $(k=1,2,3,4)$. Cuts (a) and (b) are shown in Table 1. We have calculated the SM backgrounds for various values of E_{T1}, E_{T2}, E_{T3}, E_{T4}, and $E_T^{\rm miss}$ using PYTHIA 5.7 [16]. We have considered two values of $\tan\beta=5$ and $\tan\beta=35$ ($\tan\beta\equiv\langle H_t\rangle/\langle H_b\rangle$). We have analyzed both the case of a heavy and the case of a relatively light gluino. We have considered different values of LSP and the ratio $\tilde\chi_2^0/\tilde\chi_1^0$. In our calculations, we took $m_{\tilde q_{1,2}}=3800$ GeV for the masses of the first and second squark generations, but the results are virtually independent of the value of $m_{\tilde q_{1,2}}$ for $m_{\tilde q_{1,2}}\geq2500$ GeV.

5. RESULTS

The results of our calculations are shown in Tables 2 and in Figs. 1–4. Note that there is a crucial difference between a "future" experiment and the "real" experiment [17]. In the "real" experiment, the total number of events $N_{\rm ev}$ is a given number, and we compare it with the expected N_b when we test the validity of standard physics. Under the condition of a "future" experiment, we know only the average number of background events, N_b, and the average number of signal events, N_s; therefore we have to compare the Poisson distributions $P(n,N_b)$ and $P(n,N_b+N_s)$ to determine the probability of finding new physics in a future experiment. According to the general definition, the discovery potential for new physics corresponds to the case where the probability

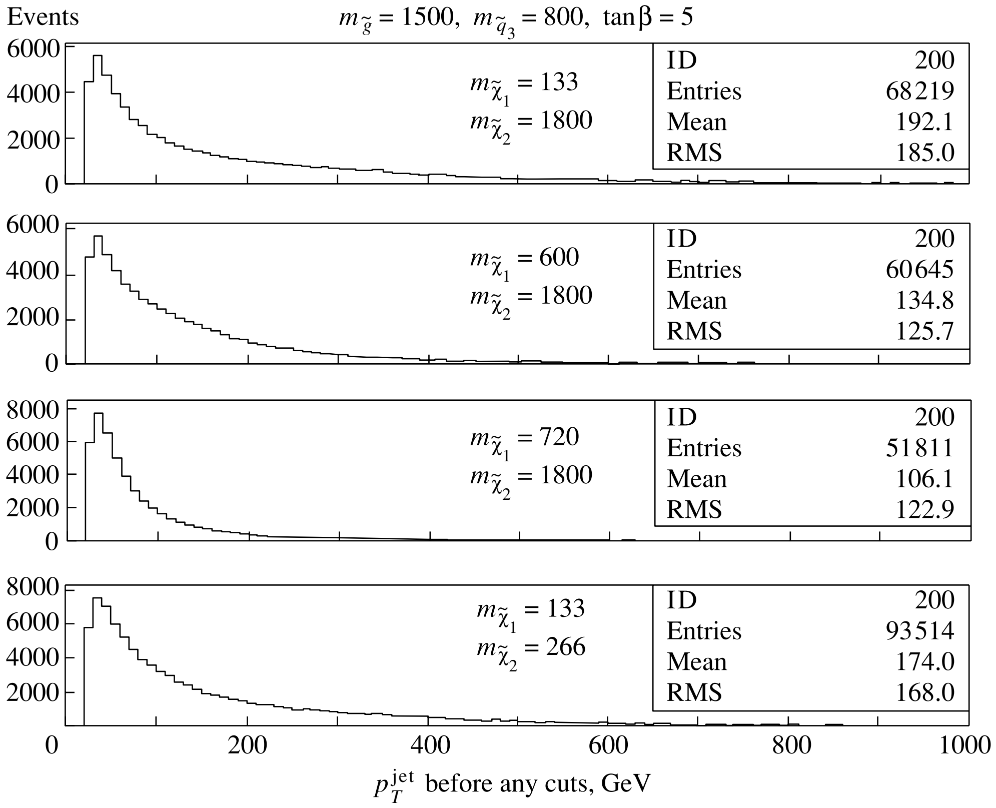

Fig. 3. p_T^{jet} distribution before any cuts on different masses of $\tilde\chi_1^0$ and $\tilde\chi_2^0$.

that the background can mimic the signal is less than $\Delta = 5.6 \times 10^{-7}$. This means that the signal with a background has a 5σ excess over a pure background in terms of standard deviations. Thus, we require that the probability $\beta(\Delta)$ of background fluctuations for $n > n_0(\Delta)$ be less than Δ, namely,

$$\beta(\Delta) = \sum_{n=n_0(\Delta)+1}^{\infty} P(n, N_b) \leq \Delta.$$

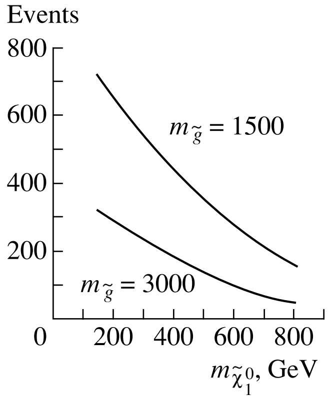

Fig. 4. Dependence of the number of signal events on the LSP mass for $m_{\tilde q_3} = 900$ GeV, $m_{\tilde q_{1,2}} = 3800$ GeV, $\mu = 1500$ GeV, $\tan\beta\ = 5$, $m_{\tilde\chi_2^0} = 1800$ GeV, and $L = 10^5$ pb^{-1} for cut 10b (Table 1) and $n_{\text{jet}} \geq 4$.

The discovery probability $1 - \alpha(\Delta)$ that the number of signal events will be larger than $n_0(\Delta)$ is equal to

$$1 - \alpha(\Delta) = \sum_{n=n_0(\Delta)+1}^{\infty} P(n, N_b + N_s).$$

We suppose that the signal is detectable if $1 - \alpha(\Delta) \geq 0.5$ and $N_s/N_b \geq 0.25$.

It follows from our results that, for fixed values of the squark and gluino masses, the visibility of the signal decreases with increasing LSP mass. This fact has a trivial explanation. Indeed, in the rest frame of the squark or the gluino, the jet spectrum becomes softer with increasing LSP mass. Furthermore, pair-produced squarks and gluino are produced with total transverse momentum close to zero in the parton model. For large LSP masses, the missing transverse momenta from two LSPs partly cancel.

Note that, for the case of relatively light third-generation squarks, b quarks dominate in the final state. In our calculations, we have not used b tagging to suppress the background and to make the signal more observable.

6. CONCLUSION

We have presented the results of an investigation of the LHC (CMS) SUSY discovery potential for models with effective supersymmetry. We have considered the general case of nonuniversal gaugino masses. We have found that the visibility of a signal through an excess over SM backgrounds in jets + isolated leptons + $E_T^{\rm miss}$ events depends rather strongly on the relation between the LSP, second-neutralino, gluino, and third-generation-squark masses, and it decreases with increasing LSP mass. For a relatively heavy gluino, it would be very difficult, or even impossible, to detect a SUSY signal even for light third-generation squarks ($m_{\tilde{q}_3} \leq 1$ TeV) if the LSP mass is close to the third-generation squark mass.

ACKNOWLEDGMENTS

We are indebted to participants of Daniel Denegri's working group on physics simulations at LHC for valuable comments.

This work was supported by the Russian Foundation for Basic Research (project no. 99-02-16956) and by the INTAS–CERN grant no. 99-377.

REFERENCES

1. S. Abdullin *et al.*, CMS NOTE 1998/006.
2. R. Barbieri *et al.*, Nucl. Phys. B **367**, 28 (1993); H. Baer, C. Chen, F. Paige, and X. Tata, Phys. Rev. D **50**, 2148 (1994); **52**, 2746 (1995); **53**, 6241 (1996).
3. R. Barbieri, Riv. Nuovo Cimento **11**, 1 (1988); A. B. Lahanas and D. V. Nanopoulos, Phys. Rep. **145**, 1 (1987); H. E. Haber and G. L. Kane, Phys. Rep. **117**, 75 (1985); H. P. Nilles, Phys. Rep. **110**, 1 (1984); N. V. Krasnikov and V. A. Matveev, Fiz. Élem. Chastits At. Yadra **28**, 1125 (1997) [Phys. Part. Nucl. **28**, 441 (1997)].
4. S. I. Bityukov and N. V. Krasnikov, Phys. Lett. B **469**, 149 (1999); Nuovo Cimento A **112**, 913 (1999).
5. M. Dine, A. Kagan, and D. Samuel, Phys. Lett. B **243**, 250 (1990); A. G. Cohen, D. B. Kaplan, and A. E. Nelson, Phys. Lett. B **243**, 588 (1990); J. Bagger, J. L. Feng, and N. Polonsky, Nucl. Phys. B **563**, 3 (1999).
6. S. I. Bityukov and N. V. Krasnikov, hep-ph/0005246; in *Proceedings of the International Seminar "Quarks-2000"* (in press).
7. B. C. Allanach, J. J. van der Bij, A. Dedes, *et al.*, J. Phys. G **26**, 1 (2000).
8. U. Chattopadhyay, Am. Datta, An. Datta, *et al.*, Phys. Lett. B **493**, 127 (2000).
9. V. S. Kaplunovsky and J. Louis, Phys. Lett. B **306**, 269 (1993).
10. N. Polonsky and A. Pomarol, Phys. Rev. Lett. **73**, 2292 (1994).
11. N. V. Krasnikov and V. V. Popov, hep-ph/9611298.
12. C. Kolda and J. March-Russell, Phys. Rev. D **55**, 4252 (1997).
13. H. Baer, M. A. Diaz, P. Quintana, and X. Tata, JHEP **0004**, 016 (2000).
14. S. Abdullin, A. Khanov, and N. Stepanov, CMS NOTE TN/94-180 (1994).
15. H. Baer, F. Paige, S. Protopopescu, and X. Tata, Preprint No. EP-930329 (Florida State University, 1993).
16. T. Sjostrand, Preprint CERN-TH.7112193 (Geneva, 1993).
17. S. I. Bityukov and N. V. Krasnikov, Mod. Phys. Lett. A **13**, 3235 (1998); Nucl. Instrum. Methods Phys. Res. A **452**, 518 (2000).

Physics of Atomic Nuclei, Vol. 65, No. 7, 2002, pp. 1352–1358. Translated from Yadernaya Fizika, Vol. 65, No. 7, 2002, pp. 1385–1391.

ELEMENTARY PARTICLES AND FIELDS
Theory

Polarization Effects in Proton–Proton Collisions

R. Kh. Muradov, A. I. Akhmedov, and R. M. Burdjaliev
Baku State University, ul. Z. Khalilova 23, Baku, 370145 Azerbaijan
Received January 30, 2001

Abstract—The single-spin and double-spin asymmetries in $pp \longrightarrow (\gamma^*, Z) + X$ processes induced by collisions of polarized protons are investigated on the basis of QCD and electroweak interaction by using the method of helicity amplitudes. Analytic expressions for the single-spin (A_L) and double-spin (A_{LL}) asymmetries are obtained, and their dependence on the dilepton transverse momentum is investigated at three values of the dilepton invariant mass. The results obtained in this study make it possible to explore the spin structure of the proton. © *2002 MAIK "Nauka/Interperiodica".*

Since the appearance of the data obtained in the EMC experiment [1], many studies have been devoted to the spin structure of the proton. In the lowest order of perturbative QCD, the spin of the proton can be represented as the sum of three terms; that is,

$$S_p = S_q + S_g + \langle L_z \rangle,$$

where S_q and S_g are, respectively, the quark and the gluon contribution to the proton spin and $\langle L_z \rangle$ is the contribution of the orbital angular momentum of the quarks and gluons.

The experimental results reported in [2–4] suggest that the gluon spin and orbital interaction contribute significantly to the proton spin. Naturally, these experimental results call for a theoretical explanation.

Gehrmann [5] calculated $O(\alpha_s)$ corrections to the x_{F} and y distributions of dileptons produced in collisions of longitudinally polarized hadrons. He also showed that measurement of the longitudinally polarized cross section for the Drell–Yan process would make it possible to investigate the distribution of polarized sea quarks in hadrons.

In [6], the longitudinal–transverse spin asymmetries A_{LT} in Drell–Yan processes were calculated in the leading order for nucleon–nucleon collisions at RHIC and HERA energies. It was shown that A_{LT} is much less than the respective transverse–transverse asymmetry A_{TT}.

The Drell–Yan process at high transverse momenta of the dilepton was studied in [7], where the effect of γZ interference was also taken into consideration. Both single-spin and double-spin asymmetries were investigated there. It was shown that the double-spin asymmetry at small invariant masses of the lepton pair and the single-spin asymmetry at the Z peak become significant.

Collisions of polarized hadrons are among processes of greater importance for studying the spin structure of the proton and for calculating the distributions of polarized quarks in the proton.

In the present study, single-spin and double-spin asymmetries in $pp \longrightarrow (\gamma^*, Z) + X$ processes induced by collisions of polarized hadrons are analyzed on the basis of QCD and electroweak interaction. This analysis is performed in the reference frame comoving with the center of mass of primary particles. In order to describe experiments that study the scattering of polarized particles, it is necessary to specify a helicity basis. Here, we use the method of helicity amplitudes. It should be noted that, in [5, 6], the asymmetries were studied with allowance for the polarizations of primary particles. Here, we consider asymmetries, taking into account the polarizations of all particles that participate in the reaction under study. We begin our analysis by introducing the subprocesses

$$\begin{aligned} g + q &\longrightarrow l^+ l^- + q, \qquad (1)\\ q + \overline{q} &\longrightarrow l^+ l^- + g. \end{aligned}$$

The Feynman diagrams of the $pp \to l^+ l^- + X$ subprocess are shown in Fig. 1.

The matrix elements for subprocesses (1) with allowance for a virtual photon and a Z boson can be represented as

$$M_\gamma = -ie^2 g_s t^a_{ik} \Big[\overline{v}(p_4, s_4) \gamma_\mu u(p_3, s_3) \Big]$$

$$\times \frac{g_{\mu\nu}}{q^2} \overline{u}(p_2, s_2) \hat{\varepsilon} \frac{\hat{f}_1 + m}{f_1^2 - m^2} \gamma_\nu u(p_1, s_1),$$

$$M_Z = -\frac{ig^2 g_s t^a_{ik}}{4 \cos^2 \Theta_{\mathrm{W}}}$$

$$
\begin{aligned}
&\times \left[\overline{v}(p_4, s_4)\gamma_\nu(g_{V_e} + g_{A_e}\gamma_5)u(p_3, s_3)\right] \\
&\quad \times \frac{g_{\mu\nu}}{q^2 - M_Z^2 + iM_Z\Gamma_Z}\overline{u}(p_2, s_2) \\
&\times \hat{\varepsilon}\frac{\hat{f}_1 + m}{f_1^2 - m^2}\gamma_\nu(g_{V_q} + g_{A_q}\gamma_5)u(p_1, s_1); \\
&M_\gamma = -ie^2 g_s t^a_{ik}\left[\overline{v}(p_4, s_4)\gamma_\mu u(p_3, s_3)\right] \\
&\times \frac{g_{\mu\nu}}{q^2}\overline{u}(p_2, s_2)\gamma_\nu\frac{\hat{f}_2 + m}{f_2^2 - m^2}\hat{\varepsilon}u(p_1, s_1), \\
&\qquad M_Z = -\frac{ig^2 g_s t^a_{ik}}{4\cos^2\Theta_{\mathrm{W}}} \\
&\times \left[\overline{v}(p_4, s_4)\gamma_\mu(g_{V_e} + g_{A_e}\gamma_5)u(p_3, s_3)\right] \\
&\quad \times \frac{g_{\mu\nu}}{q^2 - M_Z^2 + iM_Z\Gamma_Z}u(p_2, s_2) \\
&\times \gamma_\nu(g_{V_q} + g_{A_q}\gamma_5)\frac{\hat{f}_2 + m}{f_2^2 - m^2}\hat{\varepsilon}u(p_1, s_1);
\end{aligned}
$$

$$
\begin{aligned}
&M_\gamma = -ie^2 g_s t^a_{ik}\left[\overline{v}(p_4, s_4)\gamma_\mu u(p_3, s_3)\right] \qquad (2) \\
&\times \frac{g_{\mu\nu}}{q^2}\overline{u}(p_2, s_2)\hat{\varepsilon}\frac{\hat{f}_3 + m}{f_3^2 - m^2}\gamma_\nu u(p_1, s_1), \\
&\qquad M_Z = -\frac{ig^2 g_s t^a_{ik}}{4\cos^2\Theta_{\mathrm{W}}} \\
&\times \left[\overline{v}(p_4, s_4)\gamma_\mu(g_{V_e} + g_{A_e}\gamma_5)u(p_3, s_3)\right] \\
&\quad \times \frac{g_{\mu\nu}}{q^2 - M_Z + iM_Z\Gamma_Z}\overline{u}(p_2, s_2)\hat{\varepsilon} \\
&\times \frac{\hat{f}_3 + m}{f_3^2 - m^2}\gamma_\nu(g_{V_q} + g_{A_q}\gamma_5)u(p_1, s_1); \\
&M_\gamma = -ie^2 g_s t^a_{ik}\left[\overline{v}(p_4, s_4)\gamma_\mu u(p_3, s_3)\right] \\
&\times \frac{g_{\mu\nu}}{q^2}u(p_2, s_2)\gamma_\nu\frac{\hat{f}_4 + m}{f_4^2 - m^2}\hat{\varepsilon}u(p_1, s_1), \\
&\qquad M_Z = -\frac{ig^2 g_s t^a_{ik}}{4\cos^2\Theta_{\mathrm{W}}} \\
&\times \left[\overline{v}(p_4, s_4)\gamma_\mu(g_{V_e} + g_{A_e}\gamma_5)u(p_3, s_3)\right] \\
&\quad \times \frac{g_{\mu\nu}}{q^2 - M_Z^2 + iM_Z\Gamma_Z}\overline{u}(p_2, s_2) \\
&\times \gamma_\nu(g_{V_q} + g_{A_q}\gamma_5)\frac{\hat{f}_4 + m}{f_4^2 - m^2}\hat{\varepsilon}u(p_1, s_1),
\end{aligned}
$$

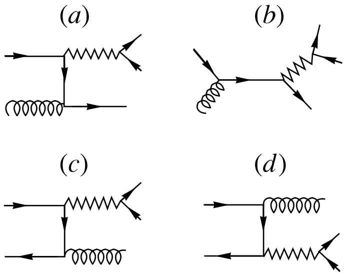

Fig. 1. Feynman diagrams for $pp \longrightarrow l^+l^- + X$ process.

where $t^a_{ik} = \lambda^a_{ik}/2$ are the Gell-Mann matrices, g_s is the strong-interaction coupling constant,

$$
f_1 = p_1 - q, \quad f_2 = p_1 + p_2,
$$
$$
f_3 = p_1 - q, \quad f_4 = p_1 - p_5.
$$

The helicity amplitudes are denoted by $M(\lambda_1, \lambda_2; \lambda_3, \lambda_4, \lambda_5)$, where λ_1 and λ_2 are the helicities of the initial partons, λ_3 and λ_4 are the helicities of two leptons, and λ_5 is the helicity of the final-state parton:

$$
M(\lambda_1, \lambda_2; \lambda_3, \lambda_4, \lambda_5) \qquad (3)
$$
$$
= \begin{cases} M(\lambda_1, \lambda_2; \lambda_3, -\lambda_3, \lambda_2) \\ \text{for } g + q \longrightarrow l^+l^- + q \\ M(\lambda_1, -\lambda_1; \lambda_3, -\lambda_3, \lambda_5) \\ \text{for } q + \overline{q} \longrightarrow l^+l^- + g. \end{cases}
$$

Positive- and negative-helicity states are denoted by $|A_\pm\rangle$; they have the following properties:

$$
\begin{aligned}
(1 + \gamma_5)|A_\pm\rangle &= 0, \\
|A_+\rangle^c &= -|A_-\rangle, \\
\langle A_\mp|B_\pm\rangle &= -\langle B_\mp|A_\pm\rangle, \qquad (4) \\
\langle A_+|\gamma_\mu|B_+\rangle &= \langle B_-|\gamma_\mu|A_-\rangle.
\end{aligned}
$$

Making use of the Fierz identities, we obtain

$$
\langle A_+|\gamma_\mu|B_+\rangle\langle C_-|\gamma_\mu|D_-\rangle = 2\langle A_+|D_-\rangle\langle C_-|B_+\rangle, \qquad (5)
$$
$$
\langle A_-|B_+\rangle\langle C_-|D_+\rangle
$$
$$
= \langle A_-|D_+\rangle\langle C_-|B_+\rangle + \langle A_-|C_+\rangle\langle B_-|D_+\rangle.
$$

The spinors $u_\pm(p)$ and $v_\pm(p)$ describing a particle of momentum p and helicity $\lambda = \pm 1$ satisfy the relations

$$
\hat{p}u(p) = \hat{p}v(p) = \overline{u}(p)\hat{p} = \overline{v}(p)\hat{p}, \quad p^2 = 0, \qquad (6)
$$
$$
\begin{aligned}
(1 \pm \gamma_5)v_\pm &= (1 \mp \gamma_5)u_\pm \\
= \overline{u}_\pm(1 \pm \gamma_5) &= \overline{v}_\pm(1 \mp \gamma_5) = 0, \\
\overline{u}_\pm(p)\gamma_\mu u_\pm(p) &= \overline{v}_\pm(p)\gamma_\mu v_\pm(p) = 2p_\mu.
\end{aligned}
$$

Here and below, we use the conventional notation

$$\begin{gathered}u_\pm(p) = v_\mp(p) = |p_\pm\rangle, \qquad (7)\\ \bar{u}_\pm(p) = \overline{v}_\mp(p) = \langle p_\pm|,\\ \langle p_-|q_+\rangle = \langle pq\rangle = -\langle qp\rangle,\\ \langle q_+|p_-\rangle = \langle pq\rangle^* = -\langle qp\rangle^*,\\ |\langle pq\rangle|^2 = 2p\cdot q.\end{gathered}$$

The gluon helicities are defined as follows:

$$\varepsilon_1^\pm = \pm\frac{\sqrt{2}}{\langle p_5^\mp|p_1^\pm\rangle}\left[|p_1^\mp\rangle\langle p_5^\mp| + |p_5^\pm\rangle\langle p_1^\pm|\right] \qquad (8)$$

for $g + q \longrightarrow l^+l^- + q$,

$$\varepsilon_5^\pm = \pm\frac{\sqrt{2}}{\langle p_1^\mp|p_5^\pm\rangle}\left[|p_5^\mp\rangle\langle p_1^\mp| + |p_1^\pm\rangle\langle p_5^\pm|\right] \qquad (9)$$

for $q + \overline{q} \longrightarrow l^+l^- + g$.

The Lagrangian describing interactions of fundamental fermions with gauge bosons has the form

$$L = \frac{e}{2}(J_\mu^\gamma A_\mu + J_\mu^Z Z_\mu), \qquad (10)$$

where

$$J_\mu^i = \overline{\Psi}_f\gamma_\mu\left[g_{L_f}^i(1+\gamma_5) + g_{R_f}^i(1-\gamma_5)\right]\Psi_f,$$

and $g_{L_f}^i$ and $g_{R_f}^i$ are the chiral coupling constants for the interaction of the fermion f with gauge bosons i ($i = \gamma, Z$). These chiral coupling constants are given by

$$\begin{gathered}g_{L_f}^\gamma = g_{R_f}^\gamma = Q_f, \qquad (11)\\ g_{L_f}^Z = \frac{2}{\sin 2\Theta_\mathrm{W}}(I_{3f} - Q_f X_\mathrm{W}),\\ g_{R_f}^Z = \frac{2}{\sin 2\Theta_\mathrm{W}}(-Q_f X_\mathrm{W}),\end{gathered}$$

where $X_\mathrm{W} = \sin^2\Theta_\mathrm{W}$ is the Weinberg angle and Q_f and I_{3f} are, respectively, the charge of the fermion f and the third component of its weak isospin.

The Mandelstam invariant variables for the subprocess under study are defined as

$$\begin{gathered}\hat{s} = (p_1+p_2)^2, \quad \hat{t} = (p_5-p_2)^2 = (Q-p_1)^2, \qquad (12)\\ \hat{u} = (p_5-p_1)^2 = (Q-p_2)^2.\end{gathered}$$

Let us consider the reference frame comoving with the center of mass of primary particles, where the momenta of primary hadrons are given by

$$\begin{gathered}P_1 = \frac{\sqrt{s}}{2}(1,0,0,1), \quad P_2 = \frac{\sqrt{s}}{2}(1,0,0,-1), \qquad (13)\\ p_1 = x_1P_1, \quad p_2 = x_2P_2,\\ p_5^\mu = p_1^\mu + p_2^\mu - Q^\mu,\\ Q^\mu = p_3^\mu + p_4^\mu,\\ q^\mu = p_3^\mu - p_4^\mu;\end{gathered}$$

p_5 is the momentum of the outgoing hadron. The momenta of the two leptons and of the final-state parton are taken to be [8]

$$\begin{gathered}p_3^\mu = \frac{1}{2}(E' - q'\cos\alpha, q'\sin\theta \qquad (14)\\ - q\sin\alpha\cos\beta\cos\theta - E'\cos\alpha\sin\theta,\\ -q\sin\alpha\sin\beta, q'\cos\theta - E'\cos\alpha\cos\theta\\ + q\sin\alpha\cos\beta\sin\theta),\\ p_4^\mu = \frac{1}{2}(E' + q'\cos\alpha, q'\sin\theta\\ + q\sin\alpha\cos\beta\cos\theta + E'\cos\alpha\sin\theta,\\ q\sin\alpha\sin\beta, q'\cos\theta + E'\cos\alpha\cos\theta\\ - q\sin\alpha\cos\beta\sin\theta),\\ p_5 = (q', -q\sin\theta, 0, -q'\cos\theta),\end{gathered}$$

where $E' = \dfrac{\hat{s}+q^2}{2\hat{s}}$ and $q' = \dfrac{\hat{s}-q^2}{2\hat{s}}$.

We now proceed to computing the square of the matrix element, taking into account all helicity states of the particles.

(i) The diagrams in Figs. 1*a* and 1*b* yield

$$\begin{gathered}|M(++;+-+)|^2 = \left[\frac{2g_s^2g^4g_{R_q}^2g_{L_e}^2}{[(q^2-M_Z^2)^2+M_Z^2\Gamma_Z^2]}\right. \qquad (15)\\ \left. + \frac{8g_s^2e^4Q_q^2}{q^4} + \frac{8g_s^2e^2g^2Q_qg_{Rq}g_{Le}(q^2-M_Z^2)}{q^2[(q^2-M_Z^2)^2+M_Z^2\Gamma_Z^2]}\right]\\ \times\left\{\frac{2\pi}{\hat{s}}\hat{t}^2 + \frac{\pi}{\hat{s}}\hat{t}\hat{u} + \pi\hat{u} + 2\pi Q^2\right.\\ + \frac{\pi}{\hat{s}}\hat{u}^2 + \frac{\pi(Q^2\hat{t}-\hat{s}\hat{u})}{3\hat{s}\hat{u}(\hat{s}-Q^2)}\\ \times(\hat{s}\hat{t}\hat{u} + Q^2\hat{s}\hat{t} - \hat{s}^2\hat{u} - \hat{s}\hat{u}^2 - Q^2\hat{u}\hat{t} - Q^2\hat{t}^2)\\ \left. + \frac{4\pi}{3}\frac{Q^2(\hat{t}^2+\hat{u}\hat{t}-\hat{s}\hat{t})}{(\hat{s}^2-Q^2)}\right\},\end{gathered}$$

$$\begin{gathered}|M(++;-++)|^2 = |M(++;+-+)|^2,\\ |M(+-;+--)|^2 = \left[\frac{2g_s^2g^4g_{L_q}^2g_{L_e}^2}{[(q^2-M_Z^2)^2+M_Z^2\Gamma_Z^2]}\right. \qquad (16)\\ \left. + \frac{8g_s^2e^4Q_q^2}{q^4} + \frac{8g_s^2e^2g^2Q_qg_{Lq}g_{Le}(q^2-M_Z^2)}{q^2[(q^2-M_Z^2)^2+M_Z^2\Gamma_Z^2]}\right]\\ \times\left\{\frac{-\pi Q^2}{\hat{s}\hat{u}}(\hat{t}+\hat{u}+2Q^2)^2 - \frac{\pi Q^2}{3\hat{s}\hat{u}(\hat{s}-Q^2)^2}\right.\end{gathered}$$

$$\times (Q^2\hat{t} + Q^2\hat{u} - \hat{s}\hat{t} - \hat{s}\hat{u})^2\Big\},$$

$$|M(+-;-+-)|^2 = |M(+-;+--)|^2$$

for $g_{R_e} \longleftrightarrow g_{L_e}$.

(ii) The contribution of the diagrams in Figs. 1*c* and 1*d* is

$$|M(+-;+-+)|^2 = \left[\frac{2g_s^2 g^4 g_{L_q}^2 g_{L_e}^2}{[(q^2 - M_Z^2)^2 + M_Z^2\Gamma_Z^2]}\right. \tag{17}$$

$$\left. + \frac{8g_s^2 e^4 Q_g^2}{q^4} + \frac{8g_s^2 e^2 g^2 Q_q g_{L_q} g_{L_e}(q^2 - M_Z^2)}{q^2[(q^2 - M_Z^2)^2 + M_Z^2\Gamma_Z^2]}\right]$$

$$\times \left\{\pi Q^2 \frac{\hat{t}}{\hat{u}} + \frac{\pi}{3}\frac{Q^2(Q^2\hat{u} - \hat{s}\hat{t})^2}{\hat{u}\hat{t}(\hat{s} - Q^2)^2} + \frac{4\pi}{3}\frac{Q^4\hat{s}}{(\hat{s} - Q^2)^2}\right\},$$

$$|M(+-;-++)|^2 = |M(+-;+-+)|^2$$

for $g_{R_e} \longleftrightarrow g_{L_e}$,

$$|M(+-;+--)|^2 = \left[\frac{2g_s^2 g^4 g_{L_q}^2 g_{L_e}^2}{[(q^2 - M_Z^2)^2 + M_Z^2\Gamma_Z^2]}\right. \tag{18}$$

$$\left. + \frac{8g_s^2 e^4 Q_g^2}{q^4} + \frac{8g_s^2 e^2 g^2 Q_q g_{L_q} g_{L_e}(q^2 - M_Z^2)}{q^2[(q^2 - M_Z^2)^2 + M_Z^2\Gamma_Z^2]}\right]$$

$$\times \Bigg\{\frac{2\pi}{3}\frac{(Q^2\hat{t} - \hat{s}\hat{u})^2}{\hat{u}(\hat{s} - Q^2)^2} + \frac{\pi}{3}\frac{\hat{s}(Q^2\hat{t} - \hat{u}\hat{s})^2}{\hat{u}\hat{t}(\hat{s} - Q^2)^2}$$

$$+ \frac{4\pi}{3}\frac{Q^2\hat{s}\hat{t}}{(\hat{s} - Q^2)^2} + \frac{4\pi}{3}\frac{Q^2\hat{s}^2}{(\hat{s} - Q^2)^2}$$

$$- 2\pi\hat{u} - 2\pi Q^2 - \pi\frac{\hat{s}\hat{u}}{\hat{t}} - 2\pi Q^2\frac{\hat{s}}{\hat{t}}\Bigg\},$$

$$|M(+-;-+-)|^2 = |M(+-;+--)|^2$$

for $g_{R_e} \longleftrightarrow g_{L_e}$.

All scalar products $p_i \cdot p_j$ can be expressed in terms of the Mandelstam variables [9]

$$s_{12} = \hat{s}, \tag{19}$$

$$s_{13} = 2p_1p_3 = \frac{1}{2}(Q^2 - \hat{t}) - \frac{Q^2\hat{u} - \hat{s}\hat{t}}{2(\hat{s} - Q^2)}\cos\alpha$$

$$- \frac{\sqrt{Q^2\hat{s}\hat{t}\hat{u}}}{\hat{s} - Q^2}\sin\alpha\cos\beta,$$

$$s_{14} = 2p_1p_4 = \frac{1}{2}(Q^2 - \hat{t}) + \frac{Q^2\hat{u} - \hat{s}\hat{t}}{2(\hat{s} - Q^2)}\cos\alpha$$

$$+ \frac{\sqrt{Q^2\hat{s}\hat{t}\hat{u}}}{\hat{s} - Q^2}\sin\alpha\cos\beta,$$

$$s_{15} = 2p_1p_5 = -\hat{u},$$

$$s_{23} = 2p_2p_3 = \frac{1}{2}(Q^2 - \hat{u}) - \frac{Q^2\hat{t} - \hat{s}\hat{u}}{2(\hat{s} - Q^2)}\cos\alpha$$

$$+ \frac{\sqrt{Q^2\hat{s}\hat{t}\hat{u}}}{\hat{s} - Q^2}\sin\alpha\cos\beta,$$

$$s_{24} = 2p_2p_4 = \frac{1}{2}(Q^2 - \hat{u}) + \frac{Q^2\hat{t} - \hat{s}\hat{u}}{2(\hat{s} - Q^2)}\cos\alpha$$

$$- \frac{\sqrt{Q^2\hat{s}\hat{t}\hat{u}}}{\hat{s} - Q^2}\sin\alpha\cos\beta,$$

$$s_{25} = 2p_2p_5 = -\hat{t},$$

$$s_{34} = 2p_3p_4 = Q^2,$$

$$s_{35} = 2p_3p_5 = -\frac{\hat{u} + \hat{t}}{2}(1 - \cos\alpha),$$

$$s_{45} = 2p_4p_5 = -\frac{\hat{u} + \hat{t}}{2}(1 + \cos\alpha).$$

Integration over the final states in phase space can be simplified by employing the relation

$$\frac{1}{(2\pi)^9}\frac{d^3p_3}{2E_3}\frac{d^3p_4}{2E_4}\frac{d^3p_5}{2E_5}\delta(p_1 + p_2 - q - p_5) \tag{20}$$

$$= \frac{1}{(2\pi)^9}\frac{1}{16}d\Omega\pi\delta(\hat{s} + \hat{t} + \hat{u} - Q^2)\frac{dQ^2d\hat{t}d\hat{u}}{\hat{s}}.$$

The effective cross section for $pp \longrightarrow l^+l^- + X$ processes can be represented in the form [10]

$$E\frac{d\sigma}{dQ^2d^3p} = \int\limits_{x_1^{\min}}^{1}\int\limits_{x_2^{\min}}^{1} dx_1dx_2G^A(x_1)G^B(x_2) \tag{21}$$

$$\times \frac{\hat{s}}{\pi}\frac{d\hat{\sigma}}{dQ^2d\hat{t}d\hat{u}}\delta(\hat{s} + \hat{t} + \hat{u} - Q^2),$$

$$\pi E\frac{d\sigma}{d^3p} = \frac{d\sigma}{dydp_T^2},$$

where y is the rapidity of the lepton pair, p_T is its transverse momentum, and $G^A(x_1)$ and $G^B(x_2)$ are the distributions of the partons in the proton. From expression (21), it follows that, in the double-spin case, the correlation effective cross section has the form

$$\frac{d\Delta\sigma}{dQ^2dydp_T^2} = \int\limits_{x_1^{\min}}^{1}\int\limits_{x_2^{\min}}^{1} dx_1dx_2 \tag{22}$$

$$\times \Delta G^A(x_1)\Delta G^B(x_2)\hat{s}\frac{d\Delta\hat{\sigma}}{dQ^2d\hat{t}d\hat{u}}\delta(\hat{s} + \hat{t} + \hat{u} - Q^2),$$

$$d\Delta\sigma = \frac{1}{2}(d\sigma^{(++)} - d\sigma^{(+-)}),$$

whereas, in the single-spin case, we obtain

$$\frac{d\Delta\sigma}{dQ^2dydp_T^2} = \int\limits_{x_1^{\min}}^{1}\int\limits_{x_2^{\min}}^{1} dx_1dx_2 \tag{23}$$

$$\begin{gathered}
\times \Delta G^A(x_1)\Delta G^B(x_2)\hat{s}\frac{d\Delta\hat{\sigma}}{dQ^2 d\hat{t} d\hat{u}}\delta(\hat{s}+\hat{t}+\hat{u}-Q^2),\\
d\Delta\sigma = d\sigma^{(+)} - d\sigma^{(-)} = \frac{1}{2}(d\sigma^{(++)}\\
+ d\sigma^{(+-)} - d\sigma^{(-+)} - d\sigma^{(--)});\\
\hat{s} = x_1 x_2 s,\\
\hat{t} = x_1 t + (1-x_1)Q^2, \qquad (24)\\
\hat{u} = x_2 u + (1-x_2)Q^2,\\
t = Q^2 - m_T\sqrt{s}e^{-y},\\
u = Q^2 - m_T\sqrt{s}e^{y},
\end{gathered}$$

where Q^2 is the invariant mass of the lepton pair and m_T is the transverse mass, which is given by $m_T^2 = Q^2 + p_T^2$

$$x_1 = \frac{x_2\sqrt{s}\sqrt{Q^2+p_T^2}e^{y} - Q^2}{x_2 s - \sqrt{s}\sqrt{Q^2+p_T^2}e^{-y}}; \qquad (25)$$

$$x_2 = \frac{x_1\sqrt{s}\sqrt{Q^2+p_T^2}e^{-y} - Q^2}{x_1 s - \sqrt{s}\sqrt{Q^2+p_T^2}e^{y}};$$

$$x_1^{\min} = \frac{-u}{s+t-Q^2} = \frac{\sqrt{s}\sqrt{Q^2+p_T^2}e^{y} - Q^2}{s - \sqrt{s}\sqrt{Q^2+p_T^2}e^{-y}}; \qquad (26)$$

$$x_2^{\min} = \frac{-t}{s+t-Q^2} = \frac{\sqrt{s}\sqrt{Q^2+p_T^2}e^{-y} - Q^2}{s - \sqrt{s}\sqrt{Q^2+p_T^2}e^{y}}.$$

In order to compute single- and double-spin asymmetries, we introduce the quantities

$$\begin{gathered}
d\hat{\sigma}^{(++)} \pm d\hat{\sigma}^{(+-)} \sim \Big\{(|M(++;+-+)|^2 \qquad (27)\\
+ |M(++;-++)|^2 \pm |M(+-;+--)|^2\\
\pm |M(+-;-+-)|^2) \pm (|M(+-;+-+)|^2\\
+ |M(+-;-++)|^2 + |M(+-;+--)|^2\\
+ |M(+-;-+-)|^2)\Big\},
\end{gathered}$$

$$\begin{gathered}
d\hat{\sigma}^{(+)} \pm d\hat{\sigma}^{(-)} \sim \Big\{(|M(++;+-+)|^2 \qquad (28)\\
+ |M(++;-++)|^2 + |M(+-;+--)|^2\\
+ |M(+-;-+-)|^2 \pm |M(-+;+-+)|^2\\
\pm |M(-+;-++)|^2 \pm |M(--;+--)|^2\\
\pm |M(--;-+-)|^2) + (|M(+-;+-+)|^2
\end{gathered}$$

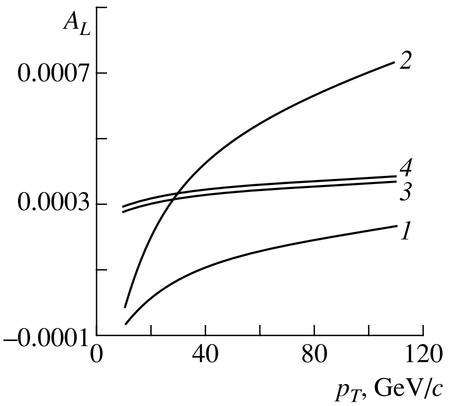

Fig. 2. Single-spin asymmetry in $pp \longrightarrow l^+l^- + X$ processes as a function of the dilepton transverse momentum $\sqrt{s} = 500$ GeV, the dilepton invariant mass of $Q = 10$ GeV, and the rapidity of $y = 0$. Shown in the figure are the results obtained on the basis of the CLW model with (curve *1*) set I and (curve *2*) set II and on the basis of the GRSV model with (curve *3*) set I and (curve *4*) set II.

$$\begin{gathered}
+ |M(+-;+--)|^2 + |M(+-;-++)|^2\\
+ |M(+-;-+-)|^2 \pm |M(-+;+--)|^2\\
\pm |M(-+;+-+)|^2 \pm |M(-+;-++)|^2\\
\pm |M(-+;-+-)|^2)\Big\}.
\end{gathered}$$

For this purpose, we also use the well-known expressions

$$A_L \frac{\left(d\sigma^{(+)}/dQ^2dydp_T^2\right) - \left(d\sigma^{(-)}/dQ^2dydp_T^2\right)}{\left(d\sigma^{(+)}/dQ^2dydp_T^2\right) + \left(d\sigma^{(-)}/dQ^2dydp_T^2\right)}, \qquad (29)$$

$$A_{LL} \qquad (30)$$

$$= \frac{\left(d\sigma^{(++)}dQ^2dydp_T^2\right) - \left(\dfrac{d\sigma^{(+-)}}{dQ^2dydp_T^2}\right)}{\left(d\sigma^{(++)}/dQ^2dydp_T^2\right) + \left(d\sigma^{(+-)}/dQ^2dydp_T^2\right)}.$$

In order to compute single- and double-spin asymmetries numerically, we employ two functions that describe the distribution of polarized quarks which were proposed by Cheng *et al.* [11] (the CLW model) and by Glück *et al.* [12] (the GRSV model). We use two sets of parameters for each function. For unpolarized quarks the distribution function was found by Martin *et al.* [13].

The dependences of the single- (A_L) and double-spin (A_{LL}) asymmetries on the dilepton transverse momentum were performed at $\sqrt{s} = 500$ GeV for various values of the invariant mass of the lepton pair: $Q = 10$, 60 GeV, and M_Z.

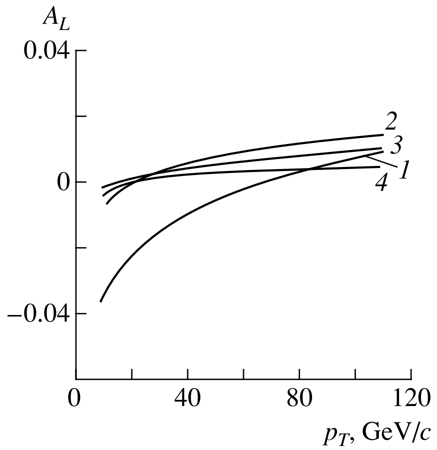

Fig. 3. As in Fig. 2, but for $Q = 60$ GeV.

The single-spin asymmetry in $pp \longrightarrow l^+l^- + X$ processes as a function of the transverse momentum of the lepton pair is shown in Figs. 2–4 at $\sqrt{s} =$ 500 GeV for three values of the dilepton invariant mass. The single-spin asymmetry A_L as a function of the dilepton transverse momentum p_T is presented in Fig. 2 at the dilepton invariant mass of $Q =$ 10 GeV and the rapidity of $y = 0$. It can be seen that, for the single-spin asymmetry A_L, the result within the CLW model differs substantially from that within the GRSV model. As the transverse momentum p_T varies within the range ~10–110 GeV/c, the single-spin asymmetry in the CLW model exhibits a smooth increase, whereas the single-spin asymmetry in the GRSV model remains constant. At the values of the dilepton invariant mass between $Q = 60$ GeV and $Q = M_Z$, the single-spin asymmetry slowly increases both in the CLW and in the GRSV model. As the dilepton mass varies from $Q = 10$ GeV to $Q = M_Z$, the single-spin asymmetry can take either positive or negative values. It should be noted that, over the entire invariant-mass range under consideration, the single-spin asymmetries in the GRSV model are virtually independent of the choice of the set of partons.

The double-spin asymmetry in $pp \longrightarrow l^+l^- + X$ processes as a function of the dilepton transverse momentum at the rapidity of $y = 0$ and the energy of $\sqrt{s} = 500$ GeV is illustrated in Figs. 5–7 for three values of the dilepton invariant mass: $Q = 10$, 60 GeV, and M_Z. For all values of the dilepton invariant mass, the double-spin asymmetry is greater than the single-spin asymmetry for p_T values considered in these figures. The double-spin asymmetries in the GRSV model are also shown in these figures. For all values considered in this study for the dilepton invariant mass and transverse momentum, they are virtually indistinguishable. In the case of the CLW model, these asymmetries show a slow decrease.

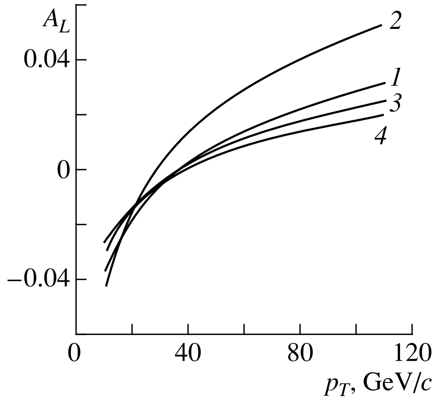

Fig. 4. As in Fig. 2, but for $Q = M_Z$.

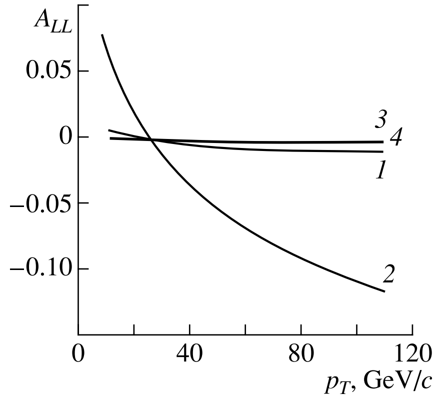

Fig. 5. Double-spin asymmetry in $pp \longrightarrow l^+l^- + X$ processes as a function of the dilepton transverse momentum at $\sqrt{s} = 500$ GeV, the dilepton invariant mass of $Q = 10$ GeV, and the rapidity of $y = 0$. Shown are the asymmetries obtained on the basis of the CLW model with (curve *1*) set I and (curve *2*) set II and on the basis of the GRSV model with (curve *3*) set I and (curve *4*) set II.

In the present study, we performed a numerical analysis of single- and double-spin asymmetries for $pp \longrightarrow (\gamma^*, Z) + X$ processes using the method of helicity amplitudes. Asymmetries were explored in the domain of high momentum transfers at RHIC energies. We employed the distributions of polarized partons within the CLW [11] and the GRSV [12] model. Both sets (CLW and GRSV) were obtained in the second order of perturbation theory. The distribution of unpolarized partons was taken from [13]. In general, the distinction between the single-spin asymmetries A_L for the two sets of partons in the CLW model is greater than that in the GRSV model. These asymmetries generally increase as the dilepton mass approaches the Z-boson mass. The distinction between the two sets in the GRSV model is small. At a fixed value of p_T, the double-spin asymmetries A_{LL} are on the same order of magnitude at the three

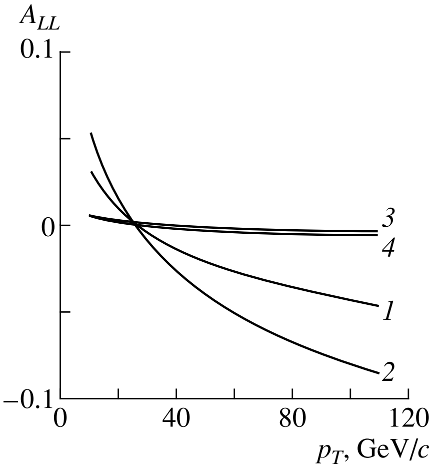

Fig. 6. As in Fig. 5, but for $Q = 60$ GeV.

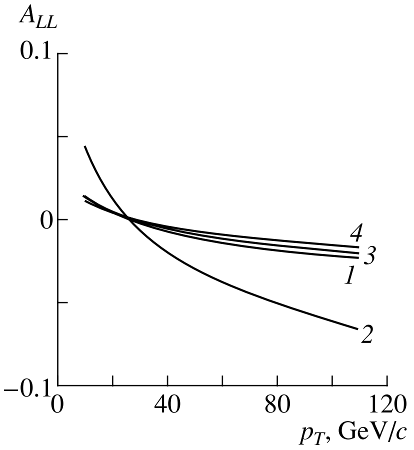

Fig. 7. As in Fig. 5, but for $Q = M_Z$.

values of Q. At various values of p_T, the difference between the asymmetries for the two sets of partons in the CLW model is greater than that in the GRSV model. The difference of the asymmetries for the two sets in the GRSV model is nearly constant. Note that these asymmetries are virtually independent of Q.

The contribution of the Z boson processes to polarized particles, in general, and to the single-spin parity-violating asymmetries, in particular, is significant. The single-spin asymmetries become large, both in the CLW and in the GRSV models, as the dilepton invariant mass approaches the Z-boson mass. Over the range of p_T under study, the double-spin asymmetry is greater than the single-spin asymmetry for all values of the dilepton mass. Therefore, measurement of the single-spin asymmetry may aid in studying the spin structure of the proton.

It should be noted that Leader and Sridhar [7] considered $pp \longrightarrow l^+l^- +$ jet processes and obtained similar results. This study was based on taking into account $O(\alpha_s)$ tree Feynman diagrams at the parton level. The calculation of one-loop radiative QCD corrections to the subprocesses involving polarized partons presents a challenge and has yet to be performed. It is worth noting that, at the energies under consideration, the $O(\alpha_s^2)$ polarization corrections to the cross section for the Drell–Yan process amount to about 10%.

REFERENCES

1. EMC Collab. (J. Ashman *et al.*), Phys. Lett. B **206**, 364 (1988).
2. K. Abe *et al.*, Phys. Rev. Lett. **74**, 346 (1995).
3. D. L. Anthony *et al.*, Phys. Rev. Lett. **71**, 959 (1993).
4. D. Adams *et al.*, Phys. Lett. B **357**, 248 (1995).
5. T. Gehrmann, Nucl. Phys. B **498**, 245 (1997).
6. Y. Kanazawa, Y. Koike, and N. Nishiyama, Phys. Lett. B **430**, 195 (1998).
7. E. Leader and K. Sridhar, Phys. Lett. B **311**, 324 (1993).
8. R. D. Carlits and R. S. Willey, Phys. Rev. D **45**, 2323 (1992).
9. E. Byckling and K. Kajantie, *Particle Kinematics* (Wiley, New York, 1973; Mir, Moscow, 1975).
10. E. Reya, Phys. Rep. **69**, 292 (1981).
11. H.-Y. Cheng, H. H. Liu, and C.-Y. Wu, Phys. Rev. D **53**, 2380 (1996).
12. M. Gluck, E. Reya, M. Stratmann, and W. Vogelsang, Phys. Rev. D **53**, 4775 (1996).
13. A. D. Martin, R. G. Roberts, and W. J. Stirling, Phys. Rev. D **50**, 6734 (1994).

Translated by R. Rogalev

Physics of Atomic Nuclei, Vol. 65, No. 7, 2002, pp. 1359–1369. Translated from Yadernaya Fizika, Vol. 65, No. 7, 2002, pp. 1392–1402.
Original Russian Text Copyright © 2002 by Dementiy.

ELEMENTARY PARTICLES AND FIELDS
Theory

On the Kinematics of $(e, e'p)$ Reactions

S. V. Dementiy[*]

Kharkov Institute for Physics and Technology, ul. Akademicheskaya 1, 61108 Kharkov, Ukraine

Received February 23, 2001; in final form, July 23, 2001

Abstract—The problem of interpreting experimental data on quasielastic electron scattering on nuclei in $A(e, e'p)(A-1)$ reactions is considered. It is shown that the existing discrepancies in experimental data on the reaction ^{4}He$(e, e'p)$T are associated with the fact that the residual-nucleus momentum p_m as determined from the law of energy—momentum conservation cannot be treated as that which is equal to the momentum p of the primary intranuclear nucleon. Under the assumption that the momentum transferred from the electron to the intranuclear nucleon is redistributed during the divergence of the products of the $(e, e'p)$ reaction in question, the method for extracting p is modified by introducing a kinematical correction, whereby the situation is considerably improved. For a first approximation, the correction can be evaluated on the basis of data on $A(e, e')$ inclusive reactions. The argument behind this evaluation is illustrated by considering the example of the reaction ^{4}He$(e, e'p)$T. *© 2002 MAIK "Nauka/Interperiodica".*

The reactions of quasielastic scattering on nuclei have been considered as a promising tool for studying the structure of nuclei since the very beginning of investigations into such reactions. By way of example, we indicate that, owing to the fact that the electromagnetic interaction of a scattered particle with nucleons is relatively weak and is well understood, both from the experimental and from the theoretical point of view, quasielastic electron scattering immediately made it possible to draw specific conclusions on the momentum distributions of intranuclear nucleons (for an overview, see [1]).

At same time, there arose difficulties in interpreting new data obtained upon the elaboration of experimental equipment and the improvement of the experimental precision. For example, the most precise experimental results known to date for the reaction ^{4}He$(e, e'p)$T, which were reported in [2, 3], present considerable difficulties not only for a global analysis of these data but also for an analysis of data from each individual study. These difficulties can be summarized as follows.

Upon the elimination of known dependences, the results of an investigation of $(e, e'p)$ reactions within the plane-wave impulse approximation (PWIA), which underlies the simplest approach, yield the momentum distribution of intranuclear nucleons. It is usually assumed that the momentum of the nucleon on which the incident electron was scattered is equal to the recoil momentum p_m of the residual nuclear system. However, the results reported in [2, 3] revealed that, within this approach, it is impossible, not only in the plane-wave impulse approximation but also upon the inclusion of final-state interaction, to match data measured under different kinematical conditions in such a way as to obtain a smooth dependence (see below for details).

The obvious dependence of the result on kinematical conditions casts some doubt on whether the plane-wave impulse approximation is applicable and on whether these results can in principle furnish information about the momentum distribution of intranuclear nucleons. At the same time, the measurements lead to momentum distributions that are by and large close to the calculated ones, thereby lending support to the plane-wave impulse approximation. Moreover, the simplicity and the physical clarity of the approach based on the plane-wave impulse approximation and the possibility of directly comparing the experimental momentum density with the results of theoretical calculations employing this approach furnish a sufficient motivation for adhering to the ideas underlying the plane-wave impulse approximation. The desire to preserve the plane-wave impulse approximation calls for clarifying the nature of the observed dependence of data on kinematics and finding, if this is possible, a means for eliminating this dependence. Although much time has passed since the appearance of data from [2, 3], the problem in question is still pressing.

That some correction may be necessary is suggested by the results presented in [4, 5], where, by studying inclusive (e, e') reactions, it was shown that the shift of the quasielastic-peak maximum can be kinematically corrected by changing the effective momentum transfer from the electron to the nucleon. On this basis, it is proposed below to normalize the

---

[*] e-mail: `svod_2000@rambler.ru`

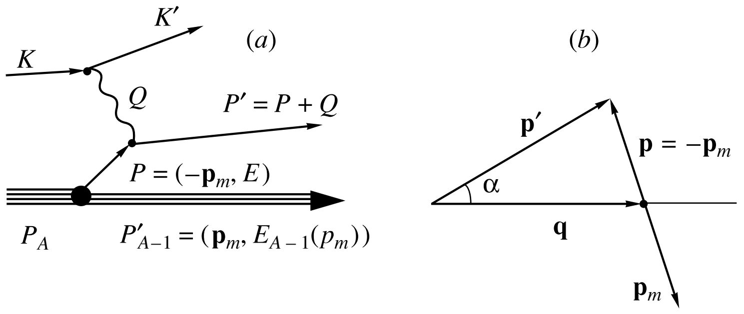

Fig. 1. (*a*) Simplest diagram describing quasielastic electron scattering and (*b*) corresponding diagram of 3-momenta.

situation by somewhat redefining the intranuclear-nucleon momentum, which, in general, proves to be different from p_m. Concurrently, this would also be a check upon the conclusions drawn in [4, 5].

1. In $(e, e'p)$ reactions, an electron of 4-momentum $K = (\mathbf{k}, k)$ is scattered by a nucleus of mass M_A into a final state with a 4-momentum $K' = (\mathbf{k}', k')$ at an angle θ in the solid-angle element $d^2\Omega_e$ and is detected in coincidence with a proton (its mass is denoted by M) knocked out from the nucleus into the solid-angle element $d^2\Omega_p$, the 4-momentum of the knocked-out proton being $P' = (\mathbf{p}', E') = P + Q$, where $P = (\mathbf{p}, E)$ and $Q = (\mathbf{q}, \omega)$ are, respectively, the 4-momentum of the intranuclear nucleon involved and the 4-momentum transfer from the electron. If the process being considered is quasielastic—that is, if the plane-wave impulse approximation is applicable to this process—it can be described in the first approximation by the diagram in Fig. 1*a*. Under the kinematical conditions corresponding to the experiments that yielded data analyzed here, this diagram is dominant [2, 3]. The cross section for the process in question is given by

$$\frac{d^6\sigma}{dk'd^2\Omega_e dT'_p d^2\Omega_p} = p'E'\sigma_{ep}(k, k', \theta) \times S(E_m, p)\delta(-E_m - \omega + T'_p + T_R), \quad (1)$$

where $\sigma_{ep}(k, k', \theta)$ is the cross section for elastic electron—proton scattering (hereafter, we set $k = |\mathbf{k}|$, $k' = |\mathbf{k}'|$, $p = |\mathbf{p}|$, etc.) and $S(E_m, p)$ is the spectral function for the primary nucleus. This spectral function depends on the following arguments: T'_p, which is the kinetic energy of the knock-on nucleon; E_m, which is the energy of nucleon separation from the nucleus with the formation of the residual nuclear system of mass M_{A-1},

$$E_m = M + M_{A-1} - M_A; \quad (2)$$

p, which is the absolute value of the intranuclear-nucleon momentum; and T_R, which is the kinetic energy of the above nuclear residue. As a matter of fact, the above spectral function is the form factor for the vertex where the primary nucleus dissociates into a proton and the residual nuclear system (see Fig. 1*a*). In the impulse approximation, $S(E_m, p)$ is the momentum distribution of intranuclear nucleons in the system formed by a nucleon and the nuclear residue, the relevant binding energy being $-E_m$.

In the particular case of proton knockout from a ^{4}He nucleus, the only existing state of the residual nuclear system is that of the tritium nucleus, the nucleon-separation energy being $E_m = 19.8$ MeV.

The kinematics of the process is determined by the law of energy—momentum conservation; that is,

$$\omega + M_A = E' + E_{A-1} = \sqrt{(\mathbf{p}')^2 + M^2} + \sqrt{\mathbf{p}_m^2 + M_{A-1}^2}, \quad (3)$$

$$\mathbf{p}' = \mathbf{q} - \mathbf{p}_m, \quad (4)$$

where $\mathbf{q} = \mathbf{k} - \mathbf{k}'$ and $\omega = k - k'$ are, respectively, the 3-momentum transfer and the energy transfer from the electron; $\mathbf{p}'$ is the 3-momentum of the knock-on nucleon; and $\mathbf{p}_m$ is the 3-momentum of the residual nucleus. Since there are only two particles in the final state, Eqs. (3) and (4) make it possible to reconstruct the missing momentum $\mathbf{p}_m$ of the undetected particle, provided that ω, $\mathbf{q}$, and $\mathbf{p}'$ are preset.

In order to define completely the kinematical conditions and to be able to specify the intranuclear-nucleon momentum in $S(E_m, p)$, the following natural assumption is usually made. As is well known, events of nucleon interaction are quite rare, whence it follows that intranuclear nucleons can be treated as (quasi)free particles for most of the time—an argument in support of this is that the applications of the nuclear model of independent particles were more or less successful. As a matter of fact, it is the quasifree character of intranuclear-nucleon motion that validates the plane-wave impulse approximation for the case being considered. Similarly, it is believed that the knock-on nucleon also has virtually no time to

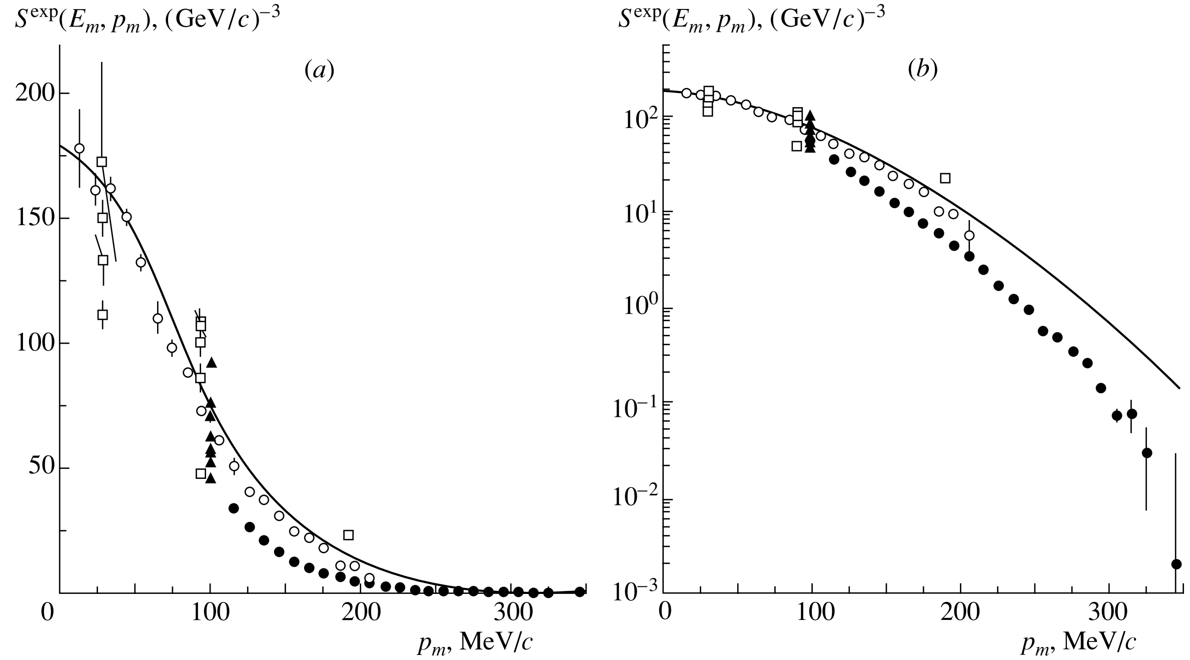

Fig. 2. Spectral function $S^{\mathrm{exp}}(E_m, p_m)$ for the ^{4}He nucleus under the kinematical conditions I, II, and A–H [2] (see Appendix, Tables 1–3) for $p_m = 15$–205, 115–345, and 100 MeV/c, respectively, and for $p_m = 30$, 90, and 190 MeV/c [3] (see Appendix, Table 4). The curves represent the results of the theoretical calculations for a model employing the Urbana V14NN potential [6]. The results are presented on (a) a linear and (b) a logarithmic scale along the ordinate. The points correspond to (open circles) kinematics I [2], (closed circles) kinematics II [2], (closed triangles) kinematics A–H [2], and (open boxes) the results calculated with the data taken from [3].

undergo interaction with the nuclear residue. Therefore, one can assume that, with a high probability, the nuclear residue, which is a spectator, does not change momentum. From the fact that the primary nucleus is at rest in the laboratory frame, we then immediately obtain (see Fig. 1b)

$$\mathbf{p} = -\mathbf{p}_m. \tag{5}$$

Taking into account relation (5) and performing in (1) integration with respect to T'_p, we arrive at

$$\frac{d^5\sigma}{dk' \cdot d^2\Omega_e \cdot d^2\Omega_p} \tag{6}$$
$$= p'E' \frac{\partial T'_p}{\partial E_m} \sigma_{ep}(k, k', \theta) S(E_m, p_m).$$

Equality (6) is a basis for extracting, within the above assumptions, the spectral function $S(E_m, p_m)$ from experimental data.

2. Let us now proceed to consider relevant experimental data (see Fig. 2). The values of the spectral function $S^{\mathrm{expt}}(E_m, p_m)$ for the ^{4}He nucleus that were measured under various kinematical conditions are displayed in Fig. 2 versus the missing momentum p_m. The data reported in [2] (see Table 2 in [2]) that were measured at values of the parameter p_m in the ranges $15 \le p_m \le 205$ and $115 \le p_m \le 345$ MeV/c are shown by, respectively, open (kinematics I, $q = 431$ MeV/c) and closed (kinematics II, $q = 250$ MeV/c) circles, whereas the data measured at the fixed value of $p_m = 100$ MeV/c (kinematics A–H; see Table 4 in [2]) are represented by closed triangles. The values of $S^{\mathrm{exp}}(E_m, p_m)$ that were calculated on the basis of data presented in [3] and measured at three values of $p_m = 30$, 90, and 190 MeV/c are shown by open boxes. The values of p_m at each experimental point are given in Tables 1–4 (see Appendix). The values of $S^{\mathrm{expt}}(E_m, p_m)$ that were extracted from the data of Ducret *et al.* [3] and which are presented in the graph are explained in the notes to Table 4 in the Appendix.

The curve in Fig. 2 represents the single-particle momentum distribution of nucleons that was calculated for the proton–tritium system bound into a ^{4}He nucleus. This calculation was performed on the basis of a model employing the Urbana V14NN potential [6]. In order to be able to consider the data both at low and at high values of p_m, they are shown on (Fig. 2a) a linear and (Fig. 2b) a logarithmic scale along the ordinate.

From Fig. 2, it can be seen that, by and large, the model calculation of the momentum distribution of intranuclear nucleons in the ^{4}He nucleus reproduces fairly well the experimental data quoted. At the same

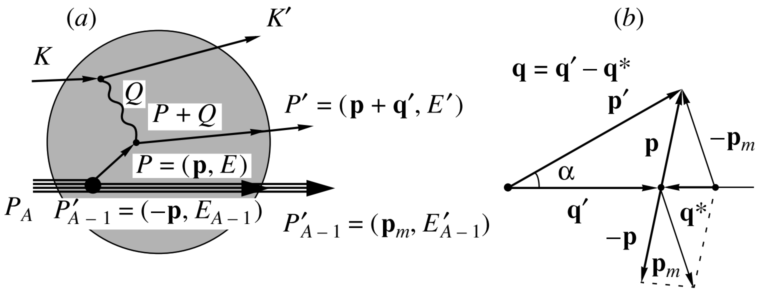

Fig. 3. (a) Diagram representing $(e, e'p)$ reactions with allowance for the fact that the absorption of a virtual photon by a nucleon occurs within the nucleus and (b) corresponding diagram of 3-momenta.

time, there are significant discrepancies—namely, the points obtained at the constant 3-momentum-transfer values of $q = 250$ and 431 MeV/c describe two smooth branches of the dependence $S^{\rm expt}(E_m, p_m)$ that do not coincide in the region of their overlap ($115 \leq p_m \leq 205$ MeV/c), where the mean value of their ratio is $r = 1.7 \pm 0.1$, with the mean relative error of measurements being about 0.2 [2]. In just the same way, points that were obtained at constant values of p_m and must in principle yield the close values of $S^{\rm expt}(E_m, p_m)$ at each value of p_m show a significant scatter that exceeds considerably the errors of the measurements. In particular, for each series of $p_m = 30$, 90, and 100 MeV/c, the ratios of the maximum values to the minimum ones are $r = 1.5$ at $p_m = 30$ MeV/c, with the maximum relative error being 0.2, and $r = 1.7$ at $p_m = 90$ and 100 MeV/c, with the maximum relative errors being 0.25 and 0.02, respectively.

Attempts of the authors of [2] at explaining this irregular behavior of experimental data by final-state interaction—in particular, by the distortion of the waves involved—did not result in matching the data. A unified dependence $S^{\rm expt}(E_m, p_m)$ could not be obtained, nor did it prove possible to describe both branches within a single approach even for kinematical conditions I and II exclusively [2]. On this basis, the authors of [2] argued that the values of $S^{\rm expt}$ depend on the kinematical conditions under which these values were obtained.

Thus, the observed behavior of experimental points is at odds either with the impulse approximation as such, within which expressions (1) and (6) for the reaction cross section were obtained, or with its part that states that the intranuclear-nucleon momentum is equal to the recoil momentum p_m of the $A - 1$ residual nucleus. But it has already been said in connection with Fig. 2 that there is fairly good overall agreement in absolute value between the experimental momentum distribution and the results of the theoretical calculation. Moreover, it is well known that $A(e, e')$ reactions, which are of the same nature, can be satisfactorily described within the plane-wave impulse approximation, apart from a modest shift of the maximum of the calculated quasielastic peak with respect to its experimental position.

The aforesaid gives sufficient grounds to hope that the impulse approximation can be kept, which would be highly desirable, as was indicated above. But in this case, the correctness of the statement specified by Eq. (5) should be questioned, and there is indeed some motivation for this.

Let us consider this point in some detail. Although the argument that has led to Eq. (5) seems natural, neither this argument nor Eq. (5) itself takes into account the fact that the nucleons constituting the nucleus are off the mass shell in the initial state. If, for example, we consider the reaction ^{4}He$(e, e'p)$T, proton knockout must result in that both particles (the proton and the triton) simultaneously go over to the mass shell. But in the above argument, it is assumed that a virtual photon is entirely absorbed by the proton, in which case only the proton can go over to the mass shell upon the energy transfer ω from the electron, with the triton state remaining completely unaffected by this. Since the free-triton mass appears in Eq. (3), it is assumed that the triton is already on the mass shell. But this assumption is difficult to validate, and it is desirable to dispense with it.

In other words, we arrive at the conclusion that a transition of final particles to the mass shell must inevitably proceed through their interaction. In the diagram in Fig. 3a, the aforesaid is represented as virtual-photon absorption by a nucleon within the nucleus, which is depicted by convention as a shaded circle. It is obvious that, at this stage, the process has the same character as that represented by the diagram in Fig. 1a. To state this otherwise, the electrodynamics of the process essentially remains the same, whence it follows that no changes are required in expressions (1) and (6). Upon the escape of the proton from the nucleus, both the proton and the nuclear residue become free, so that their kinematical

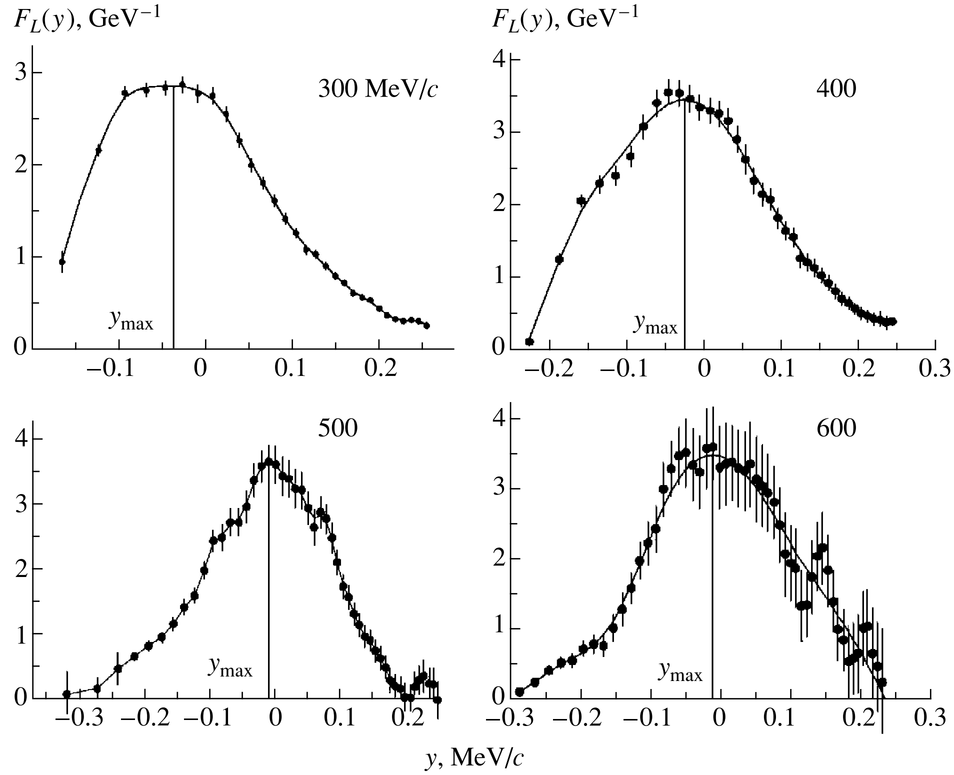

Fig. 4. Values of the scaling function $F_L(y)$ at $q = 300$, 400, 500, and 600 MeV/c [7] (for the definition of $y_{\max}$ values, see main body of the text).

features obey Eqs. (3) and (4). Within this pattern, the escape of the proton from the nucleus can be accompanied by a process where the 3-momentum transfer $\mathbf{q}$ is redistributed among the final particles, in just the same way as the redistribution of the energy transfer ω accompanies the transition of particles to the mass shell. As a result, the proton acquires the momentum

$$\mathbf{p}' = \mathbf{p} + \mathbf{q}', \tag{7}$$

where

$$\mathbf{q}' = \mathbf{q} + \mathbf{q}^*, \tag{8}$$

while the nuclear residue acquires the momentum

$$\mathbf{p}_m = -(\mathbf{p} + \mathbf{q}^*). \tag{9}$$

The above is illustrated by the diagram in Fig. 3b. As can be seen, the transformations in (7)–(9) do not disturb the momentum-conservation law (4).

Thus, the kinematics of the process would be completely specified if the momentum $\mathbf{q}^*$ that the particles escaping from the nucleus (that is going over to the mass shell) exchange were known.

Here, we do not aim at theoretically calculating $\mathbf{q}^*$. In order to solve the problem that we address, it is sufficient to obtain an experimentally justified estimate of $\mathbf{q}^*$ and to assess the effect that it exerts on the situation being considered.

It should be noted that a similar renormalization of the momentum transfer was previously performed in treating elastic electron scattering on nuclei in the one-photon approximation, in which case it is sometimes necessary to introduce the so-called Coulomb correction stemming from the fact that the effective energy of the initial (final) electron proves to be $k_{\text{eff}} = k - V_{\text{C}}$ ($k'_{\text{eff}} = k' = V_{\text{C}}$), where V_{C} is the Coulomb potential of the nucleus involved. As a result, the momentum transfer $\mathbf{q}$ undergoes a renormalization; that is, $\mathbf{q} \rightarrow \mathbf{q}_{\text{eff}} = \mathbf{k}_{\text{eff}} - \mathbf{k}'_{\text{eff}} = \mathbf{q} - V_{\text{C}}(\mathbf{k}/k - \mathbf{k}'/k')$. Such a renormalization was applied, for example by Zghiche *et al.* [7], who studied quasielastic electron scattering on a ^{208}Pb nucleus [below, we will discuss the study of those authors in connection with the analysis that they performed for the reaction ^{4}He(e, e')].

In the case considered here, the renormalization of $\mathbf{q}$ arises because of the unspecified interaction between the knock-on nucleon and the nuclear residue. This interaction cannot be specified in detail.

3. Let us now proceed to consider inclusive (e, e') reactions [which are of the same nature as $(e, e'p)$ reactions]. Their cross section is equal to the integral

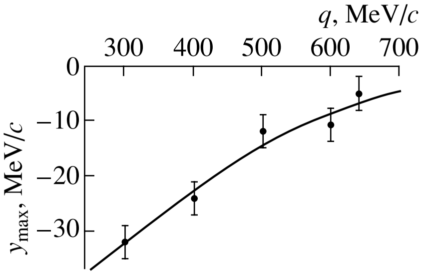

Fig. 5. Estimate of the experimental dependence $y_{\max}(q)$ on the basis of the results obtained from an analysis of y scaling for the ^{4}He nucleus [7].

of the cross section (1) over all knock-on nucleons; that is,

$$\frac{d^3\sigma}{dk'd^2\Omega_e} = N(k,k',\theta)(z\sigma_{ep} + (A-z)\sigma_{en})F(y), \quad (10)$$

where z and $(A-z)$ are, respectively, the number of protons and the number of neutrons in the nucleus; $\sigma_{ep(n)}$ is the cross section for elastic electron scattering on a proton (neutron); N is a known kinematical factor (we do not describe in detail this known function); and $F(y)$ is a scaling function that is symmetric with respect to the value of $y = 0$. Its specific form is

$$F(y) = \int\limits_{|y|}^{\infty} \rho(p)pdp, \quad (11)$$

where $\rho(p)$ is the momentum distribution of nucleons, its role in (1) and (6) being played by $S(E_m, p)$. Since $\rho(p) \geq 0$ by definition, it is obvious from (11) that $F(y)$ has a maximum at $y = 0$.

The parameter $y = p' - q$ is the $\mathbf{q}$ projection of the minimum momentum $\mathbf{p}_{\min}$ of the nucleon with which an electron can interact. Since $\mathbf{p}_{\min}$ is collinear to $\mathbf{q}$ (at given p' and q, the minimal value of $\mathbf{p}$ is achieved when $\mathbf{p}'$ and $\mathbf{q}$ are parallel), then $p_{\min} = |y|$, whereas the parameter y itself can take either positive or negative values, depending on whether the vectors $\mathbf{p}_{\min}$ and $\mathbf{q}$ are parallel ($y > 0$; that is, $p' - q > 0$) or antiparallel ($y < 0$; that is, $p' - q < 0$). The parameter y obeys the equation

$$\omega + M_A = \sqrt{(q+y)^2 + M^2} + \sqrt{y^2 + M_{A-1}^2}, \quad (12)$$

which reflects the energy-conservation law at the lower limit of integration in (11).

Since $\sigma_{ep(n)}$ and $N(k, k', \theta)$ are slowly varying functions of ω at fixed values of the scattering angle and the initial electron energy, it follows from (10) that the maximum of the cross section at the quasielastic peak must be attained at $y(q, \omega_{\max}) = 0$. At the same time, it is well known that, at the maximum of the experimental quasielastic peak (that is, at $\omega = \omega_{\max}$), y often takes negative values $y_{\max}$. In particular, such a situation was observed in studying the inclusive reactions of quasielastic electron scattering on ^{4}He and ^{12}C nuclei [4, 5]. The observed shift of the maximum of the quasielastic peak to the region of negative values of y could not be due (at least in the case of ^{4}He) to the opening of a competing channel since the two-body disintegration of ^{4}He into a proton and a triton (or into a neutron and ^{3}He) proceeds with a separation energy E_m (= 20 MeV/c) below which there are no open channels.

The data of Zghiche *et al.* [7], who studied electron scattering in the inclusive (e, e') reaction on a ^{4}He nucleus in the quasielastic region (see Fig. 4), also exhibit indications of the shift of the maximum of $F_L(y)$ to the region $y < 0$. For four values of the momentum transfer, Fig. 4 shows the values of $F_L(y)$ that were obtained for the ^{4}He nucleus by means of separating down experimental cross sections of the form (10) into the longitudinal and the transverse component. For individual graphs, the positions of the maxima are shown by vertical lines. From the graphs, it can be seen that negative values of $y_{\max}$ correspond to all of the measured distributions $F_L(y)$.

In order to restore a correct position of $F(y)$, we can proceed as follows. Redefining y as

$$y \to y_{\max} + y, \quad (13)$$

where $y_{\max}$ is found, for example, from experimental data, we can recast Eq. (12) into the form

$$\omega + M_A = \sqrt{(q'+y)^2 + M^2} + \sqrt{(y - y_{\max})^2 + M_{A-1}^2}. \quad (14)$$

It is clear that, upon this substitution, the value of $y = 0$—that is, the maximum of $F(y)$—will correspond to the maximum of the cross section (maximum of the quasielastic peak) at $\omega = \omega_{\max}$. The notation $q' = q + y_{\max}$ is used in Eq. (14). In the last equality, q' can formally be treated as the effective momentum transfer to the nucleon whose final momentum is p'.

The substitution in (13) and the values of $y_{\max}$ that were found experimentally from the spectra measured for $q > 400$ MeV/c were used to determine the experimental scaling functions for the ^{4}He [4] and ^{12}C [5] nuclei. By moving in the opposite direction and by using Eq. (10) and the single function $F^{\text{expt}}(y)$ for each nucleus, all of the spectra measured for each of these nuclei were reconstructed to a high precision in those studies. A successful description of the experimental spectra of electrons scattered quasielastically by ^{4}He

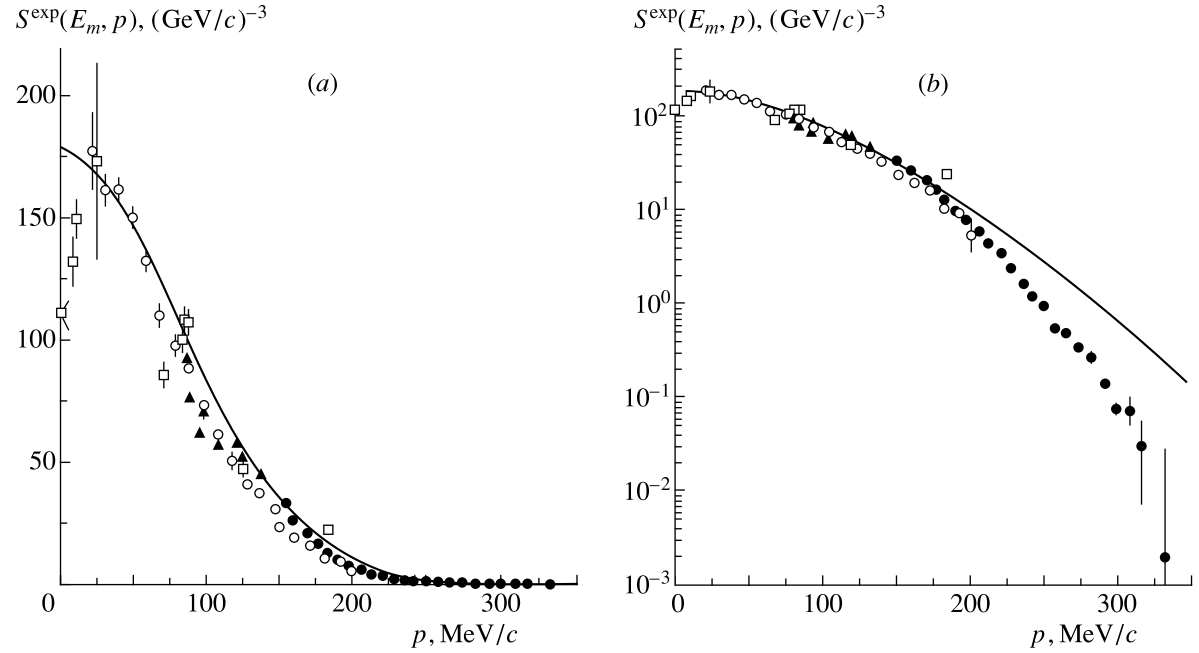

Fig. 6. As in Fig. 2, but versus the nucleon momentum p corrected by modifying the momentum transfer.

and ^{12}C gave sufficient grounds to conclude that the formally admissible combination $q' = q + y_{\max}$ has a physical meaning and can be interpreted as the actual change of $y_{\max}$ in the momentum transfer from the electron to the nucleon upon the escape of the latter from the nucleus. In a vector form, this statement can be formulated as follows:

$$\mathbf{q}' = \mathbf{q} + y_{\max}\mathbf{q}/q. \qquad (15)$$

Comparing (15) with (8), we can see that the second term on the right-hand side of Eq. (15) is analogous to the addition $\mathbf{q}^*$ in (8); that is,

$$\mathbf{q}^* = y_{\max}\mathbf{q}/q. \qquad (16)$$

In generalizing this result to $(e, e'p)$ reactions, it is natural to assume that relations (15) and (16) are valid in the case of the knockout of nucleons from a nucleus that have an arbitrary momentum $\mathbf{p}$ greater than or equal to the minimal one ($p \geq p_{\min}$). Since the correction $\mathbf{q}^*$ essentially depends only on the quantity $y_{\max}$, whose values can be found at least from experimental data, it is clear that the problem at hand has become solvable. Thus, we can see that, in interpreting data on $(e, e'p)$ reactions according to relations (7)–(9), there arises the possibility of determining, on the basis of the behavior of the maximum of the quasielastic peak in (e, e') reactions, the kinematical correction $\mathbf{q}^*$, with which one will probably be able to reconstruct the nucleon momentum $\mathbf{p}$ within the nucleus.

The experimental values of $y_{\max}$ that were determined on the basis of data reported in [7] are displayed in Fig. 5. They describe the smooth dependence of $y_{\max}$ on q and agree fairly well with the results presented in [4], where it is shown, to a precision achieved there (in [4]), that the values of $y_{\max}$ can be treated as those that depend only on the momentum transfer q. The approximating curve (solid curve in Fig. 5) enables one to assess $y_{\max}(q)$ over the entire range of momentum transfers at which the measurements in [2, 3] were performed.

4. We have formulated above the approach to quasielastic-scattering kinematics on the basis of Eqs. (7)–(9) for $A(e, e'p)(A-1)$ exclusive reactions and on the basis of Eq. (15) for $A(e, e')$ inclusive reactions. A crucial further step is to identify the equalities in (8) and (15), according to which the quantity $\mathbf{q}^* = y_{\max}\mathbf{q}/q$ (16) is just the momentum that the particles flying apart in the two reactions upon the breaking of the bond between them (that is, at the transition to the mass shell) exchange. The point is that the momentum $\mathbf{q}'$ in (15) carried away by a nucleon in (e, e') reactions can be treated, by virtue of the cylindrical symmetry of the process with respect to $\mathbf{q}$, as an effective one in the sense that it is averaged over the azimuthal angle. But in $(e, e'p)$ reactions, there is no such averaging since the reaction plane is fixed by the experimental conditions. Thus, it follows from the presumed identity of equalities (8) and (15) that only the disturbing momentum $\mathbf{q}$ is redistributed between the reaction products. This is a strong statement that requires a test, at least an experimental one.

Here, we would like to emphasize yet another point. Since, in the diagrams in Figs. 1a and 3a, the part that contains the vertex where the nucleus dissociates into a nucleon and a nuclear residue coincides with the part that contains the vertex where photon absorption occurs, it is natural to assume that the reaction cross sections in the two approaches corresponding to the two diagrams must coincide. This assumption is supported by the fact that (see above) the experimental cross sections for inclusive (e,e') reactions are accurately described (apart from a modest shift in y) in the plane-wave approximation. In other words, the redistribution of the momentum transfer $\mathbf{q}$ from the electron in $A(e,e'p)(A-1)$ and $A(e,e')$ reactions is not accompanied by changes in the cross section.

Leaving aside the possible mechanisms of the redistribution of the disturbing momentum $\mathbf{q}$ among the reaction products, we only state that the diagram in Fig. 3a represents schematically precisely this situation.

In this case, the distinction between the approaches is entirely concentrated in the difference of the kinematical parameters. In other words, the graph of the experimental dependence $S^{\rm expt}(E_m,\ p=p_m)$ in Fig. 2 (where $p_m=|\mathbf{p}'-\mathbf{q}|$) must be recast into the form of the dependence on the corrected nucleon momentum $p=|\mathbf{p}'-\mathbf{q}'|$, where $\mathbf{q}'$ is the modified momentum transfer (15).

The approach developed above makes it possible to calculate, according to (7) and (15), the corrected values of the intranuclear-proton momenta. It is assumed that these corrected values must correspond to the experimental points. Numerical values for this transition from the momentum p_m to the corrected proton momentum p are given in Tables 1–4 (see Appendix). The result of this transition is illustrated in Fig. 6, which displays the same points as in Fig. 2, but versus $p=|\mathbf{p}'-\mathbf{q}'|$. It can be seen that the situation improved considerably in relation to what occurs in Fig. 2. The two branches of experimental points for $q=250$ and 431 MeV/c [2] became matched together and now describe a smooth unified dependence $S^{\rm expt}(E_m,p)$. Almost all points measured at fixed p_m ($p_m=30, 90$, and 100 MeV/c [2, 3]) comply well with this curve; for some unknown reason, only one point at $p=185$ MeV/c ($p_m=190$ MeV/c [3]) does not fit in the observed dependence.

Thus, points that were measured over a wide region of kinematical conditions and that were obtained in different studies with different experimental facilities are matched with one another in such a way that they display a unified dependence $S(E_m,\ p)$ that is consistent, in the region $20<p<190$ MeV/c, with the theoretical prediction based on the single-particle momentum distribution of protons in the ^{4}He nucleus (needless to say, this distribution has suffered no changes, since it is independent of any assumptions made). Thereby, the hypotheses used as a basis in our calculations have been justified to a considerable extent.

Quite unexpectedly, the above modification of the method for extracting the intranuclear-nucleon momentum p from reaction kinematics revealed that the points obtained on the basis of data from [3] at $p_m=30$ MeV/c exhibit a trend toward the reduction of $S^{\rm expt}$ values for $p<30$ MeV/c. If we believe that the observed reduction is not a consequence of some experimental error (which is highly improbable in the opinion of the present author), it implies either a suppression of the cross section (e.g., as a result of the final state interaction) or the presence of a considerable number of nucleons with a nonzero orbital angular momentum in the ^{4}He nucleus. Either possibility calls for an additional investigation.

Summarizing the results of this study, we can say the following. On the basis of simple and experimentally justifiable assumptions, it has proven to be possible to develop a method for extracting, from the kinematics of $(e,e'p)$ reactions, a momentum that can be interpreted as the momentum of an intranuclear nucleon. As a result, there has appeared the possibility of matching, within a unified approach, data from experimental investigations of the momentum distribution of nucleons in the ^{4}He nucleus without resort to explaining individual groups of experimental points. Moreover, it has become clear that the effect of the final-state interaction on the reaction cross section is much weaker than it was assumed previously. It follows that, if we take into account the proposed correction, the plane-wave impulse approximation becomes quite applicable to describing $(e,e'p)$ reactions in the momentum-transfer region 250–600 MeV/c.

Our empirical result consisting in that the momentum transfer in $A(e,e'p)(A-1)$ and $A(e,e')$ reactions is redistributed when the bond between the reaction products is broken and in that this redistribution does not affect the reaction cross section is of fundamental importance for understanding and interpreting data obtained by studying the aforementioned and, possibly, other direct reactions that involve systems consisting of a few particles, where kinematical relations play an important role. At the same time, the mechanism behind the observed kinematical properties has yet to be clarified. Moreover, further experimental investigations into the region of intranuclear-nucleon momenta close to zero are required for disclosing the reasons for the observed reduction of the momentum density in this region.

Table 1. Kinematics I [2] ($q = 431$ MeV/c, $y_{\max} = -11$ MeV/c)

p'	p_m	α	p	p'	p_m	α	p
430	15	1.99	24	423	115	15.44	113
	25	3.33	31		125	16.80	122
	35	4.66	39		135	18.16	132
	45	5.99	48		145	19.52	142
	55	7.32	57		155	20.89	152
	65	8.66	66		165	22.25	161
427	65	8.67	65	417	155	20.98	151
	75	10.02	75		165	22.36	161
	85	11.36	84		175	23.75	170
	95	12.70	94		185	25.13	180
	105	14.05	104		195	26.52	190
	115	15.40	113		205	27.92	200

APPENDIX

Here, we are going to present the values of the kinematical parameters that are required for analyzing experimental data reported in [2, 3]. All these parameters are compiled in Tables 1–4. All of the quantities in the tables that have dimensions of momentum (q, p', p_m, $y_{\max}$, p) are expressed in MeV/c units, while the angle α between the vectors $\mathbf{q}$ and $\mathbf{p}'$ is given in degrees. The notation for the parameters is identical to that in the main body of the text: q is the 3-momentum transfer from the electron, p' is the recoil-proton momentum beyond the nucleus, p_m is the momentum of the residual nuclear system, and $y_{\max}$ is the $\mathbf{q}$ projection of the momentum $\mathbf{q}^*$ that the reaction products exchange in going over to the mass shell. The values of these parameters are used in calculating the final result—that is, the momentum p of the primary proton within the nucleus.

Table 2. Kinematics II [2] ($q = 250$ MeV/c, $y_{\max} = -37$ MeV/c)

p'	p_m	α	p	p'	p_m	α	p
382	115	0*	152	359	235	40.67	241
	125	0*	162		245	42.96	250
	135	5.25	171		255	45.26	258
	145	11.14	178		265	47.55	267
	155	15.11	185		275	49.84	275
	165	18.43	192		285	52.14	284
376	155	16.93	183	347	275	51.80	273
	165	20.01	190		285	54.12	281
	175	22.85	198		295	56.45	290
	185	25.52	205		305	58.80	299
	195	28.09	213		315	61.16	307
	205	30.58	221		325	63.55	316
368	195	29.66	211	334	315	63.38	305
	205	32.08	219		325	65.81	314
	215	34.47	227		345	70.76	332
	225	36.82	235				
	235	39.15	243				
	245	41.46	252				

Table 3. Kinematical parameters at constant $p_m = 100$ MeV/c [2]

Kinematics	q	p'	α	$y_{\max}$	p
A	416	313	0	−21	82
B	538	434	0	−11	93
C	262	361	2.63	−35	135
D	385	484	1.87	−24	124
E	400	308	6.40	−23	79
F	400	380	14.44	−23	95
G	400	442	12.39	−23	109
H	400	498	2.55	−23	123

From the outset, we note that, from Figs. 1*b* and 3*b*, we can see that, of all the parameters associated with the electron, only the momentum-transfer value is of importance for analyzing the kinematics that is of interest to us. Since the exact values of q, p', and α were not presented for each individual point in kinematics I and II [2], it is only possible in those cases to make use of the estimated values of q and p'. An analysis of this situation has revealed that all uncertainties associated with inaccurate knowledge of the input parameters q, p', and α can be compensated by calculating the angle α corresponding to the estimated values of q and p' and, additionally, the individual value of p_m. Within this procedure, the uncertainty in the extracted value of p proves to be commensurate with the error in determining $y_{\max}$, the estimated value of the latter being ±3 MeV/c.

As such, the method for calculating p is straightforward and is clear from Fig. 3*b*. First, the angle α between the vectors $\mathbf{q}$ and $\mathbf{p}'$ was calculated, where

Table 4. Collinear kinematics ($\alpha = 0$) [3]

Kinematics	q	p'	p_m	S^{exp}	y_{max}	p
1	299	269	30	111 ± 5.8	–30	0
2	380	350	30	133 ± 10.7	–22	8
3	421	391	30	150 ± 8.2	–19	11
4	650	620	30	173 ± 40.2	–6	24
5	299	389	90	47.3 ± 2.7	–30	120
6	380	290	90	85.5 ± 4.8	–22	68
7	544	454.6	90	100 ± 5.6	–10	80
8	572	482	90	108 ± 5.7	–9	81
9	650	560	90	107 ± 5.8	–6	84
10	680	490	190	22.4 ± 1.3	–5	185

this was possible (see explanations to Table 2), for each point on the basis of the estimated values of q and p' and the value of p_m, whereupon the quantity $q' = q + y_{\mathrm{max}}$ was found according to (15). After that, the quantity p was determined, at the resulting value of α, from the equality

$$p = |\mathbf{p}' - \mathbf{q}'|. \qquad \text{(A.1)}$$

In the case of collinear kinematics, where $\alpha = 0$, Eq. (A1) reduces to the following simplified equalities for determining p:

$$p = |p_m - y_{\mathrm{max}}| \quad (q < p'), \qquad \text{(A.2)}$$

and

$$p = |p_m + y_{\mathrm{max}}| \quad (q > p'). \qquad \text{(A.3)}$$

Table 1 gives kinematical parameters for the data from [2], which were measured in the orthogonal kinematics I at the momentum transfer of $q = 431$ MeV/c. According to the graph in Fig. 5, the value of $y_{\mathrm{max}} = -11$ MeV/c corresponds to this momentum transfer. In Table 1, the first, the second, the third, and the fourth column present, respectively, the estimated values of the recorded-proton momentum p', the values of the residual-nucleus momentum p_m from [2], the corresponding values of the angle α between the vectors **q** and **p**′, and the values of the nucleon momentum p in the ^{4}He nucleus.

From Table 1, it can be seen that, owing to the comparatively small value of $y_{\mathrm{max}} = -11$ MeV/c corresponding to $q = 431$ MeV/c and owing to the smallness of α, which corresponds to a nearly right angle between **q** and **p** (or $\mathbf{p}_m$), the values of p differ insignificantly from the values of p_m.

Table 2 corresponds to measurements in kinematics II [2] at the momentum transfer of $q = 250$ MeV/c and the value of $y_{\mathrm{max}} = -37$ MeV/c corresponding to it. The structure of Table 2 is identical to the structure of Table 1.

In what is concerned with the first two rows in Table 2 at $p' = 382$ MeV/c, the following comment is in order. The point is that, at the estimated values of $q = 250$ MeV/c and $p' = 382$ MeV/c and the above values of $p_m = 115$ and 125 MeV/c, the vector diagram of the momenta cannot be closed (for the reasons indicated above) at any value of α, since $p' > p_m + q$, the difference of the right-hand and the left-hand side of the inequality being 17 MeV/c at the first point. In this situation, α was set to zero (in Table 2, these values were labeled with an asterisk), and p was determined from Eq. (A.2), without using the values of q and p', which are not matched with p_m. From Fig. 6, it can be seen that this procedure did not lead to inconsistencies between the first two and the remaining points associated with kinematics II.

Since the measurements in kinematics II were performed at a sizably lower momentum transfer (accordingly, $y_{\mathrm{max}} = -37$ MeV/c), the distinctions between the values of p and p_m that are presented in Table 2 are more pronounced than in Table 1.

Data in Table 3 correspond to the measurements under the kinematical conditions A–H [2] at $p_m = 100$ MeV/c. The first, the second, and the third column of the table display, respectively, the notation for kinematics, the estimated values of the momentum transfer q, and the estimated value of the recorded-proton momentum p' [2]. The fourth, the fifth, and the six column give, respectively, the values of the angle α between the vectors **q** and **p**′, the values of y_{max} corresponding to q, and the values of the nucleon momentum p in the ^{4}He nucleus.

Table 4 presents the values of the kinematical parameters corresponding to the conditions of the measurements that were reported in [3] and which were performed in collinear kinematics ($\alpha = 0$). The labels of the kinematical conditions in the first column of this table correspond to the labels in Table 2 in [3], with the only exception of kinematics 10, which has label 11 in [3]. The parameters q, p', p_m, y_{max}, and p included in Table 4 (columns 2–4, 6, and 7) have already appeared in the preceding tables; therefore, they require no special comment.

In what is concerned with the fifth column in Table 4, it is worthwhile to note the following. In [3], the values of the spectral function were presented separately for the transverse and for the longitudinal component of the cross section (6) (S_L^{expt} and S_T^{expt}, respectively). If the values of S_L^{expt} (S_T^{expt}) are plotted on a graph like that in Fig. 2 or in Fig. 6, they will prove to be systematically underestimated (overestimated) in relation to the data from [2], which were obtained without a separation into the longitudinal and the transverse component. This is because the values of S_T^{expt} proved to be, for some reasons that have remained unknown to date, 30–40% greater (this is far beyond the corridor of the experimental errors) than the values of S_L^{expt}. By the way, a similar distinction was also observed between the longitudinal $[F_L(y)]$ and the transverse $[F_T(y)]$ scaling function measured in inclusive $A(e, e')$ reactions—in particular, in the reaction $^4\text{He}(e, e')$ [7]. In order to avoid this underestimation (overestimation) and to have the possibility of directly comparing the results from [3] with those from [2], it was decided that it would be advisable to take, from [3], the experimental cross sections of the form (6) that were measured at forward electron-scattering angles (see Table 3 in [3]) that were close to those at which the measurements were performed in [2] and to calculate, on the basis of these data, the unseparated values of the spectral function S^{expt}. The resulting values of S^{expt} in $(\text{GeV}/c)^{-3}$ units are given in the fifth column of Table 4. In extracting the values of the unseparated spectral function S^{expt} from the experimental cross sections according to Eq. (6), the cross section σ_{cc1} [8] for electron scattering on a nucleon occurring off the mass shell was taken for σ_{ep}, in just the same way as in [2, 3]. It is precisely these values of $S^{\text{expt}}(p)$ that were plotted in Figs. 2 and 6.

REFERENCES

1. S. Frullani and J. Mougey, Adv. Nucl. Phys. **14**, 1 (1984).
2. J. F. J. van den Brand, H. P. Blok, *et al.*, Nucl. Phys. A **534**, 637 (1991).
3. J. F. Ducret, M. Bernheim, *et al.*, Nucl. Phys. A **556**, 373 (1993).
4. S. V. Dementiĭ, Yad. Fiz. **48**, 609 (1988) [Sov. J. Nucl. Phys. **48**, 389 (1988)].
5. S. V. Dementiĭ, in *Proceedings of the VII Workshop "Electromagnetic Interactions of Nuclei at Low and Intermediate Energies," Moscow, 1988* (Inst. Yad. Issled. Akad. Nauk SSSR, Moscow, 1990), p. 5.
6. R. Shiavilla, V. R. Pandharipande, and R. B. Wiringa, Nucl. Phys. A **449**, 219 (1986).
7. A. Zghiche, J. F. Danel, *et al.,* Nucl. Phys. A **572**, 513 (1994).
8. T. De Forest, Nucl. Phys. A **392**, 232 (1983).

Translated by A. Isaakyan

Physics of Atomic Nuclei, Vol. 65, No. 7, 2002, pp. 1370–1372. Translated from Yadernaya Fizika, Vol. 65, No. 7, 2002, pp. 1403–1405.
Original Russian Text Copyright © 2002 by Okun.

On the Article of G. Gamow, D. Ivanenko, and L. Landau "World Constants and Limiting Transition"

L. B. Okun *

Institute of Theoretical and Experimental Physics,
Bol'shaya Cheremushkinskaya ul. 25, Moscow, 117218 Russia

Received November 19, 2001

Abstract—This brief preface explains why the editorial board of the journal *Yadernaya Fizika (Physics of Atomic Nuclei)* decided to reprint the article of the three authors, which was published in 1928 and which is hardly accessible to the present-day reader; tells briefly the history of its creation; and traces, from 1881 to 2001, the fate of the questions discussed in it and the impact of this article on modern fundamental physics. *© 2002 MAIK "Nauka/Interperiodica".*

On October 20, 1927, the article "World Constants and Limiting Transition" [1] of Georgii Antonovich Gamow (1904–1968), Dmitrii Dmitrievich Ivanenko (1904–1994), and Lev Davidovich Landau (1908–1968) was submitted to the journal *Zhurnal Russkogo Fiziko-Khimicheskogo Obshchestva pri Leningradskom Universitete: Chast' Fizika (Journal of the Russian Physicochemical Society at the Leningrad University: Section Physics)* (the table of contents of the journal also contained the German title of the article: "Über die Weltkonstanten und den Grenzübergang"). The article was written as a humorous present to a female student that the three young friends courted (shortly before Ivanenko passed away, I had asked him, in a telephone conversation, about the history of creation of the article; however, he could not, or he did not want to, recall the name of that student). In the following years, the paths of the authors parted, but none of them had ever referred to the article in question in his subsequent publications; nor was it included in the collection of Landau's works in two volumes [2]. The initials of Mr. Tompkins, a hero of some science fiction books written by Gamow, were the only trace that the world constants c, G, and h had left in the legacy of Gamow.

But the article, which the authors themselves considered as a trifle, contained quite serious ideas that had profound historical roots, ideas that had a strong impact on the development of fundamental physics and which have been hotly debated in the community of professional theoretical physicists to date.

George Johnston Stoney (1826–1911), a famous Irish physicist, who had been Secretary of the Irish Royal Society for many years, was the first to indicate the importance of world constants. He coined the term "electron," introduced it in physics, and measured the magnitude of the elementary electric charge e. By using this quantity and the known values of the speed of light c and of the gravitational constant G, Stoney proposed [3] natural units of length, time, and mass (that is, those that are given by nature itself):

$$l_{\rm S} = e\sqrt{G}/c^2, \quad t_{\rm S} = e\sqrt{G}/c^3, \text{ and}$$
$$m_{\rm S} = e/\sqrt{G}.$$

The expression for $m_{\rm S}$ was obtained by equating the Coulomb and the Newtonian potential:

$$\frac{e^2}{r} = G\frac{m_{\rm S}^2}{r}.$$

The expression for $l_{\rm S}$ was derived on the basis of dimensional considerations by equating the so-called "maximum kinetic energy" $m_{\rm S}c^2$ and the Coulomb energy $e^2/l_{\rm S}$. As to $t_{\rm S}$, it is obviously equal to $l_{\rm S}/c$. It is interesting to note that the expression for energy in the form mc^2 had appeared long before the advent of the theory of relativity (as a matter of fact, it was implicitly present in the discussion of black holes by Laplace [4]).

On discovering, in 1899, the constant h[1], Max Planck (later on, this constant was named after him) introduced [5] four natural world units for length, time, mass, and temperature. In the present-day notation, they are given by

$$l_{\rm P} = \hbar/(m_{\rm P}c), \quad t_{\rm P} = \hbar/(m_{\rm P}c^2), \quad m_{\rm P} = \sqrt{\hbar c/G},$$
$$T_{\rm P} = m_{\rm P}c^2/k.$$

---

*e-mail: `okun@heron.itep.ru`

[1] In the following, we will use $\hbar = h/2\pi$.

Here, k is the known Boltzmann constant,

$$k \simeq 8.6 \times 10^{-5}\ \mathrm{eV/K},$$

K being a Kelvin degree.

In all probability, Planck was unaware of Stoney's units, which, as can easily be verified, differ from Planck's units by a factor $\sqrt{\alpha}$, where $\alpha = e^2/(\hbar c) \simeq 1/137$. A. Eddington [6] was a steadfast partisan of Planck's units. On the contrary, P. Bridgman [7] deemed that these units have nothing to do with the physics of real world. A further development of physics has revealed that it was Eddington who was right.

In [1], the authors of the article return from Planck's units to the universal world constants c, G, and $\hbar$ and discuss the logical structure of a future theory in terms of these constants. The ideas of Gamow, Ivanenko, and Landau were adopted and developed in a number of studies by their friend Matvei Petrovich Bronshtein (1906–1938), who was executed during the years of Stalin's repressions. Bronshtein represented his classification of physical theories in a graphical form on a plane [8–10]. His graphical representation was similar to the development of a cube. For the first time, the spatial picture of such a cube was given by A. Zel'manov [11, 12] and was discussed by G. Gorelik [13] and by the present author [14].

If c (more precisely, $1/c$), $\hbar$, and G are plotted along three orthogonal axes, the vertices at (000), (c00), (0$\hbar$0), ($c\hbar$0), and (c0G) can be associated with, respectively, nonrelativistic mechanics, the special theory of relativity, nonrelativistic quantum mechanics, quantum field theory, and the general theory of relativity. The $c\hbar G$ vertex, which corresponds to relativistic quantum gravity, is of greatest interest. It is the realm that attracts the attention of those numerous theoretical physicists who try to construct the so-called theory of everything (TOE). They hope that, within such a theory, they would be able to develop a fundamental approach to superstrings and to calculate many fundamental parameters of the Standard Model (such as gauge coupling constants like α and ratios of the lepton and quark masses; see, for example, [15, 16]).

In recent years, Jurg Martin Frölich, a renowned German theoretical physicist, independently arrived at the idea of a cube. He put forth his consideration in the lecture that he delivered on the occasion of the investiture of him with the Max Planck medal [17]. In contrast to the aforementioned studies, Frölich supplements the cube of theories with the fourth dimension (for the Boltzmann constant k) and refers to the resulting construction as Planck's hypercube. It is the opinion of the present author that, in modern physics, the status of k differs drastically from the status of c, $\hbar$, or the Planck mass. According to statistical mechanics, temperature is the mean energy of an ensemble of particles. Therefore, k is the factor of rescaling from electronvolt or Joule units into Kelvin degrees. Needless to say, c, G, and $\hbar$ also play the role of scaling factors, but this role is of secondary importance for them. The main role of c is that it is the limiting velocity of signal propagation in a vacuum. When the velocity of a particle is close to c, its behavior is governed by the special theory of relativity. The role of the quantum $\hbar$ of action or angular momentum is that, when these quantities are close to $\hbar$, quantum mechanics comes into play. At an energy of order $m_{\mathrm{P}}c^2$, quantum relativistic effects in gravity become significant. As to k, there is no physical quantity of dimension k such for which k would be a critical value. Planck included k in the set of four fundamental constants since it appears in the ratio $\hbar\omega/kT$ on equal terms with $\hbar$ and since neither quantum mechanics nor the theory of relativity was known a century ago.

In conclusion, I would like to dwell upon yet another important point associated with the article by Gamow, Ivanenko, and Landau. The reader that has deeply thought over its content would have never agreed with the point of view according to which the international system of units SI [18–21] must serve as a basis for teaching physics (see critical comments on this system in [22–24]).

REFERENCES

1. G. Gamov, D. Ivanenko, and L. Landau, Zh. Russ. Fiz.-Khim. O-va., Chast Fiz. **60**, 13 (1928).
2. L. D. Landau, *Collection of Works* (Nauka, Moscow, 1969), Vols. 1, 2.
3. G. J. Stoney, Philos. Mag. J. Sci. **11**, 381 (1881).
4. P. S. Laplace, *Exposition du systeme du monde,* Ed. by J. B. M. Duprat (Paris, 1976), Vol. 2.
5. M. Planck, *Selected Works* (Nauka, Moscow, 1975), p. 232.
6. A. S. Eddington, Proc. Phys. Soc. London **30**, 91 (1918).
7. P. W. Bridgman, *Dimensional Analysis* (Yale Univ. Press, New Haven, 1931; Leningrad, 1934), Chap. 8, p. 105.
8. M. P. Bronshteĭn, in *Progress in Astronomical Sciences* (Gostekhizdat, Moscow, 1933), Vol. 3, pp. 3–30.
9. M. P. Bronshteĭn, *Basic Problems of Cosmic Physics* (ONTI, Kiev, 1934), pp. 186–218.
10. M. Bronshtein, Phys. Z. Sowjetunion **9**, 140 (1936).
11. A. Zel'manov, in *Development of Astronomy in USSR* (Nauka, Moscow, 1967), pp. 320–390.
12. A. Zel'manov, in *Infinity and Universe* (Mysl', Moscow, 1969), pp. 274–324.
13. G. E. Gorelik, *Space Dimension* (Mosk. Gos. Univ., Moscow, 1983), Chap. 5; JHEP **03**, 023 (2002).

14. L. B. Okun, Usp. Fiz. Nauk **161** (9), 177 (1991) [Sov. Phys. Usp. **34**, 818 (1991)].
15. S. Weinberg, Philos. Trans. R. Soc. London, Ser. A **310**, 249 (1983).
16. M. J. Duff, L. B. Okun, and G. Veneziano, physics/0110060.
17. J. Fröhlich, Phys. Bl. **57** (7/8), 53 (2001).
18. *International Union of Pure and Applied Physics. Commission for Symbols, Units and Nomenclature,* Document U.I.P. 20 (1978).
19. Review of Particle Properties, Phys. Rev. D **45** (Pt. II), III.4 (1992).
20. *Symbols, Units, and Nomenclature in Physics: Document U.I.P. 20* (International Union of Pure and Applied Physics, S.U.N. Commission, 1978); Usp. Fiz. Nauk **129**, 289 (1979) [Sov. Phys. Usp. **22**, 833 (1979)].
21. *The NIST Reference on Constants, Units, and Uncertainty,* http://physics.nist.gov/cuu/Units/international/html.
22. D. I. Sivukhin, Usp. Fiz. Nauk **129**, 335 (1979) [Sov. Phys. Usp. **22**, 834 (1979)].
23. M. A. Leontovich, Vestn. Akad. Nauk SSSR **6**, 123 (1964).
24. L. B. Okun, *Particle Physics* (Nauka, Moscow, 1988; Harwood, Chur, 1985), Suppl. 1, p. 141.

Translated by A. Isaakyan

Physics of Atomic Nuclei, Vol. 65, No. 7, 2002, pp. 1373–1375. Translated from Yadernaya Fizika, Vol. 65, No. 7, 2002, pp. 1406–1408.
Original Russian Text Copyright © 2002 by Gamow, Ivanenko, Landau.

KEY PROBLEMS IN FUNDAMENTAL PHYSICS

World Constants and Limiting Transition*

G. Gamow, D. Ivanenko, and L. Landau

§ 1. In constructing a system of units in physics, there exist two basic methods for choosing units of any new quantity:

(i) One merely specifies an arbitrary standard of measure (this is the way in which one introduces the usual definitions of, say, gram or ohm).

(ii) By employing some law—we denote it by A—that relates the quantity in question to those that are known and which involves a numerical coefficient, one chooses a satndard in such a way as to reduce this coefficient to unity (this is exemplified by the definition of a charge unit in terms of the Coulomb law).

Technical difficulties apart, one can always make use of either method of the above two.1) In the first case, we have a new arbitrary satndard; that is, we increase the number of units forming the basis of the theory of dimensions. Moreover, the coefficient in the law A then takes a specific numerical value that appears to be a new world constant.

In the second case, both the number of basic arbitrary standard and the number of world constants remain unchanged; for measuring the quantity in question, we only obtain a unit that is natural with respect to preceding ones. This unit will change in response to changes in basic standard. The character of this variation is studied within a dimensional analysis that introduces the concept of dimensions of a given physical quantity.

Constants of zero dimensions are independent of the choice of basis units and can therefore be treated as mathematical constants (numbers). One can hope that all these numerical constants can be obtained theoretically. Within a given system of dimensions, world constants from which one can compose a combination of zero dimension must therefore obey a mathematical relation, so that they are not independent.

From the aforesaid, it follows that we can always reduce the number of basic standard (number of dimensions) using one of the world constants for this and setting it to unity. Below, this process, which is equivalent to going over from the first definition to the second one, will be referred to as a reduction.

For a complete reduction (that is, a reduction to the number of standard that is equal to zero) to be possible, it is necessary that the number of independent constants not be less than the number of dimensions forming the basis of the system of units being considered. Obviously, the number of independent constants cannot be greater than the number of basic independent basic units in our system of dimensions.

For example, only the reduction to two units was possible in Newtonian mechanics, since, in the presence of three basic dimensions of T, L, and M, there was only one law featuring a world constant; that is,

$$f = \chi \frac{mm'}{r^2}.$$

A second constant, which enables a reduction to one dimension is introduced by the special theory of relativity via the relation

$$x_i = ict.$$

Finally, the last missing constant h appears in the framework of quantum mechanics:

$$\varphi = \frac{2\pi W}{h}$$

(this is the expression for the phase φ in terms of the action W).

Usually, we are dealing with the case where the number of constants known from experiments and not yet reduced to a smaller number by establishing mathematical relations is much greater than the adopted number of basic units. In this case, it is advisable to choose the most general constants for performing complete reduction.

The quartic system $CGS1°$ is employed in modern experimental physics. In technologies, however, practical considerations dictate the use of a much greater number of standards (cm, g, s, 1°, Ω, A, ...); there, one adopts some $CGS1°\Omega\ldots$ system.

Yet another example of choosing a basic system is provided by Planck's natural system of units (c, χ, h, k).

§ 2. We have seen above that each constant is a representative of a physical law (theory), a world

---

*Translated from the Journal of Russian Physicochemical Society, Ser. Phys., **LX**, 13 (1928).

1)Of course, this is so if there is a law that relates the new quantity being considered to some known previously.

1063-7788/02/6507-1373$22.00 © 2002 MAIK "Nauka/Interperiodica"

constant symbolizing the generality of a law. More universal constants correspond to more general laws (theories)—to illustrate, one can compare the Rydberg constant with the Planck constant $\hbar$. The introduction of new constants and their reduction to a smaller number were reflected in the history of physics as a changeover of theories and their gradual unification.[2] By way of example, we can indicate the introduction of the constant $\hbar$ and the reduction of the Rydberg constant. Fixing the number of dimensions as above, we thereby constrain the number of genuine constants: among the available constants, we take n ones (n is equal to the number of dimensions) for basic ones, reducing the remaining to genuine (that is, independent) ones. From the point of view of reduction, it obviously does not matter which constants are taken for basic ones. Here, however, we are guided by two heuristic principles. The first of these is that which is based on the degree of generality of the theory that these constants represent: it is natural to reduce the Rydberg constant to the Planck constant, but not vice versa, because the theory of atomic spectra is obviously of lower order with respect to the general theory of atoms. The other principle tests a constant for a limiting transition (see below). By way of example, we will trace the history of the constant h (that is, the development of the quantum theory from the point of view of the introduction of this constant). Classical mechanics and electrodynamics can be considered as an initial stage. Bohr's theory (old quantum mechanics) introduced h as an empirical constant in its equations, pursuing only ad hoc purposes: h symbolized discontinuity, jumps, etc. Only in Schrödinger–Heisenberg wave mechanics did h appear quite naturally as a constant associated with dimension. No requirements of discontinuity are introduced, and the empirical significance of h is clarified only a posteriori. We are inclined to deem the theory of the constant h completed. Imagine a completed (!) physics. We will construct it on the basis of n dimensions; there will obviously remain n world constants in it that appear in a natural way—that is, as mere dimensional rather than empirical coefficients. All extra constants will be reduced. As to the world constants in question, we can set them to unity according to the proposal of Planck, whereby we go over to physics without dimensions. Let us construct a physics system that is in a limiting relation to the above completed physics. To do this, we apply the limiting-transition method, making the world constant in question tend to zero (of course, such a constant must first be introduced if it was initially equal to unity). The theory obtained via this limiting transition will be referred to as a classical theory with respect to the world constant being considered. For example, conventional mechanics is classical with respect to h, while wave mechanics is completed in the above sense; as to Bohr's theory, with its h introduced in an ad hoc manner, it can be called a vulgar theory. In the same way, the theory of relativity is a completed theory with respect to $1/c$ ($1/c$ appears in the metric as a dimensional coefficient); for a limiting theory, we have here conventional mechanics, as in the preceding case, and nonrelativistic quantum mechanics. It should be emphasized that, for a genuinely basic constant in the sense of the limiting transition, we have here $1/c$ rather than c, since it is the former that is made to tend to zero. As to theories that are vulgar with respect to $1/c$, these include a number of prerelativistic formulations of electrodynamics. Further, geometric optics is a classical theory with respect to the constant of wavelength ($\lambda_0 \to 0$), while wave optics is a completed theory. From this point of view, the Fresnel theory of diffraction is a vulgar theory. On the basis of this method, we can construct new classical theories by introducing new constants and making them tend to zero. Such classical theories can be doubly, triply, etc., limiting ones (rank of a classical theory). For example, conventional mechanics is triply limiting—with respect to quantum theory, the special theory of relativity, and the theory of gravity (the corresponding constants are h, $1/c$, and χ). Since a combination of constants is also a constant, there arises the question of elementary constants.

We have seen that a normal course of the development of a theory was from a limiting through a vulgar to a completed one. Having constructed parallel schemes, we notice gaps—some theories skipped a "vulgar" period, while, in the history of others, there were no limiting case. Historically, we have the L, M, T system of dimensions (temperature apart) and, hence, three genuine world constants. According to the aforesaid, the choice of the three dimensions was accidental from the lofty point of view; as to the choice of "genuine" constants, we may heuristically follow the generality of theories and the limiting-transition principle. From both points of view, one is led to adopt h, $1/c$, and χ for "genuine" constants (all three of them represent the most advanced theories, and all three meet the limiting-transition test).

§ 3. If, following the aforesaid, we lay the basic constants h, $1/c$, and χ in the foundation of the theory of dimensions, we can obtain "natural units" for all other physical quantities, including mass and electric charge. The charge and mass units deduced in this way do not coincide with "elementary" values obtained for these quantities experimentally (the charges and masses of the electron and of the proton).

---

[2] In a sense, one can associate each new law with a new irreducible constant, introducing the corresponding new dimension.

However, this coincidence could hardly be expected because the mass of the electron differs from the mass of the proton—it would have been strange if one of them had proved to be a basic one.

The only thing that is natural to expect is that either of these masses will be expressed, in one way or another, in terms of the "natural unit" of mass. The origin of two mass values (m_+, m_-) may be that the equation from which they will be determined has two different roots corresponding to two charge values ($+e$, $-e$).

Not yet having the theory of the electron at our disposal, we may deduce, however, some conclusions about the character of this theory from a dimensional analysis. Let us find the dimensions of charge and mass in terms of our basic dimensions $[h]$, $[1/c]$, and $[\chi]$. After some simple algebra, we obtain

$$[e] = \sqrt{[h]\cdot[c]}; \quad [m] = \sqrt{\frac{[h]\cdot[c]}{[\chi]}}; \quad \left[\frac{e}{m}\right] = \sqrt{[\chi]}$$

or

$$e = \lambda\sqrt{h\cdot c}; \quad m = \nu\sqrt{\frac{hc}{\chi}},$$

where λ and ν are numerical constants that are different for the proton and for the electron. (It is obvious that $\lambda_- = -\lambda_+$.)

The above formulas for the dimensions may also furnish valuable guidelines in constructing the theory of the electron on the basis of an incomplete system of theoretical physics where some world constants are set to zero.

It can easily be seen that the only incomplete system leading to finite values of charge and mass is

$$\left\{h = 0; \quad \frac{1}{c} = 0; \quad \chi \neq 0\right\};$$

that is, this is a nonquantum, nonrelativistic, gravitating electron. In this case, the electron charge becomes a new world constant.

As to other incomplete systems, they lead to indefinitely small (or indefinitely large) charges or masses. In particular, frequent attempts at constructing a theory of a nonquantum electron in the general theory of relativity cannot be successful ($h = 0$, $c \neq \infty$, $\chi \neq 0$, whence it follows that $e = m = 0$).

Leningrad.
October 20, 1927

Translated by A. Isaakyan